

A MULTIDISCIPLINARY INVESTIGATION OF THE
FORMATION, GROWTH AND EVOLUTION OF
NEOARCHEAN CRUST, SNARE RIVER TERRANE:
SOUTHWESTERN SLAVE PROVINCE

VENESSA ROSE CHARLENE BENNETT

**A Multidisciplinary Investigation of the Formation, Growth and Evolution of Neoproterozoic
Crust, Snare River terrane: Southwestern Slave Province**

by

©Venessa Rose Charlene Bennett

A thesis submitted to the
School of Graduate Studies
In partial fulfillment of the
requirements for the degree of
Doctor of Philosophy

Department of Earth Sciences
Memorial University of Newfoundland
St John's, Newfoundland

Submitted: January, 2006

Defended: June 2006





“Admittedly, geoscience cannot flourish without the vitamins and drugs of tectonofanciful models, but the science receives its basic nourishment from the bread-and-butter observations of open-eyed field geologists, the foot-slogging infantry who spare no effort in describing and illustrating the capriciousness of Nature”.

Asger Berthelsen, Preface to “Precambrian Tectonics Illustrated”

Abstract

The hypothesis that Neoproterozoic crust (~ 3.0 – 2.5 Ga) is the expression of a global thermotectonic event that led to cratonization of crustal nuclei and the transition to a 'modern' style of plate tectonic processes is tested through a multidisciplinary study of the Snare River terrane, a ca. 2.67-2.56 Ga crustal fragment in the southwestern Slave Province. Integration of datasets defining the temporal, geochemical, architectural and thermal evolution reveals crust formation was initiated in an oceanic tectonic regime (TR1) and terminated with collision with an older Mesoproterozoic crustal fragment (TR2).

U-Pb zircon crystallization ages for thirteen intrusive units provide tight constraints on the timing of crust formation and orogenic evolution. Seven metaluminous plutons were emplaced over ca. 90 M.y. from ca. 2674-2589 Ma, whereas six peraluminous plutons were emplaced over ca. 15 M.y. from ca. 2598-2585 Ma. Collectively they define four stages of crustal development: (i) 2674-2635 Ma — proto-arc formation and early turbidite sedimentation; (ii) 2635-2608 Ma — juxtaposition of turbidites and proto-arc; (iii) 2608-2597 Ma — collision of proto-arc with Central Slave Basement Complex, crustal thickening, metamorphism and plutonism; and (iv) 2597-2586 Ma — orogenic collapse and mid-crustal exhumation.

Deformation histories of low- and high-grade domains illustrate younging of structural age with paleodepth and a progression from steep structures in the upper crust to gently-dipping structures in the mid crust due to diachronous polyphase deformation. A migmatitic transition zone is characterized by structural elements from both crustal levels. The proposed tectonic model involves: (i) protracted thin-skinned shortening (D1); (ii) crustal thickening by nappe tectonics and orogenic plutonism (D2); and (iii) post-orogenic collapse and mid-crustal exhumation (D3).

Geochemical and Nd isotopic data for magmatic units support initiation of crust formation by plume-related mafic magmatism, evolution to a protoarc by subcretion, and

establishment of subduction magmatism. Protoarc–continent collision heralded emplacement of sanukitoid, metaluminous and peraluminous suites, whereas only sanukitoid and peraluminous magmatism accompanied orogenic collapse. Mantle-melting events demarcate the four stages of crustal evolution, implying linkage between crustal and mantle tectonics, and a time-space analysis demonstrates that the oldest magmas occur in the upper crust and younger syn-orogenic magmas intruded at mid-crustal levels.

Ages of inherited zircon cores are used to isotopically profile Neoproterozoic crustal evolution. The datasets illustrate that metaluminous and peraluminous magmas were derived from discrete lower- and mid-crustal reservoirs at different times. Secular changes in inherited zircon in metaluminous magmas fingerprint lower crustal growth from both ‘local’ magmatic additions and intercalated ‘exotic’ material, and the absence of Neoproterozoic inherited cores in metaluminous magmas indicates crust formation was distal from the Central Slave Basement Complex. With respect to peraluminous magmas, the similarity between their inheritance profiles and detrital zircon spectra confirm metaturbidites as the source for peraluminous magmatism.

Zircon saturation thermometry is used to constrain the thermal contributions of magmas to the crustal heat budget, after refinement of the raw data using whole-rock geochemistry, BSE imaging and petrographic analysis. Results, confirmed by independent metamorphic data, reveal moderate-temperature magmatism during crustal growth, both low-temperature H₂O-rich and high-temperature H₂O-poor magmatism during the orogenic phase, and low-temperature magmatism in the post-orogenic stage. Low-temperature plutons emplaced into the upper crust did not significantly affect the existing thermal regime, whereas high-temperature plutons in the mid crust provided the principal heat source for metamorphism.

Recognition of mid- and upper-crustal levels separated by a transition zone has permitted reconstruction of a ‘crustal stratigraphy’ that exhibits: (i) depth-dependent magmatic growth, (ii) compositional zonation; (iii) secular magmatic evolution; (iv) metamorphic zonation, and (v)

diachronous polyphase deformation. Collectively, these results demonstrate intimate feedback between crustal levels and the interplay among magmatism, sedimentation, metamorphism and deformation in crustal evolution. Neoproterozoic crustal growth in the Snare Rive terrane was characterized by a prolonged period of lateral accretion in an oceanic realm (TR1), followed by rapid crustal thickening during accretion of the oceanic terranes to the Central Slave Basement Complex (TR2). Thus a primary control on the Neoproterozoic crustal evolution was the presence of a Mesoproterozoic nucleus around which cratonization occurred.

Acknowledgements

Many people have contributed their time, resources, advice and friendship throughout the course of my studies. I would like to express my sincerest gratitude to everyone who has helped me reach this goal. Firstly, I would like to thank my supervisors, Toby Rivers and Carolyn Relf, who placed their faith and confidence in me and helped steer the thesis in directions it would not have otherwise gone. Their support, engaging discussions and excitement concerning all components of the research were invaluable and provided me with the impetus to complete the thesis. Additionally, I would like to thank Carolyn and all the staff of the NWT Geoscience Office who made my time in Yellowknife enjoyable and stimulating. I am indebted to Valerie Jackson for integration into the Snare River mapping project and her support, friendship and willingness to forgive the misgivings of a crazy foreigner. My two field assistants, Darrell Hyde and Lara Lewis, made completion of the field studies memorable. Greg Dunning, Aphrodite Indares and Marc Wilson initiated my involvement in this project and provided advice and instruction during the early stages of the Ph.D. candidacy. I would particularly like to thank the former Dean of Graduate Studies, Dr. Greg Kealey, who made a concerted effort to assist my progress. Staff of Earth Sciences Department were central to the success of the analytical program, particularly Robbie Hicks, Pat Horan, Mike Tubrett, Helen Gillespie, Pam King and Rick Soper. The flexibility and friendship of Lisa Lee (Biology Department) allowed me to collect detailed grain images that subsequently proved crucial to the research. Sally Pehrsson is acknowledged for her interest and several enlightening discussions. Wouter Bleeker introduced me to the regional geology of the Slave Province during the first field season, provided advice, encouragement and generously made available a rocksaw that quickly became an indispensable sampling tool. Richard Flood is thanked for his input on various parts of the thesis and for always keeping tabs on my whereabouts and wellbeing. Ron Vernon is thanked for staying in touch whenever possible and reviewing Chapters 3 and 6. Special thanks to my office mates, Marisca Vanderkamp and Chris Buchanan, whose friendship and lively discussions made long hours in the Earth Sciences Department pass quickly and enjoyably. Elliot Burden provided a constant sympathetic ear, friendship and accommodation during one of my intermittent stays in the Province.

I could not have succeeded in this journey without the encouragement, support and love of my family and friends, particularly my mum and sister, Agnes Walsh, Richard Geeve, Evelyne Benais, Rondi Davies, Elizabeth Noseworthy and Ron Tobin. Fiona McLeod and Kim Smale welcomed me into their lives and home during my stay in Yellowknife. I will always be grateful for their love and faith in me. Kelly Emon is thanked for her friendship, advice, musical taste and for treating me to many sumptuous international feasts. Trevor and Nicole Machattie, Susan Pfister, Agnes Walsh, Evelyne Benais and Derek Weir provided me with a place to stay during my travels across the country. Finally, I am forever indebted to my loyalist, most unwavering support (especially at dinner time), who brings a smile to my face every single day. This work was supported by a Lithoprobe grant, an NSERC Discovery grant to Toby Rivers for field analytical and other costs, a Canadian Commonwealth Scholarship and graduate student bursaries from Memorial University of Newfoundland.

Table of Contents

Abstract.....	i
Acknowledgments.....	iv
List of Tables.....	x
List of Figures.....	xii
List of Appendices.....	xvii
Chapter 1: Prologue.....	1-2
1.1 Preamble.....	1-2
1.2 The Polarized World of Archean geology: Uniformitarianism versus secular change.....	1-3
1.2.1 Paleo- to Mesoarchean geology.....	1-6
1.2.2 Neoproterozoic geology.....	1-9
1.2.3 Summary.....	1-18
1.3 Crustal cross-sections: A four dimensional understanding of Archean crustal evolution.....	1-20
1.4 Geological setting of study area.....	1-26
1.4.1 Slave Province.....	1-26
1.4.2 Snare River terrane.....	1-28
1.5 Study objectives and thesis outline.....	1-34
1.5.1 Objectives.....	1-34
1.5.2 Thesis outline.....	1-36
1.5.3 Appendices.....	1-38
References	1-41
Chapter 2: Geology and U-Pb Geochronology of the Late Archean Snare River Terrane: Tracking Evolving Tectonic Regimes and Crustal Growth Mechanisms.....	2-2
2.1 Abstract.....	2-3
2.2 Introduction.....	2-4
2.3 Geological setting.....	2-5
2.4 Metamorphic gradients and relationship to the Lithoprobe SNORCLE transect.	2-8
2.5 Snare River terrane.....	2-9
2.5.1 Geology of the Snare River terrane.....	2-11
2.5.2 Tectonic history of the Snare River terrane.....	2-15
2.6 U-Pb geochronology.....	2-16
2.7 Analytical procedures.....	2-18
2.8 Results.....	2-25
2.8.1 Metaluminous intrusions.....	2-26
2.8.2 Peraluminous intrusions.	2-48
2.8.3 Detrital zircon study.....	2-64
2.9 Discussion.....	2-68

2.9.1 Temporal and spatial correlations: construction of orogenic stratigraphy	2-68
2.9.2 Duration of sedimentation.....	2-76
2.9.3 Regional provenance implications.....	2-77
2.9.4 Implications for the Lithoprobe SNORCLE transect.....	2-80
2.10 Conclusions.....	2-82
2.11 Acknowledgements.....	2-85
References.....	2-86

Chapter 3: Bridging the mid to upper crustal gap – Structural Correlations between late Archean low and high grade domains in the Snare River terrane, Slave Province, NWT, Canada.....

3.1 Abstract.....	3-3
3.2 Introduction.....	3-4
3.3 Geological setting.....	3-6
3.3.1 Exposed Crust Levels.....	3-8
3.3.2 Deformation and metamorphism.....	3-10
3.3.3 Timing of Metamorphism.....	3-15
3.4 Deformation history of the Snare River terrane.....	3-16
3.4.1 Labelling generations of folds and fabrics.....	3-20
3.4.2 Belt-scale structural elements.....	3-24
3.4.3 Deformation history.....	3-26
3.4.3.1 Upper Crust – Kwejinne Lake supracrustal belt..	3-30
3.4.3.2 Transition zone.....	3-41
3.4.3.3 Mid crust – Ghost subdomain.....	3-51
3.4.4 Correlations and crustal architecture.....	3-63
3.4.4.1 Structural correlations.....	3-63
3.4.4.2 Crustal Architecture.....	3-66
3.5 Interpretation and tectonic model.....	3-68
3.5.1 D0-D1 – Lateral Crustal Shortening.....	3-68
3.5.2 D2 – Nappe tectonics.....	3-74
3.5.3 D3 – Crustal Thinning.....	3-75
3.6 Discussion.....	3-79
3.6.1 Structural and metamorphic diachroneity.....	3-79
3.6.2 Migmatitic transition zone: Bridging the crustal gap.....	3-82
3.6.3 The paradox of steep low-grade and shallow high-grade structures.....	3-83
3.6.4 Crustal evolution and secular change in deformation mechanisms.....	3-86
3.6.5 Regional implications.....	3-87
3.7 Conclusions.....	3-91
References.....	3-96

Chapter 4: Formation, Growth and Evolution of Neoproterozoic crust: Geochemical and isotopic constraints from the Snare River terrane, Slave Province, Canada.....	4-2
4.1 Abstract.....	4-3
4.2 Introduction.....	4-4
4.3 Geological setting.....	4-5
4.3.1 Regional geological setting.....	4-5
4.3.2 Geological setting of the Snare River terrane.....	4-8
4.4 Magmatic groups of the Snare River terrane.....	4-11
4.5 Analytical techniques.....	4-12
4.6 Results.....	4-20
4.6.1. Group 1: 2674 –2654 Ma magmatism.....	4-20
4.6.2. Group 2: 2637 – 2608 Ma magmatism.....	4-35
4.6.3. Group 3: 2608 – 2597 Ma magmatism.....	4-39
4.6.4. Group 4: 2597 - 2585 Ma magmatism.....	4-46
4.6.5. Metaturbidites.....	4-53
4.7 Interpretation.....	4-53
4.7.1 Crust Formation: Metaluminous magmatism.....	4-54
4.7.1.1 2674 Ma tholeiites.....	4-54
4.7.1.2 2658 Ma tholeiites.....	4-57
4.7.1.3 Calc-alkaline basalt – basaltic andesite.....	4-58
4.7.1.4 Calc-alkaline intermediate - felsic magmas.....	4-58
4.7.1.5 ‘Depleted’ TTG suite.....	4-60
4.7.1.6 Synthesis: Crust formation ~ 2674-2654 Ma.....	4-62
4.7.2 Growth of the Snare protoarc.....	4-66
4.7.2.1 Disco intrusive suite.....	4-66
4.7.2.2 Mafic intrusive complexes.....	4-68
4.7.2.3 Synthesis: Magma diversification in response to maturation of protoarc.....	4-68
4.7.2.4 The Snare protoarc.....	4-70
4.7.3 Protoarc-Continent Collision – The Snare orogen.....	4-71
4.7.3.1 Group 3: Metaluminous magmas.....	4-71
4.7.3.2 Group 3: Peraluminous magmas.....	4-73
4.7.3.3 Synthesis - Collisional magmatism.....	4-75
4.7.4. Post-orogenic magmatism.....	4-79
4.7.4.1 Metaluminous magmatism.....	4-79
4.7.4.2 Peraluminous magmatism.....	4-80
4.7.4.3 Post-orogenic magmatism: summary model.....	4-81
4.8 Tectonic implications of magmatism.....	4-82
4.8.1 Pan-Slave implications.....	4-85
4.9 Conclusions.....	4-88
4.10 Acknowledgements.....	4-91
References.....	4-93

Chapter 5: Fingerprinting lower crustal evolution: Integrating inherited zircon analysis, zircon saturation thermometry and Sm-Nd isotopes, Snare River Terrane, Slave Province, NWT	5-2
5.1 Abstract.....	5-3
5.2 Introduction.....	5-4
5.3 Zircon inheritance.....	5-5
5.4 Geological context.....	5-7
5.4.1 Regional setting.....	5-7
5.4.2 Magmatic rocks in the Snare River terrane.....	5-10
5.5 Analytical techniques.....	5-12
5.6 Results and methods of data treatment.....	5-15
5.6.1 Inherited zircon results.....	5-15
5.6.2 ϵ Nd modelling data.....	5-34
5.7 Interpretation.....	5-35
5.7.1 Zircon inheritance in metaluminous magmas – Implications for Neoproterozoic lower crustal evolution	5-37
5.7.1.1 Lower crustal profile at ca. 2674 Ma.....	5-37
5.7.1.2 Lower crustal profile at ca. 2637 Ma.....	5-39
5.7.1.3 Lower crustal profile at ca. 2600 Ma.....	5-40
5.7.1.4 Inheritance in 2589 Ma sanukitoid suite.....	5-42
5.7.2 Zircon inheritance in peraluminous magmas – Identifying metaturbitite contributions in inherited zircon spectra.....	5-46
5.7.2.1 Two-mica granite suite – deciphering the detrital connection.....	5-46
5.7.2.2 Megacrystic granite suite – A record of mid-crustal heterogeneity.....	5-49
5.7.2.3 Cordierite leucogranite – A record of turbidite evolution.....	5-50
5.7.3 Applications of inherited zircon data to deconstruct ϵ Nd mixing models.....	5-52
5.7.3.1 Binary mixing.....	5-53
5.7.3.1 Multicomponent mixing.....	5-53
5.7.3.1 Discussion.....	5-56
5.8 Conclusions.....	5-59
References.....	5-62

Chapter 6: Thermal Effects of Neoproterozoic Magmatism on Crustal Evolution and Orogenesis: Constraints from Zircon Saturation Thermometry	6-2
6.1 Abstract.....	6-3
6.2 Introduction.....	6-4
6.3 Geological setting.....	6-6
6.4 Zircon saturation thermometry.....	6-17
6.5 Results.....	6-18

6.5.1 Orthopyroxene granite suite.....	6-34
6.6 Interpretation.....	6-38
6.6.1 Secular variations in magma crystallization temperatures.....	6-38
6.6.1.1 Crust-forming TTG magmatism (ca. 2674 – 2608 Ma).....	6-40
6.6.1.2 Orogenic magmatism (ca. 2608 – 2597 Ma).....	6-41
6.6.1.3 Post-orogenic magmatism (ca. 2585 Ma).....	6-46
6.6.2 Orogenic magmatism, HT/LP metamorphism and thermal structure.....	6-47
6.6.2.1 Upper-crustal magmatism – buffering a pre-existing thermal regime?.....	6-48
6.6.2.2 Mid-crustal pluton-driven metamorphism.....	6-49
6.6.2.3 Orogenic thermal structure.....	6-54
6.7 Conclusions.....	6-59
References.....	6-62

Chapter 7: Highlights and Conclusions.....	7-2
7.1 Preliminary statement.....	7-2
7.2 Highlights of research methods.....	7-3
7.2.1 Field mapping.....	7-3
7.2.2 LAM ICP-MS.....	7-5
7.2.3 Integration of multidisciplinary studies.....	7-6
7.3 Detailed Contributions.....	7-7
7.3.1 Zircon geochronology: Magmatic, detrital and inherited studies.....	7-8
7.3.2 Three dimensional architecture.....	7-10
7.3.3 Magma geochemistry.....	7-12
7.3.4 Thermal evolution of crust.....	7-14
7.4 Four-Dimensional Crustal Evolution in the Snare River Terrane.....	7-16
7.4.1 Tectonic Evolution.....	7-16
7.4.2 Implications of crustal stratigraphy.....	7-25
7.5 Future Work.....	7-29
References.....	7-31

List of Tables

CHAPTER 2

Table 2.1:	U-Pb ID TIMS Analytical Results, Metaluminous Intrusions.....	2-27
Table 2.2:	U-Pb ID TIMS Analytical Results, Peraluminous Intrusions.....	2-28
Table 2.3:	ID TIMS and LAM ICP-MS U-Pb crystallization age datasets ignoring and including U decay constant uncertainties.....	2-29
Table 2.4:	Summary table of nine defined detrital zircon age populations.....	2-67

CHAPTER 3

Table 3.1:	Summary of P-T conditions and U-Pb age constraints for Archean metamorphic events M1 to M3 in the Snare River terrane.....	3-13
Table 3.2:	Summary table of deformational fabric at different crustal levels during D1 to D3 and M1 to M3	3-17
Table 3.3:	Physical characteristics of fold generations F1 – F4.....	3-21

CHAPTER 4

Table 4.1:	Petrographic characteristics of magmatic rocks in the SRT.....	4-13
Table 4.2:	Major and trace element composition of metaluminous volcanic and plutonic rocks (Groups 1-4) in the SRT.....	4-21
Table 4.3:	Major and trace element compositions of peraluminous plutonic rocks in the SRT.....	4-23
Table 4.4:	Major and trace element geochemistry of metaturbidites.....	4-24
Table 4.5:	Nd isotopic compositions, crystallization ages and rock types.....	4-25

CHAPTER 5

Table 5.1:	Summary of geochemical characteristics of magmatic groups.....	5-13
Table 5.2:	Summary of $^{206}\text{Pb}/^{207}\text{Pb}$ ages of inherited components in metaluminous samples.....	5-21
Table 5.3:	Summary of $^{206}\text{Pb}/^{207}\text{Pb}$ ages of inherited components in peraluminous samples.....	5-30
Table 5.4:	Summary data to constrain binary and multicomponent mixing models for PVB9 and VB1357.....	5-36

CHAPTER 6

Table 6.1:	Summary of peak metamorphic conditions (M2) at different crustal levels during the ca. 2600 Ma orogenic peak6-14
Table 6.2:	Summary of whole-rock trace-element composition, mineralogy, and zircon petrographic observations.....6-21
Table 6.3:	Metaluminous samples – summary of age data, M values, Zr concentrations and zircon saturation temperatures..... 6-28
Table 6.4:	Peraluminous samples – summary of age data, M values, Zr concentrations and zircon saturation temperatures.....6-30
Table 6.5:	Comparison of maximum uncorrected, corrected, and average zircon saturation temperatures for metaluminous and peraluminous samples associated with zircon U-Pb age data 6-35

List of Figures

CHAPTER 1

Figure 1.1:	Greenstone eruption histogram.....	1-10
Figure 1.2:	Evolution of continental crust composition plots.....	1-12
Figure 1.3:	Evolution of crustal products throughout the Archean.....	1-19
Figure 1.4:	Schematic crustal stratigraphy of the Kapuskasing Uplift.....	1-22
Figure 1.5:	General geological map of the Slave Province.....	1-25
Figure 1.6:	Schematic time – space framework of the SRT.....	1-30
Figure 1.7:	Generalized geology of the southwestern Slave Province and the Snare River Terrane.....	1-31

CHAPTER 2

Figure 2.1:	Simplified geological map of the Slave Province.....	2-6
Figure 2.2:	*Geological and geophysical maps of the Snare River terrane.....	2-10
Figure 2.3:	*Geological transect maps showing locations of 10 geochronological sampling sites.....	2-12
Figure 2.4:	Relative sequence of plutonism.....	2-17
Figure 2.5:	Field relationships of seven metaluminous intrusive units.....	2-32
Figure 2.6:	Transmitted light, BSE and SE images of zircon populations and single grains in metaluminous intrusions.....	2-35
Figure 2.7:	Concordia diagrams for metaluminous samples VB165, (a-d) VB166, VB1359A and VJ375.....	2-36
Figure 2.7:	Concordia diagrams for metaluminous samples VB1363 (e-h) and VB1841	2-38
Figure 2.7:	Concordia diagrams for metaluminous sample VB1357.....	2-46
Figure 2.8:	Field relationships of peraluminous intrusions, with polished slabs of representative samples (inset) and metaturbidite.....	2-50
Figure 2.9:	Transmitted light BSE and SE images of zircon populations and single grains in peraluminous samples.....	2-52
Figure 2.10:	Concordia diagrams for peraluminous samples VB1358 and (a-d) PVB9.....	2-54
Figure 2.10:	Concordia diagrams for peraluminous samples VB1688 and (e-h) VB161.....	2-59
Figure 2.10:	Concordia diagrams for peraluminous samples VB1229A and (i-j) VB1864.....	2-63
Figure 2.11:	Histogram and cumulative probability diagram illustrating $^{207}\text{Pb}/^{206}\text{Pb}$ ages in detrital zircon population from metaturbidite...	2-65

Figure 2.12:	U-Pb concordia diagrams for 9 detrital age components.....	2-66
Figure 2.13:	*Schematic orogenic stratigraphy of the Snare River terrane.....	2-70
Figure 2.14:	Time versus tectonic setting diagram linking the inferred evolution of plutonism and deformation in the SRT.....	2-71

CHAPTER 3

Figure 3.1:	Simplified structural trend map of metasedimentary belts in the Slave Province.....	3-7
Figure 3.2:	*(a) Simplified structural trend map and (b) distribution of different crustal levels in the Snare River terrane.....	3-9
Figure 3.3:	*Relative sequence of plutonism with respect to D1-D3 deformational episodes.....	3-11
Figure 3.4:	Structural elements and related fabrics in mafic volcanic and turbidite packages northwest of the Wijinnedi antiformal closure.....	3-28
Figure 3.5:	*Geological map and cross-section of southwestern closure of the upper-crustal Wijinnedi antiform.....	3-32
Figure 3.6:	Structural elements and related deformational fabrics observed in metaturbidite of the Kwejinne Lake supracrustal belt.....	3-34
Figure 3.7:	*Geological map and cross-section illustrating the closure of the Hinscliffe antiform and the transition zone.....	3-43
Figure 3.8:	Structural elements and related deformational fabrics observed in metaturbidite of the transitional migmatite zone.....	3-46
Figure 3.9:	*Geological map and cross-section of the central mid-crustal Ghost subdomain.....	3-53
Figure 3.10:	Structural elements and related deformational fabrics observed across the Ghost subdomain.....	3-57
Figure 3.11:	Summary correlation diagram illustrating diachronous relationships between deformation, fabric formation and metamorphism.....	3-65
Figure 3.12:	*Distribution of conjugate shear zones and decompression metamorphic assemblages.....	3-67
Figure 3.13:	*Summary crustal cross-section across the Kwejinne Lake supracrustal belt, transition zone, and Ghost subdomain.....	3-69
Figure 3.14:	Deformation history of the Snare River terrane depicted in six schematic crustal profiles.....	3-72
Figure 3.15:	Distribution of fold interference patterns and relative structural age map.....	3-81

CHAPTER 4

Figure 4.1:	*Simplified geological maps of the Slave Province and the Snare River terrane.....	4-7
Figure 4.2:	Relationship between temporal magmatic group, tectonic regime and tectonometamorphic evolution of the SRT.....	4-10
Figure 4.3:	Field and textural relationships of magmatic suites in the SRT	4-18
Figure 4.4:	Relationship of SRT temporal magmatic groups to SRT geochemical suites and their correlative geochemical suite within the Slave Province	4-26
Figure 4.5:	Geochemical classification diagrams of volcanic rocks	4-27
Figure 4.6:	Geochemical classification diagrams of plutonic rocks	4-28
Figure 4.7:	Chondrite-normalized incompatible element patterns for (Group 1) (a-d) magmatic rocks.....	4-31
Figure 4.7:	Chondrite-normalized incompatible element patterns for (Group 1) (e-h) magmatic rocks.....	4-34
Figure 4.8:	Chondrite-normalized incompatible element patterns for (a-d) Group 2-4 metaluminous plutonic rocks	4-37
Figure 4.8:	Chondrite-normalized incompatible element patterns (e-h) for Group 2-4 metaluminous plutonic rocks.....	4-41
Figure 4.8:	Chondrite-normalized incompatible element patterns (i-l) for Group 1-4 metaluminous plutonic rocks.....	4-42
Figure 4.9:	Chondrite-normalized incompatible element patterns for Groups 3 and 4 peraluminous plutonic rocks.....	4-45
Figure 4.10:	ϵNdT vs age diagrams for magmatic and sedimentary rocks.....	4-49
Figure 4.11:	Incompatible element patterns for average compositions of SRT tholeiites, Banting and Kam Group tholeiites and SRT calc-alkaline basalts.....	4-55
Figure 4.12:	$(\text{Nb}/\text{Th})_N$ vs. $(\text{La}/\text{Nb})_N$ data for the KLSB and RSSB tholeiites, Kam and Banting group tholeiites.....	4-56
Figure 4.13:	Chondrite normalized incompatible element diagram: average TTG vs modern adakite and SRT Group 1 TTG.....	4-61
Figure 4.14:	*Time-space model of crust development of the SRT.....	4-65
Figure 4.14:	Time-space model of crust development of the SRT.....	4-78
Figure 4.15:	*Sequence of crustal development imaged through schematic crustal profiles depicting the four main phases of evolution in the Snare River terrane.....	4-84

CHAPTER 5

- Figure 5.1:** Simplified geological maps of the Slave Province and the Snare River terrane..... 5-8
- Figure 5.2:** Relationship between temporal magmatic group, tectonic regime and tectonometamorphic evolution of the SRT.....5-11
- Figure 5.3:** BSE images of representative inherited zircon grains in metaluminous intrusions.....5-16
- Figure 5.4:** Resolved U-Pb age populations for metaluminous samples.....5-19
- (a-b)**
- Figure 5.4:** Resolved U-Pb age populations for metaluminous samples.....5-23
- (c-d)**
- Figure 5.4:** Resolved U-Pb age populations for metaluminous samples.....5-25
- (e)**
- Figure 5.5:** Resolved U-Pb age populations for peraluminous samples.....5-28
- (a-b)**
- Figure 5.5:** Resolved U-Pb age populations for peraluminous samples.....5-32
- (c-d)**
- Figure 5.6:** Summary diagram of the evolution of the SRT during crust formation, growth and orogenesis.....5-38
- Figure 5.7:** Comparison of premagmatic zircon component in VJ375 with Magmatic zircon.....5-44
- Figure 5.8:** Comparison of cumulative probability diagrams and frequency histograms of turbidite detrital zircon spectra with peraluminous magma inherited zircon age spectra.....5-48
- Figure 5.9:** Simplified diagram showing the principles behind two-component and multi-component mixing using inherited zircon data to determine the age and number of components.....5-55

CHAPTER 6

- Figure 6.1:** Geological maps of the Slave Province and the Snare River terrane..... 6-7
- Figure 6.2:** Field and petrographic relationships of magmatic suites in the Snare River Terrane.....6-11
- Figure 6.3:** Representative images of metamorphic indicators for each metamorphic zone in the SRT6-16
- Figure 6.4:** Zircon morphologies and representative inherited zircon zonation trends for magmatic suites..... 6-20
- Figure 6.5:** Petrographic relationships between zircon and host minerals..... 6-24
- Figure 6.6:** Zr vs M-value plot with experimental zircon solubility curves.....6-31
- Figure 6.7:** Temperature histograms - zircon saturation temperature estimates for metaluminous and peraluminous samples..... 6-32

Figure 6.8:	Proportion of inherited zircon to magmatic zircon.....	6-33
Figure 6.9:	Temperature histogram - corrected and uncorrected zircon saturation temperatures for individual samples	6-36
Figure 6.10:	Temperature vs time diagram - evolution in zircon saturation temperatures.....	6-39
Figure 6.11:	P-T diagram - dehydration melting reactions for pelitic rocks and calculated T_{Zir} estimates for two-mica and megacrystic granite suites.....	6-43
Figure 6.12:	Comparison of P-T constraints for each metamorphic zone in the SRT and the upper- and mid-crustal orogenic magmatic suites.....	6-51
Figure 6.13:	Schematic diagram illustrating the variation in ca. 2600 Ma orogenic magma temperature and ambient metamorphic grade with depth...	6-56
Figure 6.14:	Temperature versus depth diagram with steady-state geotherms from Kramers et al (2001).....	6-58

CHAPTER 7

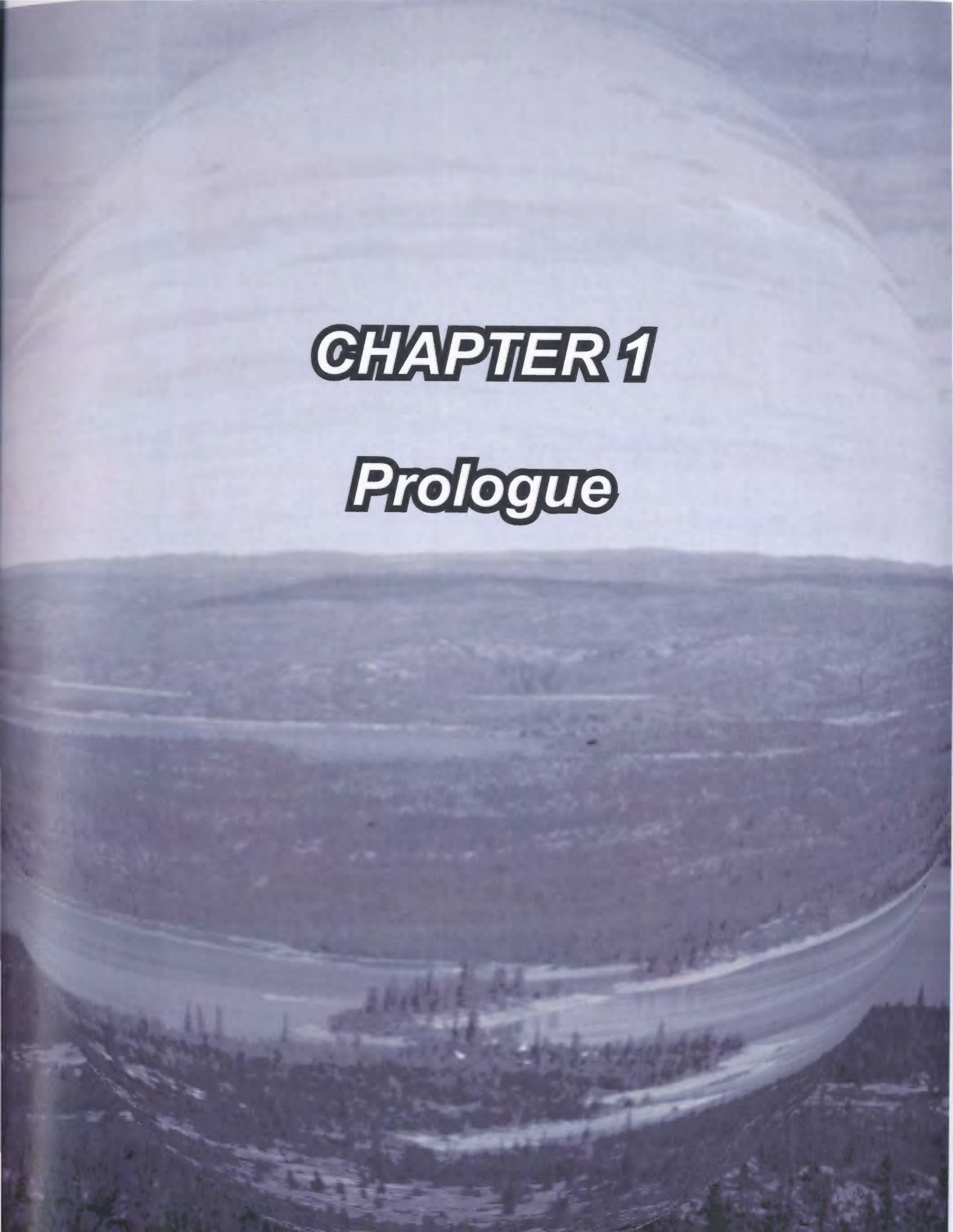
Figure 7.1:	Geological maps of the Snare River terrane.....	7-4
Figure 7.2:	Schematic model of the evolution of the SRT.....	7-20
(a-c)		
Figure 7.2:	Collisional orogenesis.....	7-23
(d)		
Figure 7.2:	Post-orogenic collapse.....	7-24
(e)		
Figure 7.3:	Schematic crustal stratigraphy of the Kapuskasing structure and the SRT.....	7-27

* 11 x 17in insert

List of Appendices

Appendix A: U-Pb LAM ICP-MS Data Table	<i>CD database</i>
Table A1: Metaluminous Intrusions.....	A2
Table A2: Peraluminous Intrusions.....	A3
Table A3 : Detrital Zircon Dataset.....	A5
Appendix B: Reverse Discordance in U-Pb LAM – ICP-MS Datasets	B1
Figure B1: Figure B1: Time-resolved diagram of $^{206}\text{Pb}/^{238}\text{U}$ and $^{207}\text{Pb}/^{206}\text{Pb}$ ratio.....	B4
Figure B2: Concordia plots and BSE images (VB165) – standards.....	B11
Figure B3: Time-resolved analyses of VB165.....	B15
Table B1: LAM ICP-MS U-Pb age data - Standard 02123.....	B6
Table B2: LAM ICP-MS U-Pb age data - VB165.....	B7
Appendix C: ID TIMS size-weight reference table.....	C1
Figure C1: Zircon reference groups.....	C3
Table C1: Size-weight data for zircon reference groups.....	C5
Table C2: Weight estimate comparison table.....	C6
Appendix D: Geochemical analytical techniques.....	D1
Table D1: XRF standards geochemical data.....	D4
Table D2: ICP-MS standards geochemical data.....	D5
Table D3: Snare River Terrane composite database.....	<i>CD database</i>
Figure D1: XRF vs ICP-MS trace element concentration comparison.....	D7
Appendix E: Field relations and petrography of magmatic groups.....	<i>CD database</i>
Table E1: Sources of U-Pb age data used to subdivide groups.....	E2
Appendix F: Inherited zircon U-Pb age LAM ICP-MS data.....	<i>CD database</i>
Table F1: Metaluminous Intrusions.....	F1
Table F2: Peraluminous Intrusions.....	F7
Table F3: Geochemical database – eNd modelling.....	F11
Appendix G: Inherited zircon population descriptions and age summaries.....	G1

Appendix H: ϵNd modelling methodology	H1
Appendix I: Supplementary P/T data	I1
Figure I1a-j: Photomicrographs and polished slabs (upper amphibolite facies).....	I4
Figure I1k-u: Photomicrographs and polished slabs (granulite facies).....	I13
Figure I2a: Petrogenetic grid for Chl, Bt, Crd, Sil zones.....	I5
Figure I2b: Petrogenetic grid for Crd (2) and Grt + Kfs zones.....	I11
Figure I2c: Summary diagram – metamorphic field gradient.....	I15
Appendix J: Zircon saturation thermometry, methodology and sample descriptions	J1
Appendix K: Sample numbers, descriptions and UTM locations	<i>CD database</i>
Appendix L: Summary LAM ICP-MS report monazite pilot studies	<i>CD database</i>
Appendix M: Zircon BSE images, pit locations and pit morphologies	<i>CD database</i>
Appendix N: PhD research proposals	<i>CD database</i>
Appendix O: Composite field database (notebooks, field and selected petrographic photos, thin section and polished and stained slab images)	<i>CD database</i>
Appendix P: Snare River Terrane presentations and publications	<i>CD database</i>
Appendix Q: Indian and Northern Affairs, Geology Division, open file reports- U-Pb and P/T datasets	<i>CD database</i>
Appendix R: 1:250 000 geological map, Snare River Terrane	<i>map pocket</i>

An aerial, wide-angle photograph of a vast, flat landscape, likely a river valley or a large plain. A winding river or road cuts through the center of the scene. The terrain is covered in dense vegetation, possibly a forest or scrubland. The image is framed by a circular fisheye lens effect, creating a curved horizon and a sense of depth. The overall color palette is muted, with shades of green, brown, and grey.

CHAPTER 1

Prologue

1 PROLOGUE

1.1 Preamble

The research presented in this thesis seeks to provide new insight into several fundamental aspects of Archean geology, specifically the mode, scale and timing of crust-formation and subsequent development during the Neoproterozoic era (~ 3.0 – 2.5 Ga). Neoproterozoic rock assemblages, which occur in Archean terranes worldwide, have been interpreted to represent the crustal expression of a global thermotectonic event that resulted in widespread stabilization of cratonic regions (Frei et al. 2003) and the transition to a more ‘modern’ style of plate processes in the Paleoproterozoic. In addition to major reworking of pre-existing crustal blocks, large quantities of new crust were generated during this period. Growth of the cratonic nuclei occurred both vertically through mantle additions and density-driven redistribution of magmas, and laterally by tectonic amalgamation and accretion of crustal fragments of contrasting age and provenance.

It has been suggested that the geometry and distribution of the pre-existing Paleoproterozoic to Neoproterozoic (~ 4.0 – 3.0 Ga) crustal blocks imparted significant control on the crustal evolution of the younger Neoproterozoic terranes (e.g., de Wit et al. 1992; Horstwood et al. 1999; Chadwick et al. 2000; Kramers et al. 2001). However, the nature and extent of this control, although commonly identified in the evolutionary histories of many cratons, remains one of the least well understood and documented aspects of Neoproterozoic geology.

This study adopts a multidisciplinary approach to analyzing these problems in an attempt to constrain the timing and mechanisms of crust-formation, growth and evolution in the Snare River terrane, a ca. 2.67 – 2.56 Ga assemblage of upper- and mid-crustal rocks exposed in the southwestern Slave Province. The primary datasets presented include: (1) 1:30 000 scale field mapping, with emphasis on crustal architecture and the relative chronology of magma emplacement and fabric formation; (2) U-Pb zircon geochronology of representative magmatic suites, (3) major- and trace-element geochemistry, (4) Sm-Nd isotopic analyses, (5) zircon inheritance ages of representative igneous suites and (6) zircon saturation thermometry data. Integration of these datasets illuminates the nature, diversity, and interconnections among the processes responsible for crustal growth and evolution in the southwestern Slave Province, which it is hoped will serve as a model for comparison with other Neoproterozoic terranes.

1.2 The polarized world of Archean geology: Uniformitarianism versus secular change

Aside from ongoing isotopic studies related to the search for, and characterization of the Hadean (~ 4.0 – 4.5 Ga) crust and the effect of its extraction on the Hadean mantle (e.g., Compston and Pidgeon 1986; Bowring and Williams 1999; Wilde et al. 2001; Valley et al. 2002; Frei et al. 2004), Archean geology is essentially polarized into two schools that focus on specific problems in the Paleo- to Mesoarchean and Neoproterozoic eras, respectively. Many of the problems addressed are unique to either the Paleo- to Mesoarchean or the Neoproterozoic, with only minor overlap of certain issues between the

two eras, e.g., tonalite-trondhjemite-granite (TTG) and greenstone genesis. However, one fundamental problem plagues the interpretation of all Archean geology, namely the application of uniformitarian (i.e., plate tectonic) principles and whether they adequately account for the exposed Archean crustal record. Crustal products and average crustal compositions varied significantly in the Archean compared to the present, and hence the extrapolation of a plate tectonic framework back to the Archean has sparked vigorous debate (e.g., de Wit 1998; Hamilton 1998). Apart from the absence of directly comparable Archean and Palaeozoic (or younger) sequences, one of the principal arguments against the operation of modern-style plate tectonics in the early Earth is the inference of hotter ambient mantle temperatures at that time. At least four lines of evidence imply that the Hadean Earth was hot and extremely energetic (Pollack 1997), including: (a) the kinetic and gravitational energy associated with planetary accretion and core formation, (b) the inferred early meteorite bombardment, (c) radiogenic heat production from short-lived nuclides, and (d) the scarcity of crust of Hadean and Paleoproterozoic age. Since the Hadean, the Earth's interior has been steadily cooling as a result of the decline in radiogenic heat production (Davies 1992; Pollack 1997). Radiogenic heat production from the Paleoproterozoic to the present, and from the Paleoproterozoic to the end of the Neoproterozoic, are estimated to have declined by factors of ~ 6 - 3 and 3 - 2 , respectively (Pollack 1997). The continuing challenge is to constrain the time at which the Earth attained the thermal and mechanical properties favourable for the onset of a plate tectonic dynamic.

It has been proposed that the elevated mantle temperatures in the Archean would have resulted in a more voluminous and hence thicker basaltic crust than currently occurs (Davies 1992). Thick 'unsubductable' buoyant basaltic crust is surmised to have been ubiquitous throughout the Paleo- and Mesoarchean Earth (e.g., Anderson 1979; Vlaar et al. 1994; Zegers and van Keken 2001), precluding the operation of plate tectonics as it is understood from the modern record. Thus, if a plate tectonic regime did not exist during the Archean era, what mode of tectonism did?

Archean literature is replete with both uniformitarian (i.e., plate tectonic) and non-uniformitarian interpretations of Archean sequences (e.g., Komiya 1999; Chadwick et al. 2000; Zegers and van Keken 2001; Percival et al. 2001; Bédard et al. 2003), with proportionately more uniformitarian interpretations invoked for late Mesoarchean and Neoarchean terrains. It seems likely that some form of mobile plate-like tectonics had evolved at least by the end of the Archean (e.g., Bleeker 2002; Griffin et al. 2003; Smithies et al. 2003). Three pertinent questions arise in regard to the emergence of this Archean quasi-plate tectonic regime: (1) Are there any localities where the transition between the two tectonic regimes can be observed? (2) What crustal products, or perhaps more correctly, what 'assemblage and /or sequence of crustal products' characterize this change in tectonic regime, i.e., how does Paleo- to Mesoarchean crust differ from Neoarchean crust? And (3) do any specific relationships exist between the pre-plate tectonic regime and the onset of the plate tectonic regime? These fundamental questions represent the central themes examined in this thesis. The following sections briefly outline the major characteristics and problems associated with the Paleo- to Mesoarchean

and Neoproterozoic eras. The purpose is to introduce the necessary background relevant to the questions addressed above and to provide the broader geological context in which to assess the research presented in this study.

1.2.1 Paleo- to Mesoarchean geology

Paleo- to Mesoarchean terranes (> 3.0 Ga) are a volumetrically subordinate, yet a compositionally distinct component of Archean crust. Supracrustal assemblages consist predominantly of basaltic – komatiitic greenstone belt sequences and minor associated banded iron formation, clastic sediments and felsic volcanic rocks. In addition to the classic ca. 3.71 Ga Isua supracrustal belt in West Greenland (e.g., Nutman et al. 1997; Frei and Kastbjerg Jensen 2003), the ca. 3.7 – 3.3 Ga greenstone belts of the Pilbara (Western Australia) and Kaapvaal (South Africa) cratons are perhaps the best preserved and documented successions (e.g., de Wit et al. 1987; Kröner et al. 1992; Buick et al. 1995; Parman et al. 1997; Green et al. 2000). These belts are interpreted as new crustal additions derived from pre-existing variably depleted/enriched mantle, implying the occurrence of Hadean crust-forming episodes. Geological and geochemical evidence from the Coonterunah and Warrawoona greenstones in the Pilbara craton indicate emplacement on pre-3.5 Ga continental basement (Green et al. 2000), supporting the potential for more widespread existence of Eoarchean crust. The tectonic setting of, and the driving forces behind thermal perturbations responsible for early greenstone genesis are poorly constrained, although mantle plume events, catastrophic mantle overturn, and lower crustal delamination have all been invoked as potential causes (e.g., Davies 1992,

1995; Stein and Hoffman 1994; Tomlinson and Condie 2001; Zegers and Van Keken 2001). Similarly, the corresponding crustal tectonic setting remains a controversial issue. Island arcs, oceanic plateaux, intra-oceanic obduction, and intra-continental extensional settings have all been proposed to account for greenstone belt tectonics (e.g., de Wit et al. 1992; Condie 1997; Kusky and Polat 1999; Bleeker 2002).

Mid-crustal Paleo- to Mesoarchean assemblages consist of the 'grey gneiss' suite (Martin 1994), which consist of poly-deformed and -metamorphosed assemblages of tonalite-trondhjemite-granodiorite (TTG) plutonic rocks, interlayered with less abundant mafic to ultramafic components. The oldest known grey gneiss terrane is the ca. 4.03 Ga Acasta Gneiss Complex in the Slave Province of northwestern Canada. Other well-documented Paleoproterozoic examples include the ca. 3.82 Ga Amitsoq gneisses of West Greenland and the ca. 3.9 Ga Napier Complex of Antarctica. U-Pb zircon data for the Acasta gneisses reveal overprinting events at ~3.75, 3.6, 3.36 and 1.7 Ga (Bowring et al. 1989; Bowring and Williams 1999). Isotopic data for the Amitsoq gneisses demonstrate at least seven resolvable overprinting events between 3.9 and 3.6 Ga (Nutman et al. 1993), and the ca. 3.9 Ga tonalitic orthogneisses from Enderby Land in the Napier Complex, Antarctica, similarly show evidence for polyphase overprinting, in this case at ca. 2.95, 2.48 and 1.0 Ga (Black et al. 1986). A comparable overprinting pattern also exists for Mesoarchean gneiss terranes. For instance, Mesoarchean tonalites (~ 3.27 Ga) from the Mt. Riiser-Larsen region of the Napier Complex have undergone successive stages of crustal reworking at ca. 3.07, 2.8 and 2.5 Ga. Collectively, the U-Pb age data from ancient grey gneiss terranes illustrate that their formation took place over extended

periods and that they were characterized by several overprinting thermal pulses. Perhaps most importantly, the data highlight incremental crustal growth, prolonged mid-crustal residence, and the enduring nature of these TTG-dominant grey gneiss terranes.

It is widely accepted that TTGs formed by partial melting of hydrated basaltic crust at pressures where garnet and amphibole co-exist and remain in the residue (e.g., Martin 1987, 1994; Drummond and Defant 1990; Rapp et al. 1991; Springer and Seck 1997; Smithies 2000). Debate revolves around the tectonic setting in which such melting took place. Two current models include: (a) dehydration melting of a subducted mafic slab (e.g., Martin 1986, 1994; Martin and Moyen 2002; Smithies et al. 2003), which inherently implies the existence of a plate tectonic regime; and (b) melting at the base of magmatically or tectonically thickened crust (e.g., de Wit et al. 1992; Atherton and Petford 1993; Turkina and Nozhkin 2003). No clear resolution to this problem is evident in the literature and both geodynamic settings may be realistic alternatives that apply to individual cratons.

The Paleo- and Mesoarchean was an interval characterized by intermittent and progressive crustal growth and the development of protocratons, possibly driven in part by large mantle overturn events (Stein and Hofmann 1994). Isotopic and geochemical data from Paleo- and Mesoarchean crust provide evidence for older Hadean crust-formation and mantle perturbations that resulted in early development of depleted and enriched mantle reservoirs from which younger crust was subsequently extracted (Bowring and Housh 1995; Bowring and Williams 1999; Frei et al. 2004). Greenstone and TTG assemblages appear to have been the predominant crustal products formed

during this era and together represent the 'staple' components of early cratonic nuclei onto which younger crust amalgamated. Application of uniformitarian plate tectonic principles cannot be entirely ruled out; however their acceptance a priori is also inappropriate since the Paleo- and Mesoarchean rock record indicates that both crustal products and average crustal composition contrast with crust formed subsequently.

1.2.2 Neoarchean geology

Overall, Neoarchean crust predominates the Archean crustal record, most notably in the abundance of greenstone belts (Condie 1995; Rey et al. 2003; Fig. 1.1). Furthermore, the Neoarchean era was characterized by a voluminous global tectonothermal episode (Rey et al. 2003) involving polyphase reworking of the older protocratonic blocks in addition to the formation of new continental crust. This global tectonothermal episode is considered to represent a terminal stage of cratonization that ultimately led to the stabilization of vast regions of continental crust. Estimates of the combined areal extent of Archean crust exceed ca. $2.6 \times 10^6 \text{ km}^2$ (Condie 1981; Eriksson 1995) prior to breakup and fragmentation during the Proterozoic.

In addition to the voluminous magmatic products, the Neoarchean also marked the onset of a more evolved suite of crustal lithotectonic units including thick sedimentary sequences, heterogeneous polyphase high-grade terranes, and voluminous syn- to post-tectonic granitic plutonism, including K-rich granite-granodiorite-monzonite (GGM) suites and sanukitoid suites. The onset of such diverse crustal products coincided with a major change in the average composition of Archean crust exposed at the surface

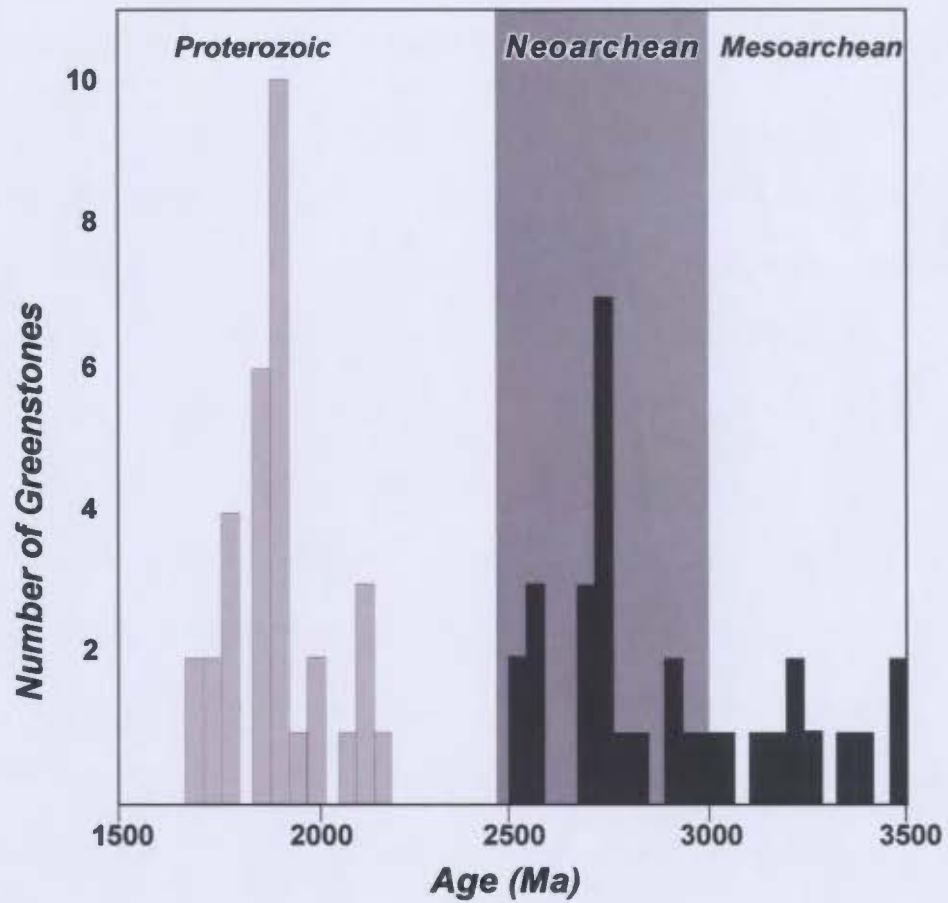


Figure 1.1: Greenstone eruption frequency during the Mesoproterozoic, Neoproterozoic and Paleoproterozoic, after Condie (1994). Diagram illustrates a major peak in greenstone formation at ~ 2.7 - 2.6 Ga.

and incorporated into sediments (Taylor and McLennan 1985; Fig. 1.2). In particular, the K-rich GGM suite has been estimated to comprise ~ 20% of the exposed Archean crust (Condie 1993).

Clastic sedimentary sequences are a minor component of the Paleo- to Mesoproterozoic record, their increased abundance in the Neoproterozoic being attributed to the formation of emergent buoyant protocratons that could sustain appreciable loads of clastic detritus in their flanking submarine basins. Sedimentary successions are speculated to have increased in abundance and volume from ca. 4.0 to 2.5 Ga in response to the progressive growth of the continents (Eriksson and Fedo 1994; Windley 1998), with a notable increase in basin formation and preservation at the onset of the Neoproterozoic. A variety of sedimentary associations have been recognized in the Neoproterozoic stratigraphic record, including a syn-rift to syn-orogenic association, a calc-alkaline association, and 'Timiskaming' types, which are briefly discussed here.

In regard to syn-rift to syn-orogenic successions, the ca. 3.1–2.8 Ga lower Witwatersrand and Dominion groups of the Kaapvaal Craton, the Steep Rock Group of the Superior Province, and the Central Slave Cover Group in the Slave Province, which represent the best known examples, were all deposited on 'protocratonic' crust (de Wit et al. 1992; Eriksson and Fedo 1994; Eriksson et al. 1997; Bleeker et al. 1999). Syn-rift successions are characterized by conglomerate, mudstone, sandstone and intercalated (ultra-)mafic and/or felsic volcanic rocks, whereas those deposited after rifting on a stable continental shelf consist of quartz arenite, mudstone, iron formation and stromatolitic carbonate (Eriksson and Fedo 1994). Extension of the underlying basement is typically

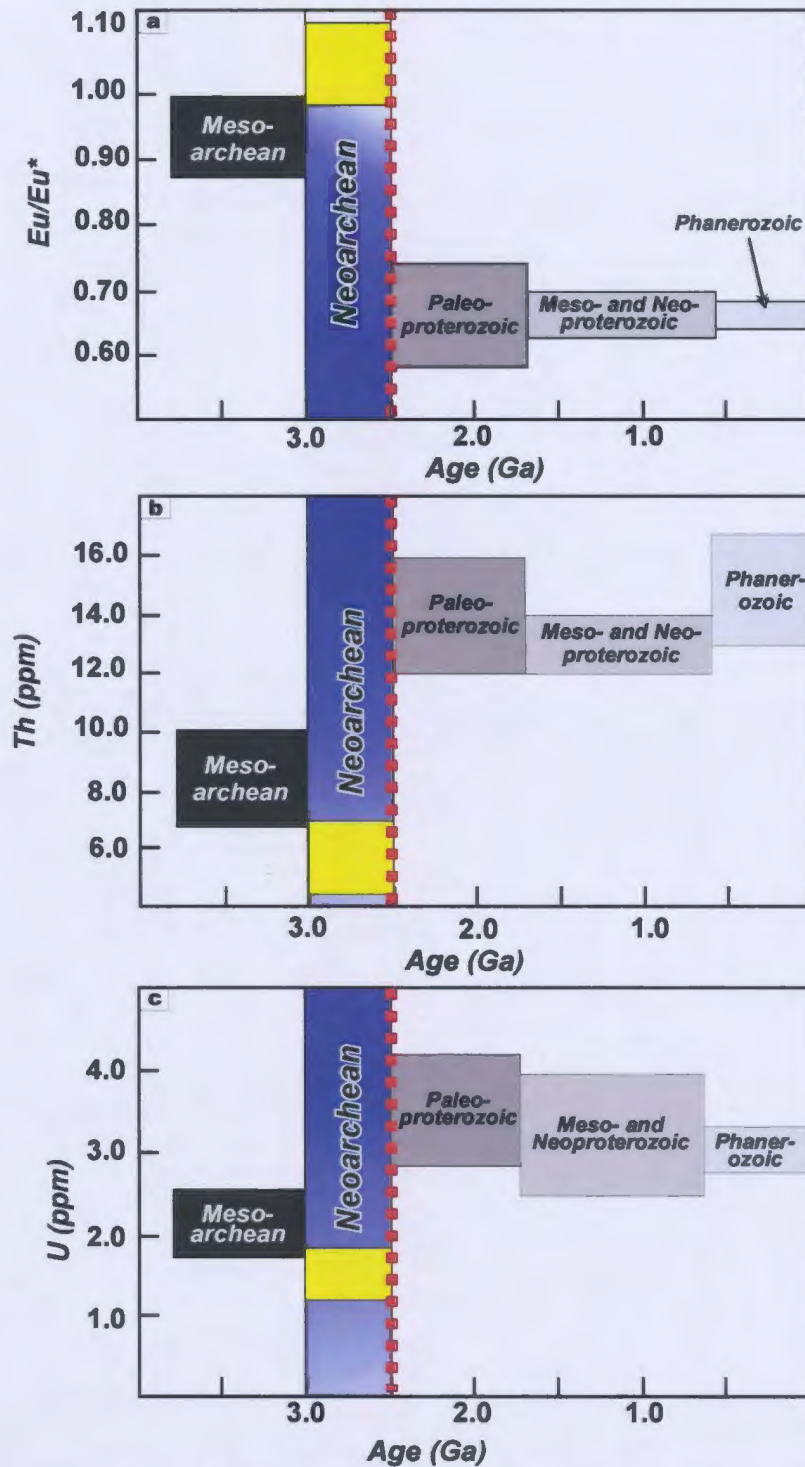


Figure 1.2: Plots illustrating the change in average composition of continental crust as sampled in sedimentary rocks through geological time, modified after Taylor and McLennan (1985). (a) Secular evolution of the Eu/Eu^* ratio, ($\text{Eu}/\text{Eu}^* = \text{Eu}_N / (\text{Sm}_N \times \text{Gd}_N)^{0.5}$); (b) and (c) secular evolution of Th and U abundances in continental shales. Data for the Neoproterozoic era are highlighted in each figure to emphasize the distinctive compositions at that time.

Invoked as the principal basin-formation mechanism, although the ultimate cause of extension is poorly understood. It has recently been suggested that it may have been due to enhanced mantle plume activity in response to wholesale mantle overturn (Bleeker 2002).

Sedimentary successions associated with calc-alkaline magmatism range in age from ca. 2.75–2.65 Ga and are widespread throughout the Superior and Slave cratons, Canada and the Yilgarn block, Australia (Langford and Morin 1976; Henderson 1981; Barley and Groves 1990). These successions are typically composed of greywacke – mudstone turbidite, banded iron formation and conglomerate (Eriksson et al. 1997) and they have been interpreted as analogues to modern fore-arc basin sequences. Their similarity with modern sediments and their association with calc-alkaline volcanic rocks have further been suggested to provide unequivocal evidence for the operation of subduction-related processes during their sedimentation (Eriksson et al. 1997). However, Bleeker (2002) invoked vertical diapirism similar to that outlined by Campbell and Hill (1988) to account for the setting of these sedimentary successions in the Slave Province, noting that the commencement of turbidite sedimentation coincided with the onset of TTG magmatism.

The ‘Timiskaming’ association consists of volumetrically minor, but distinctive assemblages of largely late kinematic conglomerate, cross-bedded sandstone and mudstone (Bleeker 2002). These sediments occur in elongate structural basins, display unconformable contacts with the underlying basement and strike-slip contacts with younger supracrustal rocks (Eriksson et al. 1997). Examples include the ~ 2.7 Ga

Timiskaming Group in the type location in the Superior Province (Legault and Hattori 1994), the ~ 3 Ga Lalla Rookh Supersequence in the Pilbara Block (Krapez 1989), and the ~ 2.59 Ga Jackson Lake Formation in the Slave Province (Isachsen and Bowring 1994). Depositional settings invoked for these sediments include pull-apart basins associated with late tectonic strike-slip faulting (e.g., Krapez and Barley 1987) and subsidence basins peripheral to regions of doming in granite – greenstone belts (e.g., Bleeker 2002).

Mid-crustal high grade terranes, although not absent from the Paleo- and Mesoarchean (e.g., ~3.65 Ga granulites, southern West Greenland; Nutman et al. 1993), are widespread in Neoproterozoic crust. These exhumed granulite-facies terranes typically exhibit evidence for high temperature / low to medium pressure (HT/LP) metamorphism and retain average peak P - T conditions of approximately 7.5 ± 1 kbar and $800 \pm 50^\circ\text{C}$, respectively (Harley 1989). Voluminous plutonism coeval with high-grade metamorphism is typical of some belts, as is a record of polyphase metamorphism and deformation. Kramers et al. (2001) demonstrated in their analysis of the Limpopo belt that Neoproterozoic high-grade terranes exhibit a high degree of lithological, structural, and metamorphic heterogeneity such that each one is unique. However, Percival (1994) distinguished two end-member types: (a) terranes that formed in response to juvenile crust-forming processes (e.g., southern west Greenland; Nutman et al. 1993); and (b) terranes resulting from crustal reworking, particularly in collisional orogenic settings (e.g., Limpopo Belt; Kamber et al. 1996). Neoproterozoic granulite formation is thus considered to be intimately associated with the same diverse array of processes that

operated on the low grade, upper crustal sequences. With increasing acceptance of an incipient mobile plate regime in the Neoproterozoic, recent tectonic interpretations of the granulite terranes have largely been uniformitarian in approach, for example, an inferred collisional setting for the Limpopo belt (Kamber et al. 1996) and a magmatic arc setting for the Neoproterozoic rocks exposed in the Kapuskasing Uplift of the Superior Province (Percival 1994). The marked increase of granulite genesis, as is preserved in the exposed Neoproterozoic crustal record, is surmised to reflect the shift in the prevailing tectonics in place at that time. The onset of dynamic plate interaction tectonics greatly influenced and controlled the processes responsible for the production and exhumation of these high-grade mid- and lower-crustal fragments.

Interpreting the geothermal gradients recorded in mid-crustal granulite terranes is perhaps the foremost contentious issue surrounding these belts. Initially, the widespread occurrence of HT/LP metamorphic terranes in the Archean record was inferred to directly reflect the elevated heat production levels of the early Earth. Comparison of gradients calculated from P - T estimates in the high-grade terranes and the present-day stable continental geotherm revealed that granulite geotherms were strongly perturbed above those of the stable continental crust (e.g., Harley 1989; Mezger 1992). Subsequent discussion revolved around physico-chemical conditions and tectonic settings compatible with such elevated geothermal gradients. End-member models include those that add heat to the lower- and mid-crust by magmatic under-plating, intra-plating, and accretion (e.g., Harley 1989; Bohlen and Mezger 1989; Ashwal et al. 1992) and those in which the excess heat is generated internally in the crust due to increased radioactive decay induced

by a variety of tectonic thickening mechanisms that result in redistribution of heat-producing material (e.g., England and Thompson 1984; Harley 1989; Sandiford 1989a; Ashwal et al. 1992; Percival 1994; Jamieson et al. 1998).

Neoproterozoic Granites: GGMs comprise up to ~ 20% of the currently exposed Neoproterozoic crust (Condie 1993) and are considered to have played a leading role in crustal stabilization due to their propensity to remove the heat producing elements U, Th and K from deeper crustal levels and transport them to the mid- and upper-crust, thus promoting crustal cooling (Bohlar 2001). They are compositionally diverse, typically ranging from quartz-rich compositions such as granodiorite, alkali feldspar granite and syenogranite to quartz-poor compositions such as monzogranite and syenite (Sylvester 1994), but also including relatively anhydrous magmas (charnockite suite) and Mg-rich types (sanukitoid association). Individual suites may exhibit calc-alkaline, strongly peraluminous or peralkaline affinities and generally show evidence for syn- to post-tectonic emplacement with respect to major orogenic compressional deformation (Sylvester 1994; Rey et al. 2003). On average, the time lag between greenstone formation and granite emplacement in many cratons is ~ 20-40 M.y. (Rey et al. 2003).

Moyen et al. (2003) subdivided Neoproterozoic granites into five groups: (1) Na-rich TTGs (discussed above); (2) K-rich biotite granite; (3) two-mica granite; (4) sanukitoid suite; and (5) volumetrically minor peralkaline granite. Biotite granite, including charnockitic types, and two-mica granite represent crustal melts of TTG and metasedimentary sources, respectively. Sanukitoids were initially identified in the western Superior Province (Shirey and Hanson 1984; Stern et al. 1989), but have been

subsequently recognized as an important component of the Neoproterozoic plutonic record elsewhere (e.g., Krogstad et al. 1995; Smithies and Champion 1999). The suite has been suggested to represent partial melting of metasomatized mantle (Shirey and Hanson 1984; Stern and Hanson 1991; Stevenson et al. 1999), with subsequent fractionation and crustal assimilation producing the evolved granodioritic to granitic members of the suite. Sanukitoid genesis, however, remains a widely debated issue, with some authors preferring a multistage model involving an initial TTG slab melt that hybridized with mantle peridotite before final fractionation in the crust (e.g., Rapp et al. 1999; Moyen et al. 2003). Regardless of the exact mode of origin, the sanukitoid suite is unique amongst the Neoproterozoic melts of the GGM suite in that it formed by initial extraction from the mantle. Charnockitic suite magmas, which range from granitic to tonalitic in composition and contain igneous orthopyroxene, are intimately associated with mid- to lower-crustal high-grade metamorphic terranes. Mid-crustal emplacement of these dry and hot (e.g. >1000 °C; Kilpatrick and Ellis 1992) magmas, provides a mechanism for advection of excess heat through the crustal column and initiation of partial melting in the adjacent host rocks (Percival 1994).

Neoproterozoic granites differ in composition from their Phanerozoic counterparts, indicating secular evolution of magmatic processes, which may partially reflect the change in average crustal composition over time (Sylvester 1994; Fig. 1.2). In part, these differences are also surmised to result from the elevated geothermal gradients present during the Archean (Sylvester 1994). The anatectic biotite and two-mica granites are recognized to have modern correlatives, whereas TTGs and sanukitoids are not

commonly identified in the Phanerozoic record (Moyen et al. 2003). Geochemical similarities between the Neoproterozoic intracrustal anatectic suites and Phanerozoic calc-alkaline granites that occur in collisional settings (Sylvester 1994) imply a plate tectonic framework may be applicable for these older suites. Tectonic settings of the TTG and sanukitoid suites are less well constrained, but petrogenetic interpretations requiring slab-melt and mantle interaction, if correct, dictate a plate tectonic paradigm.

1.2.3 Summary

Crustal growth mechanisms evolved throughout the Archean, in parallel with the inferred secular change in crustal heat production. The variation in crustal processes over this interval led to a corresponding increase in the diversity of crustal products (Fig. 1.3). Tonalite-trondjemite-granodiorite and greenstone belt genesis occurred throughout the Archean and is considered to be the 'staple' crust-forming mechanism. Arguments for both uniformitarian and non-uniformitarian interpretations of TTGs and greenstone are numerous, but in the opinion of the author a plate tectonic scenario less than adequately accounts for the Paleo- and Mesoarchean geological record. In an Archean context, the deposition of thick sedimentary sequences, formation and exhumation of mid-crustal granulite belts, and emplacement of voluminous K-rich magmas are processes unique to the Neoproterozoic and imply a change in the tectonic regime controlling crust formation and growth (Fig. 1.3). A plate tectonic interpretation most readily accounts for many of the first-order characteristics of these belts, but parallels between modern plate tectonics are not exact and require variations of standard uniformitarian models (e.g., shallow

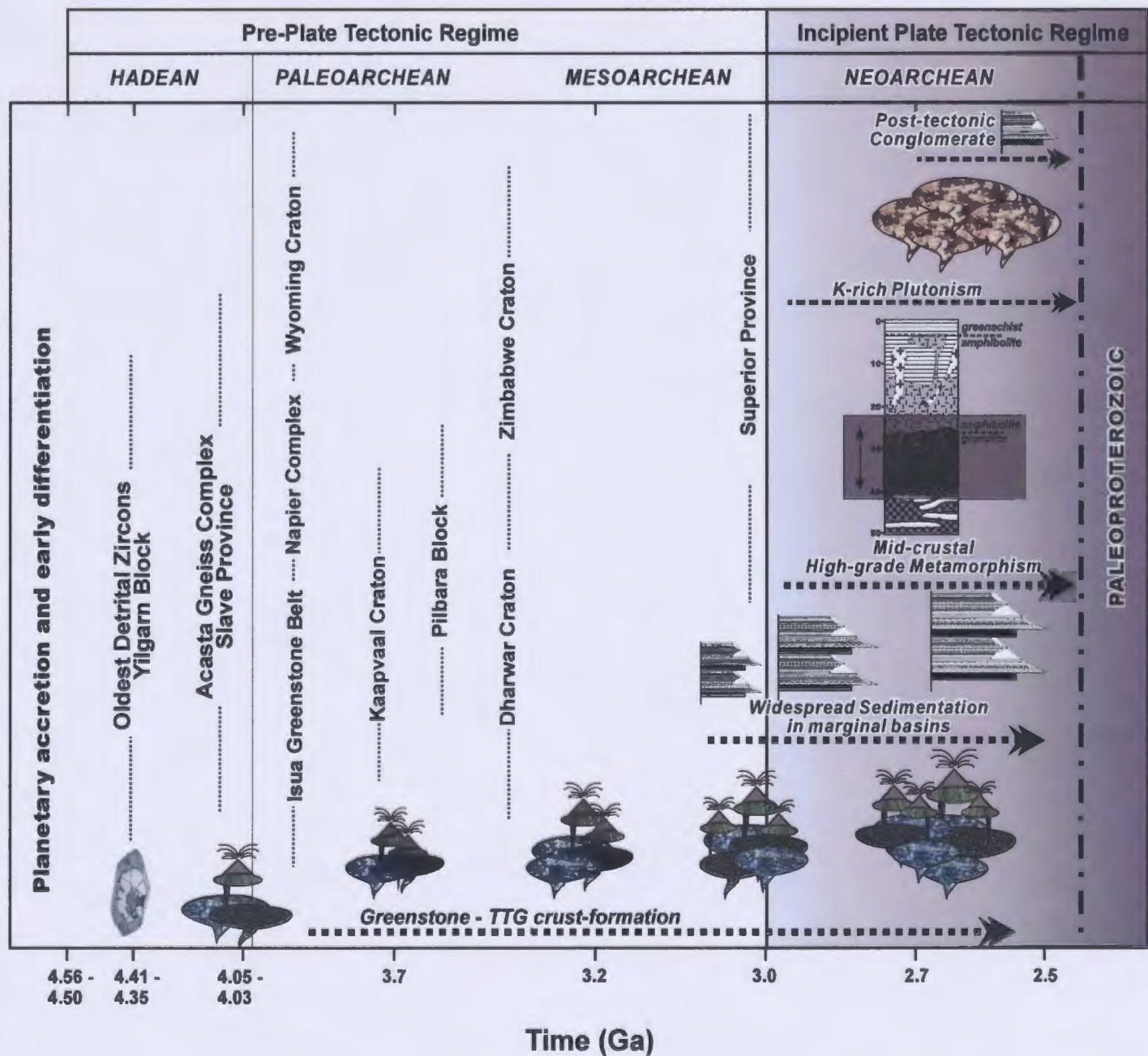


Figure 1.3: Summary one dimensional diagram illustrating the evolution of crustal products through the Archean eon and the timing of the oldest crust-forming events in Archean cratons worldwide. TTG-greenstone belt formation dominated crust-formation throughout the Archean, culminating in a major Neoproterozoic peak. During the Neoproterozoic crustal products increase in diversity and abundance, including widespread marginal basin sedimentation, high-grade metamorphism, voluminous plutonism and late extension-related sedimentation. Major events in early Earth history discussed in the text are noted.

subduction; Smithies et al. 2003). Collectively, these observations imply that the Neoproterozoic represents a window that images a transitional tectonic stage in Earth history where the pre-plate tectonic, Paleo- to Mesoproterozoic TTG –greenstone dynamic evolved into the Neoproterozoic incipient plate-tectonic regime.

1.3 Crustal cross-sections: A four-dimensional understanding of Archean crustal evolution.

Our understanding of the continental crust and the way it has evolved since its origin in the Hadean has been significantly advanced by information obtained from crustal cross-sections, oblique sections through tilted continental crust exhumed to the Earth's surface. They are characterized by an increase in metamorphic grade with depth and provide a surface view of the lithological and structural constitution of the crust at different levels and times. Crustal cross-sections are relatively rare, particularly those exposing Archean crust, but two in particular, i.e., the Kapuskasing structure in the Superior Province (Percival and Card 1983) and the Vredefort structure in the Kaapvaal craton, (Hart et al. 1981; Lana et al. 2003), have provided invaluable information about the vertical constitution of Archean crust and the processes involved in its formation (Percival and West 1994). Temporal, structural and metamorphic data presented in this thesis support the interpretation that a partial crustal section, (i.e. from upper- to mid-crustal levels) is exposed in the Snare River terrane. The information that such terranes reveal is reviewed in the text that follows.

The importance of crustal sections is three-fold:

1. They allow the variations in composition, structure and metamorphic grade to be mapped out as a function of depth, which, in turn, provide the necessary data to reconstruct the crustal-scale stratigraphy (e.g., Fig. 1.4) and interpret key tectonometamorphic relationships among crustal levels;
2. Comparison of the observed crustal stratigraphy with reflection and refraction seismology, where available, permits extrapolation of geophysical interpretations of deep crustal structure away from the region of the exposed crustal section;
3. Crustal cross-sections provide a unique opportunity to investigate lateral and vertical variations in pressure, temperature and the timing of evolution at different crustal levels. Integration of such datasets allows for a four dimensional understanding (three spatial dimensions and time) of Archean crustal evolution. Importantly, the protracted histories recorded in Archean crustal cross-sections are windows into the processes of cratonization, i.e., the formation and stabilization of thick sialic continental nuclei. For instance, multidisciplinary data obtained from the Kapuskasing structure not only validated the presence of a continuous crustal section down to ~ 35 km depth, but also provided constraints on the sequence of Archean evolution and subsequent Proterozoic cooling and uplift.

Crustal sections (Fig. 1.4) are distinguished by their second-order metamorphic fabric imposed on the first-order lithological architecture (Fountain and Salisbury 1981).

Studied sections exhibit an increase in pressure from ~2 kbar at the highest structural levels to ~12 kbar at the base (Kapuskasing structure; Percival et al. 1992; Percival et al.

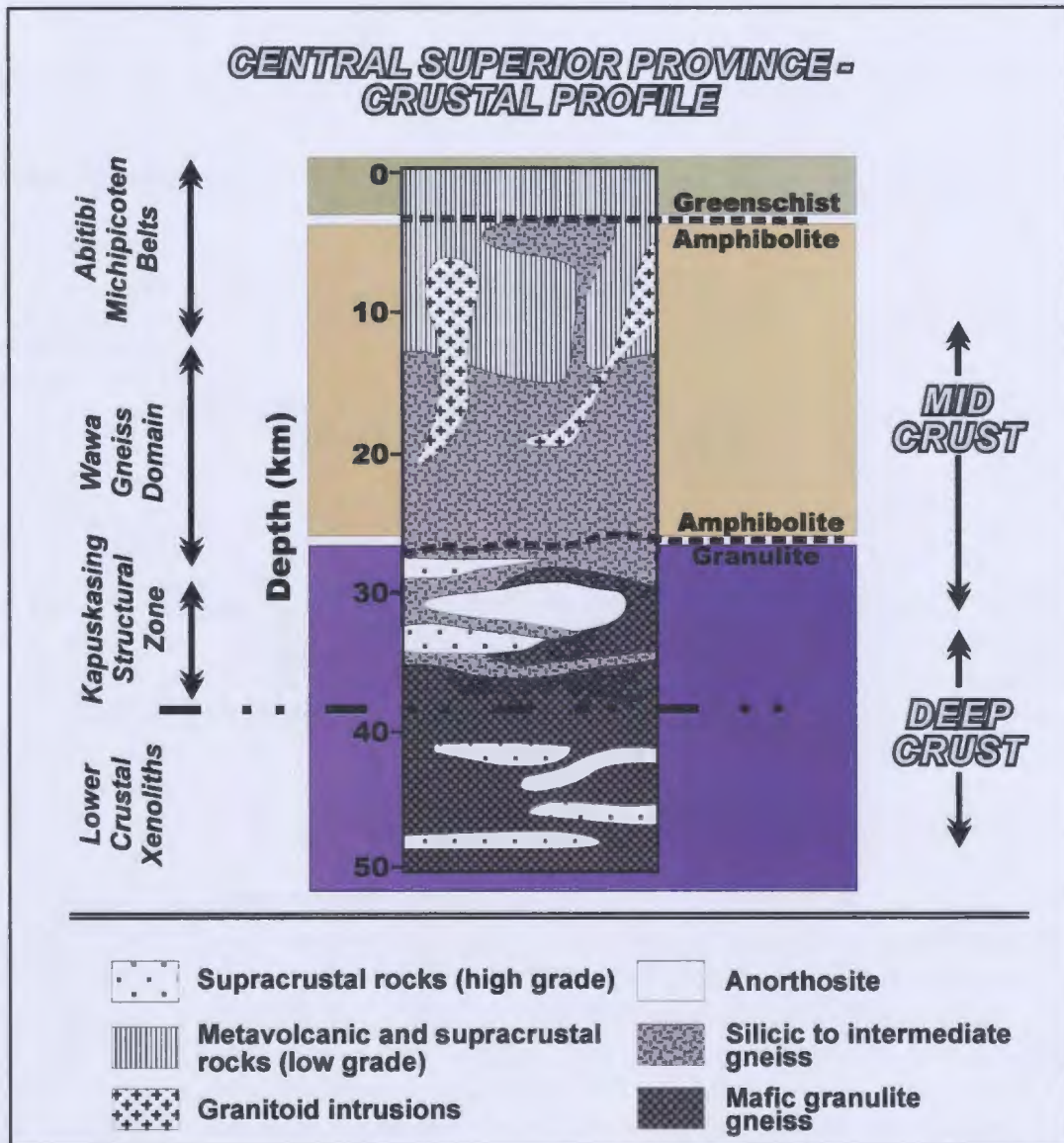


Figure 1.4 : Schematic crustal stratigraphy of the Kapuskasing Uplift, Superior Province (modified after Percival et al. 1992, Krogh and Moser 1994; Moser 1994). Diagram illustrates second-order structural - metamorphic layering of the crust, subvertical in the upper crust, subhorizontal in the lower crust, superimposed on the broad first-order compositional stratification that comprises a predominantly felsic upper crust to mafic to ultramafic lower-crust.

1997), with granulite-facies assemblages in the lower- and mid-crust giving way to amphibolite- and greenschist-facies assemblages in the upper mid- and upper-crust respectively (Fig. 1.4). Peak temperature estimates at the base of the crustal profiles range from 750 °C to ≥ 850 °C, but these should be regarded as minimum values due to the possible effects of diffusional resetting of geothermometers during cooling (i.e., the granulite uncertainty problem; Frost and Chacko 1989). Where detailed isotopic datasets are available, mineral U-Pb ages systematically decrease with increasing paleodepth (e.g., Corfu 1987; Krogh 1993). However, such datasets are relatively few in number and it is not known if this is a general phenomenon.

Exhumation of crustal sections has been reported from three tectonic settings: (a) compressional exhumation along deep-rooted thrust faults, typically in convergent plate-margin settings (e.g. Kapuskasing Uplift, Percival and West 1994); (b) extensional exhumation along crustal-scale detachment faults in orogenic settings (e.g. Cordilleran core complexes, Henry and Dokka, 1992); and (c) impactogenic uplift due to crustal rebound after a bolide impact (e.g., Vredefort Dome, Lana et al. 2003). In (a) and (c), the crust is tilted to provide a relatively intact cross-section upon erosion, whereas in (b) the upper crust is displaced laterally from the uplifted mid-crust along detachment faults and two possible crustal geometries can result. In the first scenario, contrasting crustal-levels are juxtaposed in the hanging- and footwalls of a steep crustal-scale fault system. In contrast, if a low angle detachment fault exists, such that extensive preservation of the footwall occurs, then a continuous crustal section will be preserved.

A review of the literature pertaining to exposed crustal sections demonstrates that individual crustal levels represent heterogeneous collages of crustal- and/or mantle-derived material that have undergone pervasive polyphase deformation and metamorphism. Magmatic components typically dominate, with upper-crustal felsic compositions grading into intermediate, mafic and/or ultramafic compositions at mid- and lower-crustal levels (e.g. Percival et al. 1992). Supracrustal relics are widespread at middle and lower structural levels of several sections, emphasizing the importance of tectonic juxtaposition of crustal components of dissimilar origin and burial of supracrustal rocks (Fountain and Salisbury 1981).

A fundamental structural dilemma in several terranes, notably including those of Archean age, is the contrast between steep structures observed in the upper-crust and the sub-horizontal structures characteristic of the mid- and lower-crust that have been widely imaged in deep seismic reflection experiments. This dilemma has been termed the 'structural versus seismic paradox' by Culshaw et al. (2004). Low-angle structures in mid-crustal terranes have often been attributed to orogenic extension (e.g., Sandiford 1989b; Moser et al. 1996) or crustal-scale thrusting (e.g., Kelly et al. 2000; Culshaw et al. 2004) in different orogens. The challenge is to systematically correlate structures both temporally and kinematically throughout the crustal profile in order to understand the role of deformation during orogenesis.

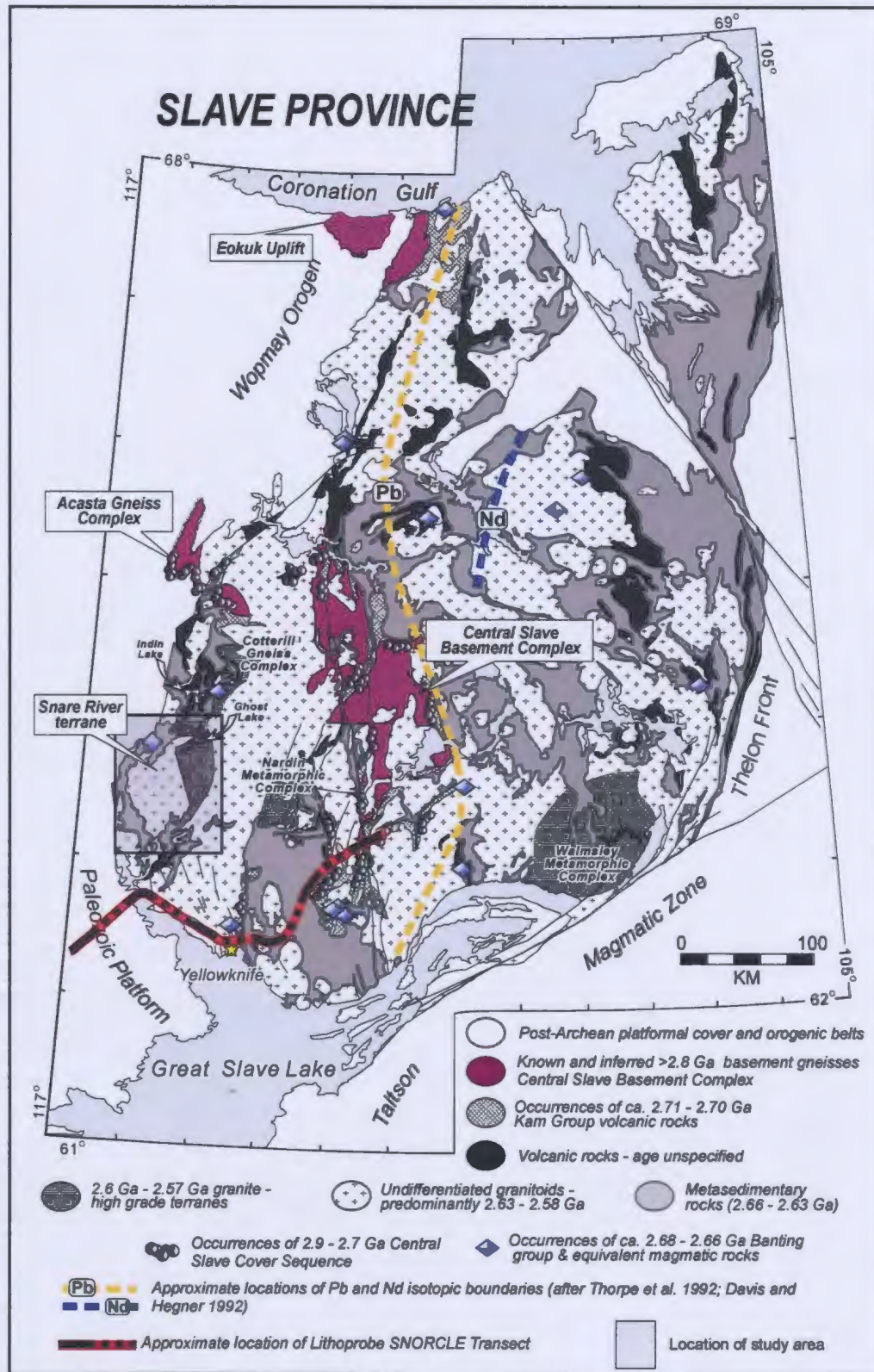


Figure 1.5: General geological map of the Slave Province. Locations of the Lithoprobe SNORCLE transect, Pb and Nd isotopic boundaries, and the study area are shown. Modified after Bleeker et al. (1999a).

1.4 Geological setting of study area

1.4.1 Slave Province.

The Slave Province, located in the northwestern Canadian Shield (Fig. 1.5), is a small Archean craton of approximately 190 000 km² (Padgham and Fyson 1992) that preserves a record of crustal growth and reworking spanning more than 1.5 Ga. It consists of three chronologically distinct domains: (a) ca. 4.031 - 2.8 Ga (Henderson et al. 1982; Frith et al. 1986; Bowring and Williams 1999; Bleeker et al. 1999) inliers and xenoliths of sialic basement that predominantly occur in the western half of the province and structurally underlie and predate the Meso- and Neoproterozoic supracrustal assemblages. The pre-2.8 Ga rocks, typically of TTG affinity, have collectively been termed the Central Slave Basement Complex (CSBC) and are overlain by a thin cover sequence termed the Central Slave Cover Group (CSCG; Bleeker et al. 1999a, b; Ketchum and Bleeker 1999, 2000; Sircombe et al. 2001); (b) ca. 2.71 – post-2.65 Ga (Mortensen et al. 1988; Isachsen et al. 1991) greenstone - supracrustal belts, comprising greywacke - mudstone and volcanic lithologies sequences (collectively referred to as the Yellowknife Supergroup; e.g., Henderson 1998) that crop out over ~ 33% of the province; and (c) widespread ca. 2.63 - 2.58 Ga granitic plutons constituting ~ 65% of the province (Davis and Bleeker 1999). The oldest known sialic basement is the Acasta Gneiss complex, located in the west of the province in a basement culmination associated with the Proterozoic Wopmay Orogen. The extent of the sialic basement terranes in the western half of the province is roughly demarcated by the Pb and Nd isotopic boundaries (Fig. 1.5). The Pb boundary of Thorpe et al. (1992) is based on data from estimates of initial

Pb compositions of galena in syn-volcanic sulphide deposits, whereas the Nd line (Davis and Hegner 1992) was determined from initial ϵNd values of lower-crustally-derived granitoid rocks. Both indicate that the sialic basement in the eastern Slave Province is younger than that in the west (Davis and Hegner 1992), compatible with the outcrops of old sialic basement in the west and implying growth of the Slave craton during the Archean. Specifically, with respect to Nd, supracrustal sequences and Neoproterozoic plutonic rocks from east of the Nd boundary yield positive ϵNd values ($\epsilon\text{Nd} = +0.3$ to $+3.6$) implying derivation from juvenile sources, whereas those from west of the Nd line yield negative initial ϵNd values ($\epsilon\text{Nd} = -1.0$ to -5.3) compatible with derivation from, or contamination by, pre-2.8 Ga basement (Davis and Hegner 1992). Complementary Pb isotopic studies of granitoid plutons support the Nd isotopic studies, with plutons in the east - central regions having initial $^{207}\text{Pb}/^{204}\text{Pb}$ compositions of 14.8 - 14.9, suggesting derivation from juvenile source material, whereas those in the west have $^{207}\text{Pb}/^{204}\text{Pb} = 15.1 - 15.2$, demonstrating recycling of pre-2.8 Ga crust (Davis et al. 1996).

Three major periods of deformation have been identified in the Slave Province: (a) pre-2.7 Ga polyphase deformation preserved in basement rocks; (b) craton-wide compressional deformation at ca. 2.64 - 2.58 Ga, associated with local deformation related to pluton emplacement and late extension (King and Helmstaedt 1997); and (c) overprinting Proterozoic deformation. Pre-2.7 Ga deformation in the basement terranes is poorly constrained and is not considered further here. Deformation of Neoproterozoic (ca. 2.64-2.58 Ga) supracrustal rocks resulted in multiple sets of isoclinal folds, foliations and faults that were refolded by regional open cross-folds (Davis et al. 1996). Large turbidite

domains preserve polyphase, tight to isoclinal folds, multiple cleavages and layer-parallel faults, all of which indicate major horizontal shortening. Proterozoic deformation overprints the eastern and western flanks of the province and predominantly involved crustal-scale open refolding of the underlying and adjacent Archean rocks. Narrow brittle and mylonitic fault zones related to ~1.84 - 1.74 Ga conjugate transcurrent faulting occur locally within the craton and delineate its southeastern and northeastern margins (King and Helmsteadt 1997).

Low pressure, andalusite - sillimanite metamorphism at ca. 2.6 Ga was associated with compressional deformation throughout the Slave Province. Estimated maximum temperature conditions in the greenstone belts vary from ca. 400 °C to 750 °C (Thompson 1978; Relf 1992). Early Proterozoic metamorphism related to the Wopmay and Thelon orogens overprints both the eastern and western margins (King and Helmsteadt 1997).

1.4.2 Snare River terrane

Until the work of Henderson (1994, 1998), the limited recognition of granulites in the Slave Province was considered inconsequential to the broader tectonic development of the craton. Since then, several workers (e.g., Stublely et al. 1995; Pehrsson 1998; Emon et al. 1999; Cairns et al. in press; Bennett et al. in press), have demonstrated the occurrence of considerable areas of high-temperature - low pressure (*HT-LP*) granulite-facies rocks in the Slave Province, of which the Snare River terrane represents one of the largest and best exposed. Additionally, the Snare River Terrane represents part of a larger

entity, the Snare domain (Pehrsson et al. 2000) consisting of discontinuous exposures of high-grade rocks and associated plutons, juxtaposed against low-grade supracrustal belts.

The Snare River terrane is situated in the southwestern Slave Province, approximately 150 km NNW of Yellowknife, 100 km north of the Lithoprobe SNORCLE transect line, and west of the Nd and Pb isotopic boundaries (Fig. 1.5). The western margin of the terrane is defined by the onlapping and fault-bound Proterozoic Wopmay orogen, whereas the eastern margin is defined by a curvilinear fault system (Eastern Boundary Fault; EBF) at least in part also of Proterozoic age. Approximately 100 M.y. of crustal growth and development, about 7% of the temporal history of the Slave Province, is recorded in the Snare River terrane (Fig. 1.6). It consists of a high-grade mid-crustal core, comprising HT-LP granulite- and amphibolite-facies grade rocks outcropping in Ghost and Bigspruce subdomains, surrounded by the greenschist- to amphibolite-facies Kwejinne Lake (*KLSB*), Labrish Lake (*LLSB*) and Russell-Slemon (*RSSB*) supracrustal belts (Fig. 1.7). A 1:30 000 scale geological transect was completed by the author across the contiguous low- and high-grade domains in conjunction with a multi-year 1:50 000 mapping project carried out by the NWT Geoscience Office (Jackson 2003). The transect was staggered so as to incorporate key representative components of the Snare River terrane and mapping was conducted over the course of three summers (1998 – 2000). The Snare River terrane is significant in that it represents one of the few places in the Slave Province where the mid-crust is exposed and where Neoproterozoic crustal evolution can be documented and correlated with that in the adjacent supracrustal belts.

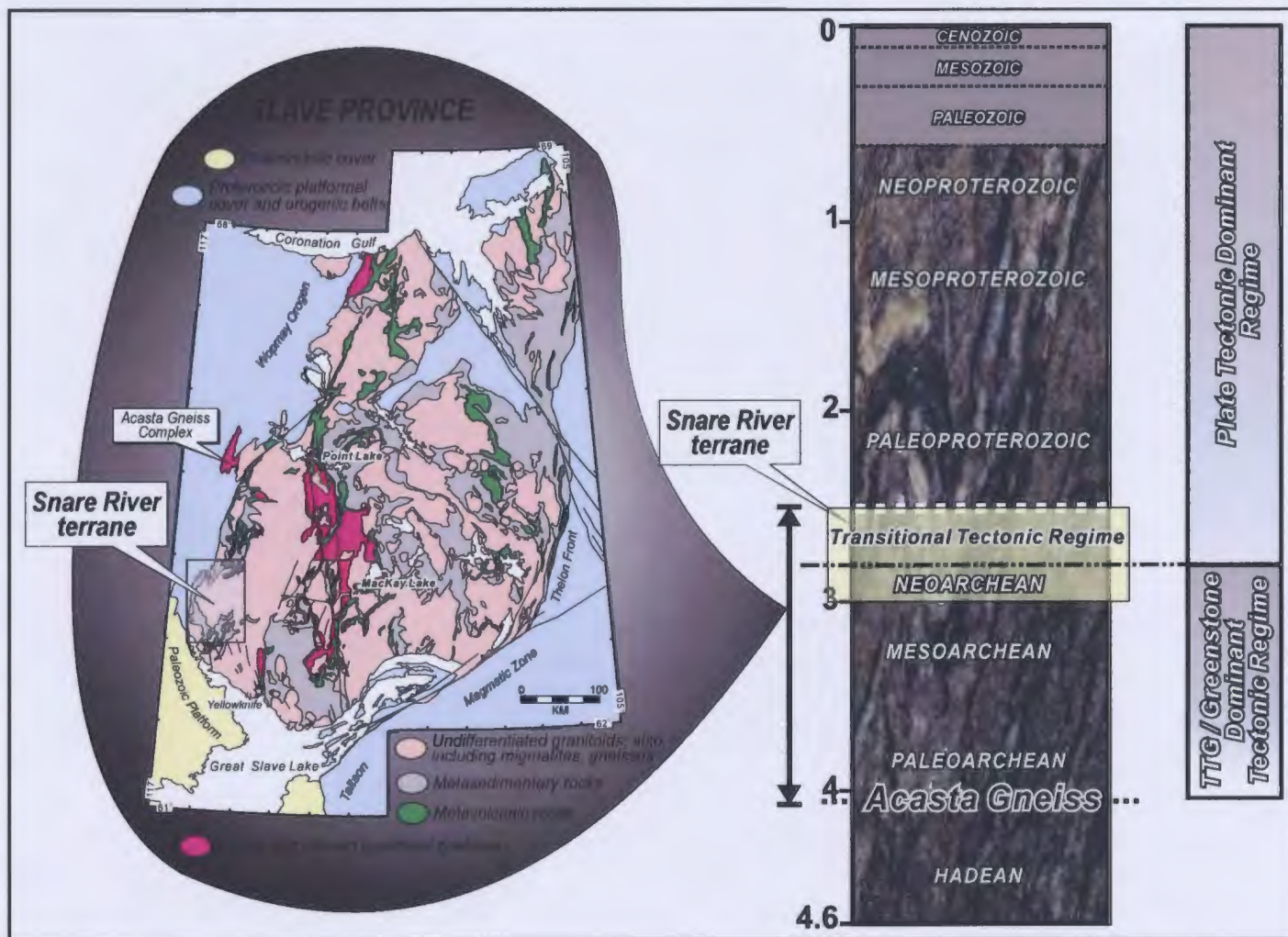


Figure 1.6 : Geological map and time scale illustrating the ~ 100 M.y time-frame in which crustal evolution occurred in the SRT. The location of the Acasta Gneiss Complex is noted on both map and time scale for reference. Also highlighted is the timing of the inferred transitional tectonic regime from a predominantly TTG-greenstone dynamic to an incipient plate

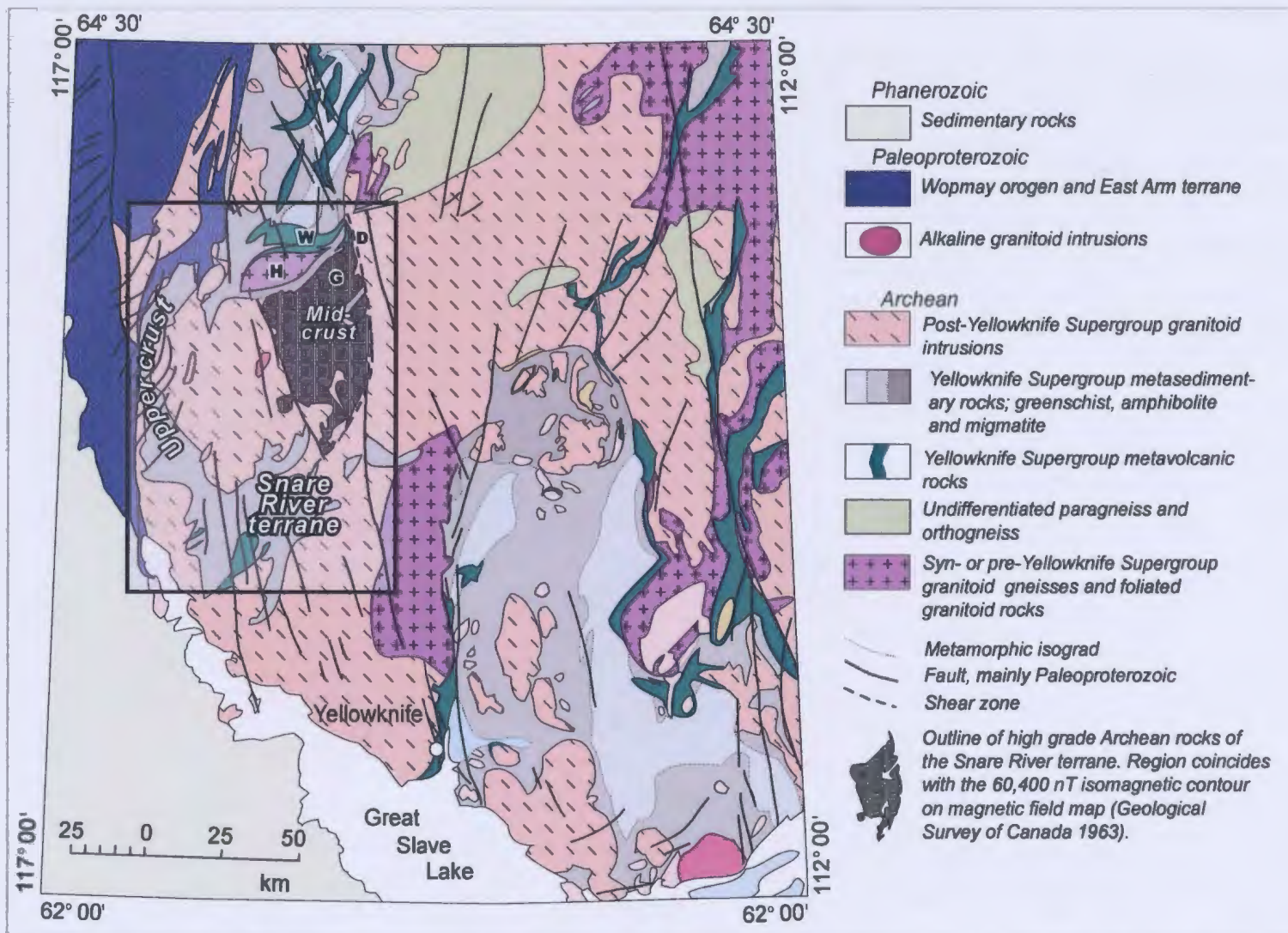


Figure 1.7: Geological map of the southwestern Slave Province illustrating the general geology of the the Snare River terrane, after Henderson (1998). Regions of upper- and mid-crust are indicated. Domains of Henderson (1994, 1998) are marked: W (Wijinnedi), H (Hinscliffe), G (Ghost), and D (Dauphinee).

Initial mapping of the Snare River terrane was completed by Lord (1942) at a scale of 1 inch to 4 miles. Lord and co-workers grossly subdivided the region into two broad domains consisting of an arcuate supracrustal package partially surrounding an undifferentiated granite domain. Wright (1950, 1954) mapped the Ghost Lake area in more detail (1 inch to 1 mile) and M^cGlynn and Ross (1962) documented the overprinting effects of the Proterozoic Wopmay orogen on sedimentary rocks at Basler Lake and northwest of the Kwejinne Lake supracrustal belt. The earliest records of the high-grade metamorphic assemblages were by Folinsbee (1940, 1941a and b), who reported on gem quality cordierite (iolite) from the Ghost Lake area. Robertson and Folinsbee (1974) carried out a Pb isotope study on granulite gneisses from the Ghost Lake area and obtained an age of 2540 ± 50 Ma, which they interpreted as the time the gneiss became a closed system during the last metamorphic event to affect the area.

Henderson (1994, 1998) conducted 1:50 000 scale mapping of the Wijinnedi Lake area and was able to subdivide the region into four main fault-bound blocks, which he termed the Wijinnedi, Hinscliffe, Ghost and Dauphinée domains (Fig.1.7). The Wijinnedi domain consists of greenschist- and amphibolite-facies metasedimentary and volcanic rocks that adjoin the northern part of the Kwejinne Lake supracrustal belt. The Hinscliffe domain, which consists of granitic plutons and amphibolite-facies gneisses, is separated from the Wijinnedi domain by a curvilinear high strain zone. The Ghost domain represents the northernmost exposure of the larger unit referred to as Ghost subdomain by Pehrsson et al. (2000). It is located to the southeast of the Wijinnedi and Hinscliffe domains and consists of heterogeneous and highly deformed granulite grade rocks. The

Dauphinée domain is separated from the Ghost domain by a prominent cataclastic shear zone and consists of a heterogeneous assemblage of massive to weakly foliated granitoid rocks that truncate the Ghost domain at a high angle (Henderson and Schaan 1993). Float-plane reconnaissance was carried out by Henderson and Chacko (1995) to better define the regional extent of granulite-facies assemblages south of Ghost Lake.

U-Pb age dating of representative magmatic rocks in the Wijinnedi map area, reported by Villeneuve and Henderson (1998), indicated that magmatism took place in the interval ca. 2.67 to 2.58 Ga. Initial quantitative *P-T* work on metapelitic and migmatitic rocks from the Ghost domain (Farquhar et al. 1993) suggested maximum pressures of 5.2 kbar and a thermal peak of 850 - 870°C. Farquhar and Chacko et al. (1995) subsequently revised these estimates to 5.9 - 7.4 kbar and 845 -920 °C. Pb isotopic data for ca. 2.6 Ga plutonic rocks near MacNaughton Lake, southwest of the Ghost Lake, were used to suggest the involvement of crust older than 3.2 Ga in the source regions (Yamashita et al. 1999), compatible with their location west of the Pb boundary of Thorpe et al. (1992). In contrast, Sm-Nd isotopic data from the same study imply significant input from juvenile crustal sources. The authors explained the discrepancy by surmising that the melt regions from which the granites were derived consisted of mixtures of juvenile and pre-2.8 Ga material. Finally, Perks (1997) revealed some of the complexity of the mid-crustal rocks at Forked Lake south of Ghost Lake in an integrated mapping and isotopic (U-Pb and Sm-Nd) analytical study on magmatic and metasedimentary rocks.

1.5 Study objectives and thesis outline

1.5.1 Objectives

This thesis is an investigation into the formation, growth and evolution of Neoproterozoic crust in the Snare River terrane, southwestern Slave Province. It is primarily an examination of evolving tectonic styles and an analysis of the corresponding increased diversity of crustal products. The three core objectives of this study are:

1. To produce multidisciplinary datasets that constrain the chronological, structural, geochemical and thermal evolution of the Snare River terrane, and to utilize these to elucidate the processes characterizing the transition from an early TTG – greenstone regime to a granite-granulite regime with turbidites as the most abundant supracrustal lithology, or more simply to evaluate the transition from classical Paleo- to Neoproterozoic tectonics to an incipient neo-plate-tectonic regime;
2. To evaluate the relationships, if any, that may exist among the Paleo- to Neoproterozoic '*protocratonic*' blocks of the Central Slave Basement Complex and the Snare River terrane and to determine to what extent these older blocks controlled the sequence of crustal evolution in the Snare River terrane.
3. To investigate the juxtaposed low- and high-grade domains of the Snare River terrane in the context of present understanding of crustal sections and to investigate, using the multidisciplinary datasets, the associations that exist between the two crustal levels. A major focus is to document the sequence of

crust-formation and subsequent reworking as it occurs within the contrasting mid- and upper-crustal levels;

Six principal datasets are presented in this study: (a) the results of 1:30 000 scale mapping across from the upper-crustal Kwejinne Lake Supracrustal Belt to the Eastern Boundary Fault Ghost sub-domain; (b) detailed zircon U-Pb crystallization ages of 13 magmatic rocks selected on the basis of well-defined cross-cutting relationships observed in the field; (c) structural data that constrain the deformational and fabric-formation history of the Snare River terrane; (d) geochemical and Sm-Nd isotopic datasets for the principal magmatic suites; (e) inherited zircon age data determined for a suite of nine plutons that punctuate the different stages of evolution of the region, and (f) the results of zircon saturation thermometry determined for representative magmatic suites to characterize thermal behaviour of magmatism during crustal evolution. The six datasets serve to characterize the major temporal, geochemical, architectural, thermal and tectonic conditions that prevailed during crustal evolution. Moreover, each chapter provides an independent analysis of each of these features / processes in order to (i) assess the degree of reproducibility in the sequence of crustal evolution as revealed by each dataset, and (ii) to investigate the interconnections between each dataset.

Finally, it is hoped that the research presented will highlight a spectacular, previously little-known, Neoproterozoic HT-LP crustal terrane in which some of the deepest and hottest exhumed exposures of mid-crustal rocks in the Slave Province have retained their first-order compositional, temporal, geochemical and geometric relationships to adjacent exposures of the upper crust.

1.5.2 Thesis outline

The thesis is arranged into seven chapters and related appendices. Field and analytical datasets collected for the Snare River terrane are presented in chapters 2 to 6 and major conclusions and impacts of this study in addition to suggestions for future work are provided in chapter 7.

Chapter 2 presents the results of 1:30 000 scale field mapping and U-Pb zircon geochronology from 13 representative magmatic units and a detrital zircon study. The chapter serves as a broad overview of the geology and field relationships in the Snare River terrane and establishes the absolute time frame for the major deformation and metamorphic events. With respect to the zircon geochronology, all samples were extensively imaged prior to analysis by one of two methods, conventional isotope dilution - thermal ionization mass spectrometry (ID-TIMS) and/or laser ablation microprobe inductively coupled plasma - mass spectrometry (LAM ICP-MS), in order to constrain crystallization ages in the complex zircon populations. Integration of the relative sequence of pluton emplacement from field observations with the absolute ages derived from U-Pb geochronology field provides the necessary data to construct the crustal stratigraphy for the Snare River terrane.

Chapter 3 examines the polyphase deformation history and deformation mechanics that account for the structural evolution of the upper- and mid-crust in the Snare River terrane, with particular attention paid to the significance of metamorphic isograd patterns, the contrast between the steep upper-crustal and shallow mid-crustal

structures, and metamorphic and structural diachroneity between different crustal levels. Deformation histories are documented for the upper and mid crust and the intervening transition zones. The chapter concludes by presenting a model that resolves the seemingly disparate structural behaviour of the exposed crustal levels in the Snare River terrane.

Chapter 4 presents major- and trace-element geochemistry and Sm-Nd isotopic data for the plutons that intrude the Snare River terrane in order to investigate crustal and mantle evolution during crust formation and subsequent orogenic evolution. All analysed samples were previously dated, adding a temporal dimension to the understanding of the chemical evolution of the various suites. The aim is to employ a systematic geochemical evaluation of magmatism at different times and crustal levels to define the processes that controlled early TTG – greenstone genesis and subsequent granitic magmatism during the ensuing incipient plate tectonic regime. Secular variations in ϵNd are used to evaluate the role played by Paleo- to Mesoarchean basement during the Neoproterozoic magmatic evolution of the Snare River terrane.

Chapter 5 presents a new method to characterize the evolution of both the cryptic (unexposed) lower crust and orogenic mid-crust by studying inherited zircon populations in plutons that intruded at different stages of crustal development. U-Pb analyses of the inherited cores of zircons by LAM ICP-MS from five metaluminous and four peraluminous plutons are presented in order to evaluate the secular evolution of the lower and mid crust with time, and to determine linkages with the Central Slave Basement Complex on the basis of published geochronological data. The chapter concludes with a

demonstration of how inherited zircon datasets may be applied to enhance interpretation of magmatic ϵNd values.

Chapter 6 utilizes the zircon saturation thermometer of Watson and Harrison (1983), whole-rock geochemical data from magmatic suites across the Snare River terrane, and zircon Back Scattered Electron (BSE) and transmitted light image database to determine magma crystallization temperatures. Integration of these results with U-Pb age data and the crustal stratigraphy constructed in Chapter 2 permits: (i) an assessment of the secular magmatic variations that occurred during crustal evolution and a consideration of the implications with regard to magma petrogenesis, and (ii) an evaluation of the controls of *HT-LP* metamorphism at different crustal levels, specifically a qualitative understanding of the magnitude of heat advection at different crustal levels. Together, these temporal and spatial observations allow for a first-order characterization of the thermal stratigraphy the Snare River terrane.

Chapter 7 summarizes the main contributions and conclusions of this study with regard to the current understanding of Neoproterozoic geology and suggests where future work in the Snare River terrane will enhance and build on the major findings presented in this thesis.

1.5.3 Appendices

A comprehensive suite of appendices (A – R) is provided with the thesis. Unless otherwise indicated, all digital appendices are provided in PDF format.

Appendix A presents LAM ICP-MS zircon crystallization U-Pb age data for samples discussed in chapter 2. Appendix B provides supplementary information on the phenomenon of reverse discordance in some of the LAM ICP-MS analyses. U-Pb dating by LAM ICP-MS is an actively evolving field of research in geochronology and the data presented in this study provide novel documentation on the phenomenon of reverse discordance and its possible causes. Appendix C provides detail on the construction of a size-weight reference chart designed by the author, which became crucial to estimate zircon grain weights after BSE imaging and prior to dissolution during the ID-TIMS procedure. Appendix D outlines the analytical techniques used to generate major- and trace-element and Sm-Nd isotopic data presented in Chapter 4. Detailed petrographic descriptions of the magmatic rocks discussed in chapters 2, 4 and 5 are given in Appendix E. Inherited zircon U-Pb age data tables and inherited zircon age populations descriptions, the subject of Chapter 5, are presented in Appendices F and G. Appendix H outlines the methodology for ϵ Nd modelling using inherited zircon and geochemical datasets. Appendix I provides supplementary data on metamorphic assemblages, isograd reactions, petrogenetic grids and P - T data for metamorphic rocks across the Snare River terrane. Description of zircon saturation thermometry results is given in Appendix J. Appendix K provides descriptions and UTM co-ordinates of all samples collected during the study. Appendix L is a supplementary report completed during the course of LAM ICP-MS data collection. Significant advances were made as a result of this study to increase the precision, accuracy and spatial resolution of the laser dating technique conducted at Memorial University of Newfoundland. The report addresses some of the

problems that were encountered and the developments that were achieved during the period of data collection. Appendix M is an integrated digital database that presents all BSE images, laser pit localities and representative SEM images of laser pit morphologies for the zircon grains analyzed by the LAM ICP-MS technique during the course of this study. Appendix N includes the two versions of the original Ph.D. project proposal submitted in at the onset of the research. Appendix O integrates all field data, related field photographs, polished slab and thin section images into an integrated digital database. Appendix P outlines the current (at time of writing) publications related to the Snare River terrane, including conference abstracts and associated poster and oral presentations. Appendix Q presents two INAC reports, compiled by the author, which were completed to accompany the 1:50 000 scale government mapping project. Appendix R (in the map pocket at the back of the thesis) is a 1:125 000 copy of the NWT open file 2003 – 2004: *Compilation of the Geology of the Snare River Area (1998 – 2002 results)*.

1 References

- Anderson, D.L., 1979. Upper mantle transition region – Eclogite: *Geophysical Research Letters*, **6**: 433- 436.
- Ashwal, L.D., Morgan, P., and Hoisch, T.D., 1992. Tectonics and heat sources for granulite metamorphism of supracrustal bearing terranes. *Precambrian Research*, **55**: 525-538.
- Atherton, M.P., and Petford, N., 1993. Generation of Na rich magmas from newly underplated basaltic crust. *Nature*, **362**: 144 – 146.
- Barley, M.E and Groves, D.J., 1990. Deciphering the tectonic evolution of Archean greenstone belts: the importance of contrasting histories to the distribution of mineralization in the Yilgarn Craton, Western Australia. *Precambrian Research*, **44**: 3-20.
- Bedard, J.H., Brouillette, P., Madore, L., and Berclaz A., 2003. Archean cratonization and deformation in the Superior Province Canada: an evaluation of plate tectonic versus vertical tectonic models. *Precambrian Research*, **127**: 61 - 87.
- Bennett, V., Jackson, V.A., Rivers, T., Relf, C., Horan, P and Tubrett, M, 2005. Geology and U-Pb Geochronology of the Late Archean Snare River Terrane: Tracking Evolving Tectonic Regimes and Crustal Growth Mechanisms. *Canadian Journal of Earth Sciences, Lithoprobe SNORCLE Special Edition* **42**: 895-934.
- Black, L.P., Williams, I.S., and Compston, W., 1986. Four zircon ages from one rock: the history of a 3930 Ma – old granulite from Mt Sones, Enderby Land Antarctica. *Contributions to Mineralogy and Petrology*, **94**: 427 – 437.
- Bleeker W., Ketchum, J.W.F., Jackson, V.A., and Villeneuve, M.E. 1999a. The Central Slave Basement, Part I: its structural topology and autochthonous cover. *Canadian Journal of Earth Sciences*, **36**: 1083-1109.
- Bleeker W., Ketchum, J.W.F., and Davis, W.J. 1999b. The Central Slave Basement, Part II: Age and tectonic significance of high strain zones along the basement-cover contact. *Canadian Journal of Earth Sciences*, **36**: 1111-1130.
- Bleeker, W., 2002. Archean tectonics: a review, with illustrations from the Slave craton. *Geological Society of London Special Publication* **199**: 151 - 181
- Bohlar, R., 2001. Archean Mafic Magmatism and Crust Formation in the Eastern Pilbara Craton (Western Australia) and Belingwe Greenstone Belt (Zimbabwe). Unpublished Ph.D. Thesis, University of Melbourne.
- Bohlen, S.R., and Mezger, K., 1989. Origin of granulite terranes and the formation of the

- lowermost continental crust. *Science*, **222**: 326-329
- Bowring, S.A., Williams, I.S., and Compston, W. 1989. 3.96 Ga gneisses from the Slave Province Canada, Northwest Territories, Canada. *Geology*, **17**: 971-975
- Bowring, S.A. and Housh, T.B., 1995. Earth's early evolution: *Science*, **269**: 1535-1540.
- Bowring, S.A., and Williams, I.S., 1999. Priscoan (4.00 – 4.03 Ga) orthogneisses from northwestern Canada: *Contributions to Mineralogy and Petrology*, **134**: 3-16.
- Buick, R., Thronett, J.R., McNaughton, N.J., Smith, J.B., Barley, M.E., and Savage, M., 1995. Record of emergent continental crust ~ 3.5 billion years ago in the Pilbara craton of Australia. *Nature*, **375**: 574 - 577
- Cairns, S., Relf, C., MacLachlan, K., and Davis, W., 2005. Late Archean decoupling of upper and mid crustal tectonothermal domains in the southeast Slave Province; evidence from the Walmsley Lake area. *Canadian Journal of Earth Sciences, Lithoprobe SNORCLE Special Edition* **42**: 869-894.
- Campbell, I.H., and Hill, R.I., 1988. A two-stage model for the formation of the granite-greenstone terrains of the Kalgoorlie-Norseman area, Western Australia. *Earth and Planetary Science Letters*, **90**: 11–25.
- Chacko, T., Creaser, R.A., Farquar, J., and Muehlenbachs, K., 1995. The deep crust of the western Slave Province - initial petrological and isotopic data from the high grade rocks of the Ghost Domain. SNORCLE, lithoprobe report, **44**: 4 -7.
- Chadwick, B., Vasudev, V.N., Hegde, G.V., 2000. The Dharwar craton, southern India, interpreted as the result of Late Archean oblique convergence. *Precambrian Research*, **99**: 91-111
- Compston, W., and Pidgeon, R.T., 1986. Jack Hills evidence of more very old zircons in Western Australia. *Nature*, **321**: 766 - 769
- Condie, K.C., 1981. Archean Greenstone Belts. *Developments in Precambrian Geology* 3, Elsevier, Amsterdam
- Condie, K.C., 1993. Chemical composition and evolution of the upper continental crust: contrasting results from surface samples and shales. *Chemical Geology* **104**: 1- 37
- Condie, K., 1994. Greenstones through time, In: K.C. Condie (Editor), *Archean Crustal Evolution*, Elsevier, Amsterdam, pp. 85-120.
- Condie, K.C., 1995. Episodic ages of greenstones: a key to mantle dynamics? *Geophysical Research Letters*, **22**: 2215 – 2218.
- Condie, K.C. 1997. Contrasting sources for upper and lower continental crust: The greenstone connection. *The Journal of Geology*, **105**: 729 – 736.

- Corfu, F., 1987. Inverse age stratification in the Archean crust of the Superior Province: Evidence for infra- and subcrustal accretion from high resolution U-Pb zircon and monazite ages. *Precambrian Research*, **36**: 259 – 275.
- Culshaw, N.G., Beaumont, C., and Jamieson, R.A. 2004. Geodynamic models of contrasting structural styles and ages in the upper- and lower- crust of collisional orogens: resolution of the structural vs. seismic paradox. GAC - MAC Joint annual meeting, St Catharines, program and abstracts v.29, p331.
- Davies, G.F., 1992. On emergence of plate tectonics. *Geology*, **20**: 963 – 966.
- Davies, G.F., 1995. Punctuated tectonic evolution of the earth. *Earth and Planetary Science Letters*. **136**: 363-379
- Davis, W.J., and Hegner, E., 1992. Neodymium isotopic evidence for the tectonic assembly of the Late Archean crust in the Slave Province, northwest Canada. *Contributions to Mineralogy and Petrology*, **111**: 493 - 504.
- Davis, W.J., and Bleeker, W., 1999. Timing of plutonism, deformation and metamorphism in the Yellowknife Domain, Slave Province, Canada. *Canadian Journal of Earth Sciences*, **36**: 1169-118
- Davis, W.J., Gariépy, C., and van Breeman, O., 1996. Pb isotopic composition of late Archean granites and the extent of recycling early Archean crust in the Slave Province, northwest Canada. *Chemical Geology*, **130**: 255-269.
- de Wit, M.J., Hart, R.A., and Hart, R.J., 1987. The Jamestown Ophiolite complex, Barberton Mountain Belt: a section through 3.5 Ga oceanic crust. *Journal of African Earth Sciences*, **5**: 681 - 730
- de Wit, M.J., Roering, C., Hart, R.J., Armstrong, R.A., de Ronde, C.E.J., Green, R.W.E., Tredoux, M., Peberdy, E., and Hart, R.A., 1992. Formation of an Archean continent. *Nature*, **357**:553-562
- de Wit, M.J., 1998. On Archean granites, greenstones, cratons and tectonics: does the evidence demand a verdict? *Precambrian Research*, **91**: 181 - 226
- Drummond, M.S., and Defant. M.J., 1990. A model for trondhjemite-tonalite-dacite genesis and crustal growth via slab melting: Archean to modern comparisons, *Journal of Geophysical Research*, **95**: 21 503 – 21 522.
- Emon, K.E., Jackson, V.A., and Dunning, G.R., 1999. Geology and U-Pb geochronology of the Eukok Uplift: a pre-2.8 Ga basement terrane in the northwestern Slave Structural Province, Northwest Territories, Canada. *Canadian Journal of Earth Sciences*, **36**: 1061-1082.
- England, P.C. and Thompson, A.B., 1984. Pressure - temperature time paths of regional

- metamorphism 1. Heat transfer during the evolution of regions of thickened continental crust. *Journal of Petrology*, **25**: 894-928.
- Eriksson, K.A., 1995. Crustal growth, surface processes and atmospheric evolution on the early Earth. In: M.P. Coward and A.C. Ries (Editors), *Early Precambrian Processes*, Geological Society, Special Publication **95**: 11-25.
- Eriksson, K.A., and Fedo, C.M., 1994, Archean synrift and stable-shelf successions. In: K.C. Condie (Editor), *Archean Crustal Evolution*: Elsevier, p. 171-204.
- Eriksson, K.A., Krapez, B. and Fralick, P.W., 1997. Sedimentological aspects of greenstone belts. In: de Wit, M.J. and Ashwal, L. (Editors.), *Tectonic Evolution of Greenstone Belts*. Oxford University Press, p. 33-54.
- Farquhar, J., Snavely, J.A., and Chacko, T., 1993. Granulite facies metamorphism near Ghost Lake area, NWT. GAC - MAC Joint annual meeting, program and abstracts V18, pA-28.
- Farquhar, J., and Chacko, T., 1996. Thermobarometry of high-temperature granites and granulites of the western Slave Province, District of Mackenzie, NWT, Canada. In 1996 spring Meeting, EOS, American Geophysical Union, V. 77, no. 17, supplement, p 283 – 284.
- Frei, R., and Kastbjerg Jensen, B., 2003. Re-Os, Sm-Nd and REE systematics on ultramafic rocks and pillow basalts from the Earth's oldest oceanic crustal fragments (Isua Supracrustal Belt and Ujargssuit nunat area, western Greenland). *Chemical Geology*, **196**: 163 – 191.
- Frei, R., Polat, A., and Meiborn, A., 2004. The Hadean upper mantle conundrum; Evidence for source depletion and enrichment from Sm-Nd, Re-Os, and Pb isotopic compositions in the 3.71 Gy boninite-like metabasalts from the Isua Supracrustal Belt, Greenland. *Geochimica et Cosmochimica Acta*, **68**: 1645 – 1660.
- Folinsbee, R.E., 1940. Gem cordierite from the Great Slave Lake area, N.W.T., Canada; *American Mineralogist*, **25**: 216.
- Folinsbee, R.E., 1941a. The chemical composition of garnet associated with cordierite. *American Mineralogist*, **26**: 50 - 53.
- Folinsbee, R.E., 1941b. Optic properties of cordierite in relation to alkalies in the cordierite - beryl structure. *American Mineralogist*, **26**: 485 - 500.
- Fountain, D.M., and Salisbury, M.H., 1981. Exposed cross-sections through the continental crust: implications for crustal structure, petrology, and evolution. *Earth and Planetary Science Letters*, **56**: 263 – 277.
- Frost, B.R., and Chacko, T. 1989. The granulite uncertainty principle: limitations on

- thermobarometry in granulites. *Journal of Geology*, **97**: 435 – 450.
- Geological Survey of Canada, 1963. Ghost Lake, District of Mackenzie, Northwest Territories; Aeromagnetic Series. Geological Survey of Canada, Geophysics Paper 2955, Map 2955G, (scale 1:50 000).
- Green, M. G., Sylvester, P.J., and Buick R., 2000. Growth and recycling of early Archean Continental crust: geochemical evidence from the Coonterunah and Warrawoona Groups, Pilbara Craton, Australia. *Tectonophysics*, **322**: 69 – 88.
- Griffin, W.L., O'Reilly, S.Y., Abe, N., Aulbach, S., Davies, R.M., Pearson., N.J., Doyle, B.J., and Kivi, K., 2003. The origin and evolution of Archean lithospheric mantle. *Precambrian Research*, **127**: 19 - 41.
- Hamilton, W.B., 1998. Archean magmatism and deformation were not the products of plate tectonics. *Precambrian Research*, **91**: 143 – 179
- Harley, S.L., 1989. The origins of granulites: a metamorphic perspective. *Geological Magazine*, **126**: 215 – 247.
- Hart, R.J., Welke, H.J., and Nicolaysen, L.O., 1981. Geochronology of the deep profile through Archean basement of the Vredefort structure. *Journal of Geophysical Research*, **86**: 10663 – 10 680
- Henderson, J.B., 1981. Archean basin evolution in the Slave Province, Canada. In; A. Kroner (Editor) *Precambrian Plate Tectonics*, Elsevier, Amsterdam, pp. 213-236.
- Henderson, J.B., 1994. Geology of the Wijinnedi Lake area - a Palaeoproterozoic (?) asymmetrical uplift of Archean rocks in the southwestern Slave Province, District of Mackenzie, NWT; In: *Current Research 1994-C*; GSC, p71-79.
- Henderson, J.B., 1998. Preliminary geology, Wijinnedi Lake area, District of Mackenzie, NWT, GSC, Open file 3609, scale 1:50 000.
- Henderson, J.B., and Schaan, S.E., 1993. Geology of the Wijinnedi lake area : a transect into mid-crustal levels in the western Slave Province, District of Mackenzie, Northwest Territories. In: *Current Research 1993-C*; GSC, p83-91.
- Henderson, J.B., and Chacko, T., 1995. A reconnaissance of the high grade metamorphic terrane south of Ghost Lake, southweatern Slave Province, Northwest territories. In: *Current Research 1995-C*; GSC, p77 - 85.
- Henry, D.J., and Dokka, R.K., 1992. Metamorphic evolution of exhumed middle and lower crustal rocks in the Mojave extensional belt, southern California, USA. *Journal of Metamorphic Geology* **10**: 347-364.
- Hokada, T., Misawa, K., Shiraishi, K., and Suzuki, S., 2003. Mid to late Archean (3.3 –

- 2.5 Ga) tonalitic crustal formation and high-grade metamorphism at Mt Riiser-Larsen, Napier Complex, East Antarctica. *Precambrian Research*, **127**: 215 - 228
- Horstwood, M.S.A., Nesbitt, R.W., Noble., S.R., and Wilson, J.F., 1999. U-Pb zircon evidence for an extensive early Archean Craton in Zimbabwe: a reassessment of the timing of craton formation, stabilization and growth. *Geology*, **26**: 883 – 886.
- Isachsen, C.E., Bowring, S.A., and Padgham, W.A., 1991. Geochronology of the Yellowknife Volcanic Belt, N.W.T., Canada : new constraints on the timing and duration of greenstone belt magmatism. *Journal of Geology*, **99**: 55 - 67.
- Isachsen, C.E., and Bowring, S.A., 1994. Evolution of the Slave craton. *Geology*, **22**: 917 – 920.
- Jackson, V.A., 2003. Preliminary compilation of the geology of the Snare River (1998-2002 results), Winjinnedi Lake, Labrish Lake and Russell Lake area; parts of 85N and 85O. C.S. Lord Northern Geoscience Centre, Yellowknife, NT. NWT Open Report 2003-002. Map, scale 1:100 000.
- Jamieson, R.A., Beaumont, C., Fullsack, P., and Lee, B., 1998. Barrovian regional metamorphism: where's the heat? In: Treloar, P.J., and O'Brien, P.J. (eds). What drives metamorphism and Metamorphic reactions? Geological Society, London, Special Publications **138**, 23-51.
- Kamber, B.S., Biino, G.G., Wijbrans, J.R., Davies, G.R., and Villa, I.M. 1996. Archean granulites of the Limpopo Belt, Zimbabwe: One slow exhumation or two rapid events? *Tectonics*, **15**: 1414- 1430
- Kelly, N.M., Clarke, G.L., Carson, C.J., & White, R.W., 2000. Thrusting in the lower crust: evidence from the Oygarden Islands, Kemp Land, East Antarctica. *Geological Magazine*, **137**: 219-234
- Ketchum, J., and Bleeker, W. 1999. The Central Slave Cover Group and Central Slave Basement Complex: a progress report on U-Pb geochronological studies, *In* Slave – Northern Cordillera Lithospheric Evolution Workshop (SNORCLE) Transect and Cordilleran Tectonics Workshop Meeting, 5 – 7 March, Calgary. *Compiled by* F. Cook and P. Erdmer. Lithoprobe Report 69, pp. 21-29.
- Ketchum, J., and Bleeker, W. 2000. New field and U-Pb data from the Central Slave Cover Group near Yellowknife and the Central Slave Basement Complex at Point Lake, *In* Slave – Northern Cordillera Lithospheric Evolution Workshop (SNORCLE) Transect and Cordilleran Tectonics Workshop Meeting, 25 – 27 February, Calgary. *Compiled by* F. Cook and P. Erdmer. Lithoprobe Report 72, pp. 27-31.
- Kilpatrick, J.A., and Ellis, D.J., 1992. C-type magmas: igneous charnockites and their extrusive equivalents. *Transactions of the Royal Society of Edinburgh, Earth Sciences*, **83**: 155 – 164.

- King, J., and Helmstaedt, . 1997. The Slave Province, North West Territories, Canada. *In*: J.M. De Wit and L.D. Ashwal (Editors), *Greenstone Belts. Oxford Monographs on geology and geophysics*, no.35, Oxford Science Publications, Oxford, pp 459-479.
- Komiya, T., Maruyama, S., Masuda, T., Nohda, S., Hayashi, M., and Okamoto, K., 1999. Plate Tectonics at 3.8 -3.7 Ga: Field Evidence from the Isua Accretionary Complex, Southern West Greenland. **107**: 515 – 554.
- Krapez, B., and Barley, M.E., 1987. Archean strike-slip faulting and related ensialic basins: Evidence from the Pilbara Block, Australia. *Geological Magazine* **124**: 555-567.
- Krapez, B., 1989. Depositional styles and geotectonic settings of Archean metasedimentary sequences: evidence from the Lalla Rookh basin, Pilbara Block, Western Australia. Unpublished Ph.D. thesis, University of Western Australia, Nedlands.
- Kramers, J.D., Kreissig, K., and Jones, M.Q.W., 2001. Crustal heat production and style of metamorphism between two Archean high grade provinces in the Limpopo Belt, southern Africa. *Precambrian Research*, **112**: 149 – 163.
- Krogh, T.E., 1993. High precision U-Pb ages for granulite metamorphism and deformation in the Archean Kapuskasing structural zone, Ontario: implications for structure and development of the lower crust. *Earth and Planetary Science Letters*, **119**: 1 – 18.
- Krogh, T.E., and Moser, D.E. 1994. U-Pb zircon and monazite ages from the Kapuskasing Uplift: age constraints on deformation within the Ivanhoe Lake fault zone. *Canadian Journal of Earth Sciences*, **31**: 1096 – 1103.
- Krogstad, E.J., Hanson, G.N., and Rajamani, V., 1995. Sources of continental magmatism adjacent to the late Archean Kolar Suture Zone, South India: distinct isotopic and elemental signatures of two late Archean magmatic series. *Contributions to Mineralogy and Petrology*, **122**: 159 – 173.
- Kroner, A., Byerly, G.R., and Lowe, D.R., 1992. Chronology of early Archean granite – greenstone evolution in the Baberton Mountain Land, South Africa, based on precise dating by single zircon evaporation. *Earth and Planetary Science Letters*, **103**: 41-54.
- Kusky, T.M., and Polat, A., 1999. Growth of granite – greenstone terranes and convergent margins and stabilization of Archean cratons. *Tectonophysics*, **305**: 43 –73.
- Lana, C., Gibson, R.L., Kisters, A.F.M., and Reimold. W.U., 2003. Archean crustal structure of the Kaapvaal craton, South Africa – evidence from the Vredefort dome. *Earth and Planetary Science Letters*, **206**: 133 – 144.
- Langford, F.F., and Morin, J.A., 1976. The development of the Superior Province northwestern Ontario by merging island arcs. *American Journal of Science*, **276**: 1023 – 1034.

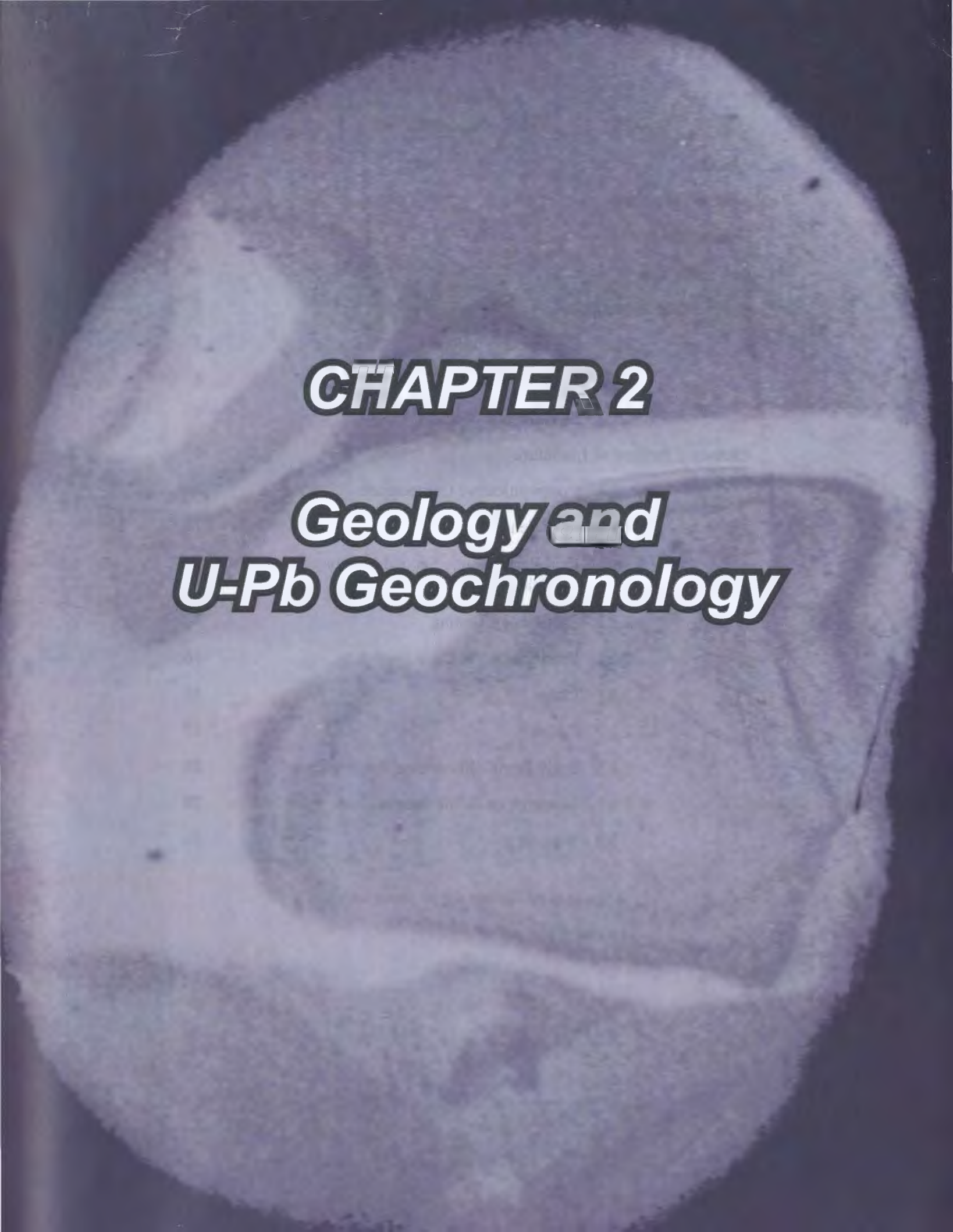
- Legault, M.I. & Hattori, K., 1994. Provenance of igneous clasts in conglomerates of the Archean Timiskaming Group, Kirkland Lake area, Abitibi greenstone belt, Canada, *Canadian Journal of Earth Science*, **31**: 1749-1762
- Lord, C.S. 1942. Snare and Ingray Lake map areas, Northwest Territories. Geological Survey of Canada, Memoir 235.
- Martin, H. 1986. Effect of steeper Archean geothermal gradient on geochemistry of subduction zone magmas. *Geology* **14**: 753 – 756.
- Martin, H. 1987. Petrogenesis of Archean trondhjemites, tonalites and granodiorites from eastern Finland: Major and trace element geochemistry. *Journal of Petrology* **228**: 921-953.
- Martin, H., 1994. The Archean gneisses and genesis of the continental crust. In Condie, K.C., (Ed), *Archean Crustal Evolution*: Amsterdam, Elsevier, 205-259.
- Martin, H., and Moyen, J-F., 2002. Secular changes in tonalite - trondhjemite – granodiorite composition as markers of the progressive cooling of Earth. *Geology*, **30**: 319 – 322.
- McGlynn, J.C., and Ross, J.V., 1962. Geology, Basler Lake, District of Mackenzie, Geological Survey of Canada, Map 18-1962, 1 inch to 1 mile map with marginal notes.
- Mezger, K., 1992. Temporal evolution of regional granulite terranes: Implication for the formation of the lowermost continental crust. In: D.M. Fountain, R. Arculus and R.W. Kay (Editors), *Continental Lower Crust*. Elsevier, Amsterdam, pp. 447 – 478.
- Mortensen, J.K., Thorpe, R.I., Padgham, W.A., King, J.E. and Davis, W.J., 1988. U-Pb zircon ages for felsic volcanism in the Slave Province, N.W.T., In *Radiogenic age and isotopic studies: Report 2*. Geological Survey of Canada, Paper 88-2, pp 85-95.
- Moser, D.E. 1994. The geology and structure of the mid-crustal Wawa gneiss domain: a key to understanding tectonic variation with depth and time in the late Archean Abitibi-Wawa orogen. *Canadian Journal of Earth Sciences*, **31**: 1064-1080.
- Moser, D.E., Heaman, L.M., and Krogh, T.E., 1996. Intracrustal extension of an Archean Orogen revealed using single grain U-Pb zircon geochronology. *Tectonics*, **15**: 1093 – 1109.
- Moyen, J.-F., Martin, H., Jayananda, M, and Auvray, B., 2003. Late-Archean granites: a typology based on the Dharwar Craton (India). *Precambrian Research* **127**: 103 - 123.
- Nutman, A.P., Friend, C.R.L., Kinny, P.O., and McGregor, V.R., 1993. Anatomy of an early Archean gneiss complex: 3900 to 3600 Ma crustal evolution in southern West Greenland. *Geology*, **21**: 415 – 418.
- Nutman, A.P., Bennett, V.C., Friend, C.R.L., and Rosing, M.T., 1997. Approximately

- ~3710 and >3790 Ma volcanic sequences in the Isua (Greenland) Supracrustal Belt; structural and Nd isotope implications. *Chemical Geology*, **141**: 271 - 287.
- Padgham, W.A., and Fyson, W.K. 1992. The Slave Province: a distinct Archean craton. *Canadian Journal of Earth Sciences*, **29**: 2072 – 2086.
- Parman, S.W., Dann, J.C., Grove T.L., and de Wit, M.J., 1997. Emplacement conditions of komatiite magmas from the 3.49 Ga Komati formation, Barberton Greenstone belt, South Africa. *Earth and Planetary Science Letters*, **150**: 303 – 323.
- Percival, J.A., 1994. Archean high grade metamorphism. In : K.C. Condie (Ed), *Archean crustal evolution*, chapter 9. *Developments in Precambrian Geology* 11. Elsevier, Amsterdam, pp 357 - 409.
- Percival, J.E., and Card, K.D., 1983. Archean crust as revealed in the Kapuskasing uplift, Superior Province, Canada, *Geology*, **11**: 323 - 326
- Percival, J.A., and West, G.F., 1994. The Kapuskasing Uplift: a geological and geophysical synthesis. *Canadian Journal of Earth Science*, **31**: 1256 – 1286
- Percival, J.A., Fountain, D.M., and Salisbury, M.H., 1992. Exposed crustal cross sections as windows on the lower crust. In D.M. Fountain and R.J. Arculus and R.W. Kay (eds). *Continental lower crust*. Elsevier, Amsterdam, pp. 317 – 362.
- Percival, J.A., Roering, C., van Reenen, D.D., and Smit, C.A., 1997. Tectonic Evolution of Associated Greenstone Belts and High-Grade Terrains. In: de Wit MJ and Ashwal LD (eds), *Greenstone belts*. Oxford University Press, pp 398 – 420.
- Percival, J.A., Stern, R.A. and Skulski, T., 2001. Crustal growth through successive arc magmatism; reconnaissance U-Pb SHRIMP data from northeastern Superior Province, Canada. *Precambrian Research*, **109**: 203 – 238.
- Pehrsson, S.J., 1998. Deposition, deformation and preservation of the Indin Lake supracrustal belt, Slave Province, Northwest Territories. Unpublished Ph.D. thesis, Queens University, Kingston, Ontario.
- Pehrsson, S.J., Chacko, T., Pilkington, M., Villeneuve, M.E. and Bethune, K., 2000. Anton terrane revisited: Late Archean exhumation of moderate-pressure granulite terrane in the western Slave Province. *Geology*, **28**: 1075-1078.
- Perks, M.A., 1997. The mid crust of the western Slave Province - Geological Mapping, geochemistry and U - Pb Geochronology of the Forked Lake Area, Southwestern Slave Province, NWT. Masters Thesis, University of Alberta, 95p.
- Pollack, H.N., 1997, Thermal characteristics of the Archean Earth, in *Tectonic Evolution of Greenstone Belts*. In: M. deWit and L. Ashwal, (Editors), Oxford University Press, pp.223-232.

- Rapp, R.P., Watson, E.B., and Miller, C.F., 1991. Partial melting of amphibolite/eclogite and the origin of Archean trondhjemites and tonalites. *Precambrian Research*, **51**: 1 – 25.
- Rapp, R.P., Shimizu, N., Norman, M.D., and Applegate, G.S., 1999. Reaction between slab-derived melts and peridotite in the mantle wedge: Experimental constraints at 3.8 GPA. *Chemical Geology*, **160**: 335 – 356.
- Relf, C., 1992. Two distinct shortening events during late Archean orogeny in the west-central Slave Province, Northwest Territories, Canada. *Canadian Journal of Earth Sciences*, **29**: 2104 – 2117.
- Rey, P.F., Philippot, P., and Thebaud, N., 2003. Contribution of mantle plumes, crustal thickening and greenstone blanketing to the 2.75 – 2.65 Ga global crisis. *Precambrian Research*, **127**: 43-60
- Robertson, D.K., and Folinsbee, R.E., 1974. Lead Isotope ratios and crustal evolution of the Slave Craton at Ghost lake, Northwest Territories. *Canadian Journal of Earth Sciences*, **11**: 819 - 827.
- Sandiford, M.A., 1989a. Secular trends in the thermal evolution of metamorphic terranes. *Earth and Planetary Science Letters*, **95**: 85-96.
- Sandiford, M.A., 1989b. Horizontal structures in granulite terranes : A record of mountain building or mountain collapse? *Geology*, **17**: 449-452.
- Shirey, S.B., and Hanson, G.N., 1984. Mantle-derived Archean monzodiorites and trachyandesites. *Nature* **310**: 222-224.
- Sircombe, K.N., Bleeker, W. Stern, R.A., 2001. Detrital zircon geochronology and grain-size analysis of a ~ 2800 Ma Mesoarchean proto-cratonic cover succession, Slave Province, Canada. *Earth and Planetary Science Letters*, **189**: 207-220.
- Smithies, R.H., and Champion, D.C., 1999. Archean high-Mg diorite (sanukitoid) suite, Pilbara craton, Western Australia: petrogenesis and links to tonalite-trondhjemite-granodiorite and alkaline magmatism. *Journal of Petrology*, **41**: 1653 – 1671.
- Smithies, R.H., 2000. The Archean tonalite – trondhjemite – granodiorite (TTG) series is not an analogue of Cenozoic adakite. *Earth and Planetary Science Letters*, **182**: 115 – 125.
- Smithies, R.H., Champion, D.C., and Cassidy, K.F., 2003. Formation of Earth's early Archean continental crust. *Precambrian Research*, **127**: 203 – 238
- Springer, W., and Seck, H.A., 1997. Partial fusion of basic granulites at 5 to 15kbar: implications for the origin of TTG magmas. *Contributions to Mineralogy and Petrology*, **127**: 30 – 45.
- Stein, M., and Hofmann, A.W., 1994. Mantle plumes and episodic crustal growth.

- Nature, **372**: 63 – 68.
- Stern, R.A., and Hanson, G.N., 1991. Archean high-Mg granodiorite: a derivative of light Rare Earth Element enriched monzodiorite of Mantle origin. *Journal of Petrology*, **32**: 201-238.
- Stern, R.A., Hanson, G.N. and Shirey, S.B., 1989. Petrogenesis of mantle-derived, LILE-enriched Archean monzodiorite and trachyandesites (sanukitoids) in southwestern Superior Province. *Canadian Journal of Earth Sciences*, **26**: 1688 – 1712.
- Stevenson, R., Henry, P., and Gariépy, C., 1999. Assimilation-fractional crystallization origin of Archean Sanukitoid Suites: Western Superior Province, Canada. *Precambrian Research*, **96**: 83 – 99.
- Stubley, M.P., Jaegli, S., Bilben, S. & Tyler, T. 1995. Geology of the Nardin Lake area, south-central Slave Province, parts of NTS 85P/5&12, 85O/8&9. EGS Open File 1995-04. 1:50 000 map with marginal notes. Yellowknife: DIAND NWT Geology Division.
- Sylvester, P.J., 1994, Archean granite plutons. In: K.C. Condie (Editor), *Archean Crustal Evolution*, pp. 261-314, Elsevier Press, Amsterdam.
- Taylor, S.R., and McLennan, S.M., 1985. *The continental crust: Its composition and evolution*. Oxford, Blackwell Scientific Publications, 312p.
- Thompson, P.H. 1978. Archean regional metamorphism in the Slave Structural Province - a new perspective on some old rocks; *Metamorphism in the Canadian Shield*. Geological Survey of Canada, Paper 78-10, pp85 - 102.
- Thorpe, R.I., Cumming, G.L., and Mortensen, J.K., 1992. A significant Pb Isotope boundary in the Slave Province and its probable relation to ancient basement in the western Slave Province. In *Project Summaries, Canada - Northwest Territories Mineral Development Agreement 1987 - 91*. Geological Survey of Canada, Open File Report no. 2484: 179-184
- Tomlinson, K.Y., and Condie, K.C., 2001. Archean Mantle Plumes: evidence from greenstone belt geochemistry. *Geological Society of America, Special Paper* **352**: 341 – 357.
- Turkina, O.M., and Nozhkin, A.D., 2003. Genesis of Archean tonalite - trondhjemite – suites: Plume or subduction related? *Russian Journal of Earth Sciences*, **5**: 93 - 100.
- Valley, J.W., Peck, W.H., King, E.M and Wilde, S.A., 2002. A cool early Earth. *Geology*, **30**: 351 – 354.
- Villeneuve, M.E., and Henderson, J.B., 1998. U-Pb geochronology of the Wijinnedi Lake area, Slave Province, District of Mackenzie, NWT. In *Radiogenic Age and Isotopic studies: Report 11*. Geological Survey of Canada, 1998-F, pp. 99-106.

- Vlaar, N.J., van Keken, P.E., and van den Berg, A.P., 1994. Cooling of the earth in the Archean: *Earth and Planetary Science Letters*, **121**: 1 – 18.
- Watson, E.B., and Harrison, T.M., 1983. Zircon saturation revisited: temperature and composition effects in a variety of crustal magma types. *Earth Planetary Science Letters* **64**: 295-304.
- Wilde, S.A., Valley, J.W., Peck, W.H., and Graham, C.M., 2001. Evidence from detrital zircons for the existence of continental crust and oceans on the earth 4.4 gyr ago. *Nature*, **409**: 175 – 178.
- Wright, G.M., 1950. Ghost Lake map area, Northwest Territories; Geological Survey of Canada, Paper 50 -13, 10p.
- Wright, G.M., 1954. Ghost Lake, District of Mackenzie, NWT, GSC, Map 1021A.
- Yamashita, K., Creaser, R.A., Stemler, J.U. and Zimaro, T.W. 1999. Geochemical and Nd-Pb isotopic systematics of Late Archean granitoids, southwestern Slave Province, Canada: Constraints for granitoid origin and crustal isotopic structure. *Canadian Journal of Earth Sciences*, **36**: 1131-1147
- Zegers, T.E., and van Keken, P.E., 2001. Middle Archean continent formation by crustal delamination. *Geology*, **29**: 1083 – 1086.



CHAPTER 2

**Geology and
U-Pb Geochronology**

Appendix 2
Table of Contents

Abstract	ii
Acknowledgments	v
List of Tables	vi
List of Figures	vii
Chapter 1 Introduction	1
1.1 Background of Study	3
1.2 Purpose of Study	4
1.2 Significance of Study	5
Chapter 2 Review of Literature	7
2.1 Communicative Competence	7
2.2 Proficiency	11
2.2.1 Oral Performance/Second Language Proficiency	11
2.2.2 Proficiency Testing	13
2.2.3 Proficiency Testing Research	16
2.2.3.1 Cadre 1	16
2.2.3.2 Cadre 2	17
2.3 Early French Immersion Research	23
2.3.1 Research on Achievement	24
2.4 Summary	31

[Contents above are for example only!]

2 Geology and U-Pb Geochronology of the Late Archean Snare River Terrane: Tracking Evolving Tectonic Regimes and Crustal Growth Mechanisms.

V. Bennett¹, V. A. Jackson², T.Rivers¹, C. Relf², P. Horan^{1,3} and M. Tubrett¹

1. Department of Earth Sciences, Memorial University of Newfoundland, St. John's,
NL, A1B 3X5
2. NWT Geoscience Office, Yellowknife, NT, X1A 2R3
3. Now at: Department of Earth Sciences, Dartmouth College, 6105 Fairchild Hall,
Hanover, NH, 03755, USA

Canadian Journal of Earth Sciences, Lithoprobe SNORCLE

Special Edition, vol. 42: 895-934 (2005).

NWT Geoscience Office Contribution number 0008.

2.1 Abstract

U-Pb zircon crystallization ages determined by isotope dilution – thermal ionization mass spectrometry (ID-TIMS) and laser ablation microprobe – inductively coupled mass spectrometry (LAM ICP-MS) for thirteen intrusive units in the Neoproterozoic Snare River terrane (SRT) provide tight constraints on the timing of crust formation and orogenic evolution. Seven metaluminous plutons were emplaced over ~80 M.y. from ca. 2674-2589 Ma, whereas six peraluminous bodies were emplaced in a ~15 M.y. interval from ca. 2598-2585 Ma. A detrital zircon study yielded an age spectrum with peaks correlative with known magmatic events in the Slave Province, with the ca. 2635 Ma age of the youngest detrital population providing a maximum estimate for the onset of sedimentation. This age contrasts with evidence for pre-2635 Ma sedimentation elsewhere in the SRT, indicating that sedimentation was protracted and diachronous. Evolution of the SRT can be subdivided into four stages: (i) 2674-2635 Ma – formation of a metaluminous proto-arc in a TTG/granite-greenstone tectonic regime (TR1), coeval with early turbidite sedimentation; (ii) 2635-2608 Ma – continued turbidite sedimentation, D1/M1 juxtaposition of turbidites and proto-arc lithologies prior to ~2608 Ma, and metaluminous granitoid plutonism; (iii) 2608-2597 Ma – onset of TR2, collision of Snare proto-arc with Central Slave Basement Complex, D2/M2 crustal thickening and mid-crustal granulite-facies metamorphism synchronous with voluminous metaluminous and peraluminous plutonism; (iv) 2597-2586 Ma – orogenic collapse, D3/M3 mid-crustal uplift, granulite-facies metamorphism, and waning metaluminous and peraluminous

plutonism. The distribution of igneous rocks yields an 'orogenic stratigraphy' with an older upper crust underlain by a younger synorogenic mid-crust. These data can be used to provide constraints for the interpretation of the SNORCLE Lithoprobe transect.

Key Words: *Snare River terrane; Neoproterozoic; Slave Province; evolving tectonic regimes; ID TIMS; LAM ICP-MS; crustal stratigraphy.*

2.2 Introduction

The Neoproterozoic is a critical period in Earth evolution in which fundamental changes in the styles of tectonism, crust formation and reworking took place. For much of the Paleo- and Neoproterozoic, crustal growth principally occurred in a tectonic regime dominated by episodic formation and accretion of tonalite-trondhjemite-granodiorite (TTG) complexes and granite-greenstone terranes, referred to here as proto-arcs, with subordinate formation of thin platformal supracrustal sequences composed of ultramafic volcanics, fuchsite quartzite and banded iron formation (e.g. Eriksson and Fedo 1994; Buick et al. 1995; Horstwood et al. 1999). The gradual accumulation of buoyant crust is inferred to have culminated in the stabilization and emergence of differentiated crustal blocks that acted as nuclei for further crustal growth during the latest Neoproterozoic and into the Proterozoic. It appears likely that these crustal blocks were responsible for the change from the prevailing TTG / granite-greenstone styles of tectonism to an incipient plate tectonic regime involving the formation and reworking of crust through subduction, collision and extensional processes. Correspondingly, crustal products also changed. Thick successions of turbidites, bimodal volcanic sequences, voluminous granitic

plutonism and exhumed mid-crustal, high-grade terranes first appear abundantly in the Neoproterozoic. Although this change in tectonic regime probably took place over a period of several hundred million years across the Archean Earth as a whole, there is evidence locally, where appropriate parts of the geological record are preserved, that the change was geologically quite rapid. One such area is the Slave Province in northwestern Canada, in which an extensive record of Archean crustal growth is preserved.

In this paper we examine the Neoproterozoic evolution of the Snare River terrane, southwestern Slave Province, with the aim of documenting chronologically the transition from crustal growth in a TTG / granite-greenstone proto-arc regime to the emergence and interaction of stable crustal blocks that became nuclei for subsequent crustal growth in an incipient plate-tectonic regime.

2.3 Geological Setting

The Slave Province (Fig. 2.1) is a small Archean craton that preserves a record of crustal growth and reworking spanning more than 1.5 Ga. It consists of three lithologically and chronologically distinct crustal elements: (i) inliers and xenoliths of 4.06 - 2.8 Ga sialic basement terranes (Henderson et al. 1982; Frith et al. 1986; Lambert and van Breemen 1991; James and Mortensen 1992; Isachsen and Bowring 1997; Relf et al. 1994, 1999; Bleeker et al. 1999a; Emon et al. 1999), including the Acasta gneisses (Bowring et al. 1989; Stern and Bleeker 1998; Bowring and Williams 1999) and a sedimentary cover sequence known as the Central Slave Cover Group (Bleeker et al.

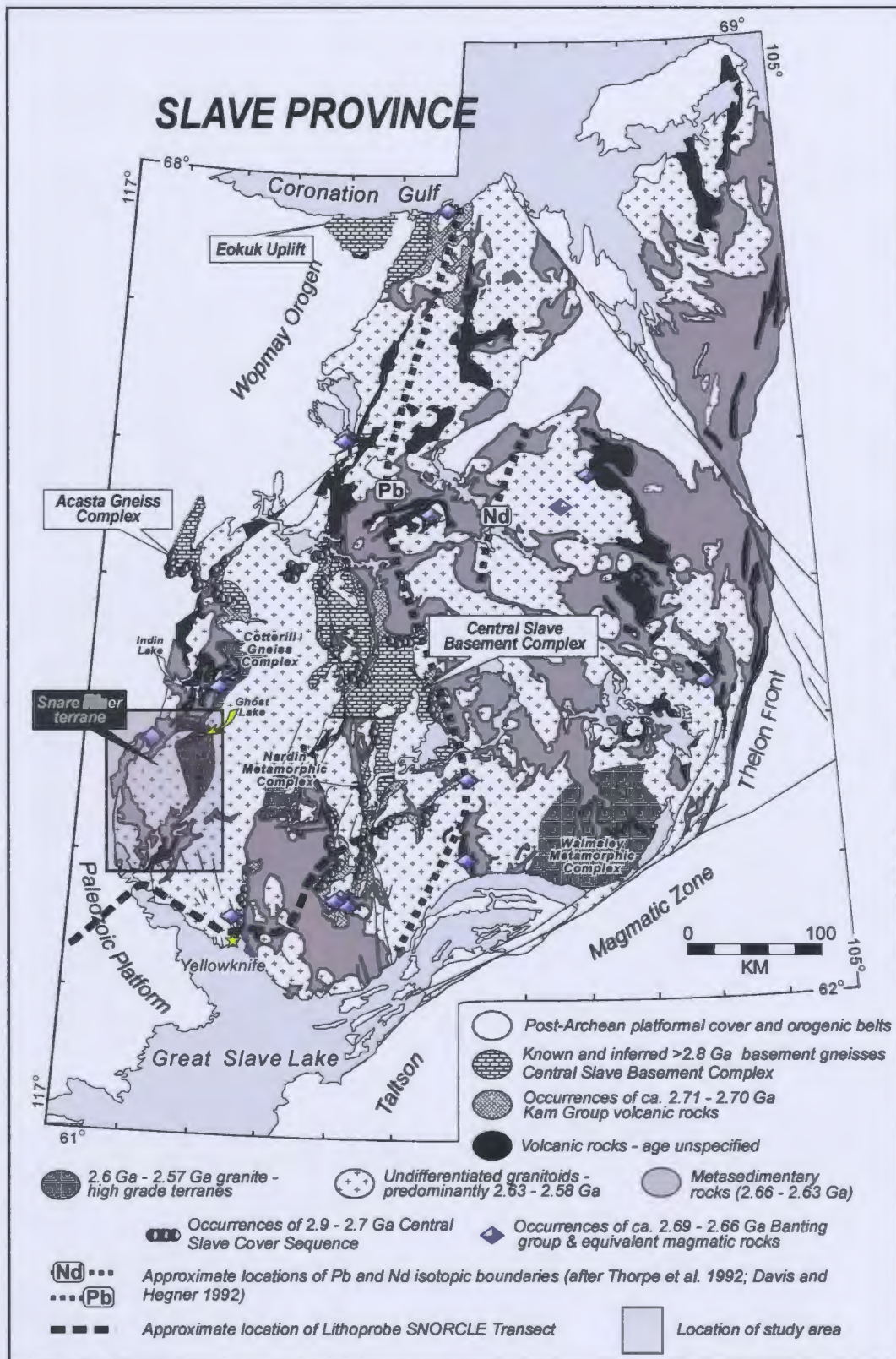


Figure 2.1: Simplified geological map of the Slave Province (modified after Bleeker et al. 1999) showing location of Snare River terrane and Figs. 2.2a and b.

1999a, b; Ketchum and Bleeker 1999, 2000; Sircombe et al. 2001); (ii) 2.71 - 2.65 Ga greenstone belts (Mortensen et al. 1988; Isachsen et al. 1991; Villeneuve et al. 1997); and (iii) widespread 2.62 - 2.58 Ga granitic plutons (Davis 1992; Davis et al. 1994; Davis and Bleeker 1999; van Breemen et al. 1992; Villeneuve et al. 1997). The Slave Province has been broadly subdivided on the basis of Pb and Nd isotopic signatures (Fig. 2.1; Thorpe et al. 1992; Davis and Hegner 1992; Davis et al. 1996) into a western domain composed of inliers and xenoliths of pre-2.8 Ga sialic material in 2.7-2.5 Ga crustally-contaminated magmatic rocks with negative ϵNd values and high $^{207}\text{Pb}/^{204}\text{Pb}$ ratios, and an eastern domain lacking pre-2.8 Ga basement inliers or contaminated geochemical signatures and characterized by juvenile or positive ϵNd values and low $^{207}\text{Pb}/^{204}\text{Pb}$ ratios.

Much of the Slave Province is underlain by greenschist- to upper amphibolite-facies metamorphic rocks, thus the occurrence of granulite-facies terranes west of the Pb and Nd isotopic boundaries is of particular interest. Work by Stubbley et al. (1995) and Stubbley and Cairns (1998) in the Nardin metamorphic complex, by Pehrsson and Chacko (1997), Pehrsson (1998), Pehrsson and Villeneuve (1999), Pehrsson et al. (2000) in the Cotterill gneiss complex (Fig. 2.1), and by Henderson (1994, 1998, 2004), Henderson and Chacko (1995), Chacko et al. (1995a and b), Perks (1997), Yamashita et al. (1999), Jackson (1998a,b, 1999, 2000a-c, 2001, 2002a,b), and Bennett and Dunning (1998), and Bennett et al. (2000, 2002) in the Snare River terrane has highlighted two features suggesting that the crustal architecture and evolutionary history of the southwestern Slave Province are different to those elsewhere in the craton: (i) the granulite-facies rocks are fault-bounded and are juxtaposed against low grade supracrustal and / or granitic rocks;

and (ii) in the southwestern Slave Province, they lack significant evidence of ≥ 2.8 Ga basement at the erosion surface and/or analytical evidence of significant ($> 10-30\%$) basement contamination (Pehrsson and Villeneuve 1999, Yamashita et al. 1999), despite their locations west of the Pb and Nd isotopic boundaries.

The significance of these granulite-facies terranes has not previously been considered in tectonic models of the Slave Province. Their relatively recent discovery and widespread exposure in the southwestern Slave Province provides an opportunity to: (i) examine the mid-crustal response to Neoproterozoic orogenesis, an aspect previously addressed only in lower crustal xenolith studies (e.g. Davis 1997); and (ii) assess their relationship to the adjacent Mesoproterozoic, pre-2.8 Ga crustal blocks.

2.4 Metamorphic gradients and relationship to the Lithoprobe SNORCLE transect.

Exceptional exposure and unified regional aeromagnetic coverage significantly aided in mapping the Snare River terrane (SRT), which consists of a greenschist- to granulite-facies metamorphic terrane with an apparently unbroken metamorphic transition from the upper-crustal northern and southern regions towards a mid-crustal core. Understanding of Archean crustal growth and evolution has been significantly advanced by information gleaned from areas where different crustal levels are juxtaposed at the Earth's surface. Such areas are significant because they allow the variations in composition, structure and metamorphic grade to be directly mapped out as a function of depth, thereby providing the data to reconstruct a crustal-scale 'orogenic stratigraphy'.

Comparison of such a stratigraphy with seismic and magnetotelluric data allows geologically realistic constraints to be placed on interpretations of crustal-scale sections constructed from these datasets. This is particularly relevant in the case of the SRT, which lies less than 100 km north of the Lithoprobe SNORCLE transect (Fig. 2.1). Furthermore, metamorphic gradients that correspond to different crustal levels are windows into the processes of cratonization, i.e., the formation and stabilization of thick sialic continental nuclei, providing a natural laboratory in which to observe temporal and spatial changes in crustal growth processes and products.

The purpose of this paper is to present the findings of recent geological mapping in the southwestern Slave Province, integrated with a geochronological dataset resulting from U/Pb analyses of intrusive phases that bracket the main stages of deformation and evolution of the SRT as determined from field relationships. In so doing, it is hoped that this study will shed light on the origin of the southwestern Slave Province and concurrently, advance understanding of Neoproterozoic crustal growth mechanisms.

2.5 Snare River terrane

1:50 000 scale mapping of the Snare River terrane (Henderson 1998; Jackson 2003 and references therein; Appendix R), integrated with regional aeromagnetic coverage (GSC 1963; Robinson et al. 2002), has revealed a plutonic-gneiss core with high-grade supracrustal remnants and encircling low-grade supracrustal belts (Figs. 2.2a, b). The plutonic core can be subdivided into the granulite-facies Ghost subdomain (Henderson and Schaan, 1993; Pehrsson et al. 2000) and the amphibolite-facies

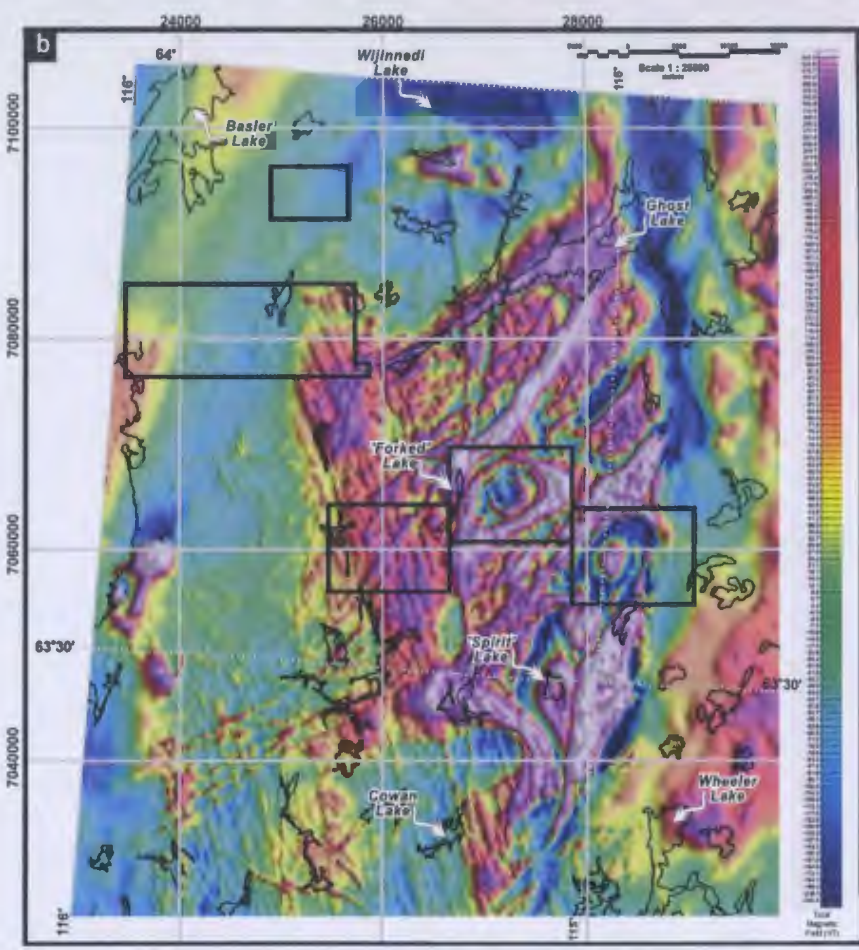
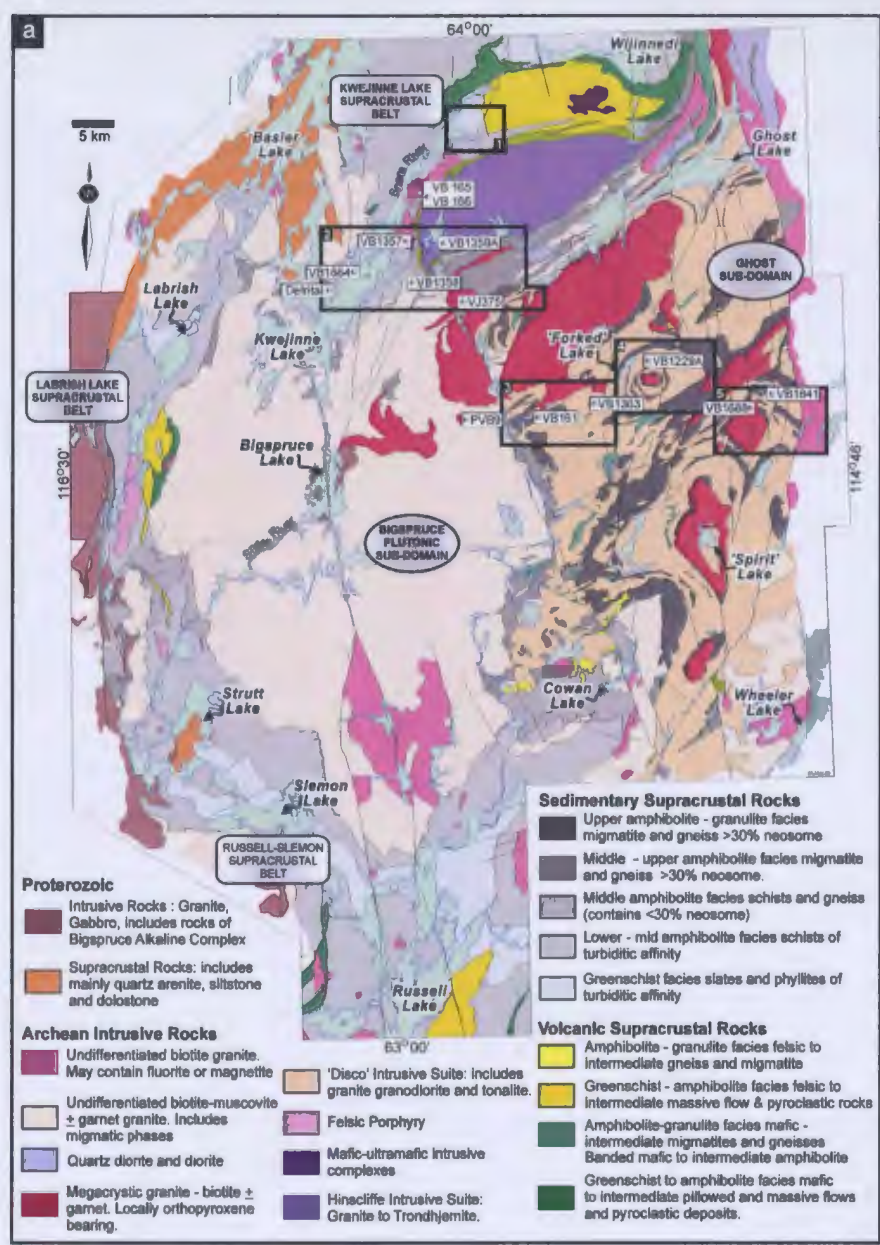


Figure 2.2: Geological and geophysical maps of the Snare River terrane. (a) Simplified geological map of the Snare River terrane, showing location of transect (boxes numbered 1-5, Figure 3). Sources of information: Snare River area (Jackson 2003); Wijnnedi Lake area (Henderson, 1998); Labrish Lake area (Brophy and Pell 2002); Russell Lake area (Jackson 1999); Basler Lake area (McGlynn and Ross 1962, Lord 1942). (b) Total magnetic field map of the Snare River terrane (data compilation - Robinson et al. 2002). Transect shown as boxes.

Bigspruce subdomain (Fig. 2.2a), and the low grade rocks are subdivided into the Kwejinne Lake, Labrish Lake and Russell-Slemon supracrustal belts.

A 1:30 000 scale geological transect (Figs. 2.2a, b, and 2.3) across key localities of the SRT was undertaken to better define the nature of and relationships among the wedge of high temperature – low pressure (*HT-LP*) granulites, associated plutonic rocks and the adjacent supracrustal belts (Bennett and Dunning 1998; Bennett et al. 2000, 2002). The transect consists of 5 staggered segments that cross the greenschist- to mid-amphibolite-facies rocks of the Kwejinne Lake supracrustal belt and the upper amphibolite- to granulite-facies Bigspruce and Ghost subdomains. A complete database of field observations is presented in Appendix O.

2.5.1 Geology of the Snare River terrane

The broad subdivision of the SRT into supracrustal belts and plutonic complexes is used as the context for the description of important field relationships. Well-preserved supracrustal sequences occur in all three belts, but the Kwejinne Lake belt was selected for study as it contains all representative lithologies. The three main protolith groups in the supracrustal belts are: bimodal volcanic rocks, syn-volcanic plutons and sedimentary rocks, principally greywacke – mudstone turbidites. Remnants of metasedimentary and metavolcanic units that occur as lensoid and irregular bodies throughout the Ghost subdomain are interpreted as high-grade equivalents of the low-grade rocks.

Thermobarometric studies on samples from Ghost Lake (Chacko et al. 1995a, b) revealed that the thermal peak of the M2 metamorphic event (ca. 850 – 900 °C) was attained at

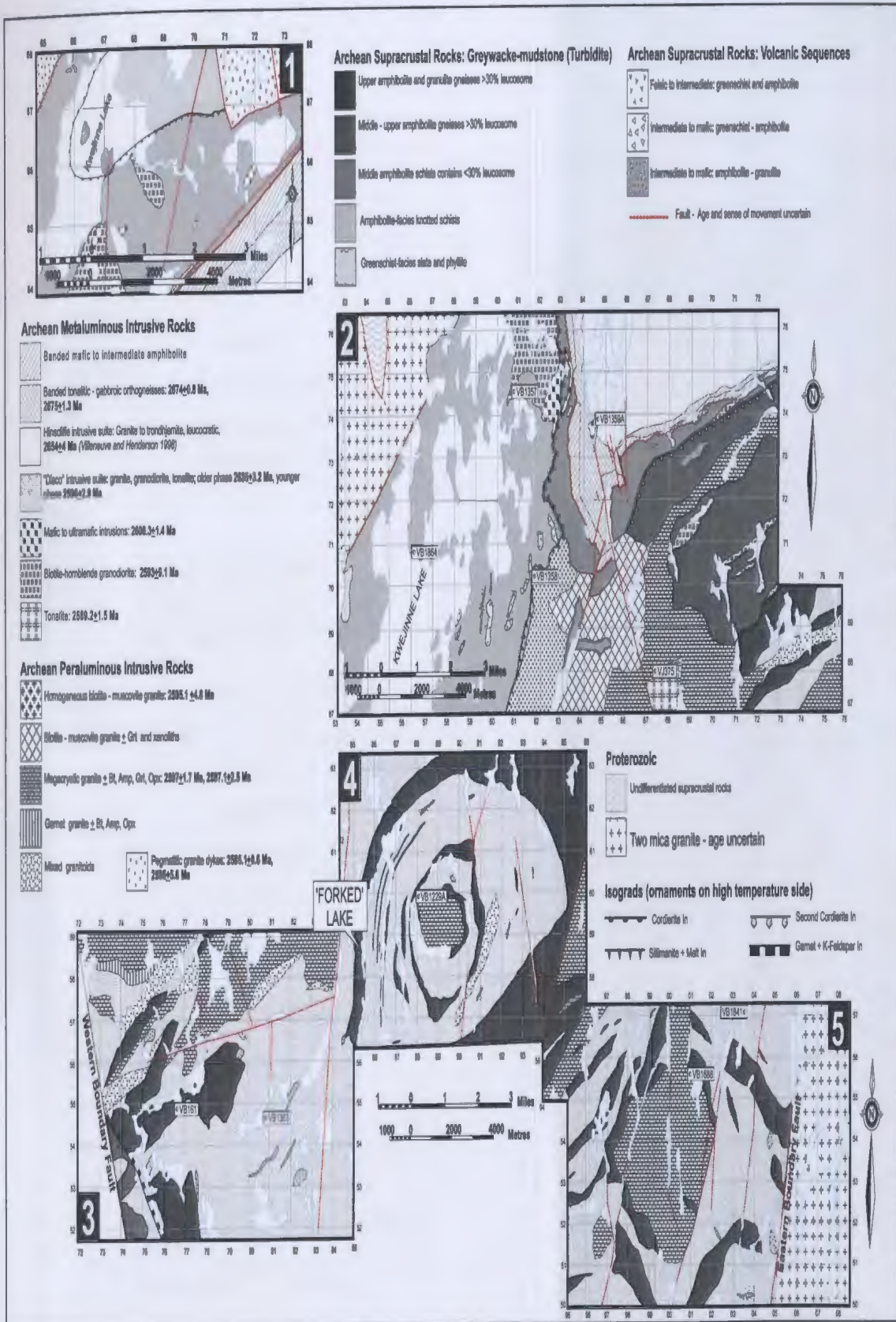


Figure 2.3: Geological transect maps showing locations of 10 geochronological sampling sites (remaining three shown on Fig. 2.2a). Legend incorporates crystallization ages of units determined in this study. Bt - biotite, Amp - amphibole, Grt - garnet, Opx - orthopyroxene.

pressures of approximately 6.5 to 7 kbar, implying a midcrustal origin for the granulite-facies rocks and, hence for the coeval interlayered magmatic rocks in the Ghost subdomain. The presence of supracrustal rocks that can be correlated with reasonable confidence across the SRT due to excellent exposure (70 – 80%) provides a rare opportunity to correlate tectonic evolution across a metamorphic gradient.

Supracrustal rocks: Turbidites, composed of greywacke-mudstone and discontinuous iron formations are the dominant supracrustal lithology. They commonly display sedimentary structures (e.g., graded bedding, flame and load structures, cross-bedding) in the low-grade part of the belt, some of which (e.g., graded bedding) are locally preserved in granulite-facies rocks, aiding lithological correlations. Contacts with adjacent volcanic units are both conformable and faulted. Metavolcanic lithologies were derived from mafic pillow and sheet flows, mafic to intermediate hyaloclastic breccia, rhyolite lava domes, andesitic to rhyodacitic pyroclastic flows, lapilli and ashfall tuff. Primary volcanosedimentary features, including pillows, brecciated flow tops, stratification in tuffs, and cross-bedding in volcanoclastic rocks, are common. Mafic to felsic gneisses that occur as discrete lenses and irregular bodies throughout the Ghost subdomain are inferred to be related to these volcanic protoliths. Two ages of felsic volcanism in the SRT have been determined: $2658 \pm [1.2/-0.8]$ Ma in the Russell Lake belt (Mortensen et al. 1992) and $2673 \pm [1.5]$ Ma in the Kwejinne Lake belt (Villeneuve and Henderson 1998) [square brackets indicate that uncertainties in U decay constants are not included in the error estimate].

Syn-volcanic intrusions: A polydeformed assemblage of mafic – tonalitic orthogneiss occurs in a prominent high strain zone in the Kwejinne Lake supracrustal belt. The orthogneiss unit is spatially associated with a finely banded amphibolite schist, which is considered to represent highly strained mafic - intermediate volcanic rocks. On the basis of field relationships and geochemical data (chapter 4), the orthogneiss is interpreted as a syn-volcanic intrusive package. The high-strain orthogneiss—schist package mantles the trondhjemitic to granodioritic Hinscliffe plutonic complex (Henderson and Schaan 1993; Figs. 2.2, 2.3), which has a U/Pb age of $2654 \pm [4]$ Ma (Villeneuve and Henderson 1998).

Younger plutons: Younger plutons in the SRT have been divided into nominal ‘metaluminous’ or ‘peraluminous’ groups on the basis of their varietal mineralogy. Intrusions are denoted as metaluminous if their mineralogy lacks muscovite and consists predominantly of hornblende and/or biotite, or peraluminous if muscovite, cordierite or garnet occur as varietal phases. No inference with respect to the geochemistry or petrogenesis of the groups is implied by the usage of this terminology. The two groups have important cross-cutting and overprinting field relationships that bracket the main stages of evolution of the SRT from crust formation through collision to post-orogenic collapse.

Three metaluminous suites are recognized (Fig. 2.3): (a) a suite of heterogeneous, ultramafic to granodioritic complexes; (b) a biotite-hornblende granite suite; and (c) biotite-hornblende±orthopyroxene granodiorite/granite of the Disco Intrusive suite characterized by abundant mafic enclaves. Four peraluminous suites have been identified

(Fig. 2.3): (a) a homogeneous, enclave-free, biotite-muscovite granite; (b) a muscovite-dominant, two-mica granite with abundant metasedimentary enclaves; (c) a coarse-grained, foliated K-feldspar megacrystic to porphyritic granite; and (d) late stage bodies of cordierite-muscovite granite and dykes of unfoliated, pegmatitic granite. For additional lithological information, the reader is referred to the reports of Jackson (1998a, 1999, 2000a, 2000b, 2002a).

2.5.2 Tectonic history of the Snare River terrane

The complex history of magmatism, polyphase deformation and metamorphism of the SRT was investigated by dating critical cross-cutting and structural overprinting relationships among the metaluminous and peraluminous suites observed in the field. Metaluminous bodies were particularly useful because of their protracted intrusive history and multiple overprinting relationships. Field evidence indicates that peraluminous magmas clearly post-date the early structures and intruded relatively late in the evolution of the SRT. The summary of the tectonic evolution that follows is based on the work of Jackson (1998a,b, 1999, 2000a-c, 2001, 2002a,b), Bennett and Dunning (1998), and Bennett et al. (2000, 2002).

Three widespread deformation episodes, D1 – D3, have been recognized in the SRT. D1, which is inferred to have taken place in a proto-arc tectonic regime, spans the interval from the formation of the early bimodal volcanic-plutonic sequence to the onset of D2. D1 was a protracted event culminating in the assembly of the volcanic and sedimentary components of the supracrustal belts and greenschist- and amphibolite-facies

metamorphism (M1). D2 was a crustal shortening episode that resulted in structural reworking of the supracrustal sequences assembled during D1, major crustal thickening and medium-*P*, high-*T* granulite-facies metamorphism (M2). Evidence for an episode of post-orogenic collapse, D3, is inferred from a third metamorphic episode (M3) that overprints D2 features in the Ghost subdomain and the lower structural levels of the Kwejinne Lake and Russell-Slemon supracrustal belts. M3 metamorphism has a low-*P*, high-*T* character, but preservation of D3 structures is limited. This chronology of deformation and metamorphism was used as a framework in which to place the relative sequence of pluton emplacement (Fig. 2.4).

2.6 U-Pb Geochronology

In this study, two geochronological approaches were adopted. First, U-Pb zircon igneous crystallization ages were determined on selected intrusive bodies, inferred from field relationships to punctuate the tectonic evolution of the SRT, using both ID-TIMS and LAM ICP-MS methods. Second, LAM ICP-MS U-Pb data were collected from the detrital zircon population of a low grade turbidite to determine provenance ages and the maximum age of sedimentation.

Samples from seven metaluminous and six peraluminous intrusions were selected from across the transect (Figs. 2.2a, 2.3) on the basis of: (a) crustal level of the intrusion; (b) observed age relationships with respect to other intrusions and major structural and metamorphic events; and (c) so as to obtain a representative selection of the principal the intrusive suites. Figure 2.4 outlines the sequence of emplacement and relative timing of

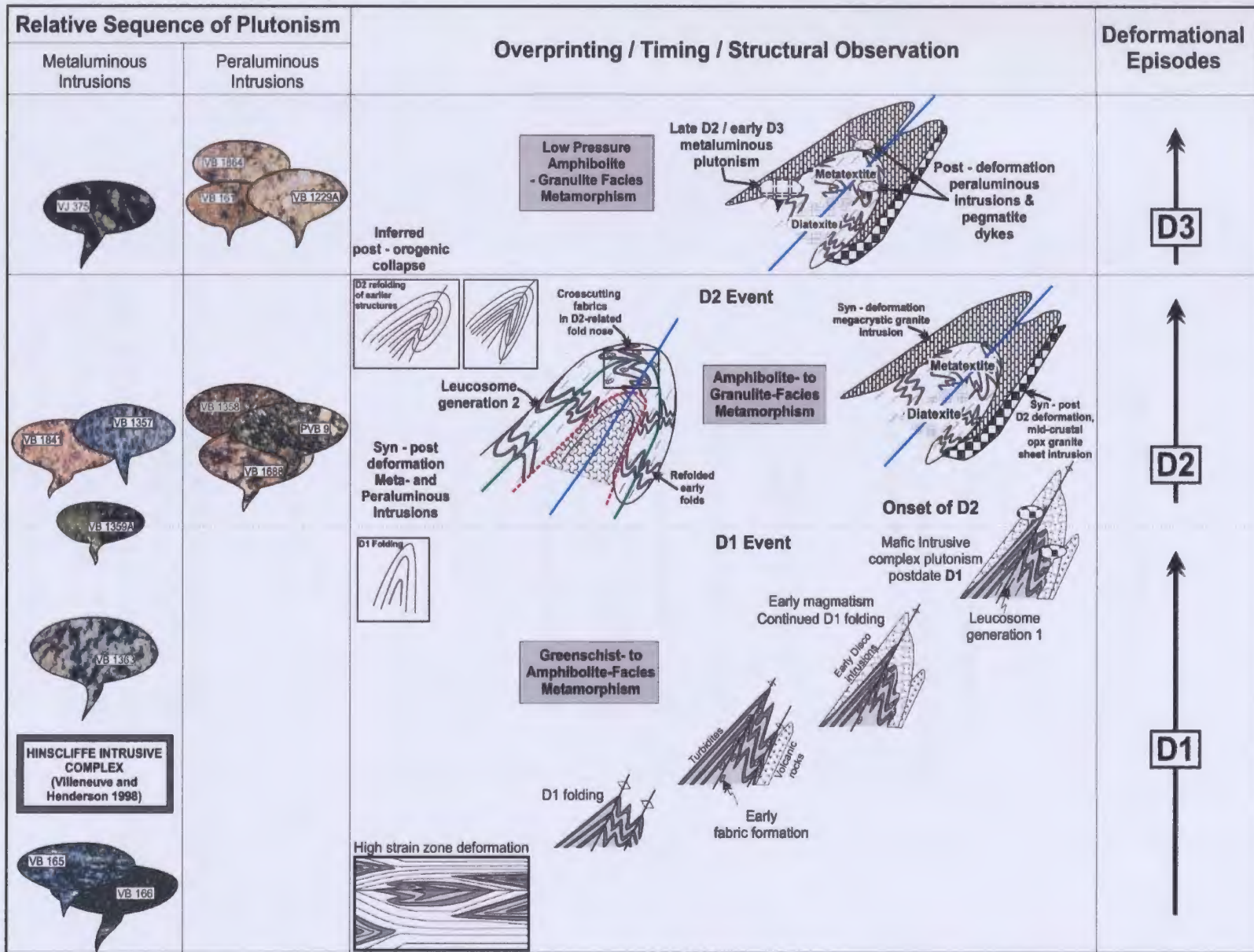


Figure 2.4: Relative sequence of metaluminous and peraluminous intrusions with respect to D1-D3 deformational episodes as interpreted from crosscutting and overprinting field relationships.

the thirteen intrusive units with respect to the polyphase deformation and metamorphism, as determined from field relationships.

Metaluminous intrusions (Figs. 2.5a-c) punctuate various stages of the D1 event. Syn-D1 plutons have undergone at least two episodes of folding and metamorphism, depending on their crustal level, and were subsequently intruded by younger plutons during D2 and D3. Magmatism during D2 was both metaluminous and peraluminous, the latter predominating. Syn-D2 magmatism for the most part occurred at mid-crustal levels. Truncation of upper-crustal D2 structures by intrusions with syn-D2, mid-crustal correlatives that have D2 fabrics suggests that D2 was a diachronous event. Late metaluminous and peraluminous intrusions were syn-D3. These small-volume bodies are variably affected by the M3 metamorphic episode, with mid-crustal intrusions in the Ghost subdomain being recrystallized, whereas upper-crustal counterparts in the Kwejinne Lake belt exhibit no significant metamorphic overprint. The youngest intrusions in the SRT are the undeformed, peraluminous, pegmatitic dykes and irregular bosses that postdate D3 structures. The metasedimentary sample selected for the detrital study comes from the lower-amphibolite-facies part of the Kwejinne Lake supracrustal belt. Sample locations are shown in Figs. 2.2a and 2.3.

2.7 Analytical Procedures

Zircon separates were extracted using standard crushing techniques, and heavy mineral concentrates were produced using a WilfleyTM table, heavy liquids and a FrantzTM isodynamic separator before hand-picking in ethanol under a binocular

microscope. All extraction and analyses were conducted at the Department of Earth Sciences, Memorial University of Newfoundland.

ID-TIMS: Isotope Dilution – Thermal Ionization Mass Spectrometry was the first technique employed to establish emplacement ages of the 13 intrusive bodies. The occurrence of multiple complex zircon populations in all samples necessitated rigorous grain characterization before selection of target fractions. Subdivision of zircon populations was initially carried out using a binocular microscope and standard optical criteria (i.e., colour, morphology, inclusion characteristics). The highest quality zircon crystals from populations considered on the basis of these criteria to have crystallized during emplacement were then air abraded for 12-24 hours to remove high U rims that may have suffered low-temperature Pb loss, following the method of Krogh (1982). In an attempt to better understand the zircon populations in the samples and thereby increase the chances of selecting appropriate grains that would yield precise crystallization ages using ID-TIMS, a maximum of ten high quality abraded grains, together with representative unabraded grains, was selected for back-scattered electron (BSE) imaging to investigate their internal structures. The grains were mounted in epoxy resin, polished to expose their central regions, and carbon coated prior to BSE analysis. Back scattered electron imaging reveals contrasts in mean atomic number that, in the case of zircon, are typically a result of Hf and to a lesser extent U, Th and Y zoning (Hancher and Miller 1993). This procedure, which until recently was not commonly employed in standard U-Pb TIMS studies, considerably enhanced the quality of the resultant dataset as it provided an independent source of information with which to interpret the U-Pb data.

Following grain characterization, the decision as to whether to analyse single or multiple grains was made. Where zircon populations appeared relatively straightforward, multigrain fractions, composed of between 3 and 15 grains, were prepared. In other cases, abraded imaged single grains were carefully plucked from the grain mount and placed in cleaned glass petri dishes for cleaning and dissolution. In order to minimize handling of these small, single grain fractions, individual grain weights were estimated using a size-weight table constructed in-house (Appendix C). Grain weight estimates using the table were within error of sample weights measured with an electronic balance. All fractions were washed in 4N HNO₃ and doubly distilled H₂O and distilled acetone before loading, under a microscope, into teflon™ bombs. Each zircon fraction was spiked with a mixed ²⁰⁵Pb/²³⁵U tracer solution and dissolved with 8 N HNO₃ and concentrated HF for at least 5 days at 210 °C. Ion exchange chemistry was completed using the method of Krogh (1973), but with ion exchange columns and reagent quantities 1/10th the volume (see also Emon et al. 1999). The purified U and Pb were mounted on Re filaments with silica gel and H₃PO₄. Isotope ratios were measured on a Finnigan-Mat 262 thermal ionization mass spectrometer in static mode with faraday cups calibrated against the NBS 981 standard. ²⁰⁴Pb and the majority of the single grain fractions were measured by peak jumping using the secondary electron multiplier-ion counter, which was calibrated using known faraday data. Measured isotopic ratios were corrected for U and Pb fractionation at 0.1%/AMU using repeated measurements of NBS standards, and for laboratory blanks (2-12 pg Pb, 1 pg U; Cox et al. 1998). Stacey and Kramers' (1975) model Pb isotopic compositions were used to correct for common lead in excess of the laboratory blank. Uncertainties in

isotopic ratios were calculated using an in-house error propagation program. Linear regressions follow the method outlined in Isoplot v2.06 (Ludwig 1999). Estimated uncertainties on the U decay constants are presented graphically in concordia plots, and decay constants used are those of Jaffey et al. (1971).

LAM ICP-MS: Complex U-Pb systematics in seven of the thirteen samples analysed by ID-TIMS resulted in a spread of ages, from concordant to slightly discordant, likely a result of inheritance, variable Pb loss, and/or new metamorphic zircon growth. The spread of data for these samples made it difficult to confidently infer their crystallization ages, so additional U-Pb data were collected using the LAM ICP-MS (approximately 20-50 grains per sample). Prior to LAM analysis, the target grains were examined by BSE imaging. In order to define crystallization ages, distinctive populations were singled out and core-rim relationships characterized; in particular, an attempt was made to select undisturbed, growth-zoned portions of grains. Zircon samples and standards to be analyzed were polished to a 0.25 μm finish, washed in ethyl alcohol and placed in an ultrasonic bath for 2-5 minutes before removal to a positive-pressure clean box. The sample cell was disassembled in the clean box, soaked in warm 2N HNO_3 and washed in doubly distilled H_2O . The cell pieces were air-dried before reassembly and sample loading. The sample and standards to be analyzed were washed in doubly distilled H_2O , polished surfaces to be ablated were washed in 4N HNO_3 and double distilled H_2O and left to air-dry before loading into the sample cell. Handling of the cell and samples was minimized and clean techniques were employed during the loading process to reduce surface contamination to a minimum. After cell assembly, the ends were sealed with

parafilm prior to attachment to the LAM ICP-MS. Isotopic ratios (U/Pb and Pb/Pb) of the zircon standards and samples were measured using a VG PlasmaQuad 2S+ mass spectrometer coupled to an in-house custom built, Q switched Nd:YAG ultraviolet 266 nm laser. Most operating conditions were similar to those described by Košler et al. (2001, 2002). Zircon surfaces were ablated using a 10-20 μm diameter laser beam focused 100 μm above the surface and operating at a repetition rate of 10 Hz. The sample cell was mounted on the computer-driven, motorized stage of an optical microscope, and the stage was moved beneath the stationary laser beam at variable speeds (0.00075 to 0.0015 mm s^{-1}). Laser energies varied from 0.15 to 1.2 mJ/pulse, depending on the spatial resolution required and U and Pb isotope concentrations. The sample surface was passed under the laser beam once only, as this technique was observed to result in very efficient ablation. Slower velocity rastering was found to increase spatial resolution and significantly reduce elemental fractionation at the ablation site. Pit depths varied from 5-15 μm , dependent on laser energy, and were therefore close to the depth of penetration of the electron beam during acquisition of the BSE images. The sample introduction system, modified after Horn et al. (2000), enabled simultaneous nebulization of an internal standard tracer solution and laser ablation of the solid sample. The tracer solution, consisting of a mixture of natural Tl ($^{205}\text{Tl}/^{203}\text{Tl} = 2.3871$) and enriched ^{233}U , ^{209}Bi and ^{237}Np (concentrations of ca. 10 ppb per isotope) transported in a mixed Ar-He carrier gas, was employed to correct for instrumental mass bias. Time-resolved data acquisitions (180-340 s experiments) consisted of ca. 60 s measurement of the Ar-He gas blank and aspirated tracer solution prior to introduction of ablated material. Data were collected on

unknown zircon samples and two zircon standards, 02123 (ca. 295 Ma) and VB165 (ca. 2674 Ma) whose U-Pb and Pb-Pb ages had been previously determined by ID-TIMS. VB165, a sample initially treated as an unknown and analyzed by ID-TIMS in this study, was selected as a secondary internal standard due to its abundance and near concordant behaviour. Typically 7-8 unknowns were collected for every 3-4 analyses of the standards to monitor instrument variability and drift in operating conditions during a session. Laser ablation analyses of internal standards 02123 and VB165, calculated ages and comparisons with their ID-TIMS ages are presented on concordia diagrams in Figure B1 in Appendix B. During ablation, U and Pb isotopes and tracer solution signals were acquired in time-resolved peak-jumping, pulse-counting mode with one point measured per peak using PQVision v. 4.30 software. The range of masses measured for each analysis was: 201 (flyback), 202(Hg), 203(Tl), 205(Tl), 206(Pb), 207(Pb), 209(Bi), 233(U), 237(Np), 238(U). Three oxide masses, 249(UO), 253(NpO) and 254(UO) were measured to correct for oxide formation. Quadrupole settling time was 1 ms for all masses and dwell time was 8.3 ms for all masses except 207 for which it was 24.9 ms. Raw counts were corrected for electron multiplier dead time (20 ns) and gas blank. Isotopic ratios were calculated from the average integrated counts using the natural $^{238}\text{U}/^{235}\text{U}$ ratio of 137.88. The intercept method of Sylvester and Ghaderi (1997), which is commonly used to correct for Pb/U fractionation of LAM analyses, was not readily applicable to the slow raster analyses performed in this study due to the minimization of elemental fractionation at the ablation site. Li et al., (2001) also noted the reduction in U and Pb fractionation in a study utilizing similar slow, linear single pass ablation protocols

and estimated elemental fractionation to be less than 5% for the $^{206}\text{Pb}/^{238}\text{U}$ and <1% for $^{207}\text{Pb}/^{206}\text{Pb}$ isotopic ratios, respectively. Similar fractionation rates were observed in this study (see Appendix B). ID-TIMS analyses suggested common Pb was in low enough concentrations within individual grains so as not to pose a significant problem for reduction of the LAM ICP-MS dataset. $^{207}\text{Pb}/^{235}\text{U}$ and $^{206}\text{Pb}/^{238}\text{U}$ ratios were corrected for mass bias using the tracer solution and internal standard 02123 and were cross-calibrated with the known intercept age (ca. 2674 Ma) of internal standard VB165. $^{207}\text{Pb}/^{206}\text{Pb}$ ratios were corrected for mass bias using the tracer solution and internal standard VB165. Isoplot v. 2.06 of Ludwig (1999), in conjunction with the LAMdate Excel spreadsheet program (Košler et al. 2002), were used to calculate U-Pb ages of unknowns.

Detrital zircon methodology: Sample preparation, instrumentation and data reduction for the detrital zircon study were as described above for LAM ICP-MS. A total of 104 grains were analyzed, and one analysis per grain was acquired in an attempt to sample the full range of provenance ages and not bias the results. A cumulative frequency diagram based on the 1σ errors in the $^{207}\text{Pb}/^{206}\text{Pb}$ ages was employed to analyze the results. Provenance ages presented on concordia plots are at the 95% confidence interval and also consider the U decay constant uncertainties.

Reverse discordance: A noticeable feature of the LAM dataset is the occurrence of reversely and normally discordant analyses from a single grain. Two features may account for the data; (a) The results may be real and occur as a result of within-grain diffusion of U and/or Pb during secondary recrystallization of zircon; or (b) the reversely

discordant data are an artifact of the LAM ICP-MS method. A discussion is provided in Appendix B. For all LAM ICP-MS results, where a concordia age was not able to be calculated, the $^{207}\text{Pb}/^{206}\text{Pb}$ age is considered to be the most robust age calculation as this ratio exhibits limited time-resolved elemental fractionation. All ID-TIMS and LAM ICP-MS data points are presented in concordia plots and data tables.

2.8 Results

Isotope dilution – thermal ionization mass spectrometry analytical results are presented in Tables 2.1 and 2.2 for both metaluminous and peraluminous magmatic suites, and LAM ICP-MS data for seven plutonic samples and the detrital zircon study are presented in Appendix A (Tables A1, A2 and A3). Uncertainties reported for ID-TIMS data in Tables 2.1 and 2.2 and plotted on associated concordia diagrams are at the 2σ uncertainty level unless stated otherwise. LAM ICP-MS uncertainties are reported at both 1 and 2σ values in Tables A1-A3 for isotopic ratios and calculated ages for individual analyses are quoted at 1σ levels. Calculated LAM ICP-MS ages presented on concordia diagrams are reported at 2σ confidence levels unless otherwise stated. Ellipses are plotted at 2σ for ID-TIMS data and 1σ for LAM ICP-MS data. For both data sets, two error estimates are given for each age determination, excluding and including U decay constant uncertainties respectively. Decay constant uncertainties are plotted graphically on concordia plots and reported in the text. The concordia age that includes U decay constant uncertainties is considered the best estimate of the crystallization age of a sample. Where a concordia age cannot be calculated, the weighted mean of the

$^{207}\text{Pb}/^{206}\text{Pb}$ age, calculated on the basis of the measurement error, or the intercept age is considered the best estimate of the crystallization age. Uncertainties associated with the U decay constant are typically ignored when calculating U-Pb age data, however we believe that these uncertainties are significant (Ludwig 2000; Begemann et al. 2001) and should be included as they effect accuracy of the resultant datasets and hence, associated interpretations. Table 2.3 summarizes the ID-TIMS and LAM ICP-MS concordia, intercept and weighted mean $^{207}\text{Pb}/^{206}\text{Pb}$ ages (both ignoring and including U decay constant uncertainties) that correspond to the emplacement ages of the 13 intrusive samples. In the following text and associated concordia diagrams two errors are quoted, one including U decay constant uncertainties (not in square brackets) and the other ignoring decay constant uncertainties (in square brackets), the latter to facilitate comparison with results in the published literature. The complete database of BSE grain images and associated laser pit locations, in addition to selected secondary electron (SE) images of pit morphologies, is presented in Appendix M. A detailed account of the deformation history of the Snare River terrane is provided in Chapter 3. Hence, only a brief summary of the crosscutting relationships is given for each of the following samples.

2.8.1 Metaluminous Intrusions

Synvolcanic tonalitic gneiss - VB165: Sample VB165 is from a ~ 1 m wide body of medium-grained, biotite–hornblende tonalite gneiss (Fig. 2.5a) enclosing the Hinscliffe plutonic complex. The unit occurs in a high-strain zone and has a well-developed

Table 2.1: U-Pb ID TIMS Analytical Results, Metaluminous Intrusions

Concentration Measured				Corrected Atomic Ratios										Disc %					
*Fraction	Weight (mg)	U (ppm)	Pb _{rad} (ppm) ^b	Pb (pg)	²⁰⁶ Pb/ ²⁰⁴ Pb	²⁰⁸ Pb/ ²⁰⁶ Pb	Th (model)	Th/U	²⁰⁷ Pb/ ²³⁵ U	2σ	²⁰⁶ Pb/ ²³⁸ U	2σ	²⁰⁷ Pb/ ²⁰⁶ Pb		2σ	ρ	²⁰⁷ Pb/ ²³⁵ U	²⁰⁶ Pb/ ²³⁸ U	²⁰⁷ Pb/ ²⁰⁶ Pb
VB 165 - syn volcanic tonalite (115° 39.1 E, 63° 51.1' N)																			
Z1 sgl abr pm	0.011	158	91.4	9	6225	0.1298	71.9	0.46	12.8767	0.226	0.5123	0.210	0.1823	0.062	0.9622	2671	2666	2674	0.4
Z2 sgl abr pm	0.008	94	54.7	8	3093	0.1328	43.9	0.47	12.9244	0.252	0.5140	0.256	0.1824	0.118	0.8922	2674	2673	2675	0.1
Z3 sgl abr pm	0.006	163	94.3	8	4007	0.1353	80.1	0.49	12.8071	0.310	0.5095	0.314	0.1823	0.116	0.9310	2666	2654	2674	0.9
Z4 sgl abr pm	0.006	153	86.3	7	4284	0.093	50.1	0.33	12.8971	0.298	0.5129	0.312	0.1824	0.138	0.8986	2672	2669	2675	0.3
VB 166 - syn-volcanic Gabbro (115° 39.1 E, 63° 51.1' N)																			
Z1 mlt abr (9)	0.0018	200	115.7	23	517	0.1373	95.8	0.48	12.7953	0.402	0.5091	0.4200	0.1823	0.2120	0.8679	2665	2653	2674	1.0
Z2 mlt abr (11)	0.0003	409	235.9	15	265	0.1513	212.7	0.52	12.6625	0.904	0.5029	0.9060	0.1826	0.2300	0.9677	2655	2626	2677	2.3
Z3 sgl unabr imgd	0.002	136	75.8	14	659	0.1507	68.1	0.50	12.2168	0.460	0.4855	0.4640	0.1825	0.1520	0.9459	2621	2551	2676	5.7
Z4 sgl abr imgd	0.002	140	79.2	11	778	0.1399	66.6	0.48	12.5476	0.402	0.4989	0.3980	0.1824	0.1100	0.9622	2646	2609	2675	3.0
VB 1363 - biotite-hornblende granodiorite (115° 22.2' E, 63° 36.5' N)																			
Z1 sgl abr imgd	0.004	137	74.1	9	2024	0.0985	46.7	0.34	11.9009	0.3520	0.4916	0.3200	0.1756	0.1940	0.8375	2597	2578	2611	1.6
Z2 sgl abr imgd	0.004	222	120	44	701	0.0646	50.8	0.23	12.4241	0.3160	0.5059	0.3120	0.1781	0.1380	0.9035	2637	2639	2635	-0.2
Z3 sgl abr imgd	0.003	130	64.7	6	1958	0.1012	42.2	0.32	10.8387	0.3400	0.4519	0.3580	0.1740	0.1740	0.8770	2509	2404	2596	8.9
VB 1359A gabbro (115° 41.6' E, 63° 47.4' N)																			
Z1 mlt abr ndl (8)	0.003	403	237.1	26	1529	0.2523	342.5	0.85	11.5273	0.3320	0.4792	0.3260	0.1745	0.0960	0.9576	2567	2524	2601	3.6
Z2 mlt abr ndl (6)	0.003	405	230.5	12	2991	0.2181	295.1	0.73	11.4083	0.3120	0.4753	0.3140	0.1741	0.1140	0.9337	2557	2507	2597	4.2
Z3 sgl abr imgd pm	0.004	178	95.2	26	950	0.0687	43.0	0.24	12.0381	0.2820	0.4984	0.2760	0.1752	0.1120	0.9196	2607	2607	2608	0.0
Z4 sgl abr imgd pm	0.007	169	90.4	34	1097	0.0702	41.7	0.25	12.0646	0.2700	0.4992	0.2760	0.1753	0.1460	0.8572	2609	2610	2609	-0.1
Z5 sgl abr imgd pm	0.005	102	54.7	8	2112	0.0766	27.4	0.27	12.0387	0.4320	0.4983	0.4580	0.1752	0.1920	0.9085	2607	2606	2608	0.1
VB 1357 - biotite - hornblende granite (115° 46.3' E, 63° 47.8' N)																			
Z1 sgl abr imgd	0.006	293	150.3	16	3342	0.0522	52.5	0.18	11.6119	0.3180	0.4864	0.3260	0.1732	0.1260	0.9237	2574	2555	2588	1.6
Z2 sgl abr imgd	0.004	230	97	34	660	0.1056	66.1	0.29	8.9353	0.3280	0.3837	0.3420	0.1689	0.2080	0.8080	2331	2094	2547	20.8
Z3 sgl abr imgd	0.002	116	63.6	7	996	0.1136	46.0	0.40	12.2521	0.3040	0.4949	0.3020	0.1796	0.1700	0.8426	2624	2592	2649	2.6
Z4 sgl abr imgd	0.002	381	143.8	41	335	0.0441	43.4	0.11	7.7992	0.4760	0.3659	0.4660	0.1546	0.2060	0.9046	2208	2010	2397	18.8
VB 1841 - Orthopyroxene Granite (114° 55.8' E, 63° 37.4' N)																			
Z1 sgl abr imgd	0.002	371	194	15	1150	0.0922	116.9	0.32	11.4013	0.4080	0.4811	0.4260	0.1719	0.1740	0.9138	2557	2532	2576	2.1
Z2 sgl abr imgd	0.002	136	73.6	8	1255	0.1036	49.4	0.36	11.6516	0.3020	0.4914	0.3040	0.1720	0.1400	0.8933	2577	2577	2577	0.0
Z3 sgl abr imgd	0.001	228	123.2	11	792	0.1085	86.3	0.38	11.5790	0.3860	0.4899	0.3820	0.1714	0.1220	0.9496	2571	2570	2571	0.1
Z4 sgl abr imgd	0.001	212	113.7	14	467	0.1054	77.5	0.37	11.6378	0.5200	0.4889	0.4540	0.1726	0.2320	0.8952	2576	2566	2583	0.8
VJ 375 Tonalite (115° 37.2' E, 63° 43.7' N)																			
Z1 mlt abr (8)	0.002	246	149.9	8	1729	0.2634	226.0	0.92	11.7767	0.3060	0.4928	0.3140	0.1733	0.1360	0.9041	2587	2583	2590	0.3
Z2 mlt abr (10)	0.001	243	143.2	18	472	0.2071	176.7	0.73	11.8227	0.4540	0.4959	0.4600	0.1729	0.1960	0.9081	2590	2596	2586	-0.5
Z3 mlt abr (11)	0.001	239	147.2	5	338	0.2673	224.2	0.94	11.8336	0.6020	0.4951	0.5900	0.1734	0.1520	0.9677	2591	2593	2590	-0.1

Notes : Latitude / longitude for each sample are presented in parentheses.

^a Z, zircon; sgl, single grain; mlt, multi grain; abr, abraded; unabr, unabrased; imgd, BSE imaged. Number in brackets after mlt fractions denotes number of grains in fraction.^b Total radiogenic Pb after correction for blank, common Pb and spike.^c Ratios corrected for fractionation, spike, 4 - 10 pg laboratory blank, initial common Pb (calculated using Stacey and Kramers (1975) model Pb composition at ²⁰⁷Pb/²⁰⁶Pb age) and 1 pg U blank.^d ρ: Rho is associated error correlation (Ludwig 1980).^e Disc%, discordance along a discordia to origin

Uncertainties quoted at 2σ confidence level for measured ratios. Errors of sample weight are + 0.0015 mg.

Table 2.2: U-Pb ID TIMS Analytical Results, Peraluminous Intrusions

Concentration Measured				Corrected Atomic Ratios																
*Fraction	Weight (mg)	U (ppm)	Pb _{rad} (ppm) ^b	Pb (pg)	²⁰⁶ Pb/ ²⁰⁶ Pb	²⁰⁸ Pb/ ²⁰⁶ Pb	Th (model)	Th/U	²⁰⁷ Pb/ ²³⁵ U	2σ	²⁰⁶ Pb/ ²³⁸ U	2σ	²⁰⁷ Pb/ ²⁰⁶ Pb	2σ	ρ	²⁰⁷ Pb/ ²³⁵ U	²⁰⁶ Pb/ ²³⁸ U	²⁰⁷ Pb/ ²⁰⁶ Pb	^d Disc %	
VB 1358 - Two mica granite (115° 45.0' E, 63°45.3' N)																				
Z1 sgl abr imgd	0.001	155	74.9	18	288	0.1503	69.6	0.45	10.3043	0.712	0.4243	0.6680	0.1762	0.3160	0.8971	2463	2280	2617	15.3	
Z2 sgl abr imgd	0.001	304	118.2	7	1290	0.1518	111.3	0.37	7.9952	0.430	0.3421	0.4380	0.1695	0.1740	0.9198	2230	1897	2553	29.6	
Z3 sgl abr imgd	0.002	123	69.3	55	115	0.1861	77.9	0.63	11.6425	1.236	0.4802	0.6640	0.1758	0.8940	0.7124	2528	2528	2614	4.0	
Z4 sgl abr imgd	0.001	79	41.9	8	306	0.0877	24.0	0.30	11.7433	0.902	0.4890	0.8740	0.1742	0.3480	0.9237	2566	2566	2598	1.5	
PVB9 - Amphibolite Facies megacrystic granite (115° 38.6' E, 63° 43.8' N)																				
Z1 mlt abr (4)	0.006	235	123.7	6	7055	0.074	60.5	0.26	11.7180	0.3340	0.4914	0.3540	0.1730	0.1580	0.8961	2582	2577	2586	0.5	
Z2 mlt abr (4)	0.006	124	68.1	7	3217	0.1215	52.6	0.42	11.7435	0.2680	0.4914	0.2700	0.1733	0.1160	0.9070	2584	2577	2590	0.6	
Z3 sgl abr imgd	0.002	123	67.3	14	426	0.1213	51.9	0.42	11.7443	0.5780	0.4914	0.5320	0.1733	0.2480	0.9034	2584	2577	2590	0.6	
Z4 sgl abr imgd	0.002	74	40.9	12	475	0.131	33.8	0.46	11.7732	0.5200	0.4901	0.5280	0.1742	0.1780	0.9424	2587	2571	2599	1.3	
Z5 sgl abr imgd	0.001	207	110.4	14	644	0.0947	67.8	0.33	11.7079	0.3900	0.4882	0.3840	0.1739	0.1320	0.9419	2581	2563	2596	1.5	
VB 1688 - Granulite Facies megacrystic granite (114° 57.7' E, 63° 36.7' N)																				
Z1 sgl abr imgd	0.005	297	151.8	13	3650	0.0384	39.6	0.13	11.6856	0.2640	0.4900	0.2620	0.1730	0.1080	0.9157	2580	2571	2587	0.8	
Z2 sgl abr imgd	0.003	178	92.6	12	1284	0.0416	26.1	0.15	11.9160	0.2820	0.4966	0.3060	0.1740	0.1640	0.8475	2598	2599	2597	-0.1	
Z3 sgl abr imgd	0.007	380	195.3	29	3007	0.368	48.9	0.13	11.8329	0.3000	0.4938	0.2880	0.1738	0.0640	0.9771	2591	2587	2594	0.3	
VB1229A- Granulite facies pegmatitic granite dyke (115° 12.6' E, 63° 38.9' N)																				
Z1 sgl abr imgd	0.0031	853	443.2	7	12521	0.073	214.1	0.25	11.5431	0.3540	0.4843	0.3560	0.1729	0.1080	0.9537	2568	2545	2585	1.7	
Z2 sgl abr imgd	0.008	1039	552.5	70	3676	0.0889	320.3	0.31	11.6776	0.2600	0.4900	0.2440	0.1728	0.0600	0.9736	2579	2571	2585	0.7	
Z3 sgl abr imgd	0.009	1002	327.4	21	7886	0.0839	180.4	0.18	7.1991	0.2760	0.3025	0.2340	0.1726	0.1180	0.9059	2136	1703	2584	38.7	
Z4 sgl abr imgd	0.009	1029	532.7	19	15645	0.0745	262.5	0.26	11.4987	0.2720	0.4827	0.2800	0.1728	0.0720	0.9664	2564	2539	2585	2.1	
VB161 - muscovite-cordierite granite (115° 27.4' E, 63° 36.8' N)																				
Z1 sgl abr imgd	0.001	1902	765	30	1625	0.0023	12.5	0.01	9.1384	0.3840	0.4007	0.3980	0.1654	0.1720	0.9039	2352	2172	2512	15.9	
Z2 sgl abr imgd	0.002	1066	496.4	45	1045	0.0025	8.9	0.01	10.6839	0.3100	0.4630	0.3020	0.1674	0.1220	0.9209	2496	2453	2531	3.8	
Z3 sgl abr imgd	0.001	428	183	19	798	0.0048	3.8	0.01	10.9805	0.5000	0.4686	0.5000	0.1699	0.3100	0.8078	2414	2283	2527	11.5	
Z4 sgl abr imgd	0.001	279	131.9	13	652	0.004	6.3	0.02	9.7787	0.2860	0.4249	0.2660	0.1669	0.0840	0.9563	2521	2478	2557	3.7	
Z5 sgl abr imgd	0.001	530	253.1	37	431	0.019	34.0	0.06	11.0224	0.3200	0.4670	0.3000	0.1712	0.1840	0.8258	2525	2471	2569	4.6	
VB 1864 : Amphibolite facies pegmatitic dyke (115° 52.1' E, 63° 45.8' N)																				
Z1 sgl abr imgd	0.002	140	142.6	6	1869	1.0972	537.5	3.85	13.2130	0.3200	0.5178	0.3120	0.1851	0.1060	0.9441	2695	2690	2699	0.4	
Z2 sgl abr imgd	0.008	60	30.4	5	2761	0.0779	14.8	0.25	11.9297	0.3440	0.4673	0.3840	0.1852	0.2020	0.8516	2599	2472	2700	10.2	
Z3 sgl abr imgd	0.004	94	54.7	8	1527	0.1101	36.6	0.39	13.3824	0.4320	0.5210	0.4800	0.1863	0.2840	0.8111	2707	2703	2710	0.3	
Z4 sgl abr imgd	0.003	86	48.4	11	838	0.0815	24.5	0.28	13.1936	0.3860	0.5150	0.3920	0.1858	0.1500	0.9258	2694	2678	2705	1.2	
Z5 sgl abr imgd	0.002	394	195.5	13	1322	0.1242	154.4	0.39	10.5907	0.3840	0.4442	0.4820	0.1729	0.3460	0.7025	2488	2369	2586	10.0	

Notes : Latitude / longitude for each sample are presented in parentheses.

* Z, zircon; sgl, single grain; mlt, multi grain; abr, abraded; imgd, BSE imaged. Number in brackets after mlt fractions denotes number of grains in fraction.

^bTotal radiogenic Pb after correction for blank, common Pb and spike.

^cRatios corrected for fractionation, spike, 4 – 10 pg laboratory blank, initial common Pb (calculated using Stacey and Kramers (1975) model Pb composition at ²⁰⁷Pb/²⁰⁶Pb age) and 1 pg U blank.

^dρ: Rho is associated error correlation (Ludwig 1980).

^eDisc%, discordance along a discordia to origin

Uncertainties quoted at 2σ confidence level for measured ratios. Errors of sample weight are + 0.0015 mg.

Table 2.3: ID TIMS and LAM ICP-MS U-Pb crystallization age datasets ignoring and including U decay constant uncertainties

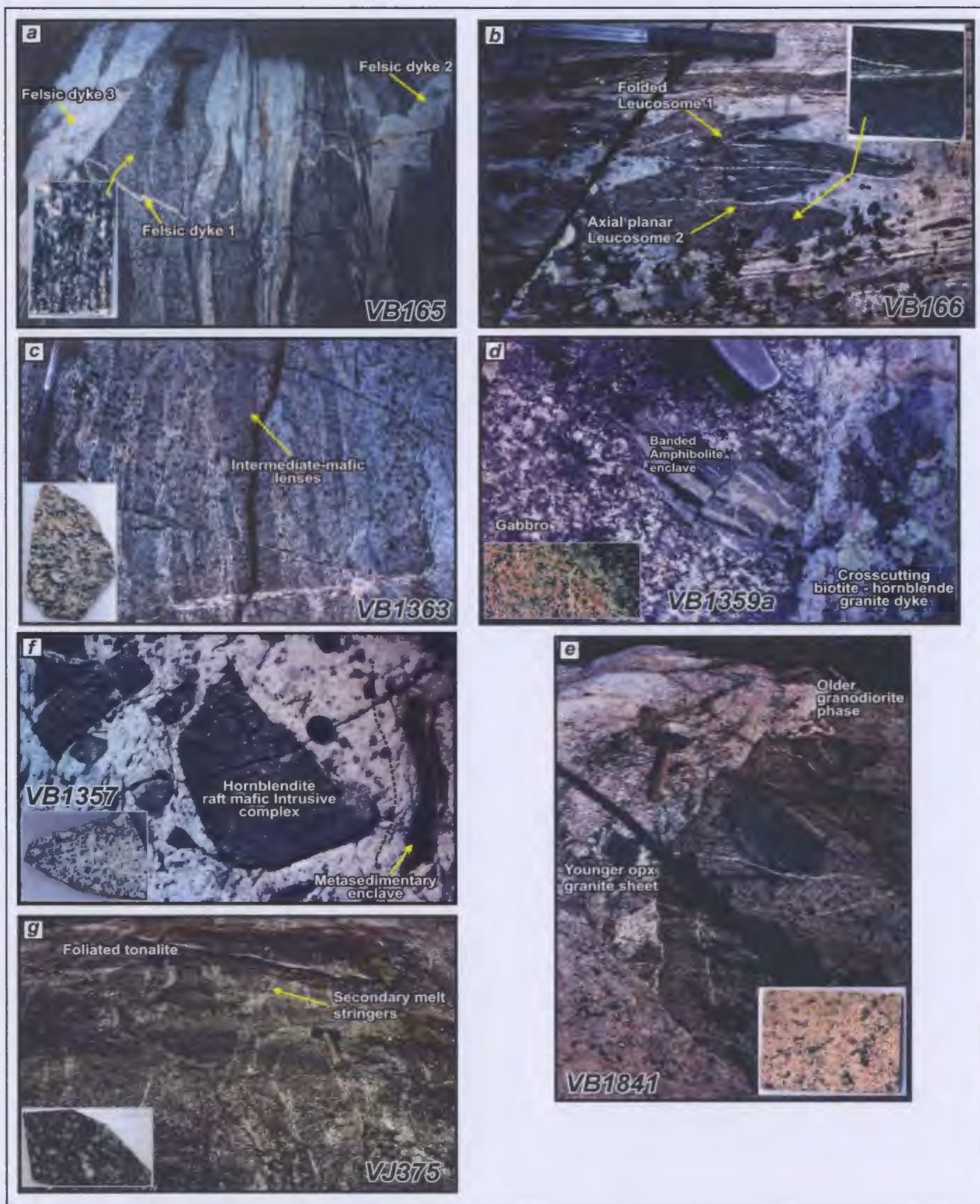
Metaluminous Intrusions						
2σ Without U Decay Constant Uncertainties				2σ With U Decay Constant Uncertainties		
	Concordia Age	Intercept Ages	Weighted ²⁰⁷Pb/²⁰⁶Pb age	Concordia Age	Intercept Ages	Weighted ²⁰⁷Pb/²⁰⁶Pb age
VB 165 <i>IDTIMS</i>	2673.9 ± 0.8 Ma	U: 2674.4 ± 1.4 Ma L: 172 ± 740 Ma	2674.3 ± 0.8 Ma	* 2671 ± 3.2 Ma	U: 2674.4 ± 7.1 Ma L: 172 ± 740 Ma	2674.3 ± 6.8 Ma
VB 166 <i>IDTIMS</i>	<i>n.a.</i>	U: 2674.3 ± 2.9 Ma L: -74 ± 210 Ma	2675.3 ± 1.3 Ma	<i>n.a.</i>	U: 2674.3 ± 7.2 L: -74 ± 210 Ma	* 2675.3 ± 6.9 Ma
VB 1363	2636 ± 2 Ma <i>IDTIMS</i>	<i>n.a.</i>	2635.4 ± 3.2 Ma	* 2637.2 ± 4.6 Ma	<i>n.a.</i>	2635.5 ± 6.9 Ma
	2631.5 ± 7.4 Ma <i>LAM ICP-MS</i>	U: 2635.9 ± 4.8 Ma L: -73 ± 150 Ma	2639.4 ± 4.3 Ma	2630.4 ± 8.8 Ma	U: 2635.9 ± 8.2 Ma L: -73 ± 150 Ma	2639.5 ± 8 Ma
VB 1359A <i>IDTIMS</i>	2608.4 ± 1.1 Ma	U: 2608 ± 3 Ma L: 1295 ± 3700 Ma	2608.1 ± 1.3 Ma	* 2608.2 ± 3.4 Ma	U: 2608 ± 11 Ma L: 1295 ± 3700 Ma	2608.1 ± 6.8 Ma
VB 1841 <i>LAM ICP-MS</i>	<i>n.a.</i>	U: 2598 ± 3 Ma L: -3 ± 58 Ma	2596.7 ± 2.9 Ma	<i>n.a.</i>	U: 2598 ± 7.3 Ma L: -3 ± 58 Ma	* 2596.7 ± 7.3 Ma
VB 1357 <i>LAM ICP-MS</i>	2594 ± 7.3 Ma	U: 2597.1 ± 7.7 Ma L: 129 ± 280 Ma	2604.2 ± 7.4 Ma	* 2594 ± 9 Ma	U: 2597.1 ± 10 Ma L: 129 ± 280 Ma	2604.2 ± 10 Ma
VJ 375 <i>IDTIMS</i>	2589 ± 1.3 Ma	U: 2588.8 ± 1.5 Ma L: <i>n.a.</i>	2589 ± 4.8 Ma	* 2589 ± 3.9 Ma	U: 2588.8 ± 5.1 Ma L: <i>n.a.</i>	2589.2 ± 8.2 Ma
Peraluminous Intrusions						
VB 1358	<i>n.a.</i> <i>IDTIMS</i>	<i>n.a.</i>	2598 ± 5.8 Ma	<i>n.a.</i>	<i>n.a.</i>	2598 ± 8.7 Ma
	<i>n.a.</i> <i>LAM ICP-MS</i>	U: 2592 ± 4.2 Ma L: -6 ± 49 Ma	2595.1 ± 4.8 Ma	<i>n.a.</i>	U: 2592 ± 8.2 Ma L: -6 ± 49 Ma	* 2595 ± 8.2 Ma
PVB 9	<i>n.a.</i> <i>IDTIMS</i>	U: 2597.1 ± 2 Ma L: 44 ± 94 Ma	2596.9 ± 1.7 Ma	<i>n.a.</i>	U: 2597.1 ± 7 Ma L: 44 ± 94 Ma	* 2596.9 ± 6.9 Ma
	2598 ± 7.9 Ma <i>LAM ICP-MS</i>	U: 2596.5 ± 4.4 Ma L: -35 ± 77 Ma	2596.5 ± 3.7 Ma	2598 ± 9.2 Ma	U: 2596.5 ± 7.9 Ma L: -35 ± 77 Ma	2596.5 ± 7.6 Ma
VB 1688	2598 ± 2 Ma <i>IDTIMS</i>	U: 2596.3 ± 3.3 Ma L: 57.2 ± 95.3 Ma	2597 ± 2.7 Ma	* 2598 ± 4.3 Ma	U: 2596.3 ± 9.2 Ma L: 57.2 ± 95.3 Ma	2597 ± 7.2 Ma
	2596 ± 4.1 Ma <i>LAM ICP-MS</i>	U: 2597.1 ± 2.5 Ma L: -19 ± 51 Ma	2597 ± 2.4 Ma	2594 ± 6.7 Ma	U: 2597.1 ± 7.1 Ma L: -19 ± 51 Ma	2597 ± 7.1 Ma
VB 161 <i>LAM ICP-MS</i>	<i>n.a.</i>	U: 2580.1 ± 5.7 Ma L: -2 ± 41 Ma	2585.1 ± 5.5 Ma	<i>n.a.</i>	U: 2580.1 ± 8.7 Ma L: -2 ± 41 Ma	* 2585 ± 8.6 Ma
VB 1229A <i>IDTIMS</i>	<i>n.a.</i>	U: 2585.2 ± 0.7 Ma L: 8.9 ± 8.6 Ma	2585 ± 0.7 Ma	<i>n.a.</i>	U: 2585.2 ± 6.7 Ma L: 8.9 ± 8.6 Ma	* 2585 ± 6.7 Ma
VB 1864 <i>IDTIMS</i>	<i>n.a.</i>	<i>n.a.</i>	2586 ± 5.8 Ma	<i>n.a.</i>	<i>n.a.</i>	* 2586 ± 8.7 Ma

Note: *n.a.*, not available for calculation; *U*, upper intercept; *L*, lower intercept. * denotes preferred crystallization age.

foliation defined by biotite, hornblende and stretched quartzofeldspathic segregations. Field and microstructural evidence indicate that it has undergone an extended deformational history, as it displays evidence for D1 and D2 folding and is cross-cut by late-D1, and syn-D2 and D3 intrusions.

The sample yielded abundant, high quality, light pink to brown zircon crystals that were grouped into four populations (Figs. 2.6a and 2.7a): (i) clear to light pink elongate prisms 100-200 μm long with aspect ratios of 4:1; (ii) stubby, moderately faceted, euhedral prisms 100-200 μm in diameter with aspect ratios of 1:1; (iii) light pink to translucent needles 100-200 μm long and with aspect ratios of 6:1; and (iv) pyramids 100-150 μm diameter with aspect ratios of 2:1, dark brown cores and light pink to translucent euhedral rims. The two prismatic populations were selected for ID-TIMS analysis. Back scattered electron imaging (Fig. 2.6a) revealed planar growth zoning among the elongate prisms and concentric and sector zoning in the stubby prisms. Featureless, bright embayed rims exhibiting irregular zonation patterns truncate the planar, growth or sector zoned cores. Representative BSE images of abraded grains showed successful removal of overgrowths. Four single grain fractions (3 elongate prisms and 1 stubby prism) with moderate U concentrations (91-163 ppm) yielded near concordant analyses (0.06 – 0.9% discordant). An error weighted regression of the data yields an upper intercept of 2674.4 ± 7.1 [± 1.4] Ma. A weighted average (mean square of weighted deviates (MSWD) = 0.42) of the $^{207}\text{Pb}/^{206}\text{Pb}$ ratios yielded an age of 2674.3 ± 6.8 [± 0.8] Ma (Table 2.1, Fig. 2.7a). A concordia age of 2671 ± 3 [2673.0 ± 0.8] Ma was calculated using fractions Z1, Z2 and Z4 and is considered the best estimate of the

Figure 2.5: Field relationships of seven metaluminous intrusive units, with polished slabs of representative samples (inset). Hammer is approximately 45 cm in length. Lens cap is approximately 5 cm in diameter. (a) *VB165*: Synvolcanic tonalite, high strain zone, Kwejinne Lake supracrustal belt. Three cross-cutting felsic dykes are indicated. (b) *VB166*: Synvolcanic gabbro within high-strain zone, Kwejinne Lake supracrustal belt. Two felsic vein generations are present, one folded and the other parallel to the regional foliation. (c) *VB1363*: Biotite-hornblende granodiorite, an older phase of the Disco Intrusive Suite. (d) *VB1359A*: Coarse-grained gabbro - monzonite, Mafic Intrusive Complexes, Kwejinne Lake supracrustal belt. Gabbro incorporates amphibolite enclaves from adjacent high-strain zone and is crosscut by biotite-hornblende granite dyke, inferred to be coeval with VB1357. (e) *VB1841*: Mid-crustal orthopyroxene granite, youngest phase of the Disco Intrusive Suite. A sharp contact between older and younger phases is indicated. (f) *VB1357*: Upper-crustal biotite-hornblende granite with metasedimentary and hornblendite enclaves the latter from Mafic Intrusive Complexes. A weak foliation is parallel to the regional D2 fabrics. (g) *VJ375*: Foliated tonalite within megacrystic granite, Kwejinne Lake supracrustal belt.



crystallization age.

Synvolcanic gabbroic gneiss - VB166: Sample VB166 consists of medium- to coarse-grained hornblende–biotite gabbroic gneiss (Fig. 2.5b) from a 1m wide lens in the high strain zone surrounding the Hinscliffe complex. The gneiss displays a foliation defined by the alignment of biotite, hornblende and sparse elongate leucosomes, which were avoided during sample preparation. The unit shares the same deformational history as VB165, including at least two episodes of folding and overprinting by late-D1 and younger intrusions.

VB166 yielded moderate quality tan to light brown zircon grains that were separated into two populations (Fig. 2.6b): (i) small, light brown to translucent needles, 100-200 μm long with aspect ratios of 6:1 – 8:1, longitudinal and transverse cracks, and thin euhedral terminations on the largest needles; and (ii) a subordinate population of well-faceted, translucent to light-brown prisms, 100-120 μm in length with aspect ratios of 3:1. Both populations were selected for analysis by ID-TIMS. Back scattered electron imaging of the needle population shows an internal structure dominated by planar growth zoning parallel to crystal faces, with irregular and patchy and heterogeneous bright zones truncating primary growth zonation. The prism population displayed weak growth zoning with patchy featureless, bright cores. Four fractions, 2 multigrain fractions (9 and 11 grains, Z1 and Z2 respectively) and 2 single-grain fractions (Z3 unabraded and Z4 abraded) with low to moderate U concentrations (136-409 ppm) yielded variably discordant results (0.97 to 5.65 % discordance). An error weighted regression of the data yields an upper intercept of 2674.3 ± 7.2 [± 2.9] Ma. A weighted average (MSWD= 0.59)

Figure 2.6: Transmitted-light, BSE and SE images of zircon populations and single grains in metaluminous intrusions. Some grains show elongate laser pits. *(a) VB165.* Ai, elongate prisms, planar growth zoning; aii stubby prisms, broad concentric sector zoning. *(b) VB166:* bi & bii needles and prisms, respectively; diffuse planar zoning with patchy recrystallization. *(c) VB1363:* ci & cii needles and prisms, respectively; ci-1, patchy recrystallized core, fine oscillatory zoned rim; ci-2a and ci-b, BSE and SE images, respectively, of laser ablation pit, rim - crystallization age; cii-1 oscillatory zoning; cii-2, disturbed, patchy recrystallized core, weak oscillatory zoned rim; cii-3, relict sector zoned core, weak oscillatory zoned rim; cii-4, nebulous, wispy core recrystallization. *(d) VB 1359A.* di, prisms, planar growth zoning, minor secondary recrystallization (right hand corner), faint oscillatory zoned outer - rim and featureless overgrowth (low BSE); dii needles, homogeneous core with a thin, weak oscillatory zoned outer rim recrystallized tip. *(e) VB1841.* ei-1 and ei-2, needle - relict primary oscillatory zoning, secondary recrystallization, homogeneous - planar growth zoned rim; ei-3a and ei-3b - BSE & SEM images of laser ablation pit, inherited core; eii-1, prisms, diffuse, sector zoned inherited core, broad planar zoned rim (emplacement age); eii-2, prisms, relict oscillatory zoned core, homogeneous rim; eiii-3, diffuse concentric planar zoning - metamorphic age. *(f) VB1357.* fi & fii needles and prisms, respectively; fi-1 and fi-3, oscillatory zoning; fi-2, diffuse sector zoned core, oscillatory zoned rim; fi-4a and fi-4b, BSE and SEM images of laser ablation pit, crystallization age grain; fii-1, oscillatory zoning; fii-2, secondary recrystallized core, oscillatory zoned rim; fii-3, wispy secondary zoning; fii-4, oscillatory zoning, patchy recrystallization. *(g) VJ375.* gi, needles, diffuse oscillatory zoning, patchy recrystallization; gii, prisms, weak sector zoning, patchy recrystallization.

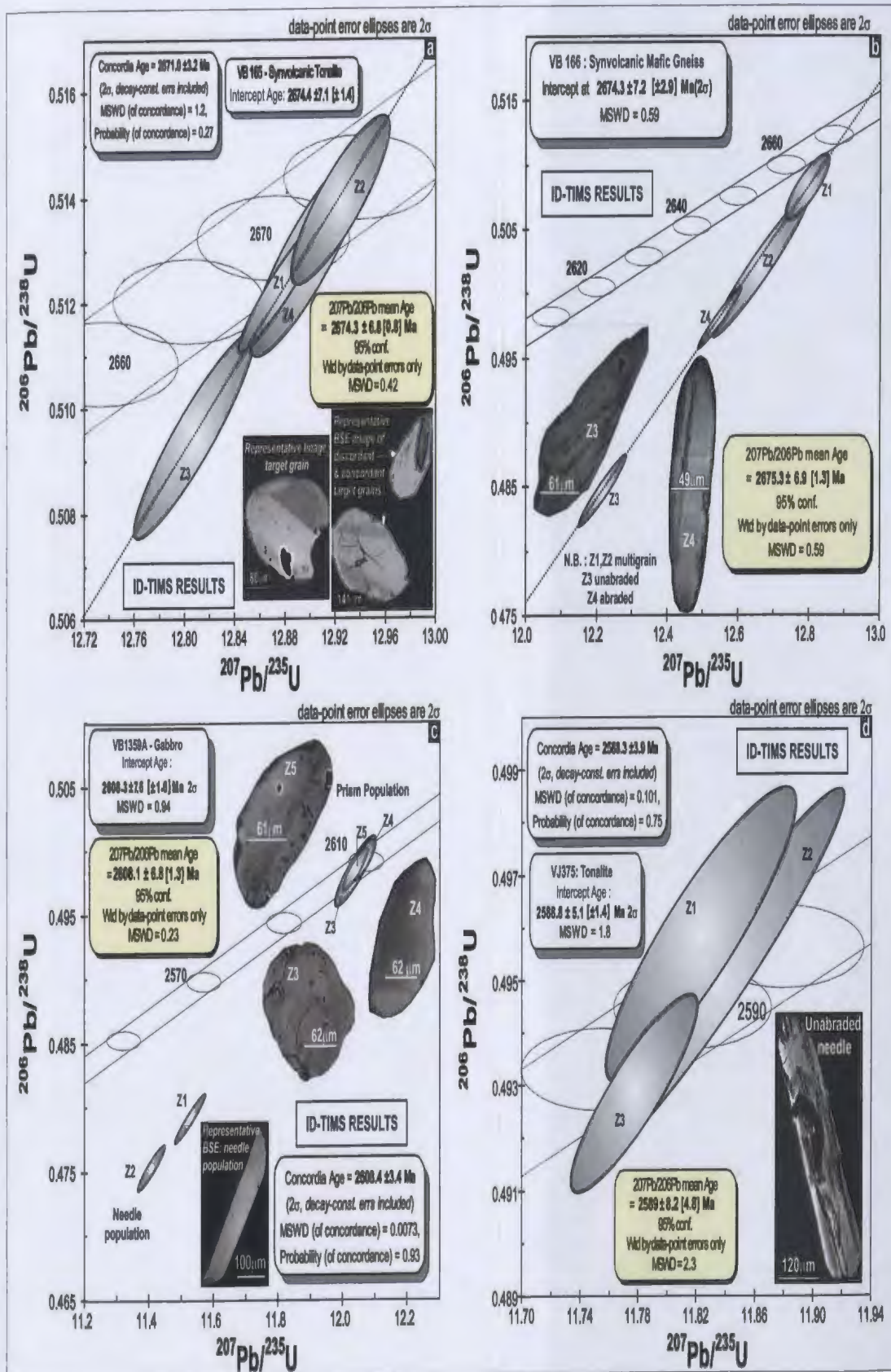
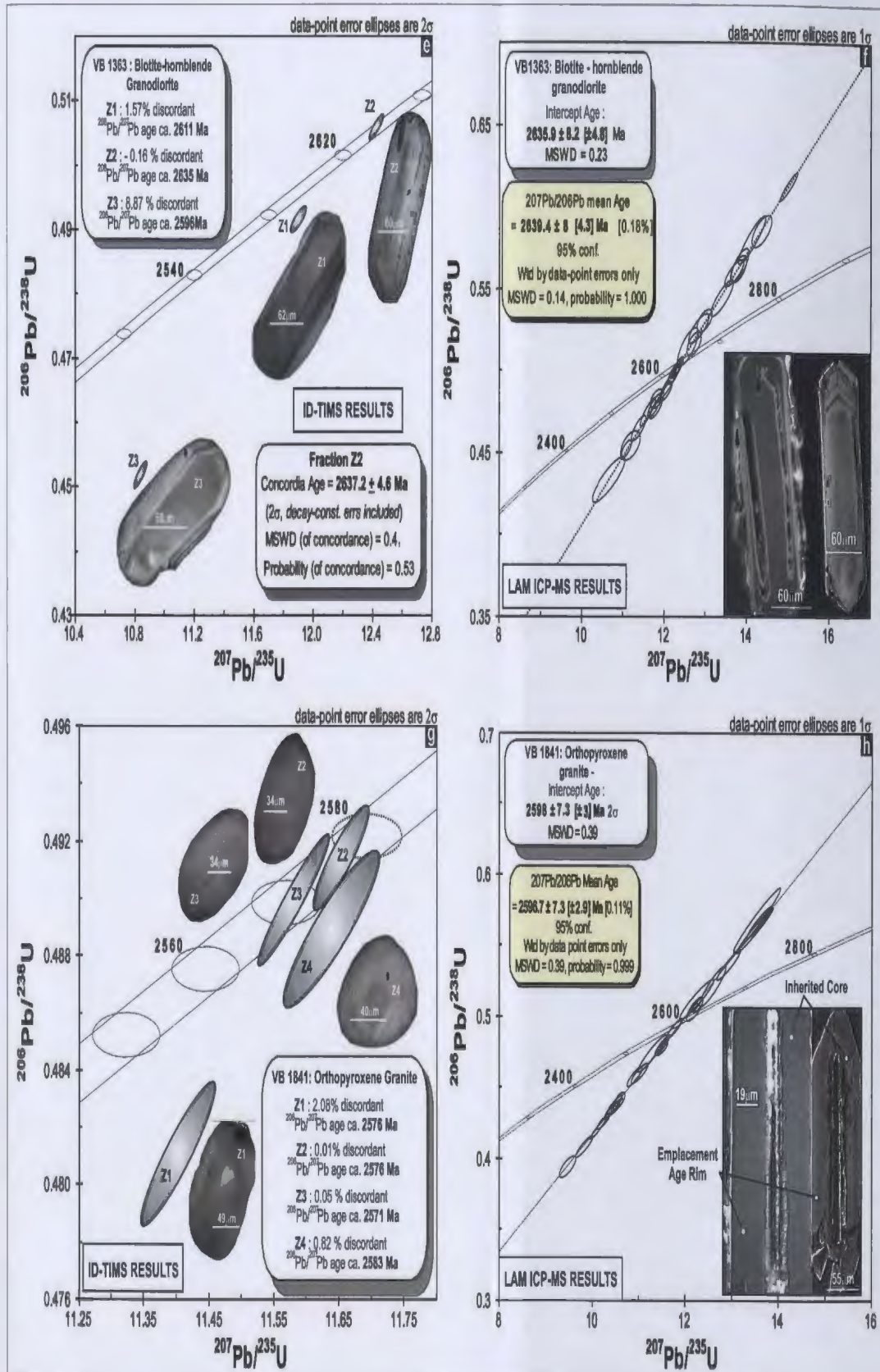


Figure 2.7a - d: ID-TIMS concordia diagrams for metaluminous intrusions, samples VB165, VB166, VB1359A, VJ375. Decay constant uncertainties of concordia are indicated and representative images of analyzed zircons are shown.

of the $^{207}\text{Pb}/^{206}\text{Pb}$ ratios yields an age of 2675.3 ± 6.9 [± 1.3] Ma (Table 2.1, Fig. 2.7b), which is interpreted as the best estimate of the crystallization age.

Biotite–hornblende granodiorite - VB1363: Sample VB1363 is from one of numerous bodies and sheets of homogeneous fine- to medium-grained biotite-hornblende granodiorite (Fig. 2.5c), which constitutes an older phase of the Disco Intrusive Suite in the Ghost subdomain. Mafic enclaves are abundant near the margins of the intrusions and the unit exhibits a fabric defined by alignment of biotite, hornblende and mafic enclaves. Foliations in the granodiorite are axial planar to the D2 regional fabric, with earlier fabrics and folds occurring locally. VB1363 is intruded by syn-D2 and D3 intrusions.

The sample yielded reasonable quality, light brown to pink zircon grains that were separated into two populations (Fig. 2.6c): (i) needles, 100–200 μm long with aspect ratios of 4:1 and euhedral overgrowths on the largest grains; and (ii) well-faceted translucent stubby prisms 100–120 μm in length with aspect ratios of 3:1. Both populations were imaged. The needle population contains dull cores with diffuse, patchy or weak growth zoning, mantled by sharply defined concentric, growth-zoned brighter rims, whereas the prism population had cracked, dull cores with relict planar, sector and growth zoning, mantled by growth-zoned rims. Internal structures in the prism cores are similar to those in recrystallized zircon described by Pidgeon et al. (1998), with subdued primary growth zoned structures cross-cut by lobate unzoned regions. The needle population was targeted for ID-TIMS, and three imaged and abraded, single grain fractions with low to moderate U concentrations (130–222 ppm) yielded discordant data (-0.16 to 8.87 %) with $^{207}\text{Pb}/^{206}\text{Pb}$ ages ranging from 2635 to 2596 Ma. Back scattered



electron images of abraded fractions Z1 and Z3 (Fig. 2.6c) had inherited, dull cores with minor heterogeneous zoning mantled by brighter rims that were not entirely removed by abrasion, and as a result the $^{207}\text{Pb}/^{206}\text{Pb}$ ages are not considered reliable estimates of the time of crystallization. The near concordant Z2 fraction (U = 222 ppm, Table 2.1), which was predominantly composed of the brighter, growth zoned, rim component of the abraded needle, yielded a $^{207}\text{Pb}/^{206}\text{Pb}$ age of 2635 ± 6.9 [3.2] Ma. No definitive age can be assigned on the basis of the ID-TIMS dataset.

The complex core/rim relationships and evidence for either dissolution / reprecipitation or recrystallization processes within these zircon grains suggested that additional analyses by ID-TIMS would be unlikely to resolve the age of this sample, so the LAM ICP-MS technique, with its enhanced spatial resolution, was utilized. Twenty-four analyses of rims were obtained from 20 needles and prisms (Table A1, Fig. 2.7f). The analyses have $^{207}\text{Pb}/^{206}\text{Pb}$ ages within error of a single value and a weighted mean of 2639.4 ± 8 [± 4.3] Ma (MSWD = 0.37). The data are normally to reversely discordant (12 to 16 %) and spread along a chord with an upper intercept of 2635.9 ± 8.2 [± 4.8] Ma and a lower intercept of -73 ± 150 Ma. The laser data are in good agreement with fraction Z2 of the ID-TIMS data and the concordia age of 2637.2 ± 4.6 [2636 ± 2] Ma is considered the most precise estimate of the crystallization age.

Gabbro – monzonite mafic complex - VB1359A : Sample VB1359A is from a small stock <1 km in diameter, composed of coarse-grained, relatively homogeneous hornblende gabbro-monzonite (Fig. 2.4d), one of nine bodies that intrude meta-turbidites in the Kwejinne Lake belt. As a group, these intrusions are compositionally variable,

ranging from ultramafic to granodioritic. Deformation fabrics are not strongly developed, but where present, they parallel the regional D2 fabrics in the adjacent high strain zone. The stock appears to truncate a D1 mica fabric in cordierite-bearing meta-turbidites and locally straddles the M2 sillimanite + melt-in isograd. No grade change or fabric development was observed in the hornblende-plagioclase-biotite mineralogy across the stock, suggesting that emplacement post-dated M1. Rare enclaves that preserve D1 folds typical of the adjacent high-strain zone indicate that emplacement postdated D1, and the arcuate arrangement of the nine intrusions, of similar composition and character, around the antiformal fold nose of the Hinscliffe complex (Figs. 2.2a, 2.3) suggests that emplacement of this plutonic suite was pre- to syn-D2. The unit is intruded by late D2 and syn-D3 intrusions.

Sample VB1359A yielded good quality, dark pink to brown zircon crystals that were subdivided into three populations (Fig. 2.6d): (i) euhedral prisms 100-300 μm long, with aspect ratios of 3:1 and narrow, faceted, translucent overgrowths on some grains; (ii) needles 50-150 μm long, with aspect ratios of 5:1 and thin translucent prismatic overgrowths on the largest grains; and (iii) a population of stubby prisms ca. 100 μm in diameter and aspect ratios of 2:1, with dark pink cores and lighter pink rims and overgrowths. BSE imaging of the prism population (Figs. 2.6d, 2.7c) revealed cores with diffuse planar, concentric or patchy zoning truncated and mantled by fine growth-zoned bands and featureless dull tips, whereas the needle population had unzoned, homogeneous cores mantled by faint growth zoning parallel with recrystallized grains tips showing dull patchy zoning. Three single prisms (Z3, Z4 and Z5) and 2 multigrain

fractions (Z1 and Z2) consisting of 8 and 6 needles were selected for analysis by ID TIMS. Back scattered electron imaging of the three single grain prism fractions after abrasion indicated that the outer rims were successfully removed. Fractions Z3, Z4 and Z5 (Fig. 2.6c, Table 2.1), which had low to moderate U concentrations (102-178 ppm), yielded near concordant analyses (0.03, -0.07 and 0.08% discordant, respectively) and $^{207}\text{Pb}/^{206}\text{Pb}$ ages ranging from 2608 - 2609 Ma. Multi-grain fractions Z1 and Z2, which had higher U concentrations, yielded discordant data (3.59 to 4.19% discordant) and $^{207}\text{Pb}/^{206}\text{Pb}$ ages ranging from 2597 - 2601 Ma. An error weighted regression of the single grain fractions yields an upper intercept age of 2608.3 ± 7.6 [1.6]. The weighted average (MSWD = 0.23) of the $^{207}\text{Pb}/^{206}\text{Pb}$ ages is 2608.3 ± 6.8 [1.3] Ma (Table 2.1, Fig. 2.6a). The concordia age, calculated using single grain fractions Z3-5, is 2608 ± 3.4 [2608.4 \pm 1.1] Ma, represents the most precise estimate of the crystallization age.

Orthopyroxene granite - VB1841: Sample VB1841 is from a sheet of medium- to coarse-grained, homogeneous, pink orthopyroxene granite with abundant mafic enclaves (Fig. 2.5e) and represents the youngest phase of the Disco Intrusive Suite. Locally, the enclaves have thin rims with the assemblage orthopyroxene-plagioclase \pm quartz mantling hornblende-biotite-plagioclase \pm quartz cores, suggesting the rims originated by contact metamorphism during emplacement. A weak to moderate biotite foliation within the orthopyroxene granite parallels the D2 regional fabric in the surrounding country rocks. The granite intrudes an older biotite – hornblende granodiorite, which shows evidence for earlier deformation, in part associated with D1 and one leucosome-forming event interpreted to have formed syn-D2. Emplacement of the orthopyroxene granite is

therefore, considered to postdate D1 and be synchronous with D2 / M2; the unit is cut by syn-D3 intrusions.

The sample yielded abundant, good quality, dark pink to brown zircon crystals that were separated into four groups (Fig. 2.6e): (i) prisms ca. 50-150 μm in length with aspect ratios of $\sim 3:1$ and rounded terminations; (ii) well faceted stubby prisms ca. 100 μm in diameter; (iii) elongate needles 150-300 μm long, with aspect ratios of $\sim 5:1$, rounded terminations, pervasive longitudinal cracks, and orange cores; and (iv) aggregated grains ca. 100 -150 μm in length, aspect ratios of $\sim 3:1$ and indistinct rounded crystal terminations. Back scattered electron imaging of the two prism morphologies showed that cores are present in some grains in population (i), which is characterized by internal structures with diffuse concentric sector zoning modified by secondary patchy recrystallization; and that population (ii) has ubiquitous, small cores exhibiting disturbed concentric oscillatory or planar growth zoning, mantled by brighter rims with weak diffuse concentric growth zoning, suggesting that the latter are of metamorphic origin. The needle population (iii) revealed cores with complex zoning patterns including relict oscillatory and planar growth zoning overprinted by irregular recrystallized domains, and the grain aggregates (iv) displayed featureless and homogeneous cores mantled by thin, dull rims with diffuse growth zoning. Prism population (i) was chosen for ID-TIMS analysis based on the relative simplicity of the internal structures, and BSE imaging of the selected grains (Fig. 2.7g) illustrates the lack of inherited cores. Four single grain fractions with low to moderate U concentrations (136-371 ppm) yielded near concordant to slightly discordant analyses (0.01 to 2.08% discordant) and $^{207}\text{Pb}/^{206}\text{Pb}$ ages ranging

from 2583-2571 Ma (Fig. 2.7g, Table 2.1). An error weighted regression of fractions Z1 and Z2 yields an upper intercept age of 2576.9 ± 7.1 [± 2.4]. However, the spread of concordant and near concordant U-Pb ages in this sample is similar to that reported by Ashwal et al. (1999), which they attributed to high temperature Pb-loss during an extended episode of granulite-facies metamorphism. This is compatible with field relationships, which indicate the orthopyroxene granite was emplaced during D2 and subsequently underwent the high-temperature M3 metamorphism, and with petrographic evidence for zircon recrystallization. Therefore, it is possible that the ID-TIMS date does not reflect the time of emplacement, but is rather an estimate of the age of the M3 metamorphic event. Independent field evidence supporting this suggestion is based on the crosscutting relationships of the syn-D3 pegmatite dykes, and the fact that the ID-TIMS age determined for this sample is ca. 10 M.y. younger than the emplacement age of these dykes (samples VB1229A and VB161 discussed below).

In an attempt to resolve the emplacement age of sample VB1841, additional U-Pb data were collected from approximately 50 needles and prisms (population i) using the LAM ICP-MS. The metamorphic prism population (ii) was avoided. Initially cores were analyzed, but the resultant data were found to yield inheritance ages (see Chapter 5). Consequently rims on prisms and needles that were either unzoned or displayed growth zoning were sampled. Twenty eight analyses (Table A1, Fig. 2.7h) gave $^{207}\text{Pb}/^{206}\text{Pb}$ ages within error of a single value, clustering around a weighted mean (MSWD = 0.39) of 2596.7 ± 7.3 [2.9] Ma. The U/Pb analyses spread along a chord and exhibit both normal and reverse discordance (17.5 to -11.7 %) with an upper intercept of 2598 ± 7.3 [± 3] Ma

and a lower intercept of 14 ± 82 Ma. This age is consistent with field relations and the estimated emplacement ages of younger intrusions (see below). The $^{207}\text{Pb}/^{206}\text{Pb}$ date of 2596.7 ± 7.3 [± 2.9] Ma is considered the best estimate of the emplacement age of the orthopyroxene granite.

Biotite-hornblende granite - VB1357: Sample VB1357 is from one of several small intrusions of biotite-hornblende granite to granodiorite that occur as sheets and small plutons emplaced in the supracrustal belts of the SRT. The sampled body is a ca. 6 km² granodiorite sheet with an arcuate geometry that intrudes both the turbidites and a gabbro-monzonite complex in the Kwejinne Lake supracrustal belt. A weak to moderate foliation, defined by alignment of hornblende and biotite, is parallel to the margins of the body (Fig. 2.5f) and the regional foliation in adjacent cordierite-bearing metaturbidites. The granodiorite truncates the gabbro-monzonite pluton in addition to D1 and early D2-mica and cordierite deformational fabrics, respectively, in adjacent metaturbidites and is cut by syn-D3 intrusions. Based on these constraints the pluton is interpreted to be broadly syn-D2 in age.

The sample yielded a modest quantity of moderate to poor quality zircon crystals that were separated into three populations (Fig. 2.5): (i) dark brown to pink prisms ca. 50-150 μm in length with aspect ratios of 2:1 and rounded terminations; (ii) light pink to brown, elongate prisms ca. 50-200 μm in length with aspect ratios of 3:1 and well faceted terminations; and (iii) light pink to translucent needles 50-250 μm long with aspect ratios of 5:1 and rounded to moderately well-faceted terminations. Back scattered electron imaging of the prism populations revealed cores with faint oscillatory, sector and planar

growth zoning truncated and overgrown by dull recrystallized rims with wispy or patchy zoning. The needle population showed cores with oscillatory and planar growth zoning truncated and overgrown by featureless recrystallized rims. Fractions from both the prism and needle populations were selected for ID-TIMS analysis. Four single grain fractions, with low to moderate U concentrations (116-381 ppm), yielded discordant analyses (1.57 to 20.79% discordant) and $^{207}\text{Pb}/^{206}\text{Pb}$ ages ranging from 2649-2397 Ma (Fig. 2.7i, Table 2.1). The least discordant fraction Z1, which showed fine planar growth zoning, yielded a $^{207}\text{Pb}/^{206}\text{Pb}$ age of ca. 2588 Ma. This age corresponds to the time of emplacement of syn-D3 intrusions that crosscut the granodiorite and is, therefore, not considered to represent the crystallization age. In fractions Z2 and Z4 there was incomplete removal of the outer recrystallized rims and significant cracking in the cores. The discordance of these analyses is interpreted to be due to a combination of variable Pb loss and mixing of different age domains. Fraction Z3, with a featureless cracked core mantled by a faint, growth zoned outer rim, yielded a $^{207}\text{Pb}/^{206}\text{Pb}$ age of ca. 2649 Ma, which is significantly older than the gabbro-monzonite intrusion (ca. 2608 Ma) cross-cut by this granodiorite, suggesting that it is an inheritance age.

In an attempt to resolve the crystallization age of the granodiorite, additional U-Pb age data were collected from approximately 50 needles and prisms, using LAM ICP-MS. Cores were sampled, particularly where BSE imaging revealed primary growth structures (Fig. 2.7j) and minimal secondary recrystallization or dissolution and reprecipitation. Of the 67 analyses, only 8 are interpreted to represent the crystallization age. Inherited grain populations dominate this unit, which appears to have had minimal

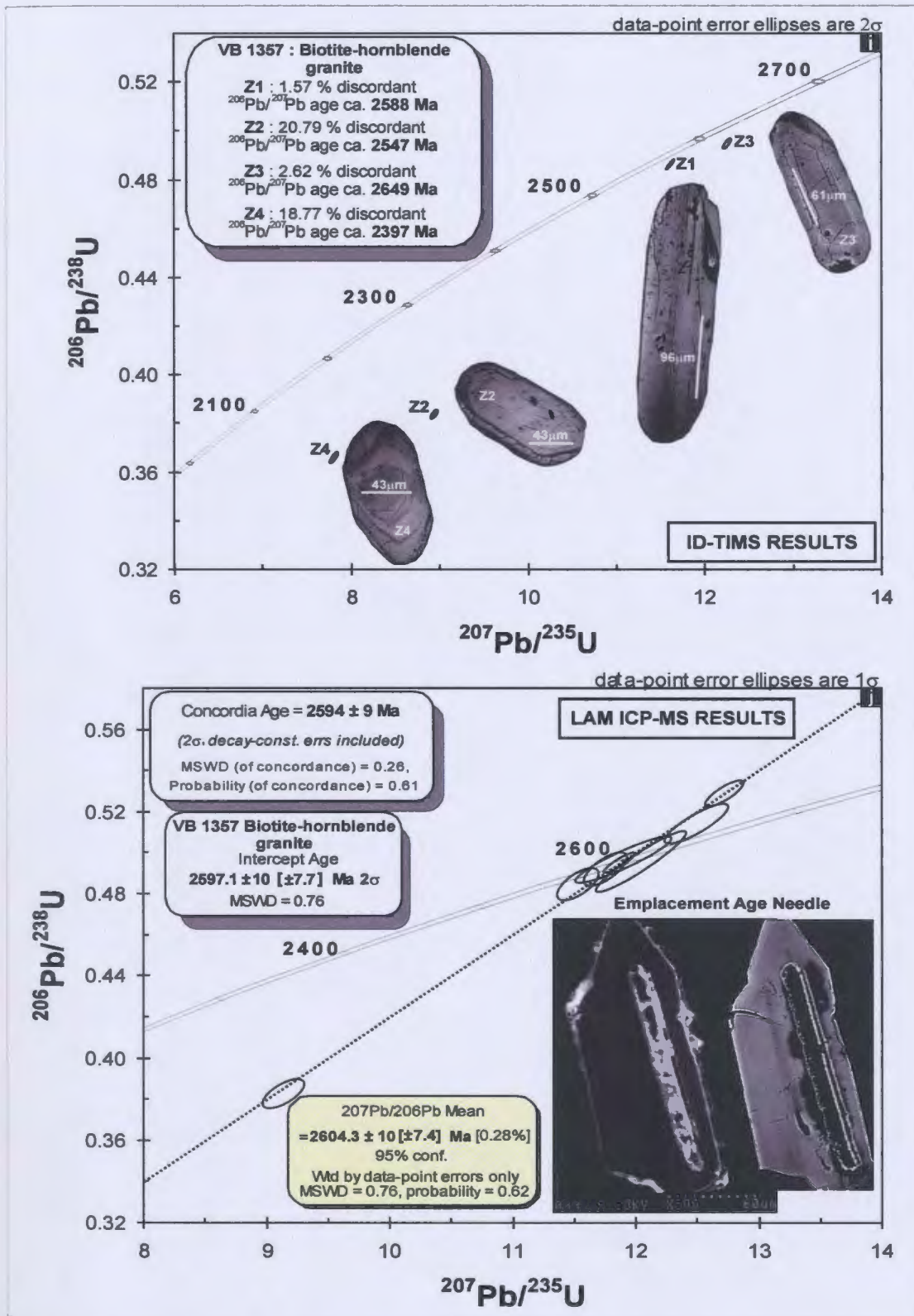


Figure 2.7i-j: ID TIMS and LAM ICP-MS concordia diagrams for metaluminous intrusions samples VB1357. Decay constant uncertainties of concordia are indicated and representative images of analyzed zircons are shown.

new zircon growth during emplacement. The eight analyses (Table A1, Fig. 2.7j) yielded $^{207}\text{Pb}/^{206}\text{Pb}$ ages within error of a single value, clustering around a weighted mean (MSWD=0.76) of 2604.3 ± 10 [± 7.4] Ma. The analyses, which lie on a chord and are both normally and reversely discordant (19.5 to -5.6%), yield an upper intercept of 2597.1 ± 10 [± 7.7] Ma and a lower intercept of 129 ± 280 Ma. The concordia age of 2594 ± 9 Ma for these eight analyses is considered to represent the best estimate of the emplacement age of the granite.

Tonalite - VJ 375: Sample VJ375 is from a sheet of medium- to coarse-grained homogeneous biotite tonalite in a large body of megacrystic granite (Fig. 2.5g). Where sampled, the intrusion has a northwest-striking foliation defined by the alignment of biotite aggregates, plagioclase phenocrysts with rounded terminations and secondary melt segregations. A northwest-trending mineral lineation is also present. Contact relations are ambiguous as a result of post-emplacement deformation. The tonalite is intruded by peraluminous dykes, indicating emplacement occurred pre- to syn-D3.

The sample yielded abundant reasonable quality zircon grains that were separated into two populations (Fig. 2.6g): (i) tan to dark brown needles 100-300 μm long with aspect ratios of 6:1, rounded, symmetrical terminations, and longitudinal and transverse cracks; (ii) tan to pink prisms ca. 150 μm long with aspect ratios of 3:1. Overgrowths were not observed in either population. Back scattered electron imaging (Figs. 2.6g, 2.7d) showed faint planar, growth and weak sector zoning overprinted by heterogeneous patchy domains. The three multigrain fractions (Z1-Z3), consisting of mixtures of 8, 10 and 11 of needles and prisms with moderate U concentrations (239-246 ppm), yielded near

concordant analyses (-0.46 to 0.32% discordant) with $^{207}\text{Pb}/^{206}\text{Pb}$ ages ranging from 2586 – 2590 Ma. An error weighted regression of the data yields an upper intercept age of 2588.3 ± 5.1 [± 1.5] Ma. The weighted average (MSWD = 2.3) of $^{207}\text{Pb}/^{206}\text{Pb}$ ratios 2589.2 ± 8.2 [± 4.8] Ma. The concordia age of 2588.3 ± 3.9 [± 1.3] Ma is considered the most precise estimate of the crystallization age for this sample.

2.8.2 Peraluminous Intrusions

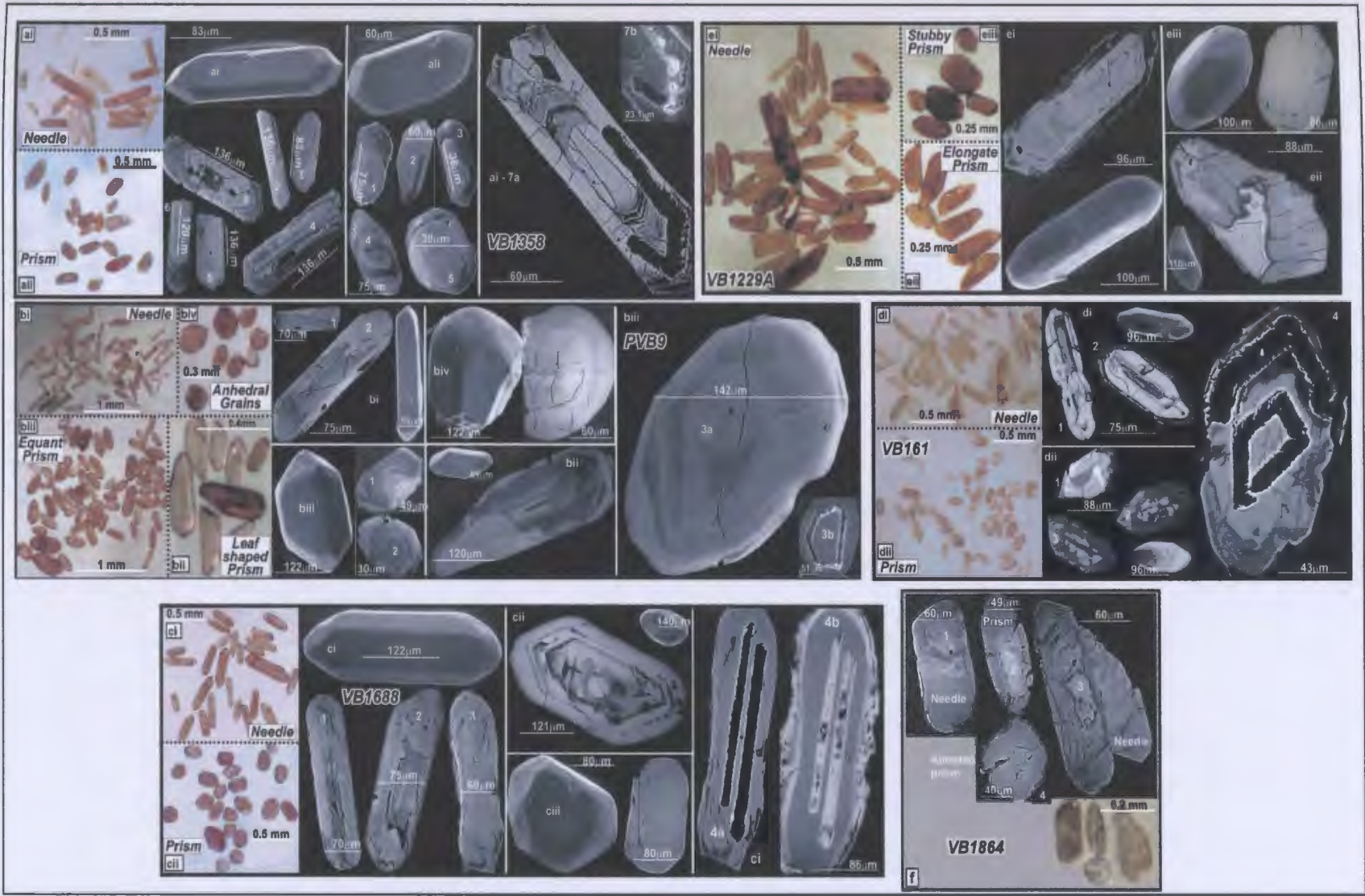
Two Mica Granite - VB 1358: Sample VB1358 is from a biotite-muscovite granite batholith in Bigspruce subdomain. The batholith, the largest peraluminous body in the SRT, is situated in the mid to upper crust and intrudes the lower structural levels of the Kwejinne Lake belt. Individual intrusions in the batholith range from large, irregular masses to small discordant sheets. The main body principally consists of two phases (Fig. 2.8a): a variably foliated, equigranular to porphyritic phase with abundant metasedimentary enclaves and a younger enclave-free, equigranular phase with a weak mica foliation. The younger phase was sampled for this study. Minor D2 folds are observed locally and it is crosscut by syn- to post-D3 intrusions. Based on these relationships the two-mica granite is interpreted to have been emplaced post-D1/M1 and syn- to late D2.

The sample yielded a minor amount of zircon that was subdivided into two populations (Fig. 2.9a): (i) translucent to light pink needles 100 - 200 μm long with aspect ratios of 5:1, well faceted terminations and translucent to light pink, euhedral overgrowths on the largest grains; and (ii) elongate, light pink to brown, euhedral to

Figure 2.8. Field relationships of peraluminous intrusions, with polished slabs of representative samples (inset) and meta-turbidite used for detrital study; hammer is approximately 45 cm in length, lens cap is approximately 5 cm in diameter. *(a)* **VB1358:** Two-mica granite, Kwejinne Lake supracrustal belt. Older foliated phase (top), amphibolite-grade metasedimentary enclaves (center) and equigranular two-mica granite (bottom). *(b)* **PVB 9:** Irregular, sharp contact between megacrystic granite (bottom) and two-mica granite (top) Bigspruce subdomain. *(c)* **VB1688:** Contact between megacrystic granite and metasedimentary enclaves (granulite grade), Ghost subdomain. *(d)* **VB1229A:** Undeformed pegmatitic granite dyke cross-cutting diatexite (granulite grade), Ghost subdomain. *(e)* **VB161:** Cordierite-muscovite granite incorporating metasedimentary enclaves (granulite grade), Ghost sub-domain. *(f)* **VB1864:** Undeformed pegmatitic granite dyke truncating D2 fabric in turbidite, Kwejinne Lake supracrustal belt. *(g)* **VB18A:** Polished slab of amphibolite-grade meta-turbidite. Field of view is approximately 7 cm.



Figure 2.9: Transmitted-light, BSE and SE images of zircon populations and single grains in peraluminous intrusions. **(a) VB1358.** ai, needle; 1, oscillatory-zoned rim, sector zoned core and secondary recrystallization; 2 and 4, planar growth zoning, thin featureless overgrowths; 3, inherited core, faint diffuse oscillatory zoned rim; 5, broad oscillatory zoning, homogeneous overgrowth; 6, planar growth-zoned core, oscillatory-zoned, but disturbed tip; ai-7a and ai-7b, BSE and SE images, respectively, of laser ablation pit, emplacement age zone; aii, prism; 1, oscillatory zoning with minor disturbance in core; 2, homogeneous growth-zoning minor secondary recrystallization; 3, inherited core, secondary transgressive recrystallization; 4, inherited core - relict diffuse oscillatory zoning, homogeneous overgrowth; 5, broad planar growth zoning and unzoned rim. **(b) PVB9.** Bi, needle; 1, planar growth zoning and secondary convoluted zoning (top of grain image); 2, planar growth-zoned core, weak oscillatory-zoned outer rim, secondary transgressive recrystallization; bii, leaf-shaped prisms, broad oscillatory zoning, secondary transgressive recrystallization; biii, prism 1 and 2, concentric sector zoning, broad growth bands; 1, transgressive recrystallization; 3a and 3b, BSE and SE images, respectively, of laser ablation pit, emplacement age grain; biv, stubby prism, faint diffuse concentric planar growth zoning. **(c) VB1688.** ci, needle; 1, concentric planar growth zoning with patchy recrystallization; 2, inherited core with diffuse relict planar zoning, oscillatory zoned rim, secondary transgressive recrystallization (top); 3, faint planar growth zoning with minor secondary overgrowth (bottom right hand corner); 4a & b, BSE and SE images, respectively, of laser ablation pit, emplacement age grain; cii, prism, oscillatory zoning, disturbed, recrystallized core; ciii, prism population with exhibiting an equant and subrounded habit. **(d) VB161.** di, needle; 1, relict fine oscillatory zoning, transgressive secondary recrystallization within lower portion of grain; 2, broadened oscillatory zoning; dii, prism; 1, 2, and 3, bright BSE core mantled by recrystallized - disturbed rim of variable thickness. **(e) VB1229A.** ei, needle - fine oscillatory zoning, secondary recrystallization on rim; eii, elongate prism, extensive transgressive recrystallization 'fronts'; eiii, stubby prism, unzoned. **(f) VB1864.** Selected needles and prisms; 1, oscillatory-zoned inherited core, zonation altered by secondary processes, volumetrically abundant homogeneous mantle; 2, oscillatory-zoned inherited core, homogeneous overgrowth; 3, relict oscillatory-zoned needle, secondary patchy recrystallization; 4, homogeneous abraded prism.



subhedral prisms ca. 100-120 μm in length, aspect ratios of 4:1 and abundant overgrowths. Two grains of each population were analysed by ID-TIMS. Back scattered electron imaging of both needles and prisms (Figs. 2.9a, 2.10a) revealed cores with diffuse growth and planar growth zoning mantled by oscillatory zoned, dull rims, indicative of recrystallization. All four grains were abraded. U concentrations were moderate (79-304 ppm; Table 2.2) and the analyses were variably discordant (1.48 – 29.6% discordance) with $^{207}\text{Pb}/^{206}\text{Pb}$ ages ranging from 2617-2553 Ma. The $^{207}\text{Pb}/^{206}\text{Pb}$ ages of fractions Z1 and Z3 agree within error suggesting the presence of a population with an age of 2614.2 ± 8.2 [± 3.8] Ma (MSWD = 0.14). Z2 exhibits relatively undisturbed primary structures but has undergone extensive Pb loss precluding meaningful interpretation of the data. Z4, which exhibits faint planar zoning and a dull recrystallized domain on one of the grain tips, yielded a near-concordant analysis (1.48% discordant) with a $^{207}\text{Pb}/^{206}\text{Pb}$ age of 2598 ± 8.7 [± 5.8] Ma. The spread of data did not permit conclusive resolution of the emplacement age, so additional analyses of core and rim compositions were undertaken using LAM ICP-MS. Fifty-nine analyses were collected from approximately 40 needles and prisms. Fifteen of these analyses (Table A2, Fig. 2.10b) are interpreted to represent the crystallization age, based on their locations (bright rims on needles) and the presence of fine growth zoning. The analyses are normally to reversely discordant (19.5 to -5.6%) and lie on a chord with an upper intercept of 2592 ± 8.2 [± 4.8]. The analyses have $^{207}\text{Pb}/^{206}\text{Pb}$ ages within error of a single value, clustering around the weighted mean (MSWD = 0.24) of 2595.1 ± 8.2 [± 4.8] Ma,

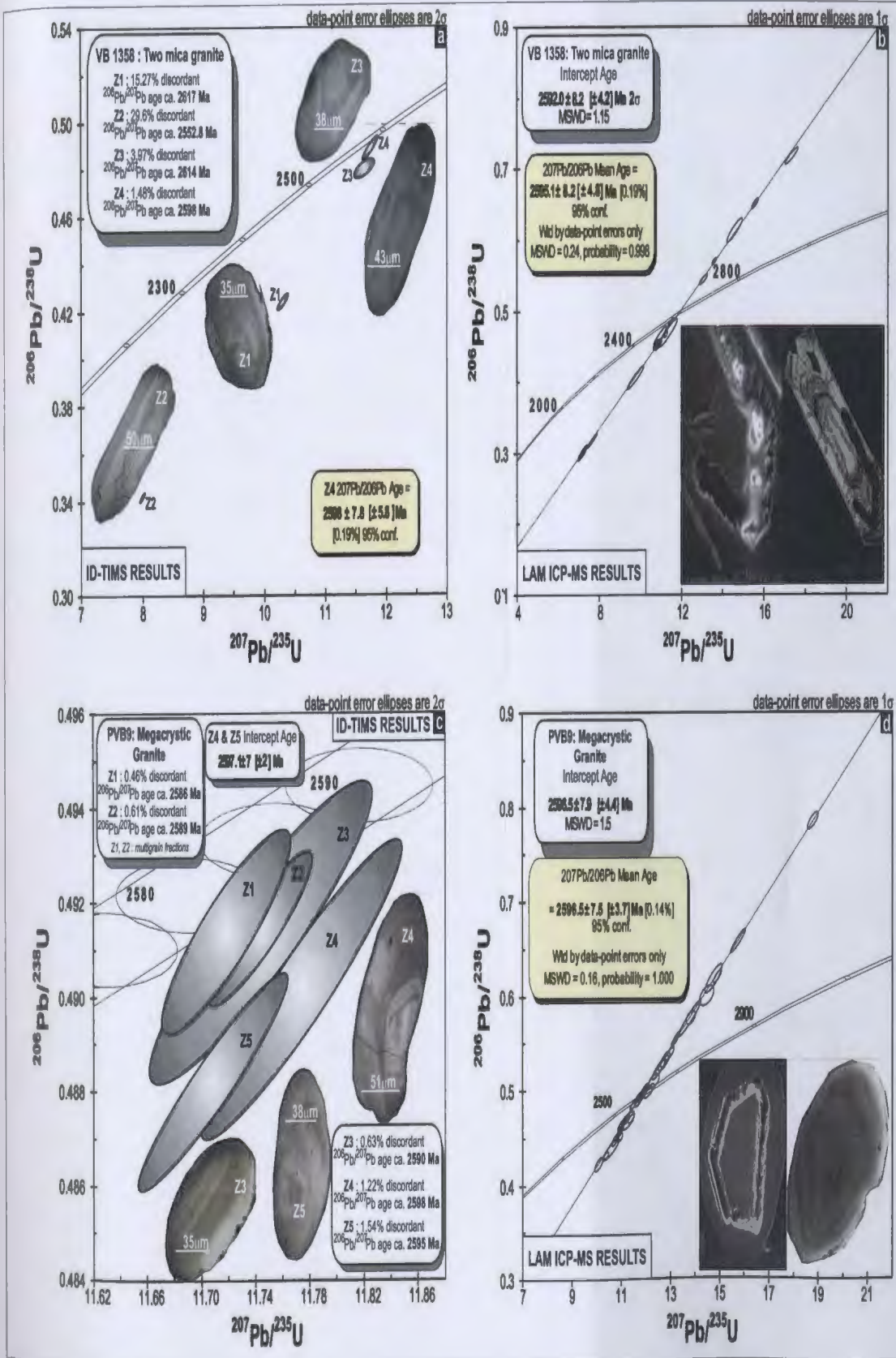


Figure 2.10a - d: ID-TIMS and LAM ICP-MS concordia diagrams for peraluminous intrusions, samples VB1358 and PVB9. Decay constant uncertainties of concordia are indicated and representative images of analyzed zircons are shown.

which is considered the most precise estimate of the crystallization age.

Megacrystic granite - PVB9: Sample PVB9 is from an irregular sheet-like intrusion of coarse-grained megacrystic granite, which occurs in Bigspruce and Ghost subdomains. In the Bigspruce subdomain, the granite has both transitional and sharp contacts with the surrounding two-mica granite (Fig. 2.8b), but intrusive relationships between the two units are unclear. The megacrystic granite consists of 2-10 cm K-feldspar phenocrysts and megacrysts that define both flow and deformational fabrics at different localities. Rounded crystal terminations indicate a strong component of deformation, whereas sharp, euhedral crystals, where aligned, are indicative of magmatic flow. Fabrics in the megacrystic granite parallel the regional D2 fabric in adjacent metaturbidites, implying emplacement was syn-D2. The granite is cut by syn- to post- D3 intrusions.

The sample yielded abundant, high quality brown to light pink zircon crystals that were separated into four populations (Fig. 2.9b): (i) needles 100-200 μm long, with aspect ratios of 5:1, well faceted crystal terminations and clearly defined overgrowths; (ii) elongate leaf-shaped prisms 100-120 μm long, a 4:1 aspect ratio and slightly rounded terminations; (iii) euhedral prisms ca. 100 μm in length and aspect ratios of 3:1; and (iv) subhedral to anhedral prisms 100-120 μm in length and aspect ratios of 3:1 – 2:1. Back scattered electron imaging of needle and prism populations revealed diffuse primary structures overprinted by unzoned recrystallized domains and rims. The euhedral prism population was analysed by ID-TIMS. Five fractions, two multigrain (Z1 and Z2) consisting of 4 grains each and three single grain (Z3-Z5) with low to moderate U

concentrations (74 - 235 ppm) yielded discordant data (0.46 – 1.54%) with $^{207}\text{Pb}/^{206}\text{Pb}$ ages ranging from 2586 to 2599 Ma (Table 2.2, Fig. 2.10c). Back scattered electron images of the single grain fractions (Fig. 2.10b) showed internal sector zoning with slight secondary modification, suggesting the spread in ages is due to mixed age domains in individual fractions. Two of the single grain fractions, in which the brighter outer rims were removed (Z4 and Z5), yielded an average $^{207}\text{Pb}/^{206}\text{Pb}$ age (MSWD = 2.8) of 2597 ± 7 [± 1.7] Ma. Fraction Z3, however, in which only part of the rim was removed, yielded a near concordant younger $^{207}\text{Pb}/^{206}\text{Pb}$ age of 2590 ± 7.7 [± 4] Ma. Fraction Z3 overlaps with multigrain fractions Z1 and Z2, which together yield a weighted average (MSWD = 3.1) $^{207}\text{Pb}/^{206}\text{Pb}$ age of 2588 ± 7.8 [± 5.5] Ma, suggesting that the younger age is caused by partial recrystallization. Additional LAM ICP-MS data were collected on the needle and prism populations to resolve the emplacement age. Of the 56 analyses collected from ~40 needles and prisms, 30 are inferred to correspond to the crystallization age and have $^{207}\text{Pb}/^{206}\text{Pb}$ ages within error of a single value, clustering around a weighted mean (MSWD = 0.16) of 2596.5 ± 7.6 [± 3.7] Ma (Fig. 2.10d). The analyses are normally to reversely discordant (11 to -25 %) and lie on a chord with an upper intercept of 2596.5 ± 7.9 [± 4.4] Ma. The $^{207}\text{Pb}/^{206}\text{Pb}$ date of 2596.9 ± 7.6 [± 3.7] Ma, considered the best estimate of the crystallization age from the laser dataset, is in agreement with the weighted average $^{207}\text{Pb}/^{206}\text{Pb}$ age of 2597 ± 6.9 [± 1.7] Ma determined by ID-TIMS for fractions Z4 and Z5, which is the most precise estimate of the crystallization age.

Lower mid-crustal megacrystic granite – VB 1688: Sample VB 1688 is from a deformed sheet of coarse-grained megacrystic granite in the core of a prominent

structural dome in Ghost sub-domain (Figs. 2.3, 2.8c). The granite consists of K-feldspar megacrysts with rounded terminations in a medium-grained groundmass of quartz, biotite and garnet. Orthopyroxene locally replaces garnet indicating the unit has undergone granulite-facies metamorphism. Narrow high-strain zones marked by augen textures and cm-scale mylonite zones are pervasive. The dominant foliation, defined by alignment of elongate quartz grains and K-feldspar megacrysts, parallels the latest penetrative D2 leucosomal fabric in the adjacent meta-turbidites and is truncated by syn- to post-D3 intrusions. Additionally, the megacrystic granite suite within the Ghost subdomain is locally observed to truncate the older syn-D1 magmas of the Disco Intrusive suite and is deformed by late D2 open folding. Therefore, emplacement of these mid-crustal plutons is considered to be broadly syn-D2.

The sample yielded abundant, high quality light pink to brown zircon crystals that were separated into three populations (Fig. 2.9c): (i) needles 100-250 μm long, with aspect ratios of 4:1, slightly rounded crystal faces, and overgrowths with euhedral terminations; (ii) euhedral prisms 100-200 μm in length, with aspect ratios of 3:1, slightly rounded terminations and ubiquitous translucent overgrowths; and (iii) stubby prisms 100 μm in diameter, aspect ratios of 2:1, and slightly rounded, indistinct crystal faces. Back scattered electron imaging of the needle and elongate prism populations revealed faint primary growth zoning locally truncated and overprinted by dull patchy recrystallized domains, whereas the stubby prism population is homogeneous and unzoned. The needle population was analysed by ID-TIMS. Three single-grain fractions with low to moderate U concentrations (93-195 ppm) yielded concordant to near concordant data (-0.1 – 1.75%

discordant) with $^{207}\text{Pb}/^{206}\text{Pb}$ ages ranging from 2587 to 2594 Ma (Table 2.2, Fig. 2.10e). This spread in ages can be related to the BSE images (Fig. 2.10e). Fractions Z2 and Z3, which yielded $^{207}\text{Pb}/^{206}\text{Pb}$ dates of 2597 ± 7.2 [± 2.7] and 2594 ± 6.7 [± 1.2] Ma, exhibited primary growth zoning, whereas Z1, with a $^{207}\text{Pb}/^{206}\text{Pb}$ date of 2587 ± 6.9 [± 1.7] Ma, is recrystallized. Additional analyses by LAM ICP-MS were collected to resolve the emplacement age. Of the 99 analyses collected from 36 needles and prisms, 36 analyses (Table A2, Fig. 2.10f) are interpreted to correspond to the crystallization age. They have $^{207}\text{Pb}/^{206}\text{Pb}$ ages within error of a single value, clustering around a weighted mean (MSWD = 0.17) of 2597 ± 7.1 [± 2.4] Ma. The analyses are normally to reversely discordant (15 to -26 %) along a chord with an upper intercept of 2597.1 ± 7.1 [± 2.5] Ma. The weighted average of $^{207}\text{Pb}/^{206}\text{Pb}$ ages of the laser data (2597 ± 2.4 Ma) is considered to be the best estimate of the crystallization age from the laser data and is in agreement with the ID-TIMS concordia age for fraction Z2 of 2598 ± 4.3 [± 2] Ma, which is considered the most precise estimate of the crystallization age.

Cordierite-muscovite granite – VB161: Sample VB161 is from a 50 m wide, undeformed, irregular boss of fine- to medium-grained cordierite-muscovite granite with abundant metasedimentary enclaves from the western margin of Ghost subdomain (Figs. 2.3, 2.8e). The unit is unfoliated and truncates D1 and D2 structures in the adjacent meta-turbidites, thereby providing a minimum age for the cessation of deformation in these granulite-facies rocks.

The sample yielded abundant, tan to yellow zircon crystals that were separated into two populations (Fig. 2.9d): (i) needles 50-100 μm long, with aspect ratios of 4:1 and

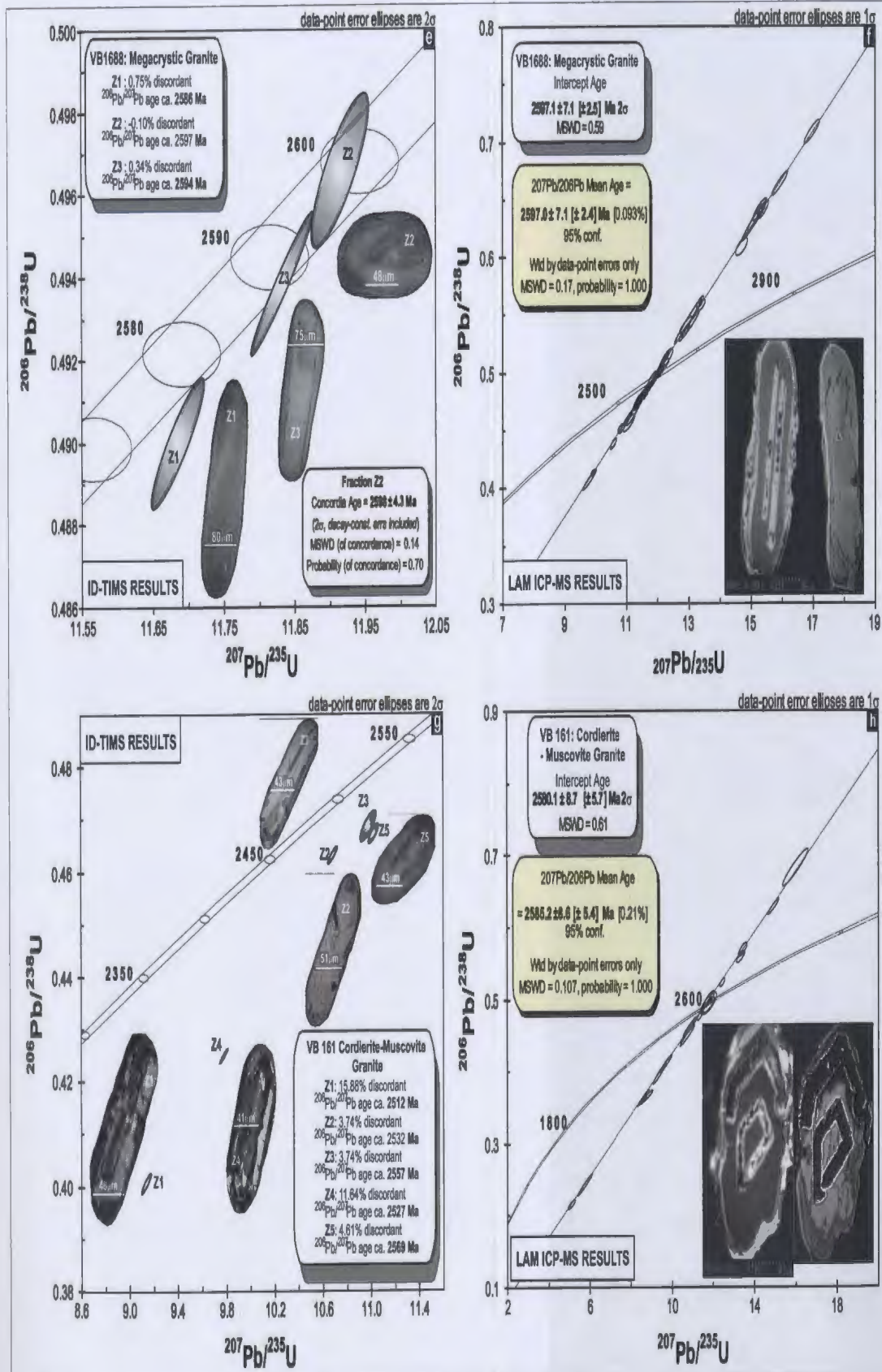


Figure 2.10e - h: ID-TIMS and LAM ICP-MS concordia diagrams for peraluminous intrusions, samples VB1688 and VB161. Decay constant uncertainties of concordia are indicated and representative images of analyzed zircons are shown.

subrounded crystal faces; and (ii) prisms 50-150 μm in length, with aspect ratios of 3:1 and well faceted terminations. Translucent overgrowths were present in both populations. BSE imaging (Fig. 2.10) revealed similar internal structures in both populations, with primary concentric growth and planar zoning extensively modified by secondary broadening and widening. Typically dull, featureless cores and rims retain relics of primary growth structures (Fig. 2.9d) that are partially overprinted by recrystallized domains. The needle population was analysed by ID-TIMS. Five single grain fractions with a wide range of U concentration (279 - 1902 ppm) yielded discordant data (3.74 – 15.88%) with $^{207}\text{Pb}/^{206}\text{Pb}$ ages ranging from 2512 – 2569 Ma (Table 2.2, Fig. 2.10g). The complicated internal structures, significant Pb loss and inheritance suggested that additional ID-TIMS analyses would not resolve the crystallization age, so LAM ICP-MS data were collected on both populations. Fifty-five analyses were collected from 38 grains. Inheritance and resetting were common, despite the careful selection of ablation locations. However, 17 analyses (Table A2, Fig. 2.10h) were interpreted to represent the crystallization age based on within-grain sampling location and internal structures. The analyses have $^{207}\text{Pb}/^{206}\text{Pb}$ ages within error of a single value, clustering around the weighted mean (MSWD = 0.107) of $2585 \pm 8.6 [\pm 5.4]$ Ma. They are normally to reversely discordant (46 to -30 %) and lie on a chord with an upper intercept of $2580.1 \pm 8.7 [\pm 5.7]$ Ma. The weighted average of $^{207}\text{Pb}/^{206}\text{Pb}$ ages of the laser data, $2585 \pm 8.6 [\pm 5.4]$ Ma, is considered the best estimate of the crystallization age.

Pegmatitic granite dyke – VB 1229A: Sample VB1229A is from a 0.5-1 m wide dyke of coarse-grained pegmatitic granite in the granulite-facies Ghost sub-domain (Figs.

2.3, 2.8d). It consists of a coarse-grained graphic intergrowth of K-feldspar and quartz with minor biotite and garnet–magnetite aggregates. The dyke crosscuts all D2 fabrics and fold events in adjacent country rocks. Additionally, intrusions of the suite post-date D3 northwest trending shear fabrics that are associated with uplift of the Ghost subdomain (see Chapter 3). Hence, the sample provides an upper limit for the cessation of Archean deformation across the mid-crustal granulite domain.

The sample yielded abundant brown zircon grains that were separated into three populations (Fig. 2.9e): (i) needles 100-200 μm long with aspect ratios of 5:1 and indistinct crystal faces; (ii) prisms ca. 100-150 μm in length, with aspect ratios of 3:1 and anhedral, tan overgrowths; and (iii) stubby prisms 100-150 μm in diameter, aspect ratios of \sim 2:1 and subrounded terminations. Back scattered electron imaging of the needle and prism populations revealed primary growth zoning variably overprinted by patchy and featureless, dull, structureless domains, whereas the stubby prism population was unzoned. The needle population was analysed by ID-TIMS. Four single-grain, high U fractions (853 - 1039 ppm) yielded discordant data (0.69 – 38.66%) with $^{207}\text{Pb}/^{206}\text{Pb}$ ages ranging from 2584 to 2585 Ma (Table 2.2, Fig. 2.10i). An error weighted regression of the data yield an upper intercept age of 2585.2 ± 6.7 [± 0.71]. A weighted average (MSWD = 0.94) of $^{207}\text{Pb}/^{206}\text{Pb}$ ratios yields an age of 2584.7 ± 6.7 [± 0.56] Ma. Both the $^{207}\text{Pb}/^{206}\text{Pb}$ and intercept ages provide good estimates of the crystallization age for this sample.

Pegmatitic granite dyke – VB1864: Sample VB1864 is from a 0.5-1 m wide, undeformed dyke of pegmatitic alkali feldspar muscovite-biotite granite that crosscuts

amphibolite-facies metaturbidites in the Kwejinne Lake supracrustal belt (Figs. 2.3, 2.8f). The dyke crosscuts D1 and D2 structures, thereby providing a constraint on the cessation of deformation and plutonism in upper crustal levels of the Snare River terrane.

Zircon yield from this sample was low and only 10 useable grains, comprising needles and prisms of variable quality, were retrieved. Needles consisted of brown to pink grains 100-200 μm long, with aspect ratios of \sim 4:1 and subhedral, indistinct crystal faces, and the prism population consisted of fractured, light pink grains ca. 50 -100 μm in diameter, with aspect ratios of 2:1 and subhedral, indistinct terminations. Back scattered electron imaging of needles revealed rare cores with concentric, oscillatory and sector growth zoning overprinted by irregular, featureless domains, whereas the prism population exhibited faint traces of sector and growth zoning.

Five single grain fractions with low to moderate U concentrations (60-394 ppm) yielded near-concordant to discordant data (0.4 – 10.15%) with $^{207}\text{Pb}/^{206}\text{Pb}$ ages ranging from 2710 – 2586 Ma (Table 2.2, Fig. 2.10j). Results for fractions Z1 to Z4, which yielded $^{207}\text{Pb}/^{206}\text{Pb}$ ages of 2699 ± 6.9 [± 1.8] Ma, 2700 ± 17 [± 16] Ma, 2710 ± 8.3 [± 4.6] Ma and 2705 ± 7.3 [± 2.5] Ma, respectively, are incompatible with field relationships and are inferred to indicate inheritance. Fraction Z5, which exhibits growth zoning, yielded a $^{207}\text{Pb}/^{206}\text{Pb}$ age of 2586 ± 8.7 [± 5.8] Ma. Poor zircon yield prevented further analysis of the sample by LAM ICP-MS. Based on field observations and the overlap of the $^{207}\text{Pb}/^{206}\text{Pb}$ age of fraction Z5 with the crystallization ages of samples VB1229A and

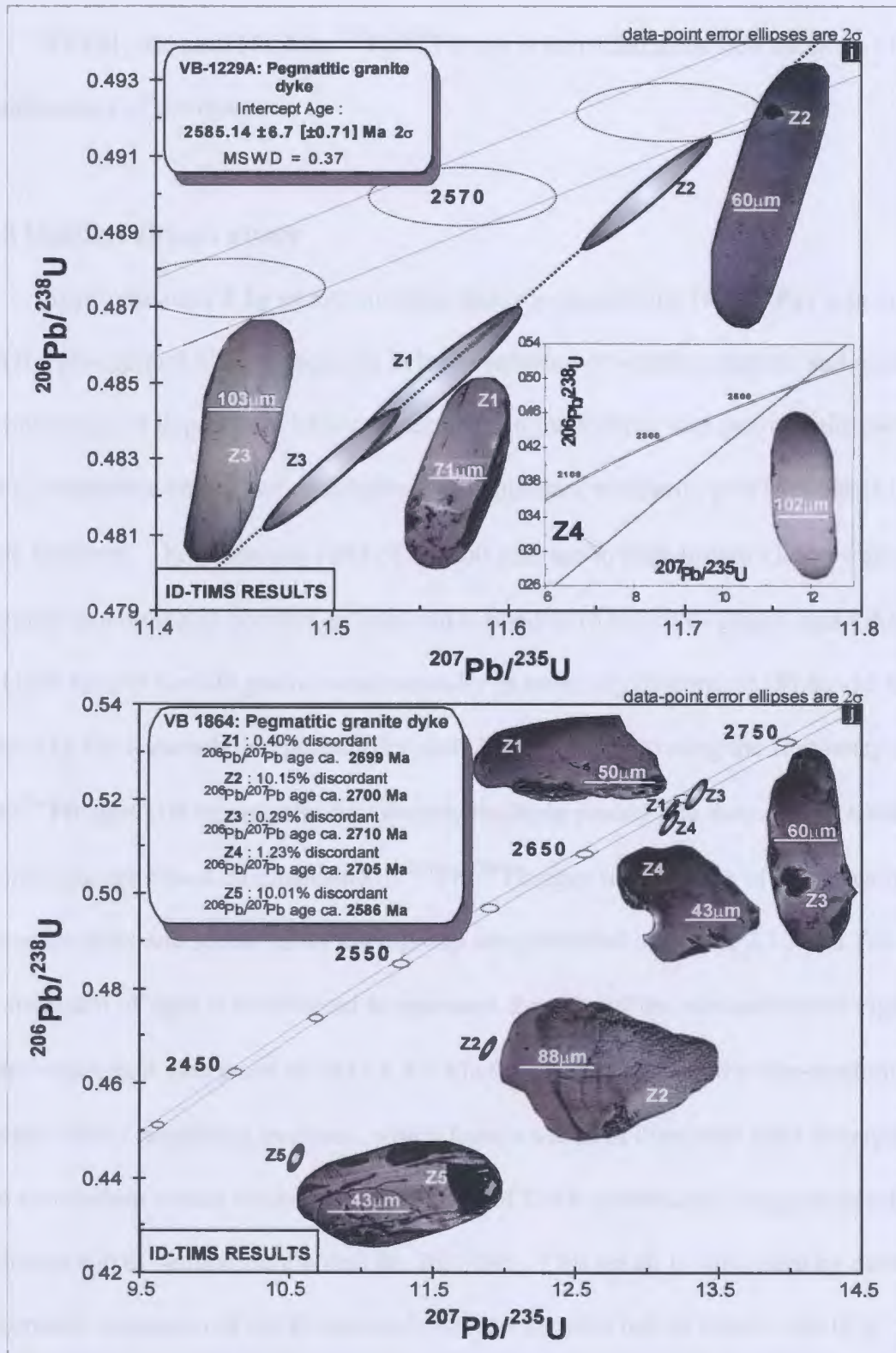


Figure 2.10i-j: ID TIMS concordia diagrams for peraluminous intrusions, samples VB1229A and VB1864. Decay constant uncertainties of concordia are indicated and representative images of analyzed zircons are shown.

VB161, the ca. 2586 Ma $^{207}\text{Pb}/^{206}\text{Pb}$ age is considered the best estimate of crystallization of the dyke.

2.8.3 Detrital zircon study

Approximately 8 kg of amphibolite-facies metaturbidite (Fig. 2.8g) was sampled from the Kwejinne Lake supracrustal belt to evaluate provenance sources and establish a maximum age of deposition. Major mineralogy in the sample was quartz, feldspar, biotite, muscovite and minor andalusite, with abundant cordierite porphyroblasts in pelitic horizons. The moderate yield of 50-100 μm , tan to dark brown zircon was separated into euhedral needles, prisms and subhedral to anhedral grains, and LAM ICP-MS U-Pb results for 100 grains were normally to reversely discordant (81 to -16.6 %; Table A3). On a cumulative probability plot (Fig. 2.11) illustrating the frequency of $^{207}\text{Pb}/^{206}\text{Pb}$ ages (1σ errors), the data display multiple peaks. The dataset was subdivided into nine groups based on clustering of $^{207}\text{Pb}/^{206}\text{Pb}$ ages within error of single values. Concordia plots and statistics for each group are presented in Figure 2.12 and Table 2.4. The spectrum of ages is considered to represent the ages of the various source regions. A single concordant data point at 2633 ± 9.3 Ma (1σ), together with the non-random dispersal of the remaining analyses, which form a series of discordia lines through one or more concordant points implying preservation of U-Pb systematics, suggest that the maximum age of sedimentation was ca. 2635 Ma. This result is supported by data from the northern extension of the Kwejinne Lake supracrustal belt at Indin Lake (Fig. 2.1), where Pehrsson and Villeneuve (1999) determined a ca. 2629 Ma age for the maximum

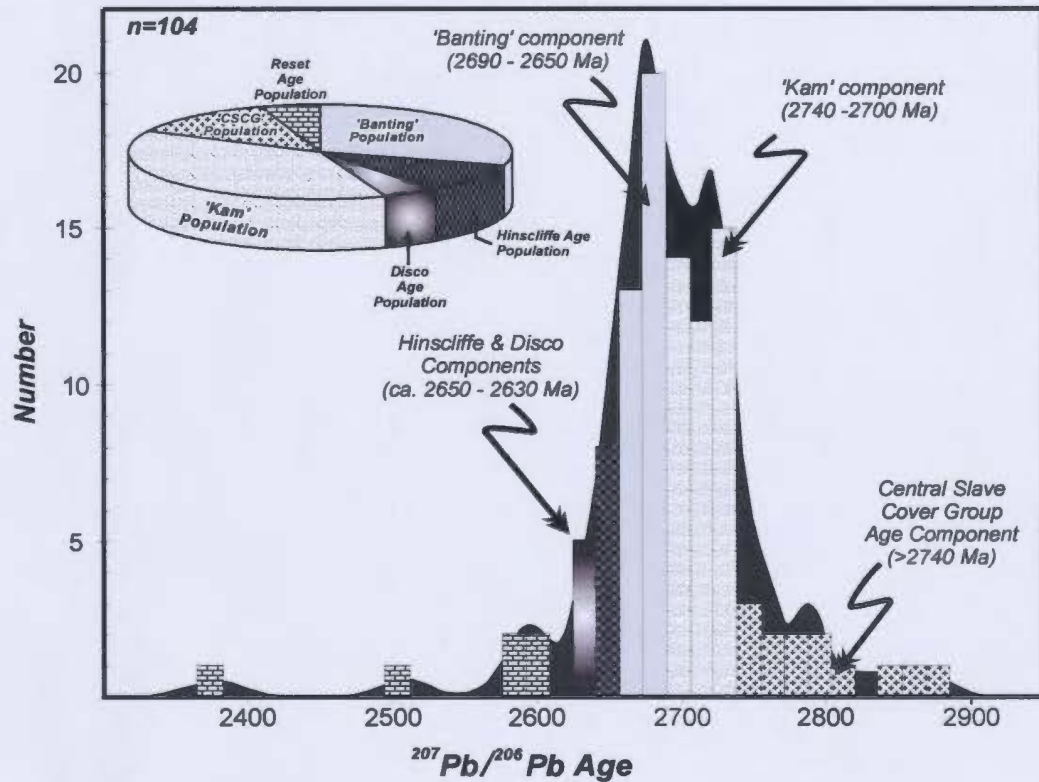


Figure 2.11: Histogram and cumulative probability diagram illustrating $^{207}\text{Pb}/^{206}\text{Pb}$ ages in detrital zircon population from meta-turbidite. $^{207}\text{Pb}/^{206}\text{Pb}$ ages are variably discordant (see text, Table 2.3) and correlate with known events elsewhere in the Slave Province labelled in Fig. 2.1.

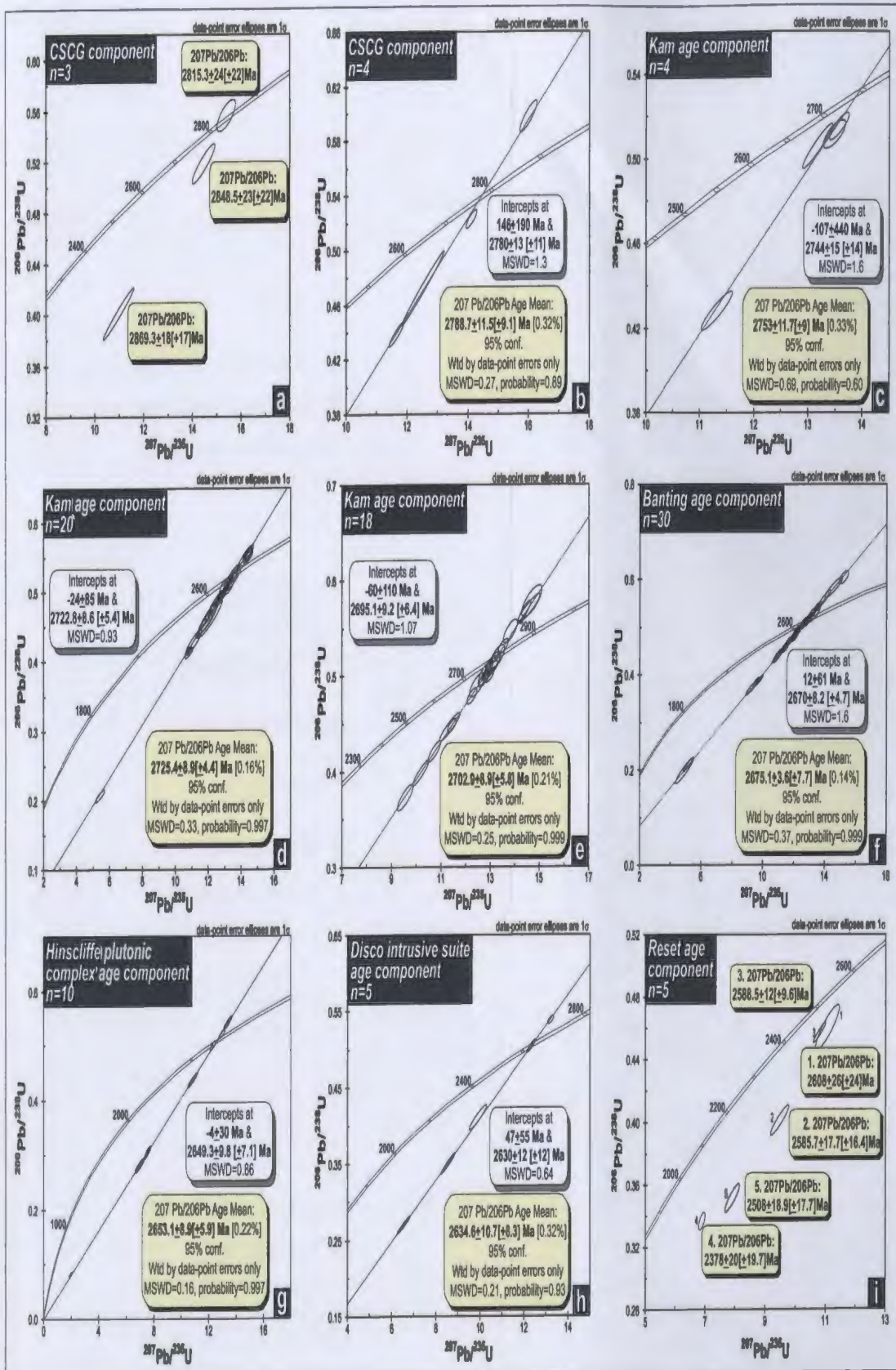


Figure 2.12a-i. U-Pb concordia diagrams for 9 detrital age components distinguished in Fig. 11. Decay constant uncertainties of concordia are indicated. Ellipses reflect 1 σ uncertainties.

Table 2.4: Summary table of nine defined detrital zircon age populations. Confidence levels are specified.

Age Grouping	Concordia figure number	Discordance Range (%)	Upper Intercept Age (2σ)		Weighted $^{207}\text{Pb}/^{206}\text{Pb}$ age (2σ) or $^{207}\text{Pb}/^{206}\text{Pb}$ age range (quoted errors at 1σ)	Correlations / Comments
			Without decay constant uncertainties	With decay constant uncertainties		
>2800 Ma $n=3$	2.12a	-0.1 to 22.8 %	n/a	n/a	Age range : 2815 \pm 22 Ma to 2869 \pm 16.6 Ma	Oldest & least abundant population. Age range correlative with Central Slave Cover Group.
2780 - 2794 Ma $n=4$	2.12b	-8.1 to 10.3%	2780 \pm 11 Ma	2780 \pm 13 Ma	Weighted Mean - 2788.7 \pm 9.1 Ma (MSWD = 0.27)	Calculated ages correlative with Central Slave Cover Group.
2740 - 2760 Ma $n=4$	2.12c	8.6 to 14.3%	2744 \pm 14 Ma	2744 \pm 15 Ma	Weighted Mean - 2753 \pm 9 Ma (MSWD = 0.79)	Calculated ages correlative with Kam Group Magmatism, Central Slave Province.
2718 - 2736 Ma $n=20$	2.12d	-4.5 to 55%	2722.8 \pm 5.4 Ma	2722.8 \pm 8.6 Ma	Weighted Mean - 2725.4 \pm 4.4 Ma (MSWD = 0.33)	Calculated ages correlative with Kam Group Magmatism, Central Slave Province.
2693 - 2712 Ma $n = 18$	2.12e	-9.4 to 25.4%	2695.1 \pm 6.4 Ma	2695.1 \pm 9.2 Ma	Weighted Mean - 2702.9 \pm 5.8 Ma (MSWD = 0.25)	Calculated ages correlative with Kam Group Magmatism, Central Slave Province.
2661 - 2687 Ma $n = 29$	2.12f	-13.6 to 55%	2670.0 \pm 4.7 Ma	2670.0 \pm 3.9 Ma	Weighted Mean - 2675.1 \pm 3.6 Ma (MSWD = 0.25)	Calculated ages correlative with Pan-Slave Banting Age Magmatism.
2641 - 2658 Ma $n = 10$	2.12g	-5.5 to 81.7%	2649.3 \pm 7.1 Ma	2649.3 \pm 9.8 Ma	Weighted Mean - 2653.1 \pm 5.9 Ma (MSWD = 0.16)	Calculated ages correlative with Hinscliffe Plutonic complex, Snare River Terrane.
2628 - 2639 Ma $n = 5$	2.12h	6.3 to 22.5 %	2630 \pm 12 Ma	2630 \pm 14 Ma	Weighted Mean - 2634 \pm 8.3 Ma (MSWD = 0.16)	Calculated ages correlative with Disco Intrusive Suite, Snare River Terrane.
2608 - 2379 Ma $n= 5$	2.12i	6.3 to 22.5 %	n/a	n/a	Age range : 2378 \pm 19.7 to 2608.3 \pm 24.7 Ma	Disturbed and reset age population

Note: Sources of U-Pb age data: 2.7 - 2.9 Ga basement cover sequence ages and >2.9 Ga basement complex ages (Isachsen and Bowring 1997; Ketchum and Bleeker 1999 and 2000; Bleeker et al 1999a and b; Sircombe et al. 2001); 2.75 - 2.70 Ga Kam age and equivalents (Isachsen 1992; Isachsen et al. 1991a; Isachsen and Bowring 1997; Ketchum and Bleeker 1999; Bleeker et al 1999b); 2.69 - 2.66 Ga Banting age and equivalent (Henderson et al. 1987; van Breemen et al. 1992; Isachsen 1992; Mortensen et al. 1992; Ketchum and Bleeker 1998 and 1999; Villeneuve and Henderson 1998; Bleeker et al. 1999b; Pehrsson and Villeneuve 1999; Yamashita et al. 2000; Ootes and Lentz 2002).

age of sedimentation, which is within error of the value determined in this study. Field relationships at the sampling locality demonstrate that the metaturbidites are crosscut by ca. 2585 Ma pegmatite dykes, a magmatic event which may account for the younger reset $^{207}\text{Pb}/^{206}\text{Pb}$ ages in the detrital dataset. It is significant to note the older age of metaturbidite units in the Ghost subdomain. Within this subdomain metasedimentary enclaves are observed in ca. ~2635 – 2640 Ma plutonic rocks (see sample VB1363; Perks 1997), emplacement of which pre-date the youngest interpreted detrital zircon age in the sample described above (ca. 2633 Ma). Additional interpretations are integrated with the pluton emplacement age results below.

2.9 Discussion

2.9.1 Temporal and spatial correlations: construction of orogenic stratigraphy

The metamorphic gradient exposed in the SRT provides a window into the origin and geometry of the upper and mid-crustal levels of the orogen. Detailed mapping and U-Pb dating of representative units has enabled correlations to be made between these levels and also provides the opportunity to construct an ‘orogenic stratigraphy’ (Fig. 2.13). A crucial observation is that *temporal* and *tectonic* contrasts in crust formation correspond to spatial stratification into upper- and mid-crustal levels (Fig. 2.14). We propose that an early tectonic regime (TR1), involving formation of TTG complexes, bimodal volcanic belts and turbidite deposition, was followed by juxtaposition and deformation of these

Figure 2.13: Schematic orogenic stratigraphy of the Snare River terrane summarizing links among lithology, age, metamorphic grade and crustal level. Age constraints provided from Villeneuve and Henderson (1998), Perks (1997) and this study. Stratigraphic thickness is not implied, but the overall increasing abundance of granitoid rocks and decreasing abundance of supracrustal rocks with depth is evident. Note that ca. 2670 - 2650 Ma intrusions are restricted to the upper-crustal Kwejinne Lake supracrustal belt and that most intrusions in the mid-crustal Ghost subdomain are < 2600 Ma, implying migration of the locus of magmatic emplacement from the upper crust to the mid crust with time.

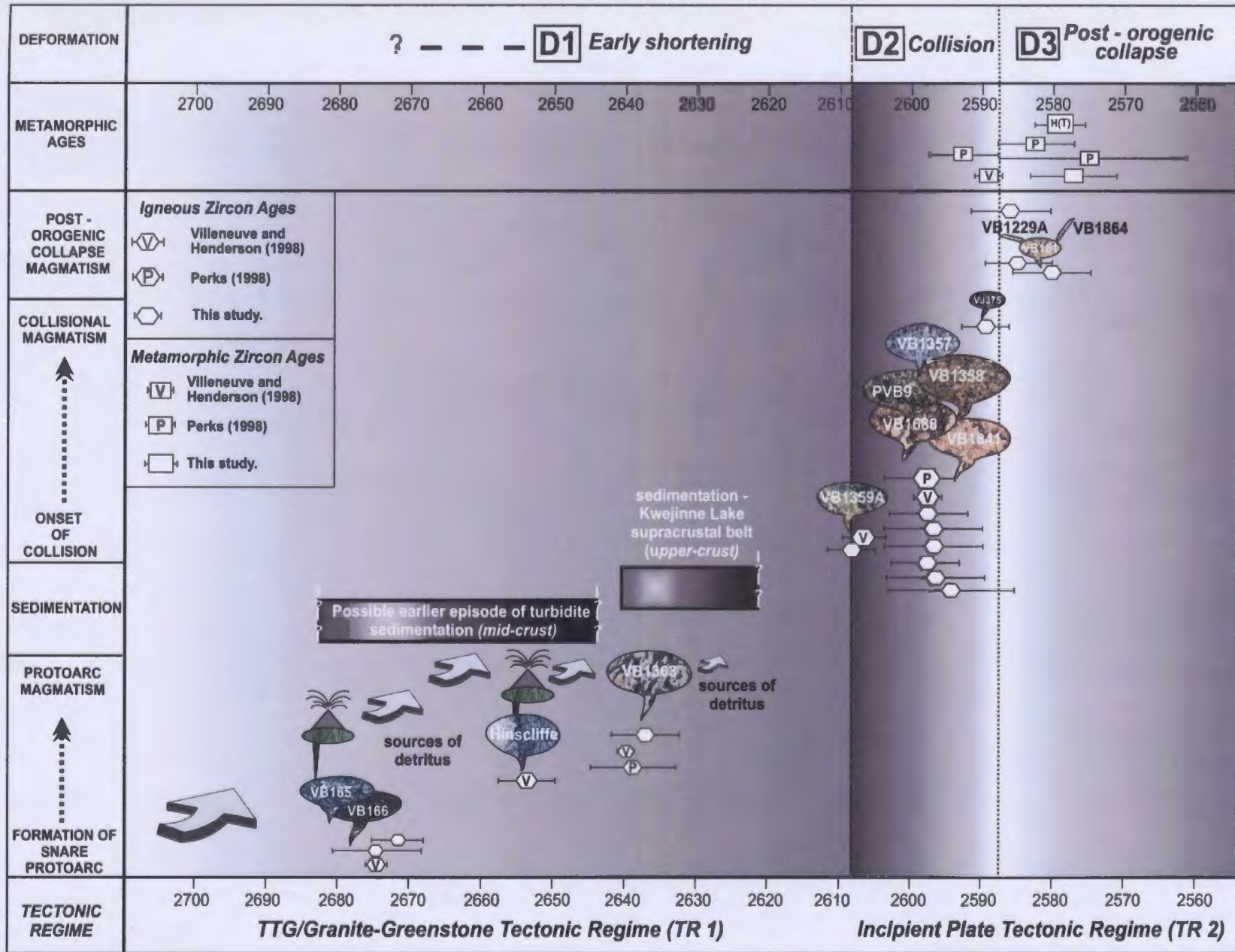


Figure 2.14. Time versus tectonic setting diagram linking the inferred evolution of plutonism and deformation in the SRT. Error bars at 2 sigma confidence level and include U decay constant uncertainties.

components during the D1 event, giving rise to the '*Snare proto-arc*'. [We use the term proto-arc to distinguish it from modern arcs that develop by steep subduction. We make no specific connotation regarding the tectonic setting of the TTG-granite greenstone regime]. Remnants of this D1 orogen, which likely formed in an oceanic setting, are well-preserved in the low grade, upper-crustal component of the SRT. In TR2, the Snare proto-arc collided with another crustal block in a plate-tectonic style collisional orogeny, giving rise to crustal thickening (D2) and associated magmatism, followed by orogenic collapse (D3), for which evidence is best preserved in the mid crust. In the following sections, the evidence for this model is evaluated in more detail.

Upper Crustal Stratigraphy and Tectonic Regime 1

TR1 lasted from ca. 2675 to 2608 Ma and involved the following events:

- i) Two early episodes of metaluminous magmatism in the interval ca. 2675 to 2654 Ma. In the Kwejinne Lake belt, tonalitic and gabbroic plutonism, dated in this study at ca. 2671 and ca. 2675 Ma respectively, was coeval with felsic volcanism dated at $2673 \pm [1.5]$ Ma (Villeneuve and Henderson 1998). A second magmatic episode is indicated by the $2658 [+1.2/-0.8]$ Ma age of felsic volcanic rocks in the Russell Lake belt (Mortensen et al. 1992), which is within error of the $2654 [\pm 4]$ Ma age for the Hinscliffe complex in the Kwejinne Lake belt (Villeneuve and Henderson 1998);

- ii) Subsequent pulses of metaluminous plutonism at ca. 2637 Ma and 2608 Ma (early phases of the Disco suite and mafic to ultramafic complexes respectively; this study). This record of apparently episodic metaluminous plutonism suggests that early crust formation and evolution took place in a long-lived proto-arc setting, in which periods of quiescence were longer lived than the periods of active magmatism;

- iii) Turbidite deposition was coeval with proto-arc formation, with detrital age peaks at ~2670, 2654 and 2634 Ma correlating closely with dated magmatic activity (gabbroic and tonalitic plutonism, Hinscliffe complex and Disco suite respectively), permitting the interpretation that the turbidites formed in part by erosion of the proximal proto-arc. The youngest detrital grain (ca. 2633 Ma) provides an estimate for the maximum age of turbidite sedimentation in the upper structural levels of the SRT. However, the observation of intrusive contacts between ca. 2635 Ma plutons and foliated metaturbidites in the mid-crustal Ghost subdomain, and the presence of metasedimentary enclaves in these plutons, implies that deposition of metasediments preserved in the mid crust pre-dated 2635 Ma (see below);

- iv) D1 deformation and greenschist- to amphibolite-facies metamorphism, poorly constrained between ~ 2674 and 2608 Ma, involved assembly and imbrication of igneous and metasedimentary lithologies, and formation of the Snare proto-arc.

Mid-Crustal stratigraphy and Tectonic Regime 2

TR2 lasted from ca. 2608-2570 Ma and involved the following events:

- i) Emplacement of large volumes of magma at mid-crustal levels, reworking and / or imbrication of the TR1 stratigraphy by synchronous D2 shortening and M2 metamorphism, and development of thermal stratification between cold upper crust and thermally weakened mid-crust;
- ii) Syn-D2 magmatism was both metaluminous, i.e., 2605 [\pm 3] Ma quartz diorite at Ghost Lake (Villeneuve and Henderson, 1998), ca. 2594 Ma hornblende-biotite granite and ca. 2597 Ma orthopyroxene-bearing granite (this study), and peraluminous, i.e., ca. 2597 Ma mid-crustal megacrystic granite (Perks 1997; Villeneuve and Henderson 1998; this study), ca. 2598 Ma two-mica granite (Villeneuve and Henderson 1998; this study). Metaluminous intrusions were predominantly emplaced into the granulite-facies mid crust, whereas peraluminous intrusions were emplaced into all crustal levels, particularly the amphibolite-facies boundary region between the mid and upper crust;
- iii) Renewed magmatism between ~2589-2586 Ma involved small-volume metaluminous and peraluminous intrusions, i.e., ca. 2589 Ma tonalite, ca. 2586 Ma two-mica pegmatite and cordierite-muscovite granite (this study) and was associated with M3 granulite-facies metamorphism in the mid crust;
- iv) M3 involved partial to complete resetting of older zircon populations at ~2586 Ma and the growth of new metamorphic zircon until ~2571 Ma. M3 was widespread, as it is also recorded in the ID-TIMS data of Perks (1997) and Villeneuve and

Henderson (1998) in the Forked Lake and Ghost Lake areas, respectively (Fig. 2.2a). Perks (1997) reported $^{207}\text{Pb}/^{206}\text{Pb}$ dates of 2587 to 2562 Ma from prismatic metamorphic zircon in mafic granulite, and a population of zircon needles from the same unit yielded an age of $2592 [\pm 5]$ Ma, which he also interpreted as a metamorphic age. In addition, Perks (1997) reported three zircon fractions from a megacrystic granite with $^{207}\text{Pb}/^{206}\text{Pb}$ ages of ~ 2586 Ma, which overlap with a metamorphic monazite age of 2589 ± 2 Ma reported by Villeneuve and Henderson (1998). Finally, zircon data obtained from two orthopyroxene granite bodies yielded ages of $2589 [+1/-2]$ Ma (Perks 1997) and ~ 2587 to 2577 Ma (Villeneuve and Henderson 1998), similar to the orthopyroxene granite analyzed in this study (VB1841; Fig. 2.7c), for which an emplacement age of ca. 2598 Ma was determined. The ca. 2589 Ma dates were interpreted as crystallization ages by Perks (1997) and Villeneuve and Henderson (1998), but in the light of the evidence for pervasive zircon recrystallization identified in this study it is considered likely that they represent metamorphic ages;

- v) This evidence for syn-D3 thermal reworking apparently unrelated to plutonism supports an interpretation that it was a consequence of crustal overthickening following D2. The available structural data are compatible with a widespread episode of post-orogenic collapse following the ~ 2597 Ma D2 orogenic peak that was accompanied by thermal reworking of the mid-crust (M3) and subsequent uplift of the granulite-facies Ghost subdomain associated with crustal extensional, e.g., Pehrsson et al. (2000).

2.9.2 Duration of sedimentation

In this section, we address the apparent contradiction between field evidence, which indicates that ca. 2635 Ma plutons of the Disco suite intrude metaturbidites in the mid-crustal Ghost subdomain, and the detrital zircon study which indicates a maximum age of turbidite sedimentation in the Kwejinne Lake belt of ca. 2633 Ma. These results can be accounted for in either of two ways: (i) pre- and syn-D1 periods of sedimentation that took place before and after 2635 Ma; or (ii) one protracted diachronous episode of sedimentation coeval with shortening deformation (i.e., analogous to an accretionary wedge setting). Evidence for early turbidite sedimentation in the Slave Province includes the 2692 [± 5], 2689 [± 3] and 2661 [± 2] Ma ages of volcanic rocks interbedded with turbidites in the Hackett River and Clan Lake areas (Mortensen et al. 1988; van Breemen et al. 1992), and the interlayered Watta Lake tuff dated at 2661 [$+2/-3$] Ma (Bleeker and Villeneuve 1995). No evidence for a younger phase of sedimentation is observed at these localities. However a maximum age of sedimentation of ca. 2629 Ma has been determined for the Damoti greywacke at Indin Lake (Pehrsson and Villeneuve 1999), immediately north of the SRT. These data suggest that sedimentation took place at different times across the Slave Province, but do not directly resolve whether there were two discrete episodes of sedimentation separated by a phase of deformation or a single protracted diachronous episode of sedimentation coeval with deformation. In the latter case, sedimentation would have been synchronous with magmatism in the Snare proto-arc and have continued until ocean-basin closure at the onset of D2. In such a setting, older turbidites would have been deformed and intercalated into the Snare proto-arc,

buried to mid-crustal levels, and intruded by ca. 2635 Ma plutons before deposition of the younger turbidites in the upper crustal Kwejinne Lake supracrustal belt. Neither scenario can be ruled out because of the paucity of relevant data across the SRT and the Slave Province as a whole. However, the protracted sedimentation model (i.e., the accretionary wedge analogue) is preferred for three reasons: (i) no distinct period of deformation has been identified between the two ages of sediments, with both upper- and mid-crustal turbidites exhibiting a similar style and orientation of D1 structures; (ii) Meta-turbidite succession comprise ca. 70-80% of supracrustal belts that occur across the Slave Province (Padgham and Fyson 1992; Davis et al, 1996). Such a large volume of material that was apparently deposited over a wide lateral extent would require a longer depositional time-frame in which to accumulate significant thicknesses; and (ii) by analogy with modern turbidite environments, in which sedimentation is sustained as long as a trigger mechanism (i.e., earthquakes) exists to initiate turbidity currents, the ca. 66 M.y. period of proto-arc growth in the SRT could have provided a suitable tectonic setting for coeval turbidite sedimentation and deformation.

2.9.3 Regional provenance implications

The multi-mode detrital zircon results in this study indicate that turbidites in the southwestern Slave Province had a mixed provenance. As noted above, the majority of ages correlate well with magmatism in the Snare proto-arc, and in this section we investigate possible correlations in the wider context of the Slave Province. Fig. 2.1 illustrates the distribution of major age domains in the western Slave Province. Three

lithotectonic units bounding the SRT to the north and east are: (i) the 4.03-2.9 Ga Central Slave Basement Complex; (ii) the unconformably overlying ca. 2.9-2.75 Ga Central Slave Cover Group (CSCG); and (iii) numerous overlying granite–greenstone belts with ca. 2.73-2.70 Ga ('Kam') and 2.69-2.66 Ga ('Banting') ages (terminology after Henderson 1970; Helmstادت and Padgham 1985; ages from Isachsen et al. 1991; Isachsen 1992). The U-Pb detrital age spectrum determined in this study exhibits remarkable overlap with three of the major age groups occurring in two of these lithotectonic units, suggesting that the nine peaks in Fig. 2.11 can be regrouped into three modes corresponding to the CSCG (ii) and the Kam and Banting (iii) igneous events. The detrital age data presented in this study also correlate well with detrital age determinations from the Damoti Formation at Indin Lake (Pehrsson and Villeneuve 1999). These correlations are discussed in more detail below.

2900 – 2750 Ma: CSCG correlations.

There is widespread recognition that a tectonomagmatic event involving ultramafic to felsic volcanism and granitoid plutonism accompanied by high-grade metamorphism affected the Slave Province in the interval 2.9-2.8 Ga (Henderson et al. 1987; Emon et al. 1999; Northrup et al. 1999; Ketchum and Bleeker 1999, 2000; Bleeker et al. 1999a, b; Sircombe et al. 2001). Detrital zircon grains with this age range have been identified in this study (Figs. 2.12a-c), suggesting that the CSCG was exposed and shedding detritus during deposition of the SRT turbidites. Although Pehrsson and Villeneuve (1999) did not recognize a detrital zircon population of this age in the Indin

Lake region, one of their zircon fractions yielded an age of 3048 [\pm 2] Ma, which correlates with the underlying pre-2.9 Ga Central Slave Basement Complex.

2730 –2700 Ma: Kam correlations

‘Kam’ volcanism from ca. 2.73-2.70 Ga was ubiquitous throughout the central Slave Province, resulting in the eruption of large quantities of submarine tholeiitic basalt onto the Central Slave basement and its platformal cover and the onset of extensive granite–greenstone development (e.g., the Yellowknife, Cameron River, Beaulieu River, Beniah Lake, Camsell Lake, Courageous Lake, Desteffany Lake, Winter Lake, Point Lake and Emile River belts), in an inferred extensional setting (Bleeker et al. 2000). The detrital spectrum presented in this study has a strong Kam age-component (Figs. 2.11; 2.12d, e), as does the Damoti greywacke in the Indin Lake belt (Pehrsson and Villeneuve 1999), but Kam-age rocks have not been identified in either area suggesting that the two units had similar distal source regions.

2690 – 2630 Ma: Banting (2690 –2660 Ma) and local (<2660) age correlations

Extensive bimodal ‘Banting’ magmatic activity between 2690-2660 Ma marked the onset of a pan-Slave tectonomagmatic event of which the Snare arc was a part. Banting-age zircon grains are the dominant component in the SRT turbidite age spectrum, and detritus of this age was probably derived principally from local sources. Similarly, subordinate components of ca. 2650 Ma (Hinscliffe complex age) and 2635 Ma (Disco Intrusive Suite age) can be correlated to magmatic events in both the SRT and

the broader Slave Province. Pehrsson and Villeneuve (1999) also documented these components in the Damoti greywacke, again suggesting similar source regions for the two areas at that time.

In summary, the similarity of the SRT detrital age spectrum with known local and regional events suggests that sediment detritus in the southwestern Slave Province had both proximal and distal provenance, with sedimentation continuing until tectonic assembly of the turbidites with magmatic rocks into the Snare proto-arc.

2.9.3 Implications for the Lithoprobe SNORCLE transect

Exposure of Neoproterozoic upper and mid crust in the Snare River terrane provides an opportunity to correlate the geologic datasets of the study area with the seismic reflection dataset acquired along the Lithoprobe SNORCLE transect approximately 100 km to the south (Fig. 2.1), where greenschist- to amphibolite-facies upper-crustal rocks of probable Neoproterozoic age are exposed at the surface.

Seismic reflection data at the western end of the seismic line reveal a largely non-reflective upper crust overlying gently undulating reflectors at mid-crustal depths, i.e., 4-8 s two-way travel time (see Figs. 3a, b of van der Velden and Cook 2002). To a first approximation, this pattern correlates well with surface geological information from the Snare River terrane, where steep structures in the upper crustal belts (which are expected to be non-reflective on account of their geometry) structurally overlie gently to moderately dipping dome-and-basin structures in the mid-crustal rocks in Ghost subdomain (Figs. 2.2a, b). Thus on the basis of these correlations, it is permissible to

suggest that the mid-crustal Ghost subdomain may be representative of the type of mid crust imaged in the SNORCLE transect. Furthermore, seismic reflection data at the western edge of the SNORCLE line exhibit a marked change in apparent reflectivity and dip at ca. 13-15 km depth, which in the study area would correspond to the paleodepth of the amphibolite to granulite transition and the presence of abundant magmatic rocks, including the large two-mica batholith in Bigspruce subdomain and the sheets of coarse-grained megacrystic granite interlayered with metasedimentary rocks (Figs. 2.2b, 2.3). However, in their interpretation of the seismic data, van der Velden and Cook (2002) suggested that the Paleo- to Mesoarchean Central Slave Basement Complex occurred in the subsurface at mid-crustal depths beneath much of the western Slave Province in the SNORCLE transect. Data presented in this study indicate that this interpretation is not tenable for the Snare River terrane, implying that if the conclusions of van der Velden and Cook (2002) are correct, there must be a transitional region of complex crustal geometry between the study area and the SNORCLE line.

This study demonstrates the diversity in age and composition that exists in the upper- and mid-crust in the southwestern Slave Province. As such it provides an excellent opportunity to directly test the physical properties (e.g., seismic velocity, conductivity and heat flow) of these crustal levels and ultimately compare and integrate these data with the indirect geophysical datasets of the Lithoprobe SNORCLE transect

2.10 Conclusions

Integrated field mapping and U-Pb age dating have permitted construction of a 4D framework for the evolution of the SRT. Integrating the well-preserved metamorphic gradient that exposes a section through mid and upper orogenic crust, with new U-Pb age data, we have defined the occurrence of and transition between two contrasting tectonic regimes responsible for successive phases of crustal growth in the SRT and provided a detailed sequence of magmatic events in each regime. The upper crustal stratigraphy delineated for the Kwejinne Lake supracrustal belt is a window into the early history of a predominantly TTG/granite–greenstone tectonic regime (TR1) that prevailed from ca. 2674–2608 Ma. This regime was characterized by progressive accumulation of new crust through episodic metaluminous magmatism and coeval, but diachronous, turbidite sedimentation in an adjacent basin. TR1 concluded with tectonic imbrication (D1) of the turbidites and TTG/greenstones, coeval with greenschist- to amphibolite-facies metamorphism (M1), and led to formation of the imbricated Snare proto-arc.

The onset of extensive mid-crustal peraluminous and metaluminous granitoid plutonism, rapid crustal thickening, D2 refolding of earlier structures and M2 granulite-facies metamorphism, marked the transition from the early TR1 to an incipient plate tectonic regime, TR2. Defined from the lower structural levels of the Kwejinne Lake supracrustal belt and the mid-crustal, granulite-facies Ghost subdomain, TR2 occurred between 2608 and 2597 Ma and is interpreted as a consequence of collision between the Snare proto-arc and an adjacent crustal block that comprised the Central Slave Basement Complex and its younger cover components. During TR2, the locus of magmatism and

metamorphism shifted to the mid crust, resulting in intra-crustal thickening by thrusting and magmatic injection, reworking of TR1 crust and generation of a hot and weak mid-crustal layer. D2 shortening and M2 granulite-facies metamorphism terminated in post-orogenic collapse between ca. 2597-2586 Ma, characterised by upper crustal extension, mid-crustal uplift, renewed small-volume, bimodal plutonic activity between 2590-2586 Ma, and high temperature – low pressure metamorphism (M3) from ca. 2586-2571 Ma.

Metaluminous plutonism spanned the entire ~80 M.y. magmatic history of the SRT, indicating the prolonged influence of lower crustal and/or mantle melting on crust-formation. Metaluminous magma compositions ranged from tonalite to granodiorite during the early stages of TR1, through granodiorite and granite at the 2597 Ma magmatic peak, and reverted to tonalitic compositions during post-orogenic collapse. In contrast, peraluminous plutonism, which was predominantly granitic, was restricted to TR2 and occurred in two discrete pulses at ca. 2597 and 2586 Ma, suggesting that generation of peraluminous magmas occurred when peak temperatures were achieved during D2/M2 and during orogenic collapse (D3/M3) as a result of decompression melting.

With regard to the detrital zircon study, four age groupings have been defined, i.e., 2.85-2.74, 2.74-2.70, 2.69-2.66 and 2.66-2.635 Ga, that correlate with the known ages of the CSCG sequence, overlying Kam- and Banting-age greenstone belts and local post-2.66 Ga ages of magmatism in the SRT. Of these, only Banting-age and younger rocks are present in the SRT, implying a distal provenance for a proportion of the detritus. The youngest detrital zircon determined from a sample in the upper-crustal

Kwejinne Lake supracrustal belt has an age of ~2633 Ma, which defines the maximum age of sedimentation for that part of the SRT. However, intrusion of ca. 2635 Ma plutons of the Disco Intrusive Suite into metaturbidites in the mid-crustal Ghost subdomain suggests either that two phases of sedimentation occurred or that a single protracted sedimentation event was coeval with deformation. The presence of a small population of detrital grains with ages correlative with dated ash horizons in the platformal CSCG suggests a distal continental influence on the Snare proto-arc during TR1 that evolved into a proximal influence in the stages preceding the proto-arc—continent collision of TR2.

Gently undulating reflections imaged at mid-crustal levels in the Lithoprobe SNORCLE experiment correlate well with the dome-and-basin geometry of the exhumed mid crust in the Ghost subdomain. However, in this study we demonstrate an absence of pre-2.8 Ga crust in the region, at least at upper and mid-crustal levels, which contrasts with the published interpretation of the crustal structure of the southwestern Slave Province under the SNORCLE transect, in which the continuation of the Central Slave Basement Complex at mid to lower crustal levels is proposed beneath much of the region. Further work involving measurement of the physical properties of the Neoproterozoic upper- and mid-crustal lithologies exposed at the erosion surface in the Snare River terrane could provide the information necessary to reconcile the results of this study with those of the SNORCLE dataset.

In conclusion, the Neoproterozoic Snare River terrane has proved an exemplary natural laboratory in which to observe and document the relatively rapid transition from a

TTG / granite–greenstone tectonic regime and associated mechanism of crustal growth into a plate-tectonic collisional regime of crustal growth and reworking that principally involved collision of the leading edge of an older crustal block with a younger outboard, proto-arc terrane.

2.11 Acknowledgements

The NWT Geoscience Office and the Geological Survey of Canada provided logistical support for the ~ 8 months of fieldwork associated with the project. The NWT Geoscience Office also provided financial assistance, office space and a stimulating work environment for V.B. to complete the research presented. John Ketchum, Jim Connelly and Ken Ludwig are thanked for discussions regarding U decay constant uncertainties, and Sally Pehrsson is acknowledged for her ongoing interest in the project and several enlightening conversations. Wouter Bleeker introduced V.B. to the regional geology of the Slave Province during the first field season, and also generously made available the use of a rock saw, which quickly became an indispensable sampling tool. Richard Flood is thanked for his suggestions on various parts of the manuscript. Bill Griffin, an anonymous reviewer, and the associate journal editor Kevin Ansdell are thanked for their constructive assessments of the manuscript. This work was supported by a Lithoprobe grant and a Natural Sciences and Engineering Research Council Discovery grant to T.R. for field, analytical and other costs. V.B. acknowledges receipt of a Canadian Commonwealth Scholarship and graduate student bursaries from MUN.

2 References

- Ashwal, L.D., Tucker, R.D., and Zinner, E.K. 1999. Slow cooling of deep crustal granulites and Pb loss in zircon. *Geochimica et Cosmochimica Acta*, **63**: 2839-2851.
- Begemann, F., Ludwig, K.R., Lugmair, G.W., Min, K., Nyquist, L.E., Patchett, P.J., Renne, P.R., Shih, C.-Y., Villa, I.M., and Walker, R.J. 2001. Call for an improved set of decay constants for geochronological use. *Geochimica et Cosmochimica Acta*, **65**: 111-121.
- Bennett, V.R.C., and Dunning, G.R. 1998. Geological Transect across the southern Indin Lake supracrustal belt to the central Ghost Lake granulite domain. *In* 26th Yellowknife Geoscience Forum. Indian and Northern Affairs Canada, NWT Chamber of Mines and Resources, Wildlife and Economic Development, Program and Abstracts of Talks and Posters, pp. 14-16.
- Bennett, V., Dunning, G.R., and Indares, A. 2000. Preliminary data from the Kwejinne Lake supracrustal belt-Ghost Lake granulite domain transect: impact of a steep thermal gradient on upper crustal rocks. *In* 28th Yellowknife Geoscience Forum ; Indian and Northern Affairs Canada, NWT Chamber of Mines and Resources, Wildlife and Economic Development, Program and Abstracts of Talks and Posters, pp. 10-11.
- Bennett, V., Rivers, T., Relf, C. 2002. Where East meets West: Formation, growth and collapse of the Snare River Terrain, southwestern Slave Province. *In* 30th Yellowknife Geoscience Forum ; Indian and Northern Affairs Canada, NWT Chamber of Mines and Resources, Wildlife and Economic Development, Program and Abstracts of Talks and Posters, pp. 1-2.
- Bleeker, W., and Villeneuve, M. 1995. Structural studies along the Slave portion of the SNORCLE Transect; in Slave-NORthern Cordillera Lithospheric Evolution (SNORCLE), Report of 1995 Transect Meeting, April 8-9, University of Calgary, edited by F. Cook and P. Erdmer, LITHOPROBE Report No. 44, p. 8-14.
- Bleeker W., Ketchum, J.W.F., Jackson, V.A., and Villeneuve, M.E. 1999a. The Central Slave Basement, Part I: its structural topology and autochthonous cover. *Canadian Journal of Earth Sciences*, **36**: 1083-1109.
- Bleeker W., Ketchum, J.W.F., and Davis, W.J. 1999b. The Central Slave Basement, Part II: Age and tectonic significance of high strain zones along the basement-cover contact. *Canadian Journal of Earth Sciences*, **36**: 1111-1130.
- Bleeker W., Stern R., and Sircombe, K. 2000. Why the Slave Province got a little bigger. *In* Current Research, 2000-C. Geological Survey of Canada, 9 pp.
- Bowring, S.A., and Williams, I.S. 1999. Priscoan (4.00 – 4.03 Ga) orthogneisses from northwestern Canada: Contributions to Mineralogy and Petrology, **134**: 3-16.
- Bowring, S.A., Williams, I.S., and Compston, W. 1989. 3.96 Ga gneisses from the Slave Province Canada, Northwest Territories, Canada. *Geology*, **17**: 971-975

- Brophy, J.A., and Pell, J. 2002. Preliminary Geology of the Labrish Lake area, Southwestern Slave Province; Parts of 85N/09. NWT Open File 2002-06. DIAND, NWT Geology Division, Yellowknife. 1 map plus legend scale 1: 50 000.
- Buick, R., Thornett, J.R., McNaughton, N.J., Smith, J.B., Barley, M.E., and Savage, M. 1995. Record of emergent continental crust ~ 3.5 billion years ago in the Pilbara craton of Australia. *Nature*, **375**: 574-577.
- Carson, C.J., Ague, J.J., and Coath, C.D. 2002. U-Pb geochronology from the Tonagh Island, East Antarctica: implications for the timing of ultra high temperature metamorphism of the Napier Complex. *Precambrian Research*, **116**, p. 237-263.
- Carson, C.J., Ague, J.J., Grove, M., Coath, C.D., and Harrison, T.M. 2002. U-Pb isotopic behaviour of zircon during upper-amphibolite facies fluid infiltration in the Napier Complex, east Antarctica. *Earth and Planetary Science Letters*, **199**: 287-310.
- Chacko, T., Creaser, R.A., Farquhar, J. and Muehlenbachs, K. 1995a. The deep crust of the western Slave Province – Initial petrological and isotopic data from high grade rocks of the Ghost Domain. *In Slave – Northern Cordillera Lithospheric Evolution Workshop (SNORCLE) Transect and Cordilleran Tectonics Workshop Meeting, 8 – 9 April, Calgary. Compiled by F. Cook and P. Erdmer. Lithoprobe Report 44, pp.4-7.*
- Chacko, T., Farquhar, J., and Creaser, R.A. 1995b. A petrological study of granulites and associated rocks from the Ghost Lake area, southwestern Slave Province; *In Geological Association of Canada – Mineralogical association of Canada (GACMAC) Annual Meeting, Victoria 1995, Program with Abstracts, 20: A-15.*
- Cherniak, D.J., and Watson, E.B. 2000. Pb Diffusion in zircon. *Chemical Geology*, **172**, p. 5-24.
- Cox, R.A., Dunning, G.R., and Indares, A. 1998. Petrology and U-Pb geochronology of mafic, high-pressure metamorphic coronites from the Tshenukutish domain. Eastern Grenville Province. *Precambrian Research*, **90**: 59-83.
- Crowley, J.L. 2002. Testing the model of late Archean terrane accretion in southern West Greenland: a comparison of the timing of geological events across the Qarliit nunaat fault, Bukesefjorden region. *Precambrian Research*, **116**: 57-79
- Davis, W.J. 1992. Granitoid geochemistry and crustal evolution in the central Slave Province, Ph.D. thesis. Memorial University of Newfoundland, St John's, N.L.
- Davis, W.J. 1997. U-Pb zircon and rutile ages from granulite xenoliths in the Slave Province : Evidence for mafic magmatism in the lower crust coincident with Proterozoic Dyke Swarms. *Geology*, **25**: 343-346.
- Davis, W.J. and Hegner, E. 1992. Neodymium isotopic evidence for the tectonic assembly of Late Archean crust in the Slave Province, northwest Canada. *Contributions to Mineralogy and Petrology*, **111**: 493 –504.

- Davis, W.J., and Bleeker, W. 1999. Timing of plutonism, deformation and metamorphism in the Yellowknife Domain, Slave Province, Canada. *Canadian Journal of Earth Sciences*, **36**: 1169-1187.
- Davis, W.J., and Hegner, E. 1992. Neodymium isotopic evidence for the tectonic assembly of the Late Archean crust in the Slave Province, northwest Canada. *Contributions to Mineralogy and Petrology*, **111**: 493 - 504.
- Davis, W.J., King, J.E., and Fryer, B.J. 1994. Geochemistry and evolution of Late Archean plutonism and its' significance to the tectonic development of the Slave craton. *Precambrian Research*, **67**: 207 -241.
- Davis, W.J., Gariepy, C., and van Breeman, O. 1996. Pb isotopic composition of late Archean granites and the extent of recycling early Archean crust in the Slave Province, northwest Canada. *Chemical Geology*, **130**: 255-269.
- Emon, K.E., Jackson, V.A., and Dunning, G.R. 1999. Geology and U-Pb geochronology of the Eukok Uplift: a pre-2.8 Ga basement terrane in the northwestern Slave Structural Province, Northwest Territories, Canada. *Canadian Journal of Earth Sciences*, **36**: 1061-1082.
- Eriksson, K.A., and Fedo, C.M. 1994. Archean synrift and stable shelf sedimentary successions. *In Archean Crustal Evolution. Edited by K.C. Condie, Developments in Precambrian Geology*, **11**: 171-204.
- Frith, R.A., Loveridge, W.D., and Van Breeman, O. 1986. U-Pb ages from basement granitoids of the western Slave Structural Province, northwestern Canadian Shield, *In Current Research, Part A. Geological Survey of Canada, Paper 86-1A*, pp. 113 - 119.
- Geological Survey of Canada, 1963. Ghost Lake, District of Mackenzie, Northwest Territories; Aeromagnetic Series. Geological Survey of Canada, Geophysics Paper 2955, Map 2955G, (scale 1:50 000).
- Hanchar, J.M., and Miller, C.F. 1993. Zircon zonation patterns as revealed by cathodoluminescence and backscattered electron images: Implications for interpretation of complex crustal histories. *Chemical Geology*, **110**: 1-13.
- Hawkins, D.P., and Bowring, S.A. 1997. U-Pb systematics of monazite and xenotime: case studies from the Palaeoproterozoic of the Grand Canyon, Arizona. *Contributions to Mineralogy and Petrology*, **127**: 87-103.
- Helmstaedt, H., and Padgham, W.A., 1985. A new look at the stratigraphy of the Yellowknife Supergroup at Yellowknife, N.W.T. - implications for the age of gold-bearing shear zones and Archean basin evolution. *Canadian Journal of Earth Sciences*, **23**: 454-475.
- Henderson, J.B. 1970. Stratigraphy of the Yellowknife Supergroup, Yellowknife Bay - Prosperous Lake area, District of Mackenzie: Geological Survey of Canada, Paper 70-26.

- Henderson, J.B. 1994. Geology of the Wijinnedi Lake area – a Paleoproterozoic (?) asymmetric uplift of Archean rocks in the southwestern Slave Province, District of Mackenzie, Northwest Territories. *In* Current Research, 1994-C. Geological Survey of Canada, pp. 71-79.
- Henderson, J.B. 1998. Preliminary geology, Wijinnedi Lake area, District of Mackenzie, Northwest Territories; Geological Survey of Canada, Open File 3609 (scale 1: 50 000).
- Henderson, J.B. 2004. Geology of the Wijinnedi Lake area, District of Mackenzie, Northwest Territories. Geological Survey of Canada, Bulletin 576,
- Henderson, J.B. and Chacko, T. 1995. A reconnaissance of the high grade metamorphic terrane south of Ghost Lake, southwestern Slave Province, Northwest Territories. *In* Current Research, 1995-C. Geological Survey of Canada, pp. 77-85.
- Henderson, J.B. and Schaan, S.E. 1993. Geology of the Wijinnedi Lake area: a transect into mid-crustal levels in the western Slave Province, District of Mackenzie, Northwest Territories. *In* Current Research, Part C. Geological Survey of Canada, Paper 93-1C, pp. 83-91.
- Henderson, J.B., Loveridge, W.D., and Sullivan, R.W. 1982. U-Pb study from granitic basement beneath the Yellowknife Supergroup, Point Lake, District of Mackenzie, *In* Rb-Sr and U-Pb Isotopic Age Studies, Report 5. Geological Survey of Canada, Paper 82-1C, pp. 173 – 178.
- Henderson, J.B., van Breemen, O., and Loveridge, W.D. 1987. Some U-Pb zircon ages from Archean basement, supracrustal and intrusive rocks, Yellowknife – Hearne Lake area, District of Mackenzie. *In* Radiogenic Age and Isotopic Studies: Report 1. Geological Survey of Canada, Paper 87-2, pp. 111-121.
- Horn, I., Rudnick, R.L., and McDonough, W.F. 2000. Precise elemental and isotope ratio determination by simultaneous solution nebulization and laser ablation-ICP-MS: application to U-Pb geochronology. *Chemical Geology*, **167**: 405-425.
- Horstwood, M.S.A., Nesbitt, R.W., Noble., S.R., and Wilson, J.F. 1999. U-Pb zircon evidence for an extensive early Archean Craton in Zimbabwe: a reassessment of the timing of craton formation, stabilization and growth. *Geology*, **26**: 883 – 886.
- Isachsen, C.E., 1992. U-Pb Zircon Geochronology of the Yellowknife Volcanic Belt and Subjacent Rocks, N.W.T., Canada: Constraints on the Timing, Duration, and Mechanics of Greenstone Belt Formation. Ph.D. thesis, Washington University, St Louis, Mo.
- Isachsen, C.E., and Bowring, S.A. 1997. The Bell Lake group and Anton Complex: a basement – cover sequence beneath the Archean Yellowknife greenstone belt revealed and implicated in greenstone belt formation. *Canadian Journal of Earth Sciences*, **34**: 169-189.
- Isachsen, C.E., Bowring, S.A., and Padgham, W.A. 1991. Geochronology of the Yellowknife

- Volcanic Belt, N.W.T., Canada : new constraints on the timing and duration of greenstone belt magmatism. *Journal of Geology*, **99**: 55 - 67.
- Jackson, V.A. 1998a. Preliminary Geology of the Kwejinne Lake area (parts of 85O/11, 12, 13): EGS Open File 1998-19. DIAND, NWT Geology Division, Yellowknife. 1 sheet with descriptive notes.
- Jackson, V.A. 1998b. The Snare River Project : Objectives and initial results *In* 26th Yellowknife Geoscience Forum. Indian and Northern Affairs Canada, NWT Chamber of Mines and Resources, Wildlife and Economic Development, Program and Abstracts of Talks and Posters, pp. 61-63.
- Jackson, V.A. 1999. Preliminary 1:100 000 scale compilation of the geology of the Snare River area (1998 and 1999 results); EGS Open File 1999-18. DIAND, NWT Geology Division, Yellowknife.
- Jackson, V.A. 2000a. Descriptive Notes for the Snare River 1:50 000 scale maps to accompany EGS Open File 1998-18 and EGS Open File 2000-10. DIAND, NWT Geology Division, Yellowknife.
- Jackson, V.A. 2000b. Preliminary Geology of the part of the Snare River area; Parts of 85N/16 and 85O/5-7; 10-13: EGS Open File 2000-10. DIAND, NWT Geology Division, Yellowknife. Data on 3 maps and assay tables, scale 1:50 000 and CD in Autocad R14 and .pdf formats.
- Jackson, V.A. 2000c. The Snare River Project: results from mapping; *In* 28th Yellowknife Geoscience Forum. Indian and Northern Affairs Canada, NWT Chamber of Mines and Resources, Wildlife and Economic Development, Program and Abstracts of Talks and Posters, pp.33-34.
- Jackson, V.A. 2001. The 2001 Snare River Project: Mapping results with focus on the high grade rocks. *In* 29th Yellowknife Geoscience Forum. Indian and Northern Affairs Canada, NWT Chamber of Mines and Resources, Wildlife and Economic Development, Program and Abstracts of Talks and Posters, pp. 28-29.
- Jackson, V.A. 2002a. Preliminary Geology of the part of the Snare River area, Southwestern Slave Province; Parts of 85O and 85N. NWT Open File 2002-02. DIAND, NWT Geology Division, Yellowknife. 4 maps plus legend, scale 1:50 000. Assay tables to accompany maps.
- Jackson, V.A. 2002b. The Snare River project (parts of 85N and 85O): Results from 2002 mapping, the final field season. *In* 30th Yellowknife Geoscience Forum. Indian and Northern Affairs Canada, NWT Chamber of Mines and Resources, Wildlife and Economic Development, Program and Abstracts of Talks and Posters, pp. 27-28.

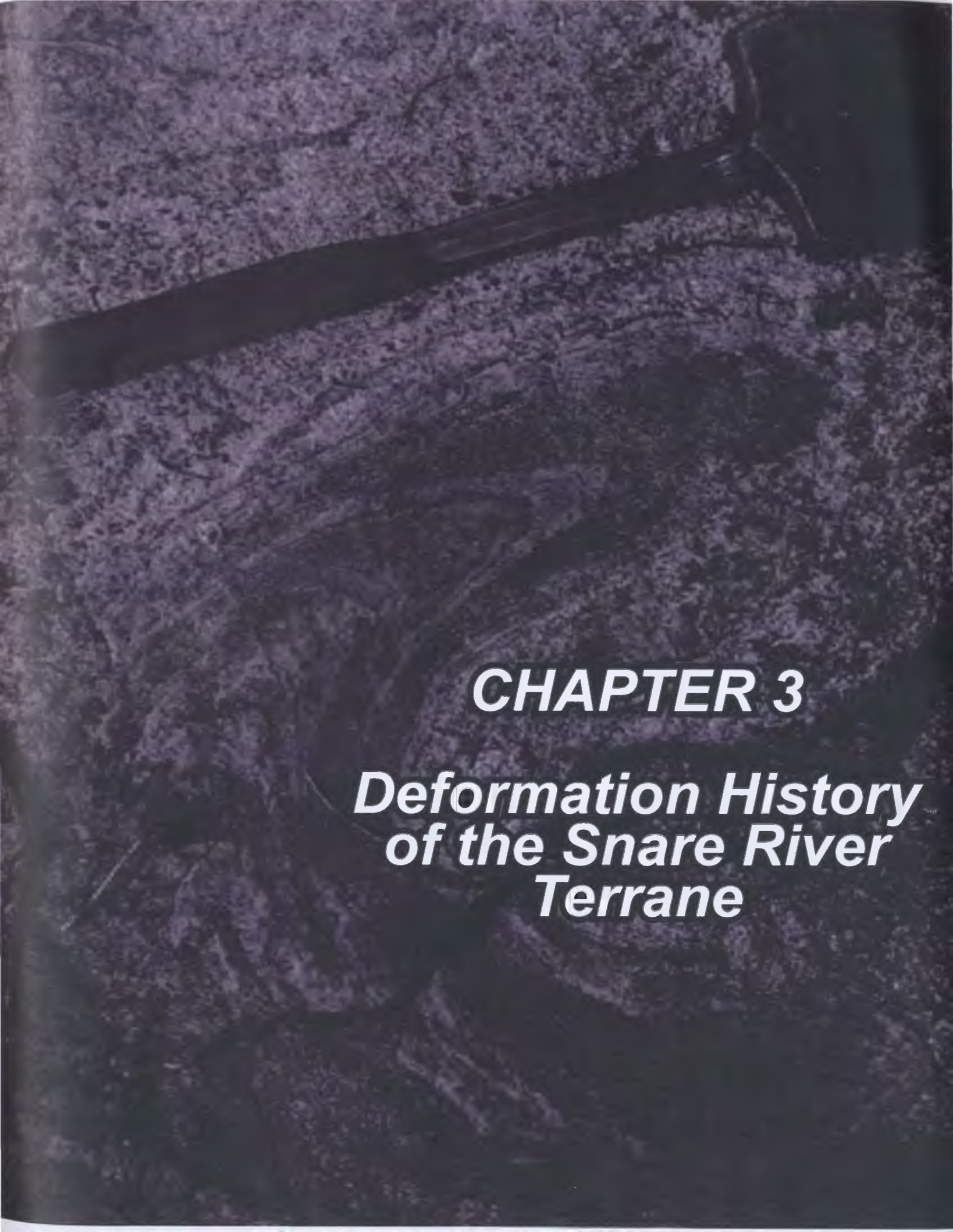
- Jackson, V.A., 2003. Preliminary compilation of the geology of the Snare River (1998-2002 results), Winjinnedi Lake, Labrish Lake and Russell Lake area; parts of 85N and 85O. C.S. Lord Northern Geoscience Centre, Yellowknife, NT. NWT Open Report 2003-002. Map, scale 1:100 000.
- Jaffey, A.H., Flynn, K.F., Glendenin, L.E., Bentley, W.C., and Essling, A.M. 1971. Precision measurements of half lives and specific activities of ²³⁵U and ²³⁸U. *Physical Reviews C: Nuclear Physics*, **4**: 1889 – 1906.
- James, D.T., and Mortensen, J.K. 1992. An Archean metamorphic core complex in the southern Slave Province: basement-cover structural relations between the Sleepy Dragon Complex and the Yellowknife Supergroup, *Canadian Journal of Earth Sciences*, **29**: 2133 – 2145.
- Ketchum, J., and Bleeker, W. 1998. U-Pb geochronology of the Sleepy Dragon complex in the Morose – Patterson Lake areas, southwestern Slave Province, with tectonic implications. *In Slave – Northern Cordillera Lithospheric Evolution Workshop (SNORCLE) Transect and Cordilleran Tectonics Workshop Meeting*, 6 – 8 March, Simon Fraser University. *Compiled by F. Cook and P. Erdmer*. Lithoprobe Report 64, pp. 25-30.
- Ketchum, J., and Bleeker, W. 1999. The Central Slave Cover Group and Central Slave Basement Complex: a progress report on U-Pb geochronological studies. *In Slave – Northern Cordillera Lithospheric Evolution Workshop (SNORCLE) Transect and Cordilleran Tectonics Workshop Meeting*, 5 – 7 March, Calgary. *Compiled by F. Cook and P. Erdmer*. Lithoprobe Report 69, pp. 21-29.
- Ketchum, J., and Bleeker, W. 2000. New field and U-Pb data from the Central Slave Cover Group near Yellowknife and the Central Slave Basement Complex at Point Lake. *In Slave – Northern Cordillera Lithospheric Evolution Workshop (SNORCLE) Transect and Cordilleran Tectonics Workshop Meeting*, 25 – 27 February, Calgary. *Compiled by F. Cook and P. Erdmer*. Lithoprobe Report 72, pp. 27-31.
- Kosler, J., Tubrett, M., and Sylvester, P. 2001. Application of Laser Ablation ICP-MS to U-Th-Pb Dating of Monazite. *Geostandards Newsletter, The Journal of Geostandards and Geoanalysis*. **25**, no.2 , pp. 12.
- Kosler., J., Fonneland, H., Sylvester, P., Tubrett, M., and Pedersen, R. 2002. U-Pb Dating of detrital zircons for sediment provenance studies – a comparison of laser ablation ICP-MS and SIMS techniques. *Chemical Geology*, **182**: 605-618.
- Krogh, T.E. 1973. A low contamination method for hydrothermal decomposition of zircon and extraction of U and Pb for isotopic age determination. *Geochimica and Cosmochimica Acta*, **37**: 485-494.
- Krogh, T.E. 1982. Improved accuracy of U-Pb ages by the creation of more concordant systems using an air abrasion technique. *Geochimica and Cosmochimica Acta*, **46**: 637-649.
- Lambert, M.L., and van Breemen, O. 1991. U-Pb zircon ages from the Sleepy Dragon Complex

- and a new occurrence of basement rocks within the Meander Lake Plutonic Suite, Slave Province, N.W.T. *In* Radiogenic age and isotopic studies: Report 4. Geological Survey of Canada, Paper 90-2, pp 79 - 84.
- Lee, J.K.W., Williams, I.S., and Ellis, D.J. 1997. Pb, U and Th diffusion in natural zircon. *Nature*, **390**: 159-161.
- Li, X., Liang, X., Sun., M and Malpas, J.G., 2001. Precise $^{206}\text{Pb}/^{238}\text{U}$ age determination on zircons by laser ablation microprobe – inductively coupled plasma – mass spectrometry using continuous laser ablation. *Chemical Geology*, **175**: 209 – 219.
- Lord, C.S. 1942. Snare and Ingray Lake map areas, Northwest Territories. Geological Survey of Canada, Memoir 235.
- Ludwig, K.R. 1980. Calculation of uncertainties of U-Pb isotope data. *Earth and Planetary Science Letters*, **46**: 212-220.
- Ludwig, K.R. 1999. User's manual for Isoplot/Ex, v2.06. A geochronological toolkit for microsoft excel. Berkeley Geochronological Centre Special Publication No. 1a.
- Ludwig, K.R. 2000. Decay constant errors on U-Pb concordia-intercept ages. *Chemical Geology*, **166**: 315-318.
- Mattinson, J.M., Graubard, C.M., Parkinson, D.L., and McClelland, W.C. 1996. U-Pb reverse discordance in zircons: the role of fine scale oscillatory zoning and submicron transport of Pb. *Geophysical Monograph*, **95**: 355-370.
- McGlynn, J.C., and Ross, J.V. 1962. Geology, Basler Lake, District of Mackenzie, Geological Survey of Canada, Map 18-1962, 1 inch to 1 mile map with marginal notes.
- Mortensen, J.K., Thorpe, R.I., Padgham, W.A., King, J.E. and Davis, W.J. 1988. U-Pb zircon ages for felsic volcanism in the Slave Province, N.W.T. *In* Radiogenic age and isotopic studies: Report 2. Geological Survey of Canada, Paper 88-2, pp. 85-95.
- Mortensen., J.K., Henderson, J.B., Jackson, V.A., and Padgham, W.A. 1992. U-Pb geochronology of the Yellowknife Supergroup felsic volcanic rocks in the Russell Lake and Clan Lake areas, southwestern Slave Province, Northwest Territories. *In* Radiogenic Age and Isotopic studies, Report 5. Geological Survey of Canada, Paper 91-2, pp. 1-7.
- Northrup, C.J., Isachsen, C., and Bowring, S.A. 1999. Field relations, U-Pb geochronology and Sm-Nd isotope geochemistry of the Point Lake greenstone belt and adjacent gneisses, central Slave craton, N.W.T., Canada. *Canadian Journal of Earth Sciences*, **36**: 1043-1059.
- Ootes, L., and Lentz, D. R. 2002. Occurrence of bleached mafic flows and their association with stockwork sulphides and banded iron-formation in the Crestaurum Formation of the late Archean Yellowknife Greenstone Belt, Northwest Territories. Geological Survey of Canada, Current Research No. 2002-E5, 12 pages.

- Padgham, W.A., and Fyson, W.K., 1992. The Slave Province: a distinct Archean craton. *Canadian Journal of Earth Sciences*, **29**, pp 2072 - 2086.
- Pehrsson, S.J. 1998. Deposition, deformation and preservation of the Indin Lake supracrustal belt, Slave Province, Northwest Territories. Unpublished Ph.D. thesis, Queens University, Kingston, Ontario.
- Pehrsson, S.J., and Chacko, T. 1997. Contrasting styles of deformation and metamorphism between mid and upper crustal rocks of the western Slave Province, Northwest Territories. *In Current Research, 1997-C*. Geological Survey of Canada, pp. 15-25.
- Pehrsson, S.J., and Villeneuve, M.E. 1999. Deposition and imbrication of a 2670-2629 Ma supracrustal sequence in the Indin Lake area, southwestern Slave Province, Canada. *Canadian Journal of Earth Sciences*, **36**: 1149-1168.
- Pehrsson, S.J., Chacko, T., Pilkington, M., Villeneuve, M.E. and Bethune, K., 2000. Anton terrane revisited: Late Archean exhumation of moderate-pressure granulite terrane in the western Slave Province. *Geology*, **28**: 1075-1078.
- Perks, M.A. 1997. The mid crust of the western Slave Province - Geological Mapping, geochemistry and U - Pb Geochronology of the Forked Lake Area, Southwestern Slave Province, NWT. M.Sc. thesis, University of Alberta, Edmonton, Alberta.
- Pidgeon, R.T., Nemchin, A.A., and Hitchen, G.J. 1998. Internal structures of zircons from Archean granites from the Darling Range batholith: implications for zircon stability and interpretation of zircon U-Pb ages. *Contributions to Mineralogy and Petrology*, **132**: 288-299.
- Relf, R., Chouinard, A., Sandeman, H., and Villeneuve, M. 1994. Contact relations between Anialik River volcanic belt and the Kangguyak gneiss belt, northwestern Slave Province, Northwest Territories, *In Current Research, 1994-C*. Geological Survey of Canada, pp 49 – 59.
- Relf, R., Sandeman, H., and Villeneuve, M. 1999. Tectonic and thermal history of the Anialik River area, northwestern Slave Province, Canada. *Canadian Journal of Earth Sciences*, **36**: 1207 – 1226.
- Robinson, J., Covello, L., and Falck, H. 2002. Compilation of airborne total field magnetic geophysical data for the Yellowknife basin; NTS 85 I, J, O and P. *In 30th Yellowknife Geoscience Forum*. Indian and Northern Affairs Canada, NWT Chamber of Mines and Resources, Wildlife and Economic Development, Program and Abstracts of Talks and Posters, p. 53.
- Sircombe, K.N., Bleeker, W. Stern, R.A., 2001. Detrital zircon geochronology and grain-size analysis of a ~ 2800 Ma Mesoarchean proto-cratonic cover succession, Slave Province, Canada. *Earth and Planetary Science Letters*, **189**: 207-220.

- Stacey, J.S., and Kramers, J.D. 1975. Approximation of terrestrial Pb isotope evolution by a two stage model. *Earth and Planetary Science Letters*, **26**: 207-221.
- Stern, R.A., and Bleeker, W. 1998. Age of the world's oldest rocks refined using Canada's SHRIMP: The Acasta Gneiss Complex, Northwest Territories, Canada. *Geoscience Canada*, **25**: 27-31.
- Stubbley, M.P., and Cairns, S.R. 1998. Geology of Fishing Lake area, southern Slave Province; Parts of NTS 85 O/1 and 8 and 85P/5. Economic Geology Series, EGS Open File 1998-05. DIAND NWT Geology Division.
- Stubbley, M.P., Jaegli, S., Bilben, S. and Tyler, T. 1995. Geology of the Nardin Lake area, south-central Slave Province, parts of NTS 85P/5 and 12, 85O/8 and 9. EGS Open File 1995-04. 1:50 000 map with marginal notes. Yellowknife: DIAND NWT Geology Division.
- Sylvester, P.J., and Ghaderi, M. 1997. Trace element analysis of scheelite by excimer laser ablation-inductively coupled plasma-mass spectrometry (ELA-ICP-MS) using a synthetic glass standard. *Chemical Geology*, **141**: 49-65.
- Thorpe, R.I., Cumming, G.L., and Mortensen, J.K. 1992. A significant Pb Isotope boundary in the Slave Province and its probable relation to ancient basement in the western Slave Province. *In* Project Summaries, Canada - Northwest Territories Mineral Development Agreement 1987 - 91. Geological Survey of Canada, Open File Report no. 2484: 179-184
- van Breemen, O., Davis, W.J., and King, J.E. 1992. Temporal distribution of granitoid plutonic rocks in the Archean Slave Province, northwest Canadian Shield. *Canadian Journal of Earth Sciences*, **29**: 2186 – 2199.
- van der Velden, A.J., and Cook, F.A. 2002. Products of the 2.65 – 2.58 Ga orogenesis in the Slave Province correlated with Slave – Northern Cordillera Lithospheric Evolution (SNORCLE) seismic reflection patterns. *Canadian Journal of Earth Sciences*, **38**: 1189 – 1200.
- Villeneuve, M.E., and Henderson, J.B. 1998. U-Pb geochronology of the Wijnnedi Lake area, Slave Province, District of Mackenzie, NWT. *In* Radiogenic Age and Isotopic studies: Report 11. Geological Survey of Canada, 1998-F, pp. 99-106.
- Villeneuve, M.E., Henderson, J.R., Hrabí, R.B., Jackson, V.A., and Relf, C. 1997. 2.70 – 2.58 Ga plutonism and volcanism in the Slave Province, District of Mackenzie, Northwest Territories. *In* Radiogenic Age and Isotopic studies: Report 8. Geological Survey of Canada, 1997-F, pp. 37-60.
- Yamashita, K., Creaser, R.A., Stemler, J.U. and Zimaro, T.W. 1999. Geochemical and Nd-Pb isotopic systematics of Late Archean granitoids, southwestern Slave Province, Canada: Constraints for granitoid origin and crustal isotopic structure. *Canadian Journal of Earth Sciences*, **36**: 1131-1147.
- Yamashita, K., Creaser, R.A., Jensen, J.E. and Heaman, L.M. 2000. Origin and evolution of the

mid- to late-Archean crust in the Hanikahimajuk Lake area, Slave Province, Canada; evidence from U-Pb geochronological, geochemical and Nd-Pb isotopic data. *Precambrian Research* **99**, 197-224.



CHAPTER 3

***Deformation History
of the Snare River
Terrane***

**3. Bridging the crustal gap: Structural correlations
between Neoproterozoic low- and high-grade domains,
Snare River terrane, Slave Province, Canada**

V. Bennett¹, V. A. Jackson², T. Rivers¹ & C. Relf².

1. Department of Earth Sciences, Memorial University of Newfoundland, St Johns', NL.

A1B 3X5

2. C.S. Lord Northern Geoscience Centre, Yellowknife, NT, X1A 2R3

To submit to Tectonics

NWT Geoscience Office Contribution number 0012.

3.1 Abstract

Synthesis of deformation histories from juxtaposed low- and high-grade domains in the Neoproterozoic Snare River terrane, southwestern Slave Province has enabled reconstruction of the events responsible for the contrasting structural architecture of the upper and mid crust, providing a means to reconcile the 'seismic versus structural' paradox. Superposition of three Neoproterozoic tectonothermal events (D1/M1 – D3/M3) resulted in a relative younging of structural age as a function of paleodepth, such that the oldest deformation events (D0, D1, early D2) are preserved in upper-crustal domains and younger events (late D2, D3) occur at progressively deeper levels. Structural analysis reveals a progression from steep upper-crustal structures to gently-dipping mid-crustal structures resulting from the combined effects of polyphase coaxial and non-coaxial progressive strain, and deformational and metamorphic diachroneity. Correlation of deformation histories between contrasting crustal levels was facilitated by the presence of the migmatitic transition zone, which carries structural attributes of both the overlying and underlying crust. A four-stage tectonothermal model is proposed for the architecture of the Snare River terrane: (i) protracted, diachronous thin-skinned shortening (D1) involving lateral telescoping of supracrustal belts against a protocratonic nucleus; (ii) crustal thickening by nappe tectonics and voluminous orogenic plutonism resulting from collision of the Snare River terrane (superstructure) with the Central Slave Basement complex (infrastructure); (iii) post-orogenic collapse, mid-crustal uplift and crustal thinning as a result of extension on conjugate sets of ductile shear zones; and (iv) overprinting by Paleoproterozoic deformation involving steep open folding and cleavage formation at all crustal levels. The distribution of regional fold interference patterns in the Snare River terrane tracks the migration of the D2 deformation front to increasing crustal depths during crustal thickening. Craton-wide correlations reveal that crustal growth in the Neoproterozoic involved horizontal accretion and reworking of outboard crustal terranes about a central

Mesoarchean protocratonic nucleus. Compressive strain was largely accommodated by thickening in marginal supracrustal terranes that subsequently underwent orogenic collapse. The distribution of these 'overthickened' regions has significant implications for diamond exploration in the Slave Craton.

Keywords: Seismic versus structural paradox, structural and metamorphic diachroneity, progressive deformation and metamorphism, crustal overthickening, core complex, diamond exploration.

3.2 Introduction

Published interpretations of Neoproterozoic crustal evolution in the Slave Province have principally been based on tectonic analyses of the low-grade supracrustal belts and intervening regions of granitoid rocks that constitute more than 90% of the craton at the present level of exposure. As far back as 1971, however, Windley and Bridgewater noted that a solely upper-crustal focus resulted in an unbalanced or biased perspective of Archean crustal architecture and evolution, and emphasized the need to integrate tectonic interpretations from the low-grade upper crust with those from medium- to high-grade, mid and lower crustal domains. Since then, studies of exhumed Archean crustal sections (e.g., Fountain and Salisbury 1981; Percival and West 1994; Lana et al. 2003) have shed light on some aspects of Neoproterozoic crustal architecture and confirmed that orogenesis occurs throughout the entire crustal column, while also emphasizing that different crustal levels responded in distinctive ways and at different times. In particular, although the geometry of juxtaposition of the upper and mid crust at the erosion surface in all analyzed crustal sections ranges from gradational (i.e., tilted crustal section) to sharp (i.e., rotated

fault block), a common attribute is the variation of structural style with paleodepth, involving the transition from steep brittle-ductile structures in the upper crust to subhorizontal ductile structures in the mid crust. Seismic profiles across Archean cratons have also revealed that reflectors become increasingly shallow dipping with depth, indicating that the gently-dipping mid-crustal structures in exhumed crustal sections originated prior to exhumation (e.g., Percival and West 1994; Sénéchal et al 1996; van der Velden and Cook 2002). The contrast between the steep structures observed at the surface in many upper-crustal Archean terranes and the sub-horizontal fabrics imaged seismically at depth beneath them has been termed the seismic versus structural paradox by Culshaw et al. (2004) and remains a poorly understood attribute of Archean crust. In the Neoproterozoic Snare River terrane, southwestern Slave Province, juxtaposed high- and low-grade domains separated by a transition zone exhibit strikingly similar first-order geometry to the crustal structures revealed in seismic profiles and provide an opportunity to contribute to resolution of this paradox by elucidating the range of deformation mechanisms and their variation with depth during crustal evolution.

In this contribution we correlate the sequence of polyphase deformation and metamorphism among the three exposed crustal levels and relate the contrasting structural styles, deformation mechanisms and overprinting metamorphic events to the regional crustal evolution. We have paid particular attention to four themes: (1) coaxial and non-coaxial progressive deformation; (2) structural and metamorphic overprinting; (3) the transition zone, which exhibits features characteristic of both the upper and mid crust enabling correlation between them; and (4) structural and metamorphic diachroneity at different structural levels.

An analysis of the crustal architecture in the context of these themes is essential to define the variation in structural style with depth, and the processes that resulted in the formation and juxtaposition of these structurally contrasting crustal levels. We present a model that provides a solution to these issues and contributes to understanding the crustal-scale tectonic evolution of Archean low- and high-grade domains.

3.3 Geological setting

The Slave Province (Fig. 3.1) is a small, predominantly granite–greenstone Archean craton that preserves a record of crustal growth and reworking from ca. 4.06 to 2.5 Ga (Bowring et al. 1989; Bowring and Williams 1999; Bleeker et al. 1999a, b; Pehrsson et al. 2000). The Snare River terrane (Fig. 3.2a), southwestern Slave Province, consists of a core of high-temperature low-pressure (HT/LP) granulite- and amphibolite-facies supracrustal and plutonic rocks with moderately to shallowly dipping structures (Ghost and Bigspruce subdomains) surrounded by steeply inclined greenschist- to amphibolite-facies volcano-sedimentary belts (Kwejinne Lake, Labrish Lake and Russell-Slemon supracrustal belts; Henderson and Schaan, 1993; Pehrsson et al. 2000; Bennett et al. 2005). The wedge-shaped Ghost subdomain is an uplifted mid-crustal block approximately 35 x 80 km in size bounded by the curvilinear Eastern and Western Boundary faults (Fig. 3.2a). Abrupt metamorphic transitions across these faults and the presence of cataclastic fabrics on the Eastern Boundary Fault imply that they are the sites of post-Archean reactivation

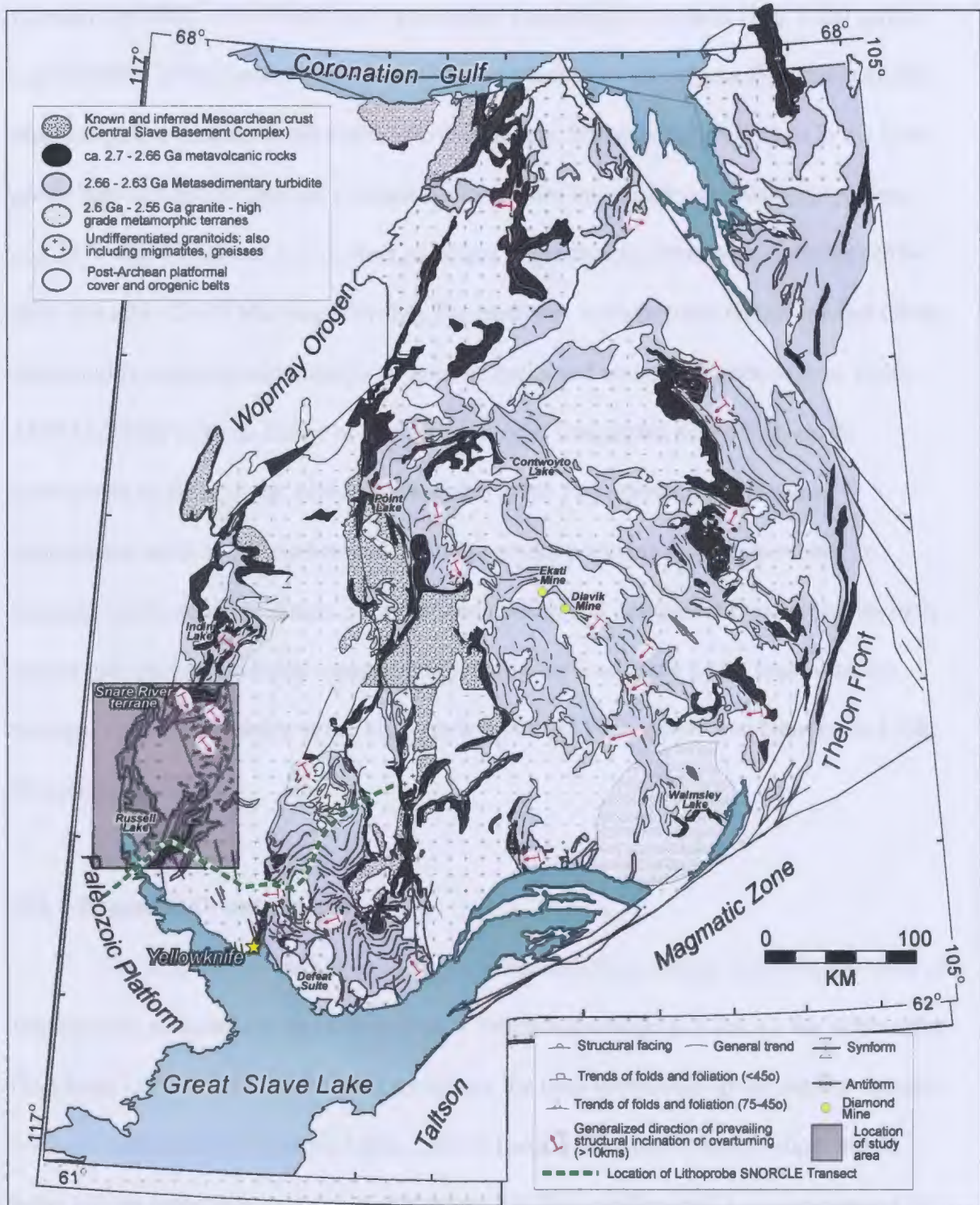


Figure 3.1: Simplified structural trend map of metasedimentary belts in the Slave Province. Modified after Bleeker et al. (1999) and Fyson and Jackson (2004). Location of Snare River terrane, lithoprobe SNORCLE transect and two of the largest diamond mines are shown.

(Henderson 2004). A 1:30 000 scale geological transect in three parts (Fig. 3.2a) across key localities of the Snare River terrane was undertaken to investigate the structural and metamorphic evolution in the exposed crustal levels. Supracrustal sequences in the low-grade belts consist of bimodal volcanic rocks and are intruded by syn-volcanic plutons (ca. 2674–2658 Ma) and two distinct packages of greywacke–mudstone turbidite (2674–2635 Ma and < 2635 Ma, respectively). The medium- to high-grade Bigspruce and Ghost subdomains consist predominantly of granitic rocks and associated gneisses (ca. 2640–2589 Ma) with tectonic lenses of supracrustal rocks interpreted as the high-grade equivalents of those in the adjacent low-grade belts. The presence of the same supracrustal units at greenschist and granulite grades provides a rare opportunity to integrate the tectonic evolution of upper- and mid-crustal domains. Previous studies have shown that the oldest crustal components occur in the low-grade upper crust whereas younger units predominate in the high-grade mid crust (Villeneuve and Henderson 1998; Bennett et al. 2005).

3.3.1 Exposed Crust Levels

The Snare River terrane can be subdivided into three crustal levels on the basis of lithotectonic associations and paleopressure determinations (Fig. 3.2b): (i) the upper crust (2–4 kbar; ca. 7–14 km paleodepth) comprises the low- to medium-grade, narrow arcuate volcano-sedimentary Kwejinne Lake, Labrish Lake and Russell–Slemon supracrustal belts; (ii) the transition zone (ca. 4–5 kbar; ca. 14–20 km paleodepth) is characterized by upper amphibolite-facies metamorphism, widespread anatexis and the presence of abundant migmatite and sparse granite sheets; and (iii) the mid crust (ca. 6.5–

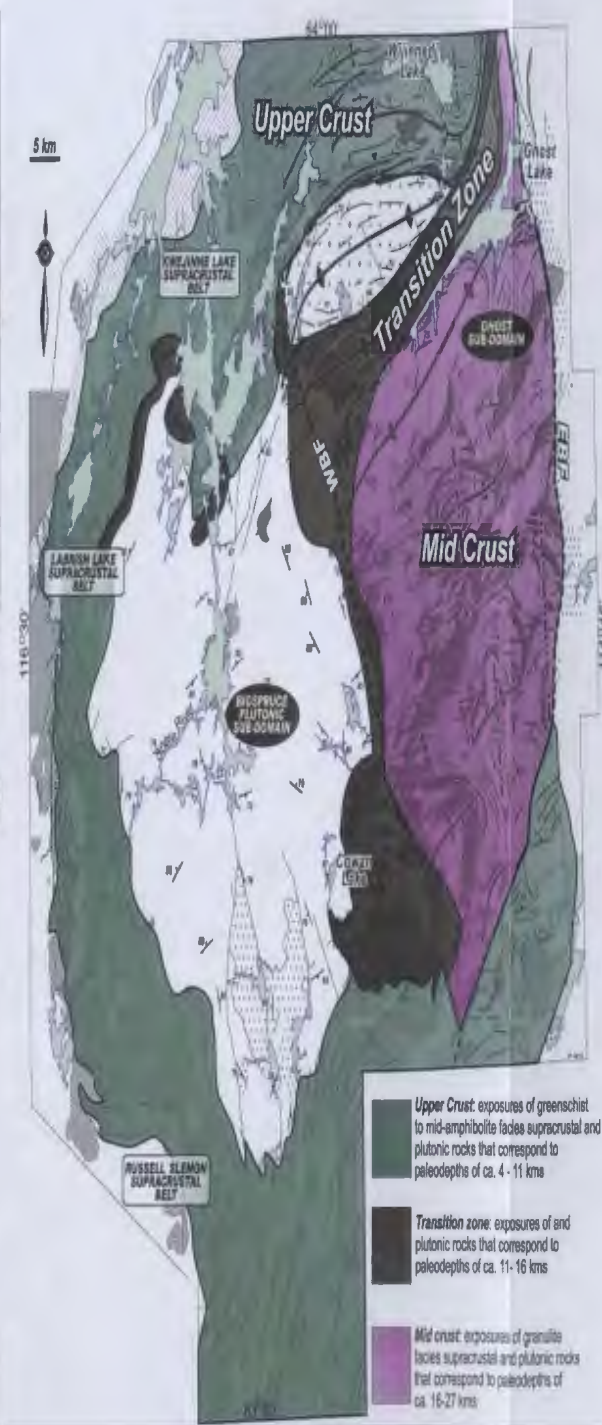
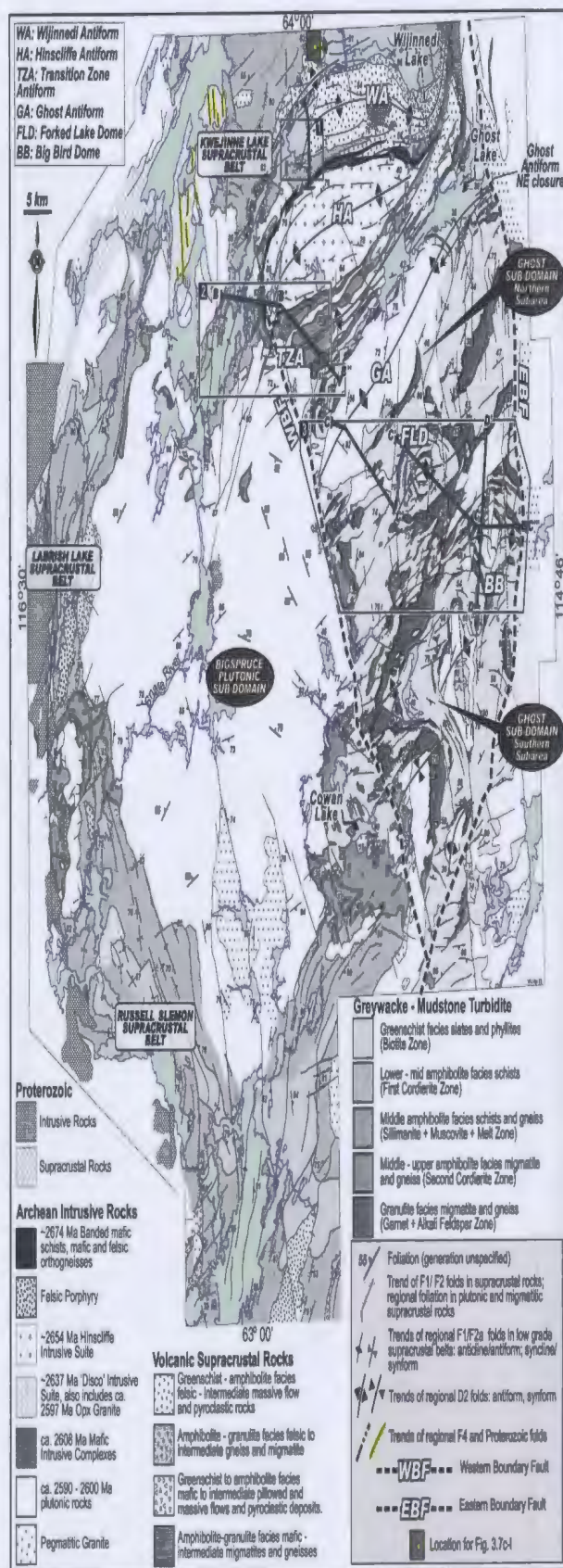


Figure 3.2: (a) Simplified structural trend map outlining major folds and foliations in the Snare River terrane. Modified after Jackson (2003 and references therein) and Fyson and Jackson (2004). Labelling and ages of structures are discussed in the text and shown in Figs. 3.4 and 3.5. Locations of transect maps and cross-sections indicated. (b) Interpretative map of distribution of crustal levels in the Snare River terrane. Data used to determine paleodepth are given in Appendix I.

7 kbar; ca. 22–25 km paleodepth), exposed in the Ghost subdomain, consists of uppermost amphibolite- to granulite-facies ortho- and paragneisses and massive to foliated plutonic rocks. Voluminous plutonism in Bigspruce subdomain, although occurring at the level of the transition zone, has obliterated continuity with adjacent crustal levels and so this subdomain is not discussed in detail here.

In two areas of the Snare River terrane, near Kwejinne and Cowan lakes, there is an unbroken transition from the low-grade upper-crustal belts through the transition zone to the mid-crustal Ghost subdomain (Fig. 3.2). Elsewhere the boundaries of the Ghost subdomain are tectonic: for instance, the Eastern Boundary Fault (which may represent the southern continuation of the Daran Lake Fault; Pehrsson et al. 2000), juxtaposes mid- and upper-crustal levels east of the area shown in Fig. 3.2, and the Western Boundary Fault juxtaposes the Bigspruce and Ghost subdomains locally.

3.3.2 Deformation and Metamorphism

The Snare River terrane exhibits a similar Neoproterozoic deformation history to the Slave Province as a whole, with three major events (D1 to D3; e.g., Davis and Bleeker 1999). In addition, a pre-D1 event, labelled D0, is recognised locally in metavolcanic lithologies (see below). The relative and absolute timeframes of these deformation events in the Snare River terrane are illustrated in Fig. 3.3. D1/M1 involved progressive fabric formation, isoclinal folding and associated greenschist- to lower-amphibolite-facies metamorphism between ca. 2640–2610 Ma, but for the most part has been overprinted by M2. D2/M2 involved refolding of D1 structures, major crustal thickening and metamorphism up to HTLP granulite-facies

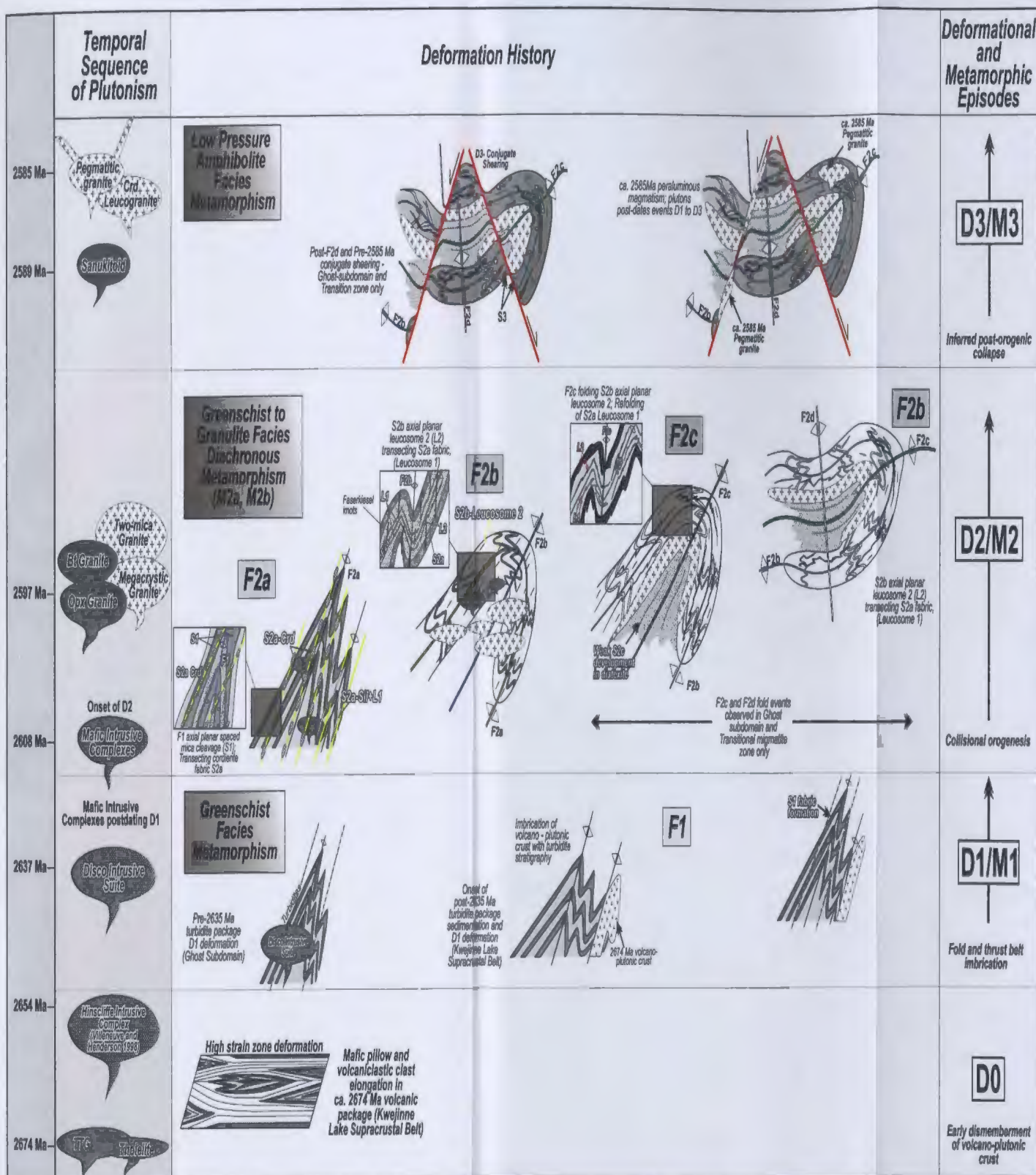


Figure 3.3: Relative sequence of metaluminous and peraluminous intrusions with respect to D1-D3 deformational episodes as interpreted from crosscutting and overprinting field relationships.

conditions from ca. 2610–2600 Ma. Preliminary metamorphic results indicate that M2 temperatures ranged from 300–570 °C in the low-grade supracrustal belts, 550–770 °C in the transition zone, and 740–920 °C in the high-grade Ghost subdomain (Table 3.1; Chacko et al. 1995; Appendix I). Additionally, M2 can be subdivided temporally into M2a, characterized by lower to mid-amphibolite-facies conditions that pre-dated intrusion of voluminous ca. 2597 Ma upper-crustal plutons, and M2b, characterized by upper-amphibolite to granulite-facies conditions that were contemporaneous with the ca. 2597 Ma synorogenic plutonism. Further details of this metamorphic diachroneity are discussed in Chapter 6. Evidence for D3 includes post-2597–pre-2586 Ma E- and NW-trending conjugate shear sets. D3 was associated with a HT/LP decompression-related metamorphic episode (M3) that overprinted D2/M2 in the Ghost subdomain and the transition zone between ca. 2597–2580 Ma. Overprinting disequilibrium textures and assemblages throughout both crustal levels indicate that M3 was associated with exhumation to depths of 6–13 km under quasi-isothermal conditions (Table 3.1). The relationship of M1-M3 to Neoproterozoic fold and fabric formation in the Snare River terrane is summarized in Tables 3.2 and 3.3. D4 structures are correlated with Paleoproterozoic deformation that effected the adjacent Wopmay orogen. North to northwest trending regional folding in Paleoproterozoic sedimentary rocks unconformably overlying the Snare River terrane are characterized by similar open geometry and orientation as F4 fold sets occurring at all crustal levels in the study area (Fig. 3.2a; Appendix R). Pehrsson (1998) documented an equivalent D4 open NW trending fold set at Indin Lake, which was correlated with steeply plunging, NW trending

Table 3.1: Summary of P-T conditions and U-Pb age constraints for Archean metamorphic events M1 to M3 in the Snare River terrane. Mineral abbreviations after Kretz (1983).

METAMORPHIC ZONE	METAMORPHIC MINERAL ASSEMBLAGE	REACTIONS	⁽⁴⁾ P-T RANGE	CRUSTAL LEVEL	TIMING OF METAMORPHISM
M1					
GREENSCHIST FACIES – Kwejinne Lake Supracrustal Belt					
	Chl-Qtz-Kfs (inclusion trails in M2a biotite) porphyroblasts	n/a	n/a	Upper Crust	2635 - >2608Ma (young turbidite package) <i>Thermal peak:</i> ca. 2610 Ma (Villeneuve & Henderson 1998; <i>Minimum age constraint</i>)
M2a					
GREENSCHIST FACIES – Kwejinne Lake Supracrustal Belt					
Chl Zone Bt Zone	Chl - Ms Chl - Ms - Bt	(1) Chl + Kfs = Ms + Bt + Qtz + H ₂ O	300 – 400°C ≤ 2 kbar	Upper Crust (4 – 7 km)	~2608 Ma - < 2598 Ma. Prior to emplacement of ca. 2597 Ma magmas. No age constraint on thermal peak
LOWER AMPHIBOLITE FACIES – Kwejinne Lake Supracrustal Belt					
Crd (1) Zone	Crd - Bt - Ms ± And	(2) Mg-Chl + And = Mg-Crd + H ₂ O (3) Mg-Chl + Ms = Mg-Crd + Phl + H ₂ O (4) Chl + Ms = Crd + Bt + And + H ₂ O (5) Phl + Ms = Crd + Kfs + H ₂ O	500 – 570°C 2 – 3.2 kbar	Upper Crust (7 – 11 km)	~2608 Ma - < 2598 Ma. Prior to emplacement of ca. 2597 Ma magmas. No age constraint on thermal peak
MIDDLE AMPHIBOLITE FACIES – Kwejinne Lake Supracrustal Belt					
Sil + Melt Zone	Sil - Bt - Ms - Melt ± Crd	(6) Ms + Crd = Sil + Bt + Qtz + H ₂ O (Faserkeisel Crd replacement) (7) H ₂ O Pelite saturated solidus (8) Ms + Qtz = Sil + Kfs + L	550 – 650°C 3.2 – 4 kbar	Transition Zone (11 – 14 km)	~2608 Ma - < 2598 Ma. Prior to emplacement of ca. 2597 Ma magmas. No age constraint on thermal peak

Table 3.1: continued

METAMORPHIC ZONE	METAMORPHIC MINERAL ASSEMBLAGE	REACTIONS	^(a) P-T RANGE	CRUSTAL LEVEL	TIMING OF METAMORPHISM
M2b					
UPPER AMPHIBOLITE FACIES – Kwejinne Lake Supracrustal Belt					
Crd (2) + Melt Zone	Crd (2) – Bt – Sil ± Kfs	(9) Bt + Sil + Qtz = Crd + Kfs + H ₂ O (10) Bt + Kfs + Sil + H ₂ O = Crd + L (11) Bt + Sil + Qtz + H ₂ O = Crd + L (12) Bt + Crd + Kfs + H ₂ O = Sil + L	650 – 770°C 4 – 4.7 kbar	Transition Zone (14 – 16.5 km)	ca. 2597 Ma to < 2585 Ma Thermal peak ca. 2596 – 2590 Ma (Perks 1997; Villeneuve and Henderson 1998; Bennett et al. in press; Henderson 2004)
GRANULITE FACIES – Upper Ghost subdomain					
Grt + Kfs Zone	Grt – Kfs - Crd - Melt	(13) Bt + Sil + Pl + Qtz = Grt + Kfs + L (14) Bt + Sil = Grt + Crd + Kfs + L	740 – 830°C 4.7 – 5.9 kbar	Mid Crust (16.5 – 21)	ca. 2597 Ma to < 2585 Ma Thermal peak ca. 2596 – 2590 Ma (Perks 1997; Villeneuve and Henderson 1998; Bennett et al. in press; Henderson 2004)
GRANULITE FACIES – Lower Ghost subdomain					
Crd + Opx Associated with Reactions (13) & (14)	Crd – Opx – Kfs - Grt	(15) Grt + Bt + Qtz = Opx + Kfs + Crd + L	^(c) 845 – 920°C 5.9 – 7.4 kbar	Mid Crust (22 – 27 km)	ca. 2597 Ma to < 2585 Ma Thermal peak ca. 2596 – 2590 Ma (Perks 1997; Villeneuve and Henderson 1998; Bennett et al. in press; Henderson 2004)
<hr/>					
M3					
Crd (2) Decompression	Crd-Spl-Sil-Bt-ilm	(16) Crd + Bt = Sil + Spl +/- Ilm	600 – 800°C 2 – 4 kbar, <i>n.b.</i> <i>maximum estimates only</i>	Upper Crust Uplift to ca. <13 kms depth	2589 Ma - 2585 Ma: Onset of M3 Decompression event. 2583 – 2563 Ma (Perks 1997; Villeneuve and Henderson 1998; Henderson 2004; Bennett et al. in press)
Grt Decompression	Crd-Spl-Sil-Bt-ilm	(17) Grt + Sil = Crd + Spl (18) Grt + Kfs + Crd + H ₂ O = Bt + Spl	600 – 800°C 2 – 4 kbar, <i>n.b.</i> <i>maximum estimates only</i>	Upper Crust Uplift to ca. 6 to <13 kms depth	2589 Ma - 2585 Ma: Onset of M3 Decompression event. 2583 – 2563 Ma (Perks 1997; Villeneuve and Henderson 1998; Henderson 2004; Bennett et al. in press)

Notes: (a) P/T determination based on petrologic considerations. Details presented in Appendix I. (b) P-T estimate of Grt + Kfs isograd. (c) Thermobarometric determinations of Chacko et al. (1995, 1996) for the northern Ghost Subdomain. P-T estimates calculated using Grt-Pl-Opx-Qtz barometer and aluminum-in-Opx thermometer (Fitzsimmons and Harley 1994; Pattison and Begin 1994).

cross-folds that deform the Archean – Proterozoic unconformity, immediately NW of the Indin Lake supracrustal belt.

3.3.3 Timing of Metamorphism

U-Pb constraints on the duration of metamorphism in the Snare River terranes support a polyphase history. A titanite cooling age of 2610 ± 4 Ma (Villeneuve and Henderson 1998) from the Hinscliffe plutonic complex is interpreted to represent a minimum age for M1 in the upper-crustal Kwejinne Lake supracrustal belt. The M2 thermal peak is constrained by 2592 ± 5 Ma metamorphic zircon in mafic granulite at Forked Lake (Perks 1997) and ca. 2596–2590 Ma metamorphic monazite in tonalitic gneiss north of Ghost Lake (Henderson 2004), both of which are coeval within error of voluminous syn-M2 magmatism at ca. 2597 Ma. U-Pb data from both igneous and metamorphic rocks in the Snare River terrane indicate M3 was a prolonged event that affected all crustal levels. Metamorphic zircon and monazite from the mid-crustal orthopyroxene granite and megacrystic granite suites cluster between ca. 2589–2585 Ma (Perks 1997; Villeneuve and Henderson 1998; Bennett et al. 2005; Henderson 2004), which is interpreted as the minimum age for the onset of M3. However, metamorphic monazite from tonalitic gneiss (2582 ± 1.5 Ma; Henderson 2004) and amphibolite- to granulite-facies pelite (2570–2568 Ma; V. Bennett unpublished data), and metamorphic zircon in orthopyroxene granite (ca. 2583–2571 Ma; Bennett et al. 2005) and mafic granulite (ca. 2563 Ma; Perks 1997), demonstrate that M3 persisted at high temperatures in the mid crust for a minimum of ca. 26 M.y. from ca. 2589–2563 Ma. A titanite age of 2579 ± 1.25 Ma determined from mafic volcanic rocks in the Kwejinne Lake supracrustal belt (Hyde 2000) places an age

constraint on cooling of the upper crust during M3. These data, summarized in Table 3.1 and Fig. 3.3, demonstrate that M3 was a protracted thermal event that involved continued elevated temperatures in the mid-crust which remained at temperatures of ca. 700–900 °C approximately 16 M.y. after the upper crust had cooled through ~600 °C.

The concept of a tectonic regime (TR) was proposed in Chapter 1 to describe a tectonic episode involving one or more deformation and metamorphic events and/or several episodes of magmatism, all of which occur in a similar tectonic setting. The tectonic history of the Snare River terrane consists of two broad tectonic regimes, an accretionary regime TR1 and a collisional regime TR2. The deformational history of the Snare River terrane outlined in the following text is discussed within this framework.

3.4 Deformation history of the Snare River terrane

In this section we describe the Neoproterozoic structural evolution in each crustal level of the Snare River terrane. The local complexity of polyphase deformation in the transition zone, where structural competency was severely reduced, renders application of traditional structural analysis difficult, so we have used a composite approach to define structural events involving the number of discrete fold events, overprinting fold and fabric associations, and the change in meso- and macroscale structural style with crustal depth. In our analysis, we draw on and incorporate the data of Fyson and Jackson (1991, 2004), Pehrsson (1998) and Henderson (2004). Correlation of their results with data presented in this study is given in Table 3.2.

Table 3.2: Summary table of deformation fabric developed at different crustal levels during D1 to D3 deformational and M1 to M3 metamorphic events. Mineral abbreviations after Kretz (1983).

M2 Metamorphic Zone	Deformational Fabric (this study)	Fabric- Forming Minerals	Related Fold Event	Relative Timing of Porphyroblast Growth	Timing of Fabric Formation	Correlation to Previous Work		
						<i>Fyson & Jackson 2003</i>	<i>Pehrsson 1998</i>	<i>Cairns et al. 2005</i>
Upper Crust (Kwejinne Lake Supracrustal Belt)								
Recognized in D2/M2 Biotite Porphyroblasts	S1 (<i>inclusion trails in M2a biotite</i>)	Qtz-Kfs	F1 (tight- isoclinal folds of bedding)	Pre-M2 porphyroblast growth	^a 2635 – 2608 Ma	S1, S2; F, F2	S1 F1	S1 F1 (pre-2614 Ma)
Recognized in D2/M2 Biotite Porphyroblasts	S4 (locally developed)	Crenulation cleavage	F4 (open NW folds of bedding)	Post-M3 porphyroblast growth	Post Archean ^b (2035 – 1830 Ma)	-not recognized-	S4 F4	
Upper Crust (Kwejinne Lake Supracrustal Belt - Above Hinscliffe Antiform)								
Biotite Zone (M2a)	S2a Penetrative	Bt porphyroblast Ms-Chl-Qtz-Kfs matrix (syn-def)	F2a (isoclinal refolds of F1)	Pre-M2a Crd porphyroblast growth; Syn-F2a	^a 2608 - <2597 Ma	S3 F3	S2 F2	S2 F2 (pre-2603 Ma)
	^b S2b(?) spaced	Pressure solution	F2b (?)	Post-Crd growth	unconstrained	— not recognized —		
Cordierite Zone (M2a)	S2a Penetrative	^c Crd porphyroblast Ms-Bt-Qtz-Kfs matrix (syn-def)	F2a (isoclinal refolds of F1)	Pre-M2a Sil growth (<i>faeserkasil replacement of Crd</i>); Syn-F2a	^a 2608 -	S3 F3	S2 F2	S2 F2 (pre-2603 Ma)
	^b S2b(?) spaced	Pressure solution	F2b (?)	Post-Crd growth	unconstrained	-not recognized-	S2b F2b domainal	-not present-
Sillimanite + Melt Zone (M2a)	S2a Penetrative	^d Sil+ Leucosome 1 Ms-Bt-Qtz-Kfs matrix (syn-def)	F2a (isoclinal refolds of F1)	Pre-M2b Leucosome 2 development; Syn-F2a	^a 2608 - <2597 Ma	-not recognized-	S2 F2 local	S2

Table 3.2: continued

M2 Metamorphic Zone	Deformational Fabric (<i>this study</i>)	Fabric- Forming Minerals	Related Fold Event	Relative of Porphyroblast Growth	Timing	Timing of Fabric Formation	Contemporaneous Structural Elements		
							<i>Fyson & Jackon 1991 Russell Lake</i>	<i>Pehrsson 1998 Indlin Lake</i>	<i>Cairns et al. 2005 Walmsley Lake</i>

Sillimanite + Melt Zone (M2b)	S2b sporadic development	Leucosome 2 crosscuts Leucosome 1 in F2b fold hinge	F2b (isoclinal refolds of F2a)	Syn-F2b/M2b	^e 2597 Ma - <2585	————not present————			
-------------------------------------	--------------------------------	--	---	-------------	---------------------------------	---------------------	--	--	--

Transition Zone (Kwejinne Lake Supracrustal Belt – Below Hinscliffe Antiform)

Cordierite (2) + Melt Zone (M2a)	S2a	Leucosome 1 (Crd-absent) Crd-Bt-Qtz-Kfs matrix (syn-def)	F2a (refolded folds in F2c hinge zones)	Pre-M2b Leucosome 2; development; Syn-F2a	^a 2608 - <2597 Ma	————not recognized————		Rare crenulation in F3 hinges
Cordierite (2) Melt Zone (M2b)	S2b	Leucosome 2 (Crd-bearing) Crd-Bt-Qtz-Kfs matrix (syn-def)	F2b (folded by F2c)	Syn-F2b/M2b	^e 2597 Ma - <2585	————not recognized————		transposed S2-S3 (2603 – 2583 Ma)
Cordierite (2) Melt Zone (M2b)	S2c weakly developed	spaced biotite segregation fabric; aligned metasedimentary rafts	F2b (axial planar to F2c)	Syn-F2c	^f post-2597 Ma; pre-F2d	————not recognized————		-not present-
Cordierite (2) Melt Zone (M2b)	S3 Sporadic developed	Shear fabric	D3 Conjugate shearing	post-F2d Ma	^g pre-2585Ma	————not recognized————		-not present-

Mid Crust (Ghost Subdomain)

Garnet + Kfs Zone (M2a)	S2a	Grt-Leucosome 1 (Crd-absent) Crd-Bt-Qtz-Kfs matrix (syn-def)	F2a (refolded folds in F2c hinge zones)	Pre-M2b Leucosome 2; development; Syn-F2a	^a 2608 - <2597 Ma	————not recognized————		-not present-
----------------------------	-----	---	--	--	---------------------------------	------------------------	--	---------------

Table 3.2: continued

M2 Metamorphic Zone	Deformational Fabric (<i>this study</i>)	Fabric- Forming Minerals	Related Fold Event	Relative Timing of Porphyroblast Growth	Timing of Fabric Formation	Correlation to Previous Work		
						<i>Fyson & Jackon 1991</i>	<i>Pehrsson 1998</i>	<i>Cairns et al. 2005</i>
Garnet + Kfs Zone (<i>M2b</i>)	S2b	Leucosome 2 (Grt-Crd-bearing) Crd-Bt-Qtz-Kfs (syn-def)	F2b (folded by F2c)	Syn-F2b/M2b	^e 2597 Ma - to pre-2585	——not recognized——		-not present-
Garnet + Kfs Zone (<i>M2b</i>)	S2c weakly developed	spaced biotite segregation fabric	F2c (axial planar to F2c)	Syn-F2c	^f post-2597 Ma; pre-F2d	——not recognized——		-not present-
Garnet + Kfs Melt	S3 Locally developed	Shear fabric	D3 Conjugate shearing	Post-F2d	Pre-2585 Ma	——not recognized——		-not present-

3.4.1 Labelling generations of folds and fabrics.

Several features conspire against the straightforward labelling of generations of structures in the Snare River terrane, including: (i) the effects of diachroneity and overprinting on folds formed during progressive coaxial deformation, which render distinction between fold sets on the basis of style and orientation unreliable; (ii) heterogeneous strain, which resulted in fold and fabric transposition in areas of high strain, obscuring overprinting relationships; and (iii) the increase in melt (leucosome) with paleodepth, which reduced structural competency leading to poorer definition of fold styles in the high-grade domains. However, despite these challenges, the presence of a prograde M2 gradient between the upper and mid crust in the transition zone enabled structural correlations to be made with reasonable confidence.

The structural nomenclature system adopted in this study is based on observed field relationships among the D1–D3 events that define the tectonic evolution calibrated with respect to dated plutonic suites (Tables 3.1, 3.2; Fig. 3.3; U-Pb ages reported in Bennett et al. 2005). Apart from this temporal framework, all correlations are relative and future work should address the absolute timing of fabric development and metamorphism across the belt. In cases where several overprinting fold generations are related to a single protracted deformation, modifications to the scheme using criteria summarised in Table 3.3 were adopted, whereby each recognizable generation of folds associated with a particular deformation event is assigned an alphabetic subscript (e.g., F2_a, F2_b etc; Fig. 3.3).

Structural and metamorphic correlations across the different structural levels in the Snare River terrane were made on the basis of: (i) meso- and macroscale geometry and

Table 3.3: Characteristic of fold generations determined from both minor and major structures in the Kwejinne Lake supracrustal belt SE across the Central Ghost subdomain and rationale for assigning F1 – F4 overprinting relationships. Timing relationships of fold events given in Tables 3.2 and 3.3.

Fold	Hinge (relative scale)	Crustal Level	^(a)Fold Axis	Fold Type and Characteristics	Generation	Map scale identification
^(b) KLSB bedding reversal folds	mesoscopic (Fig. 3.8a –c)	upper crust	041/71 003/77	Isoclinal, predominantly E to SE ^(c) vergent; locally overturned to E and S around younger fold systems; associated with spaced axial planar micaceous cleavage; overprinted by transecting or unaligned M2a cordierite porphyroblasts; variably plunging along strike due to subsequent fold superposition.	F1	^(d) Bedding reversals Correlation to other workers.
KLSB M2a folds	mesoscopic (Fig. 3.8h-k)	upper crust	246/70 224/60	Tight, SE-vergent minor fold system; near-coaxial superposition on older F1 system; limbs overturned to west; synchronous with axial planar growth of M2a porphyroblasts (biotite, cordierite, leucosome 1 (Figs. 3.8 d,g,l,p,q).	F2a	Hinge zones with definitive M2a axial planar relationships.
Wjinnedi antiform	regional (Fig. 3.2a; 3.7g-k)	upper crust	215/75 SW closure	Tight - isoclinal, SE to S vergent; limbs overturned to west; refolds earlier F1 and folds F2a; suggested to fold M2a isograds; folds S2a fabrics (Fig. 3.4); associated with low-grade axial planar spaced cleavage that varies in form (pressure solution; stylonitic; crenulation; Figs. 3.8 e-g, m-o).	F2b	Regional fold closure; identified by folds and refolds of S2a and S0, respectively.
Hinscliffe antiform	regional (Fig. 3.2a; 3.5)	upper crust	291/71 SW closure	Overturned, tight, SE vergent; near coaxial superposition on older F1/F2a fold belt; curvilinear fold hinge resulting in macroscale doubly plunging structure (Fig. 3.6c); contrasting associated S2b fabrics:– above Hinscliffe antiform S2b manifest as pressure solution - stylonitic and locally micaceous crenulation cleavage. Below Hinscliffe antiform S2b occurs as M2a second generation leucosome.	F2b	Regional fold closure; identified by folding of S2a and presence of S2b leucosome.

Table 3.3: continued

Fold	Hinge (relative scale)	Crustal Level	^(a) Fold Axis	Fold Type and Characteristics	Generation	Map scale identification
Transition zone antiform	regional (Fig. 3.5)	Transition zone	340/71 WSW closure	Overtured, tight- open, SE vergent; near-coaxial refolding of F2b and S2a fabrics; folding of S2b; local non-coaxial F2d fold superposition; characteristic mesoscopic refolded folds; higher grade melt mineralogy characteristic of S2b melts. increasing incompetency and ductility across regional F2c structure coinciding with increase in metamorphic grade (Fig. 3.9).	F2c	Regional fold closure; identified by folded S2b, refolded S2a; abundant diatexite throughout hinge regions (Fig. 3.9h,n)
Ghost antiform	regional (Fig. 3.6)	Transition zone to Mid-crust	065/72 SW closure 050/20 NE closure	Overtured and reclined – upright structure resulting from effects of non-coaxial superposition of NE plunging, open and upright ESE verging F2d on older F2c structures; map pattern of NE Ghost antiform represents a regional F2d closure; Map pattern of SW Ghost antiform represents complex interference between F2c, F2d (Fig. 3.6) and F4; No associated regional penetrative fabric development.	F2c to F2d	Regional fold closure; identified by orientation of S2b, mesoscopic fold interference and map-scale outcrop patterns.
Midcrustal Synform (SE Ghost antiform)	regional (Fig. 3.6)	Mid-crust	057/32 SW closure	Upright, close, cusate, NE plunging F2d fold; SE to ESE vergent; F2d system imparts major control on outcrop pattern of northern subarea in midcrust; F2c folded around F2d hinge zones; no penetrative fabric development attributed to F2d.	F2d	Regional fold closure; identified by orientation of S2b, mesoscopic fold interference and map-scale outcrop patterns.
Forked Lake Dome	regional (Fig. 3.6)	Mid-crust	054/20 NE closure	Upright, open, lobate, NE plunging F2d fold; SE to ESE vergent; F2c folded around F2d hinge zones; no penetrative fabric development attributed to F2d.	F2d	Regional dome; defined by S2b trends, mesoscopic fold interference and map-scale outcrop patterns.

Table 3.3: concluded

Fold	Hinge (relative scale)	Crustal Level	^(a) Fold Axis	Fold Type and Characteristics	Generation	Map scale identification
North 'Big Bird' Dome	regional (Fig. 3.6)	Mid-crust	345/60	Upright, open, steep N plunging F4 fold; E to NE vergent; non-coaxial fold superposition characterized by macroscale folding of F2d	F4	Regional dome; N closure of large structure in S subdomain; defined by regional S2b data and map-scale outcrop patterns.
			005/64 dome core	(Fig. 3.6c); no penetrative fabric development in mid-crust; local S4 in upper crust (Fig. 3.7l); F4 observed to fold all crustal levels at meso- and macroscopic scales		

Notes: (a) Fold axes represent either measured examples of mesoscopic folds or calculated from fabric data defining regional fold structures. (b) KLSB - Kwejinne Lake supracrustal belt ; (c) Vergence used to describe the general direction of movement that occurred during each discrete deformation phase; (d) F1 /F2a – n.b. reversals of bedding may represent either F1 or F2a due to effects of coaxial fold superposition. However, differences in fold type (isoclinal vs tight) and bedding-cleavage relationships were used to delineated F1 from F2a at the mesoscopic scale. Correlation of F1 from this study was made with Fyson and Jackson (1992) and Pehrsson (1998) where F1 was represented reversals of bedding.

fold style; (ii) overprinting relationships among folds and axial planar fabrics; (iii) relationships between porphyroblast-forming reactions and fabrics, and the prograde or retrograde character of reactions in which porphyroblasts are consumed; and (iv) the compositions and geometry of inclusions in porphyroblasts and their association with the surrounding matrix. In order to document the sequence of overprinting consistently, a top-down approach is followed in the text, beginning with the greenschist-facies upper crust, progressing through the amphibolite-facies transition zone, and concluding with the granulite-facies mid crust.

3.4.2 Belt-scale structural elements

Figure 3.2a illustrates the regional structural trends in the Snare River terrane. The variation in orientation of D1 and D2 structures from approximately E–W in the Wijinnedi supracrustal belt to NE–SW in Ghost Lake subdomain is in part attributed to reorientation by Paleoproterozoic NW-trending open folds (F4) that occur at all structural levels. These folds are apparent from the orientation of foliations in the oval Bigspruce subdomain, which is underlain by voluminous granite bodies emplaced after penetrative D1-D2 deformation had taken place in the adjacent supracrustal belts. The contact between Bigspruce and Ghost subdomains, the NNW-trending Western Boundary Fault (Fig. 3.2a), is inferred to be a D3 structure related to exhumation of the Ghost subdomain that was subsequently reactivated during the Paleoproterozoic (D4). On the basis of the abrupt change in metamorphic grade between the Bigspruce and Ghost subdomains across the fault in the central part of the map area, but the presence of greenschist-facies assemblages on both sides of the fault farther north and south, the Western Boundary

Fault is inferred to have accommodated a significant rotational displacement along its length.

The contrasting geometries of the steep structures in the low-grade supracrustal belts and the locally recumbent and shallow structures in the high-grade Ghost subdomain together define the first-order tectonic character of the Snare River terrane. A structural progression between these crustal levels occurs in the transition zone on the northwest side of Ghost subdomain (Fig. 3.2), across which lithological continuity is maintained. The regular progression of metamorphic isograds and the consistent change in estimated P - T conditions (Table 3.1; Appendix I) indicate that a high degree of structural continuity was also maintained.

Each crustal level can be considered as a distinct structural domain. In the upper-crustal volcano-sedimentary belts, the structures are steeply inclined and the regional grain is defined by the arcuate map pattern of the belts. D1 and early D2 axial traces rotate around the voluminous syn- to late D2 ca. syn- to late D2 plutons in the underlying Bigspruce plutonic domain, but are locally cut by them. Direction of D2 inclination or overturning in these belts is predominantly towards the west in the Kwejinne and Labrish Lake supracrustal belts, but is more variable in the Russell-Slemon supracrustal belt (Fyson and Jackson 1991), indicating no consistent sense of vergence is preserved.

The migmatitic transition zone, which outcrops over a comparatively small area compared to over- and underlying crustal levels, is well exposed near Kwejinne and Cowan lakes (Fig. 3.2), where it exhibits variable structural character. In the narrow transition zone near Kwejinne Lake southwest of the Hinscliffe antiform, the structural grain is parallel to the NE-SW regional trend in the over- and underlying crust, whereas

in the broader Cowan transition zone the structures are discordant to the regional grain suggesting that they may have been reoriented during exhumation of the Ghost subdomain (Figs. 3.2a, b).

The mid-crustal Ghost subdomain is characterized by moderately to gently dipping fabrics and has been divided into two subareas on the basis of the style of fold interference (Fyson and Jackson 2004; Fig. 3.2a), a northern subarea with type I 'dome-and-basin' interference structures (Ramsay 1967) in doubly-plunging folds with wavelengths of 12-25 km, which are subparallel to NE-SW regional grain (Ghost antiform and Forked Lake dome), and a southern subarea characterized by type II mushroom or 'crescent' interference structures (Big Bird Lake, Spirit Lake, and Cowan Lake domes) in which N-trending axial traces diverge from the prevailing NE-SW regional grain (Fig. 3.2).

3.4.3 Deformation history

Analysis of the deformation history in the three crustal levels of the Snare River terrane is based on structural datasets from three areas mapped at 1:30 000 scale in the Kwejinne Lake supracrustal belt, the transition zone, and central Ghost subdomain (Fig. 3.2a). The oldest structures (D0), which occur in volcanic units in the Kwejinne Lake supracrustal belt, predated turbidite deposition. They consist of high strain zones with L-S fabrics and a penetrative stretching lineation defined by elongate pillows and felsic clasts in breccia (Fig. 3.4a-f). Mineral assemblages defining these L-S fabrics range from upper greenschist to lower amphibolite facies indicative of a low metamorphic grade during fabric formation. The largest of these high strain zones (Figs. 3.2a, 3.4b) is

Figure 3.4: Structural elements and related fabrics in mafic volcanic and turbidite packages northwest of the Wijinnedi antiformal closure (see Fig 3.2a for location). (a) D0 pillow elongation in mafic volcanic package; (b) Pre–2654 Ma high-strain zone in ca. 2674 Ma volcano-plutonic complex located on the northwest limb of the Hinscliffe antiform. High-strain enclaves occur in Hinscliffe Intrusive Complex at the contact between the two lithologies; (c) – (e) Progressive strain partitioning and high strain zone development in discrete meter-scale zones in mafic volcanic rocks, northern Kwejinne Lake supracrustal belt; (f) Strongly lineated and foliated mafic pillow; (g) Aerial photograph of a folded (F2b) volcano-sedimentary contact NW of Wijinnedi antiform. The approximate orientation of cordierite-bearing S2a fabrics in the hinge zone of the metaturbidite package and location of Fig. 3.7h are marked on for comparison; (h) Two generations (syn- and post-deformational) of cordierite growth in an F2b hinge zone. Trend of F2b axial trace is shown; (i) Tightly folded (F2a) metaturbidites on the NW limb of F2b folded shown in Fig. 3.7h. Syn-deformational cordierite growth (shown inset) is axial planar to the mesoscopic isoclinal fold sets shown. NNW-trending F4 minor folds refold the F2a fold set at this locality; (k) Tightly folded relict S1 fabric with axial plane parallel to S0. S2a, defined by syn-deformational cordierite, transects both bedding and the older S1 fabric; (l) NNW-trending crenulation cleavage postdates cordierite growth. The S4 fabric is axial planar to the minor F4 fold set. At this site, overprinting relationships between F2a , F2b and F4 folds and S1, S2a and S4 fabrics are well preserved.

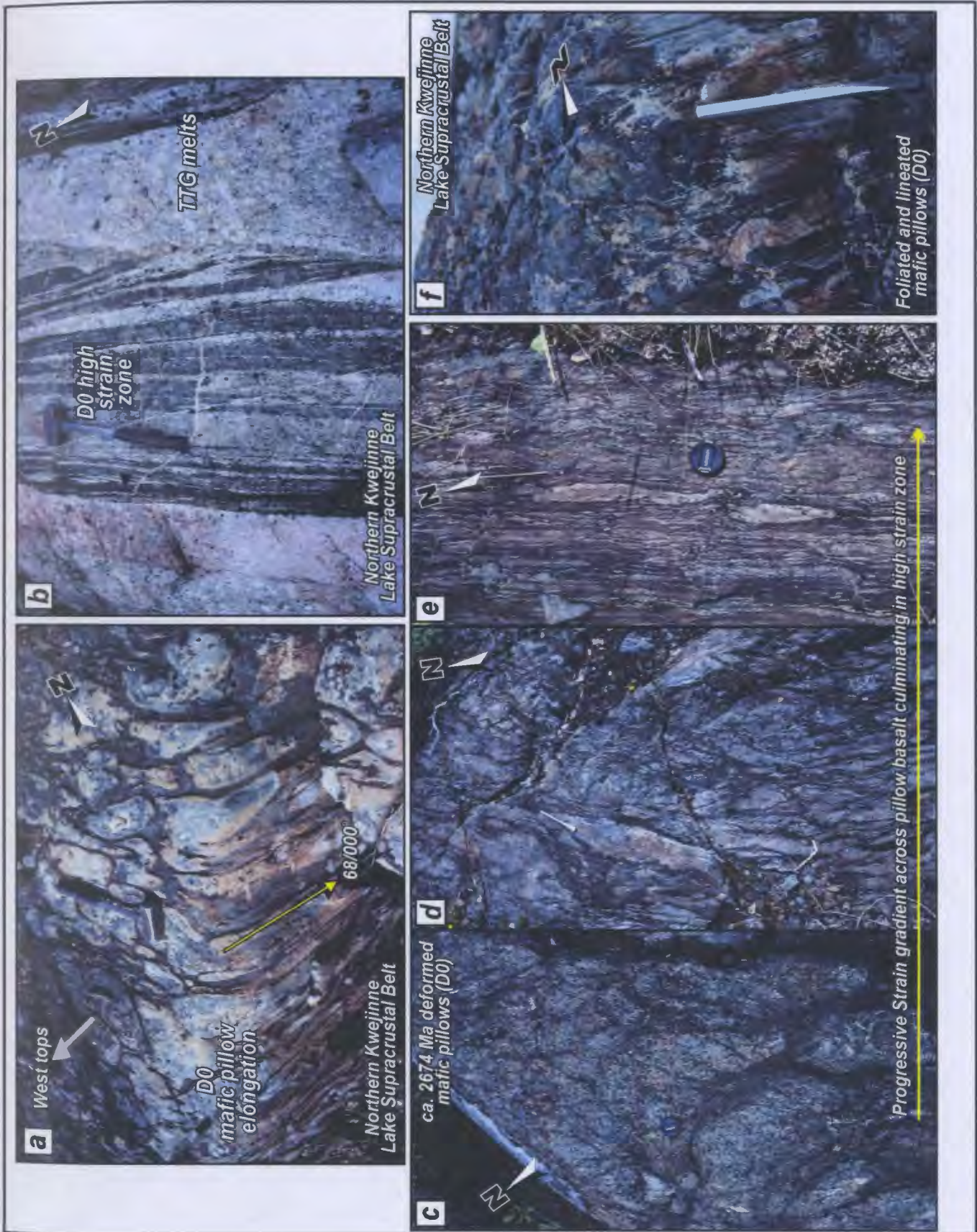


Figure 3.4: Northern KLSB

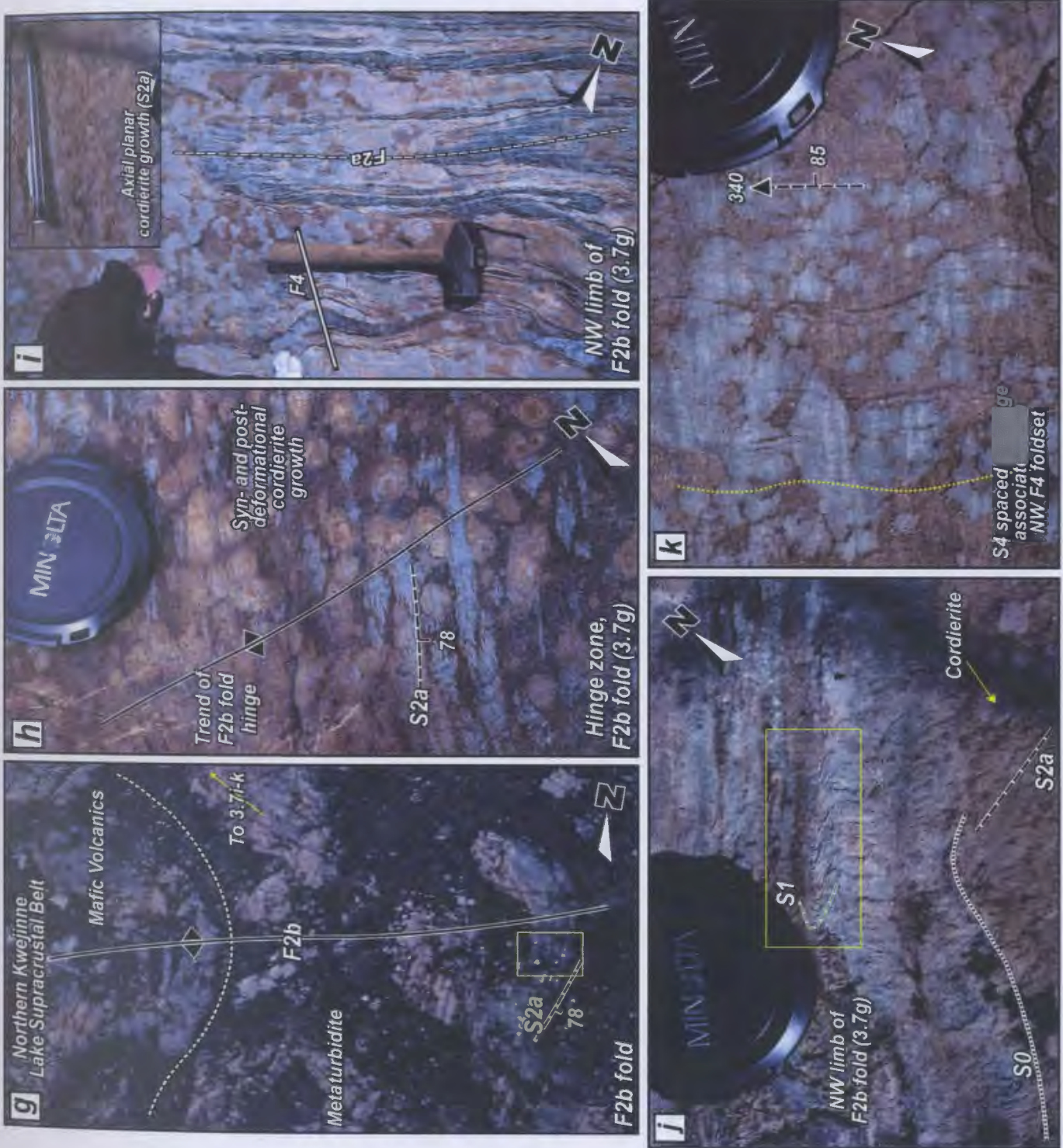


Figure 3.4: Northern KLSB

intruded by plutons of the Hinscliffe complex, which constrains the age of this phase of deformation to pre-2654 Ma. Corresponding D0 high-strain fabrics do not occur in the adjacent metaturbidites and so cannot be used for correlation across the map area. In contrast, structures in the metaturbidites exhibit continuity from the upper crust into the mid crust and are used to document the D1 to post-D3 evolution in the Snare River terrane. Apart from the contrast in their ages, pre- and post-2654 Ma, D0 and D1 structures may not have been fundamentally different, and their formation in a long-lived accretionary prism setting (*TRI*) is proposed until more detailed analysis is conducted on the D0 deformation structures.

3.4.3.1 Upper Crust – Kwejinne Lake supracrustal belt

The geometry of the low-grade upper-crustal belts is a result of polyphase refolding of D1 structures during D2 and D4 (Fig. 3.5). The earliest recognized D1 structures in the metaturbidites are tight to isoclinal, steeply plunging F1 fold sets identified by the reversal of younging directions across strike. The same criteria were used to identify F1 folding in the Indin Lake and Russell Lake supracrustal belts (Fyson and Jackson 1991; Pehrsson 1998; Tables 3.2, 3.4). Wavelengths range from a few meters to greater than 100 m (Figs. 3.6a, e) and fold hinges are curvilinear along strike. S1 is preserved as inclusion trails in M2a biotite porphyroblasts (Fig. 3.6d) and locally as a spaced mica cleavage tentatively correlated to F1 hinge zones (Fig. 3.6b, c). At one locality northwest of the Wijinnedi antiform, a folded S1 fabric is shortened perpendicular to S0 on the limbs of minor F2a folds (Fig. 3.4k). S1 fabrics are not widely preserved in context within F1 fold sets in the Kwejinne Lake supracrustal belt, having

Figure 3.5: (a) Map showing lithologic, structural and metamorphic relationships at the southwestern closure of the Wijinnedi antiform, northern Kwejinne Lake supracrustal belt (see Fig. 3.2a for location). The map highlights the regional F2b refolding of the F1 fold system and shows the relationships of M2a cordierite and S2a fabrics. No F2a closures are recognized in the map area however, stereonet analyses (equal area projections) illustrate the presence of a NE-trending overprinting cleavage (S2b) in the hinge zone of an F2b fold, which is a steep SW-plunging antiformal structure. This fabric is axial planar to folded S2b cordierite fabrics. Localities of photographs presented in Fig. 3.6 are shown. (b) Schematic NNW–SSE trending cross-section drawn approximately perpendicular to the axial trace of the Wijinnedi antiform, illustrating folding of the cordierite isograd and the absence of a regional syncline above the NW limb of the Hinscliffe antiform. The dip of folded cordierite isograd below the surface is not constrained. (c) Simplified three-dimensional diagram of the metasedimentary package defining the Wijinnedi antiform.

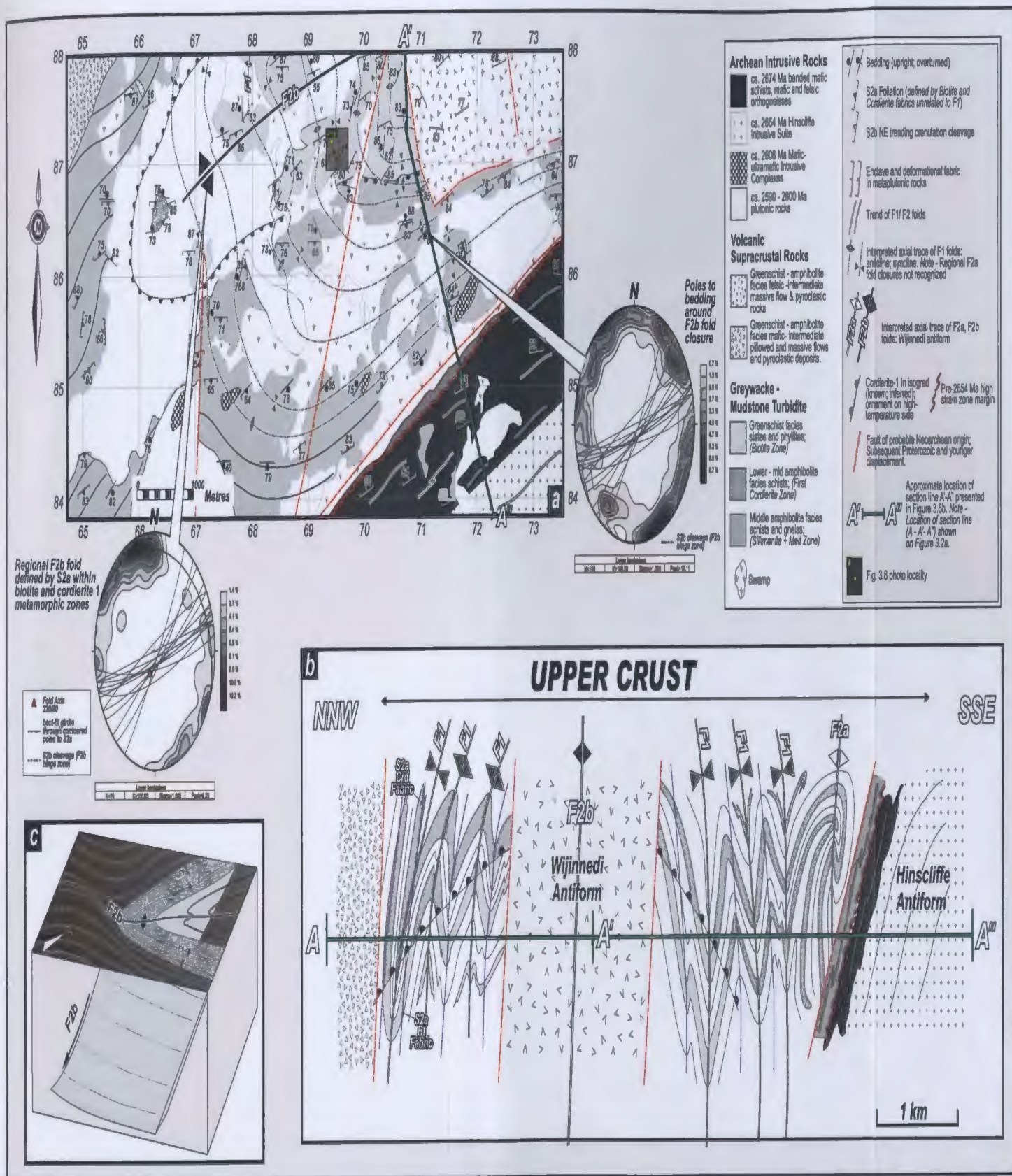


Figure 3.5

Figure 3.6: Structural elements and related deformational fabrics observed in metaturbidite of the Kwejinne Lake supracrustal belt. Hammer and lens cap are approximately 45 and 5 cm long, respectively. North arrow, scale and fields of view for polished slabs and photomicrographs, respectively, are indicated. Photo locations are marked on Figures 3.5 and 3.7. *(a)* Steep NE plunging, F1 fold closure. The NE plunging and steep isoclinal fold morphology distinguish it from younger foldsets, particularly the F2a folds which are typically SW plunging tight structures; *(b)* - *(c)* Mesoscopic S1 spaced mica cleavage overgrown by randomly oriented M2a cordierite porphyroblasts; *(d)* Relict S1 inclusion trail in M2a biotite porphyroblast, biotite zone turbidite; *(e)* Minor F1 fold overprinted by SW-NE trending F2b fold and S2b cleavage in hinge zone of Wijinnedi antiform; *(f)* and *(g)* photomicrographs of S2a mica cleavages overprinted by younger S2b cleavage. Samples located in biotite metamorphic zone in regional F2b Wijinnedi antiformal closure. Note in *(g)*, top, that S1 is preserved in S2a biotite; *(h)* and *(i)* S2a fabric relations in minor F2a fold hinge. Cordierite porphyroblast growth is axial planar to F2a fold; *(j)* Two generations of cordierite porphyroblast growth on limb of minor F2a fold. An earlier syn-tectonic generation is overgrown by a younger phase interpreted to reflect rapid renewed growth during voluminous ca. 2600 Ma pluton emplacement; *(k)* photomicrograph of two cordierite generations. The internal fabric in porphyroblast core parallels external matrix fabric suggesting initial cordierite growth was syntectonic.

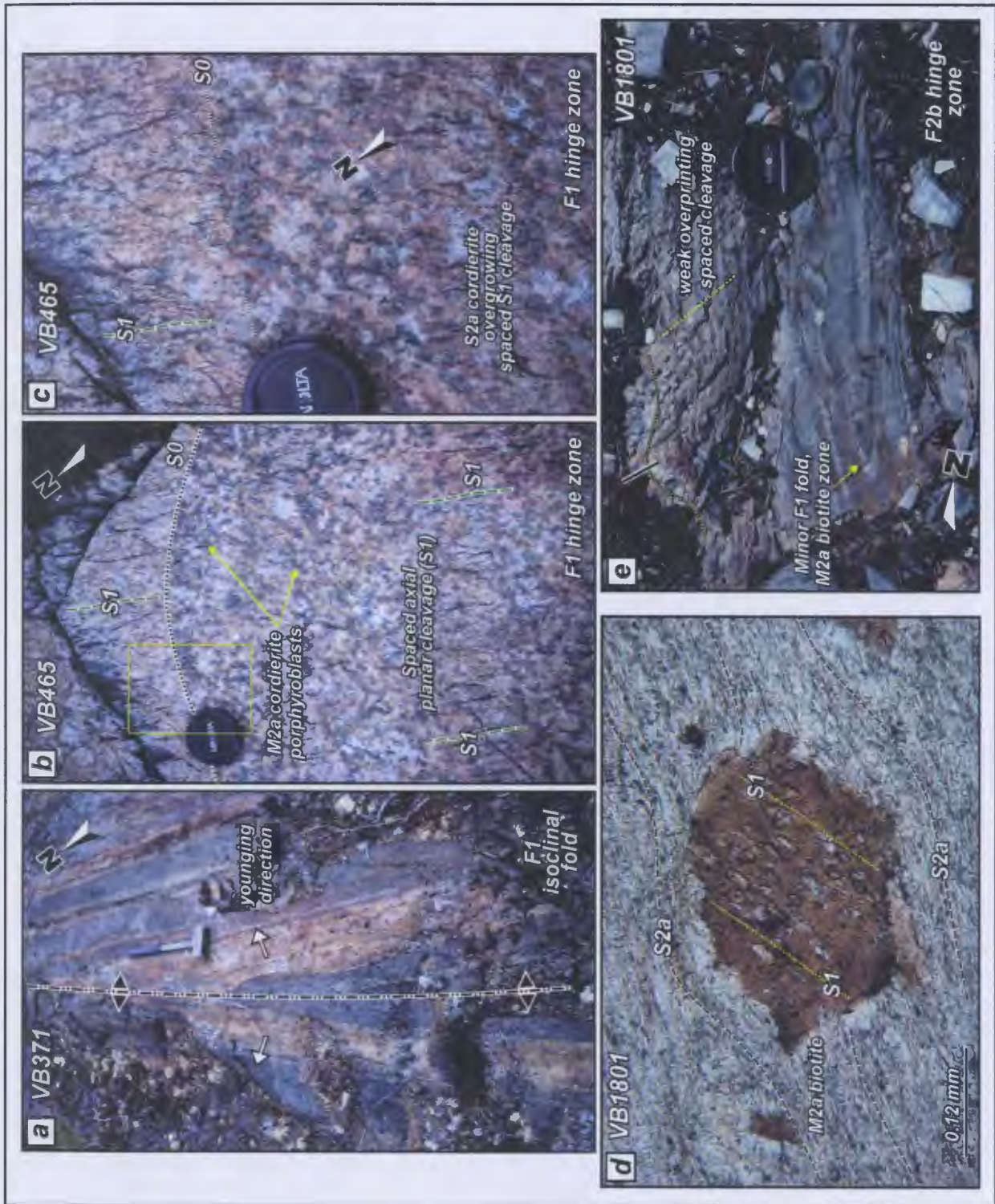


Figure 3.6: Kwejinne Lake supracrustal belt

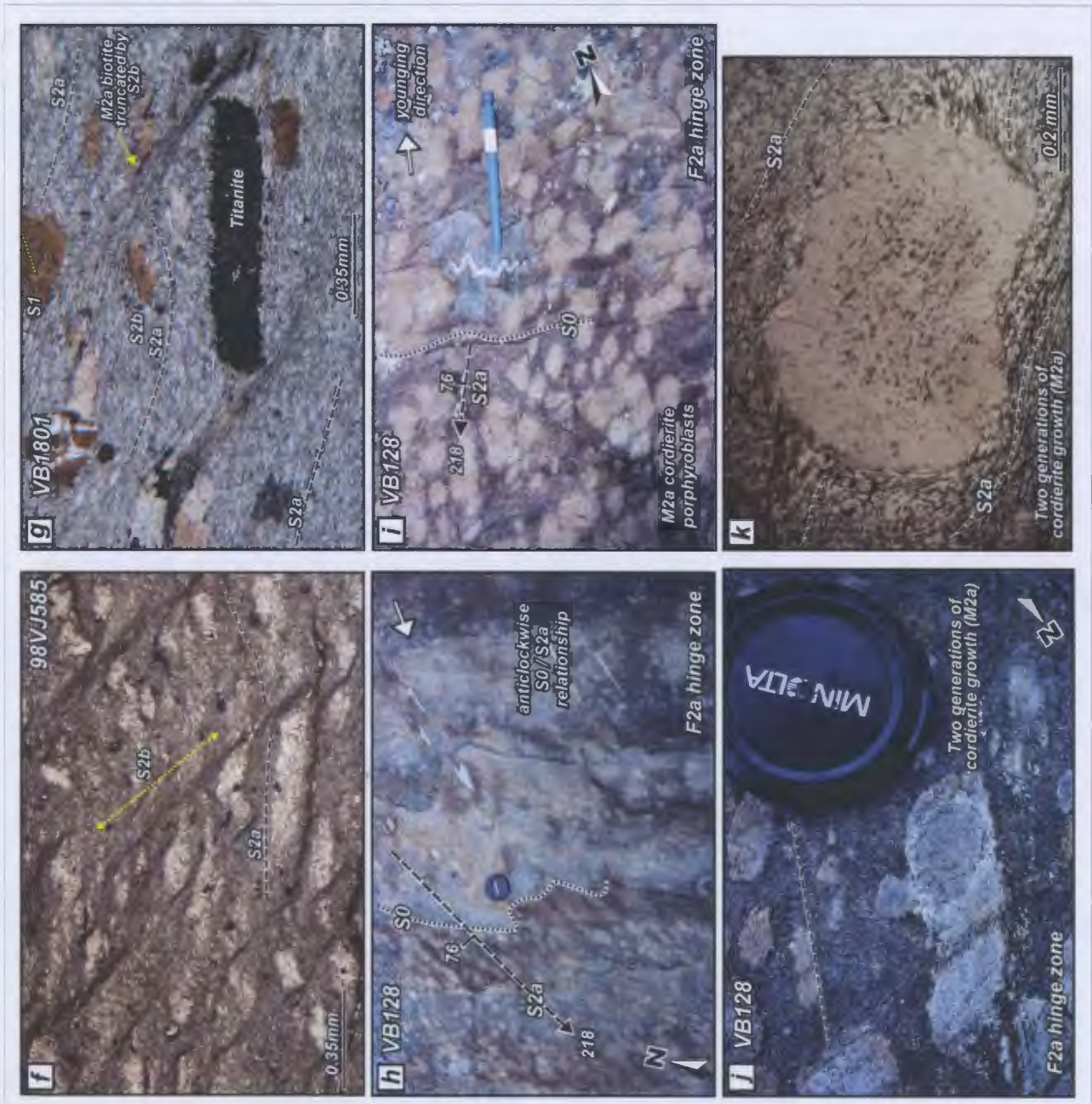


Figure 3.6: Kwejinne Lake supracrustal belt

Figure 3.6 continued: Structural elements and related deformational fabrics observed in metaturbidite of the Kwejinne Lake supracrustal belt. Hammer and lens cap are approximately 45 and 5 cm long, respectively. North arrow, scale and fields of view for polished slabs and photomicrographs, respectively, are indicated. Photo locations are marked on Figures 3.5 and 3.7. *(l)* photomicrograph of cordierite grade metaturbidite illustrating coeval progressive metamorphism and deformation. Relict S1 is preserved in an early M2a biotite porphyroblast enclosed within a larger cordierite porphyroblast. The early biotite has undergone a degree of decomposition at the margin of the cordierite porphyroblast in contrast with the younger S2a matrix; *(m)* Thinsection image showing overprinting of S2a cordierite porphyroblasts by a discontinuous, irregular pressure solution fabric oriented parallel to subparallel to S2a; *(n)* Thinsection image of transecting pressure solution cleavage interpreted as S2b and located in the Hinscliffe antiform closure; *(o)* Photomicrograph of transecting cleavage with stylolitic habit; *(p)* Faserkiesel replacement of M2a cordierite by sillimanite oriented parallel to S2a; *(q)* Mesoscopic F2a fold in M2a sillimanite + melt metamorphic zone on NW limb of the Hinscliffe antiform. Note that the S2a leucosome is oriented parallel to minor F2a axial plane; *(r)* F2b crenulation of S2a leucosome on NW limb of Hinscliffe antiform; *(s)* S0, S2a and S2b fabric relationships on limb of F2b minor fold, NW Hinscliffe antiform. The S0-parallel S2a leucosome is crenulated and has incipient axial planar S2b leucosome stringers; *(t)* Transecting S2a and S2b leucosome fabric relationships near hinge zone of minor F2b fold. The younger S2b melt overprints an older S2a sillimanite + melt fabric; *(u)* Transecting S2a and S2b leucosomes in hinge zone of minor F2b fold; *(v)* Polished slab of transecting S2a and S2b leucosome fabrics near hinge zone of Hinscliffe antiform.

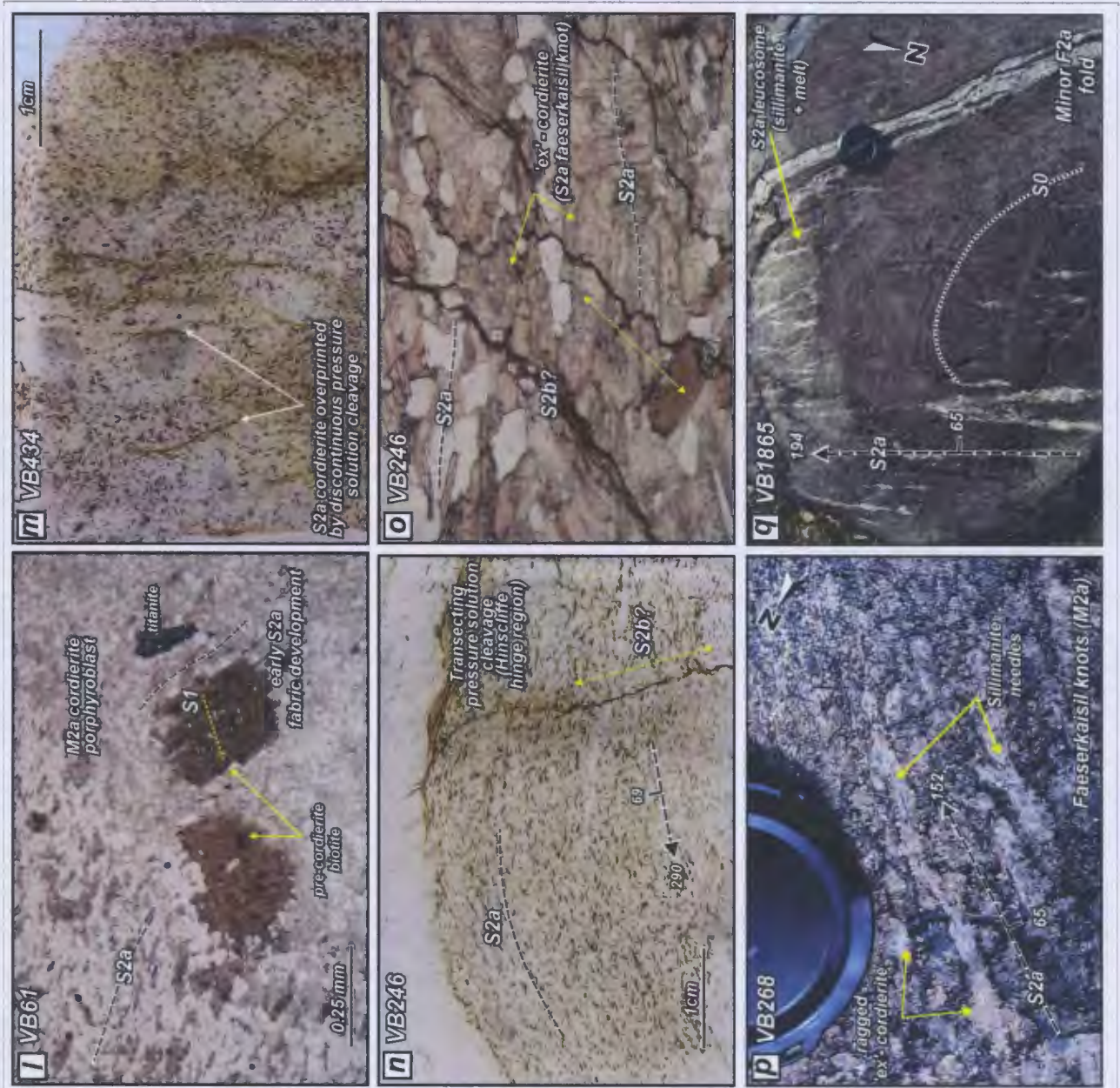


Figure 3.6: Kwejinnie Lake supracrustal belt

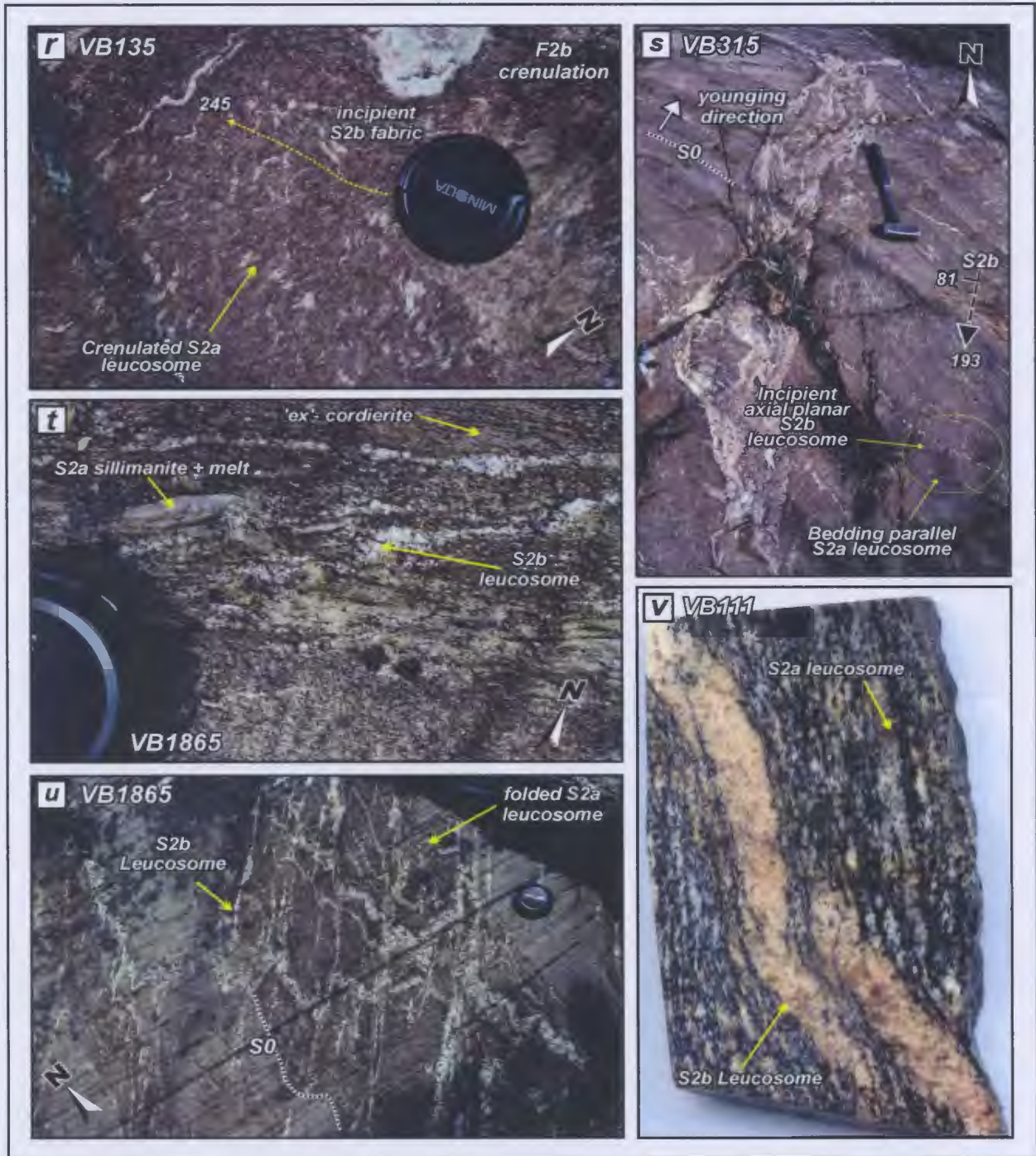


Figure 3.6: Kwejinne Lake supracrustal belt

been extensively overprinted by D2/M2. However, in the Russell–Slemon Belt two distinct D1 fold sets in turbidites (F1 and F2; Fyson and Jackson 2004; Table 3.2) are characterized by sporadic development of S1 axial planar mica and segregation cleavages. D1 was accompanied by sub-greenschist- to lower-greenschist-facies M1 metamorphism, evidence for which is preserved as inclusions trails in M2a porphyroblasts (Table 3.1; Fyson and Jackson 1991; Pehrsson 1998). F1 folds at the western margin of the Kwejinne Lake supracrustal belt occur on the limbs of D2 folds, which control the regional structural grain at this crustal level. Farther southeast, towards the underlying transition zone, this structural package becomes progressively refolded and overprinted by younger phases of D2 (Fig. 3.7).

In the Kwejinne Lake supracrustal belt, progressive refolding of D1 structures during D2/ M2 is recorded by fabrics and structures in the *Biotite*, *Crd (1)*, and *Sil + Melt* metamorphic zones (Tables 3.2 and 3.3). Two near-coaxial progressive D2 folding events have been identified, F2a and F2b. F2a fold closures are not recognized in the Kwejinne Lake supracrustal belt, but elsewhere are defined on the basis of local tight refolding of F1 axial traces (Table 3.3; Figs. 3.5, 3.7) and formation of S2a axial planar fabrics defined by biotite, cordierite, and leucosome associated with minor folds of different orientation and fold style to F1 (Figs. 3.4i, 3.6h, i, q and 3.7). The paucity of F2a regional closures is inferred to be a consequence of coaxial refolding that resulted in Type 0 (redundant superposition; Ramsay and Huber 1987) and Type III fold interference patterns. Syn- to post D2 sillimanite replaces S2a cordierite porphyroblasts with increasing metamorphic grade, and fabrics exhibit a progression across the belt such that biotite porphyroblasts that overgrew S1 are in turn overgrown by S2a cordierite, which in

turn is replaced by sillimanite (Fig. 3.6l, p), implying progressive metamorphism accompanied progressive deformation at this crustal level. Meso- to macro-scale refolding of S2a fabrics defines F2b folds in metaturbidite packages (Figs. 3.2a, 3.4g, 3.5, 3.7 and 3.6r). S2b fabrics vary with metamorphic grade across the Kwejinne Lake belt: at low grades, the S2b fabric is tentatively correlated with an anastomosing spaced pressure-solution cleavage subparallel to S2a on fold limbs and a weak non-penetrative stylolitic cleavage that transects older fabrics in F2b fold hinges (Figs. 3.5, 3.6e-g, n-o), whereas at high grades the S2b fabric is defined by axial planar leucosomes (e.g., adjacent to the Hinscliffe antiform; Fig. 3.6t-v). Absolute age constraints are needed to confirm these fabric relationships, but their consistent orientations to F2b axial planes suggest a causal link (see Fig. 3.5).

Syn- and post-D2 cordierite growth is recognized (Fig. 3.4h, 3.6j, k). Fyson and Jackson (1991, 2004) attributed post-D2 cordierite in the Russell-Slemon supracrustal belt to heating due to granite emplacement in the Bigspruce subdomain, an interpretation that is extended to the post-tectonic cordierite in the Kwejinne Lake supracrustal belt here. Cross-sections constructed approximately NW–SE across the Kwejinne Lake supracrustal belt indicate that Type 0 and Type III coaxial refolding are the dominant superposed fold styles (Figs. 3.5 and 3.7b; Ramsay 1967), but different fold generations define the regional structural grain across the belt. At the highest structural levels, the architecture of the supracrustal belt is controlled by superposition of F2a on F1, but with increasing structural depth (e.g., near the Hinscliffe antiform) F2b folds are predominant (Figs. 3.5, 3.7). D3 structures have not been identified in the Kwejinne Lake belt, suggesting that the upper crust was not penetratively reworked during this deformation

event. Paleoproterozoic D4 structures include open NW-trending folds and associated spaced segregation and local crenulation cleavages, which overprint all Archean fabric elements (Figs. 3.2a; 3.4i, k).

3.4.3.2 Transition zone

Based on observations in metaturbidites near Kwejinne Lake (Figs 3.2, 3.7), the structural topology of the transition zone is controlled by the overprinting effects of the progressively younger stages of D2, minor D3 shearing deformation and Proterozoic F4 folding. Bedding and D1 structures are not typically preserved as a result of grain coarsening, metamorphic recrystallization, and abundant leucosome in these rocks.

D2 structures in the transition zone consist of three distinct fold sets, F2b, F2c and F2d (Figs. 3.3, 3.7; Table 3.3) that increase in importance with paleodepth. Associated S2a and S2b fabrics can be correlated from the upper crust, around the Hinscliffe antiform, and into the transition zone. Meso- and microscopic S2a and S2b fabrics are defined principally by different generations of leucosome: S2a leucosomes are cordierite-absent and formed by muscovite breakdown, whereas S2b leucosomes contain cordierite and represent the breakdown of biotite + sillimanite at higher grade (Figs. 3.6t-v, 3.8a-d; Tables 3.1, 3.2). At high structural levels of the transition zone, S2b cordierite-bearing leucosomes are axial planar to tight- to isoclinally-folded cordierite-absent S2a leucosomes (Fig. 3.8a, b). Structural transposition in the northern part of the transition zone is less penetrative than farther south and oblique S2a and S2b leucosome relationships are commonly preserved (Fig. 3.8e, f, k). At progressively deeper levels, as

Figure 3.7: (a) Map showing lithological, structural and metamorphic relationships in the closure of the Hinscliffe antiform and the transition zone, central Kwejinne Lake supracrustal belt (see Fig. 3.2a for location). The map illustrates the near-coaxial superposition of F2a and F2b refolding in the western margin of the belt and F2c refolding farther southeast in the underlying transition zone. Limited displacement is evident on either side of the Western Boundary Fault. S2a is folded around the Hinscliffe antiform, which has a steep WNW-plunging fold axis. Localities of photographs in Figs. 3.6 and 3.8 are shown. (b) E-W and NW-SE-trending staggered cross-section drawn through the hinge zones of the F2b Hinscliffe and F2c transition zone antiforms. The section illustrates local refolding of S1 by F2a and minor F2b structures on the western limb of the F2b Hinscliffe antiform and folding of this structural package around the nose of the antiform, beneath which S2b fabrics are folded and S2a fabrics refolded by F2c in the transition zone. A modest degree of rotation towards the horizontal (ca. 20–30°) is evident from F1 structures through to F2c structures. (c) Simplified three-dimensional diagram of the Hinscliffe antiform. Stereonet data (equal area projections) illustrate S2a fabric orientations around the fold hinge which delineate a steep WNW-trending fold axis.

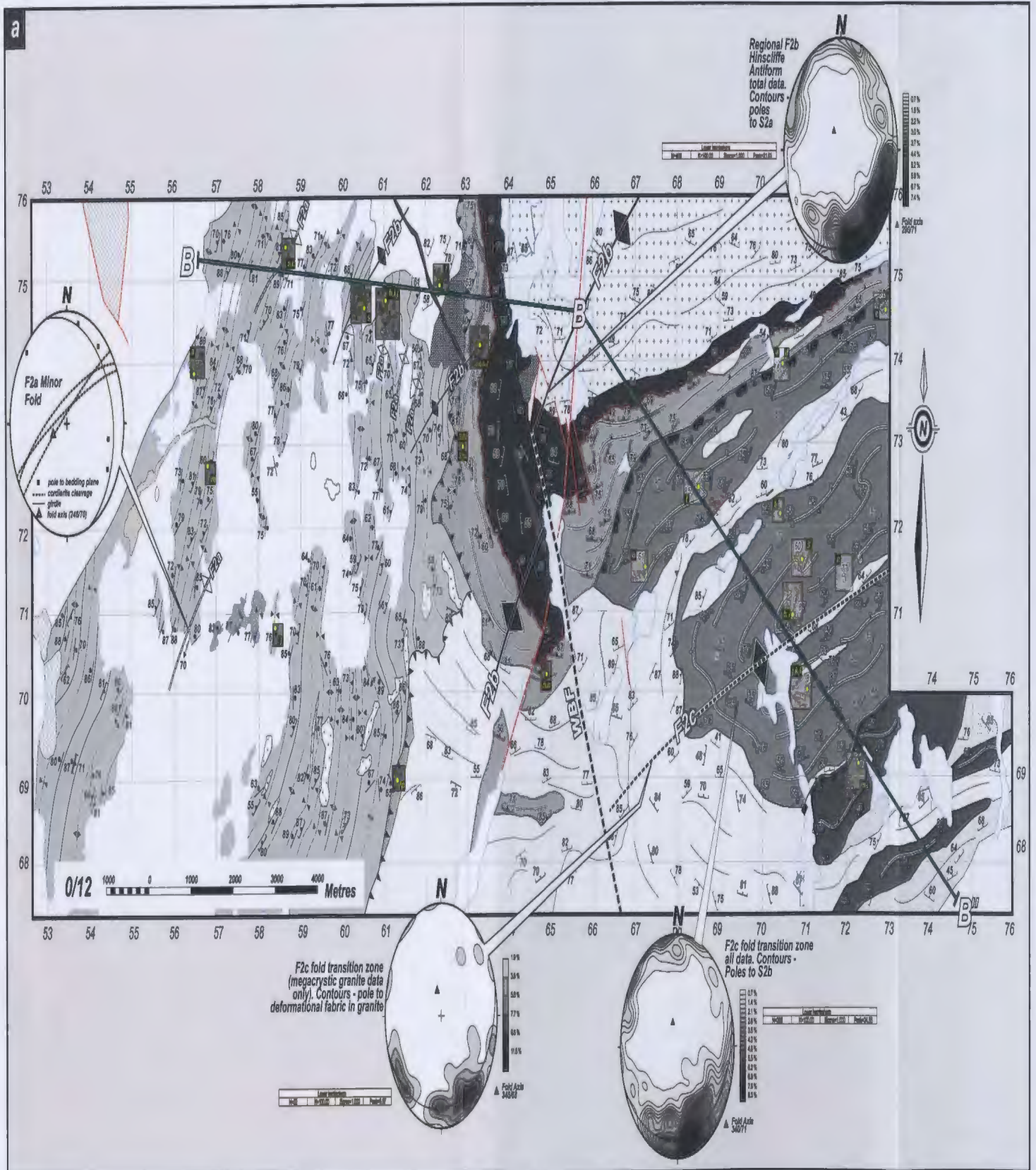


Figure 3.7

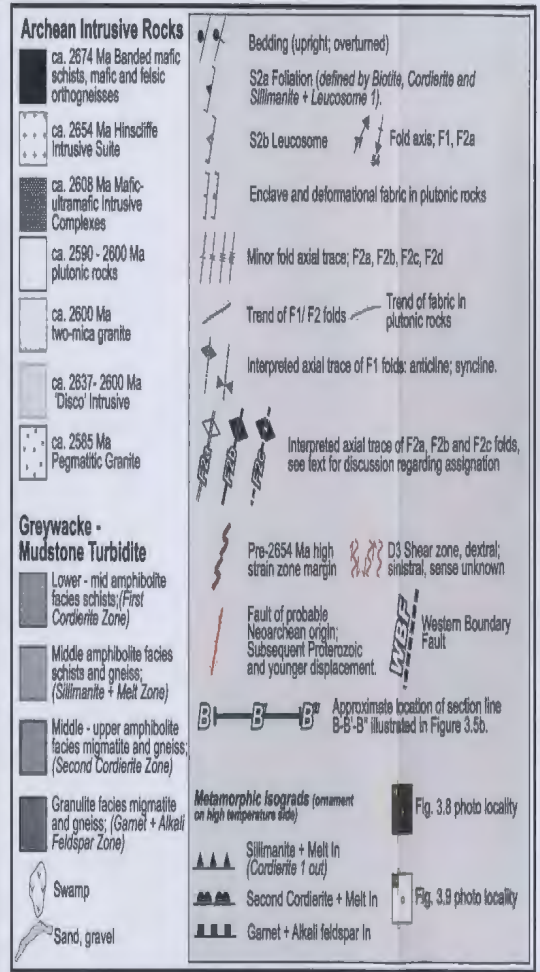
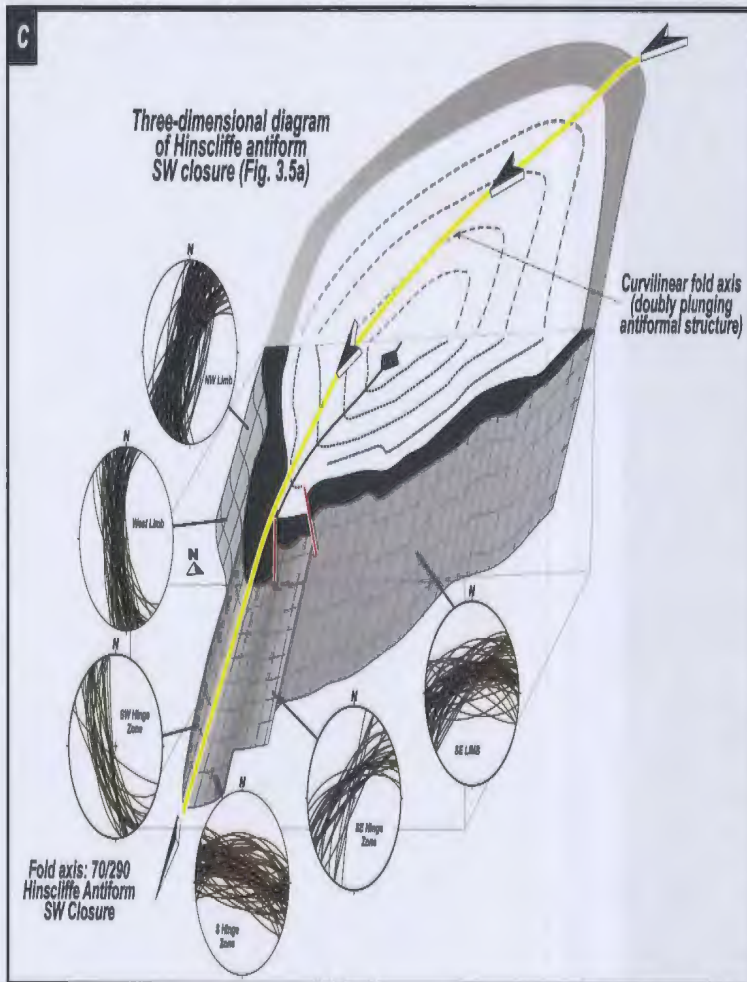
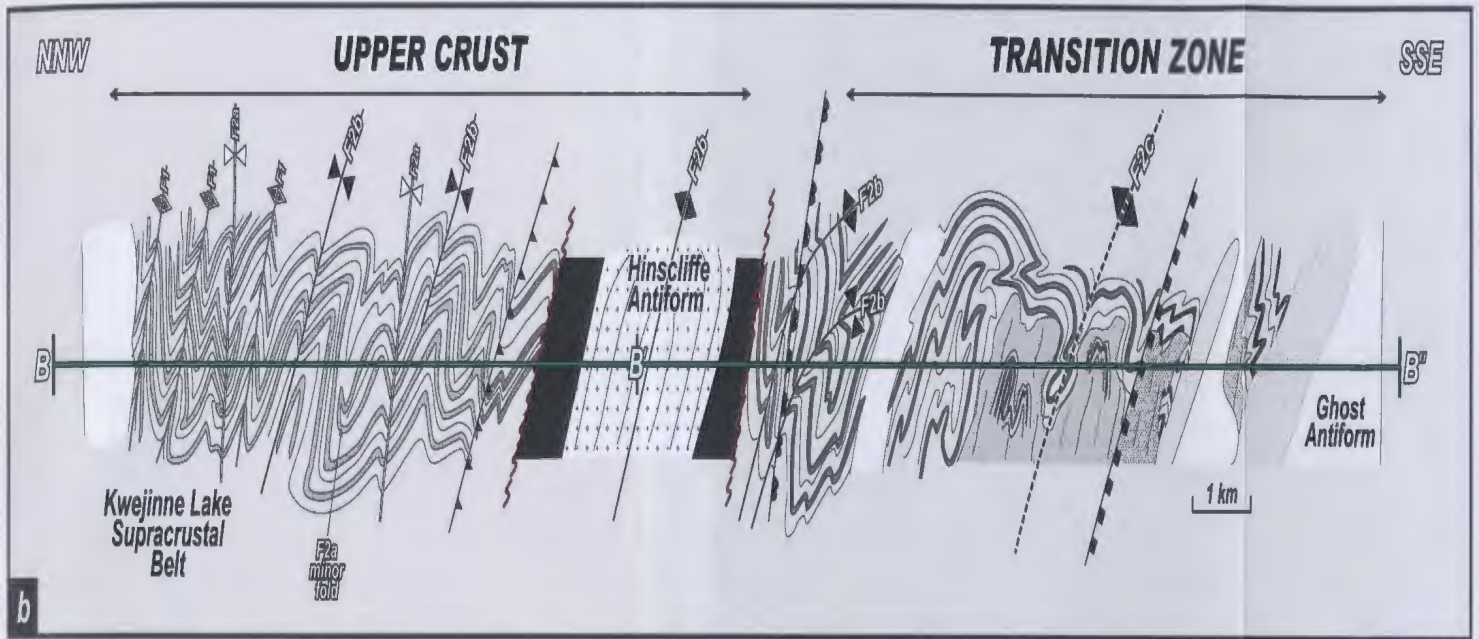


Figure 3.7

Figure 3.8: Structural elements and related deformational fabrics observed in metaturbidite of the transitional migmatite zone underlying the Kwejinne Lake supracrustal belt. Hammer and lens cap are approximately 45 and 5 cm long, respectively. North arrow, scale and fields of view for polished slabs and photomicrographs, respectively, are indicated. Photo locations are marked on Figure 3.7. *(a)* Tight minor F2b folds of S2a leucosome with axial planar formation of cordierite-bearing S2b leucosomes; *(b)* Polished slab illustrating truncation of S2a leucosome by cordierite bearing S2b leucosome; *(c)* Photomicrograph of S2a leucosomes which represent the product of muscovite breakdown during M2a; *(d)* Photomicrograph of cordierite-bearing S2b leucosome, formed during M2b as a result of fluid-present decomposition of sillimanite and biotite; *(e)* Relict S2a leucosome oblique to S2b fabric on northern limb of regional F2c fold; *(f)* Mesoscopic F2c fold of S2a and S2b leucosomes; *(g)* Mesoscopic NE trending F2d fold and D3 NW trending shear zone. Structures overprint S2a and S2b leucosome; *(h)* Mesoscopic Type III, hook, fold interference defined by folded S2b and refolded S2a leucosomes and truncated by late, unfoliated coarse grained metasedimentary diatexite; *(i)* Refolded S2a leucosomes in hinge of mesoscopic F2c fold; *(j)* F2c structure defined by folded S2b leucosome and refolded non-coaxially by minor F2d fold. Structure is overprinted by roughly E-W trending shear zone.

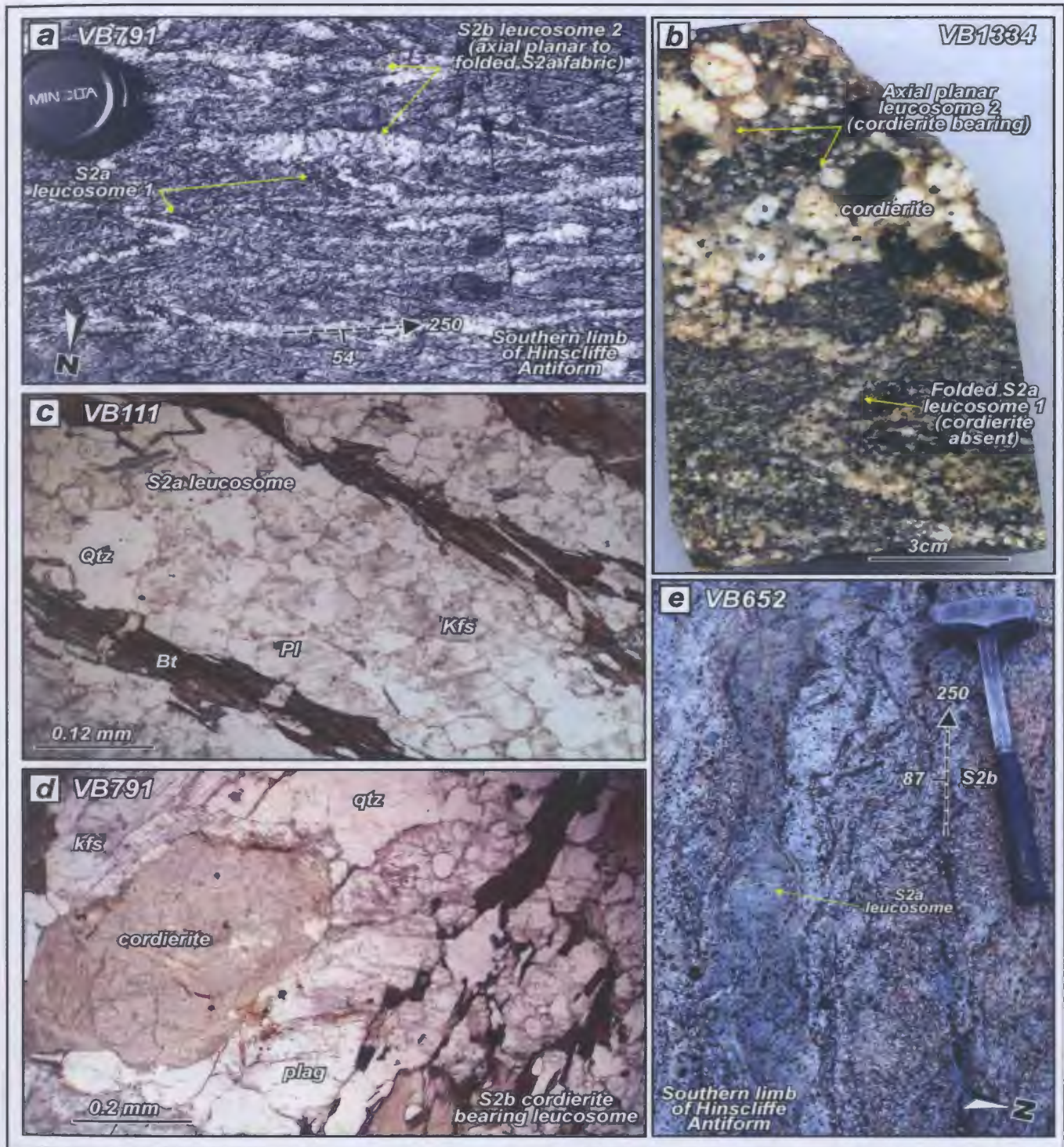


Figure 3.8

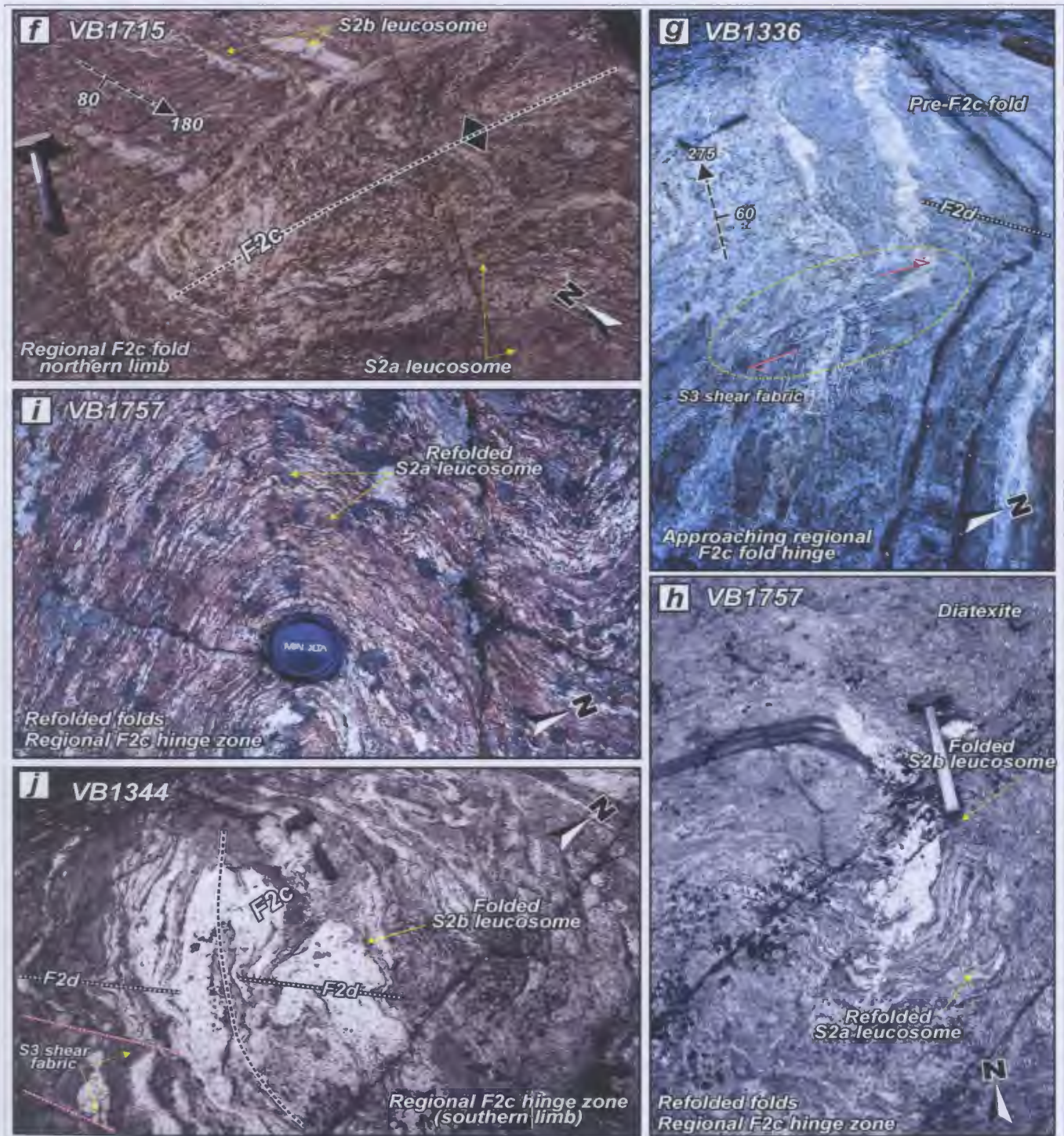


Figure 3.8

Figure 3.8 continued: Structural elements and related deformational fabrics observed in metaturbidite of the transitional migmatite zone underlying the Kwejinne Lake supracrustal belt. Hammer and lens cap are approximately 45 and 5 cm long, respectively. North arrow, scale and fields of view for polished slabs and photomicrographs, respectively, are indicated. Photo locations are marked on Figure 3.7. *(k)* Relict folded S2a leucosome that has not been transposed into S2b; *(l)* Mesoscopic F2c fold defined by folded S2b leucosome, locally refolded by F2d and overprinted by D3 E-W trending shear zone; *(m)* Close up of hinge zone of F2c fold in (l) illustrating refolded S2a leucosome; *(n)* F2c fold refolded by open NE trending F2d fold and overprinted by E-W trending shear zone; *(o)* Coarse grained, unfoliated diatexite with metasedimentary raft preserving older folded leucosome fabric; *(p)* Foliated diatexite containing flattened metasedimentary rafts and discontinuous, locally truncated S2b leucosomes; *(q)* S2a and S2b leucosomes (local fold hinge) overprinted by E-W trending shear zone. The locality represents one of the highest structural levels across the Snare River terrane that S3 shear fabrics occur.

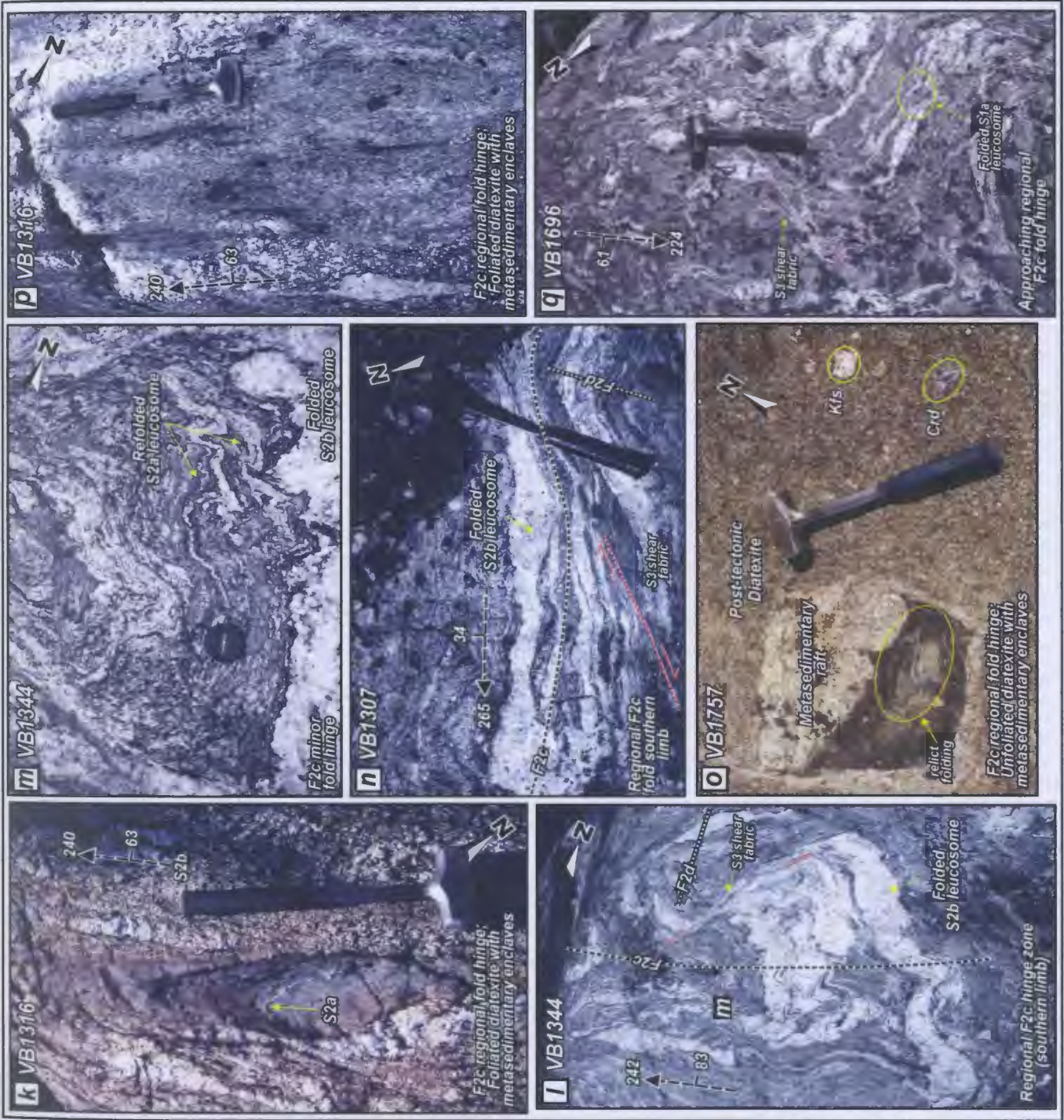


Figure 3.8

ductility and metamorphic grade increase, S2b leucosomes increase in volume and become folded into tight to isoclinal, commonly disharmonic F2c folds, overturned to the NW (Figs. 3.8d - f), which are parasitic to a regional F2c antiform structure (Fig. 3.7). The syntectonic character of S2a and S2b leucosomes contrasts with the late- to post-tectonic character of the metasedimentary diatexite (Fig. 3.8 h, o, p), which is ubiquitous across the transition zone, indicating that M2b melting reactions outlasted deformation at this crustal level. NE-trending mesoscopic open F2d folds first appear in the transition zone and increase in abundance towards the mid crust farther south (Figs. 3.8g, j, l and n). Neither F2c nor F2d folds are recognized in the upper crust, but they produce structural interference with the older F2a and F2b folds in the transition zone (Fig 3.8g, h and m). Specifically, small-scale Type II, crescent and regional Type III, hook fold interference patterns are observed which reflect superposition of F2d on F2b and F2c structures, the axial planes of which gradually rotate from subvertical towards less steep dips of about 60° with increasing paleodepth in the Ghost subdomain (Fig. 3.7). F2c structures control the overall geometry of the transition zone and the large SW-trending, steep WNW-plunging reclined, antiformal closure defined by a megacrystic granite sheet and the enclosing metaturbidite is interpreted as a regional F2c structure (see stereonet data Fig. 3.7). This regional structure gives way to macroscopic F2d structures in the underlying Ghost subdomain.

D3 structures are ubiquitous in the transition zone and consist of discontinuous E-W and NW-trending shear bands which overprint D2 structures (Fig. 3.8g, j, l, n and q). Evidence for M3 decompression metamorphism, characterized by post-D3 cordierite–sillimanite–spinel symplectite overprinting M2b assemblages, first occurs in the

transition zone at slightly higher structural levels than the first appearance of D3 shear bands (Fig. 3.11). D4 Paleoproterozoic structures include meso- to macroscale NW-trending folds that refold all earlier structures.

3.4.3.3 *Mid crust – Ghost subdomain*

The first-order geometry of the high-grade mid crust in Ghost subdomain is controlled by dome-and-basin and asymmetric crescent fold-interference patterns (Figs. 3.2a, 3.9). D1 structures cannot be confidently recognized, but D2, D3 and D4 structures all occur and the regional structural grain in Ghost subdomain is controlled by interference among F2c, F2d and F4 folds (Fig. 3.9).

D2 folding in the northern and southern subareas of the Ghost subdomain is correlated with F2c and F2d fold sets in the overlying transition zone and the structural topology is a result of superposition of F2c, F2d and D4 fold sets (Fig. 3.9). Locally pre-F2c folds occur, but they are typically strongly transposed by later fabrics and/or high strain zones (Figs. 3.10c, d, n, and p). F2c are mesoscopic irregular tight to isoclinal folds of S2a and S2b leucosomes (Fig 3.10a, b, h and i). In Ghost subdomain, the S2a and S2b leucosome fabrics result from high-grade melting reactions (Table 3.1; Appendix I). S2a leucosomes are predominantly garnet-bearing, whereas S2b leucosomes comprise garnet–cordierite assemblages that locally transect S2a leucosomes (Figs. 3.10b, j–m and v). The different leucosome assemblages across the Ghost subdomain are interpreted in terms of a progressive increase in temperature during M2b prograde metamorphism. In terms of their structural development, the granulite-

Figure 3.9: (a) Map showing lithologic, structural and metamorphic relationships across the central part of the mid-crustal Ghost subdomain, including the southwest closure of the Ghost antiform, the Forked Lake dome and the northern margin of the 'Big Bird' dome (see Fig. 3.2a for location). The map highlights the transition from steep, overturned F2c structures into upright open F2d structures that resulted in a Type I, dome-and-basin fold interference pattern in the northern subarea, and the Paleoproterozoic (F4) upright, open and steep north-plunging structures that resulted in the Type II, dome, crescent and mushroom interference patterns in southern Ghost subdomain. Localities of photographs in Fig. 3.10 are shown. Stereonet data (equal area projections) define major fold axes for each macroscopic fold structure across the map including the reclined steep NE plunging hinge zone of the Ghost antiform (southern closure), the shallow NE plunging northern Ghost antiform closure (see Fig 3.2a; data courtesy of J. Henderson). The southwest closure of the Ghost antiform is interpreted as the consequence interference between F2c structures in the overlying transition zone with regional F2d structures that predominate in the Ghost subdomain. (b) Staggered, approximately NW–SE oriented cross-section drawn through the hinge zones of major fold structures across the central Ghost subdomain. Section illustrates the prevalence of upright structures and cusped–lobate fold styles across the map area. A transition from F2c to F2d and F4 fold structures occurs from NW to SE across the section line. (c) N-S oriented section constructed through the core of the 'Big Bird' dome where a regional F2d is refolded by a NNW-trending F4 structure. The plunge of the refolded F2d fold is consistent with the inclination of the F4 fold axis (see stereonet data Fig. 3.9a). (d) Simplified three-dimensional diagram of the Big Bird dome and the sequence of fold superposition responsible for its formation.

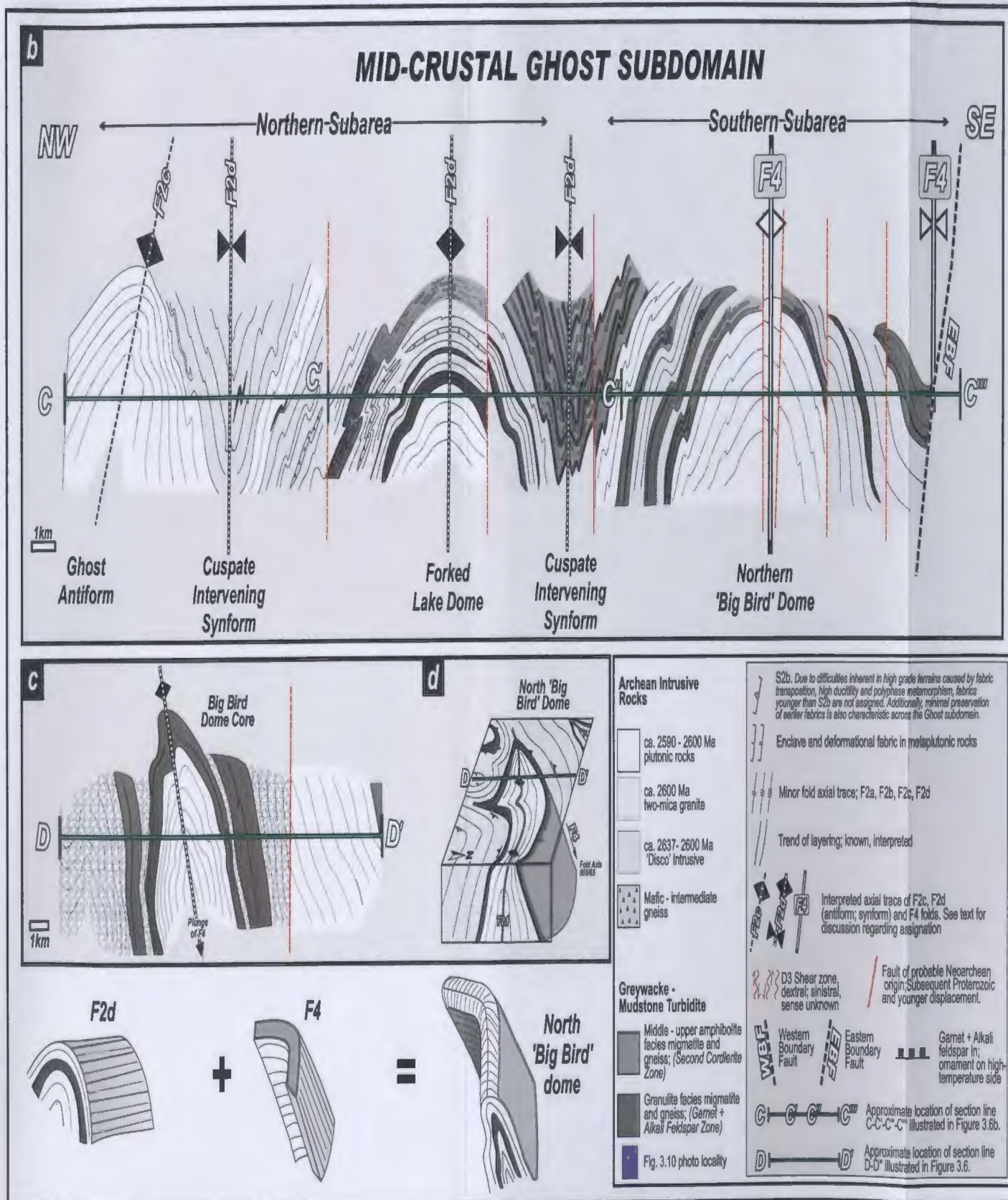


Figure 3.9

facies leucosomes contrast with their upper-amphibolite-facies counterparts in the transition zone, since S2a leucosomes do not exhibit widespread Type III refolding. F2c refolding of S2a leucosomes is difficult to demonstrate unequivocally due to the combined effects of increased strain and enhanced ductility. Timing between S2a and S2b is established on F2c fold limbs where S2a fold closures and overprinting leucosome relationships are preserved (Figs. 3.10b, l, t and v). High-strain zones are ubiquitous throughout the Ghost subdomain and are locally associated with mineral stretching lineations (e.g., Forked Lake; Figs. 3.9, 3.10p) interpreted to be a result of strain partitioning prior to regional F2d folding.

F2c folds and S2a, S2b and S2c fabrics are overprinted by open NE-trending upright F2d folds (Figs. 3.9, 3.10e, h and t; Table 3.3). The orientation of the earlier structures controls the locations of the F2d folds, which are open NE-plunging structures with longer wavelengths (12–14 km; Fyson and Jackson 2004; Fig. 3.9) in the mid crust compared to the transition zone (0.5–2 km). F2d structures control the development of Type I, dome-and-basin fold interference in the northern subarea of Ghost subdomain and are refolded by F4 folds in the southern subarea (Fig. 3.9). No penetrative fabric development is associated with F2d folding, which predated intrusion of ca. 2586 Ma pegmatite granite dykes (Fig. 3.10n). Megacrystic granite sheets that comprise the Ghost antiform and Forked Lake and Big Bird structural domes are folded by F2d, which constrains the onset of this fold event to syn- to post-emplacement. The Ghost antiform has an asymmetric dome-like geometry controlled by a large F2d fold, which has a shallow NE-plunge near Ghost Lake (Table 3.3; Fig. 3.2a), but is steeply reclined with an

Figure 3.10: Structural elements and related deformational fabrics observed across the Ghost subdomain. Hammer and lens cap are approximately 45 and 5 cm long, respectively. North arrow, scale and fields of view for polished slabs and photomicrographs, respectively, are indicated. Photo locations are marked on Figure 3.9. *(a)* Mesoscopic F2c fold defined by S2b leucosome and overprinted by both E-W and NW-SE trending D3 shear zones; *(b)* Coarse grained garnet – cordierite bearing leucosome (F2c fold) and older S2a garnet bearing stringers; *(c)* Isoclinal, rootless fold transposed parallel to the surrounding S2b fabric. Relict folded bedding plane is preserved; *(d)* Closeup of hinge zone of rootless fold illustrated in *(c)*; *(e)* Local refolded fold of mafic enclave in metaplutonic rock. Youngest NE open fold is interpreted as F2d; *(f)* Metaturbidite and metaplutonic contact overprinted by E-W trending S3 shear fabric; *(g)* Weakly foliated late-tectonic garnet – cordierite bearing diatexite; *(h)* S2a and S2b leucosomes folded by mesoscopic F2d on SW limb of Forked Lake dome.

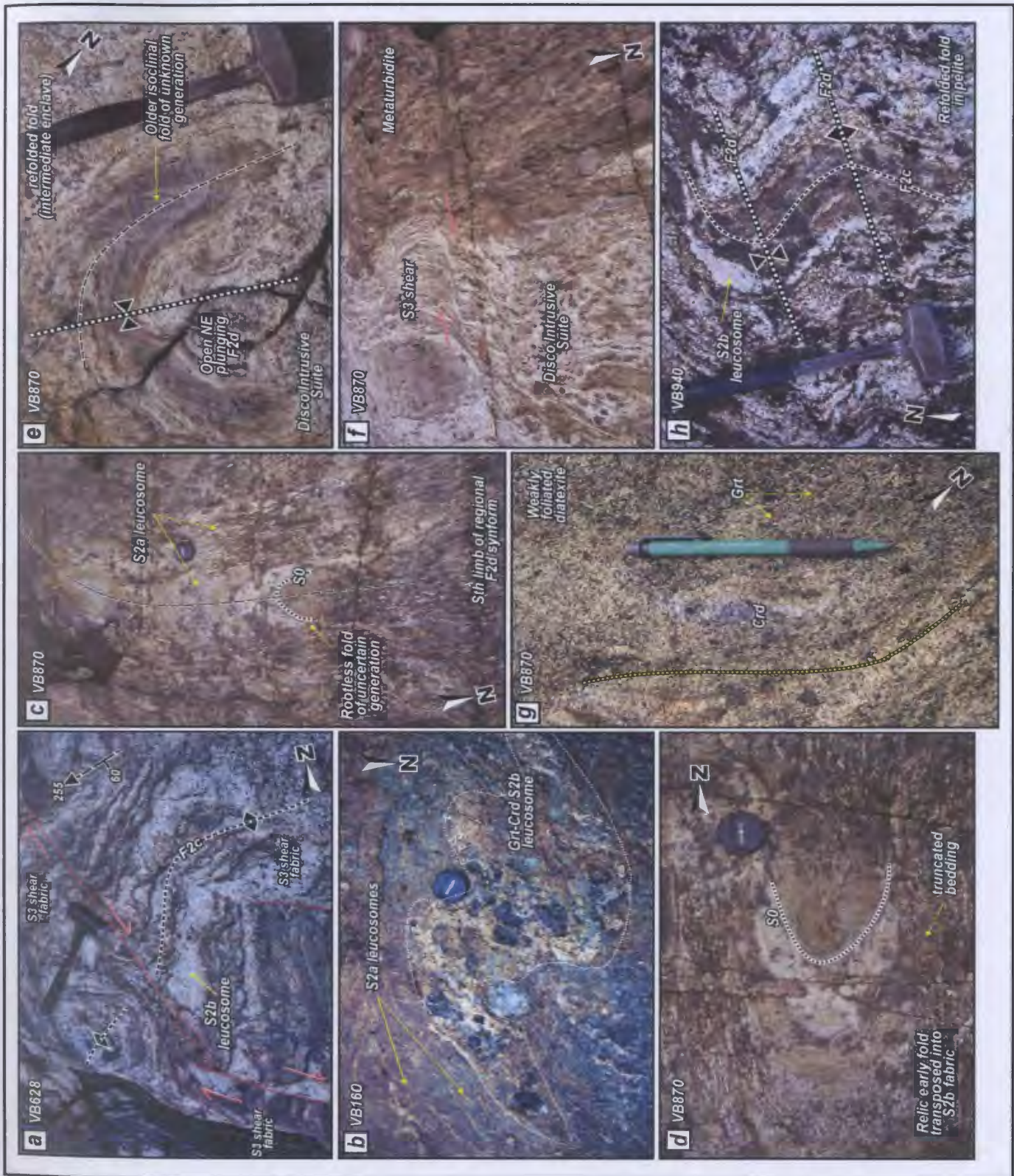


Figure 3.10: Ghost Subdomain structural features

Figure 3.10 continued: Structural elements and related deformational fabrics observed across the Ghost subdomain. Hammer and lens cap are approximately 45 and 5 cm long, respectively. North arrow, scale and fields of view for polished slabs and photomicrographs, respectively, are indicated. Photo locations are marked on Figure 3.9. *(i)* Tight – isoclinal F2c M-fold of S2b leucosome. Inset is closeup of small S2a leucosomes; *(j)* Photomicrograph of garnet- alkali feldspar bearing S2a leucosome formed in response to breakdown of biotite and sillimanite; *(k)* Photomicrograph of garnet- cordierite bearing S2b leucosome formed in response to breakdown of conituned biotite and sillimanite at higher temperature; *(l)* Outcrop photo of parallel to acutely transecting S2b and S2a leucosomes; *(m)* Polished slab and stained slab (inset) of garnet alkali-feldspar bearing S2a leucosome; *(n)* and *(o)* Isoclinal minor F2c folding of S2b leucosomes truncated by NW-SE trending D3 shear zone which is intruded by ca. 2586 Ma post-tectonic pegmatitic granite. Drag folding indicates dextral sense of motion (dip-slip); *(p)* Rootless fold in high strain zone. High strain zone fabrics across the study area are considered to be a consequence of strain partitioning in the latter stages of F2c.

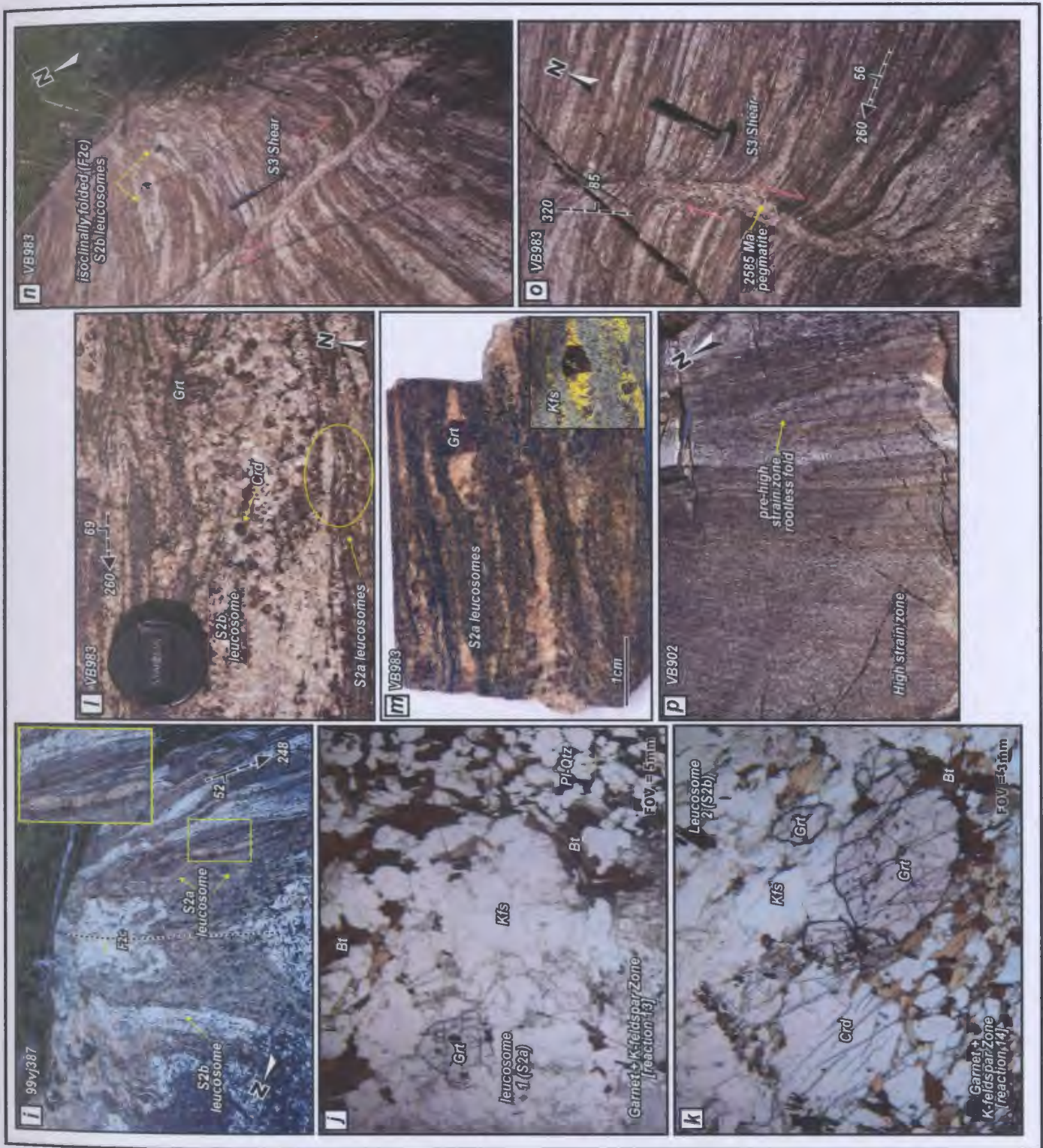


Figure 3.10: Ghost Subdomain structural features

Figure 3.10 continued: Structural elements and related deformational fabrics observed across the Ghost subdomain. Hammer and lens cap are approximately 45 and 5 cm long, respectively. North arrow, scale and fields of view for polished slabs and photomicrographs, respectively, are indicated. Photo locations are marked on Figure 3.9. *(q)* Shallow deformational fabric in megacrystic granite sheet in the core of Forked Lake dome; *(r)* Recumbent fold of mafic enclave in shallow dipping metaplutonic rock, NW of Forked Lake dome core; *(s)* NW-SE trending D3 shear zone in metaplutonic rock. Drag folds indicate dextral displacement (strike-slip); *(t)* Mesoscopic F2d fold defined by fold of S2b and local refolding of S2a leucosomes. The F2d fold is overprinted by D3 E-W trending shear zone; *(u)* Tight, irregular and discontinuous F2c fold of thin sheet of megacrystic granite that has intruded metaturbidite, northern 'Big Bird' dome; *(v)* Polished slab of S2b and S2a leucosomes. The older S2a is truncated by the larger S2b leucosome; *(w)* Sharp truncation of S2a and S2b leucosomes by coarse-grained unfoliated post-tectonic diatexite.

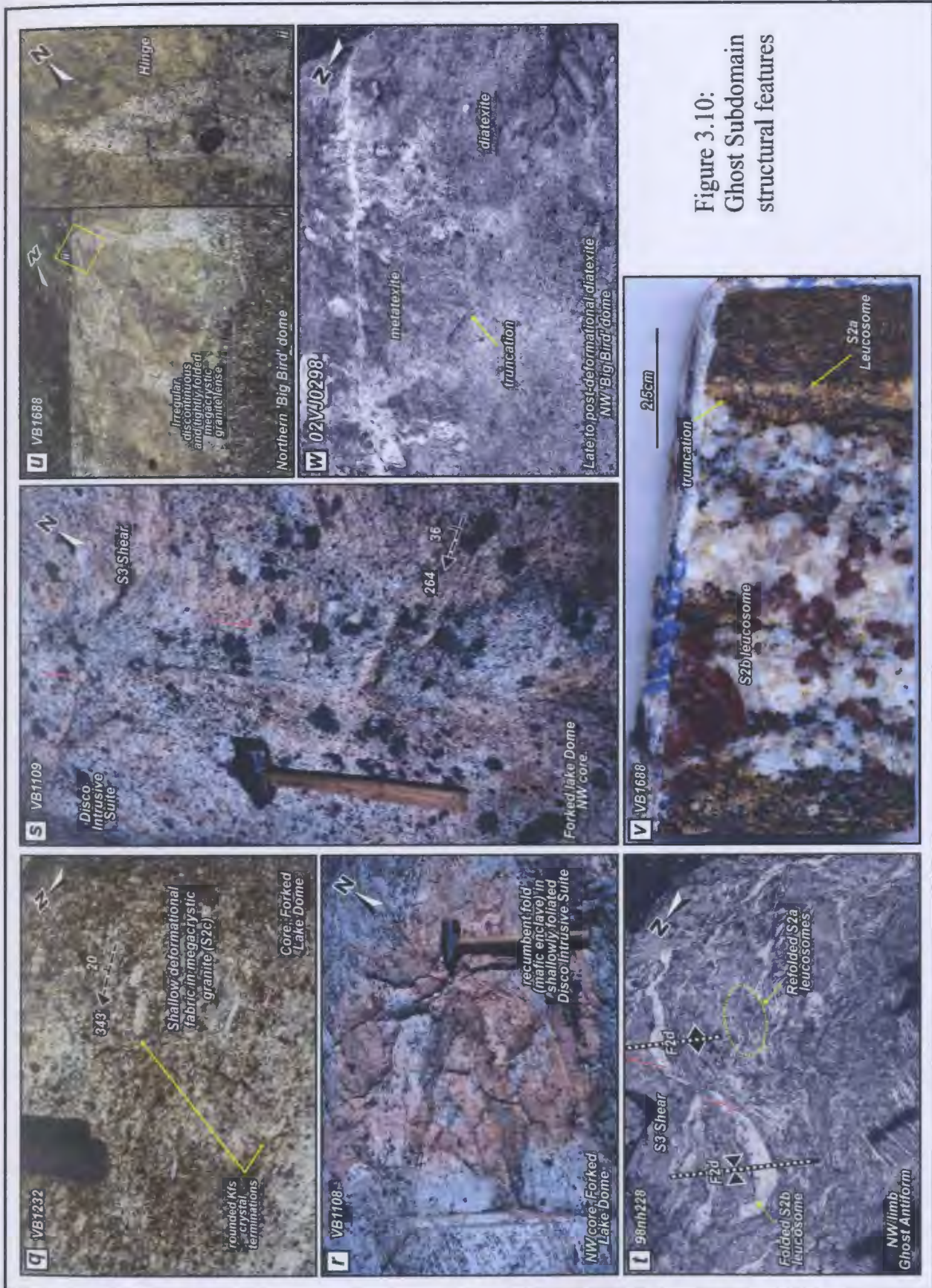


Figure 3.10: Ghost Subdomain structural features

ENE-plunging axis farther southwest (Fig. 3.9; Table 3.3). The steep inclination of fabrics defining the southwest hinge zone contrasts with the moderate to shallow fabrics of F2d regional structures (Fig. 3.10q, r), suggesting a possible correlation with F2c structures in the overlying transition zone, but the northeast plunge is more consistent with F2d folding. Collectively, these data lend support to the interpretation that the southwest closure represents a zone of incomplete transposition of a regional F2c structure into F2d (Fig. 3.9). F2c minor folds are rarely preserved in the megacrystic granite suite in Ghost subdomain (Fig. 3.10u, v), and minor S2c high-strain zones and shallow deformational fabrics support emplacement of the granite during the S2c fabric-forming episode and pre-F2d, which as noted previously, is not associated with penetrative fabrics (Fig. 3.10q). As in the transition zone, metasedimentary diatexite ranges from weakly foliated to unfoliated, suggesting that it formed late- to post-D2 (Fig. 3.10g) and that M2b outlasted D2 at deeper crustal levels. Diatexite truncates S2a and S2b folded leucosomes (Fig. 3.10w) and is overprinted by D3 shear structures, constraining the timing of melting to post-F2c and pre-D3.

D3 structures are well preserved in the Ghost subdomain and consist of NNW- and E-trending conjugate shear sets (Figs. 3.10), with associated drag folds indicating both dextral and sinistral senses of strike-slip and dip-slip displacement. Dextral and sinistral kinematics occur subequally along NW-SE-trending shears, whereas dextral motion predominates in the E-W shear set, which postdated the northwest set where crosscutting relationships are preserved and may have locally reactivated them in a dextral sense of displacement. These mid-crustal shear sets contrast with those in the

transition zone by the occurrence of large-scale conjugate pairs, their larger size and greater continuity, and also by the presence of undeformed ca. 2585 Ma pegmatite along both sets of shear planes, which indicates that shear development predated or was synchronous with melt emplacement (Fig. 3.10n, o).

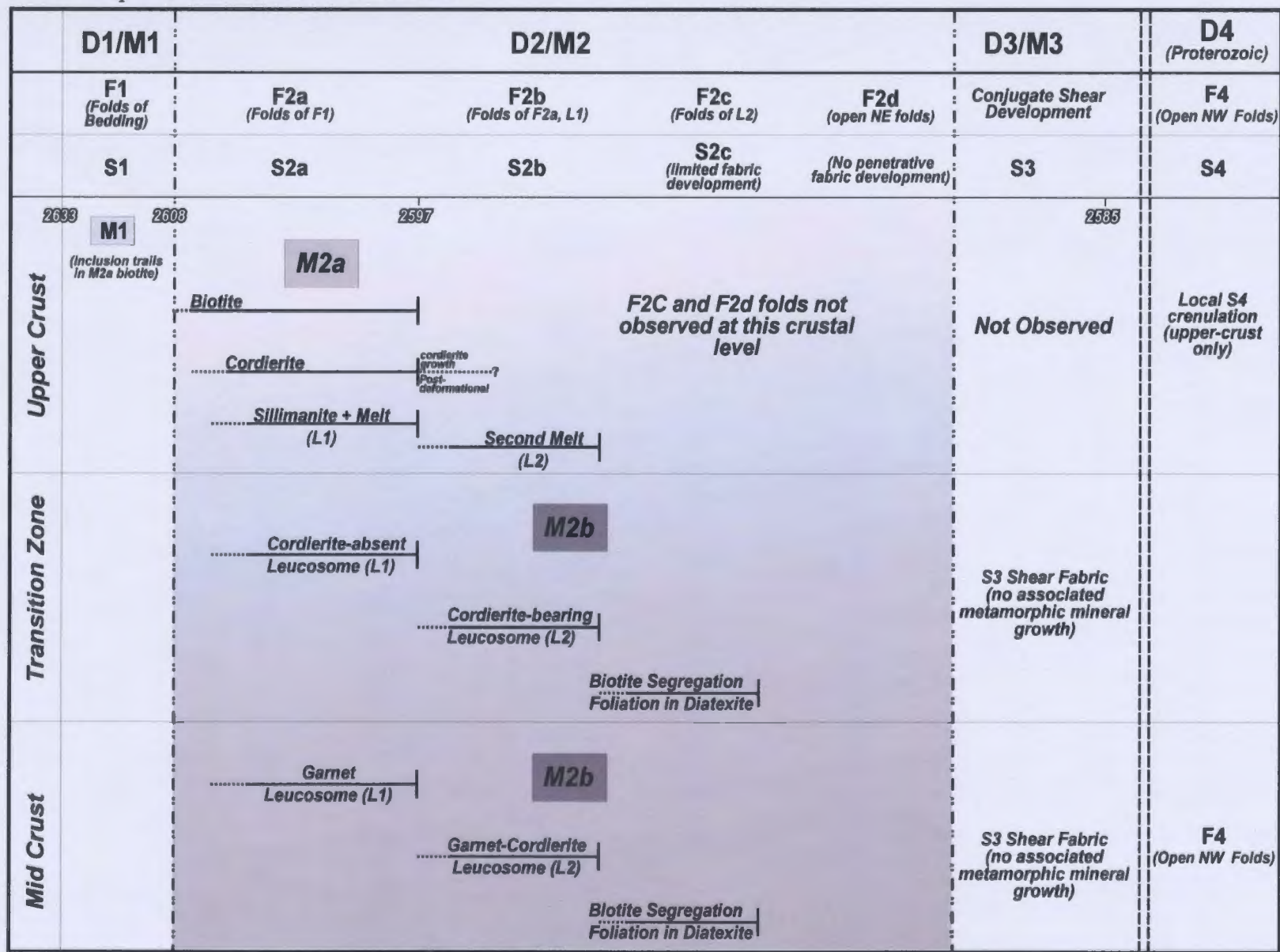
D4 Paleoproterozoic structures consist of macro-scale upright NNW-trending open folds, which imparted a major control on the distribution of fold interference across the Ghost subdomain. The Type I, dome-and-basin architecture of the northern subdomain, which is considered primarily the consequence of Neoproterozoic deformation, contrasts with the Type II, crescent interference patterns of the southern subdomain, which resulted from the superposition of a regional NNW-trending, steep north-plunging F4 fold on the older composite D2 structure. Examination of Fig. 3.9a-c reveals that open steep NNW-plunging refolding of an F2d structure accounts for the outcrop pattern of the 'Big Bird' dome. Stereonet plots of fabrics in the megacrystic granite in the core of dome demonstrate the presence of a tight overturned structure, inclined in the plunge direction of the F4 fold (Fig. 3.9d). No penetrative fabric is associated with these folds. Extrapolation of the axial trace northwards demonstrates that F4 folding was not restricted to the mid-crust, as in the vicinity of Wijinnedi Lake (Fig. 3.2a) a large, open, NNW-trending structure, also interpreted as F4, refolds upper-crustal volcano-sedimentary lithologies.

3.4.4 Correlations and crustal architecture

3.4.4.1 Structural correlations

The structural continuity (i.e., the absence of major structural–metamorphic breaks) from the upper-crustal Kwejinne Lake supracrustal belt, through the migmatitic transition zone, to the mid-crustal Ghost subdomain, enables correlation of structural generations and deformation histories among the three crustal levels (Fig. 3.11). Preservation of D0 and D1 is restricted to the low-grade upper crust and correlative regional structures are not recognized in either the transition zone or the mid crust. The earliest recognized D2 fold sets in the Kwejinne Lake supracrustal belt, F2a and F2b, are associated with axial S2a and S2b planar fabrics defined by biotite, cordierite, and melt \pm sillimanite and cordierite-bearing leucosome, respectively. At deeper levels in the transition zone and in Ghost subdomain, correlative S2a and S2b axial planar fabrics are defined by leucosomes with mineral assemblages indicative of anatexis at progressively higher temperatures. Folding of S2a and S2b leucosomes defines the younger F2c and F2d fold sets in the deeper crustal levels of the transition zone. F2c and F2d folds and S2c high-strain zones are restricted to the transition zone and the mid crust. The existence in the transition zone of both regional coaxial folding and mesoscopic non-coaxial fold interference patterns (Types I and III; Ramsay 1967) corresponds to the superposition of steep F2c structures and shallow, upright F2d folds on the composite F1–F2a–F2b structural package. The similar orientations and overprinting relationships of the D3 shear fabrics enable their correlation between the mid-crust and transition zone, but corresponding structures are not observed in the upper crust. Furthermore, occurrences of the M3 cordierite-spinel decompression assemblage in metapelites broadly coincide with the geographic distribution of D3 shear zones across the Snare River terrane, implying an

Figure 3.11: Summary diagram correlating the diachronous relationships between deformation, fabric formation and metamorphism in the Snare River terrane.



association between the two (Fig. 3.12). Importantly, M3 decompression assemblages form large radiating aggregates that overprint D2/ M2 fabrics indicating that M3 postdated D3 (Fig. 3.12). Finally, in contrast to the depth dependence of the Neoproterozoic D1–D3 events, upright Paleoproterozoic F4 fold sets can be correlated across the Snare River terrane.

3.4.4.2 Crustal Architecture

Heterogeneous superposition of three Neoproterozoic and one Paleoproterozoic deformation events has created a complex architecture in the three crustal levels of the Snare River terrane. The first-order topology of the upper crust is interpreted as a steeply westerly inclined F2b anticlinorium that refolded NNE-trending F1 and F2a structures on its northwest limb and which is itself overprinted by open D4 cross-folds with NW-trending axial traces. The first-order topology of the underlying transition zone (i.e., lower limb of Hinscliffe antiform) is characterized by a series of steep to overturned, west-dipping F2c antiforms. No intervening regional synforms of comparable scale are recognized and the limbs of the antiforms become more gently dipping as the grade of metamorphism and paleodepth increase towards the southeast. Topology of the mid-crustal Ghost subdomain is characterized by interference among F2c, F2d and F4 folds that gives rise to dome-and-basin and asymmetric crescent structures, in which basins and cusped synforms are strongly appressed in comparison to adjacent lobate domes.

When the geometries of the three crustal levels are considered together, the crustal architecture can be seen to consist of a series of overturned antiforms in the upper crust and transition zone juxtaposed against the dome-and-basin and mushroom structures

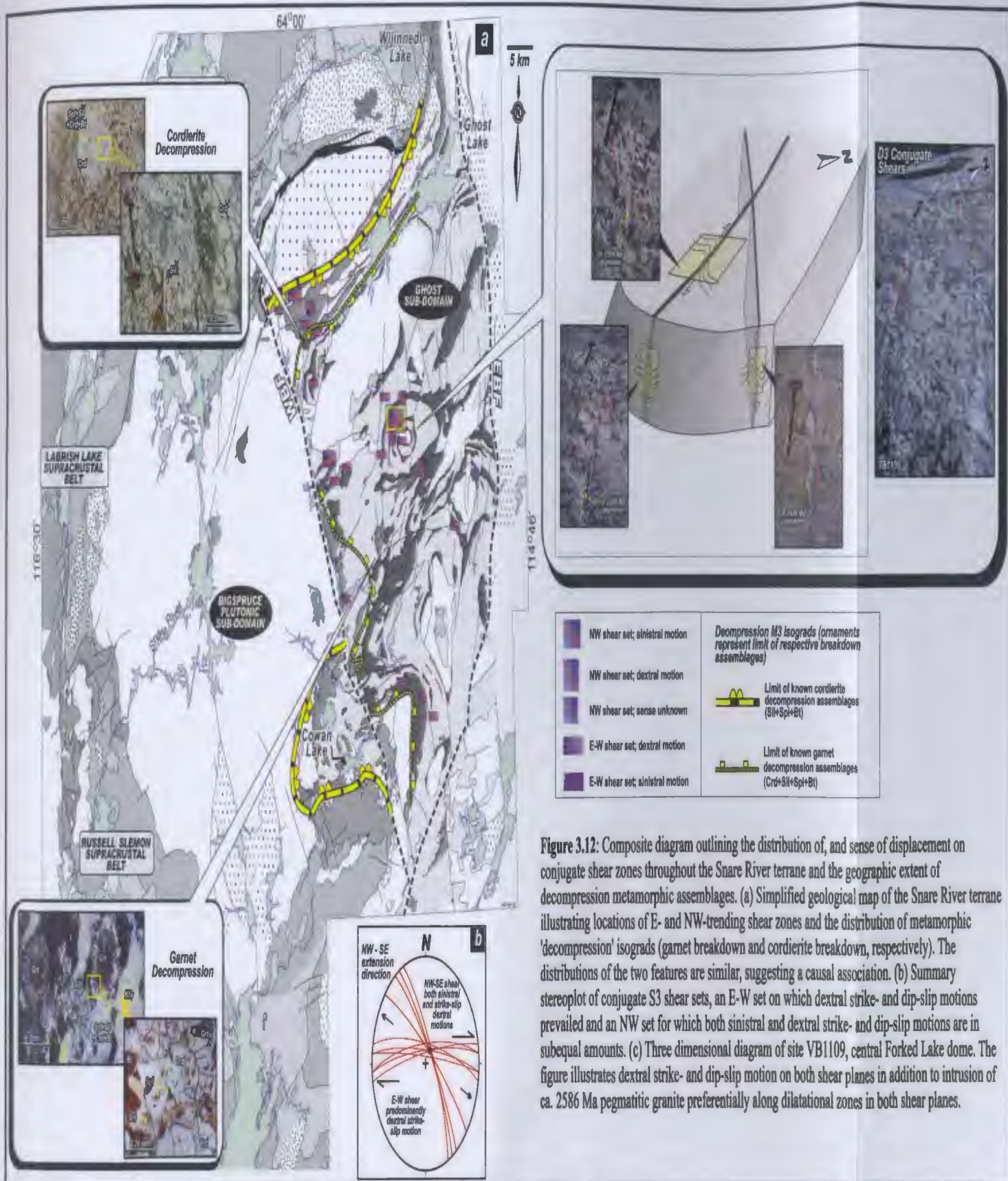


Figure 3.12: Composite diagram outlining the distribution of, and sense of displacement on conjugate shear zones throughout the Snare River terrane and the geographic extent of decompression metamorphic assemblages. (a) Simplified geological map of the Snare River terrane illustrating locations of E- and NW-trending shear zones and the distribution of metamorphic 'decompression' isograds (garnet breakdown and cordierite breakdown, respectively). The distributions of the two features are similar, suggesting a causal association. (b) Summary stereoplote of conjugate S3 shear sets, an E-W set on which dextral strike- and dip-slip motions prevailed and an NW set for which both sinistral and dextral strike- and dip-slip motions are in subequal amounts. (c) Three dimensional diagram of site VB1109, central Forked Lake dome. The figure illustrates dextral strike- and dip-slip motion on both shear planes in addition to intrusion of ca. 2586 Ma pegmatitic granite preferentially along dilatational zones in both shear planes.

of the mid-crustal Ghost subdomain (Fig. 3.13a). Additionally, major fold axes rotate progressively from steep SW-plunging F2a and F2b structures in the upper crust, through steep NW-plunging F2b and F2c structures in the transition zone, to shallow NE-plunging F2d structures in the northern subarea of the mid-crustal Ghost subdomain (Fig. 3.13b). This systematic relative rotation across crustal levels may be due to Neoproterozoic progressive D2 deformation where subsequent phases of deformation fold pre-existing and progressively shallow-dipping surfaces with increasing depth. Alternatively, the rotational trend may also be due to D4 Paleoproterozoic SW–NE shortening.

3.5 Interpretation and tectonic model

In this section, the structural correlations and deformation histories outlined for each crustal level are synthesized into a model to account for the structural evolution of the Snare River terrane and comparisons are made with data from elsewhere in the Slave Province. The three phases of Neoproterozoic deformation (D1–D3) coincide with major stages in the regional crustal development and thus the role of deformation in crustal evolution is also addressed.

3.5.1 D0-D1 – Lateral Crustal Shortening

D0 and D1 are pre- and post-turbidite stages of what is inferred to have been a protracted progressive deformation event. Pre-turbidite deformation (D0) is poorly constrained to between ca. 2674–2654 Ma and was restricted to volcanic and plutonic

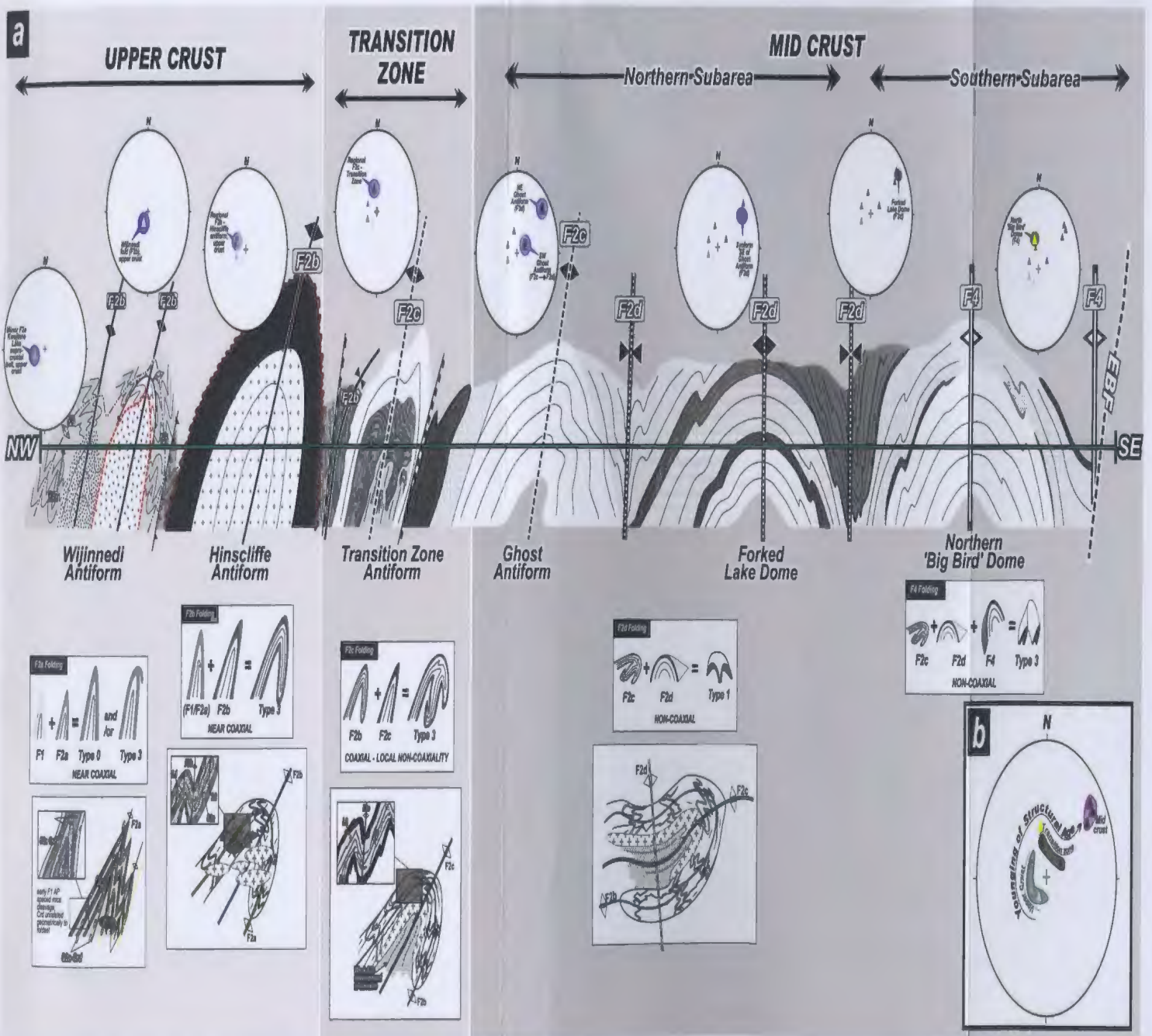


Figure 3.13: (a) Summary schematic NW-SE crustal cross-section of the Snare River terrane showing the greenschist to amphibolite-facies Kwejinne Lake supracrustal belt, the amphibolite-facies transition zone, and the granulite-facies mid-crust (Ghost subdomain), and illustrating the progressive younging of macroscopic structures (F1 to F4) that control the crustal architecture and outcrop pattern. Each structural domain is characterized by different fold interference patterns related to the younging of structures with paleodepth, such that near-coaxial refolded folds in the upper crust give way to dome-and-basin and dome, crescent and mushroom interference patterns in the mid-crust. Post-Archean brittle faults not shown. Fold axis data illustrated in summary stereoplots of each regional structure given in Table 3.4. (b) Stereoplots summarizing change in orientation of major fold axes with depth across the Snare River terrane. The plot illustrates either rotation of regional fold axes during the Neoproterozoic progressive deformation event, or refolding of Archean fold axes during later Paleoproterozoic (F4) deformation, or a combination of the two.

rocks in the supracrustal belts. The development of D0 high strain zones, mineral lineations and elongated felsic clasts and mafic pillows, features that are not observed in the adjacent metaturbidites, are interpreted to reflect the early stages of dismemberment of an oceanic plateau composed of tholeiitic and TTG magmas (Chapter 4). Initiation of compressive plate motions between the Snare River terrane and Mesoarchean crust of the Central Slave Basement Complex to the east is speculated to have been the driving force for this process and subsequent accretionary tectonics.

D1 deformation post-dated deposition of the younger turbidites and involved a protracted episode of shortening between ca. 2635–2608 Ma (Fig. 3.14a). Metamorphic grade associated with D1 was low (sub-greenschist to greenschist facies) and fabric development became more pronounced towards the end of this period; for instance, early D1 folding in the Russell-Slemon supracrustal belt lacked an axial planar cleavage (Fyson and Jackson 1991). D1 structures with similar age constraints and associated low-grade fabrics also occur in the Indin Lake supracrustal belt (Pehrsson 1998), the northern extension of the Kwejinne Lake belt, where they were interpreted to result from the imbrication of turbidites with older volcano-plutonic crust (Pehrsson and Villeneuve 1999). The low metamorphic grades imply that shortening was predominantly thin-skinned and achieved by lateral telescoping without significant crustal thickening. Lateral lithological diversity resulted in intercalation of the ca. 2640–2630 Ma Defeat Suite and pre-2635 Ma turbidite packages to the east, adjacent to the Mesoarchean Central Slave Basement Complex that were already tightly folded prior to ca. 2635 Ma. These packages graded westward into the volcano-sedimentary crust of the Snare River terrane, dominated by post-2635 Ma turbidites and devoid of Defeat Suite plutons (Fig. 3.14).

Figure 3.14: Deformation history of the Snare River terrane depicted in six schematic crustal profiles. **(a)** D1 (ca. 2635-2608 Ma) – crustal shortening of young turbidite package adjacent to the older volcano-plutonic crust in an accretionary wedge setting. Older turbidite packages and Defeat suite plutons are located to the east and underwent a more protracted D1 history compared to younger turbidite packages in the west. (i) - (iii) illustrate progressive development of F1 structures in a fold-thrust setting; in (iii) unconformable and conformable metaturbidite contacts with adjacent volcanics, observed in the northern Kwejinne Lake supracrustal belt, are shown. **(b)** Onset of collisional tectonics (D2): (D2a) primarily involved enhanced lateral shortening accompanied by HT-LP metamorphism (M2a) and formation of S2a fabrics associated with F2a folding. Resultant fold interference patterns are dominated by Type 0 redundant superposition and local Type 3 coaxial refolding. D2a pre-dated ca. 2600 Ma plutonism. **(c)** D2b involved thorough structural reworking through nappe tectonics and significant crustal thickening, and coincided with the intrusion of voluminous orogenic plutons at ca. 2600 Ma. S2b fabrics were low-temperature cleavages in the upper crust and high-temperature metamorphic fabrics and leucosomes in the migmatitic transition zone and Ghost sub-domain. The post-2635 Ma turbidite packages primarily occur at upper crustal levels, whereas the pre-2637 Ma turbidite package and the Disco Intrusive Suite (DIS) predominate at mid-crustal levels. Superposition of F2b on D1/D2a structures resulted in coaxial fold interference patterns (hook).

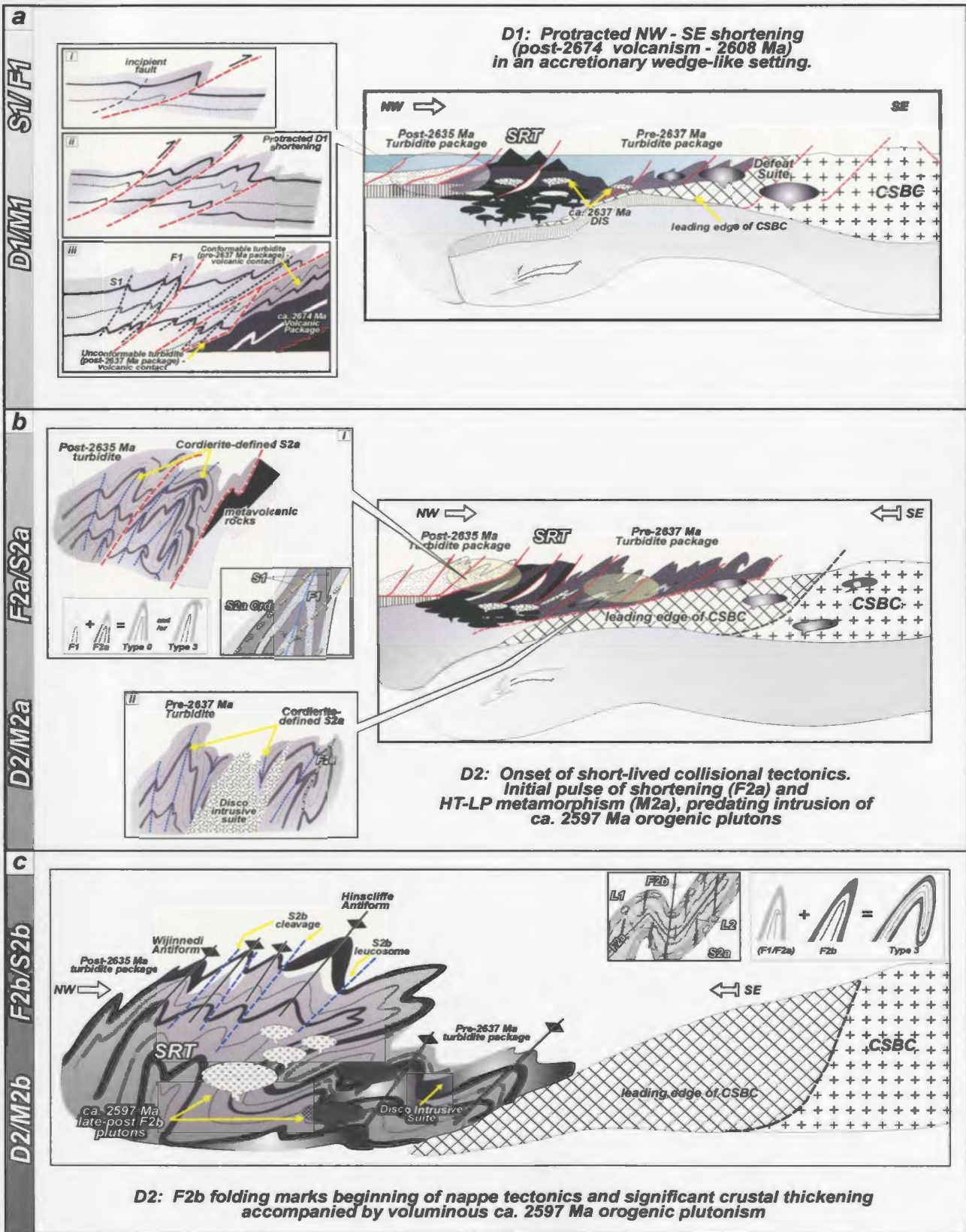


Figure 3.14

In summary D1 structures and associated low-grade metamorphism are interpreted to reflect thin-skinned crustal shortening over a ca. 45 M.y. interval, when D0 and deformation of pre-2637 Ma turbidite packages is considered. An accretionary wedge setting is invoked and resulted in intercalation of the young turbidite packages with the older volcano-plutonic crust. A lithologically and structurally distinct accretionary wedge is invoked for the Snare River terrane. Modern counterparts differ markedly in structural style, lithological diversity, the lack of major chaotic disruption zones, polymict melange and HP/LT metamorphic assemblage (Hamilton 1998). Imbricate thrust fault development is an important component of modern subduction zones and is typically facilitated by lithology-induced competency contrasts. Analogous fault systems have not been recognized in the turbidite packages of the Snare River terrane, further supporting a unique wedge setting. Subcretion, which was inferred from geochemical and inherited zircon datasets in Chapters 4 and 5 to be an important Neoproterozoic process in the study area, provides a means to reconcile the observed differences in wedge dynamics. In modern settings, the vertical component of the underthrust slab imparts significant control on trench geometry and subsequent deformation styles. In contrast, subcretion would result in greater horizontal accretion, precluding formation of a large trench. Lateral shortening rather than downward off-scraping would characterize the Neoproterozoic subcretionary wedge. In this setting, chaotic disruption would be minimal, imbricate thrusting would be less and HP-LT assemblages would not routinely form. The origin of the compressive stress regime is inferred to be continued lateral crustal motions between the Snare River terrane and the Central Slave Basement complex to the east (Fig. 3.14).

3.5.2 D2 – Nappe tectonics

The contractional event that resulted in D2 structures across the Snare River terrane differed from D1 with respect to its greater intensity and shorter duration. D2 structures in the study area share three first-order similarities with large-scale thrust nappes (e.g., Ramsay et al. 1983; Platt and Lister 1985): (i) steep structures at high structural levels and low angle structures at deeper structural levels, (ii) the absence or strong attenuation of synformal hinge zones due to repeated out-of-synform break-thrust development during nappe formation, resulting in the formation of a stacked antiform profile, and (iii) and younging of structural age within depth (e.g. nappe piles in the Alps were emplaced from top to bottom; Ramsay et al 1983; Ratschbacher et al. 1989). Given these similarities, a model involving the formation of a large-scale thrust nappe is invoked to account for the D2 structural features of the Snare River terrane. The occurrence of a metamorphic pressure gradient with depth variations in excess of 22 km indicates considerable vertical crustal thickening was associated with nappe formation. Evolution of the D2 tectonic architecture of the Snare nappe is summarized schematically in Fig. 3.14b-d.

The nappe model also provides a means to reconcile the diachroneity of D2 and M2 through the combined effects of upper-crustal decoupling and continued progressive deformation in the mid crust accompanying underthrusting. In this model, high-grade metamorphic conditions only occur after transport of the lower limb to mid-crustal levels and loading by the overlying nappe. Thus high-grade M2 metamorphism and associated F2c and F2d structures in the mid crust occurred after lower grade M2 metamorphism and associated F2a and F2b structures in the upper crust. Low-angle mid-crustal thrusting

is implied by the model and is reflected in the field by the localized development of D2 high strain zones; however the extent of these zones is poorly constrained and the role of mid-crustal thrusting is not well understood. In summary, collision involved short-duration reworking of the orogenic crust through progressive, diachronous deformation and metamorphism. Crustal imbrication and thickening played a significant role during structural evolution and resulted in welding of the Snare River terrane to the outboard regions of the older Mesoproterozoic crustal nucleus. However, the synchronicity in HT/LP M2 metamorphism and associated ca. 2600 Ma plutonism across the Slave province, specifically in regions where crustal thickening is minimal argues for an additional heat mantle heat source (Chapters 4, 6).

3.5.3 D3 – Crustal Thinning

D3 structures define a final phase of Neoproterozoic deformation that occurred after the orogenic peak and prior to emplacement of ca. 2585 Ma pegmatitic granite. Ubiquitous conjugate shear sets in the migmatitic transition zone and Ghost subdomain are interpreted to reflect mid-crustal extension and uplift prior to ca. 2585 Ma in a mode similar to core complex formation (e.g., Chery 2001; Kisters et al. 2003). In this model, mid-crustal exhumation is achieved through a combination of uplift and crustal thinning by pervasive conjugate faulting, in which the decoupled upper crust is isolated from the effects of shearing and behaves as an independent structural unit sliding off the top of the rising orogenic mid crust (Fig. 3.14). In the Snare River terrane, overprinting decompression metamorphism (M3) is restricted to the transition zone and Ghost subdomain (Fig. 3.12), supporting uplift of these crustal levels, with little or no

Figure 3.14 continued: Deformation history of the Snare River terrane depicted in six schematic crustal profiles. *(d)* During the latter stages of D2, the locus of deformation migrated to deeper crustal levels, such that the upper crust was decoupled or isolated from the effects of the F2c and F2d, which are restricted to the transition zone and Ghost subdomain. These fold events post-dated most orogenic plutonism (i.e., post-2600 Ma). The diachronous nature of D2 is best understood in terms of the superstructure–infrastructure geodynamic model of Culshaw et al. (2004), in which a highly ductile mid-crust is decoupled from a more rigid upper crust during collision with a cratonic block (the CSBC). Three segments can be distinguished, including the upper and lower limbs of the antiformal nappe (Snare River terrane; superstructure), and a lower plate (infrastructure) which the upper plate overrides during orogenesis and consists of a collage of material from both the Snare River terrane and the Central Slave Basement Complex. The occurrence of ca. 2637 Ma plutons and pre-2635 Ma turbidites in the Ghost subdomain, but not in the overlying transitional migmatite zone or supracrustal belts, provides evidence for the existence of a lithologically distinct lower plate. Furthermore, the occurrence of >2.8 Ga zircon inheritance data (Ootes et al. 2005) in lower-crustally-derived plutons east of the Snare River terrane provides additional support to the collisional model with the Central Slave Basement Complex as the lower plate and the Snare River terrane as the overriding plate. The change in fold style tight to isoclinal overturned F2c folds to gently plunging open F2d folds reflects the transition from subhorizontal transport of the Snare mid crust onto the CSBC (F2c) and limited horizontal shortening of the assembled thrust stack (F2d). Contrasting fold interference patterns resulted from the two events, with Type 3 coaxial refolding resulting from superposition of F2c in contrast to Type 1 dome-and-basin interference resulting from superposition of F2d. *(e)* Post–orogenic collapse (D3) immediately followed D2 overthickening. The initial stage involved collapse of crust overlying the Ghost subdomain along a detachment fault and coincided with uplift of a mid-crustal wedge through pervasive conjugate shearing (S3) and crustal thinning. The future site of the Snare River terrane partial crustal section occurs on the lower plate and is marked. *(f)* Impingement of the ductile migmatitic transition zone on the overlying brittle upper crust resulted in steepening of structures and telescoping of isograds in the transition zone. Crustal thinning led to a higher heat flow during D3 uplift and M3 decompression metamorphism. Intrusion of the ca. 2585 Ma pegmatite suite marks the termination of D3 in the Snare River terrane.

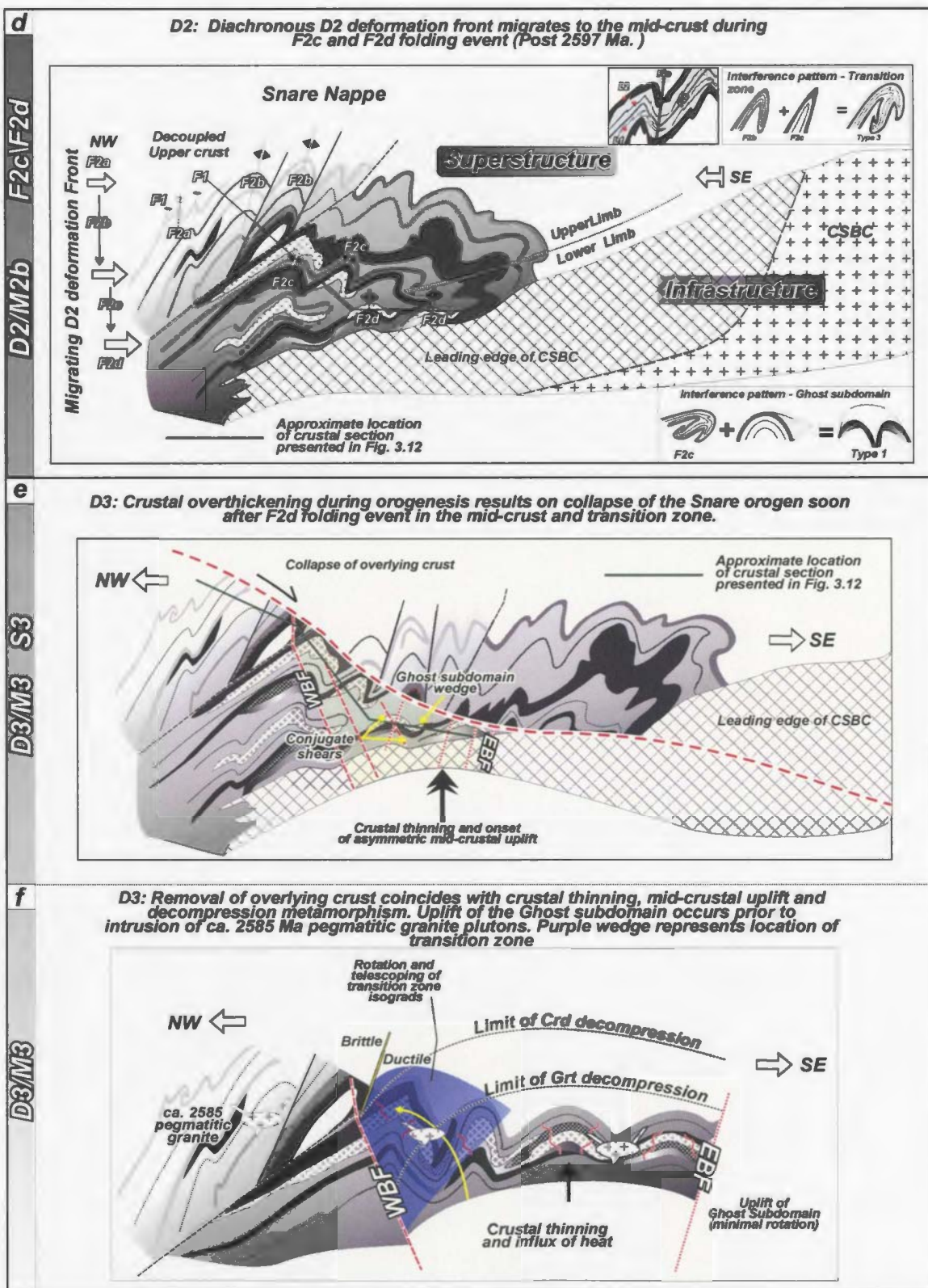


Figure 3.14

corresponding uplift of the upper crust. Uplift of the mid-crustal Ghost subdomain resulted in telescoping of M2 isograds in the transition zone (Fig. 3.14) and may in part have been localized by the brittle–ductile transition, with the brittle upper crust creating a rigid block against which the ductile transition zone was compressed. However, the appropriate structural and metamorphic continuity indicates that uplift did not involve significant relative displacement between crustal levels. In the upper crust, folds were tightened and dips steepened, whereas in the mid crust the undulating low to moderate dips were enhanced, compatible with the presence of late recumbent folds in the transition zone near Cowan Lake (Fyson and Jackson 2004). D3 structures are most readily explained by an episode of post-orogenic collapse, which took place over a period of 10–15 M.y., consistent with estimates from other orogens (e.g., Moser et al. 1996; Ketchum et al. 1998). The geometry of the uplifted core at the centre of the collapsed orogenic crust and its effect on the overlying upper crust remain poorly understood aspects of crustal evolution for the Snare River Terrane, particularly in regard to the preservation of metamorphic and structural continuity. The weakest part of the model is the removal of crust overlying the Ghost subdomain as large detachment faults (Fig. 3.14e). One candidate may be the Daran Lake Fault which extends SW into Ghost Lake, however, further work is needed to better delineate this geometry and kinematics of this fault zone (Fig. Additionally, detailed analysis of the fault zones intervening juxtaposed regional antiforms of the upper crust (e.g. Wijinnedi and Hinscliffe antiforms) are required to determine whether extension was accommodated by normal reactivation of these fault systems. Finally, F2d folding also presents a problem in that these folds may

also result from constrictional strain when the ductile Ghost subdomain was compressed against the migmatite transition zone during uplift.

3.6 Discussion

The complex sequence of polyphase deformation and the model for the structural evolution of the Snare River terrane provides insight into several fundamental problems pertaining to the evolution of high- and low-grade terranes. These include: (1) the role of structural and metamorphic diachroneity; (2) the importance of the migmatitic transition zones that link steeply dipping low-grade belts to gently dipping high-grade belts; (3) the contrasting tectonometamorphic processes that gave rise to the low-grade and high-grade belts; and (4) secular changes in deformation mechanisms during crustal evolution. These are discussed briefly below.

3.6.1 Structural and metamorphic diachroneity

The combination of overprinting fabric relationships and the restriction of certain structural elements to particular crustal levels resulted in a regional younging of structures as a function of paleodepth (Figs. 3.12, 3.13). The age-stratified crustal geometry is attributed to both the sequence of crustal evolution (i.e., D1 structures in the upper crust and D3 structures in the mid crust), and to the diachroneity of progressive D2 deformation during crustal thickening. D2 diachroneity also accounts for the transition from coaxial to non-coaxial deformation with crustal depth. Coaxial (to near-coaxial) F2a and F2b fold interference patterns (Type III, hook) that characterize the upper crust

contrast with the non-coaxial F2d (Type I, dome-and-basin) patterns in the mid crust, and simultaneously provide evidence of migration of the D2 deformation front to greater depths. In contrast, F2d dome-and-basin interference patterns exhibit decreasing amplitude from the Ghost subdomain upward into the transition zone where the F2d deformation front dissipated. Fold interference patterns in the Ghost subdomain were subsequently amplified by Paleoproterozoic cross-folding (F4) that affected the entire crust, in particular the southern subarea of Ghost subdomain where they resulted in non-coaxial Type II (crescent) interference patterns. A relative structural age map (Fig. 3.15) summarizes these observations to demonstrate the relationship between deformational diachroneity and fold interference patterns across the Snare River terrane. Additionally, high-level crustal decoupling also contributed to the observed pattern of metamorphic and deformational diachroneity as it isolated the upper crust from the effects of later orogenic events.

Diachroneity between metamorphism and deformation took place at all crustal levels. For instance, M2a metamorphism was associated with post-tectonic growth of cordierite in the upper crust (Figs. 3.4h, 3.6j,k), indicating that M2a outlasted D2 at that structural level. Similarly, in the transition zone and Ghost subdomain, post-tectonic diatexite in metaturbidites locally truncates F2a structures, indicating that M2b outlasted D2 there. These results indicate the potential for contrasting relative deformational and metamorphic ages at any crustal level.

The effects of crustal decoupling and structural / metamorphic diachroneity on crustal architecture have been well documented in the Neoarchean crustal section

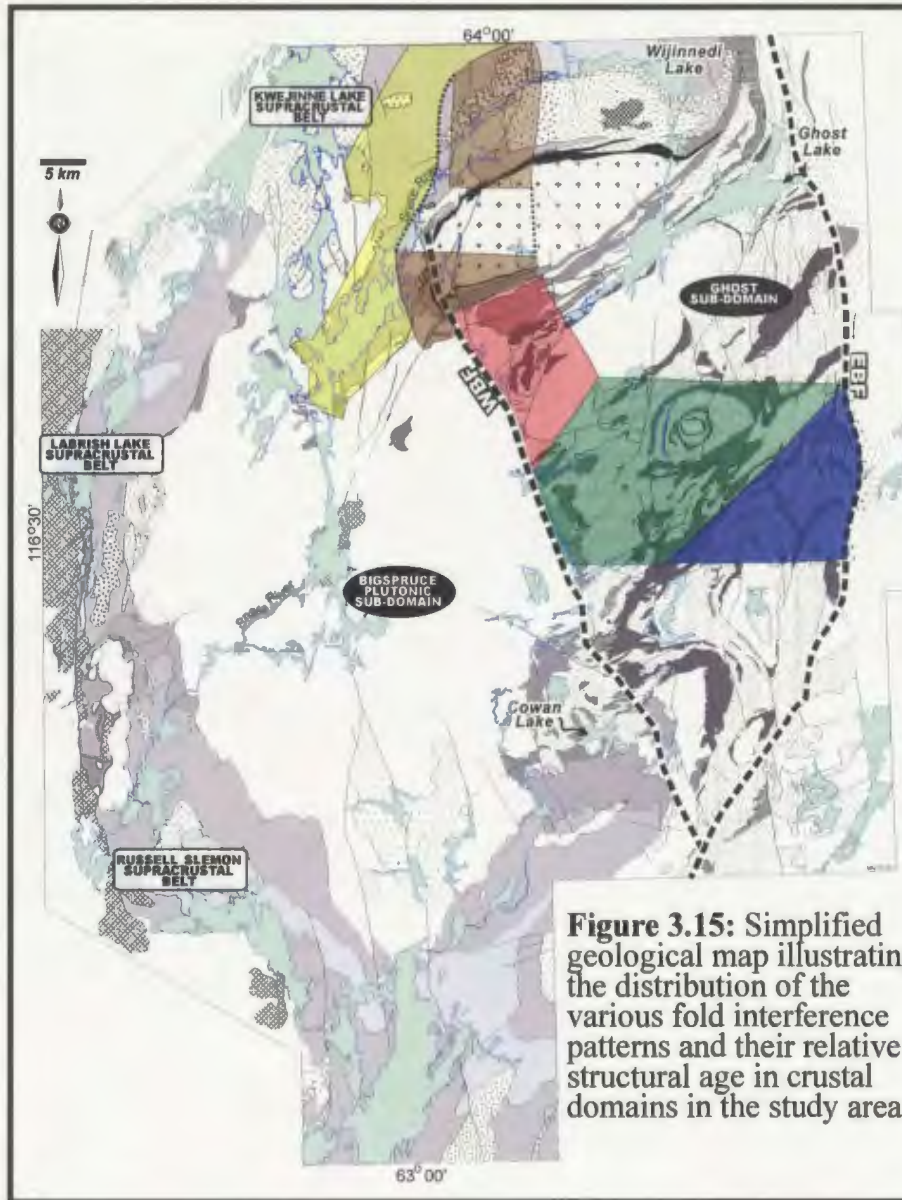
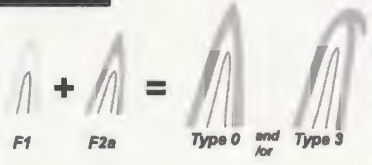
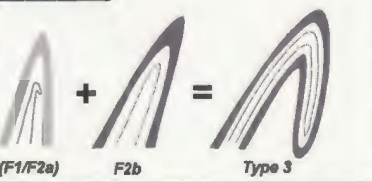
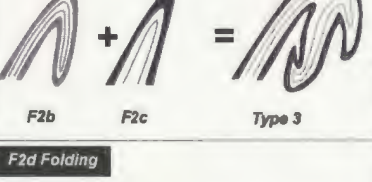
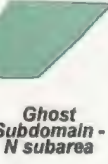


Figure 3.15: Simplified geological map illustrating the distribution of the various fold interference patterns and their relative structural age in crustal domains in the study area.

Structural domain	Sequence of Fold Superposition	Type
 KLSB - high structural level	F2a Folding 	Type 0 to 3 redundant superposition to local refolded folds NEAR COAXIAL
 KLSB - low structural level	F2b Folding 	Type 3 refolded folds NEAR COAXIAL
 Transition Zone	F2c Folding 	Type 3 refolded folds COAXIAL - LOCAL NON-COAXIALITY
 Ghost Subdomain - N subarea	F2d Folding 	Type 1 dome & basin NON-COAXIAL
 Ghost Subdomain - S subarea	F4 Folding 	Type 2 crescent, dome, mushroom NON-COAXIAL

exposed in the Kapuskasing Uplift (e.g., Corfu 1987; Bursnall et al. 1992; Krogh 1993; Moser et al. 1996). Their detailed integrated datasets demonstrate that similar processes operated in this orogen, including decoupling of the brittle upper crust with its record of old structures from the underlying ductile mid and lower crust, as well as migration of the structural and metamorphic fronts to greater crustal depths with time as a consequence of progressive downward stiffening of the orogen. Although these processes are by no means restricted to the Neoproterozoic, the occurrence of a similar tectonometamorphic evolution within broadly the same time frame (Snare Orogen, ca. 2674–2560 Ma; Kapuskasing Uplift ca. 2725–2585 Ma) implies that such processes were important elements of crust formation in the late Archean.

3.6.2 Migmatitic transition zone: Bridging the crustal gap

Exposure of the transition zone, which exhibits several structural attributes of both the low-grade supracrustal belts and high-grade Ghost subdomain, was crucial for correlating the deformation histories across the Snare River terrane. Preservation of both upper- and mid-crustal structures in the transition zone is attributed to D2 diachroneity and variable strain intensity, whereby older F2a and F2b structures were not completely transposed into F2c and F2d fabrics, resulting in a distinct structural domain characterized by complex and locally disharmonic folding.

The structurally highest level of the transition zone approximately coincides with the limit of M3 decompression metamorphism (Fig. 3.12a), lending support to the concept of upper crustal decoupling, whereby the effects of M3 were restricted to the mid crust. Telescoping of M2 isograds is evident across the transition zone, particularly in

northern Ghost subdomain (Fig. 3.2a), but structural and metamorphic continuity appears to have been maintained and no major structural or metamorphic breaks have been located. One possible interpretation is that the ductile rheology of the migmatitic transition zone facilitated uplift of the underlying mid crust and lateral extension was minimal at this crustal level. Details of the nature of the uplift remain poorly understood and further work is required to determine the extent to which the transition zone accommodated strain during uplift of the underlying mid crust.

3.6.3 The paradox of steep low-grade and shallow high-grade structures

The structural evolution outlined for the Snare River terrane provides a means to reconcile the contrasting structural styles in low- and high-grade belts. Evidence from this study suggests their genesis was a result of several protracted processes. The superstructure–infrastructure model of Culshaw et al. (2004) predicts that gently-dipping mid-crustal structures formed prior to exhumation due to the combined effects of structural diachroneity, decoupling of the upper and mid crust, and underthrusting of a lower plate, rather than to post-orogenic collapse. In the western Slave Province, prominent gently-dipping reflectors at mid-crustal depths were imaged on the LITHOPROBE *SNORCLE* transect south of the Snare River terrane (van der Velden and Cook 2002; see Fig 3.1 for location), implying they developed prior to exhumation. Furthermore, prior to superposition of F2d folding on the polydeformed mid crust of the Snare River terrane, fabrics are inferred to have been subhorizontal, compatible with crustal thickening by thrusting (Fig. 3.14; e.g. Kelly et al. 2000) and the LITHOPROBE *SNORCLE* images of the Slave crust.

However, numerous workers have proposed that prominent subhorizontal mid-crustal fabrics developed during ductile extensional flow in response to overthickening (e.g., Krogh 1993; Kelly et al. 2000; Fyson and Jackson 2004), and the process has been documented beneath Tibet, which is characterized by extensional collapse localized in the partially molten mid crust (Nelson 1992). Thermo-mechanical modelling predicts that mid-crustal channel flow and ductile extrusion are outcomes of this tectonic configuration (e.g., Beaumont et al. 2001), processes invoked by Cairns et al. (2005) to account for the subhorizontal structures in the Walmsley Lake area southeast of the Central Slave Basement complex. Although ductile flow of the mid-crust cannot be ruled out, we consider that in the Snare River terrane, subhorizontal structures developed principally during thrusting and crustal thickening, with subsequent modifications during extensional collapse being a secondary feature.

Such structural modifications of the thrust architecture occurred during both D3 extensional mid-crustal uplift and post-Archean deformational events (D4), as indicated by the telescoping of M2 isograds and the presence of late recumbent folds in the transition zone near Cowan Lake (Fyson and Jackson 2004). Mid-crustal uplift was also the mechanism principally responsible for lateral juxtaposition of the low- and high-grade domains across the belt.

The superstructure–infrastructure model of Culshaw et al. (2004) may also account for F2c and F2d folding events, which are not observed in the upper crust. In the model (Fig. 3.14d), collision of the Snare River terrane (upper plate) with a cratonic block (lower plate) resulted in overthrusting of the weakened Snare mid crust eastward onto the cratonic block. In this case, the cratonic block corresponds to the Central Slave

Basement Complex and continued underthrusting of this block generated the progressively younger structures in the mid crust of the Snare River terrane. Implicit in this model is underthrusting as the dominant driving force in the system, which resulted in migration of the deformation front to progressively deeper crustal levels as the system evolved.

Crustal thickening and decoupling are also central to understanding the origin of steeply- and gently-dipping structures. In the Snare River terrane, S2b fabric development and M2 diachroneity differ above and below the inferred zone of decoupling: in the upper crust, D2 crustal thickening was accompanied by development of low-grade pressure-solution, stylolitic and crenulation fabrics (S2b), whereas in the underlying migmatitic transition zone and mid crust, leucosome fabrics formed (S2c, S2d). Additionally, preservation of D0, D1 and the oldest phase of D2 are restricted to upper crustal levels that, together with the absence of later overprinting, suggest crustal decoupling was important. The decoupling event, although not well understood, may have been a consequence of the migration of diachronous deformational and metamorphic fronts to greater paleodepth as the leading edge of the Central Slave Basement Complex was underthrust beneath its orogenic superstructure composed of the Snare River terrane.

In summary, the similarities between the surface geometry of the Snare River terrane, the subsurface geometry displayed in the LITHOPROBE *SNORCLE* seismic reflection profile, and the crustal configuration predicted by the superstructure–infrastructure model of Culshaw et al. (2004) are striking and warrant further investigation through additional structural analysis and integrated modelling studies.

3.6.4 Crustal evolution and secular change in deformation mechanisms

Crustal evolution in the Snare River terrane took place in two contrasting tectonic regimes and can be correlated to changes in the mode of deformation and associated style of metamorphism. In tectonic regime 1 (TR1), early crustal development during D0 and D1 was characterized by protracted (>45 M.y.) lateral accretion of turbidite packages and their eventual intercalation with older volcano-plutonic crust. Metamorphic grade was low, consistent with minimal crustal thickening at this time, and the structural style exhibits *diachronous lateral imbrication* as originally distal thrust slices were successively accreted against each other in a broad shallow long-lived thrust stack. In contrast, D2 was a rapid event (<20 M.y.) involving substantial crustal thickening and reworking, and we infer that TR2 was a collisional tectonic regime characterized by diachronous *vertical imbrication* of crust. The style of metamorphism also changed and attainment of M2b granulite-facies conditions at >22 km depth implies a strong perturbation of the geothermal gradient, partly as a consequence of voluminous HT magmatic additions to the orogenic crust (Chapter 6). Crustal overthickening was followed by post-orogenic collapse, mid-crustal uplift and decompression metamorphism (M3) in which locations of isograds were dependent on the telescoped distribution of M2 high-grade cordierite in the transition zone and in Ghost subdomain. In summary, correlation of different structural processes during D1–D3 to specific stages of crustal evolution emphasizes the importance of deformation in controlling the amalgamation, metamorphic modification, and attainment of equilibrium in the Snare River terrane.

3.6.5 Regional implications

The sequence of Neoproterozoic deformation outlined for the turbidite packages of the Snare River terrane correlates well to craton-wide deformation events that similarly involved two major episodes of shortening and a terminal phase of crustal stabilization. The structural style also appears to exhibit similarities across the Slave Province despite local differences, which as discussed below appear to have been principally a function of proximity to the Mesoproterozoic cratonic nucleus, the age of the turbidite package, and diachroneity of deformation.

Turbidite sedimentation was diachronous and occurred in at least two different tectonic settings across the Slave Province: (i) in ensialic rift basins within the basement complex (Henderson 1985; Bleeker and Villeneuve 1995; Pehrsson 1998); and (ii) in ocean basins flanking the east and west sides of the Mesoproterozoic Central Slave Basement complex (Pehrsson et al. 1998; Bennett et al. 2005, this study; Cairns et al. 2005). Turbidite packages on rifted crust of the Central Slave Basement Complex were deposited at ca. 2660 Ma (e.g., at Point Lake and Watta Lake; Mortensen et al. 1991; Bleeker and Villeneuve 1995), whereas more distal turbidite successions west of the Central Slave Basement complex post-dated the ca. 2637 Ma Defeat suite plutons (e.g., Damoti Formation, Kwejinne Lake supracrustal belt to west, Pehrsson and Villeneuve 1999; Bennett et al. 2005). The age of distal turbidites east of Mesoproterozoic crust is unconstrained.

D1 fold-thrust belts provide evidence for horizontal shortening without substantial thickening, suggesting formation in an accretionary-wedge setting (e.g., King and Helmstaedt 1988; Relf 1992; King et al. 1992; Pehrsson 1998), as in the Kwejinne Lake

belt, and published data indicate that D1 deformation was diachronous, occurring both prior to and after the intrusion of Defeat Suite plutonism (~2620-2640 Ma) across the Slave Province (Bleeker and Villeneuve 1995; Bleeker et al. 1999; Pehrsson and Villeneuve 1999; Cairns et al 2005). Two main structural observations suggest that the locus of D1 deformation migrated both westward and eastward away from the Mesoarchean crustal core including post-2635 Ma D1 deformation of turbidite packages in the southwestern and southeastern Slave Province (Pehrsson 1999; Cairns et al. 2005; this study) and the occurrence of early D1 structures at Point Lake but their absence, east at Contwoto Lake (King and Helmsteadt 1988; Relf 1992). By the termination of D1 this had resulted in a new crustal configuration where outlying Neoproterozoic terranes had docked onto the margins of the Mesoarchean basement. One exception to this tectonic model of D1 lateral shortening without significant thickening occurred at Point Lake, where complex D1 structures indicate that important crustal thickening occurred at the turbidite–basement contact (King and Helmsteadt 1988; Relf 1992), suggesting that D1 strain was greatest where the outboard terranes docked against the Central Slave Basement Complex and elsewhere was partitioned with decreasing intensity throughout the fold-thrust belts.

D2 deformation histories and structural styles depend on proximity to the Mesoarchean cratonic core. In the marginal turbidite localities, significant crustal thickening occurred, as demonstrated by the formation of high-grade mid-crustal domains marginal to the Central Slave Basement Complex (Fig. 3.1). Closer to the cratonic core, crustal thickening and structural reworking were more moderate (e.g., at Contwoyto Lake). Finally, turbidite sequences overlying the central regions of the Mesoarchean core

underwent only minor F2 thickening and refolding of the D1 structures (e.g., at Watta Lake; Bleeker and Villeneuve 1995; Fig. 3.1). The NW-trending regional fold trends in the Watta Lake area contrast with the N and NE trends in the Kwejinne Lake and Indin Lake belts on the west side of the Central Slave Basement Complex and with the NNW to NW trending structural grain east of the cratonic core at Walmsley Lake (Fig. 3.1).

Collectively, these observations indicate that the bulk of D2 strain was accommodated in the marginal supracrustal belts which underwent rapid crustal thickening. Cairns et al. (2005) outlined a deformation sequence for the Walmsley Lake area that is very similar in both timing and tectonic style to that described here for the Snare River terrane. These authors demonstrated that an older upper-crustal tectonothermal domain with steep D1 and D2 structures was decoupled from a high-grade mid-crustal domain characterized by younger subhorizontal structures and metamorphism. The timing of events parallels that in the Snare River terrane (Table 3.2), with an early phase of D2 in the upper crust predating intrusion of the ca. 2597 Ma orogenic plutons and later deformation in the mid-crust (their D3) occurring after cessation of dated plutonism. Cairns et al. (2005) attributed the subhorizontal geometry of the mid-crustal domain to gravitational loading and mid-crustal flow, supporting the inference of enhanced crustal thickening in these marginal zones. This implies that post-orogenic extensional structures documented in several overthickened regions were a consequence of D2 overthickening in the external domains.

The broad synchronicity of these events over such large distances reveals much about craton-building processes during the Neoproterozoic. Recent structural datasets (e.g., Pehrsson 1998; Bleeker et al. 1999; Cairns et al. 2005; this study) have enabled

formulation of a more complete picture of the rates and processes involved in cratonization of the Slave Province. Clearly the occurrence and location of Mesoproterozoic crust was crucial to later crustal development, since it formed the nucleus onto which the younger Neoproterozoic crust was progressively accreted from both the east and west. The driving force for these compressive stresses that controlled cratonic growth remains enigmatic, but we speculate that lateral crustal accretion on both sides of the cratonic core is evidence that an embryonic form of plate tectonics involving lateral movement of microplates had evolved by the Neoproterozoic. However, the critical question of how and why apparently identical accretionary histories occurred on opposite margins of the cratonic core at the same time remains unanswered.

The contrasting tectonothermal histories across the Slave Province have significant implications with regard to diamond prospectivity. A first-order negative correlation is evident between the locations of uplifted formerly overthickened crust with perturbed geothermal gradients and the distribution of known diamond-bearing kimberlite arrays (Fig. 3.1). Specifically, in the southwest Slave Province no economic kimberlite deposits have been identified. In contrast, diamond-bearing kimberlite arrays are ubiquitous throughout the central and eastern regions, where the host supracrustal belts record only moderate crustal thickening and D3 mid-crustal uplift and orogenic collapse have not been documented. These observations may imply a relationship between the crustal tectonothermal history and the diamond stability field in the underlying mantle. Recognizing this relationship suggests that orogenic collapse structures, overthickened crust, and spinel-cordierite decompression textures may be indicators of areas with low diamond prospectivity in the Slave Province.

3.7 Conclusions

We have shown that contrasting structural topologies and deformation histories in the upper and mid crust of the Snare River terrane resulted from superposition of three Neoproterozoic tectonothermal events (D1/M1– D3/M3) and one phase of Paleoproterozoic deformation (D4). Structural analysis of the transition zone separating the low-grade supracrustal belts with steep structures from a mid-crustal granulite-facies domain with more gently-dipping structures has revealed that depth–time variations developed in a prograde M2 metamorphic gradient without obvious structural or metamorphic discontinuities. The oldest Neoproterozoic deformation events (D1, D2a-b) are preserved in the higher structural levels, whereas younger events (D2c-d, D3) occur in the mid crust. The transition zone, which is characterized by migmatitic rocks formed during M2, provides a crucial link between these structural levels, exhibiting structural elements common to both of them (i.e., F2b-F2d, S2a, S2b and F3/S3). M2 both predated (M2a) and was coeval with (M2b) voluminous ca. 2597 Ma orogenic plutonism.

Preservation of D0 and D1 structures is restricted to the upper crust of the Kwejinne Lake supracrustal belt. F1 fold successions, defined by reversals in S0 facing directions, are best developed on the northwest limbs of regional D2 folds. High-level coaxial F2a and F2b fold sets are associated with axial planar S2a fabrics defined by biotite, cordierite, and sillimanite \pm melt that formed at the M2a thermal peak. Post-tectonic cordierite is linked to ca. 2597 Ma plutonism. At deeper levels, S2a and S2b leucosome fabrics have mineral assemblages indicative of anatexis at progressively

higher temperatures, i.e., upper-amphibolite facies in the transition zone and granulite-facies in the Ghost subdomain. Folding of leucosomes defines mesoscopic F2c and F2d fold sets, which are coaxial and non-coaxial with earlier structures, respectively. Diatexite formation was post-tectonic in both the transition zone and mid-crust, demonstrating that M2b outlasted D2. Formation of F2c and F2d fold sets, S2c high strain zones, and D3 conjugate shear sets was depth-dependent and all are restricted to the lower levels of the transition zone and mid crust. Finally, the geographic distribution of M3 decompression assemblages in metapelites broadly coincides with the distribution of D3 shears in the Snare River terrane, implying a causal relationship. During the Paleoproterozoic, the D0–D3 Neoproterozoic deformations were overprinted by F4 folds, which are non-coaxial, steep northerly-plunging, upright structures at all crustal levels.

The crustal architecture of the Snare River terrane consists of a series of overturned antiforms in the upper crust and transition zone juxtaposed against the dome-and-basin and crescent structures in the Ghost subdomain. Progressive rotation of fold axes of the major deformation phases, from steep SW-plunging F2a and F2b structures in the upper crust, through steep NW-plunging F2b and F2c folds in the transition zone, to shallow NE-plunging F2d structures in mid-crust, is at least in part an effect of D4. The contrasting structural styles that characterize architecture in the low- and high-grade domains of the Snare River terrane can be explained by four-stage model:

- I) D1 – Protracted diachronous lateral thin-skinned shortening of volcanic blocks and intervening turbidite basins achieved by lateral telescoping without significant crustal thickening and resulting in intercalation of turbidite packages with older volcano-plutonic crust by ca. 2608 Ma. Compressive stresses are

inferred to have been the result of horizontal crustal motion between the Snare River terrane and the Central Slave Basement complex.

- II) D2 – Nappe tectonics and crustal thickening involving: (a) early near-coaxial refolding of the D1 fold belt into F2a folds coinciding with M2a metamorphism and minor crustal thickening, (b) large-scale coaxial F2b folding and establishment of upper and lower limb nappe geometry, accompanied by (c) voluminous ca. 2597 Ma pluton emplacement and onset of M2b metamorphism, (d) decoupling of the upper crust from the more ductile migmatitic transition zone, and (e) continued shortening of the lower limb of a crustal-scale nappe, leading to the establishment of a superstructure (Snare River terrane) and infrastructure (leading edge of the Central Slave Basement complex) crustal configuration.
- III) D3 – Post-orogenic collapse and mid-crustal uplift prior to ca. 2585 Ma, crustal thinning by displacement on conjugate shear sets, and core complex formation. M3 decompression metamorphism affected the transition zone and Ghost subdomain, demonstrating uplift of these crustal levels, with no corresponding uplift of the upper crust.
- IV) D4 – Paleoproterozoic NE-SW shortening involving low-grade cleavage formation and steep NNW-plunging open F4 folding at all crustal levels.

The combined effects of metamorphic and deformational diachroneity and depth-dependent progressive deformation resulted in a younging of the structural architecture with paleodepth. Variations in relative structural age across the Snare River terrane demonstrate a close relationship between deformational diachroneity and regional fold

interference patterns. Coaxial to near-coaxial F2a and F2b refolding (Type III, hook) that characterizes the upper-crust contrasts with non-coaxial F2d (Type I, dome-and-basin) fold superposition in the mid-crust. The occurrence of hook, dome-and-basin, and crescent fold interference patterns in the transition zone represents F2c and F2d refolding of the complex F1–F2a–F2b geometry. Collectively, the distribution of fold interference patterns across the Snare River terrane demonstrates migration of the D2 deformation front to greater depths during crustal thickening.

Structural datasets for the juxtaposed steep, low-grade upper-crust and shallow, high-grade mid-crust in the Snare River terrane conform well to the superstructure–infrastructure model of Culshaw et al. (2004). As predicted by the model, gently-dipping D2 mid-crustal structures formed after the steep polyphase D0–D2 structures in the upper crust. The presence of undulating low-angle reflectors at mid-crustal depths on the Lithoprobe SNORCLE transect demonstrates a pre-exhumation origin, which is inferred to be a consequence of mid-crustal thrusting during crustal thickening. The narrow migmatitic transition zone is critical to understanding the progression of deformation from the upper- to the mid-crust and its exposure in two areas of the Snare River terrane was essential in assessing the applicability of the superstructure–infrastructure model. In this case, the infrastructure comprising Central Slave Basement Complex and its environs underthrust the superstructure composed of the Snare River terrane, generating progressively younger and flatter structures with depth.

Crustal evolution of the Snare River terrane and the Slave Province as a whole documents secular changes in the principal modes of deformation and associated styles of metamorphism. Tectonothermal development in supracrustal belts was dependent on the

age of the turbidite package, the rate and degree of deformational diachroneity, and proximity to the Mesoarchean Central Slave Basement complex. Neoproterozoic cratonization occurred in three stages: (i) horizontal shortening during D1 resulted in docking of outboard supracrustal belts onto a Mesoarchean protocraton core, with the locus of D1 migrating away from the core as strain was partitioned through the accreted crust; (ii) during D2, nappe tectonics in the marginal terranes resulted in significant crustal thickening associated with granulite-facies metamorphism, implying strong perturbation of crustal geotherms, whereas in more proximal supracrustal belts thickening was moderate and peak conditions were attained earlier than in the marginal terranes. These observations demonstrate that the bulk of D2 strain was accommodated by rapid crustal thickening in the marginal terranes, compatible with limitation of the ensuing post-orogenic collapse to these localities. Finally, the broad synchronicity of D1-D3 across the Slave Province reveals that accretion of Neoproterozoic crust to the southeast and southwest margins of the Mesoarchean basement was essentially coeval, implying that embryonic plate tectonics processes were operating during cratonization.

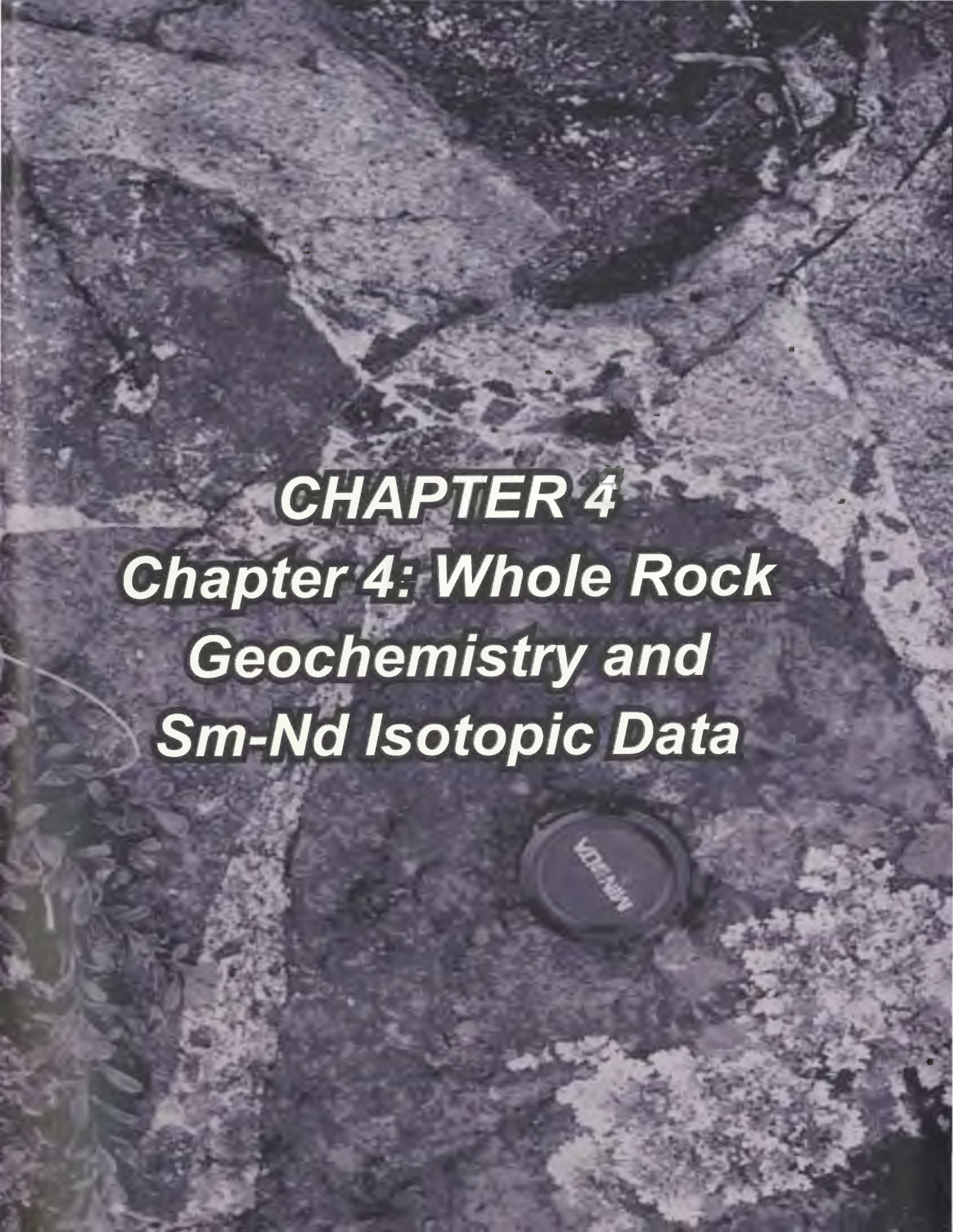
3. References

- Beaumont, C., Jamieson, R. A., Nguyen, M. H. and Lee, B., 2001. Himalayan tectonics explained by extrusion of a low-viscosity crustal channel coupled to focused surface denudation, *Nature* 414: 738-742
- Bennett, V., Jackson, V.A., Rivers, T., Relf, C., Horan, P and Tubrett, M, 2005. Geology and U-Pb Geochronology of the Late Archean Snare River Terrane: Tracking Evolving Tectonic Regimes and Crustal Growth Mechanisms. *Canadian Journal of Earth Sciences, LITHOPROBE Special Edition* 42: 895-934.
- Bleeker, W., and Villeneuve, M. 1995. Structural studies along the Slave portion of the SNORCLE Transect; in *Slave-NORthern Cordillera Lithospheric Evolution (SNORCLE), Report of 1995 Transect Meeting, April 8-9, University of Calgary*, edited by F. Cook and P. Erdmer, LITHOPROBE Report No. 44, p. 8-14.
- Bleeker W., Ketchum, J.W.F., Jackson, V.A., and Villeneuve, M.E. 1999a. The Central Slave Basement, Part I: its structural topology and autochthonous cover. *Canadian Journal of Earth Sciences*, 36: 1083-1109.
- Bleeker W., Ketchum, J.W.F., and Davis, W.J. 1999b. The Central Slave Basement, Part II: Age and tectonic significance of high strain zones along the basement-cover contact. *Canadian Journal of Earth Sciences*, 36: 1111-1130.
- Bowring, S.A., and Williams, I.S. 1999. Priscoan (4.00 – 4.03 Ga) orthogneisses from northwestern Canada: *Contributions to Mineralogy and Petrology*, 134: 3-16.
- Bowring, S.A., Williams, I.S., and Compston, W. 1989. 3.96 Ga gneisses from the Slave Province Canada, Northwest Territories, Canada. *Geology*, 17: 971-975
- Bursnall, J.T., Leclair, A.L., Moser, D.E. and Percival, J.A. 1994. Structural correlation within the Kapuskasing uplift. *Canadian Journal of Earth Sciences* 31: 1096-1103.
- Cairns, S., Relf, C., MacLachlan, K. & Davis, W. 2005. Late Archean decoupling of upper and mid crustal tectonothermal domains in the southeast Slave Province; evidence from the Walmsley Lake area. *Canadian Journal of Earth Sciences, LITHOPROBE Special Edition*, 42: 869 – 894.
- Chacko, T., Creaser, R.A., Farquhar, J. and Muehlenbachs, K., 1995. The deep crust of the western Slave Province – Initial petrological and isotopic data from high grade rocks of the Ghost Domain. *In: Slave – Northern Cordillera Lithospheric Evolution Workshop (SNORCLE) Transect and Cordilleran Tectonics Workshop Meeting, 8 – 9 April, Calgary. Compiled by F. Cook and P. Erdmer. Lithoprobe Report* 44, pp.4-7.
- Chery, J., 2001. Core complexes mechanics: from the Corinth Gulf to the Snake Range: *Geology*, 29: 439-442.

- Corfu, F. 1987. Inverse age stratification in the Archean crust of the Superior Province: evidence for infra- and subcrustal accretion from high resolution U-Pb zircon and monazite ages. *Precambrian Research* 36: 259-275.
- Culshaw, N.G., Beaumont, C., and Jamieson, R.A. 2004. Geodynamic models of contrasting structural styles and ages in the upper- and lower- crust of collisional orogens: resolution of the structural vs. seismic paradox. GAC - MAC Joint annual meeting, St Catharines, program and abstracts, volume 29, page 331.
- Davis, W.J., and Bleeker, W. 1999. Timing of plutonism, deformation and metamorphism in the Yellowknife Domain, Slave Province, Canada. *Canadian Journal of Earth Sciences*, 36: 1169-1187.
- Fountain, D.M., and Salisbury, M.H., 1981. Exposed cross-sections through the continental crust: implications for crustal structure, petrology, and evolution, *Earth and Planetary Science Letters*, 56: 263 – 277.
- Fyson, W.K., and Helmstaedt, H. 1988. Structural patterns and tectonic evolution of supracrustal domains in the Archean Slave Province, Canada. *Canadian Journal of Earth Sciences*, 25: 301 - 315.
- Fyson, W.K. and Jackson, V.A., 1991. Reorientation of structures near granitic plutons and orthogonal lineaments, Russell Lake supracrustal domain, southwestern Slave Province. *Canadian Journal of Earth Sciences*, 28: 126 - 135.
- Fyson, W.K. and Jackson, V.A., 2004. Structures in Supracrustal and Plutonic Rocks, Snare River, Archean Slave Province: Problems of Interpretation and a Tectonic Model; C.S. Lord Northern Geoscience Centre, NWT Open File 2004-03, 33 p.
- Hamilton, W.B., 1998. Archean magmatism and deformation were not the products of plate tectonics. *Precambrian Research*, 91: 143 – 179
- Henderson, J.B., 1985. Geology of the Yellowknife – Hearne Lake area, District of Mackenzie: segment across an Archean Basin. Geological Survey of Canada, Memoir 414, 135 pp.
- Henderson, J.B. and Schaan, S.E. 1993. Geology of the Wijnnedi Lake area: a transect into mid-crustal levels in the western Slave Province, District of Mackenzie, Northwest Territories. *In Current Research, Part C. Geological Survey of Canada, Paper 93-1C*, pp. 83-91.
- Henderson, J.B. 2004. Geology of the Wijnnedi Lake area, District of Mackenzie, Northwest Territories. Geological Survey of Canada, Bulletin 576, 115p.
- Hyde, D.J. 2000. Geology and geochronology of the Gooseberry Hill area, Kwejinne Lake, Northwest Territories. Unpublished B.Sc. Hons. Thesis, Memorial University of Newfoundland.
- Kelly, N.M., Clarke, G.L., Carson, C.L., and White, R.W., 2000. Thrusting in the lower crust:

- evidence from the Oygarden Islands, Kemp Land, East Antarctica. *Geological Magazine*, 137: 219 – 234.
- Ketchum, J.W.F., Heaman, L.M., Krogh, T.E., Culshaw, N.G., and Jamieson, R.A., 1998, Timing and thermal influence of late orogenic extension in the lower crust: A U-Pb geochronological study from the southwest Grenville orogen, Canada: *Precambrian Research*, 89: 25–45.
- King, J.E., and Helmstaedt, H., 1988. Deformational history of Archean fold belt, eastern Point Lake area, Slave Structural Province, N.W.T. Canada. *Canadian Journal of Earth Sciences*, 26: 106 – 118.
- Kisters, A.F.M., Stevens, G., Dziggel, A., Armstrong, R.A., 2003. Extensional detachment faulting and core-complex formation at the base of the Barberton greenstone belt: evidence for a 3.2 Ga orogenic collapse. *Precambrian Research* 127, 355-378
- Kretz, R. 1983. Symbols for rock-forming minerals. *American Mineralogist* 68: 277 – 279.
- Krogh T.E., 1993, High precision U-Pb ages for granulite metamorphism and deformation in the Archean Kapuskasing structural zone, Ontario: implications for structure and development of the lower crust., *Earth and Planetary Science Letters*, 119, 1-18
- Lana, C., Gibson, R. L., Kisters, A. and Reimold, W. U., 2003a. Archean crustal structure of the Kaapvaal craton, South Africa – evidence from the Vredefort dome. *Earth and Planetary Science Letters*, 206, 133–144
- Mortensen., J.K. Davis, D.W., Relf, C., and King, J.E., 1991. U-Pb zircon ages from the Shallow Bay volcanoclastic belt, Contwoyto Lake area: age constraints for Lupin-type iron formation. In *Radiogenic age and isotopic studies*. Geological Survey of Canada, Paper 91-2, pp. 9-15.
- Moser, D.E., Heaman, L.M., Krogh, T.E. & Hanes, J.A., 1996. Intracrustal extension of an Archean orogen revealed using single-grain U-Pb zircon geochronology. *Tectonics* 15, 1093-1109.
- Nelson, K.D., 1992. Are crustal thickness variations in old mountain belts like the Appalachians a consequence of lithospheric delamination? *Geology*, 20: 498 - 502
- Pehrsson., S.J., 1998. Deposition, deformation and preservation of the Indin Lake supracrustal belt, Slave Province, Northwest Territories. Unpublished Ph.D. thesis, Queens University, Kingston, Ontario.
- Pehrsson, S.J., and Villeneuve, M.E. 1999. Deposition and imbrication of a 2670-2629 Ma supracrustal sequence in the Indin Lake area, southwestern Slave Province, Canada. *Canadian Journal of Earth Sciences*, 36: 1149-1168.
- Pehrsson, S.J., Chacko, T., Pilkington, M., Villeneuve, M.E. and Bethune, K., 2000. Anton

- terrane revisited: Late Archean exhumation of moderate-pressure granulite terrane in the western Slave Province. *Geology*, 28: 1075-1078.
- Percival, J.A., and West, G.F., 1994, The Kapuskasing uplift: A geological and geophysical synthesis: *Canadian Journal of Earth Sciences*, 31: 1256–1286
- Perks, M.A. 1997. The mid crust of the western Slave Province - Geological Mapping, geochemistry and U - Pb Geochronology of the Forked Lake Area, Southwestern Slave Province, NWT. M.Sc. thesis, University of Alberta, Edmonton, Alberta.
- Platt, J. P. & Lister, G. S., 1985. Structural history of high-pressure metamorphic rocks in the southern Vanoise massif, French Alps, and their relation to Alpine tectonic event. *Journal of Structural Geology*, 7: 19–35
- Ramsay, J.G., 1967. *Folding and Fracturing of Rocks*, 568p. McGraw-Hill, New York.
- Ramsay, J.G., Casey, M. and Kligfield, R., 1983. Role of shear in development of the Helvetic fold-thrust belt of Switzerland. *Geology*, 11, 439-442
- Ramsay, J.G., and Huber, M.I., 1987. *The Techniques of Modern Structural Geology, Volume 2: Folds and Fractures*. Academic Press, San Diego.
- Ratschbacher, L., Frisch, W., Neubauer, F., Schmid, S. M., and Neugebauer, J., 1989. Extension in compressional orogenic belts; the Eastern Alps. *Geology*, 17: 404-407.
- Relf, C., 1992. Two distinct shortening events during late Archean orogeny in the west-central Slave Province, Northwest Territories Canada. *Canadian Journal of Earth Sciences*, 29: 2104-2117.
- Sénéchal, G., Mareschal, M., Hubert, C., Calvert, A.J., Grandjean, G. and Ludden, J.N., 1996, Integrated geophysical interpretation of crustal structures in the northern Abitibi belt: constraints from seismic amplitude analysis, *Canadian Journal of Earth Sciences*, 33: 1343-1362.
- van der Velden, A.J., and Cook, F.A., 2002. Products of 2.65 – 2.58 Ga Orogenesis in the Slave Province correlated with Slave – Northern Cordillera Lithospheric Evolution (SNORCLE) seismic reflection patterns. *Canadian Journal of Earth Sciences*, 38: 1189 – 1200.
- Villeneuve, M.E., and Henderson, J.B. 1998. U-Pb geochronology of the Wijinnedi Lake area, Slave Province, District of Mackenzie, NWT. *In Radiogenic Age and Isotopic studies: Report 11*. Geological Survey of Canada, 1998-F, pp. 99-106.
- Windley, B.F and Bridgewater, D., 1971. The evolution of Archean low- and high-grade terrains. *Geological Society of Australia Special Publication*, 3: 33 – 46.



CHAPTER 4

***Chapter 4: Whole Rock
Geochemistry and
Sm-Nd Isotopic Data***

4 Formation, Growth and Evolution of Neoproterozoic Crust: Geochemical and Isotopic Constraints from the Snare River terrane, Slave Province, Canada.

V. Bennett¹, T. Rivers¹, C. Relf², V. A. Jackson² and M. Brannstrom³

1. Department of Earth Sciences, Memorial University of Newfoundland, St. John's, NL.

A1B 3X5.

2. Northwest Territories Geoscience Office, Yellowknife, NT, X1A 2R3

3. Palatine Geological, Bowen Island, BC. V0N 1G0

Journal of Petrology (*accepted*)

NWT Geoscience Office Contribution number 0009.

4.1 Abstract

Geochemical and Nd isotopic data are used to investigate the ca. 90 M.y. magmatic evolution of the Neoproterozoic Snare River terrane, southwestern Slave Province. Early crust formation involved plume-related tholeiitic magmatism followed by initiation of a protoarc by subcretion; crustal products include juvenile, LREE-enriched tholeiites and slab-derived, HREE-depleted TTGs (Group 1 magmas). As subcretion evolved into subduction, metaluminous magmatism diversified with the emplacement of granodioritic and mafic complexes (Group 2). Protoarc–continent collision was marked by LREE-enriched sanukitoids and five diverse metaluminous to peraluminous granitoid suites (Group 3), and was succeeded by post-orogenic collapse, lower crustal delamination, renewed sanukitoid magmatism and emplacement of two peraluminous granitoid suites (Group 4).

Mantle-melting events demarcate the four stages of crustal evolution, implying a linked crust–mantle evolution. Crustally-derived magmas evolved towards quartz- and alkali-richer compositions during crustal growth and orogenesis, and peraluminous magmas became more abundant. A time-space analysis demonstrates the oldest magmas occur in the upper crust, whereas younger syn-orogenic magmas intruded at mid-crustal levels. Since the Snare River terrane developed in an oceanic setting before accretion to pre-2.8 Ga crust, the latter played a minimal role in the petrogenesis of most magmas although its distribution exerted a fundamental control on Neoproterozoic tectonic development of the Slave Province as a whole.

KEY WORDS: *Magmatic evolution; Neoproterozoic; Pre-2.8 Ga crust; Protoarc; Secular geochemical trends*

4.2 Introduction

It has been argued that formation of the Earth's crust took place predominantly during the Archean (e.g. Armstrong 1981; 1991) and that Neoproterozoic magmatism led to crustal stabilization and the formation of enduring cratonic nuclei (e.g. Nisbet 1987; Kröner et al. 1992; Davis et al. 1994). Furthermore, seismic studies of Neoproterozoic crust and upper mantle have imaged features in the upper mantle interpreted as subduction scars (e.g. Calvert et al. 1995; van der Velden and Cook 2002), indicating at least local occurrence of subduction by this time. If these inferences are correct, geochemical and isotopic studies of Neoproterozoic magmatic rocks have the potential to yield insight into mechanisms of crust formation and cratonic evolution. Recent studies of the Slave craton in NW Canada, the Dharwar craton in India, and the Kaapvaal and Zimbabwe cratons in southern Africa have demonstrated that crust formation and growth during the Paleo- and Neoproterozoic occurred predominantly by episodic accretion of tonalite-trondhjemite-granodiorite (TTG) complexes (e.g. Stern and Bleeker 1998; Horstwood et al. 1999; Chadwick et al. 2000; Poujol et al. 2003), which led to the gradual accumulation and emergence of buoyant, differentiated cratonic blocks. These blocks subsequently became sites of Neoproterozoic crustal growth with the formation of granite–greenstone and granite–volcano-sedimentary belts. In the case of the Slave Province, the granite–greenstone belts are inferred to have developed on or adjacent to the TTG basement blocks, whereas the granite–volcano-sedimentary belts formed distally and were subsequently accreted to them (e.g. Yamashita et al. 2000; Cousens 2000; Cousens et al. 2002; Pehrsson and Villeneuve 1999; Bennett et al. in press). In chapter 2, it was speculated that following the emergence

of pre-2.8 Ga ensialic basement blocks, crustal processes evolved towards an incipient plate tectonic regime during the Neoarchean. This new regime involved reworking of older TTG crust, genesis of new granite–greenstone crust, and formation of granite–volcano-sedimentary crust outboard of the composite TTG–granite–greenstone blocks. In this model, the presence of Paleo- and Mesoarchean basement is pivotal to subsequent Neoarchean crustal growth. In the Slave Province, the eastern margin of the Paleo- to Mesoarchean TTG basement, known as the Central Slave Basement Complex (Bleeker et al. 1999a, b), is demarcated by Pb and Nd isotopic boundaries defined by Thorpe et al. (1992) and Davis and Hegner (1992). However, the geometry of the western margin remains enigmatic, particularly in the southwest where the geochemical/isotopic database is limited and exposures of Paleo- to Mesoarchean crust have yet to be identified.

In this paper, we present geochemical and Nd isotopic data for magmatic and metasedimentary rocks from the Snare River terrane, a Neoarchean granite–volcano-sedimentary belt in the southwestern Slave Province. The primary objectives are to use the integrated datasets to constrain the magmatic evolution of the Snare River terrane, document the mechanisms of crust formation and growth including assessment of the role played by Paleo- to Mesoarchean basement, and evaluate the implications for the Slave Province as a whole.

4.3 Geological Setting

4.3.1 Regional Geological Setting

The Slave Province (Fig. 4.1a) consists of four principal lithotectonic components:

(i) pre- 2.8 Ga basement complexes, (ii) 2.71-2.63 Ga magmatic–sedimentary belts, (iii) 2.63-2.58 Ga plutonic rocks, and (iv) ca. 2.60-2.57 Ga granite–granulite terranes. Pre-2.8 Ga basement complexes occur west of the Nd and Pb isotopic boundaries (Fig. 4.1a) and comprise ca. 4.06-2.8 Ga orthogneiss of TTG-affinity in the Central Slave Basement Complex, and its cover, the Central Slave Cover Group (e.g. Bowring and Williams 1999; Isachsen and Bowring 1997; Bleeker et al. 1999a, b; Emon et al. 1999; Ketchum and Bleeker 1999, 2000; Sircombe et al. 2001). The ca. 2.71 - 2.63 Ga magmatic – sedimentary belts can be subdivided into two groups on the basis of age and tectonic character of the supracrustal rocks: (i) a granite–greenstone association consisting of ca. 2.71-2.70 Ga mafic volcanic rocks (Kam Group and equivalents), subordinate ca. 2.66 Ga felsic volcanic rocks (Banting Group and equivalents), and turbidites deposited after ca. 2.66 Ga (Henderson et al. 1987; Isachsen 1992; Bleeker and Villeneuve 1995); and (ii) a younger granite–volcano-sedimentary association characterized by the lack of ca. 2.7 Ga Kam Group correlatives, the presence of ca. 2.68-2.66 Ga felsic volcanic rocks (Banting correlatives), and turbidites deposited after ca. 2.63 Ga (Pehrsson and Villeneuve 1999; Bennett et al. in press; Cairns et al. 2005). 2.63 – 2.58 Ga plutonic rocks can be subdivided into a 2.63-2.60 Ga syn-D1 group (e.g. Defeat, Concession and Siege suites), and a ca. 2.60-2.58 Ga syn-D2/D3 group (e.g. Stagg, Awry, Prosperous, Contwoyto and Yamba suites; Henderson 1985; Davis and Hegner 1992; van Breemen et al. 1992; Davis et al. 1994; Villeneuve et al. 1997; Davis and Bleeker 1999) that exhibit broad secular variation from metaluminous diorite and tonalite to peraluminous granite (Davis et al. 1994; Yamashita et al. 1999, 2000). The 2.60-2.57 Ga granite terranes (e.g. Stublely and

Cairns 1998; Pehrsson et al. 2000; Jackson and Bennett 2003; Bennett et al. 2003, 2005; Henderson 2004) are composed predominantly of polydeformed plutonic rocks with minor older supracrustal remnants that exhibit HT-LP metamorphic signature. The granitic terranes typically consist of large expanses of peraluminous and subordinate metaluminous plutonic rocks coring regions characterized by amphibolite- and locally, granulite-grade country rocks.

4.3.2 Geological Setting of the Snare River Terrane

The Snare River terrane, southwestern Slave Province (Fig. 4.1b), consists of a high-grade core of HT-LP granulite- and amphibolite-facies rocks (Ghost and Bigspruce subdomains), surrounded by the greenschist- to amphibolite-facies Kwejinne Lake (KLSB), Labrish Lake (LLSB) and Russell-Slemon (RSSB) granite–volcano-sedimentary belts (Henderson and Schaan 1993; Pehrsson et al. 2000; Bennett et al. in press). Supracrustal components can be correlated with the volcanic and turbidite packages in low-grade, upper-crustal greenstone belts (Jackson 2000; Jackson and Bennett 2003; Bennett et al. in press). A 1:30 000 scale geological transect (Fig. 4.1b) across the Snare River terrane was undertaken to define the nature of, and relationships among, the granulite and amphibolite subdomains, supracrustal belts and the diverse suites of plutonic rocks (Bennett and Dunning 1998; Bennett et al. 2000, 2002, 2003, in press). The granite–volcano-sedimentary belts consist of bimodal volcanic rocks, syn-volcanic plutons, and turbidites, with tectonic lenses of these lithologies preserved in the granulite-facies Ghost subdomain. Felsic volcanism in the bimodal volcanic sequences has been dated at $2673 \pm$

1.5 Ma and $2658 \pm 1.2/-0.8$ Ma (Mortensen et al. 1992; Villeneuve and Henderson 1998); mafic to tonalitic syn-volcanic intrusions with ages of 2674.3 ± 2.9 Ma and 2673.0 ± 0.8 (Bennett et al. in press) mantle the 2654 ± 4 Ma trondhjemitic-granodioritic Hinscliffe complex (Fig. 4.1b; Villeneuve and Henderson 1998), which was coeval with the younger volcanic episode. Metaturbidite, comprising greywacke, mudstone and discontinuous iron formation, is the dominant supracrustal lithology and pre- and post ca. 2635 Ma packages are recognized in the Snare River terrane.

The Snare River terrane exhibits an Archean deformation history compatible with that defined for the Slave Province as a whole, comprising three distinct events (D1 – D3). In the Snare River terrane, D1/M1 was a greenschist- to lower-amphibolite-facies event extending from ca. 2674-2608 Ma and involving diachronous F1 folding and associated fabric development. D2/M2 involved refolding of D1 structures, major crustal thickening and granulite-facies metamorphism between ca. 2608-2600 Ma. D3/M3 involved ca. 2600-2580 Ma deformation, in part synchronous with High Temperature – Low Pressure (HT- LP) metamorphic overprinting of D2/M2 in Ghost subdomain and the lower structural levels of the granite–volcano-sedimentary belts, with metamorphism outlasting D3 by as much as 20 M.y. (e.g. 2560 Ma metamorphic zircon growth; Perks 1997). The pluton emplacement history and age relationships among the principal components of the Snare River terrane are shown schematically in Figure 4.2. An evolutionary framework involving the concept of a *tectonic regime* (TR) was proposed in Chapter 2, the term being used to embrace deformational, metamorphic and magmatic events that occurred in a similar tectonic setting. In this scheme, the tectonic history of the Snare River terrane

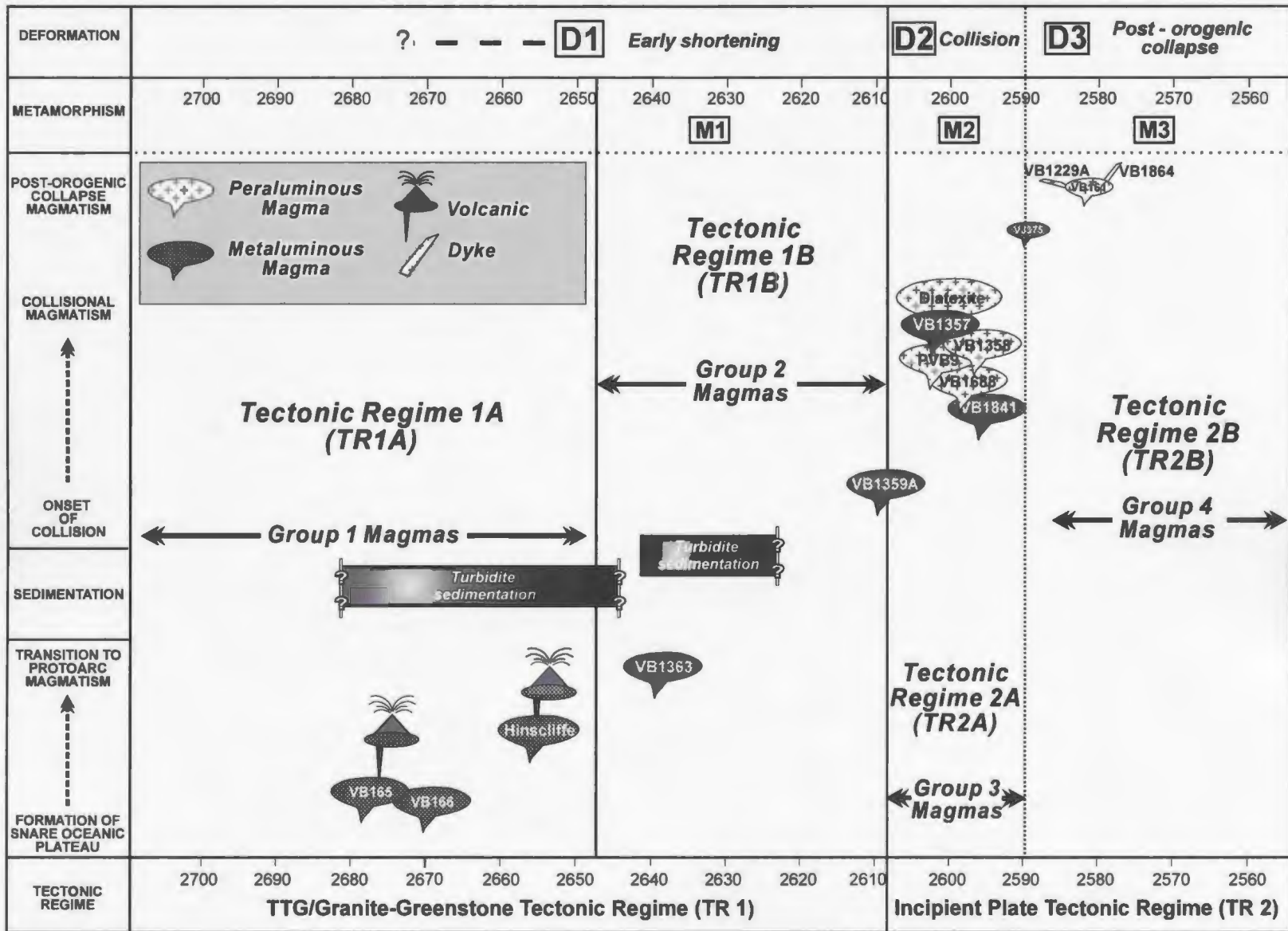


Figure 4.2: Diagram illustrating temporal relationships between magmatic group, tectonic regime and the tectonometamorphic evolution of the Snare River terrane.

encompassed two tectonic regimes, TR1 comprising D1/M1 and ca. 2674-2608 Ma magmatism, and TR2 comprising D2/M2 and D3/M3 and ca. 2600-2580 Ma magmatism. The data presented in this study permit improved definition of the magmatic aspects of these two tectonic regimes.

4.4 Magmatic Groups of the Snare River Terrane

Magmatic rocks in the Snare River terrane have been subdivided into four groups on the basis of age and tectonic regime (Fig. 4.2; Chapter 2; Table E1). Metaluminous compositions predominate in the older groups 1 and 2, whereas both metaluminous and peraluminous compositions occur in the younger groups 3 and 4. Group 1 encompasses volcanic and coeval plutonic bodies that crystallized between ca. 2674-2654 Ma and range from basalt to rhyodacite and gabbro to tonalite. Field relationships indicate this group was affected by early D1/M1. Group 2, with a compositional range from ultramafic hornblendite to granodiorite, intruded syn- to post-D1/M1 in the interval ca. 2637-2608 Ma. Group 3 is predominantly granitic and was emplaced syn-to late-D2/M2 at ca. 2597 Ma. Group 4 comprises small-volume melts of tonalitic to granitic composition that intruded syn- to post-D3/M3 from ca. 2590 to 2585 Ma.

Representative samples of each group were slabbed, stained and examined in thin section prior to analysis, permitting subdivision of the groups into suites on the basis of composition, field and petrographic criteria. A summary of important characteristics and cross-cutting relationships of each suite is given in Table 4.1 and representative features

are illustrated in Fig. 4.3. Detailed petrographic descriptions and sources of U-Pb age data used to subdivide each magmatic group are provided in Appendix E.

4.5 Analytical Techniques

Major- and trace-element geochemistry and Sm-Nd isotopic analyses were carried out for this study. All analyzed samples were related, directly or indirectly, to dated plutons. Sample locations are listed in Tables 4.2-4.4 and shown on Fig. 4.1. After clean crushing and grinding, individual powders were split into three samples for major-element, trace-element and Sm-Nd isotopic analysis. Major- and trace-element analyses of 28 representative samples were completed in the Department of Earth Sciences, Memorial University of Newfoundland using X-ray fluorescence spectrometry (XRF) and inductively coupled plasma mass spectrometry (ICP-MS). Sm-Nd isotopic analyses were completed for 13 samples at the Radiogenic Isotope Facility, Department of Earth & Atmospheric Sciences, University of Alberta, by isotope dilution thermal - ionization mass spectrometry (ID-TIMS). Details of the analytical methods employed are given in Appendix D.

In addition to data collected in this study, we have also drawn on the results of Perks (1997) and Yamashita et al. (1999), who performed Nd isotopic analyses of metasedimentary and ca. 2.64-2.59 Ga plutonic rocks from the Forked Lake area, Ghost subdomain (Fig. 4.1b), the geochemical investigations of Branstromm (2000) and Ootes

Table 4.1: Petrographic Characteristics of Magmatic rocks in Snare River terrane

Group/ Age	RockType/ Attributes	Igneous Mineralogy	Accessory Minerals	Metamorphic Mineralogy	Crustal Level / Domain	Crosscutting Relationships
GROUP 1 ca. 2674 Ma	<i>Mafic Volcanic Rocks</i> Fault-bound and conformable contacts. Lineated blocks of massive - pillowed flows, hyaloclastic breccia. (Fig. 4.3a)	Hbl + Pl + Bt + Opx + Cpx	Zrn, Ep Ttn	Amp + Tr /Act; Chl (retr)	Upper-crust KLSB	None Observed
	<i>Felsic Volcanic Rocks</i> Fault-bound contacts. Pervasively lineated pyroclastic lava, lapilli, ashfall tuff and volcanoclastic sequences. (Fig. 4.3b)	Pl + Qtz + Hbl + Bt	Zrn, Ep Ttn	Amp + Tr /Act; Chl (retr)	Upper-crust KLSB	Oldest unit dated, crosscut by ca. 2585 Ma pegmatitic granites
	<i>Mafic Plutonic Rocks</i> Metre scale pods, cgr gabbroic gneiss. (Fig. 4.3c)	Pl + Qtz + Hbl + Bt	Fe-Ti oxide	Amp + Ep	Upper-crust KLSB	HSZ mantles ca. 2654 Ma Hinscliffe intrusive complex
	<i>Felsic Plutonic Rocks</i> Meter-scale lenses of variably strained medium-grained tonalitic gneiss interlayered with gabbroic mafic gneiss. (Fig. 4.3c)	Pl + Qtz + Hbl + Bt	Zrn, Fe-Ti oxide	Amp + Ep	Upper-crust KLSB	HSZ mantles ca. 2654 Ma Hinscliffe intrusive complex
GROUP 1 ca. 2654 Ma	<i>Hinscliffe Plutonic Complex.</i> Recrystallized fgr trondhemite and mgr granodiorite (Fig. 4.3d) mafic - intermediate enclaves. Gneissic texture, pronounced on margin.	Pl + Qtz + Kfs + Bt	Zrn, Ttn, Aln	Ep; (retr chl)	Upper-crust KLSB	Incorporates enclaves of strained ca. 2674 Ma mafic to intermediate gneissic enclaves

Table 4.1: Continued

Group/ Age	RockType/ Attributes	Igneous Mineralogy	Accessory Minerals	Metamorphic Mineralogy	Crustal Level / Domain	Crosscutting Relationships
GROUP 3: ca. 2600 Ma	Megacrystic Granite Medium to large, irregular plutons and discontinuous sheets; Characteristic alkali feldspar megacrysts. (Fig. 4.3k)	Qtz + Pl + Kfs + Bt + Ms	Zm, Mnz, Ep (Fig. 4.3l)	Opx + Kfs + Grt + Mnz	Mid-Crust Ghost/ Bigspruce Sub-domains	Enclaves of Disco Intrusive suite and turbidites. Truncated by ~2585 Ma dykes
	Sedimentary Diatexite Upper amphibolite to granulite grade; Transitional to sharp contacts; Insitu and migrated melts; Abundant sedimentary enclaves (Fig. 4.3m); Upper amphibolite facies - unfoliated; Granulite facies - foliated parallel to S2 fabrics.	Amphibolite Qtz + Pl + Kfs + Bt + Ms + Crd Granulite: Qtz + Pl + Bt + Grt + Kfs + Crd	Zm, Mnz, Rt, Ttn, Ep	Ms (retr) Opx + Kfs (Rare; high-grade)	Upper-crust / Lower KLSB Mid-Crust / Ghost Sub-domain	BIF, psammite, pelite enclaves; sediments enclave truncates Disco Intrusive suite; crosscut by ~ 2585 Ma dykes
GROUP 4: ca. 2590 - 2585 Ma	Diorite-Granodiorite Small volume, mgr to cgr irregular sheets. Northwest trending foliation (Fig. 4.3n)	Pl + Bt + Kfs Hbl + Qtz	Ap, Zm, Fe-Ti oxide	-	Upper-mid crust/ Lower KLSB	Ambiguous contact relations with enclosing megacrystic and two-mica granites; truncated by ~ 2585 Ma dykes
	Cordierite Leucogranite Unfoliated small, fgr - mgr, irregular pods and bosses; Abundant metasedimentary enclaves (Fig. 4.3o)	Qtz + Pl + Kfs + Crd	Mnz, Zm, Ap	Ms + Chl (retr)	Mid-Crustal / Ghost Sub-domain	Pelite enclaves (D1- D2 fabrics)

Table 4.1: Continued

Group/ Age	RockType/ Attributes	Igneous Mineralogy	Accessory Minerals	Metamorphic Mineralogy	Crustal Level / Domain	Crosscutting Relationships
GROUP 2 ca. 2635 Ma	<i>Disco Intrusive Suite:</i> Weakly - strongly foliated, fgr to mgr massive / sheet-like bodies of tonalite to granodiorite with amphibolite enclaves (Fig. 4.3e)	Qtz + Pl + Kfs + Bt	Zrn, Mnz, Ep Mag, Tur	Grt (<i>at pelite contacts</i>); Opx + Kfs	Mid Crust / Ghost Sub Domain	Inclusions of pre-2635 Ma turbidite package;
GROUP 2 ca. 2608 Ma	<i>Mafic Intrusive Complexes:</i> small to medium, heterogeneous plutons, agmatite, intrusive breccia, magma mingling. 4 main phases - (1) cgr hornblendite; (2) mgr quartz monzodiorite; (3) cgr gabbro-monzonite; (4) Fine-grained Late aplitic dykes (Fig. 4.3h)	(1) Tr - Ed (2) Pl + Mc + Qtz + Amp + Bt (3) Hbl + Pl + Kfs + Cpx (4) Qtz + Mc + Pl + Bt	Mag, Spn, Zrn, Ap, Sulf	Hbl+Ep	Upper Crust / KLSB	Inclusions of post-2635 Ma turbidites inclusions of high strain zone lithologies
GROUP 3: ca. 2600 Ma	<i>Biotite Granodiorite</i> fgr - mgr irregular plutons and sheets; (Fig. 4.3l)	Qtz + Pl + Kfs + Bt + Hbl	Zrn, Ttn, Ep Fe-Ti oxide	Chl (retr)	Upper Crust / KLSB	Crosscuts ~2608 Ma MIC and F2 folds in turbidites
	<i>Two Mica Granite</i> Large batholith - discrete plutons and sheets; equigranular / porphyritic phases - (1) variably foliated with abundant metasedimentary enclaves (2) weak mica foliation, enclave-free (Fig. 4.3j and 4.3k, respectively)	Qtz + Pl + Kfs + Ms + Bt	Ap, Zrn, Spn	Grt + Bt (<i>pelite contacts</i>)	Upper Crust / Bigspruce Plutonic Sub-domain	Crosscuts F2 folds in turbidites
	<i>Orthopyroxene Granite</i> Mgr sheets; pink weakly foliated; abundant mafic enclaves (Fig. 4.3g)	Qtz + Pl + Kfs + Bt + Opx	Zrn, Mnz, Ap, Fe-Ti oxide		Mid-Crust / Ghost Sub-domain	Crosscuts ~2635 Ma Disco Intrusive Suite

Table 4.1: concluded

Group/ Age	RockType/ Attributes	Igneous Mineralogy	Accessory Minerals	Metamorphic Mineralogy	Crustal Level / Domain	Crosscutting Relationships
	<i>Pegmatitic Granite</i> Discontinuous lenses, irregular plugs and dykes; Extremely coarse-grained assemblages; Graphitic intergrowths (Fig. 4.3p)	Kfs + Pl + Ms + Bt ± Mag (high- grade)	Mnz, Zrn, (+ Grt + Ap)	Chl (retr)	All crustal levels & domains	Youngest magmas; truncate all lithologies / Archean structures

Retr-retrograde; Mineral abbreviations after Kretz (1983); fgr – fine-grained, mgr – medium-grained, cgr – coarse-grained.

Figure 4.3: Field and textural relationships of magmatic suites in the Snare River terrane. Hammer and pen are approximately 45 cm and 10 cm long respectively, lens cap is approximately 5 cm in diameter. *(a)* ca. 2674 mafic pillow flow in the Kwejinne Lake supracrustal belt (KLSB). Lens cap circled in white. *(b)* Polished slab of ca. 2674 Ma strongly foliated and lineated felsic volcanic in the KLSB. *(c)* Polydeformed synvolcanic gabbro and tonalite in high-strain zone mantling Hinscliffe Intrusive complex, KLSB. *(d)* Polished slab of ca. 2654 Ma Hinscliffe plutonic complex granodiorite used in this study. *(e)* Intrusive relationships between the ca. 2637 Ma Disco Intrusive Suite and younger ca. 2597 Ma orthopyroxene granite suite. *(f)* Photomicrograph illustrating breakdown of primary biotite to form orthopyroxene and alkali feldspar within Disco Intrusive Suite. *(g)* Photomicrograph: stable biotite-orthopyroxene subassemblage in ca. 2597 Ma orthopyroxene granite suite. *(h)* Textural relationships within the Mafic Intrusive Complexes in the KLSB. 3 main phases illustrated; hornblendite, quartz monzodiorite (note intrusive breccia relationships) and gabbro-monzonite (polished slab inset). *(i)* Intrusive breccia relationships (agmatite) between hornblendite of Mafic Intrusive Complex and younger ca. 2597 Ma biotite granodiorite suite. *(j)* Intrusive contact between two-mica granite and meta-turbidites. Note angular contact. *(k)* Intrusive contact between two-mica granite and megacrystic granite suites. Note irregular, but sharp contact. *(l)* Zircon inclusions in large monazite within megacrystic granite of the Ghost subdomain. *(m)* Sharp contact between sedimentary diatexite and metatexite, illustrating some migration of diatexite melts from source regions. Polished slab (inset) illustrates texture of diatexite and large cordierite (iolite) crystals that are intimately associated with these diatexites. *(n)* Intrusive relationships between ca. 2590 Ma tonalite suite and ca. 2585 Ma pegmatitic granite suite. *(o)* Granulite-grade pelite enclaves in ca. 2585 Ma unfoliated cordierite granite, Ghost subdomain. *(p)* Crosscutting dykes of ca. 2585 Ma pegmatitic granite and macroscopic pegmatite texture (see polished slab, inset).

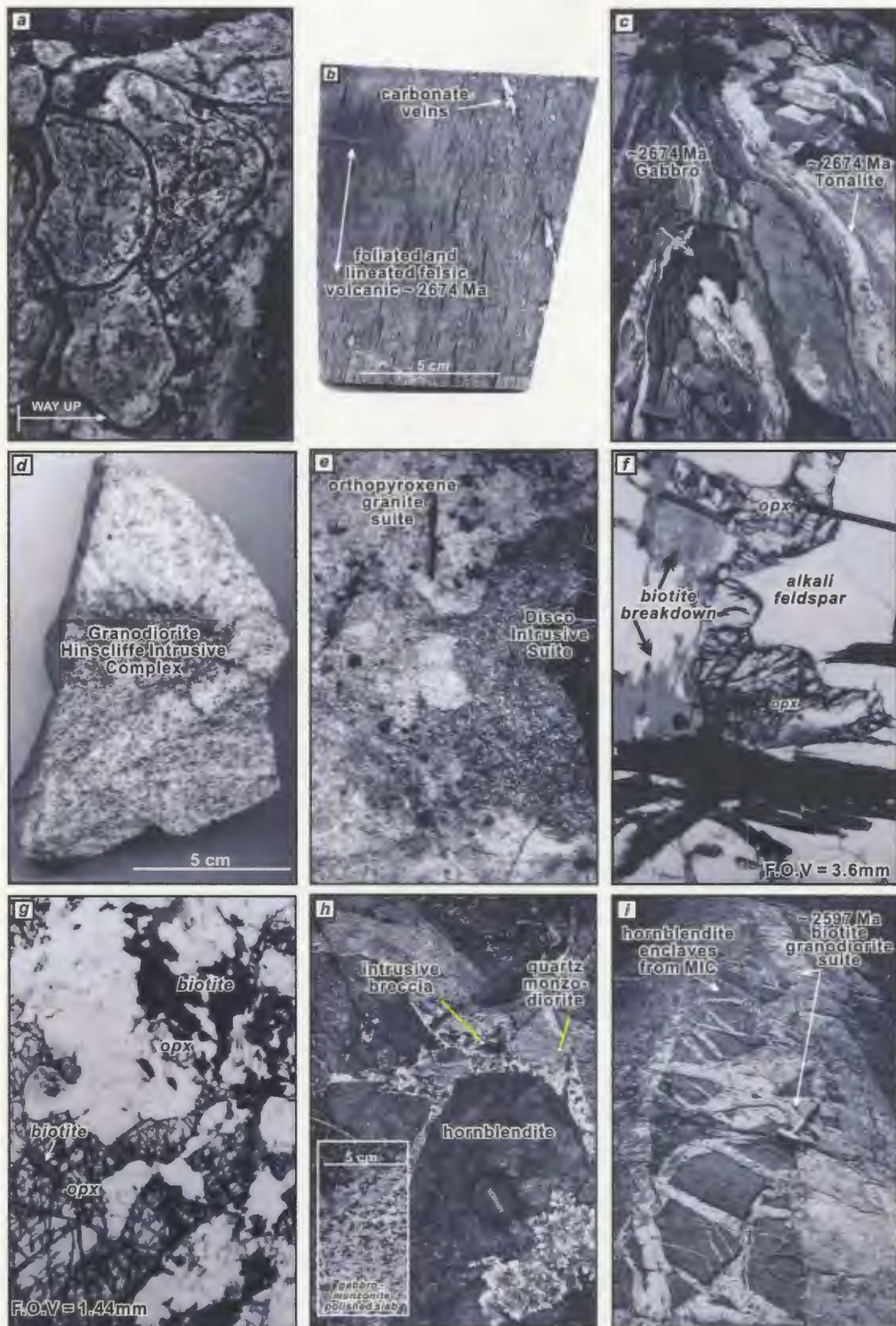


Figure 4.3: Caption see opposite

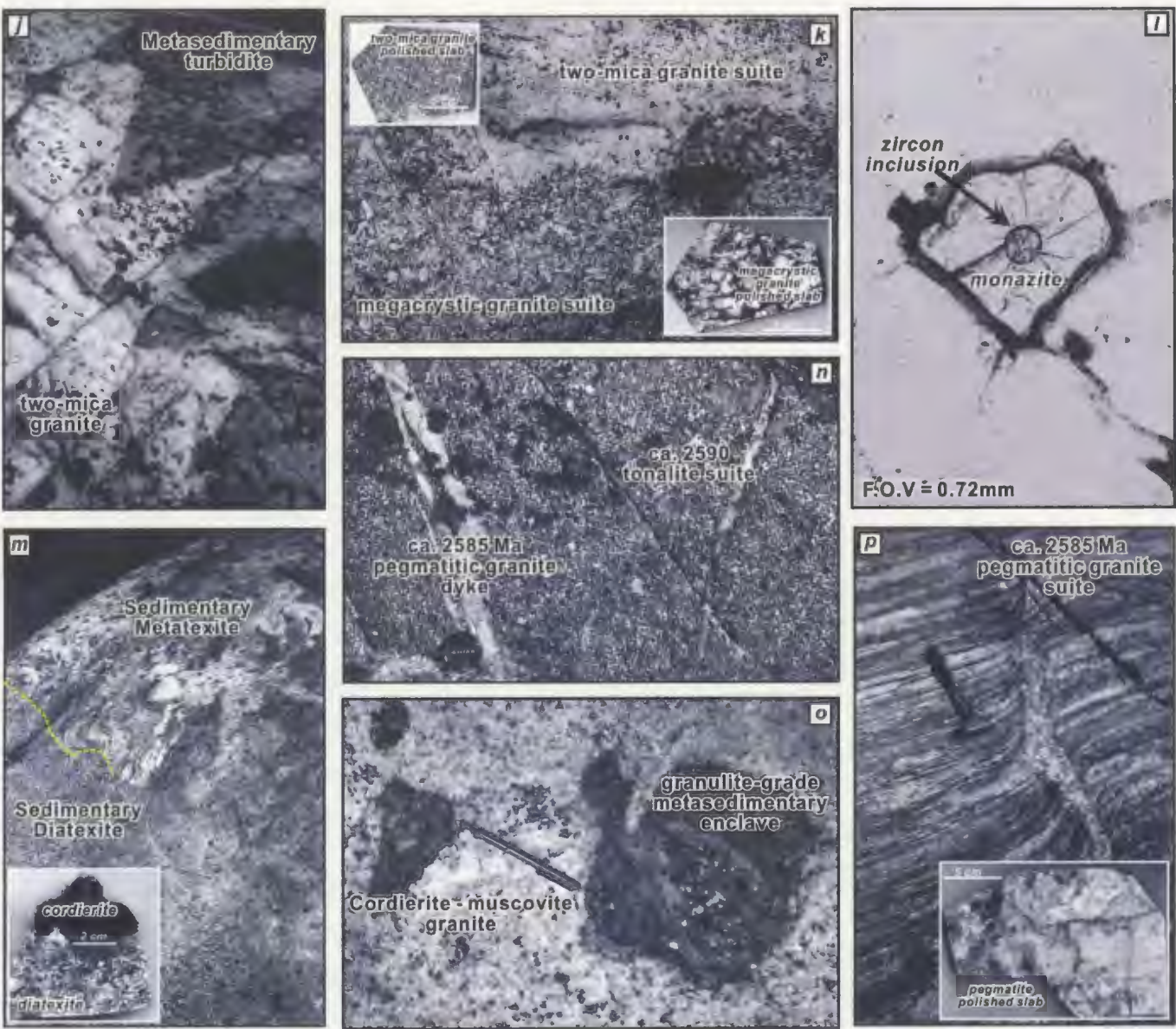


Figure 4.3: Caption see opposite

(2000) on the ca. 2.67 Ga mafic volcanic rocks and ca. 2.61 Ga mafic intrusive complexes in the Kwejinne Lake supracrustal belt, and the geochemical and Sm-Nd isotopic data of Cousens (2000) and Cousens et al. (2002) for the Banting Group, central Slave Province, and unpublished results of A. Alcazar and B. Cousens for volcanic rocks of the Russell-Slemon supracrustal belt.

4.6. Results

Relationships among suites in the four magmatic groups are summarized in Figure 4.4. Major- and trace-element data for 14 metaluminous and 7 peraluminous samples are presented in Tables 4.2 and 4.3, and data for 7 metaturbidites are in Table 4.4. Sm-Nd isotopic data for 17 samples (metaluminous and peraluminous plutons and a metaturbidite) are presented in Table 4.5. Major- and trace-element discrimination plots are presented separately for volcanic and plutonic samples (Figs. 4.5, 4.6) and chondrite-normalized, multi-element diagrams are shown in Figs. 4.7-4.9. ϵ_{Nd} data are presented graphically in Figs. 4.10a-d.

4.6.1 Group 1: 2674 –2654 Ma Magmatism

Group 1 volcanic rocks, with a compositional range from basalt to rhyolite, are mainly subalkaline (Figs. 4.3a-d, 4.5a) and can be subdivided into tholeiitic (KLSB) and calc-alkaline (KLSB and RSSB) suites (Fig. 4.5b). In the immobile-element plot of Winchester and Floyd (1977), the samples span the basalt, andesite and dacite-trachyandesite fields (Fig. 4.5c).

TABLE 4.2: Major and trace element compositions of metaluminous volcanic and plutonic rocks (Groups 1-4) in the Snare River terrane

Sample:	VB1871B	FV1806	PVB19	VB165B	VB166	VB1692	VB1363	VB1356	PVB29	VB1359A	VB158	VB1357	VB1841	VJ375
Rock:	AB	Rhd	Bthol	Ton	Gab	Grdt	Grdt	Grdt	Grdt	Gab-Monz	Gab-Monz	Grt	Grt	Ton-Di
Location:	115° 39.2' E 63°55.2' N	115° 31.9'E 63°54.4' N	115°31.2'E 63°53.3'N	115° 39.1' E 63°51.1' N	115° 39.1' E 63°51.1' N	115°38.1'E 63°48.3'N	115°22.2' E 63°36.5'N	115°16.8' E 63°39.1'N	115°05.3'E 63° 39.9' N	115°41.6'E 63°47.4'N	115° 37.7'E 63°48.1' N	115°46.3'E 63°47.8'N	114°55.8'E 63°37.4'N	115°37.2'E 63°43.7'N
Age:	2674 Ma	2674 Ma	2674 Ma	2674 Ma	2674 Ma	2654 Ma	2635 Ma	2635 Ma	2635 Ma	2608 Ma	2608 Ma	2595 Ma	2597 Ma	2589 Ma
	<i>Group 1</i>	<i>Group 1</i>	<i>Group 1</i>	<i>Group 1</i>	<i>Group 1</i>	<i>Group 1</i>	<i>Group 2</i>	<i>Group 2</i>	<i>Group 2</i>	<i>Group 2</i>	<i>Group 2</i>	<i>Group 3</i>	<i>Group 3</i>	<i>Group 4</i>
SiO ₂	53.17	65.45	44.46	57.18	47.66	71.34	71.74	68.48	68.38	54.33	51.04	69.57	72.37	56.6
TiO ₂	1.34	0.51	2.28	0.77	1.43	0.215	0.28	0.4	0.36	0.6	0.81	0.24	0.16	1.71
Al ₂ O ₃	15.35	15.62	11.78	17.02	12.03	14.76	13.87	15.49	16.57	20.3	17.89	15.99	14.51	14.28
Fe ₂ O ₃ T ^a	8.86	3.77	20.78	7.06	15.7	1.965	3.18	3.87	2.91	5.07	6.68	1.89	1.05	9.66
MnO	0.158	0.083	0.27	0.09	0.24	0.022	0.047	0.037	0.04	0.047	0.06	0.027	0.01	0.11
MgO	5.43	1.24	6.99	3.46	6.43	0.435	0.66	1.13	1.63	4.47	7.26	0.53	0.23	4.23
CaO	9.28	4.81	7.55	7.12	8.29	2.29	2.86	3.6	3.67	7.22	6.71	2.44	1.6	5.51
Na ₂ O	1.63	3.20	1.67	3.94	2.39	4.99	3.65	4.32	4.62	4.04	3.89	4.46	4.29	2.73
K ₂ O	2.68	1.95	0.73	0.76	1.23	1.09	1.52	1.21	1.54	2.51	2.18	2.58	3.06	2.49
P ₂ O ₅	0.513	0.13	0.25	0.17	0.25	0.054	0.081	0.121	0.11	0.009	0.04	0.06	0.031	0.4
LOI ^b	1.4	1.8	1.71	0.69	1.11	0.33	0.66	0.39	0.63	1.93	2.14	0.45	0.24	-2.99
Total	98.66	96.81	97.26	97.71	95.99	97.22	97.93	98.72	100.01	98.69	96.89	97.86	97.4	98.13
<i>XRF</i>														
Ni	198	10	44	8	56	0	0	0	0	108	91	0	0	22
Cu	50	14	54	19	71	0	0	7	0	62	75	2	0	28
Zn	65	24	109	32	87	8	13	18	22	20	29	9	0	64
Ga	17	20	24	20	23	19	16	21	22	21	24	25	18	21
As	2	0	0	0	0	0	7	1	0	0	0	0	6	0
Rb	61.7	56	22	13	23	31	28	30	28	79	75	49	54	75.2
Sr	294	267.8	95.5	235.7	120.8	325	157.4	467.4	317.9	492.6	421.3	603.7	476.1	299
Y	34	12.2	38.7	13	38.5	2	8	4.1	4.7	6.2	8.8	4	1.2	18.5
Zr	233.1	195.3	133.5	73.8	127.2	147.6	205.6	173.6	159.1	25.5	40.7	144.1	79.8	269.1
Nb	13.9	9.5	6.9	8.1	9.4	3	7.8	4.4	5	1.6	3.3	3.1	3.5	17.5
Ba	1428	479	260	203	204	673	406	564	424	643	538	710	971	941
Ce	119	70	0	0	0	46	31	40	0	0	0	83	56	110
Pb	0	0	9	0	0	0	0	0	0	0	0	0	5	0
Th	3	7	0	0	0	1	4	3	0	0	0	3	0	0
U	2	3	0	0	0	1	4	0	0	0	1	0	0	0
<i>ICPMS</i>														
Ba	1584	537	219	145	200	647	465	539	325	774	489	681	914	793
Ta	0.53	0.79	1.57	2.90	1.11	0.14	0.71	0.36	3.35	0.11	1.32	0.25	0.27	2.66
Nb	16.08	12.26	8.30	7.23	9.66	3.40	10.96	5.93	5.03	2.11	4.21	3.98	5.15	17.96
Hf	4.94	4.45	3.79	3.24	3.73	3.63	5.43	4.54	3.67	0.80	2.12	3.33	1.69	7.72

Table 4.2: continued

Sample:	VB1871B	FV1806	PVB19	VB165B	VB166	VB1692	VB1363	VB1356	PVB29	VB1359A	VB158	VB1357	VB1841	VJ375	
Rock:	AB	Rhd	Bthol	Ton	Gab	Grdt	Grdt	Grdt	Grdt	Gab-Monz	Gab-Monz	Grt	Grt	Ton-Di	
Location:	115° 39.2' E 63°55.2' N	115° 31.9'E 63°54.4' N	115°31.2'E 63°53.3'N	115° 39.1' E 63°51.1' N	115° 39.1' E 63°51.1' N	115°38.1'E 63°48.3'N	115°22.2' E 63°36.5'N	115°16.8' E 63°39.1'N	115°05.3'E 63° 39.9' N	115°41.6'E 63°47.4'N	115° 37.7'E 63°48.1' N	115°46.3'E 63°47.8'N	114°55.8'E 63°37.4'N	115°37.2'E 63°43.7'N	
Age:	2674 Ma	2674 Ma	2674 Ma	2674 Ma	2674 Ma	2654 Ma	2635 Ma	2635 Ma	2635 Ma	2608 Ma	2608 Ma	2595 Ma	2597 Ma	2589 Ma	
	<i>Group 1</i>	<i>Group 1</i>	<i>Group 1</i>	<i>Group 1</i>	<i>Group 1</i>	<i>Group 1</i>	<i>Group 2</i>	<i>Group 2</i>	<i>Group 2</i>	<i>Group 2</i>	<i>Group 2</i>	<i>Group 2</i>	<i>Group 3</i>	<i>Group 3</i>	<i>Group 4</i>
Zr	258	220	143	126	148	154	268	226	170	20.9	36.7	147	74.5	346	
Y	30.84	11.86	37.36	11.03	35.65	2.38	7.80	4.69	4.51	6.80	9.46	4.16	1.15	17.25	
Th	4.74	8.19	0.88	1.83	0.75	1.62	4.37	3.10	4.19	0.40	0.70	4.42	0.50	3.67	
La	37.50	27.38	5.75	9.69	6.82	9.89	25.61	22.72	31.08	3.38	5.05	15.11	12.51	32.19	
Ce	95.23	50.11	14.90	21.25	19.16	18.81	46.29	41.34	54.73	7.69	12.36	28.03	18.04	67.43	
Pr	12.89	5.45	2.37	2.53	2.94	1.96	4.84	4.41	5.42	1.20	1.83	3.46	1.50	7.13	
Nd	53.47	20.01	12.37	10.35	14.61	6.96	16.67	15.58	17.76	6.30	9.24	13.54	4.03	30.92	
Sm	9.37	3.65	4.26	2.38	4.60	1.21	2.60	2.50	2.39	2.08	2.81	2.53	0.49	6.48	
Eu	2.41	1.02	1.55	0.80	1.58	0.44	1.09	1.05	0.79	0.76	0.92	0.70	0.46	1.88	
Gd	8.01	3.32	5.78	2.28	5.80	0.93	2.17	1.66	1.57	2.18	2.89	1.74	0.30	5.44	
Tb	1.10	0.47	1.01	0.34	0.97	0.11	0.28	0.22	0.18	0.30	0.39	0.18	0.04	0.69	
Dy	6.48	2.74	6.99	2.03	6.64	0.57	1.53	1.10	0.93	1.60	2.09	0.88	0.22	3.84	
Ho	1.24	0.51	1.52	0.42	1.43	0.09	0.29	0.17	0.17	0.29	0.39	0.16	0.04	0.73	
Er	3.50	1.41	4.54	1.19	4.21	0.23	0.84	0.46	0.44	0.73	0.97	0.41	0.14	1.89	
Tm	0.51	0.21	0.67	0.18	0.63	0.03	0.13	0.06	0.06	0.09	0.13	0.06	0.02	0.26	
Yb	3.32	1.41	4.22	1.11	4.14	0.18	0.92	0.39	0.37	0.54	0.72	0.42	0.18	1.67	
Lu	0.50	0.21	0.64	0.18	0.63	0.03	0.16	0.06	0.05	0.08	0.10	0.07	0.03	0.27	
[La/Sm] _{CN} ^c	2.52	4.72	0.85	2.57	0.93	5.14	6.19	5.72	8.17	1.02	1.13	3.76	16.01	3.13	
La/Yb] _{CN}	7.63	13.15	0.92	5.88	1.11	36.92	18.89	39.42	57.23	4.27	4.27	24.09	48.04	13.00	
Mg # ^d	54.9	39.4	40	49.3	44.8	30.6	29	36.8	52.6	63.6	68.3	35.7	30.6	46.4	
A/CNK ^e	0.68	0.97	0.68	0.84	0.59	1.09	1.08	1.04	1.04	0.90	0.85	1.10	1.09	0.83	
A/NK ^f	2.75	2.12	3.33	2.33	2.29	1.57	1.81	1.84	1.79	2.17	2.04	1.58	1.40	1.99	

Notes: Major elements in wt%, trace elements in weight parts per million. AB-alkali basalt; Rhd-rhyodacite; Bthol-tholeiitic basalt; Ton-tonalite; Gab-gabbro; Grdt-granodiorite; Gab-Monz-gabbro/monzonite; Grt-granite; Di - Diorite. ^a Total Iron calculated as Fe₂O₃. ^b LOI - Loss on ignition, weight on heating to 1000°C, equivalent to total volatiles. ^c CN - Chondrite Normalized. ^d Mg # - Molar Mg/(Mg+Total Fe). ^e A/CNK - molar Al₂O₃/(CaO+Na₂O+K₂O). ^f A/NK - molar Al₂O₃/(Na₂O+K₂O). 0 values = not determined.

Table 4.3: Major and trace element compositions of peraluminous plutonic rocks in the SRT

Sample	VB1358	PVB9	VB1848	VB1688	VB161	VB1864	VB1229A
Rock	grt	mgx	mgx	mgx	grt	Peg	Peg
Location	115°45.0'E 63°45.3'N	115°38.6'E 63°43.8'N	114°57.8'E 63°36.1'N	114°57.7'E 63°36.7'N	115°27.4'E 63°36.8'N	115°52.1'E 63°45.8'N	115°12.6'E 63°38.9'N
Age	2597 Ma	2597 Ma	2597 Ma	2597 Ma	2586 Ma	2586 Ma	2586 Ma
Grouping	Group 3	Group 3	Group 3	Group 3	Group 4	Group 4	Group 4
SiO ₂	73.64	65.28	71.37	72.57	71.89	74.36	71.00
TiO ₂	0.1	0.88	0.38	0.06	0.02	0.02	0.03
Al ₂ O ₃	13.83	15.7	13.46	13.66	17.25	14.37	13.54
Fe ₂ O ₃ T ^a	1.2	5.35	2.34	0.98	0.87	0.58	3.11
MnO	0.015	0.049	0.022	0.02	0.01	0.068	0.06
MgO	0.49	2.11	0.58	0.21	0.8	0.07	0.68
CaO	0.47	2.12	1.47	0.29	0.83	0.35	0.28
Na ₂ O	3.66	3.57	2.71	1.9	2.8	4.29	1.22
K ₂ O	4.52	2.95	5.07	7.76	6.0	3.64	7.13
P ₂ O ₅	0.046	0.244	0.105	0.03	0.09	0.139	0.04
LOI ^b	0.57	2.06	0.58	0.13	0.7	0.51	0.15
Total	98.02	98.48	97.60	97.70	100.78	97.89	97.23
XRF							
Ni	0	12	0	0	0	0	0
Cu	0	7	0	0	0	0	0
Zn	0	19	0	0	0	0	0
Ga	22	20	19	14	13	24	15
As	3	16	0	0	0	6	8
Rb	117	84	147	208	68	303	202
Sr	110	263	162	223	278	11	194
Y	33	24	10	20	7	7	60
Zr	83	232	263	47	44	18	27
Nb	11	18	15	2	1	15	1
Ba	442	949	817	1840	1241	21	1124
Ce	26	53	103	35	0	14	47
Pb	6	0	0	10	29	0	13
Th	8	7	0	7	0	0	13
U	11	4	0	0	0	3	0
ICP-MS							
Ba	465	1111	935	2096	1041	13	1228
Ta	1.49	1.17	0.85	0.24	2.95	2.68	0.43
Nb	13.70	22.50	25.49	2.07	0.96	17.41	1.14
Hf	3.36	6.92	8.12	1.55	2.13	11.07	0.81
Zr	94	334	392	71	52	18	34
Y	31.71	22.15	10.33	23.10	5.42	5.35	61.59
Th	10.87	7.53	2.28	17.23	0.56	1.37	22.15
La	14.45	24.25	36.60	27.03	6.21	1.23	28.27
Ce	29.71	48.77	63.40	42.52	9.62	2.87	55.30
Pr	3.67	5.79	6.97	4.17	0.96	0.37	6.22
Nd	14.25	22.70	25.14	13.45	3.36	1.39	21.96
Sm	4.69	4.50	4.72	2.00	0.68	0.67	4.55
Eu	0.43	1.07	1.69	1.95	2.02	0.02	1.26
Gd	5.32	4.12	3.30	1.56	0.65	0.76	4.66
Tb	1.09	0.63	0.46	0.35	0.11	0.17	1.25
Dy	6.63	4.06	2.50	3.34	0.78	1.04	10.87
Ho	1.09	0.83	0.40	0.91	0.19	0.17	2.45
Er	3.00	2.61	1.11	3.79	0.56	0.51	7.86
Tm	0.42	0.39	0.15	0.72	0.09	0.10	1.15
Yb	2.60	2.56	1.05	5.65	0.67	0.89	7.05
Lu	0.39	0.36	0.18	1.07	0.11	0.13	1.07
[La/Sm] _{CN} ^c	1.94	3.39	4.88	8.50	5.79	1.15	3.91
[La/Yb] _{CN}	1.65	1.32	1.46	5.14	0.84	0.05	12.82
Mg # ^d	44.8	43.9	32.8	30.1	64.6	19.0	30.2
A/CNK ^e	1.18	1.22	1.07	1.13	1.37	1.24	1.32
A/NK ^f	1.27	1.73	1.35	1.19	1.55	1.31	1.39

Notes: Major elements in wt%, trace elements in weight parts per million. Peg-pegmatitic granite; Grt-granite(+biotite±muscovite); mgx-megacrystic granite. ^a Total Iron calculated as Fe₂O₃. ^b LOI – Loss on ignition, weight on heating to 1000°C, equivalent to total volatiles. ^c CN – Chondrite Normalized. ^d Mg # – Molar Mg/(Mg+Total Fe). ^e A/CNK – molar Al₂O₃/(CaO+Na₂O+K₂O). ^f A/NK – molar Al₂O₃/(Na₂O+K₂O). 0 values = not determined.

Table 4.4: Major and trace element geochemistry of metaturbidites

Sample:	VB18A	VB47A	VB64	VB92B	VB111	VB159O	VB160
Rock:	Tb-crd	Tb-crd	Tb-crd	TB-melt	TB-melt	Dt	Dt
Location	115°54.8'E 63°44.8'N	115°50.6'E 63°45.5'N	115°48.4' E 63°45.7'N	115°43.5'E 63°47.4'N	115°42.7'E 63°46.7'N	115°28.8'E 63°42.2'N	115° 26.2'E 63°36.7'N
SiO ₂	55.32	51.05	56.06	54.35	56.4	56.9	58.9
TiO ₂	0.79	0.89	0.72	0.94	0.84	0.89	0.89
Al ₂ O ₃	22.56	21.31	21.09	18.85	18.89	15.24	15.08
Fe ₂ O ₃ T ^a	7.05	10.78	6.56	9.08	7.92	7.93	9.71
MnO	0.04	0.05	0.04	0.07	0.06	0.1	0.06
MgO	4.93	4.95	4.83	5.06	4.53	5.32	3.88
CaO	0.91	0.57	1.02	1.75	0.94	2.7	0.66
Na ₂ O	2.38	0.69	2.21	2.38	1.79	2.74	1.25
K ₂ O	4.04	4.58	3.8	2.99	3.43	1.93	2.88
P ₂ O ₅	0.11	0.1	0.13	0.08	0.1	0.05	0.04
LOI ^b	2.93	3.97	2.99	2.76	2.49	1.47	1.38
Total	98.62	95.98	97.78	96.28	95.34	94.50	93.89
<i>XRF</i>							
Cr	264	310	255	248	209	233	264
Ni	37	83	64	58	24	58	30
V	184	191	179	180	158	161	165
Zn	58	50	42	61	40	36	45
Rb	138.1	132.5	88.5	72.3	91.2	62.6	73.7
Ba	835	846	922	706	802	747	336
Sr	191	118	198	269	171	334	97
Nb	11	8.8	9.9	8	9.3	8.2	9.7
Zr	134.5	124.9	137.8	196	128.6	118.6	157.2
Y	13.1	13	17.2	16.6	9.7	15.5	16
S	863	2880	984	1854	780	1738	1383
Cl	201	360	190	162	252	287	156
Sc	20	30	30	25	21	18	22
<i>ICP MS</i>							
Ba	689	684	684	562	653	654	258
Ta	6.63	1.27	1.33	1.66	1.65	2.33	2.39
Nb	13.23	9.47	10.66	8.58	9.26	9.04	10.07
Hf	3.41	3.23	3.17	4.97	3.28	3.48	3.77
Zr	138.7	125.2	128.8	213.1	131.2	142.5	160.7
Y	14.64	14.75	15.79	16.16	9.54	18.36	18.99
Th	8.88	8.31	8.18	8.21	7.37	14.67	9.33
La	12.26	12.02	16.26	25.90	11.52	34.37	31.35
Ce	23.70	26.92	34.78	52.55	25.72	70.69	62.98
Pr	2.85	3.46	4.23	6.02	3.05	8.33	7.44
Nd	11.23	14.94	17.28	23.16	12.09	31.00	28.35
Sm	2.49	3.64	3.54	4.27	2.37	5.55	5.28
Eu	0.99	1.04	1.12	1.28	0.82	1.44	0.83
Gd	2.42	3.26	2.97	3.59	1.87	4.33	4.16
Tb	0.42	0.50	0.45	0.52	0.28	0.61	0.60
Dy	2.75	2.93	2.95	3.07	1.75	3.65	3.64
Ho	0.59	0.59	0.64	0.64	0.38	0.74	0.74
Er	1.75	1.70	1.99	1.82	1.17	2.08	2.18
Tm	0.25	0.25	0.30	0.27	0.18	0.30	0.32
Yb	1.67	1.64	2.02	1.67	1.21	1.95	2.09
Lu	0.26	0.24	0.30	0.26	0.19	0.30	0.31
[La/Sm] _{CN} ^c	3.1	2.0	2.9	3.8	3.1	3.9	3.7
[La/Yb] _{CN}	5.0	5.0	5.5	10.5	6.4	11.9	10.1
Mg# ^d	33.60	47.6	59.3	52.5	53.1	57.1	44.2
A/CNK ^e	2.27	2.99	2.20	1.82	2.26	1.32	2.37
A/NK ^f	2.72	3.50	2.72	2.64	2.84	2.31	2.91

Notes: Major elements in wt%, trace elements in weight parts per million. ^a Total Iron calculated as Fe₂O₃. ^b LOI – Loss on ignition, weight on heating to 1000°C, equivalent to total volatiles. ^c CN – Chondrite Normalized. ^d Mg # - Molar Mg/(Mg+Total Fe). ^e A/CNK – molar Al₂O₃ /((CaO+Na₂O+K₂O)). ^f A/NK – molar Al₂O₃ /((Na₂O+K₂O)). 0 values = not determined. Tb-crd – cordierite bearing amphibolite; TB-melt: Melt – in cordierite; Dt-diatexite.

Table 4.5: Nd isotopic compositions, crystallization ages and rock types.

Sample	Rock Type	Geochemical &/or Temporal Affinity	Sm ppm	Nd ppm	$\frac{^{147}\text{Sm}}{^{144}\text{Nd}}$	$\frac{^{143}\text{Nd}}{^{144}\text{Nd}}$ ^a	uncert. 2 σ +/-	T (Ma)	ϵ_{NdT} ^b	T_{DM} ^c (Ga)
VB 165	Tonalite	Banting	2.66	12.12	0.1325	0.511572	0.000008	2674	1.3	2.97
VB 166	Gabbro	Banting	5.05	17.12	0.1784	0.512412	0.000005	2675	1.9	—
FV 1806	Rhyodacite	Banting	3.85	20.63	0.1127	0.511235	0.000009	2673	1.5	2.89
VB 1871	Basalt	Banting	9.97	55.98	0.1077	0.511140	0.000009	2673	1.4	2.89
VB 1692	Granodiorite	Olga	1.21	7.18	0.1021	0.511123	0.000008	2654	2.8	2.77
VB 1363	Granodiorite	Defeat	2.77	17.27	0.0970	0.511001	0.000007	2635	1.9	2.81
VB 1359A	Gabbro	Concession	2.04	6.52	0.1893	0.512578	0.000006	2608	1.3	—
VB 1841	Granite	n/a	0.59	4.79	0.0740	0.510515	0.000009	2597	-0.4	2.87
VB 1357	Granite	Defeat	2.37	13.27	0.1078	0.511218	0.000010	2595	2.0	2.78
VJ 375	Tonalite	Banting	6.93	33.62	0.1247	0.511450	0.000010	2589	0.8	2.91
VB 47A	Turbidite		3.65	15.03	0.1467	0.511765	0.000010	<2630	0.0	—
VB 1358	Granite	Yamba	4.41	14.11	0.1888	0.512549	0.000006	2598	0.9	—
PVB 9	Granite	Yamba	5.17	26.81	0.1166	0.511318	0.000014	2597	1.0	2.88
VB 1848	Granite	Yamba	4.66	26.95	0.1046	0.511097	0.000007	2597	0.7	2.87
VB 1864	Pegmatite	n/a	0.76	1.59	0.2898	0.514185	0.000014	2585	-0.8	—
VB 161	Crd Granite	n/a	0.47	2.40	0.1176	0.511270	0.000008	2585	-0.4	2.98
VB 1229A	Pegmatite	n/a	2.73	14.08	0.1172	0.511320	0.000009	2585	0.8	2.89

Notes: Measured $^{143}\text{Nd}/^{144}\text{Nd}$ values normalized to $^{146}\text{Nd}/^{144}\text{Nd} = 0.7219$. ^a $^{143}\text{Nd}/^{144}\text{Nd}$ at present. ^b ϵ_{Nd} at time of crystallization for magmatic rocks and at maximum age of sedimentation for sedimentary sample, VB47A. ^c T_{DM} calculated using the mantle evolution model of Goldstein et al. (1984). Present day CHUR parameters are $^{147}\text{Sm}/^{144}\text{Nd} = 0.1967$ and $^{143}\text{Nd}/^{144}\text{Nd} = 0.512638$. $\lambda_{^{147}\text{Sm}} = 6.54 \times 10^{-12} \text{ a}^{-1}$. Crd – cordierite. Co-ordinates of sample locations given in Tables 4.2, 4.3 and 4.4.

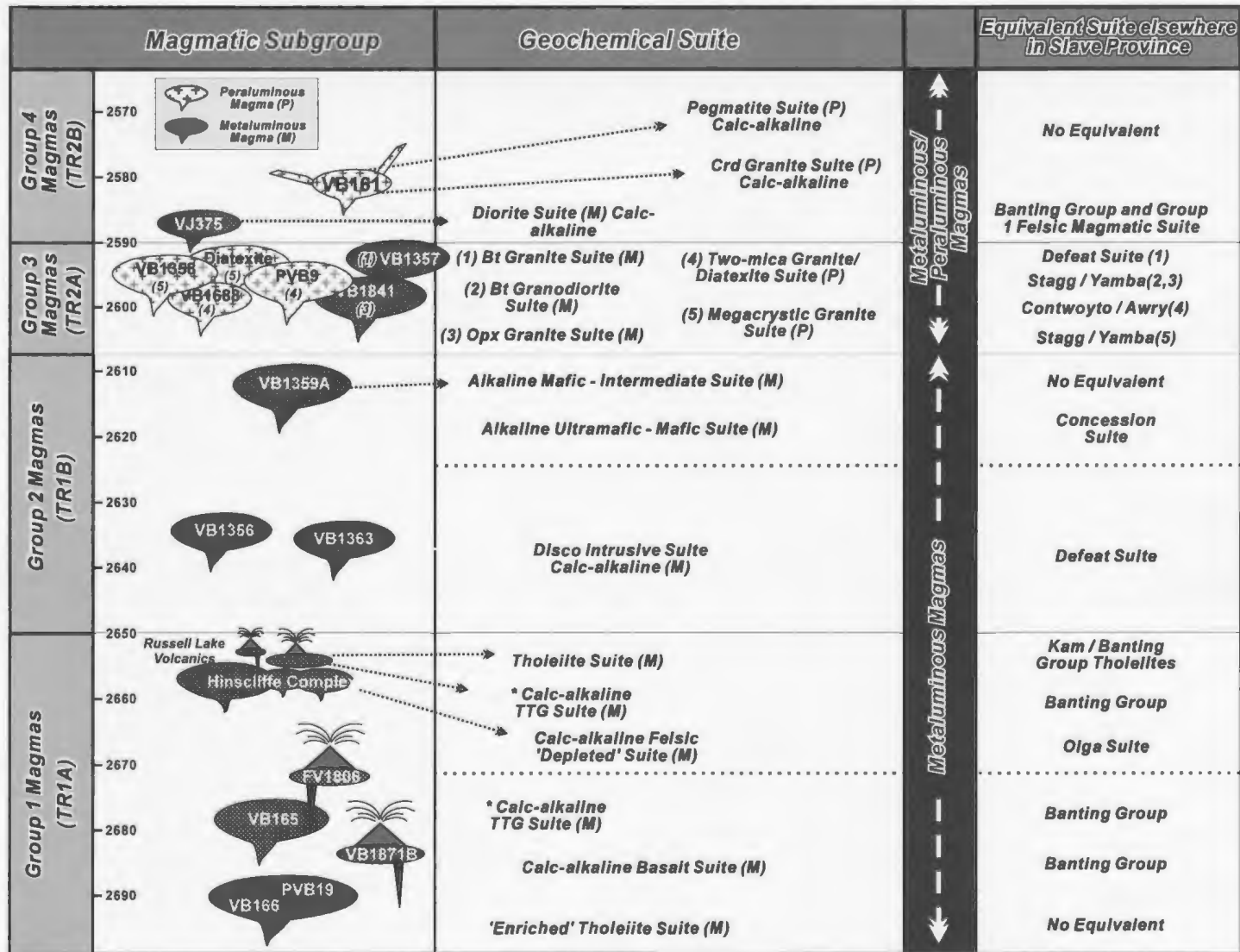


Figure 4.4: Summary diagram illustrating relationships of the sixteen magmatic suites to magmatic groups 1 to 4 defined in the text and to possible correlative magmatic suites elsewhere in the Slave Province. M, metaluminous; P, peraluminous. Numbers (1) to (5) are used to indicate main magmatic suites amongst Group 3 magmas.

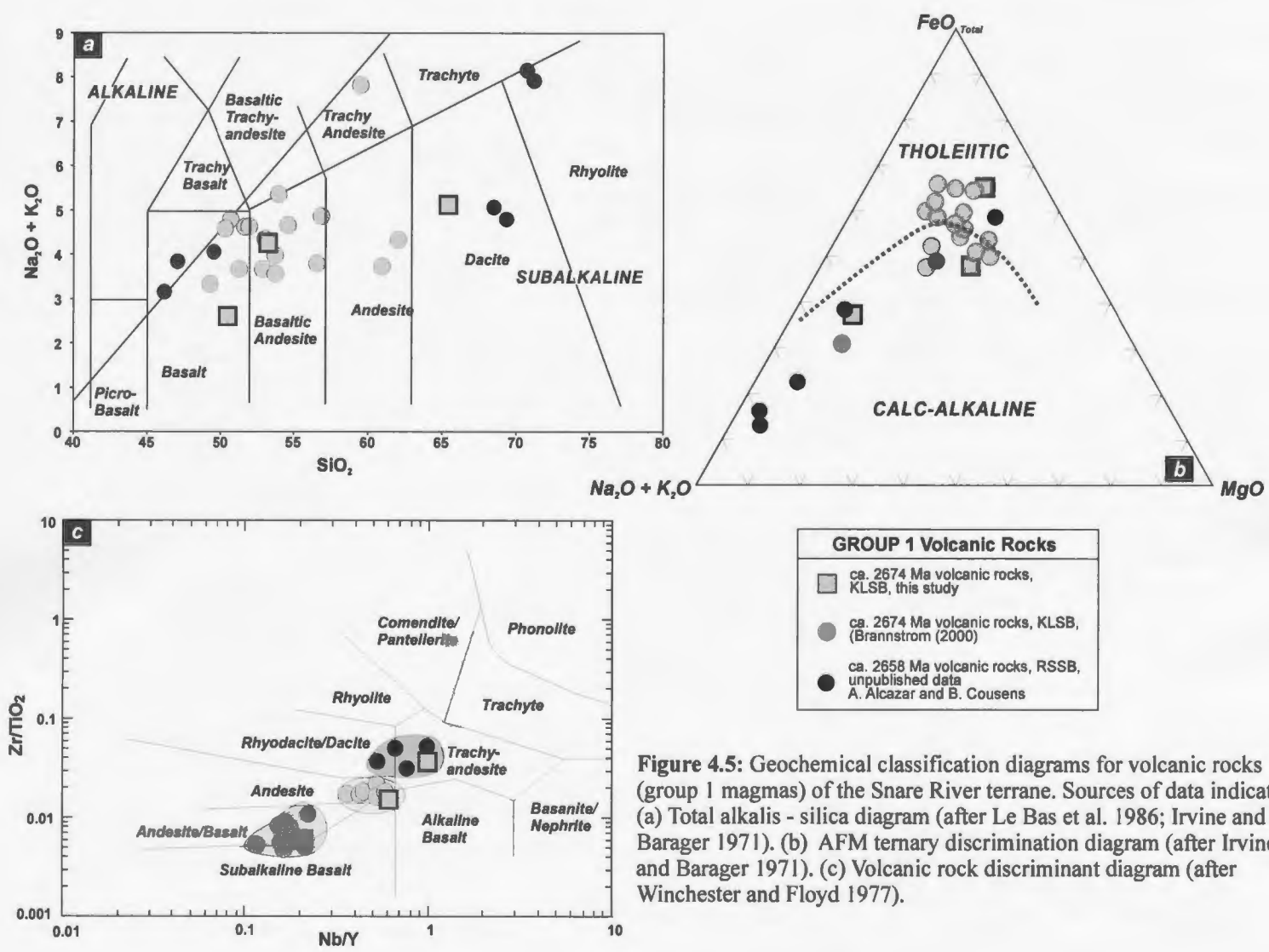


Figure 4.5: Geochemical classification diagrams for volcanic rocks (group 1 magmas) of the Snare River terrane. Sources of data indicated. (a) Total alkalis - silica diagram (after Le Bas et al. 1986; Irvine and Barager 1971). (b) AFM ternary discrimination diagram (after Irvine and Barager 1971). (c) Volcanic rock discriminant diagram (after Winchester and Floyd 1977).

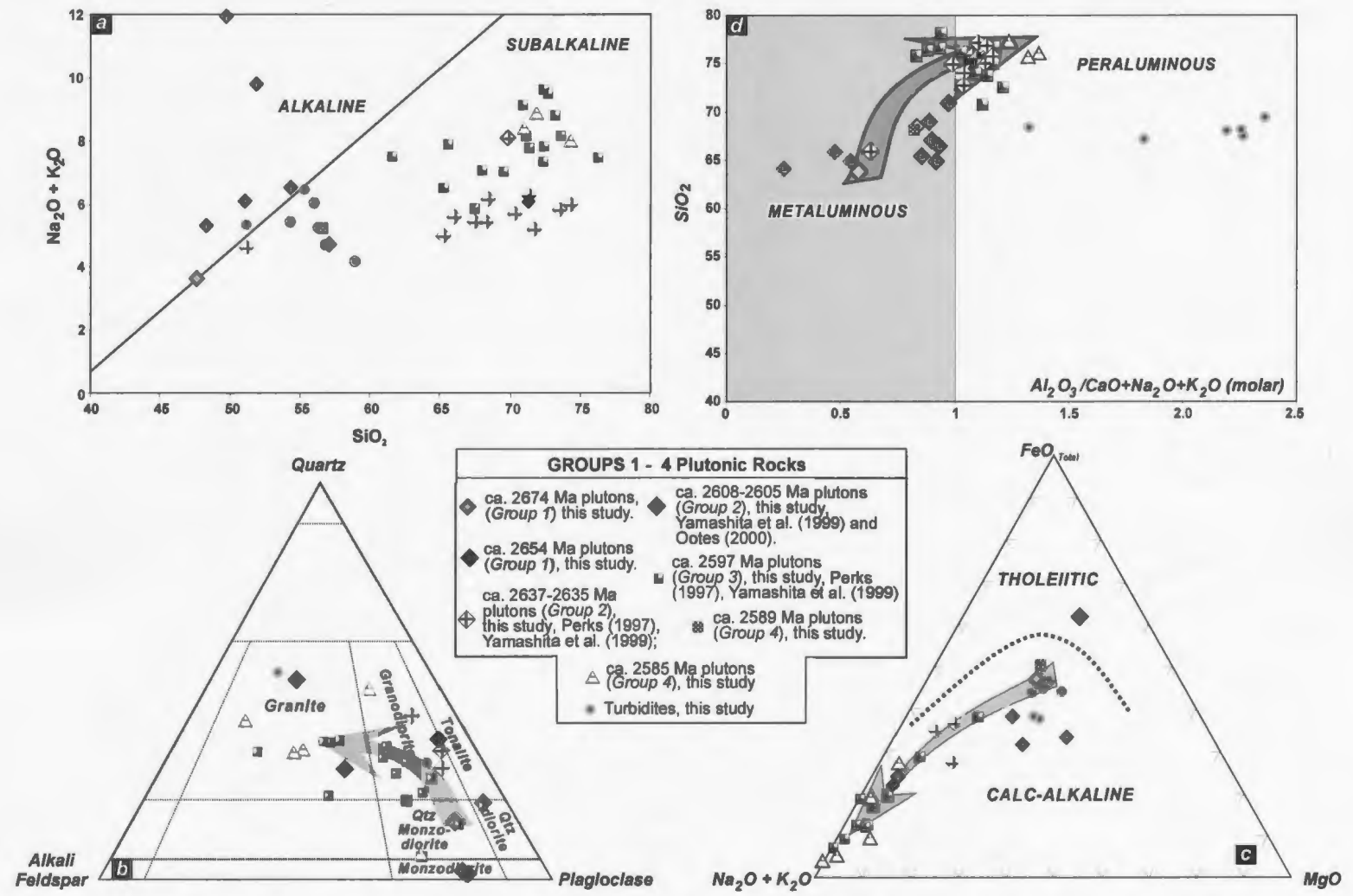


Figure 4.6: Geochemical classification diagrams for plutonic rocks in the Snare River terrane. Sources of data indicated. (a) Total alkalis - silica diagram (after Le Bas et al. 1986; Irvine and Barager 1971). (b) Normative quartz-alkali feldspar- plagioclase (IUGS granitoid classification diagram). (c) AFM ternary discrimination diagram (after Irvine and Barager 1971). (d) Silica - molar A/CNK discrimination diagram. Secular evolution trend marked on (b), (c) and (d).

Group 1 plutonic rocks are also predominantly subalkaline (Fig. 4.6a) and range from quartz monzodiorite and quartz diorite to granodiorite (Fig. 4.6b). Mafic and felsic plutons are tholeiitic and calc-alkaline respectively (Fig. 4.6c), displaying similar chemical characteristics to their volcanic counterparts. Group 1 tholeiites have lower Ni abundances (mean = 47 ppm) than calc-alkaline magmas (mean = 176 ppm; Table 4.2), whereas Y concentrations (mean = 34 ppm) are similar. All Group 1 felsic rocks (volcanic and plutonic) are calc-alkaline and have low Ni and Y abundances (mean Ni = 12 ppm, Y = 10 ppm). A/CNK ratios indicate Group 1 magmas are predominantly metaluminous (Table 4.2).

Chondrite-normalized (CN; Taylor and McClennan 1985) incompatible-element patterns for Group 1 mafic volcanic rocks are presented in Figure 4.7a and b. Three suites can be distinguished: (i) a ca. 2674 Ma *enriched* (with respect to depleted mantle; DM) tholeiite suite in the Kwejinne Lake supracrustal belt characterized by flat, unfractionated REE patterns ($[La/Yb]_{CN} = 1$), REE abundances approximately 20-30 times chondrite, absence of a Nb anomaly, and presence of a negative Sr anomaly; (ii) a ca. 2674 Ma calc-alkaline basalt/basaltic andesite suite in the KLSB, locally interlayered with the enriched tholeiitic suite, which is moderately fractionated ($[La/Yb]_{CN} = 8$), with minor LREE enrichment ($[La/Sm]_{CN} = 3$), prominent Nb and Sr depletion, little or no Eu anomaly and slightly concave-up HREE patterns; and (iii) a ca. 2658 Ma tholeiitic suite in the RSSB, which is slightly fractionated ($[La/Yb]_{CN} = 1.4 - 2.6$) with minor LREE enrichment ($[La/Sm]_{CN} = 1.2 - 2$), flat HREE profiles, a moderate Nb negative anomaly and no Sr anomaly. Figure 4.7b reveals the enriched nature of the ca. 2674 Ma tholeiitic suite and

Figure 4.7: Chondrite-normalized (Taylor and McClennan 1985) incompatible-element patterns for ca. 2674-2658 Ma (Group 1) magmatic rocks in the Snare River terrane (SRT) and Slave Province. Sources of data and symbols indicated on individual plots. Note that each diagram includes the plot from the previous diagram for comparison and the Kwejinne Lake tholeiite trend is plotted on all figures for reference. *(a)* ca. 2674-2658 Ma calc-alkaline and tholeiitic mafic rocks from Kwejinne Lake and Russell-Slemon supracrustal belts. *(b)* Comparison of ca. 2674-2658 Ma tholeiitic rocks from the SRT with tholeiites from the central Slave Province. *(c)* Comparison of ca. 2674-2658 Ma tholeiites from the SRT with Banting Group (ca. 2660 Ma) and Kam Group (ca. 2700 Ma) tholeiites. *(d)* Comparison of ca. 2674-2658 Ma calc-alkaline basalt / basaltic andesite from the SRT with Banting Group and calc-alkaline basalt and basaltic andesite of the Central Volcanic Belt, Contwoyto Lake area.

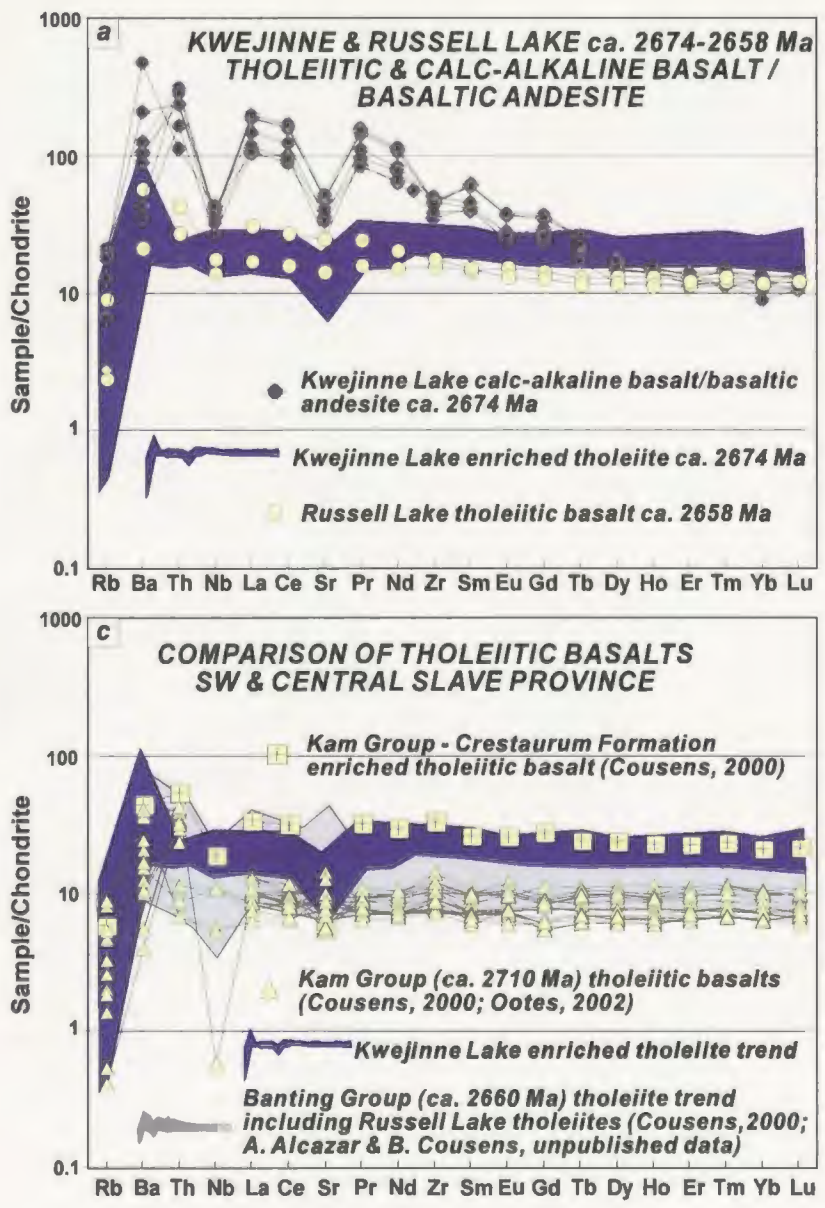


Figure 4.7: Caption see opposite

the LREE-enriched nature of the ca. 2658 Ma suite compared to the coeval tholeiitic magmas of the Banting group, central Slave Province. Figure 4.7c illustrates the similarity between the enriched tholeiites of the KLSB and basalts of the Kam Group (Crestaurum Formation). Figure 4.7d reveals the similarity between the calc-alkaline suite in the KLSB and the ca. 2660 Ma Banting Group in the southern Slave Province (data from Cousens 2000, Cousens et al. 2002) and also to andesites in the Contwoyto belt of the central Slave Province (Davis et al. 1994).

Two suites of Group 1 felsic rocks can be delineated: (i) a moderately fractionated suite (Fig. 4.7e), comprising 2674 and 2658 Ma rocks in the KLSB and RSSB respectively, with $[La/Yb]_{CN} = 6-13$, minor LREE enrichment ($[La/Sm]_{CN} = 3-5$), prominent Nb and Sr depletions and weakly concave-up HREE patterns in volcanic rocks; and (ii) a HREE-depleted, strongly fractionated ($[La/Yb]_{CN} = 35$) suite exhibiting moderate LREE-enrichment ($[La/Sm]_{CN} = 5$), a prominent negative Nb anomaly, strong positive Sr and Zr enrichments and a weak positive Eu anomaly (Fig. 4.7f), comprising ca. 2658 Ma volcanic and plutonic rocks in the KLSB and RSSB. The overlap of suite (i) felsic rocks with the field of average Archean TTG determined by Martin (1994; Fig. 4.7e) implies a TTG association, and Figure 4.7g illustrates its similarity (apart from minor Zr enrichment) to coeval felsic volcanics in the Banting Group (Cousens et al. 2002). Figure 4.7h shows that, except for its Eu signature, the HREE-depleted suite is comparable to the Olga Suite of the central Slave Province (Davis et al. 1994).

Group 1 mafic and felsic rocks have positive Nd isotopic compositions (Table 4.5, Fig. 4.10a), with ϵNd_{2674} values ranging from + 1.3 to + 1.9 and ϵNd_{2658} values from +2.2

Figure 4.7: Continued. *(e)* ca. 2674-2661 Ma calc-alkaline felsic magmatic rocks from the Kwejinne Lake and Russell-Slemon supracrustal belts. *(f)* Comparison of ca. 2658 Ma HREE depleted felsic magmas with ca. 2674-2661 Ma calc-alkaline felsic magmatic rocks from the Kwejinne Lake and Russell-Slemon supracrustal belts. *(g)* Comparison of ca. 2674-2660 Ma calc-alkaline felsic magmas from the SRT with Banting felsic magmas of the Central Slave Province. *(h)* Comparison of ca. 2660-2650 Ma HREE-depleted felsic magmas from the SRT with Olga Suite (Davis et al. 1994).

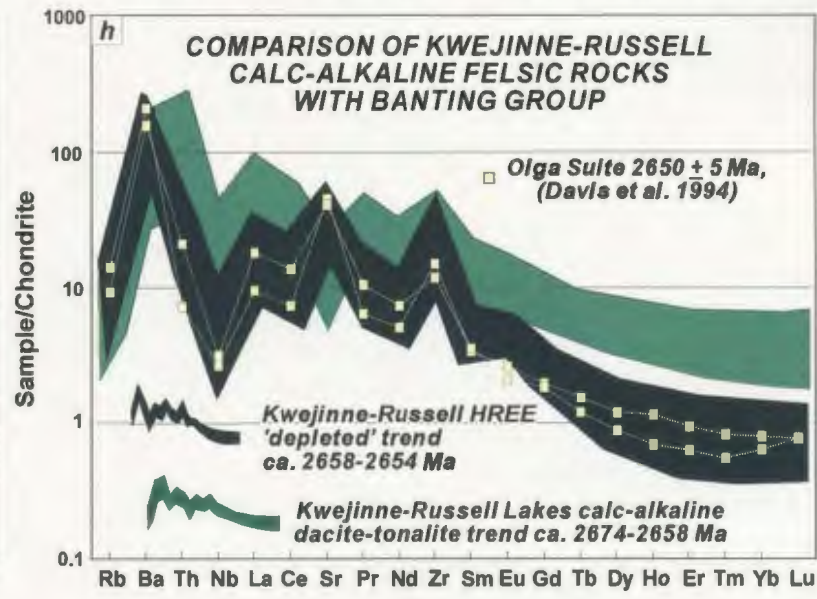
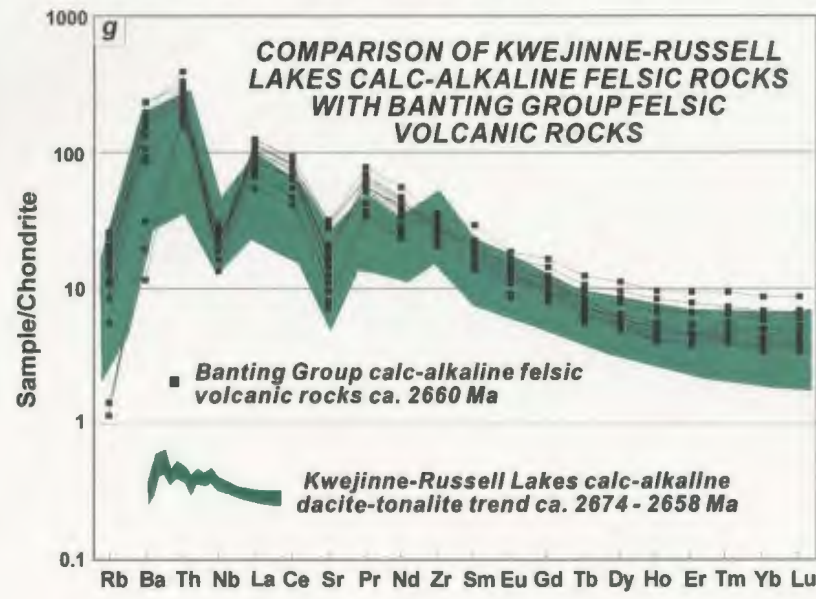
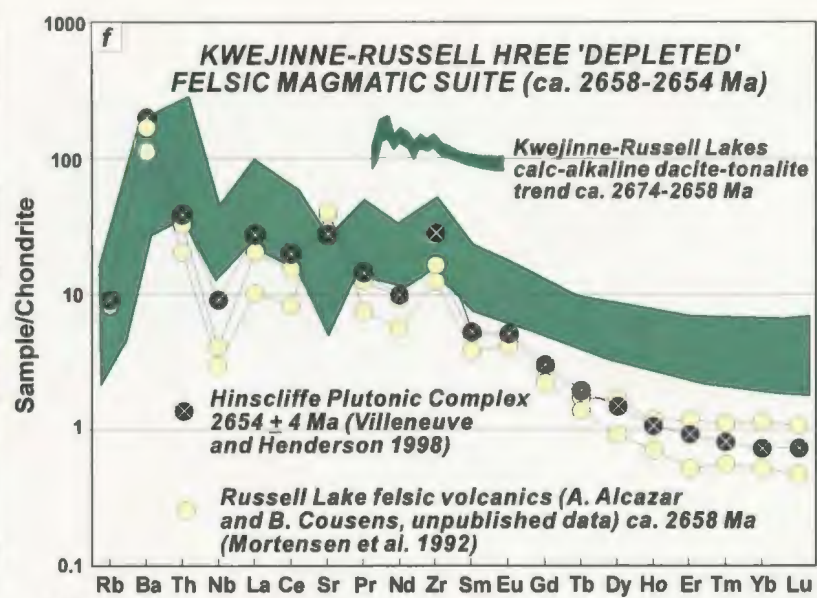
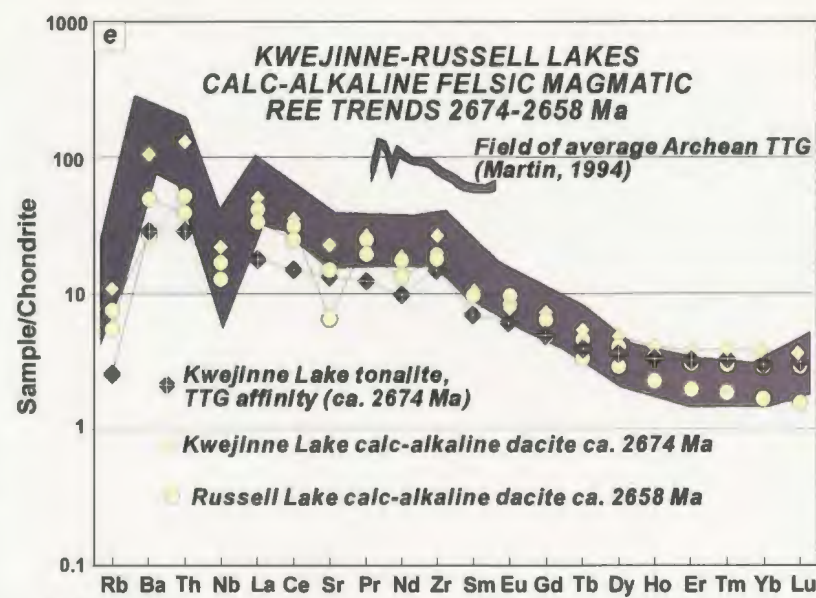


Figure 4.7: Caption see opposite

to + 3.1 (unpublished data for RSSB; A. Alcazar and B. Cousens) and + 2.8 for the ca. 2654 Ma Hinscliffe plutonic complex. They trend towards more juvenile isotopic compositions with decreasing age such that values for the ca. 2658 Ma subgroup overlap values for DM₂₆₆₀. Their ϵNd_t values overlap the range of values determined by Davis and Hegner (1992) for ca. 2.68-2.65 Ga volcanic rocks and sub-volcanic plutons from the eastern and central Slave Province ($\epsilon\text{Nd}_{2660} = + 1.2$ to + 3.6) and also with those of the variably crustally-contaminated ca. 2.66 Ga Banting Group ($\epsilon\text{Nd}_{2660} = - 0.2$ to + 4; Fig. 4.10c; Cousens et al. 2002). Davis and Hegner (1992) suggested that these rocks were mantle-derived, and Cousens et al. (2002) inferred that Banting tholeiites were melts of depleted mantle.

4.6.2 Group 2: 2637 – 2608 Ma Magmatism

Group 2 is subdivided into two suites, the 2637 Ma Disco Intrusive Suite and the 2608 Ma Mafic Intrusive Complexes. The Disco Intrusive Suite is subalkaline (Figs. 4.3e, 4.6a), granodioritic in composition, with SiO₂ contents from 65–73 % (Fig. 4.6b; Table 4.2; Perks 1997; Yamashita et al. 1999) and exhibits a calc-alkaline trend (Fig. 4.6c). It is characterized by low Rb/Sr ratios (0.063 to 0.179) and low Ni and Y contents (Ni = 0-30 ppm; Y = 2-23 ppm). A/CNK ratios are metaluminous to weakly peraluminous (Table 4.3, Fig. 4.6d), and incompatible-element patterns (Fig. 4.8a) are strongly fractionated ($[\text{La}/\text{Yb}]_{\text{CN}} = 19\text{-}57$), with moderate LREE enrichment ($[\text{La}/\text{Sm}]_{\text{CN}} = 6\text{-}8$). The suite has a strong negative Nb anomaly, moderate Sr depletion, moderate Zr and Eu enrichments and concave-up HREE abundances, similar to patterns for the broadly coeval (ca. 2620 - 2640

Figure 4.8: Chondrite-normalized (Taylor and McClennan 1985) incompatible-element patterns for Groups 2-4 metaluminous plutonic rocks in the Snare River terrane. Sources of data and symbols indicated on individual plots. *(a)* Group 2, Disco Intrusive Suite (ca. 2637 Ma) compared with Group 1, ca. 2650-2658 Ma plutons. *(b)* Comparison of Disco Intrusive Suite with the Defeat Suite of the central Slave Province. *(c)* Group 2, Mafic Intrusive Complexes (ca. 2608 Ma) compared with Disco Intrusive Suite. Note: Mafic Intrusive Complexes are subdivided into two suites using data from Ootes (2000) and this study. *(d)* Comparison of Mafic Intrusive Complexes with the ca. 2610 Ma Concession Suite (Davis et al. 1994).

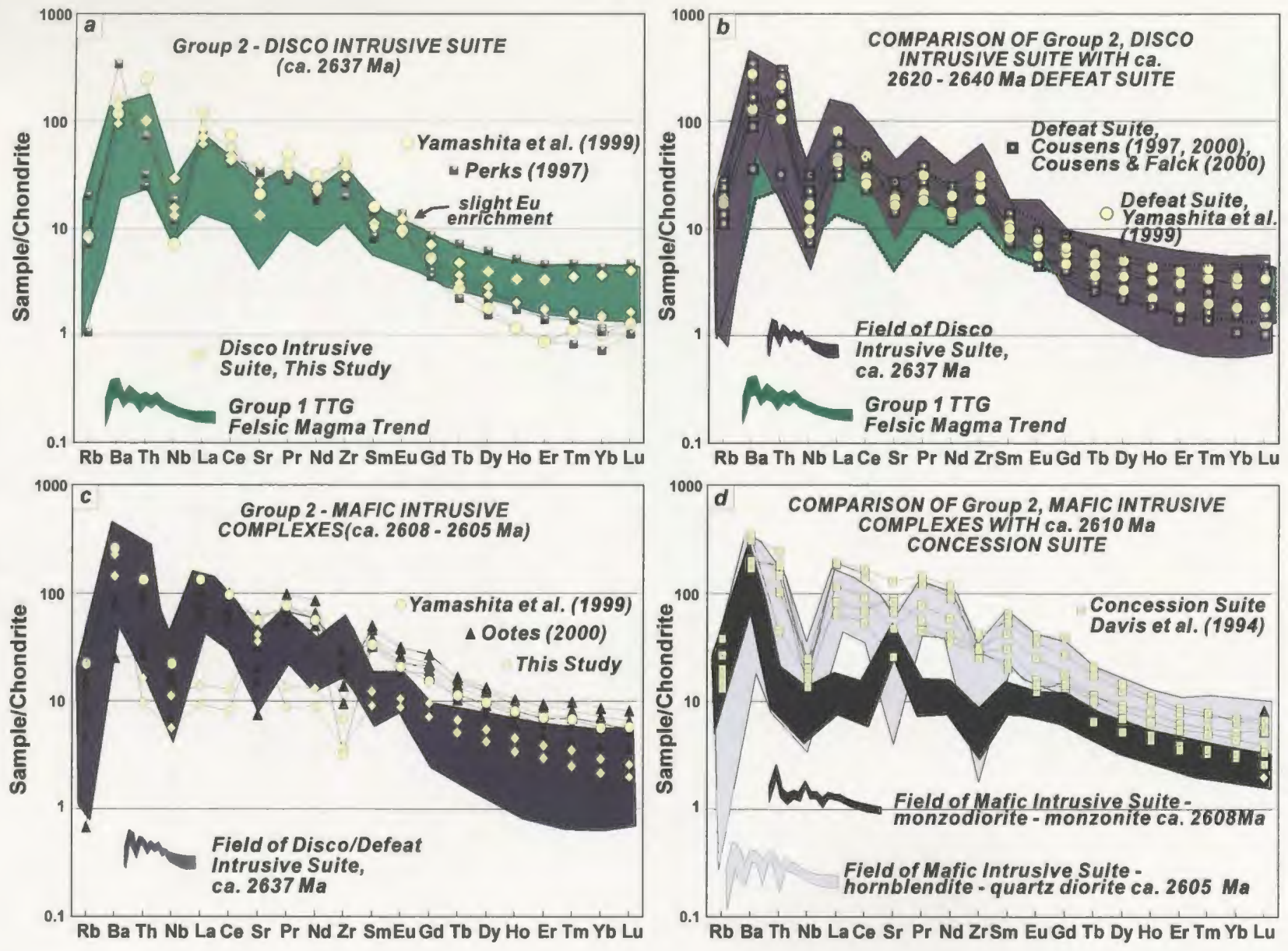


Figure 4.8: Caption see opposite

Ma) Defeat Suite in the central Slave Province (Fig. 4.8b; Cousens 1997, 2000; Yamashita et al. 1999; Cousens and Falck 2000). ϵNd_{2637} values for the Disco Intrusive Suite are predominantly positive, ranging from + 1.1 to + 1.9 (Table 4.5, Fig. 4.10a; Perks 1997; Yamashita et al. 1999), although the dataset of Perks (1997) yielded one significantly less radiogenic sample with $\epsilon\text{Nd}_{2637} = - 0.9$. Except for this sample, Nd isotopic compositions are within error of those determined for the Defeat Suite ($\epsilon\text{Nd}_{2630} = + 0.5$ to + 1.1, Fig. 4.11c; Cousens 1997, 2000; Yamashita et al. 1999; Cousens and Falck 2000).

The Mafic Intrusive Complexes comprise a distinct group of alkaline rocks (Figs. 4.3h, 4.6a) with a compositional range from gabbro and quartz diorite to monzodiorite and granite (Fig. 4.6b). They are calc-alkaline (Fig. 4.6c), have low SiO_2 (48 – 58%; Table 4.1; Ootes 2000), high Ni and low Y contents (Ni = 100 ppm; Y = 8 ppm). A/CNK ratios are metaluminous (Table 4.3, Fig. 4.6d), and incompatible-element patterns (Fig. 4.8c) permit subdivision into two sub-suites: (i) a hornblendite–quartz diorite sub-suite (Fig. 4.8c), which exhibits moderate fractionation ($[\text{La}/\text{Yb}]_{\text{CN}} = 8.2 - 23.5$; Ootes 2000; Yamashita et al. 1999), slight LREE enrichment ($[\text{La}/\text{Sm}]_{\text{CN}} = 1.3 - 4$), prominent negative Nb, Sr and Zr anomalies, no Eu anomaly, and a weakly concave-up HREE pattern, and is temporally and chemically similar to the Concession Suite (Fig. 4.8d; Davis et al. 1994); and (ii) a gabbro-monzonite sub-suite (Fig. 4.8b), which is weakly fractionated ($[\text{La}/\text{Yb}]_{\text{CN}} = 4-5$), lacks LREE enrichment ($[\text{La}/\text{Sm}]_{\text{CN}} = 1$), exhibits a weak negative Nb anomaly, prominent Sr enrichment, moderate Zr depletion and a weakly concave-up HREE pattern (Fig. 4.8c). No comparable suites are known elsewhere in the Slave Province. Nd isotopic compositions for the two sub-suites range from $\epsilon\text{Nd}_{2608} = + 1.0$ to + 1.3 (Table 4.5; Figs.

4.10 a, c), less than the calculated value of DM at ca. 2608 Ma, and overlap with the range for the Concession Suite (Fig. 4.10c; Davis et al. 1994).

4.6.3 Group 3: 2608 – 2597 Ma Magmatism

This 11 M.y. interval saw a significant increase in magmatic diversity, with contemporaneous metaluminous and peraluminous magmatism in the mid and upper crust. The metaluminous sub-group is sub-alkaline, ranges from granodioritic to granitic in composition (Fig. 4.6a-b), with SiO₂ contents of 61 – 76 % (Table 4.3; Perks 1997; Yamashita et al. 1999) and exhibits a calc-alkaline trend (Fig. 4.6c). It is characterized by low Ni and Y contents, comparatively high Sr abundances and A/CNK ratios from 0.78 to 1.1, indicating that compositions extend slightly into the peraluminous field (Table 4.3, Fig. 4.6d). Field occurrence and incompatible-element patterns permit delineation of three suites: (i) an upper-crustal biotite granite suite (Fig. 4.3i); (ii) a mid- to upper-crustal biotite granodiorite suite; and (iii) a mid-crustal orthopyroxene granite suite. (i) The biotite granite suite (Ootes 2000; Fig. 4.8e) is moderately to strongly fractionated ($[La/Yb]_{CN} = 9.8 - 24$; Table 4.3), exhibits weak LREE enrichment ($[La/Sm]_{CN} = 3 - 4.2$), a prominent negative Nb anomaly, moderate Sr and Zr enrichments, little or no Eu anomaly and a concave-up HREE pattern. The suite has chemical affinities to the Disco Intrusive Suite (Group 2; Fig. 4.8g), except for its elevated Sr content. (ii) The biotite granodiorite suite (Fig. 4.8e) is strongly fractionated ($[La/Yb]_{CN} = 22 - 75$; Yamashita et al. 1999), exhibits weak LREE enrichment ($[La/Sm]_{CN} = 3 - 5$), strong negative Nb, Sr

Figure 4.8: Continued. *(e)* Group 3 metaluminous granites, suites 1 and 2. *(f)* Group 3 metaluminous granites, suite 3, orthopyroxene granite. Fields of suites 1 and 2 shown for comparison. *(g)* Suite 2 (biotite granite) of group 3 metaluminous granites compared to ca. 2630 - 2640 Ma Defeat / Disco intrusive suites. *(h)* Comparison of group 3 metaluminous granite (suites 1 and 3) with coeval Yamba (Davis et al. 1994) and Stagg (Yamashita et al. 1999) suites. *(i)* Group 4 metaluminous tonalite compared to Group 1 magmas. *(j)* Group 4 metaluminous tonalite compared to Group 2, Defeat / Disco intrusive suites *(k)* Group 4 metaluminous tonalite compared to Group 2, Mafic Intrusive Complexes. *(l)* Group 4 metaluminous tonalite compared to Group 3, metaluminous granites (Suites 1 and 3).

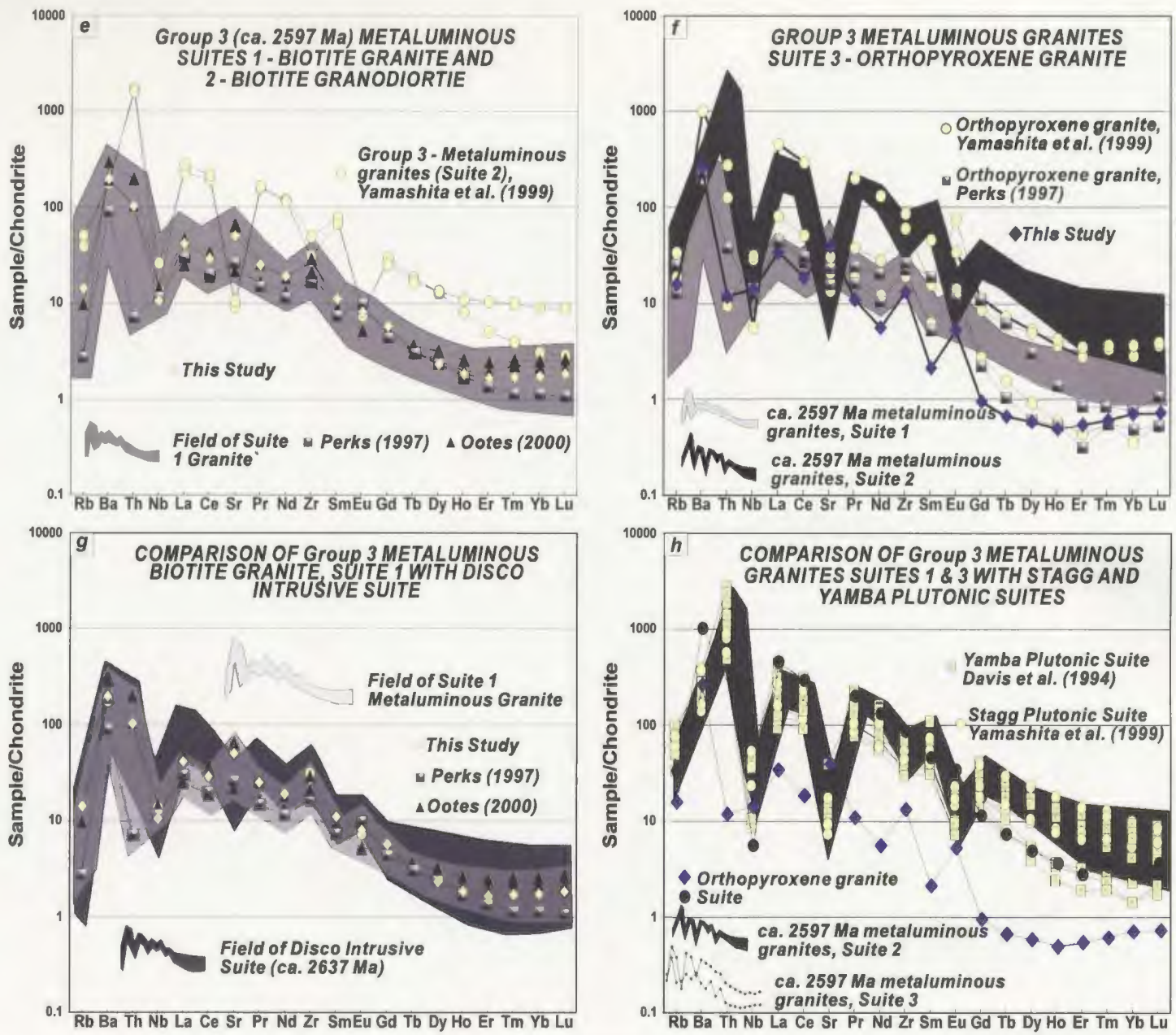


Figure 4.8: Caption see opposite

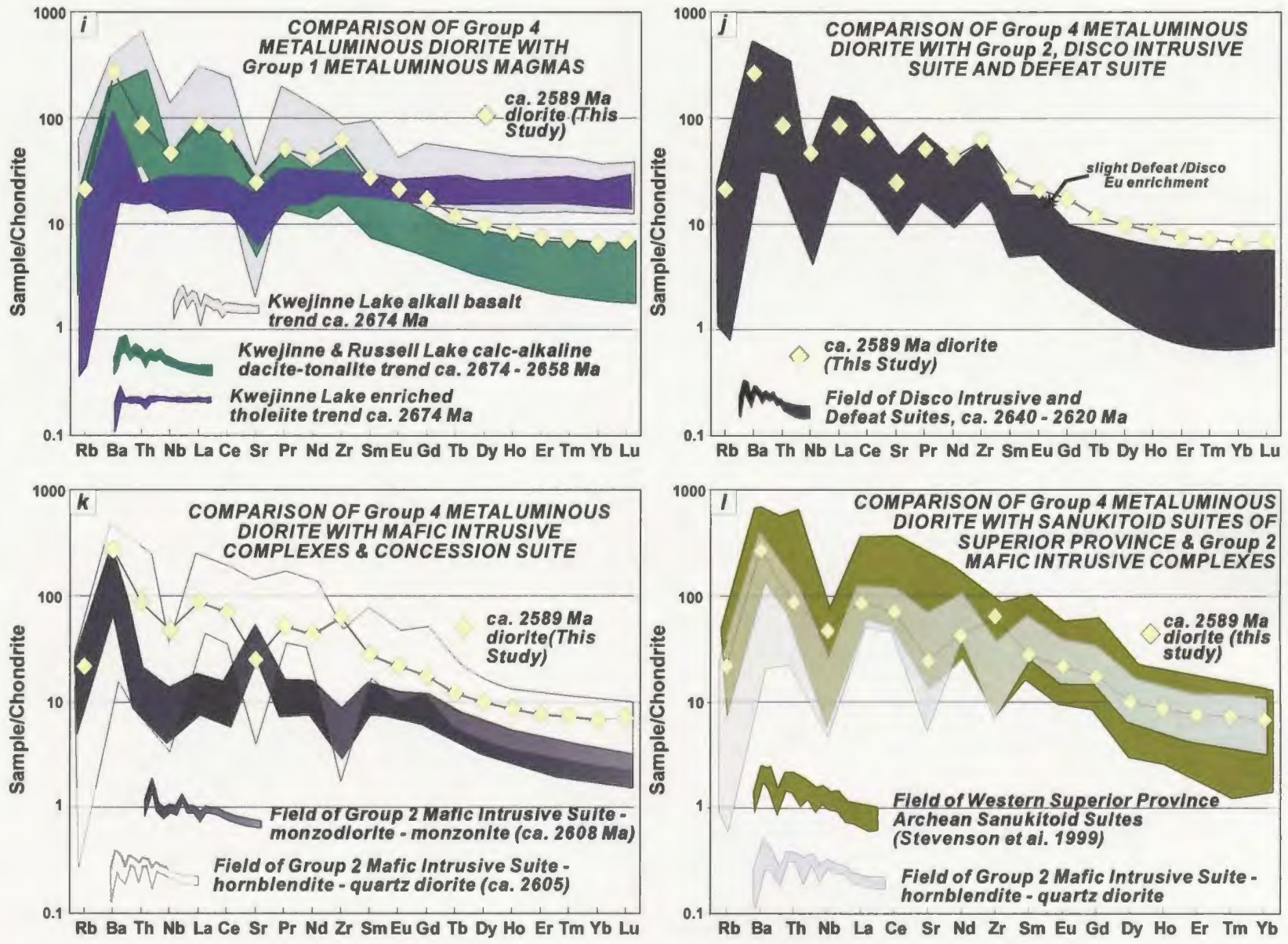


Figure 4.8: Caption see opposite

and Eu anomalies, moderate Zr depletion and a concave-up HREE pattern. Incompatible-element patterns are similar to those of the Yamba and Stagg suites (Fig. 4.8h; Davis et al. 1994; Yamashita et al. 1999). (iii) The orthopyroxene granite suite (Figs. 4.3e, 4.8f) is geochemically complex with non-parallel incompatible-element trends suggesting operation of multiple petrogenetic processes. However, all patterns are strongly fractionated ($[La/Yb]_{CN} = 48 - 159$; Table 4.3; Perks 1997; Yamashita et al. 1999), weakly to moderately LREE-enriched ($[La/Sm]_{CN} = 2 - 16$), exhibit negative Nb anomalies, strong to moderate Eu anomalies, and concave-up HREE patterns. Most samples do not have equivalents elsewhere in the Slave Province, although the most fractionated and least HREE-depleted sample (Fig. 4.8h) exhibits similarities to the coeval Yamba and Stagg suites (Davis et al. 1994; Yamashita et al. 1999). Nd isotopic compositions of Group 3 metaluminous magmas are variable, ranging from $\epsilon Nd_{2600} = -0.4$ to $+2$ (Figs. 4.10a-d; Table 4.5; Perks 1997; Yamashita et al. 1999), overlapping values determined for the Stagg Suite.

Group 3 peraluminous magmas include two-mica granite, megacrystic granite and diatexite. SiO_2 contents range from 65-74 % and they exhibit a calc-alkaline trend (Fig. 4.6b-c, Table 4.3; Perks 1997; Yamashita et al. 1999). A/CNK ratios range from 1.07-1.22 for the granites to 1.32-2.37 for diatexite, and they have low Ni and moderate Y contents (Tables 4.3, 4.4; Fig. 4.6d). Two suites can be delineated, a two-mica granite/diatexite suite and a megacrystic granite suite. (i) The two-mica granite/diatexite suite (Figs. 4.3j, k, m, 4.9a-b) has weakly to moderately fractionated incompatible-element patterns ($[La/Yb]_{CN} = 1.7 - 11.9$), weak LREE enrichment ($[La/Sm]_{CN} = 1.9-$

Figure 4.9: Chondrite-normalized (Taylor and McClennan 1985) incompatible-element patterns for Groups 3 and 4 peraluminous plutonic rocks in the Snare River terrane. Sources of data and symbols indicated on individual plots. *(a)* Group 3, peraluminous two-mica granite and metasedimentary diatexite. Comparison with incompatible-element trend of metaturbidites. *(b)* Comparison of Group 3 two-mica granite and diatexite with Contwoyto (Davis et al. 1994) and Awry (Yamashita et al. 1999) suites. *(c)* Group 3 peraluminous megacrystic granite. Comparison with trend of metaturbidites. *(d)* Comparison of Group 3 megacrystic granite with Contwoyto – Awry and Stagg - Yamba suites (Davis et al. 1994; Yamashita et al. 1999). *(e)* Group 4 peraluminous cordierite granite compared to garnet-cordierite-bearing leucosome (melt-phase) and pelite (restite) in Ghost subdomain. *(f)* Mid- and upper-crustal pegmatitic granite dykes: comparison with Contwoyto – Awry and Stagg - Yamba suites (Davis et al. 1994; Yamashita et al. 1999).

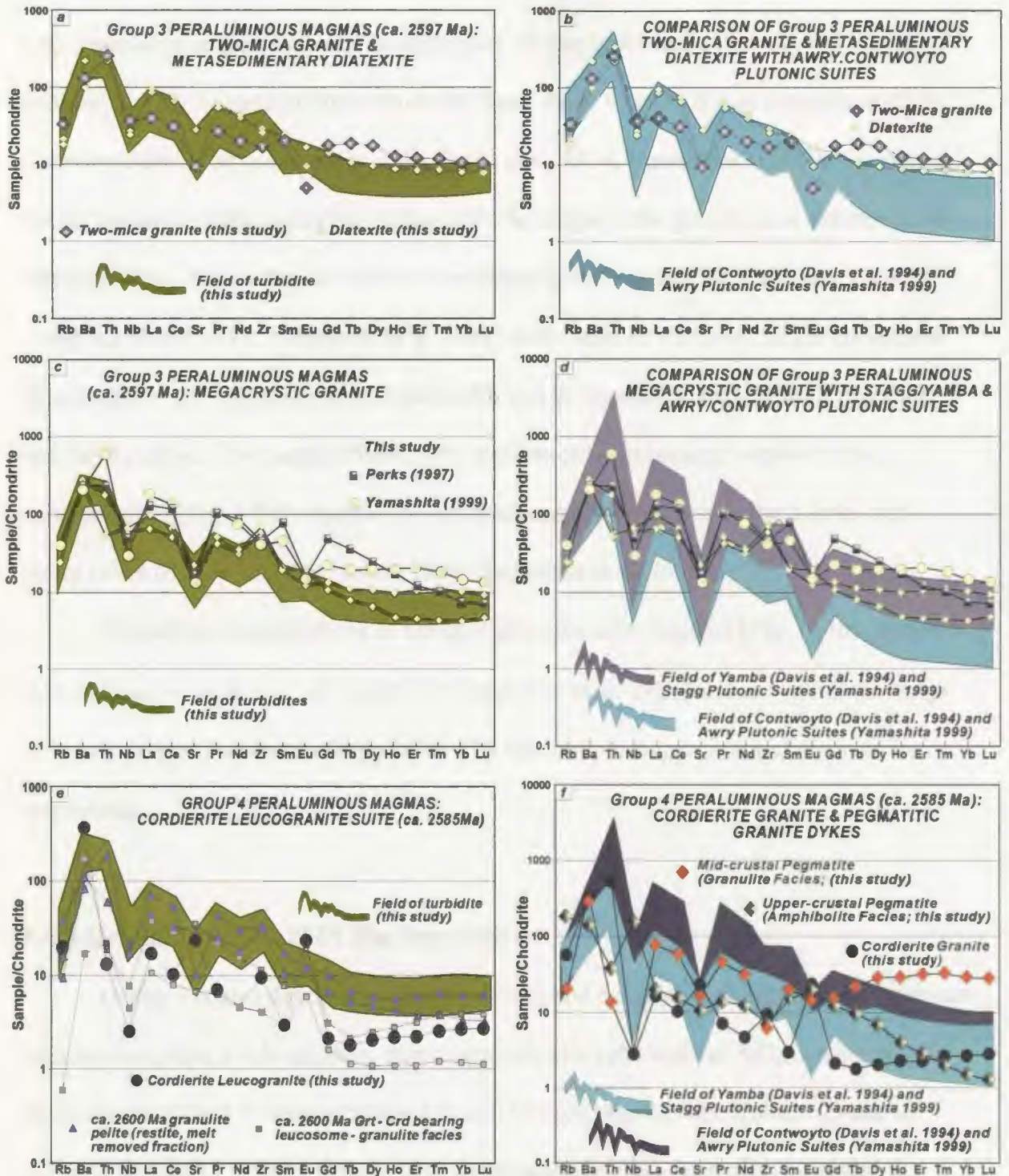


Figure 4.9: Caption see opposite

3.9), prominent negative Nb and Sr anomalies, Eu depletion and relatively flat HREE patterns, similar to metaturbidites from the Snare River terrane. It may correlate with the Contwoyto and Awry suites (Fig. 4.9b; Davis et al. 1994, Yamashita et al. 1999), although HREE contents of the former are higher. (ii) The megacrystic granite suite exhibits more variation (Figs. 4.3k, 4.9c), is weakly to moderately fractionated ($[La/Yb]_{CN} = 1.3 - 18$; Table 4.3; Perks 1997; Yamashita et al. 1999), with weak to moderate LREE enrichment ($[La/Sm]_{CN} = 1.7 - 5$), prominent negative Nb and Sr anomalies, and variable Zr values and Eu depletion. Two samples have incompatible-element patterns similar to the metaturbidites (Fig. 4.9c), whereas the remainder are more similar to the Yamba and Stagg suites (Fig. 4.10d; Davis et al. 1994; Yamashita et al. 1999).

Nd isotopic compositions of Group 3 peraluminous magmas (Figs. 4.10a, d) range from $\epsilon Nd_{2600} = +0.6$ to $+1.0$ (Table 4.5; Yamashita et al. 1999) and are within the range of values determined for the Stagg Suite. The Nd isotopic composition of diatexite was not determined.

4.6.4 Group 4: 2597 - 2585 Ma Magmatism

Group 4 is also divided into metaluminous and peraluminous suites. Metaluminous magmas comprise a calc-alkaline, diorite-granodiorite suite with an SiO_2 content of $\sim 57\%$, moderate Ni and Y concentrations (22 and 19 ppm respectively; Table 4.2) and an A/CNK ratio of 0.83 (Figs. 4.6a-d). The incompatible-element patterns (Figs. 4.8i-l) exhibit moderate fractionation ($[La/Yb]_{CN} = 13$; Table 4.2), minor LREE

enrichment ($[La/Sm]_{CN} = 3$), moderate negative Nb and Sr anomalies and concave-up HREE patterns. The suite shows some similarities with Groups 1 and 2 metaluminous magmas and with sanukitoid magmas of the western Superior Province (Figs. 4.8i-l). The ϵNd_{2590} value of + 0.8 (Table 4.5, Figs. 4.10a-d) falls in the range determined for the Awry and Stagg suites (Yamashita et al. 1999).

Group 4 peraluminous magmas are predominantly calc-alkaline and granitic (Figs. 4.6b, c). A/CNK ratios range from 1.24 – 1.37 and SiO_2 contents from ~71–75% (Table 4.3; Fig. 4.6d). Ni and Y contents are low and concentrations of some elements are extremely variable (e.g. Ba ranges from 21 to 1241 ppm). Incompatible-element patterns permit delineation of cordierite leucogranite and pegmatitic granite suites. The cordierite leucogranite suite (Fig. 4.3o) is weakly fractionated ($[La/Yb]_{CN} = 0.8$), exhibits moderate LREE enrichment ($[La/Sm]_{CN} = 5.8$), prominent negative Nb and positive Eu anomalies, moderate Sr and Zr enrichment, and a moderately positive HREE trend (Fig. 4.9e). The pegmatitic granite suite (Fig. 4.3p) exhibits complex incompatible-element patterns, variable fractionation ($[La/Yb]_{CN} = \sim 0$ to 12.8), slight LREE enrichment ($[La/Sm]_{CN} = 1.2$ to 3.9), variable Nb and Eu anomalies, and weak to moderate Sr and Zr depletions (Fig. 4.9f). Neither suite has known correlatives elsewhere in the Slave Province, although the cordierite leucogranite displays similar geochemical trends to ca. 2600 Ma, garnet-cordierite-bearing leucosomes in the Ghost subdomain, and pelitic restite is comparable to its amphibolite-facies turbidite precursor (Fig. 4.9e). Nd isotopic compositions range from $\epsilon Nd_{2585} = - 0.4$ to + 0.8 (Table 4.5, Figs. 4.10a), which are

Figure 4.10: ϵNd_T vs age diagrams for magmatic and sedimentary units in the Snare River terrane. Depleted mantle evolution trend (DePaulo 1981) and isotopic evolution of CSBC granitoids (Davis et al. 1994) plotted for reference on all diagrams. Error bars represent ± 0.5 epsilon units for data from this study, Perks (1997) and Yamashita et al. (1999) and ± 0.8 epsilon units for unpublished data of A. Alcazar and B. Cousens. *(a)* Summary diagram for magmatic suites 1-4 and two metaturbidite samples from the Snare River terrane. Data compiled from this study (Table 4.5), Perks (1997), Yamashita et al. (1999) and unpublished data of A. Alcazar and B. Cousens. Symbols and sources of data for all ϵNd_T vs age diagrams are presented in Fig. 10a. *(b)* ϵNd_T vs age diagram for Group 1 magmatic rocks and pre-2637 Ma Snare River terrane turbidites. Range of ϵNd_T values for both Kam Group tholeiites (Cousens, 2000) and Banting Group felsic volcanic rocks (Cousens et al. 2002) of the central Slave Province presented for comparison. Isotopic evolution paths of representative Kam Group tholeiites are defined in this and subsequent plots (10b-d) as: (i) oldest and least contaminated; (ii) 'average' tholeiite from Crestaurum formation; and (iii) youngest and most contaminated tholeiite from Yellowknife Bay Formation (data - Cousens, 2000). Dashed lines with arrows represent isotopic evolution trends and are plotted to examine the role of Kam Group tholeiitic magmas in Group 1 magmas petrogenesis.

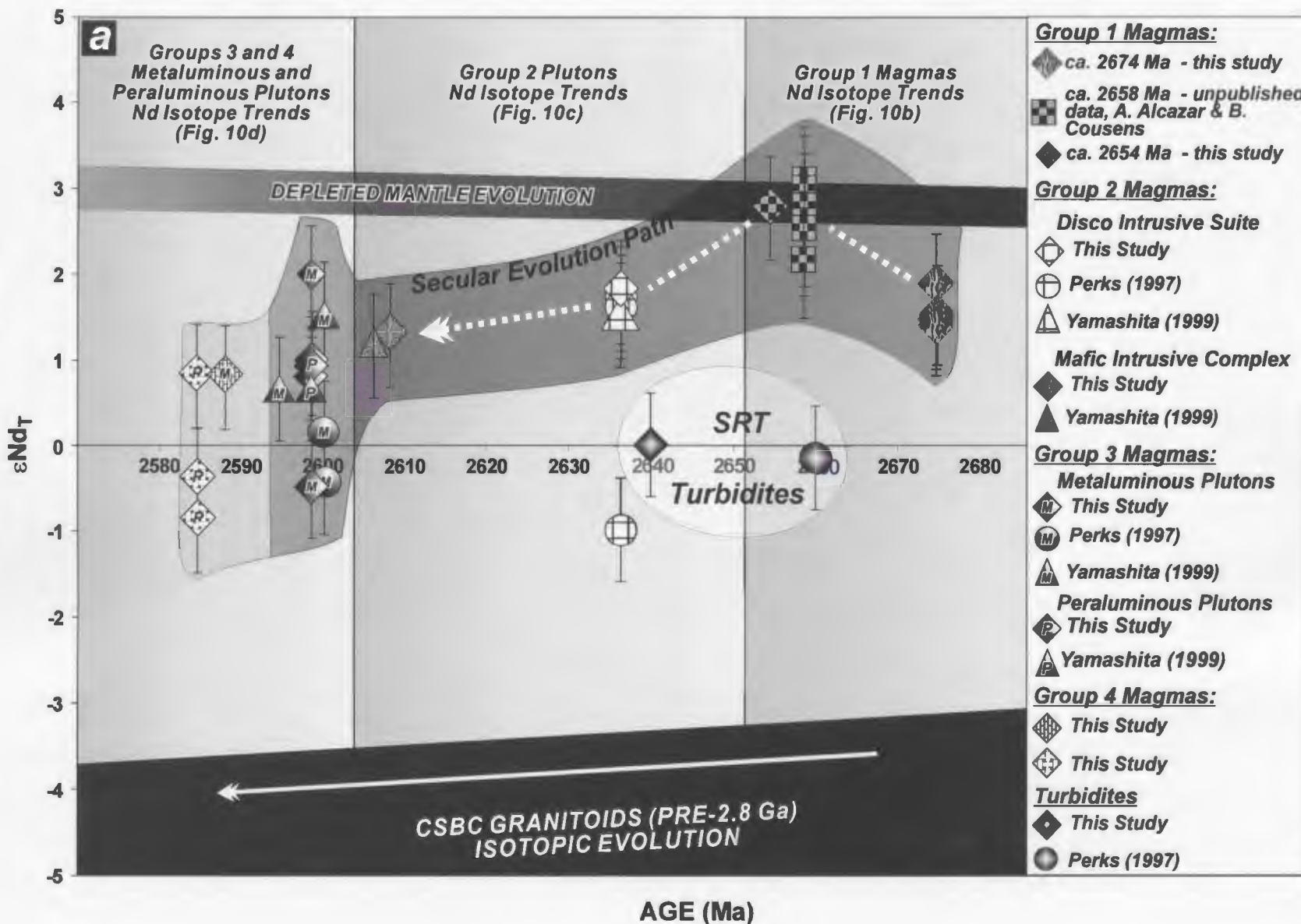


Figure 4.10: Caption see opposite

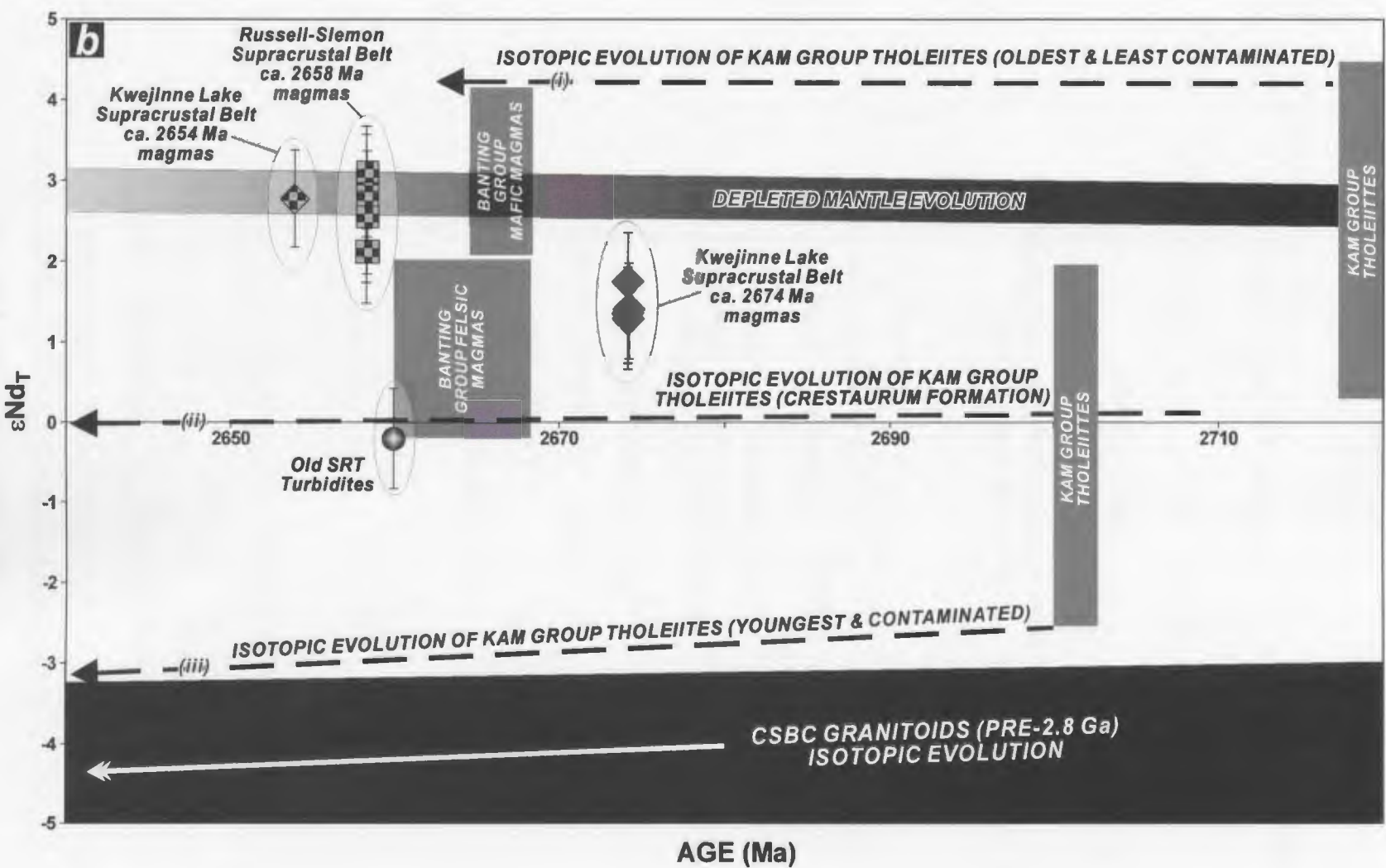


Figure 4.10: Caption see opposite

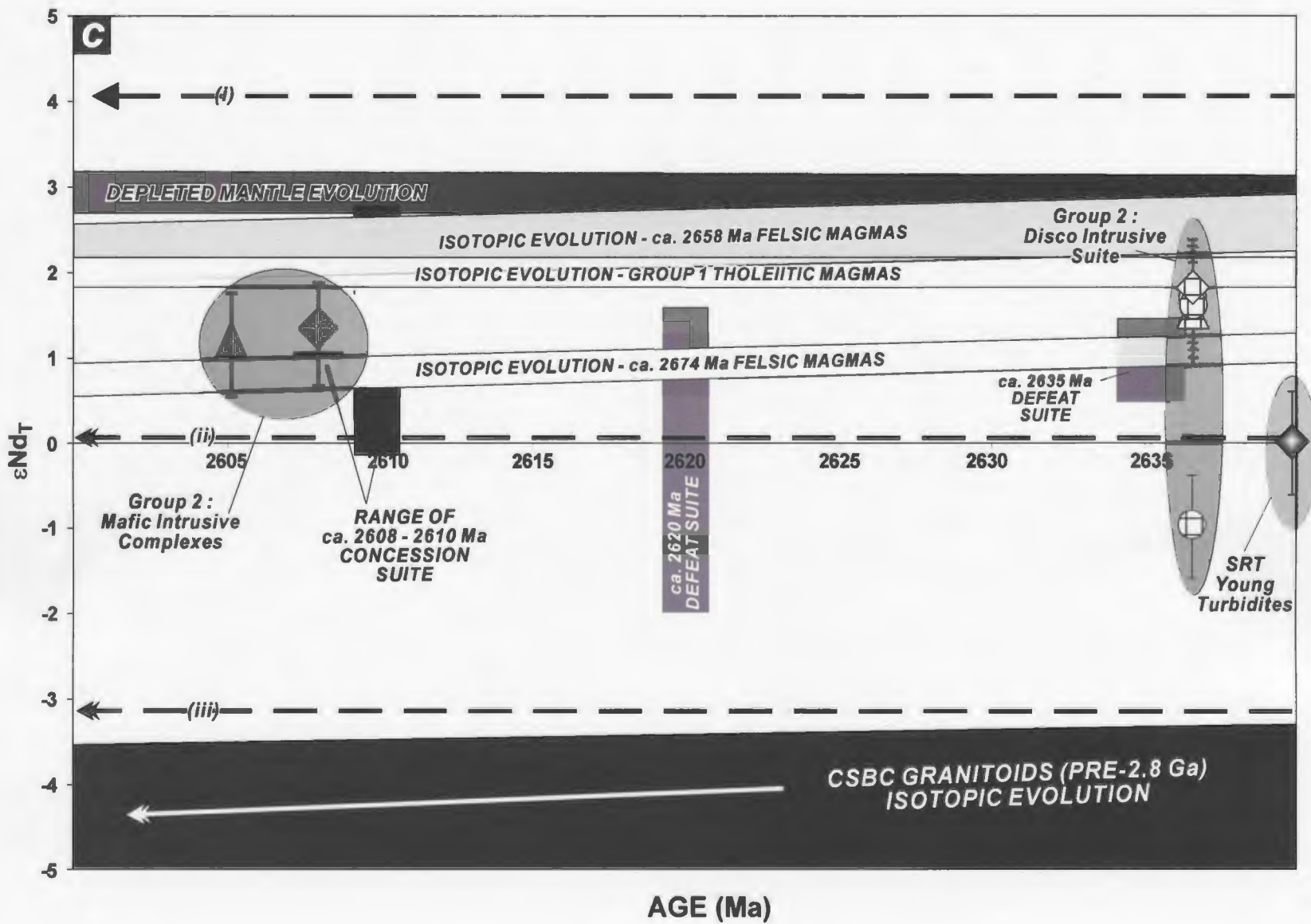


Figure 4.10: Caption see opposite

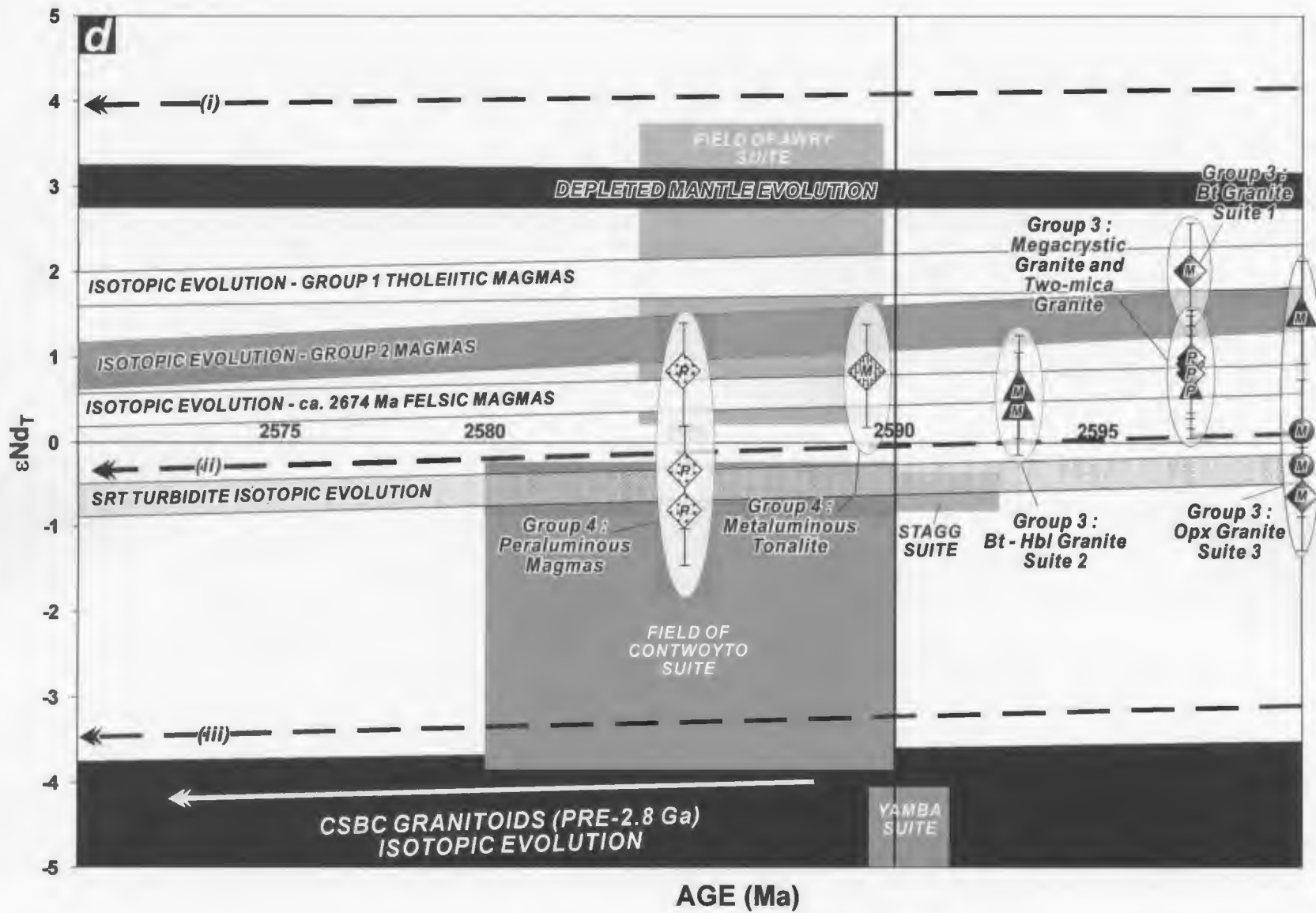


Figure 4.10: Caption see opposite

similar to values determined for the Contwoyto and Awry suites respectively (Fig. 4.10d; Davis et al. 1994; Yamashita et al. 1999).

4.6.5 Metaturbidites

Five greenschist- and amphibolite-facies metaturbidites from the KLSB were analyzed. They display a calc-alkaline trend and are strongly peraluminous ($A/CNK = 1.8$ to 3; Table 4.4, Figs. 4.6c, d). Incompatible-element patterns exhibit weak to moderate fractionation ($[La/Yb]_{CN} = 5$ to 10.5), slight LREE enrichment ($[La/Sm]_{CN} = 2$ to 3.8), prominent negative Nb and Sr anomalies, weak Zr enrichment, positive Eu anomalies and slightly concave-up HREE patterns. Nd isotopic compositions (Table 4.5; Fig. 4.10a) show little variation with ϵNd_{2635} values ranging from -0.2 to ~ 0 (Table 4.5; Perks 1997).

4.7 Interpretation

In this section, we first evaluate geochemical features that constrain magma petrogenesis and are diagnostic of particular geodynamic settings, then focus on secular variations in order to reconstruct the tectonomagmatic evolution of the Snare River terrane, before assessing the implications of the dataset for the Slave Province as a whole. Emphasis is placed on REE and HFSE data and Nd isotopic compositions, as these are more resistant to resetting during metamorphism and polyphase deformation (e.g. Condie et al. 1977; Winchester and Floyd 1977; Ludden et al. 1982; Condie 1994).

4.7.1 Crust Formation: Metaluminous Magmatism

4.7.1.1 2674 Ma tholeiites

The 2674 Ma KLSB tholeiites exhibit almost flat, elevated (20-30 times chondrite) REE patterns, they lack coupled Nb-Th anomalies, and ϵNd_{2674} values are less than DM_{2674} , features compatible with derivation from a relatively undepleted plume source removed from the influence of continental crust. These features are evaluated individually. Although the REE pattern could be generated from a mantle source that had undergone prior melting, the associated LILE depleted trends are not observed. Furthermore, pre-2674 Ma, LREE-enriched tholeiitic magmas have not been identified in the Snare River terrane. In Figure 4.11, KLSB tholeiites are normalized to tholeiites from the Ontong-Java Plateau (OJP; Mahoney et al. 1993; Tejada et al. 2002), where 20% partial melting of an undepleted peridotite source was suggested to account for tholeiite petrogenesis. For most trace elements, the KLSB tholeiites are more enriched than OJP tholeiites, indicative of a more fertile source. This is compatible with their low La/Yb and La/Sm ratios (1.5-2.2 and 1.4-1.9; Condie 2003) and their similarity to the elevated (20-50 times chondrite), REE patterns of the tholeiitic Archean Kamiskotia complex, western Abitibi subprovince (Barrie et al. 1991), which were calculated to result from 34% partial melting of chemically primitive mantle. The absence of Nb and Th anomalies argues against extensive assimilation of pre-2.8 Ga crust, an interpretation reinforced by the plot of $\text{Nb}/\text{La}_{(N)}$ vs $\text{Nb}/\text{Th}_{(N)}$ (Fig. 4.12), in which KLSB tholeiites occupy the field of oceanic plateau basalts. In contrast, Kam and Banting tholeiites spread towards the field of

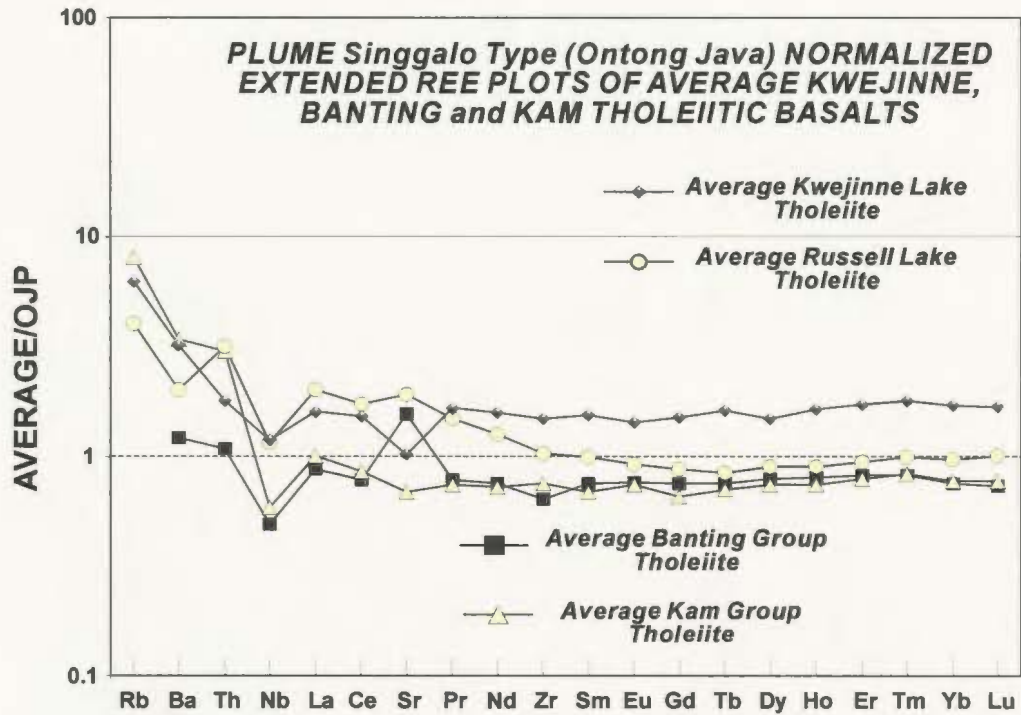


Figure 4.11. Incompatible-element patterns for average compositions of Snare River terrane tholeiites, Banting and Kam Group tholeiites and Snare River terrane calc-alkaline basalts normalized to Ontong Java Plateau (OJP) 'Singgalo-type' tholeiites (plume-source material); Data from Tejada et al. (2002). Kam and Banting data averages from Cousens (2000) and Cousens et al. (2002).

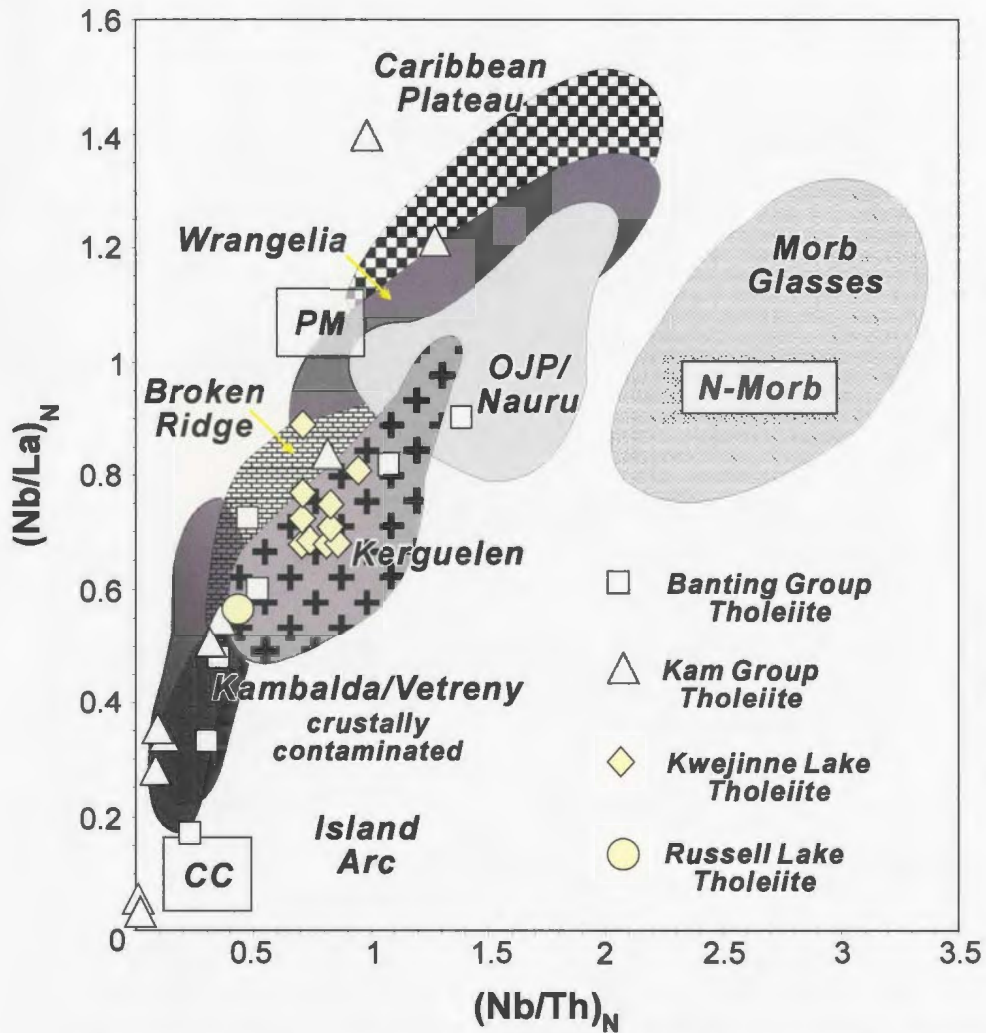


Figure 4.12: $(\text{Nb}/\text{Th})_N$ vs. $(\text{La}/\text{Nb})_N$ data for the KLSB, RSSB, Kam and Banting group tholeiites compared with modern oceanic plateaux magmas. Defined fields after Puchtel et al. (1998). Sources of data listed in Puchtel et al. (1998). CC - average continental crust (Rudnick and Fountain 1995); PM - primitive mantle, N-MORB normal mid-ocean ridge basalt (Hofmann 1988), OJP, Ontong-Java plateau

continental crust demonstrating that crustal assimilation was important in their petrogenesis (Cousens 2000; Cousens et al. 2002). Nd isotopic data for a KLSB tholeiitic gabbro ($\epsilon\text{Nd}_{2674} = + 1.9$) indicate a source more enriched than DM_{2674} (Figs. 4.10a, b). This may indicate mixing between enriched and depleted mantle reservoirs, as inferred in some modern oceanic flood basalt provinces (e.g. OJP, Caribbean and Kerguelen plateaux; Sinton et al. 1998; Mahoney et al. 1993; Tejada et al. 2002; Frey et al. 2003), and also several plume-derived Archean greenstone belts (e.g. Barrie et al. 1991; Puchtel et al. 1998; Tomlinson et al. 1998; Polat et al. 1999).

4.7.1.2 2658 Ma tholeiites

The ca. 2658 Ma tholeiites in the RSSB exhibit LREE and Th enrichment and Nb depletion, suggesting melting of an evolved mantle source, due to either crustal contamination or mantle metasomatism related to a subducting slab. In the case of crustal contamination, the positive isotopic compositions preclude significant involvement of pre-2.8 Ga crust as a contaminant, but the calc-alkaline intermediate to felsic magmas in the RSSB could be a potential contaminant as they exhibit Nb depletion and high LREE and Th abundances (Figs. 4.7e-f). Similarly, the data are permissive with respect to a subduction-zone setting, in which the descending plate is considered to be a Nb reservoir that loses LREE and Th to the overlying mantle. In summary, although their trace-element signature can be distinguished from the KLSB tholeiites, the setting of the RSSB tholeiites has not been unequivocally established.

4.7.1.3 *Calc-alkaline basalt – basaltic andesite*

In the KLSB, a suite of calc-alkaline basalt/basaltic andesite is intercalated with the plume-derived tholeiites described above. Contact and timing relationships between the two suites are ambiguous. The suite is characterized by strong Th-LREE enrichment and prominent negative Nb and Sr and moderate Zr anomalies that can potentially be generated by at least three mechanisms, i.e., melting of metasomatized mantle (e.g. Bedini et al. 1997), mixing of mafic and silicic melts (e.g. Bindeman and Davis 1999), and melting of an eclogite source followed by mantle metasomatism (e.g. Kelemen et al. submitted). On the basis of the geochemical and isotopic data, all three mechanisms could generate the basalt/basaltic andesite suite and discrimination among them is not possible from this dataset. LREE and LILE enrichments in the basalt/basaltic andesite suite from the Snare River terrane are greater than those reported elsewhere (Fig. 4.7d), which could suggest zones of variable mantle enrichment across the craton. On the other hand, Cousens et al. (2002) noted a correlation between SiO_2 , ϵNd_t , and $\text{La}/\text{Sm}_{\text{PMN}}$ (PMN – primitive mantle normalised) in evolved basalt/basaltic andesite of the Banting Group, which they attributed to crustal contamination. Hence, a combination of crustal contamination and mantle metasomatism may account for the stronger LILE-LREE enrichment in basalt/basaltic andesite suite from the Snare River terrane. Nd isotopic data, while precluding significant involvement of pre-2.8 Ga crust, are otherwise non-diagnostic.

4.7.1.4 *Calc-alkaline intermediate and felsic magmas*

Calc-alkaline intermediate and felsic magmas in the KLSB and RSSB represent the

transition from mantle to crustal melting in the interval 2674 to 2658 Ma. Two suites are identified, a TTG suite (Fig. 4.7e) that formed at ca. 2674 and 2658 Ma, and a ‘depleted’ suite (Fig. 4.7f) that formed during the ca. 2658 Ma episode. Both suites define a linear trend towards the $\text{Na}_2\text{O} + \text{K}_2\text{O}$ apex in AFM space (Fig. 4.5b), suggesting that their petrogenesis was unrelated to that of the mafic suites, which was also suggested for the calc-alkaline felsic to intermediate magmas of the ca. 2660 Ma Banting Group (Cousens et al. 2002).

The TTG-suite occurs in both the KLSB and RSSB. It exhibits the typical LREE-Zr enrichment, HREE and Nb depletion, and moderate negative Sr anomaly characteristic of Archean TTGs in general (Martin 1994), including those of the Banting Group (Fig. 4.7e, f). It is widely accepted that TTGs form by partial melting of hydrated basaltic crust at pressures where garnet and amphibole co-exist and remain in the residue (e.g. Martin 1987, 1994; Drummond and Defant 1990; Rapp et al. 1991; Springer and Seck 1997; Smithies 2000; Cousens et al. 2002). However, debate persists over the geodynamic setting, current models being: (a) dehydration melting of a mafic slab during subduction (e.g. Martin 1986, 1994; Rollinson 1997; Albarède 1998; Martin and Moyen 2002), and (b) melting at the base of magmatically or tectonically thickened crust (Atherton and Petford 1993; Condie 1994; de Wit 1998; Turkina and Nozhkin 2003). The subduction model was popular initially due to the chemical similarity between Archean TTGs and Cenozoic adakites (e.g. Drummond and Defant 1990; Yogodzinski and Kelemen 1998; Rapp et al. 1999), but the lower crustal melting model is gaining favour as a result of

estimates of crustal thicknesses of modern oceanic plateaux (up to 35 km) and the fact that TTG-affinity magmas are generated in such environments (White et al. 1999; Turkina and Nozhkin 2003). Either setting may potentially account for the TTGs in the Snare River terrane, although the average composition of Cenozoic adakites is comparatively enriched in Sr (Fig. 4.13) compared to the TTGs of the Snare River terrane and Banting Group, reflecting plagioclase stability and hence implying a shallow depth of melting (Martin and Moyen 2002). Based on the geochemistry and inferred petrogenetic settings of the coeval tholeiitic magmas, it is proposed that *both* settings may have occurred, but at different times. The 2674 Ma TTGs, which are coeval with plume-derived tholeiites, may have formed at the base of an oceanic plateau. Their positive Nd isotopic compositions ($\epsilon\text{Nd}_{2674} = +1.3$ to $+1.5$), within error of the value for the KLSB tholeiites, support this model. On the other hand, the ca. 2658 Ma TTGs are proposed to be slab-derived melts that formed in response to the onset of shallow subduction. If a subduction zone was in existence during the ca. 2658 pulse of magmatism, the tholeiitic mafic slab from which the TTGs were derived must have had corresponding ϵNd_{2660} values (i.e., between $+2.4$ and $+3.0$). A potential source for this tholeiitic material is the older, least crustally contaminated flows of 2710 – 2700 Ma Kam Group, which overlap in Nd isotopic composition with both the ca. 2674 Ma TTGs and DM₂₆₇₄ (Fig. 4.10b; $\epsilon\text{Nd}_{2660} = 0$ to $+4$; Cousens 2000).

4.7.1.5 'Depleted' TTG suite

The ca. 2658 - 2654 Ma 'depleted' suite is characterized by HREE depletion, negative Nb anomalies and Zr, Sr and Eu enrichments. This pattern can be accounted for by

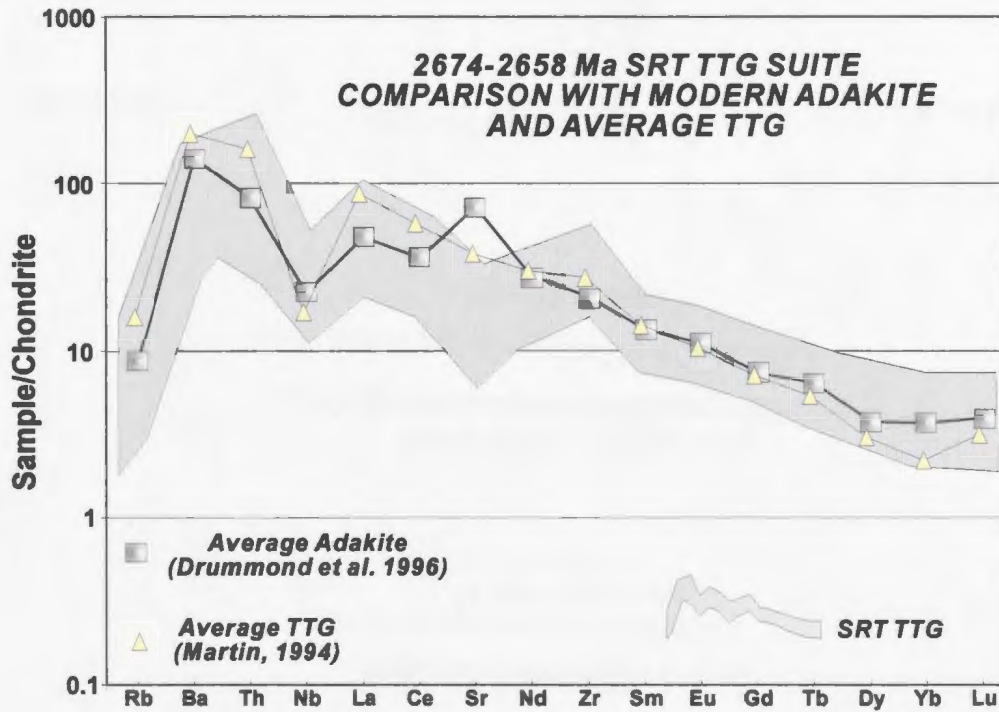


Figure 4.13: Chondrite-normalized incompatible-element diagram comparing average Archean tonalite-trondhjemite-granodiorite (TTG) composition (Martin 1994) to average modern adakite (Drummond et al. 1996) and Snare River terrane Group 1 TTG-affinity felsic magmas.

fractionation from a garnet-bearing mafic protolith (e.g. Martin 1986; Defant and Drummond 1990), similar to the Olga Suite (Davis et al. 1994), and/or partial melting of a depleted source. Sr and Eu enrichments indicate plagioclase was an important fractionating phase and suggest these depleted magmas represent differentiates as opposed to primary melts. The similar ages and overlapping Nd isotopic compositions, but contrasting geochemical signatures of the depleted and TTG suites suggest that this suite may be a differentiate of the TTG suite. The HREE depletion of the TTG suite (Fig. 4.7e,f), which would be magnified during subsequent melt fractionation, supports this interpretation.

4.7.1.6 Synthesis: Crust formation ca. 2674-2654 Ma

Two contrasting models could account for the petrogenesis of group 1 magmas generated during initial crust-formation in the Snare River terrane. In one model, tholeiite and TTG genesis is attributed to growth of an oceanic plateau as a consequence of the arrival of a mantle plume to the lithospheric mantle (Fig. 4.14a). Tholeiitic melts (ca. 2674 Ma) exhibit no definitive trace-element or Nd isotopic evidence for interaction with older sialic crust, suggesting that pre-existing crust, if present, must have been of limited extent. Tholeiite geochemistry is also consistent with partial melting of a fertile source region indicating the presence of a more chemically primitive mantle during crust-formation. The calc-alkaline basalt/basaltic andesite suite may have been generated by the interaction of ascending tholeiitic plume magmas with the overlying lithospheric, leading to enrichment and melting as the plume evolved. Rapid thickening of the crust by

volcanism and subsequent intra-crustal magma ponding resulted in the development of an oceanic plateau, which is inferred to have achieved the thickness necessary for genesis of TTGs at its base. Geochronological data (Villeneuve and Henderson 1998; Bennett et al. 2005) indicate that the plume event was short lived, possibly on the order to 2-3 M.y., similar to estimates of modern ocean-plateau-forming events (Tejada et al. 2002; Frey et al. 2003). As the plateau matured and thickened, younger tholeiitic melts were subjected to increasing crustal contamination and the growing crustal thickness led to more voluminous TTG formation, with intracrustal fractionation of TTG magmas leading to genesis of the ca. 2658 – 2654 Ma ‘depleted’ felsic suite. This is the oldest suite in the Snare River terrane to have originated by crustal differentiation and thus, is a reflection of the progress of crustal growth by this time.

An alternative model that invokes shallow subduction in an incipient arc environment is also tenable (Fig. 4.14b). Banting magmatism in the central Slave Province may have instigated lateral movements in the crust, driving it toward the Snare River area. Shallow subduction or ‘subcretion’ of this crust, originally located east of the Snare River terrane, may have resulted in the production of a ‘*protoarc*’. Material composing the slab is suggested to have been the older and least contaminated tholeiitic flows of the Kam Group, which if comparable to modern flood basalt provinces may have been extruded over an area of 200 -300 km (e.g. Columbia River Basalt Group; Reidel 1998).

Neither geodynamic setting can be ruled out. However, we invoke a model where a ca. 2674 Ma oceanic plateau evolved to a protoarc environment in response to the onset of lateral plate motion by ca. 2658 Ma. In support of this model, field evidence in the

Figure 4.14: Time-space model of crust development of the Snare River terrane. Note: due to the range of uncertainty on U-Pb detrital zircon age data and crystallization age data for the Disco Intrusive Suite, respectively, metaturbidite packages in the diagrams are referred to as pre- and post-2635 Ma groupings. *(a)* ca. 2674 Ma plume-derived crust formation in the Snare River terrane outboard of the older pre-2.8 Ga CSBC and its overlying cover sequence including the 2700 Ma Kam Group tholeiitic magmas. Crustal products include tholeiites, TTGs and basaltic andesites. *(b)* Onset of protoarc tectonics in the Snare River terrane at ca. 2660 Ma, surmised to be in part due to extension in the CSBC - cessation of TR1a and initiation of TR1b. Subcretion / subduction beneath the Snare River terrane releases LREE and Th into the overlying mantle generating an enriched mantle lithosphere beneath the Snare arc. Crustal products include tholeiites, TTGs and differentiate melts. *(c)* Continued crustal growth via protoarc tectonics. Crustal products include the ca. 2637 Ma Disco Intrusive Suite and the pre-2635 Ma (intercalation) and post-2635 Ma (deposition) turbidite packages. *(d)* Protoarc termination resulting from detachment of the subducting slab in response to collision of the Snare protoarc with the leading edge of the CBSC. Crustal products include mantle-derived sanukitoid-affinity Mafic Intrusive Complexes. Continued intercalation of pre-2635 Ma and post-2635 Ma turbidite packages into the Snare River terrane. Demarcates the end of TR1b and the initiation of TR2a.

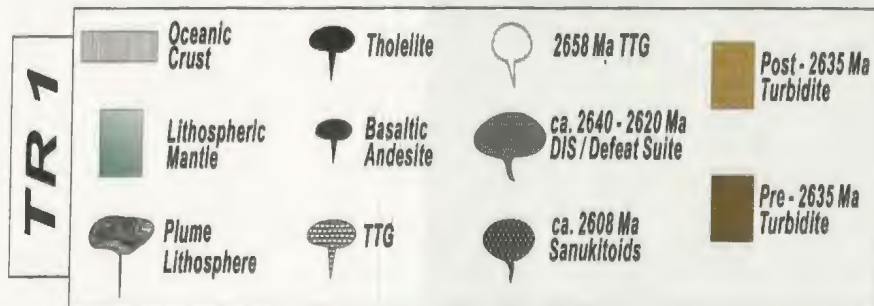
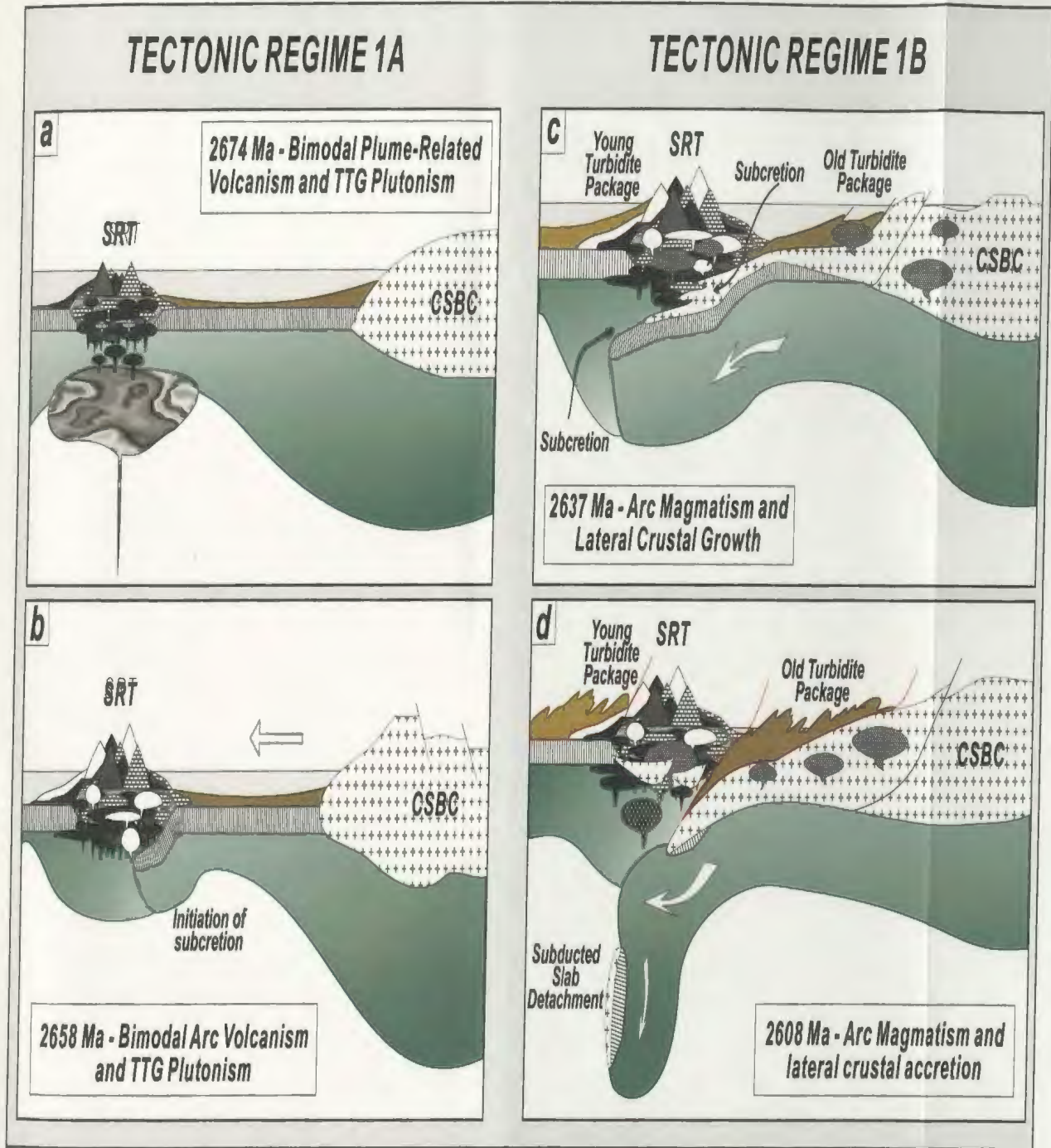


Figure 4.14: Caption see opposite

Kwejinne Lake supracrustal belt indicates that the older, ca. 2674 Ma package of tholeiite and TTG magmas experienced penetrative deformation and the formation of high-strain zones prior to regional folding and recrystallization. Younger TTGs of the ca. 2658 Ma Hinscliffe Intrusive Complex intrude one such high-strain zone with abundant highly strained enclaves of the older TTG package. This is consistent with an episode of deformation that preceded the onset of renewed TTG magmatism at ca. 2658 Ma and may represent initial subcretion of crust beneath the Snare oceanic plateau. In terms of tectonic regime, this period of early crust formation is referred to as TR1a.

4.7.2 Growth of the Snare Protoarc

Substantial crustal growth of the Snare River terrane took place between ca. 2637 and 2608 Ma. The compositionally diverse magmas that intruded during this interval exhibit evidence for significant intracrustal differentiation attributed to increased crustal thickness and residence time, which permitted operation of assimilation and fractional crystallization (AFC) processes. Although metasedimentary xenoliths have been identified in individual plutons, metaluminous magmatism prevailed, indicating the continued predominance of igneous protoliths in the magma source regions. The ca. 2637 Ma Disco Intrusive Suite and ca. 2608 Ma Mafic Intrusive Complexes represent geochemical windows into the evolving crust and mantle at this time.

4.7.2.1 Disco Intrusive Suite

The ca. 2637 Ma Disco Intrusive Suite exhibits several geochemical characteristics

similar to Group 1 TTGs (Fig. 4.8a) and is correlated with the ca. 2640-2620 Ma Defeat Suite of the central Slave Province. Yamashita et al. (1999, 2000) and Cousens et al. (2002) have argued that the steeply fractionated REE patterns of the Defeat Suite were - generated by dehydration melting of garnet amphibolite at pressures greater than 0.8 GPa, with the low K_2O/Na_2O and Rb/Sr ratios and lack of a negative Eu anomaly being consistent with garnet, hornblende, minor clinopyroxene and plagioclase as residual phases. The low K_2O/Na_2O (0.28-0.42) and Rb/Sr (0.09-0.18) ratios of the suite are compatible with this interpretation.

Minor geochemical differences between the Disco Intrusive Suite and Group 1 TTGs are indicative of slight differences in evolution. LREE abundances are greater in the Disco Intrusive Suite, implying a greater degree of crustal assimilation, and variable HREE depletion is attributed to fractionation, with the most evolved melts exhibiting the strongest depletions. The positive Eu anomaly in the Disco Intrusive Suite is inferred to be a result of plagioclase accumulation.

Most Nd isotopic compositions for the Disco Intrusive Suite ($\epsilon Nd_{2637} = + 1.0$ to $+ 1.6$) are consistent with genesis from a depleted, juvenile source such as mafic lower crust, and values fall within the isotopic evolution paths of Group 1 magmas (Fig. 4.10c), suggesting involvement of pre-2.8 Ga sialic crust was not significant. An outlier with a negative ϵNd value from Perks (1997) is not considered in the dataset as it lacks U-Pb age data and may represent a sample from the ca. 2600 Ma orthopyroxene granite suite.

4.7.2.2 Mafic Intrusive Complexes

The ca. 2608-2605 Ma Mafic Intrusive Complexes in the KLSB consist of a fractionated hornblende–quartz diorite suite, geochemically similar to Group 1 basalt/basaltic andesite and the Concession Suite (Figs. 4.8c-d), and a weakly fractionated monzodiorite-monzonite suite. The geochemical similarities among the fractionated hornblende–quartz diorite, basalt/basaltic andesite, and Concession suites suggest a similar petrogenesis. Davis et al. (1994) inferred that the elevated LILE and LREE contents of the least fractionated member of the Concession Suite were similar to modern high-Mg andesites derived from enriched mantle above a subduction zone (e.g. Kay 1978; Kelemen et al. 1993, submitted), compatible with the conclusion of Ootes (2000) for one mafic complex in the Snare River terrane (Fig. 4.3h). Figure 4.8l shows a comparison between the sanukitoids of the western Superior Province and the Mafic Intrusive Complex suite, also supporting an enriched mantle origin, with lithological diversity due to subsequent fractionation and variable degrees of greywacke assimilation.

ϵNd_{2608} values of the suite are less than the estimated DM_{2608} and may be accounted for by either mantle metasomatism during the interval ca. 2658-2608 Ma or crustal contamination. Metaturbidite xenoliths similar in composition to the samples presented in this study ($\epsilon\text{Nd}_{2608} = -0.1$) would provide a suitable contaminant.

4.7.2.3 Synthesis: Magma diversification in response to maturation of protoarc

The mafic lower crustal melts of the ca. 2637 Ma Disco Intrusive Suite differ from the calc-alkaline TTG suite in their greater degree of intracrustal fractionation and crustal

assimilation, indicating the evolving geochemical maturity of the Snare crust. The Mafic Intrusive Complexes represent a pulse of mantle magmatism that was able to penetrate the upper levels of the Snare crust, a process that had not occurred for ca. 50 M.y. However, although the lithospheric level at which magma genesis took place can be determined, the non-uniqueness of the data do not permit the geodynamic setting to be determined without supplementary evidence. In the following paragraphs, we evaluate two models, one involving a variant of the crustal delamination model of Zegers and van Keken (2001) and the other based on the subduction model of Smithies et al. (2003), briefly introducing supplementary information to discriminate between them.

In the delamination model, the Disco Intrusive Suite represents renewed thermal activity associated with the Snare oceanic plateau that resulted in mantle-derived magmas intruding and subsequently melting the thickened mafic lower crust. As noted, the TTG magmas formed by differentiation and crustal assimilation in the upper crust, where they were ultimately emplaced. A possible corollary of this model is that the crust attained a supercritical thickness some time between 2637-2608 Ma leading to lower crustal eclogitization and delamination. Flow of eclogite slabs into the lithospheric mantle could have initiated a new episode of mantle magmatism, leading to the Mafic Intrusive Complexes. This model, although satisfactorily accounting for the temporal and geochemical constraints of Group 2 magmas, is not supported by field evidence, which reveals that the interval 2637 – 2608 Ma was a time of significant crustal shortening and D1 isoclinal folding e.g. Fyson and Jackson (1990), Pehrsson and Villeneuve (1999).

The alternative subduction model implies that lateral transport of crust from outside the Snare River terrane occurred. This is compatible with field data which show that the metaturbidites from the adjacent ocean basins were intercalated with the older plume-derived volcanic in a compressional setting. A compressional setting also contrasts with the extensional environment typical of lower crustal delamination, and extensional structures of this age have not been identified in the Snare River terrane. In addition, inherited zircon U-Pb age data determined from Group 1 and Group 2 magmas (Chapter 5) demonstrate a major influx of 2700 – 2730 Ma age material into the lower crustal source region from which the Disco Intrusive Suite was generated. Collectively this information supports transport of material laterally into the Snare crust at both upper and lower crustal levels, suggesting that the original plume environment of TR1a had evolved into new tectonic regime (TR1b). On this basis, we favour a subduction-related model to account for the geochemistry of Group 2 magmas and, as noted, potentially also the Group 1, ~2658 Ma LREE enriched tholeiitic, TTG and depleted calc-alkaline magmas. However, we acknowledge that the resultant arc differed from modern arcs and hence invoke the term “protoarc” to make this distinction.

4.7.2.4 *The Snare Protoarc*

We envision the Snare protoarc (Fig. 4.14c) to be similar to the model outlined by Smithies et al. (2003) in which subduction of horizontally displaced crust occurs at a very low angle (see their Fig. 4). In the case of the Snare River terrane, crust containing both greywacke and 2720-2700 Ma mafic material (potential Kam Group correlative) was

accreted to the Snare oceanic plateau. We suggest that the mafic material was underthrust and accreted to the base of the Snare protoarc in a type of subcretion process (Fig. 4.14c), whereas the greywackes behaved in a thin-skinned manner and were shortened and intercalated with the original plateau lithologies at upper crustal levels. The Disco Intrusive Suite is inferred to be a product of this accretionary process, which is speculated to have evolved from subcretion to subduction when the slab eventually detached and descended into the lithospheric mantle. We suggest that formation of the Mafic Intrusive Complexes may represent the terminal phase of subduction that occurred in response to collision of the Snare protoarc with the leading edge of the Central Slave Basement Complex (Fig. 4.14d). At the onset of protoarc–continent collision, the subducting slab detached leading to asthenospheric mantle upwelling and renewed mantle melting in the adjacent lithosphere. Such a mechanism has been suggested for sanukitoids in the Superior Province (Corfu et al. 1995; Stevenson et al. 1999).

4.7.3 Protoarc-Continent Collision – The Snare Orogen

The cessation of protoarc magmatism in the Snare River terrane and the onset of protoarc–continent collision took place between ca. 2608 Ma and 2595 Ma. Protoarc–continent collision resulted in a new tectonic regime (TR2) involving structural reworking of existing crust and voluminous magmatic activity (Snare Orogen).

4.7.3.1 Group 3 Metaluminous Magmas

The 2595 Ma upper-crustal biotite granite suite has incompatible-element patterns

comparable to the Defeat and Disco suites (Fig. 4.8g), suggesting that its petrogenesis partly involved dehydration melting of a garnet-bearing mafic protolith in the lower crust. Sr and Eu enrichments indicate plagioclase accumulation was significant and Zr enrichment relative to Sm and Nd attests to the incompatible behaviour of Zr during partial melting (Cousens et al. 2002). The ϵNd_{2600} value (+ 2.0) falls within the isotopic evolution window of Group 1 KLSB tholeiites (Fig. 4.10d) and hence a lower crustal equivalent of this latter unit would provide suitable source material. The strongly fractionated mid- to upper-crustal biotite granodiorite suite is similar to the Yamba and Stagg suites (Davis et al. 1994; Yamashita et al. 1999). Yamashita et al. (1999) suggested the Stagg Suite formed by partial melting of a metasedimentary source. However, the incompatible-element patterns for turbidites from the Snare River terrane are less strongly fractionated than those of the Stagg Suite, lacking Eu depletion and exhibiting Zr enrichment. This may indicate a more complex petrogenetic process involving more than one protolith, as invoked by Davis et al. (1994) to account for the range of ϵNd_{2590} values in the Yamba Suite. A similar model may be applicable to the biotite granodiorite suite, for which ϵNd_{2600} values (Fig. 4.10d) plot between the isotopic evolution trends of the Mafic Intrusive Complexes and metaturbidites.

The extreme geochemical heterogeneity of the mid-crustal orthopyroxene granite suite is problematic. The broad similarity in incompatible-element patterns between some samples of this suite and the upper-crustal biotite granite suite (Fig. 4.8f) suggests dehydration melting of a lower crustal mafic source may have been important, but the more fractionated and isotopically-enriched members are comparable to the Yamba Suite

(Fig. 4.8h), suggesting magma mixing may also have been significant. Strong Eu enrichment in all samples is indicative of plagioclase accumulation. HREE concentrations are among the most depleted of all metaluminous magmas in the Snare River terrane, suggesting garnet was either an abundant residual phase or an important fractionating phase. However, the effect of metamorphism cannot be neglected, particularly as the orthopyroxene granite suite intruded granulite-facies rocks. The unit is thoroughly recrystallized and the stable coexistence of biotite and orthopyroxene is evident (Fig. 4.3g). One mechanism to generate orthopyroxene in granites is by ‘charnockitization’ or CO₂ flushing (Frost and Frost 1987; Newton 1992), a process known to cause HREE- and Y-depletion and Ba and Sr enrichment (Harlov et al. 2003), patterns characteristic of this suite. CO₂ flushing could also account for the observed heterogeneity of Nd isotopic compositions ($\epsilon\text{Nd}_{2600} = -0.5$ to $+1.3$). In this context, it is pertinent to note that the least REE-depleted sample has the most positive ϵNd_{2600} , whereas the most REE-depleted has more negative ϵNd , suggesting the isotopically positive sample was least affected by charnockitization. This sample overlaps the isotope evolution windows of the KLSB tholeiites, the Disco Intrusive Suite and the Mafic Intrusive Complexes, indicating any of these groups could have been a possible source.

4.7.3.2 Group 3 - Peraluminous Magmas

The two-mica granite *suite* is relatively HREE-enriched with a negative Eu anomaly, compatible with dry melting of greywacke (Conrad et al. 1988) with plagioclase as a residual phase. It is geochemically comparable to the Contwoyto and Awry suites,

which were interpreted as products of partial melting of metaturbidites (Figs. 4.9a, b; Davis et al. 1994; Yamashita et al. 1999). However, melting experiments involving pelitic compositions (Vielzeuf and Holloway 1988; Patiño Douce and Johnson 1991) may be more relevant to these peraluminous magmas, as mid-crustal exposures of the Snare River terrane indicate a predominance of garnet–cordierite–biotite assemblages. Dehydration melting reactions involving biotite can generate up to 50% melt by volume (Clemens and Vielzeuf 1987) and may therefore provide a source for the two-mica granite. Field relationships indicate that the diatexites are tonalitic to granodioritic in composition and that melt migration was minimal. Diatexite compositions are compatible with the results of variably water-saturated melting experiments of greywacke by Conrad et al. (1988) and almost complete melting is inferred from the similarity of incompatible-element patterns of metaturbidite and diatexite.

Nd isotopic compositions for the two-mica granite suite yield more positive ϵNd_{2600} values than the isotopic evolution window defined for the Snare River turbidites (Fig. 4.10d), implying that melting of a one-component metasedimentary source may not be realistic. Rocks of intermediate or hornblende-rich mafic compositions are highly fertile sources (Clemens and Vielzeuf 1987) and have been identified throughout Ghost subdomain. Melting of these components, which have positive ϵNd_{2600} values, and mixing/assimilation with pelitic melts may account for the ϵNd_{2600} values of the suite.

The megacrystic granite suite is characterized by variable REE contents, but overall exhibits geochemical similarities to metaturbidites and the Yamba and Stagg suites (Figs. 4.9c, d), suggesting involvement of multiple protoliths during petrogenesis. HREE

contents are not depleted, indicating that garnet was a melt phase, compatible with experiments by Patiño Douce and Johnson (1991) which showed that garnet-aluminosilicate assemblages melt incongruently to produce granitic liquid and spinel. Additionally the abundant monazite (Fig. 4.31) could be a significant contributor to both MREE and HREE abundances. The suite is also comparable to the Yamba Suite, which formed by assimilation or mixing between crustal and mafic melts (Davis et al. 1994). Average ϵNd_{2600} values (+ 0.8; Fig 4.11d) are within error of those determined for the metaluminous biotite granodiorite suite and plot between the isotopic evolution trends of Group 2 Mafic Intrusive Complexes and metaturbidites.

4.7.3.3 Synthesis - Collisional Magmatism

Protoarc–continent collision marked the onset of a new tectonic regime (TR2) involving crustal thickening and a concomitant change in magmatic style (Fig. 4.14e). Although none of the suites identified in this study represents new crustal additions extracted from the mantle, ponding of mantle-derived magmas at the crust–mantle boundary cannot be ruled out and may have been the driving mechanism for the transfer of heat necessary for lower crustal melting. In TR2a, melting of the juvenile Snare protoarc redistributed lower crustal material to the mid and upper crust. The predominantly positive Nd isotopic compositions, which indicate negligible involvement of crust pre-2.8 Ga, can be explained by mixing of metaluminous and peraluminous protoliths of the Snare protoarc in different proportions.

The onset of peraluminous magmatism during TR2 is indicative of a redistribution of material within the Snare River crust. Prior to this interval, the role of metasediments was restricted to that of a minor upper-crustal contaminant in metaluminous magmas. However, by the magmatic peak at ca. 2597 Ma, metasediments had been transported to mid-crustal depths, where they became susceptible to a high degree of partial melting (Fig. 4.14e).

The petrogenetic conditions outlined for individual suites during TR2a demonstrate heterogeneous sources, a result of tectonic juxtaposition, magma mixing and assimilation processes. Although lower-crustal melting of mafic protoliths probably continued to be an important mechanism, the locus of magma emplacement shifted to mid-crustal levels, resulting in extensive mid-crustal magmatic thickening and the transfer of heat to the upper crust. The voluminous orthopyroxene granite suite, in particular, is surmised to have advected significant amounts of heat into the mid crust and thereby buffered the ambient temperature.

Figure 4.14: Time-space model of crust development of the Snare River terrane. Note: due to the range of uncertainty on U-Pb detrital zircon age data and crystallization age data for the Disco Intrusive Suite, respectively, metaturbidite packages in the diagrams are referred to as pre- and post-2635 Ma groupings. *(e)* Orogenic peak at ca. 2600 Ma defined predominantly by voluminous metaluminous and peraluminous magmatism, mid-crustal thickening, complete structural reworking of the Snare River terrane. Represents the end of TR2a. *(f)* Post-orogenic collapse took place in the 15 M.y. following the orogenic peak and is surmised to have been driven by delamination of a dense lower crustal root and resulted in sanukitoid magmatism, crustal extension and mid-crustal exhumation.

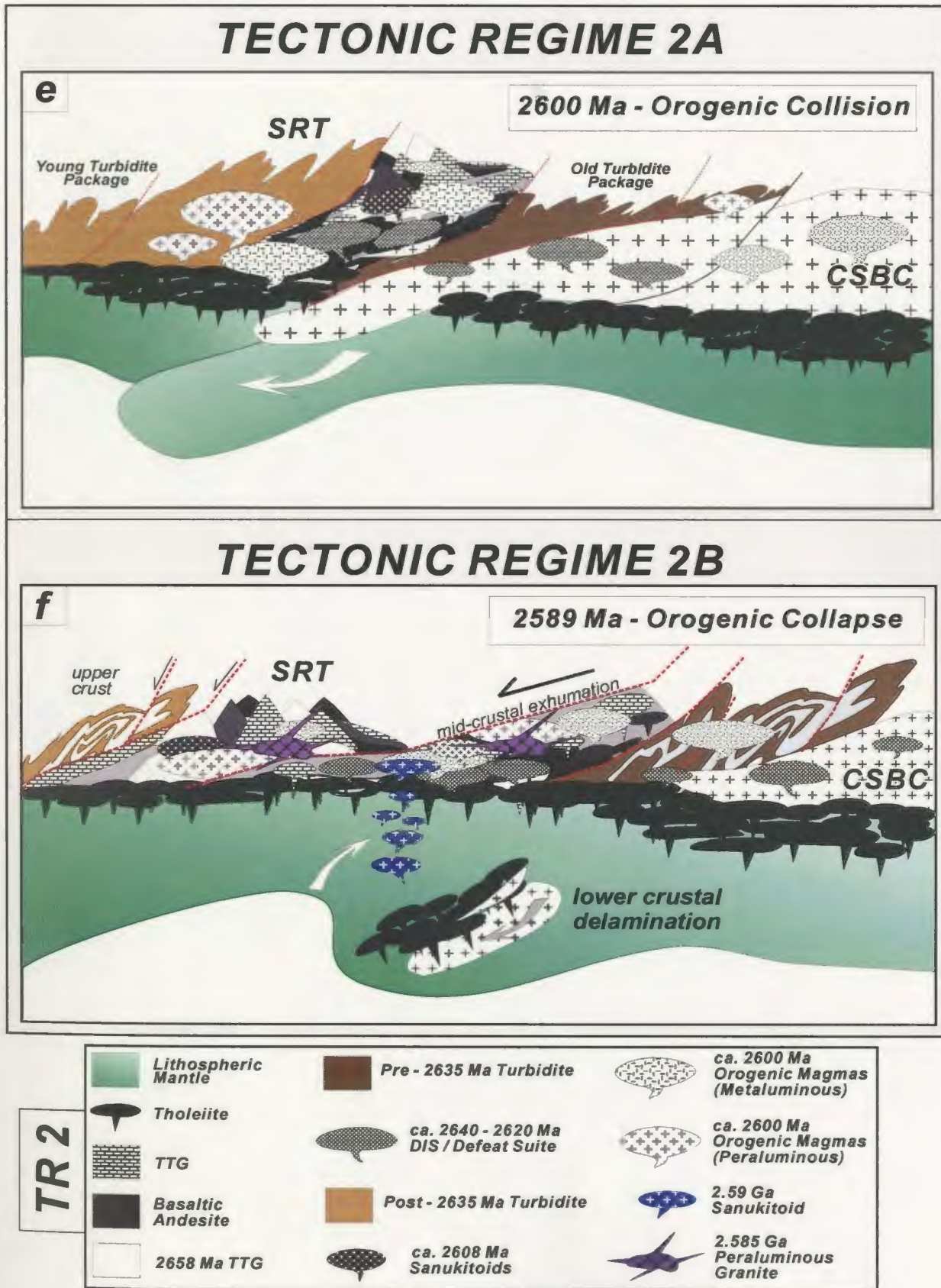


Figure 4.14: Caption see opposite

4.7.4 Post-Orogenic Magmatism

4.7.4.1 Metaluminous Magmatism

In Fig. 4.81, the 2589 Ma sanukitoid suite is compared to sanukitoids from the western Superior Province. The Snare River suite exhibits the characteristic LILE and LREE enrichment, high Mg number (0.46), high P₂O₅, Sr and Ba and low Nb concentrations, low Rb/Sr, and a weak to absent Eu anomaly. The quartz monzodioritic to granodioritic composition, Zr- and Sr-depletion, and enriched (with respect to DM₂₅₈₉) Nd isotopic compositions suggest the sanukitoids are evolved, crustally contaminated melts. The sanukitoid suite of the Superior Province is inferred to have been derived by partial melting of mantle previously metasomatized by fluid infiltration from a subducted slab (Shirey and Hanson 1984; Stern et al. 1989; Stern and Hanson 1991; Bibikova 2003). However, its post-collisional nature precludes genesis during active subduction and poses a problem with respect to the mantle heat source. Stevenson et al. (1999) suggested a model involving rise of asthenospheric mantle following delamination of the subducted slab. This mechanism cannot be ruled out for the Snare River sanukitoids, but a modification is preferred, in which delamination involved removal of an eclogitised lower-crustal root that formed in consequence to magmatic crustal thickening at ca. 2600 Ma. The emplacement of small-volume, mantle-derived, volatile-rich alkaline complexes (e.g. Villeneuve and Relf 1998; Stubbley and Cairns 1998) and lamprophyres (Armstrong 2001) across the Slave Province was approximately coeval with the sanukitoid suite, implying localized but widespread fluid activity in the mantle at ca. 2595 Ma, which may also have enhanced eclogitisation of the lower crust (Leech 2001). This model is also

compatible with exhumation of the mid-crustal Ghost subdomain during the M3 metamorphic event as crustal uplift would have been a consequence of asthenospheric upwelling as the delaminated root descended (Fig. 4.14f).

4.7.4.2 *Peraluminous Magmatism*

Major- and trace-element compositions of cordierite leucogranite are consistent with derivation from metasedimentary precursors. Positive Sr and Eu anomalies indicate plagioclase fractionation and Zr enrichment attests to the evolved state of the melt. Low La/Yb_{CN} ratios compared to peraluminous magmas formed during TR2a suggest the source was depleted in LREEs, and the prominent HREE depletion may imply garnet was restitic. The geochemical similarity between the ca. 2585 Ma cordierite leucogranite suite and the in situ ca. 2600 Ma garnet–cordierite leucosomes that were derived from the adjacent garnet-biotite-cordierite-bearing pelite (Fig. 4.9e) supports derivation from a granulite-grade pelitic source rock. Nd isotopic compositions also support derivation from metaturbidite. Analogous cordierite leucogranite in the Peña Negra complex, Central Spain (Pereira and Rodriguez Alonso 2000) formed during the waning stages of the Hercynian orogeny, where during the main orogenic stage, large melt-fraction, peraluminous granodiorite magmas were produced by partial melting of metasedimentary migmatite and assimilation of orthogneiss, and the post-tectonic cordierite leucogranite involved decompression-melting of the depleted source. A similar geodynamic setting is proposed for the Snare River terrane.

The pegmatitic granite suite is geochemically complex and a detailed analysis is beyond the scope of this study. The mineralogy and peraluminous composition suggest derivation by melting of crustal rocks. La/Yb_{CN} ratios are low, as in cordierite leucogranite, and weak Zr and Sr depletions indicate the suite is not highly evolved. Variable behaviour of garnet in the source and/or melt may explain the divergent HREE profiles of upper- and mid-crustal samples. Nd isotopic compositions for upper-crustal pegmatite ($\epsilon\text{Nd}_{2585} = -0.8$) are consistent with derivation from metaturbidite, whereas those for mid-crustal pegmatite ($\epsilon\text{Nd}_{2585} = +0.8$) suggest either the source involved more than one protolith or that the isotope systematics were disturbed during M3.

4.7.4.3 Post-orogenic magmatism: summary model

Post-orogenic magmatism took place some 10-15 M.y. after the orogenic peak at ca. 2.6 Ga. Magma geochemistry, melt volume and pluton morphology all contrast with the voluminous syntectonic magmas emplaced during TR2a, and the inferences of renewed mantle melting (sanukitoid suite) and decompression melting (cordierite leucogranite suite) indicate a change in geodynamic setting by 2589 Ma (TR2b; Figs. 4.2, 4.14f). The pegmatitic granite intrusions post-date structures attributed to extensional collapse (Chapter 3). A 10 to 25 M.y. time gap between syn- and post-orogenic magmatism was also reported in the Wawa domain of the Superior Province (Moser et al. 1996) and attributed to extension driven by delamination of the orogenic lithosphere. Such a setting is also inferred for the Snare River terrane.

4.8 Tectonic Implications of Magmatism

Secular variations in major- and trace-element chemistry and Nd isotopic composition reveal how magmatism evolved on the scale of the orogen. The AFM diagram (Fig. 4.6c) illustrates that during crust formation, magmatism began with relatively quartz- and alkali-poor compositions and evolved towards more alkali-rich magmas with increased modal quartz, compatible with the introduction of metasedimentary material and TTG into the source region and the increasing importance of AFC and remelting processes. During post-orogenic collapse, peraluminous magmas also evolved towards alkali-rich compositions, whereas metaluminous magmas reverted back to the less evolved compositions that prevailed during early crust formation. In terms of the tectonic regime concept, these variations reflect a progressive evolution of magma compositions over the ca. 66 M.y. of crust-formation and growth during TR1, culminating at the orogenic peak (TR2) in a diverse array of evolved suites (Fig. 4.14e). The secular evolution path defined by Nd isotopic compositions (Fig. 4.10a) shows a gradual change from relatively homogeneous, juvenile compositions to more evolved and enriched compositions over time as crustal sources became more heterogeneous. Of note is the large spread of compositions determined for magmas at the ca. 2600 Ma orogenic peak, implying development of multiple and complex magma source regions by that time.

The main stages of orogenic evolution are inferred from mantle melting events: i.e., 2674 Ma tholeiites define the onset of plume-related crust formation, 2658 Ma tholeiitic magmatism demarcates the onset of subcretion and protoarc formation, 2608 Ma sanukitoids formed in response to protoarc–continent collision, and 2589 Ma sanukitoids

formed in response to lithospheric delamination. The correlations between mantle-melting events and crustal evolution indicate that orogenesis was manifested in the lithospheric mantle as well as the crust, implying a coupled crust-mantle system. An enriched or metasomatized mantle source is characteristic of the four mantle-melting episodes outlined above, suggesting a correlation also between orogenesis and the chemical state of the underlying lithospheric mantle.

Crustal melting in the Snare River terrane recycled and redistributed material in the evolving crustal column. Crustal melts were predominantly metaluminous during crust formation and growth (TR1), but diversified substantially by the orogenic peak (TR2) due to mid-crustal burial and subsequent partial melting of metasedimentary material, resulting in coeval peraluminous and metaluminous magmatism. The persistent formation of HREE-depleted metaluminous magmas during TR1 indicates the progressive growth of a garnet-rich mafic lower crust. The apparent absence of such magmas post-2600 Ma suggests that a change in the lower crustal dynamics occurred after that time. Delamination of a dense lower-crustal root may account for this and furthermore is compatible with sanukitoid magmatism at ca. 2589 Ma and formation of small-volume cordierite leucogranite by decompression melting.

The exposure of an upper- to mid-crustal section in the Snare River terrane permits the establishment of a magmatic 'stratigraphy' that can be integrated with the crustal architecture to yield a time-space model of crustal evolution (Fig. 4.15a-d). The oldest components (TR1a-b) are intercalated with turbidites and preserved in the upper crust and as enclaves in mid-crustal plutons (Figs. 4.15a, b). In contrast, the mid crust

consists predominantly of magmas emplaced during the orogenic peak (TR2a; Fig. 4.15c). Post-tectonic sanukitoids and cordierite leucogranite (TR2b) are also restricted to the mid-crust, but pegmatitic granites occur throughout the exhumed section (Fig. 4.15d). Figure 4.15 reveals that crust formation was not uniform in time or space. After formation of a crustal nucleus, crustal evolution proceeded predominantly by magmatic thickening in the mid crust, and the older crustal roof may have acted as a cool dense lid that caused rising magmas to freeze as they reached its base.

4.8.1 Pan-Slave Implications

Published models for Neoproterozoic tectonic evolution of the Slave Province are focus two paradigms: (i) intracratonic rifting followed by basin closure (e.g. Henderson 1981; Thompson 1989; Padgham 1990; Yamashita et al. 2000); and (ii) arc-related tectonics (e.g. Hoffman 1986; Kusky 1989; Davis et al. 1994). The role of pre-2.8 Ga basement in the Neoproterozoic tectonic development of the Slave Province has only recently been recognized (e.g. Bleeker et al. 1999a, b; Pehrsson et al. 2000; Yamashita et al. 2000; Bennett et al. 2002, 2003) and is further developed here.

New crust-forming tholeiitic and calc-alkaline magmatism in the interval 2.68 to 2.65 Ga had similar compositions across the Slave Province. However, Banting Group and associated magmas in the south central Slave Province are characterized by trace-element and isotopic fingerprints indicative of contamination by sialic crust (Cousens et al. 2002), whereas coeval magmas farther east and west lack a crustal contamination signature, suggesting that pre-existing sialic basement was restricted to the central region of the

province (Bleeker and Davis 1999). Another contrast is that Nd isotopic ratios of Banting Group tholeiites imply derivation from an upper mantle source similar in composition to DM ($DM_{2660} = + 2.7$; Cousens et al. 2002), whereas ϵNd values of tholeiites in the Snare River terrane ($\epsilon Nd_{2674} = + 1.9$) suggest a less depleted mantle source. This implies that the Neoproterozoic mantle beneath these two components of the Slave Province was chemically different at ca. 2680-2660 Ma, possibly reflecting prior melt extraction beneath the pre-2.8 Ga Central Slave Basement Complex, leading to its more depleted signature.

Despite the similar sources of Banting magmas and their correlatives across the Slave Province, variability in trace-element and Nd isotopic data imply the existence of different crustal architecture and possibly tectonic settings across the province. It is inferred that the variable crust–mantle structure at the onset of the Neoproterozoic imparted significant control on the type of tectonic regime that evolved in response to the ca. 2.68-2.66 Ga pan-Slave thermal event, such that where pre-existing crust was present (e.g. central Slave Province), impingement of mantle plumes instigated intracratonic rifting and basin development, whereas in regions distal to basement blocks (e.g. Snare River terrane), plume activity was manifest as oceanic plateaux. Intracratonic rifting in the central part of the craton may have subsequently driven protoarc formation as a result of lateral crustal movements in response to extension (drift) and subsequent collision with juvenile outboard terranes.

Crustal growth during TR1b was characterized by lateral accretion of granite–greenstone/granite–volcano-sedimentary/TTG belts and turbidite basins in a compressive tectonic regime (Fig. 4.14). Magmas emplaced between ca. 2640-2620 Ma and 2615-2605

Ma track this accretion process. Correlation of the 2637 Ma Disco Intrusive Suite with the Defeat Suite implies that similar petrogenetic processes were involved in the formation of both suites; however, the negative ϵNd_{2630} values for the Defeat Suite compared to the positive values for the Disco Intrusive Suite imply that their tectonic settings with respect to basement were different. Similarly, the correlation between the ca. 2608 Ma Mafic Intrusive Complexes and plutons of the Concession Suite east of the Nd and Pb isotopic boundaries, indicates that a mantle-melting episode marked the termination of protoarc tectonics in juvenile terranes on either side of the Central Slave Basement Complex. Improved definition of the geographic extent of the Concession Suite is necessary to assess whether this was a pan-Slave event. In summary, the geochemical and isotopic datasets require more than one tectonic setting for Neoproterozoic crust formation and growth during TR1, potentially providing a means of reconciling the published rifting and subduction models.

Cratonization (TR2a) occurred when the major components of the Slave Province were assembled into a thick orogenic crust and stitched together by magmas largely derived by crustal reworking and recycling processes (ca. 2600 Ma). Pan-Slave correlations imply that source regions were well mixed and broadly similar in composition by this time. Additionally, the huge quantities of magmas that intruded across the province at ca. 2600 Ma in a range of tectonometamorphic settings, imply an significantly elevated crustal heat budget, which may have, in part, been a consequence of craton-wide high mantle heat flow (see chapter 6). Intrusion of the ca. 2608 Ma sanukitoid suite is suggested to demarcate the onset of this elevated geothermal regime in the Snare River

terrane. The ca. 2589 Ma sanukitoid and ca. 2585 Ma cordierite leucogranite suites provide new insight into cratonic stabilization (TR2b). Their inferred association in the Snare River terrane with lower-crustal delamination, HT-LP metamorphism, decompression melting and mid-crustal exhumation prompts a search for related features elsewhere in the Slave Province. On the basis of recent data, it appears that Neoproterozoic crust on *both* the eastern and western margins of the Central Slave Basement Complex preserves evidence of comparable stabilization processes. For instance, normal faulting at ca. 2600-2590 Ma juxtaposed the low-grade Indin Lake supracrustal belt with the high-grade Cotterill Gneiss Complex (Fig. 4.1a; Pehrsson and Villeneuve 1999), late carbonatite magmatism was associated with extensional unroofing of the high-grade Nardin metamorphic complex that straddles the western margin of the Central Slave Basement Complex (Fig. 4.1a; Villeneuve and Relf 1998; Armstrong 2001), and the Walmsley Metamorphic Complex has a strikingly similar post-2600 Ma history to the Snare River terrane (Fig. 4.1a; Cairns et al. 2005). These processes appear to have been characteristic of the juvenile Neoproterozoic belts juxtaposed against the eastern and western margins of the pre-2.8 Ga cratonic nucleus.

4.9 Conclusions

We have integrated geochemical and Nd isotopic data for representative magmatic suites that formed over ca. 90 M.y. in the Snare River terrane, western Slave Province, to elucidate the sequence, spatial distribution and tectonic setting of Neoproterozoic magmatism. Crustal evolution was punctuated by four mantle-melting episodes, permitting subdivision

into tectonic regimes associated with crust formation and growth (*TR1a-b*) and orogenesis and orogenic collapse (*TR2a-b*) respectively. Crustal magmas during *TR1a-b* were generated in the mafic lower crust, whereas those during *TR2a-b* were principally generated in the mid crust, implying that source regions and the locus of melting changed with time and that crustal magmatism redistributed material in the evolving crustal column. The persistent formation of HREE-depleted metaluminous magmas during *TR1a-b* implies progressive growth of a garnet-rich lower crust; their absence after the orogenic peak is considered evidence for lower crustal delamination.

The crust of the Snare River terrane is age and compositionally stratified, with the older, low-grade, upper crust composed predominantly of metaluminous magmas formed during *TR1a-b* and the younger, high-grade, mid crust composed of both metaluminous and peraluminous magmas formed during *TR2a-b*. Increased magma diversification during *TR2a-b* is indicated by multiple sources for several metaluminous suites. Furthermore, the initiation of voluminous peraluminous magmatism implies metasedimentary material had entered the melt region for the first time. Post-orogenic collapse, manifest by small-volume sanukitoid magmatism, was succeeded by decompression melting resulting from a second episode of lower crustal delamination. The close relationship between mantle melting and crustal evolution implies a coupled crust–mantle system, with the evidence for enriched or metasomatized mantle sources suggesting a link between orogenesis and the chemical state of the underlying mantle.

With respect to tectonic setting, crust formation was initiated at ca. 2674 Ma by tholeiitic magmatism and is speculated to have involved partial melting of chemically

primitive mantle in an oceanic plateau environment. Partial melting at the base of the thickened plateau led to coeval TTG magmatism, whereas 2658 Ma TTGs are inferred to have developed by shallow subduction or subcretion beneath the oceanic plateau, leading to the formation of a protoarc. Collision of the protoarc with the pre-2.8 Ga Central Slave Basement Complex at ca. 2608 Ma resulted in structural reworking of the Snare mid crust, granulite-facies metamorphism and voluminous orogenic magmatism prior to orogenic collapse ca. 15 M.y. later. Many elements of this tectonic scenario have counterparts in modern plate tectonics, compatible with the suggestion that the Neoproterozoic was a time of incipient plate tectonics, but we infer that the Snare protoarc was a local feature that predated the organization of subduction zones and island arcs along linear plate boundaries in the style of modern plate tectonics. Inasmuch as a similar pattern of crustal evolution also appears to have taken place on the eastern margin of the Central Slave Basement Complex (e.g. Walmsley metamorphic complex; Cairns et al. 2005), it may be representative of a mechanism of Neoproterozoic crustal growth in general, and of crustal growth distal to the Central Slave Basement Complex in particular, and it implicates an important role for crustal growth by accretionary tectonics. However, until the relative proportions of Mesoarchean basement and surrounding Neoproterozoic terranes are better delineated, it will not be possible to provide reliable estimates of the contribution of accreted Neoproterozoic terranes to the growth of the Slave craton as a whole.

Geochemical and isotopic data preclude significant involvement of Mesoarchean or older crust in petrogenesis of magmas in the Snare River terrane, but Mesoarchean crust played an important role in contemporaneous magmatism in the Central Slave Basement

Complex. Coeval suites from the two areas exhibit comparable *petrogenetic* settings, but different *tectonic* settings as a function of proximity to pre-2.8 Ga basement. For instance, crust formation between ca. 2.67-2.65 Ga resulted in the formation of intracratonic rift basins in the Central Slave Basement Complex, but oceanic plateaux in regions removed from it. Both are inferred to have developed as a result of plume activity, but the different tectonic settings are recorded in the Nd isotopes, which are juvenile in the Snare River terrane, but indicate the subtle influence of continental crust in the Central Slave Basement Complex. Thus previously published crustal-evolution models for the central Slave Province, although different from those presented here for the Snare River terrane, are not incompatible with them, but imply coeval crust formation in different tectonic settings. Recognition of this duality in tectonic setting permits reconciliation of formerly conflicting tectonic models for the evolution of the Slave Province.

4.10 Acknowledgements

The Northwest Territories Geoscience Office and the Geological Survey of Canada provided logistical support for the ~ 8 months of fieldwork associated with the project. The Northwest Territories Geoscience Office also provided financial assistance, office space and a stimulating work environment for V.B. to complete the research presented in this paper. Rob Creaser carried out the Sm-Nd analyses. Brian Cousens is particularly thanked for making available several datasets and for a constructive review of an early version of the manuscript. Richard Flood provided insight and suggestions. Luke Ootes is thanked for discussions regarding Kam group data and interpretations. This work was supported by a Lithoprobe grant, and a Natural Sciences and Engineering Research Council Discovery grant to T.R. for field, analytical and other

costs. V.B. acknowledges receipt of a Canadian Commonwealth Scholarship and graduate student bursaries from MUN.

4 References

- Albarède, F., 1998. The growth of the continental crust. *Tectonophysics*, **296**: 1-14.
- Armstrong, J.P., 2001. Alkaline magmatic events – Leith Lake carbonatite and Yellowknife lamprophyres: evidence for Archean mantle metasomatism, Southern Slave Craton. Proceedings of the Slave-Kaapvaal workshop, Merrickville, Canada, Sept 5 – 9, 2001.
- Armstrong, R.L., 1981. Radiogenic isotopes: the case for crustal recycling on a near-steady-state no-continental-growth Earth. *Philosophical Transactions of the Royal Society of London, Series A: Mathematical and Physical Sciences*, **301**: 443-472.
- Armstrong, R.L., 1991. The persistent myth of crustal growth. *Australian Journal of Earth Sciences*, **38**: 613 – 630.
- Atherton, M.P. and Petford, N., 1993. Generation of Na rich magmas from newly underplated basaltic crust. *Nature*, **362**: 144 – 146.
- Barrie, C.T., Gorton, M.P., Naldrett, A.J. and Hart, T.R., 1991. Geochemical constraints on the petrogenesis of the Kamiskotia gabbroic complex and related basalts, western Abitibi Subprovince, Ontario, Canada. *Precambrian Research*, **50**: 173 – 199.
- Bedini, R.M., Boudinier, J.L., Dautria, J.-M. and Morten, L., 1997. Evolution of LILE-enriched small melt fractions in the lithospheric mantle East African Rift. *Earth and Planetary Science Letters*, **153**: 67-83.
- Bennett, V.R.C. and Dunning, G.R., 1998. Geological transect across the southern Indin Lake supracrustal belt to the central Ghost Lake granulite domain. In: 26th Yellowknife Geoscience Forum. Indian and Northern Affairs Canada, NWT Chamber of Mines and Resources, Wildlife and Economic Development, Program and Abstracts of Talks and Posters, pp. 14-16.
- Bennett, V., Dunning, G.R. and Indares, A., 2000. Preliminary data from the Kwejinne Lake supracrustal belt-Ghost Lake granulite domain transect: impact of a steep thermal gradient on upper crustal rocks. In: 28th Yellowknife Geoscience Forum ; Indian and Northern Affairs Canada, NWT Chamber of Mines and Resources, Wildlife and Economic Development, Program and Abstracts of Talks and Posters, pp. 10-11.
- Bennett, V., Rivers, T. and Relf, C., 2002. Where East meets West: Formation, growth and collapse of the Snare River Terrain, southwestern Slave Province. In: 30th Yellowknife Geoscience Forum; Indian and Northern Affairs Canada, NWT Chamber of Mines and Resources, Wildlife and Economic Development, Program and Abstracts of Talks and Posters, pp. 1-2.
- Bennett, V., Jackson, V., Rivers, T. and Relf, C., 2003. Multidisciplinary investigations of the Snare River Terrane, southwestern Slave Province; a detailed crustal record of the formation growth and collapse of a late Archean orogen. In: Geological Association of

Canada – Mineralogical association of Canada – Society of Economic Geologists(GAC-MAC-SEG) Annual Meeting, Vancouver 2003, Program with Abstracts **28**, p.327.

- Bennett, V., Jackson, V.A., Rivers, T., Relf, C., Horan, P. and Tubrett, M. in press. Geology and U-Pb Geochronology of the Late Archean Snare River Terrane: Tracking Evolving Tectonic Regimes and Crustal Growth Mechanisms. *Canadian Journal of Earth Sciences*, **42**, LITHOPROBE Special Edition.
- Bibikova, E.V., 2003. Isotope-geochemical characteristics of Archean Sanukitoids: A review. *Geophysical Research Abstracts*, **5**: 01275
- Bindeman, I.N. and Davis, A.M., 1999. Convection and redistribution of alkalis and trace elements during the mingling of basaltic and rhyolitic melts. *Petrologiya*, **7**: 99-110.
- Bleeker, W. and Villeneuve, M., 1995. Structural studies along the Slave portion of the SNORCLE Transect. In: *Slave-NORthern Cordillera Lithospheric Evolution (SNORCLE)*, Report of 1995 Transect Meeting, April 8-9, University of Calgary, edited by F. Cook and P. Erdmer, LITHOPROBE Report No. 44, p. 8-14.
- Bleeker, W., Ketchum, J.W.F., Jackson, V.A. and Villeneuve, M.E., 1999a. The Central Slave Basement, Part I: its structural topology and autochthonous cover. *Canadian Journal of Earth Science*, **36**: 1083-1109.
- Bleeker, W., Ketchum, J.W.F. and Davis, W.J., 1999b. The Central Slave Basement, Part II: Age and tectonic significance of high strain zones along the basement-cover contact. *Canadian Journal of Earth Sciences*, **36**: 1111-1130.
- Bowring, S.A. and Williams, I.S., 1999. Priscoan (4.00 – 4.03 Ga) orthogneisses from northwestern Canada. *Contributions to Mineralogy and Petrology*, **134**: 3-16.
- Brannstrom, B.M., 2000. Chemical characteristics of Archean volcanic rocks from the Snare River Area (NTS 85O/13), S.W. Slave Province, N.W.T. Unpublished B.Sc. (Honours) Thesis. Simon Fraser University.
- Brophy, J.A., and Pell, J. 2002. Preliminary Geology of the Labrish Lake area, Southwestern Slave Province; Parts of 85N/09. NWT Open File 2002-06. DIAND, NWT Geology Division, Yellowknife. 1 map plus legend scale 1: 50 000.
- Cairns, S., Relf, C., MacLachlan, K. and Davis, W. in press. Late Archean decoupling of upper and mid crustal tectonothermal domains in the southeast Slave Province; evidence from the Walmsley Lake area. *Canadian Journal of Earth Sciences*, LITHOPROBE Special Edition, **42**.
- Calvert, A.J., Sawyer, E.W, Davis, W.J. and Ludden, J.N., 1995. Archean subduction inferred from seismic images of a mantle suture in the Superior Province. *Nature*, **375**: 670-674.
- Chadwick, B., Vasudev, V.N. and Hedge, G.V., 2000. The Dharwar craton, southern India,

- interpreted as the result of Late Archean oblique convergence. *Precambrian Research*, **99**: 91 – 111.
- Clemens, J.D. and Vielzeuf, D., 1987. Constraints on melting and magma production in the crust. *Earth and Planetary Science Letter*, **86**: 287 – 306.
- Conceição R.V., Koester E., Mallmann G., Kawashita K., Chemale Jr. F., Cingolani C., Hervé F., Bertotto G.W., Schilling M., Rodriguez A., Weber M.B.I., Morata D. and Espinoza, F., 2003. New insights on the Andean-related subcontinental lithospheric mantle and evidence of Sr-Nd decoupling: In: IV South American Symposium on Isotope Geology, Salvador, Brazil, August 2003.
- Condie, K.C., 1994. Greenstones through time. In: Condie, K.C. (ed.) *Archean Crustal Evolution*. Elsevier, Amsterdam, pp. 344.
- Condie, K.C. (2003). Incompatible element ratios in oceanic basalts and komatiites: Tracking deep mantle sources and continental growth rates with time. *Geochemistry, Geophysics, Geosystems – an electronic journal of the Earth Sciences*, **4**: 28pp.
- Condie, K.C., Viljoen, M.J. and Kable, E.J.D., 1977. Effects of alteration on element distributions in Archean tholeiites from the Barberton Greenstone Belt, South Africa. *Contributions to Mineralogy and Petrology*, **45**: 237-246.
- Conrad, W.K., Nicholls, I.A. and Wall, V.J., 1988. Water-saturated and –undersaturated melting of metaluminous and peraluminous crustal composition at 10kb: evidence for the origin of silicic magmas in the Taupo volcanic zone, New Zealand and other occurrence. *Journal of Petrology*, **29**: 765 – 803.
- Corfu, F., Stott, G.M., and Breaks, F.W., 1994. U-Pb geochronology and evolution of the English River Subprovince, an Archean low P- high T metasedimentary belt in the Superior Province. *Tectonics*, **14**: 1220 - 1233
- Cousens, B.L., 1997. An isotopic and trace element investigation of Archean supracrustal rocks of the Yellowknife Volcanic Belt, Slave Province, Northwest Territories. *Indian and Northern Affairs Canada Geology Division, EGS 1997-08, Yellowknife*, 39 p.
- Cousens, B.L., 2000. Geochemistry of the Archean Kam Group, Yellowknife Greenstone Belt, Slave Province, Canada. *Journal of Geology*, **108**: 181 – 197.
- Cousens, B.L. and Falck, H., 2000. Peeking under Yellowknife Bay: Bedrock geochemistry from drill core, southern Yellowknife Belt. In: 28th Yellowknife Geoscience Forum ; Indian and Northern Affairs Canada, NWT Chamber of Mines and Resources, Wildlife and Economic Development, Program and Abstracts of Talks and Posters, pp. 12.
- Cousens, B.L., Facey, K. and Falck, H., 2002. Geochemistry of the late Archean Banting Group, Yellowknife greenstone belt, Slave Province, Canada: simultaneous melting of upper mantle and juvenile mafic crust. *Canadian Journal of Earth Sciences*, **39**: 1635 – 1656.

- Cox, R.A., Dunning, G.R., and Indares, A., 1998. Petrology and U-Pb geochronology of mafic, high-pressure metamorphic coronites from the Tshenukutish domain. Eastern Grenville Province. *Precambrian Research*, **90**: 59-83.
- Creaser, R.A., Erdmer, P., Stevens, R.A., and Grant, S.L., 1997. Tectonic affinity of the Nisutlin and Anvil assemblage strata from the Teslin tectonic zone, northern Canadian Cordillera: Constraints from neodymium isotopic and geochemical evidence. *Tectonics*, **16**: 107-121.
- Davis, W.J. and Hegner, E., 1992. Neodymium isotopic evidence for the tectonic assembly of Late Archean crust in the Slave Province, northwest Canada. *Contributions to Mineralogy and Petrology*, **111**: 493 –504.
- Davis, W.J. and Bleeker, W., 1999. Timing of plutonism, deformation, and metamorphism in the Yellowknife Domain, Slave Province, Canada. *Canadian Journal of Earth Sciences*, **36**: 1169 – 1187.
- Davis, W.J., King, J.E. and Fryer, B.J., 1994. Geochemistry and evolution of Late Archean plutonism and its significance to the tectonic development of the Slave craton. *Precambrian Research*, **67**: 207 –241.
- Defant, M.J. and Drummond, M.S., 1990. Derivation of some modern arc magmas by melting of young subducted lithosphere. *Nature*, **347**: 662-665.
- DePaolo, D.J., 1981. Neodymium isotopes in the Colorado Front Range and crust-mantle evolution in the Proterozoic. *Nature*, **291**: 193.
- de Wit, M.J., 1998. On Archean granites, greenstones, cratons and tectonics: does the evidence demand a verdict? *Precambrian Research*, **91**: 181 – 226.
- Drummond, M.S. and Defant, M.J., 1990. A model for trondhjemite-tonalite-dacite genesis and crustal growth via slab melting: Archean to modern comparisons. *Journal of Geophysical Research*, **95**: 21 503 – 21 522.
- Drummond, M.S., Defant, M.J., Kepezhinskis, P.K., 1996. The petrogenesis of slab derived trondhjemite-tonalite-dacite/adakite magmas. *Transactions of the Royal Society of Edinburgh, Earth Sciences*, **87**: 205 – 216.
- Emon, K.E., Jackson, V.A. and Dunning, G.R., 1999. Geology and U-Pb geochronology of the Eukok Uplift: a pre-2.8 Ga basement terrane in the northwestern Slave Structural Province, Northwest Territories, Canada. *Canadian Journal of Earth Sciences*, **36**: 1061-1082.
- Frey, F.A., Coffin, M.F., Wallace, P.J. and Weis, D., 2003. Leg 183 synthesis: Kerguelen Plateau-Broken Ridge – a large igneous province. *In*: Frey, F.A., Coffin, M.F., Wallace, P.J., and Quilty, P.G. (eds) *Proceedings of the Ocean Drilling Program, Scientific Results*, **183**: 1-48.

- Frost, B.R. and Frost, C.D., 1987. CO₂, melts and granulite metamorphism. *Nature*, **327**: 503 – 506.
- Fyson, W.K. and Jackson, V.A., 1990. Reorientation of structures near granitic plutons and orthogonal lineaments, Russell Lake supracrustal domain, southwestern Slave Province, Canada. *Canadian Journal of Earth Sciences*, **28**: 126 - 135.
- Goldstein., S.L., O’Nions, R.K., and Hamilton, P.J., 1984. A Sm – Nd isotopic study of atmospheric dusts and particulates from major river systems. *Earth and Planetary Science Letter*, **70**: 221 – 236.
- Govindaraju, K., 1989. Compilation of working values and sample description for 272 geostandards. *Geostandards Newsletter - The Journal of Geostandards and Geoanalysis*, **13**: 113.
- Harlov, D.E., Forster, H-J, Johansson, L. and van der Kerkhof, A., 2003. Localised dehydration of granitic gneiss to charnockite, Sondrum, SW Sweden: implications for the fluid chemistry. *Geophysical Research Abstracts*, **5**: 03639.
- Henderson, J.B., 1981. Archean basin evolution in the Slave Province, Canada. In: Kröner, A. (ed) *Precambrian Plate Tectonics*, Elsevier, Amsterdam, pp. 213-236.
- Henderson, J.B., 1985. Geology of the Yellowknife – Hearne Lake area, District of Mackenzie: A segment across an Archean Basin. *Geological Survey of Canada, Memoir 414*, 135 pp.
- Henderson, J.B. 1998. Preliminary geology, Wijinnedi Lake area, District of Mackenzie, Northwest Territories; *Geological Survey of Canada, Open File 3609 (scale 1: 50 000)*.
- Henderson, J.B., 2003. Geology, Wijinnedi Lake area, District of Mackenzie, Northwest Territories. *Geological Survey of Canada, Map 2023A*, scale 1:50 000.
- Henderson, J.B., 2004. Geology of the Wijinnedi Lake area, District of Mackenzie, Northwest Territories. *Geological Survey of Canada, Bulletin 576*.
- Henderson, J.B. and Schaan, S.E., 1993. Geology of the Wijinnedi Lake area: a transect into mid-crustal levels in the western Slave Province, District of Mackenzie, Northwest Territories. In: *Current Research, Part C. Geological Survey of Canada, Paper 93-1C*, 83-91.
- Henderson, J.B., van Breemen, O. and Loveridge, W.D., 1987. Some U-Pb zircon ages from Archean basement, supracrustal and intrusive rocks, Yellowknife – Hearne Lake area, District of Mackenzie. In: *Radiogenic Age and Isotopic Studies: Report 1. Geological Survey of Canada, Paper 87-2*, 111-121.
- Hoffman, P.F., 1986. Crustal accretion in a 2.7 – 2.5 Ga “granite-greenstone” terrane, Slave

- Province, N.W.T.: a prograding arc – trench system? In: de Witt, M.J. and Ashwall, L.D. (eds), *Tectonic Evolution of Greenstone belts*. Lunar Planetary Institute Report 86 –10: 120.
- Hofmann, A.W., 1988. Chemical differentiation of the Earth, the relationship between mantle, continental crust, and oceanic crust. *Earth and Planetary Science Letter*, **90**: 297 – 314.
- Horstwood, M.S.A., Nesbitt, R.W., Noble., S.R. and Wilson, J.F., 1999. U-Pb zircon evidence for an extensive early Archaean Craton in Zimbabwe: a reassessment of the timing of craton formation, stabilization and growth. *Geology*, **26**: 883 – 886.
- Hyde, D., 2000. *Geology and U-Pb Geochronology of the Gooseberry Hill area, Kwejinne Lake, Northwest Territories*. Unpublished B.Sc. (Honours) thesis. Memorial University of Newfoundland.
- Isachsen, C.E., 1992. U-Pb zircon geochronology of the Yellowknife Volcanic Belt and subjacent rocks, and mechanics of greenstone formation. Unpublished Ph.D. Thesis. Washington University, St Louis.
- Isachsen, C.E. and Bowring, S.A., 1997. The Bell Lake group and Anton Complex: a basement – cover sequence beneath the Archean Yellowknife greenstone belt revealed and implicated in greenstone belt formation. *Canadian Journal of Earth Sciences*, **34**: 169-189.
- Irvine, T.N. and Baragar, R.A., 1971. A guide to the chemical classification of common volcanic rocks. *Canadian Journal of Earth Sciences*, **8**: 523-548.
- Jackson, V.A. 1999. Preliminary 1:100 000 scale compilation of the geology of the Snare River area (1998 and 1999 results); EGS Open File 1999-18. DIAND, NWT Geology Division, Yellowknife.
- Jackson, V.A., 2000. The Snare River Project: results from mapping. In: 28th Yellowknife Geoscience Forum. Indian and Northern Affairs Canada, NWT Chamber of Mines and Resources, Wildlife and Economic Development, Program and Abstracts of Talks and Posters, pp.33-34.
- Jackson, V.A., 2003. Preliminary compilation of the geology of the Snare River (1998-2002 results), Winjinnedi Lake, Labrish Lake and Russell Lake area; parts of 85N and 85O. C.S. Lord Northern Geoscience Centre, Yellowknife, NT. NWT Open Report 2003-002. Map, scale 1:100 000.
- Jackson, V.A., and Bennett, V., 2003. The Snare River Area: A unique greenschist to granulite grade Archean crustal section in the southwestern Slave Province, Northwest Territories, Canada In: Geological Association of Canada – Mineralogical association of Canada – Society of Economic Geologists(GAC-MAC-SEG) Annual Meeting, Vancouver 2003, Program with Abstracts, 28: p.365
- Jenner, G.A., Longerich, H.P., Jackson, S.E., and Fryer, B.J., 1990. ICP-MS – a powerful tool for

- high precision trace element analysis in earth sciences: evidence of analysis of selected USGS reference samples. *Chemical Geology* **83**: 133 –148.
- Kay, R.W., 1978. Aleutian magnesian andesites: Melts from subducted Pacific oceanic crust. *Journal of Volcanology and Geothermal Research*, **4**: 116-132.
- Kelemen, P.B., Shimizu, N. and Dunn, T., 1993. Relative depletion of niobium in some arc magmas and the continental crust: Partitioning of K, Nb, La and Ce during melt / rock reaction in the upper mantle. *Earth and Planetary Science Letters*, **120**: 111-134.
- Kelemen, P.B., Yogodzinski, G.M. and Scholl, D.W. accepted pending revision. Along-strike variation in lavas of the Aleutian Island Arc: Implications for the genesis of high Mg# andesite and the continental crust. AGU Geophysical Monograph Series. John Eiler (Ed).
- Ketchum, J. and Bleeker, W., 1999. The Central Slave Cover Group and Central Slave Basement Complex: a progress report on U-Pb geochronological studies, In: Slave – Northern Cordillera Lithospheric Evolution Workshop (SNORCLE) Transect and Cordilleran Tectonics Workshop Meeting, 5 – 7 March, Calgary. Compiled by F. Cook and P. Erdmer. Lithoprobe Report 69, pp. 21-29.
- Ketchum, J. and Bleeker, W., 2000. New field and U-Pb data from the Central Slave Cover Group near Yellowknife and the Central Slave Basement Complex at Point Lake, In: Slave – Northern Cordillera Lithospheric Evolution Workshop (SNORCLE) Transect and Cordilleran Tectonics Workshop Meeting, 25 – 27 February, Calgary. Compiled by F. Cook and P. Erdmer. Lithoprobe Report 72, pp. 27-31.
- Kretz, R., 1983. Symbols for rock-forming minerals. *American Mineralogist*, **68**: 277 – 279.
- Kroner, A., Byerly, G.R., and Lowe, D.R., 1992. Chronology of early Archean granite – greenstone evolution in the Baberton Mountain Land, South Africa, based on precise dating by single zircon evaporation. *Earth and Planetary Science Letters*, **103**: 41-54.
- Kusky, T.M., 1989. Accretion of the Archean Slave province. *Geology*, **17**: 63 – 67.
- Le Bas, M.J., Le Maitre, R.W., Streckeisen, A. and Zanettin, B., 1986. A chemical classification of volcanic rocks based on total alkali-silica diagram. *Journal of Petrology*, **27**: 745 – 750.
- Leech, M.L., 2001. Arrested orogenic development: eclogitization, delamination and tectonic collapse. *Earth and Planetary Science Letters*, **185**: 149 – 159.
- Longerich, H.P., Jenner, G.A., Fryer, B.J., and Jackson, S.E., 1990. Inductively coupled plasma mass spectrometric analysis of geological samples: a critical evaluation based on case studies. *Chemical Geology* **83**: 105 – 113.
- Lord, C.S. 1942. Snare and Ingray Lake map areas, Northwest Territories. Geological Survey of Canada, Memoir 235.

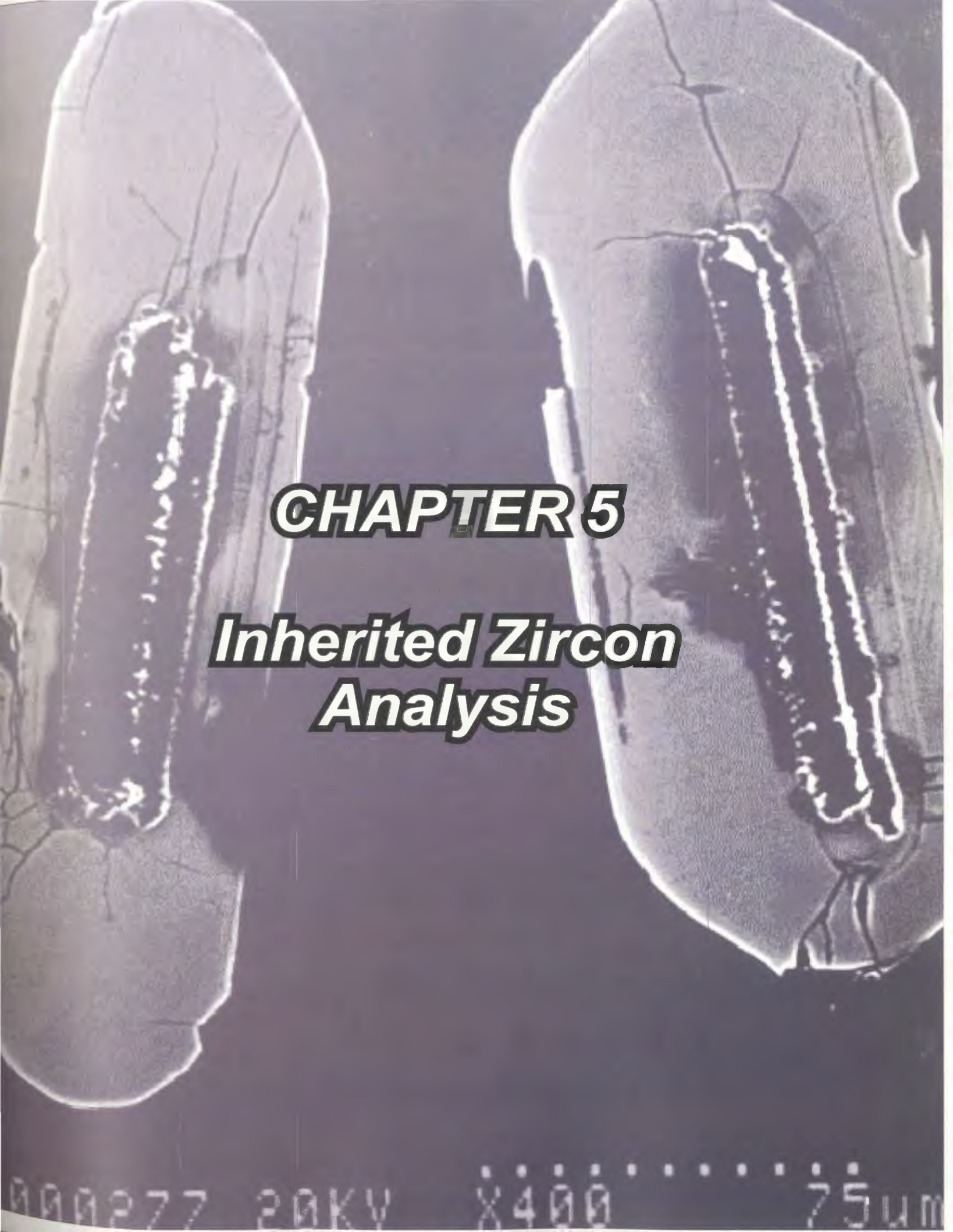
- Ludden, J.N., Gélinas, L. and Trudel, P., 1982. Archean metavolcanics from the Rouyn – Noranda district, Abitibi Greenstone Belt, Quebec. 2. Mobility of trace elements and petrogenetic constraints. *Canadian Journal of Earth Sciences*, **19**: 2276 – 2287.
- Mahoney, J.J., Neal, C.R., Petterson, M.G., McGrail, B.A., Saunders, A.D. and Babbs, T.L., 1993. Formation of an oceanic plateau; speculations from field and geophysical observations of the Ontong Java Plateau. *EOS*, **74**: 552.
- Martin, H., 1986. Effect of steeper Archean geothermal gradient on geochemistry of subduction zone magmas. *Geology*, **14**: 753 – 756.
- Martin, H., 1987. Petrogenesis of Archean trondhjemites, tonalites and granodiorites from eastern Finland: Major and trace element geochemistry. *Journal of Petrology*, **228**: 921-953.
- Martin, H., 1994. The Archean gneisses and genesis of the continental crust. In: Condie, K.C., (ed) *Archean Crustal Evolution*. Amsterdam, Elsevier, p. 205-259.
- Martin, H. and Moyen, J-F., 2002. Secular changes in tonalite - trondhjemite – granodiorite composition as markers of the progressive cooling of Earth. *Geology*, **30**: 319 – 322.
- McGlynn, J.C., and Ross, J.V. 1962. *Geology, Basler Lake, District of Mackenzie*, Geological Survey of Canada, Map 18-1962, 1 inch to 1 mile map with marginal notes.
- Mortensen., J.K., Henderson, J.B., Jackson, V.A. and Padgham, W.A., 1992. U-Pb geochronology of the Yellowknife Supergroup felsic volcanic rocks in the Russell Lake and Clan Lake areas, southwestern Slave Province, Northwest Territories. In: *Radiogenic Age and Isotopic studies, Report 5*. Geological Survey of Canada, Paper 91-2, pp. 1-7.
- Moser, D.E., Heaman, L.M., Krogh, T.E. and Hanes, J.A.. 1996. Intracrustal extension of an Archean orogen revealed using single-grain U-Pb zircon geochronology. *Tectonics*, **15**: 1093-1109.
- Newton, R.C., 1992. Charnockitic alteration: evidence for CO₂ infiltration in granulite facies metamorphism. *Journal of Metamorphic Geology*, **10**: 383 – 400.
- Nisbet, E., 1987. *The Young Earth: An introduction to Archean Geology*. Allen and Unwin, Boston, p.402.
- Ootes, L., 2000. Petrogenesis of the Sleeping Bear Intrusion, Kwejinne Lake, southwestern Slave Province, Northwest Territories. Unpublished B.Sc. (Honours) Thesis. University of Saskatchewan.
- Padgham, W.A., 1990. *The Slave Province: an overview*. Geological Survey of Canada, Open File Report **2168**, 1- 41.
- Patiño Douce, A.E. and Johnson, A.D., 1991. Phase equilibria and melt productivity in the

- pelitic system: implication for the origin of peraluminous granitoids and aluminous granulites. *Contributions to Mineralogy and Petrology*, **107**: 202 – 218.
- Pehrsson, S.J. and Villeneuve, M.E., 1999. Deposition and imbrication of a 2670-2629 Ma supracrustal sequence in the Indin Lake area, southwestern Slave Province, Canada. *Canadian Journal of Earth Sciences*, **36**: 1149-1168.
- Pehrsson, S.J., Chacko, T., Pilkington, M., Villeneuve, M.E. and Bethune, K., 2000. Anton terrane revisited: Late Archean exhumation of moderate-pressure granulite terrane in the western Slave Province. *Geology*, **28**: 1075-1078.
- Pereira, M.D. and Rodriguez Alonso, M.D., 2000. Duality of cordierite granites related to melt-restite segregation in the Peña Negra anatectic complex, Central Spain. *The Canadian Mineralogist*, **38**: 1329 – 1346.
- Perks, M.A., 1997. The mid crust of the western Slave Province - Geological Mapping, geochemistry and U - Pb Geochronology of the Forked Lake Area, Southwestern Slave Province, NWT. M.Sc. thesis, University of Alberta, Edmonton, Alberta.
- Polat, A., Kerrich, R. and Wyman, D.A., 1999. Geochemical diversity in oceanic komatiites and basalts from the late Archean Wawa greenstone belts, Superior Province, Canada: trace element and Nd isotopic evidence for a heterogeneous mantle. *Precambrian Research*, **94**: 139 – 173.
- Poujol, M., Robb, L.J., Anhaeusser, C.R. and Gericke, B., 2003. A review of the geochronological constraints on the evolution of the Kaapvaal Craton, South Africa. *Precambrian Research*, **127**: 181 – 213.
- Puchtel, I.S., Hofmann, A.W., Mezger, K., Jochum, K.P., Shchipansky, A.A. and Samsonov, A.V., 1998. Oceanic plateau model for continental crustal growth in the Archaean: A case study from the Kostomuksha greenstone belt, NW Baltic Shield. *Earth and Planetary Science Letters*, **155**: 57-74.
- Rapp, R.P., Watson, E.B. and Miller, C.F., 1991. Partial melting of amphibolite/eclogite and the origin of Archean trondhjemites and tonalites. *Precambrian Research*, **51**: 1 – 25.
- Rapp, R.P., Shimizu, N., Norman, M.D. and Applegate, G.S., 1999. Reaction between slab-derived melts and peridotite in the mantle wedge: Experimental constraints at 3.8 GPa. *Chemical Geology*, **160**: 335 – 356.
- Reidel, S. 1998. Emplacement of Columbia River basalt. *Journal of Geophysical Research*, **103**: 27393 – 27410.
- Robinson, J., Covello, L., and Falck, H. 2002. Compilation of airborne total field magnetic geophysical data for the Yellowknife basin; NTS 85 I, J, O and P. *In* 30th Yellowknife Geoscience Forum. Indian and Northern Affairs Canada, NWT Chamber of Mines and Resources, Wildlife and Economic Development, Program and Abstracts of Talks and Posters, p. 53.

- Rollinson, H., 1997. Eclogite xenoliths in west African kimberlites as residues from Archean granitoid formation. *Nature*, **389**: 173 – 176.
- Rudnick, R.L., and Fountain, D.M., 1995. Nature and composition of the continental crust – a lower crustal perspective. *Reviews in Geophysics*, **33**: 267 – 309.
- Shirey, S.B. and Hanson, G.N., 1984. Mantle-derived Archean monzodiorites and trachyandesites. *Nature*, **310**: 222-224.
- Sinton, C.W., Duncan, R.A., Storey, M., Lewis, J. and Estrada, J.J., 1998. An oceanic flood basalt province within the Caribbean plate. *Earth and Planetary Science Letters*, **155**: 221-235.
- Sircombe, K.N., Bleeker, W. and Stern, R.A., 2001. Detrital zircon geochronology and grain-size analysis of a ~ 2800 Ma Mesoarchean proto-cratonic cover succession, Slave Province, Canada. *Earth and Planetary Science Letters*, **189**: 207-220.
- Smithies, R.H., 2000. The Archean tonalite – trondhjemite – granodiorite (TTG) series is not an analogue of Cenozoic adakite. *Earth and Planetary Science Letters*, **182**: 115 – 125.
- Smithies, R.H., Champion, D.C. and Cassidy, K.F., 2003. Formation of Earth's early Archean continental crust. *Precambrian Research*, **127**: 89 – 101.
- Springer, W. and Seck, H.A., 1997. Partial fusion of basic granulites at 5 to 15kbar: implications for the origin of TTG magmas. *Contributions to Mineralogy and Petrology*, **127**: 30 – 45.
- Stern, R.A., Hanson, G.N. and Shirey, S.B., 1989. Petrogenesis of mantle-derived, LILE-enriched Archean monzodiorite and trachyandesites (sanukitoids) in southwestern Superior Province. *Canadian Journal of Earth Sciences*, **26**: 1688 – 1712.
- Stern, R.A. and Hanson, G.N., 1991. Archean high-Mg granodiorite: a derivative of light Rare Earth Element enriched monzodiorite of Mantle origin. *Journal of Petrology*, **32**: 201-238.
- Stern, R.A. and Bleeker, W., 1998. Age of the world's oldest rocks refined using Canada's SHRIMP: The Acasta Gneiss Complex, Northwest Territories, Canada. *Geoscience Canada*, **25**: 27-31.
- Stevenson, R., Henry, P. and Gariepy, C., 1999. Assimilation-fractional crystallization origin of Archean Sanukitoid Suites: Western Superior Province, Canada. *Precambrian Research*, **96**: 83 – 99.
- Stubley, M.P. and Cairns, S.R., 1998. EGS Open File 1998-05. DIAND NWT Geology Division
- Tanaka, T., Togashi, S., Kamioka, H., Amakawa, H., Kagami, H., Hamamoto, T., Yuhara, M., Orihashi, Y., Yoneda, S., Shimuzu, H., Kunimaru, T., Takahashi, K., Yanagi, T., Nakano, T., Fujimaki, K., Shinjo, R., Asahara, Y., Tanimizu, M., and Dragusanu, C., 2000. JNdi-

- 1: A neodymium isotopic reference in consistency with La Jolla neodymium: *Chemical Geology*, **168**, p. 279 – 281.
- Taylor, S.R. and McLennan, S.M., 1985. *The continental crust: Its composition and evolution*. Oxford, Blackwell Scientific Publications, 312p.
- Tejada, M.L.G., Mahoney, J.J., Neal, C.R., Duncan, R.A. and Pettersen, M.G., 2002. Basement geochemistry and geochronology of Central Malaita, Solomon Islands, with implications for the origin and Evolution of the Ontong Java Plateau. *Journal of Petrology*, **43**: 449 – 484.
- Thompson, P.H., 1989. An empirical modal for metamorphic evolution of the Slave Province and adjacent Thelon Tectonic Zone, northwestern Canadian Shield. In: Daly, J.S., Cliff, R.A. and Yardley, B.W.D. (eds) *Evolution of Metamorphic Belts*. Geological Society, Special Publication, **43**: 245 – 263.
- Thorpe, R.I., Cumming, G.L. and Mortensen, J.K., 1992. A significant Pb Isotope boundary in the Slave Province and its probable relation to ancient basement in the western Slave Province. In: *Project Summaries, Canada - Northwest Territories Mineral Development Agreement 1987 - 91*. Geological Survey of Canada, Open File Report **2484**, 179-184
- Tomlinson, K. Y., Stevenson, R.K., Huges, D.J., Hall, R.P., Thurston, P.C. and Henry, P., 1998. The Red Lake greenstone belt, Superior Province: evidence of plume-related magmatism and 3 Ga and evidence of an older enriched source. *Precambrian Research*, **89**: 59 – 76.
- Turkina, O.M. and Nozhkin, A.D., 2003. Genesis of Archean tonalite - trondhjemite – suites: Plume or subduction related? *Russian Journal of Earth Sciences*, **5**: 93 - 100.
- van Breemen, O., Davis, W.J. and King, J.E., 1992. Temporal distribution of granitoid plutonic rocks in the Archean Slave Province, northwest Canadian Shield. *Canadian Journal of Earth Sciences*, **29**: 2186 – 2199.
- van der Velden, A.J., and Cook, F.A., 2002. Products of 2.65 – 2.58 Ga orogenesis in the Slave Province correlated with Slave – Northern Cordillera lithospheric evolution (SNORCLE) seismic reflection patterns. *Canadian Journal of Earth Sciences*, **38**: 1189 – 1200.
- Vielzeuf, D. and Holloway, J.R., 1988. Experimental determination of fluid-absent melting relations in the pelitic system. *Contributions to Mineralogy and Petrology*, **98**: 257 – 276.
- Villeneuve, M.E. and Henderson, J.B., 1998. U-Pb geochronology of the Wijinnedi Lake area, Slave Province, District of Mackenzie, NWT. In: *Radiogenic Age and Isotopic studies: Report 11*. Geological Survey of Canada, 1998-F, pp. 99-106.
- Villeneuve, M.E. and Relf, C.R., 1998. Tectonic setting of the 2.6 Ga Carbonatites in the Slave Province, NW Canada. *Journal of Petrology*, **39**: 1975 – 1986.
- Villeneuve, M.E., Henderson, J.R., Hrabí, R.B., Jackson, V.A., and Relf, C. 1997. 2.70 – 2.58 Ga

- plutonism and volcanism in the Slave Province, District of Mackenzie, Northwest Territories. *In* Radiogenic Age and Isotopic studies: Report 8. Geological Survey of Canada, 1997-F, pp. 37-60.
- Wasserburg, G.L., Jacobsen, S.B., DePaolo, D.J., McCulloch, M.T. and Wen, T., 1981. Precise determination of Sm/Nd ratios, Sm and Nd isotopic abundances in standards solutions. *Geochimica et Cosmochimica Acta*, **45**: 2311-2323.
- White, R.V., Tarney, J., Kerr, A.C., Saunders, A.D., Kempton, P.D., Pringle, M.S. and Klaver, G.T., 1999. Modification of an oceanic plateau, Aruba, Dutch Caribbean: Implications for the generation of continental crust. *Lithos*, **46**: 43-68.
- Winchester, J.A. and Floyd, P.A., 1977. Geochemical discrimination of different magma series and their differentiation products using immobile elements. *Chemical Geology*, **20**: 325 – 343.
- Yamashita, K., Creaser, R.A., Stemler, J.U. and Zimaro, T.W., 1999. Geochemical and Nd-Pb isotopic systematics of Late Archean granitoids, southwestern Slave Province, Canada: Constraints for granitoid origin and crustal isotopic structure. *Canadian Journal of Earth Sciences*, **36**: 1131-1147.
- Yamashita, K., Creaser, R.A., Jensen, J.E. and Heaman, L.M., 2000. Origin and evolution of the mid- to late-Archean crust in the Hanikahimajuk Lake area, Slave Province, Canada; evidence from U-Pb geochronological, geochemical and Nd-Pb isotopic data. *Precambrian Research*, **99**: 197-224.
- Yogodzinski, G.M. and Kelemen, P.B., 1998. Slab melting in the Aleutians: implications of an ion probe study of clinopyroxene in primitive adakite and basalt. *Earth and Planetary Science Letters*, **158**: 53 – 65.
- Zegers, T.E. and van Keken, P.E. 2001. Middle Archean continent formation by crustal delamination. *Geology*, **29**: 1083 – 1086.

The image shows two large, elongated zircon crystals against a dark background. Each crystal has a prominent, dark, vertical track running through its center, which is a result of analytical techniques like laser ablation. The crystals exhibit various fractures and inclusions. The text is overlaid in the center of the image.

CHAPTER 5

***Inherited Zircon
Analysis***

000277 20KV X400 75um

5 Isotopic Profiling of Neoproterozoic Crust: Tectonic and Geochemical Applications of Inherited Zircon Analysis, Snare River Terrane, Slave Province.

*V. Bennett¹, T.Rivers¹, M. Tubrett¹, C. Relf² and V. A. Jackson²

1. Department of Earth Sciences, Memorial University of Newfoundland, St. John's,
NL. A1B 3X5.

2. NWT Geoscience Office, Yellowknife, NT, X1A 2R3

*Corresponding author

Ph: 1 709 737 8392

Fax: 1 709 737 2589

To submit to **Lithos**

NWT Geoscience Office Contribution number 0011.

5.1 Abstract

Inherited zircon analyses for nine plutonic rocks from the Neoproterozoic Snare River terrane, southwestern Slave Province, were integrated with BSE image characterization and LAM ICP-MS U-Pb age determinations to examine linkages between mid- and lower-crustal evolution. The inherited zircon age data show that metaluminous and peraluminous magmas emplaced into the mid and upper crust originated from discrete lower- and mid-crustal reservoirs at different stages of crustal development, thereby providing a temporal isotopic profile of crust formation. Secular changes in metaluminous magma inheritance trends reflect intermittent growth of a garnet-rich mafic lower crust over ca. 77 M.y. by both 'local' magmatic additions and tectonic intercalation of 'exotic' mafic material (of Kam Group tholeiite affinity). Synchronous mid- and upper-crustal TTG magmatism implies a linked mantle–crustal evolution during this interval of crustal growth. In addition, inheritance ages reveal the absence of Mesoproterozoic crust during the growth of the lower-crust in the Snare River terrane. Other conclusions derived from the inheritance data include: (i) refractory zircon in a mantle-derived sanukitoid implies longevity of chemically isolated domains in the lithospheric mantle; (ii) the similarity between inheritance profiles of peraluminous granites and detrital zircon spectra in metaturbidites demonstrates the occurrence of a major metasedimentary reservoir in the mid crust from which the peraluminous magmas were sourced; and (iii) a megacrystic granite suite is shown to have two distinct inherited components consistent with petrogenetic interpretations involving mixing of metasedimentary and mafic source rocks. A new technique is presented that utilizes inherited zircon ages to quantify the end-members used in binary and multicomponent Sm-Nd isotope mixing models. Specifically it is shown that magmas in the Snare River terrane can be derived by mixing lower- and mid-crustal sources of ca. 2700 Ma and younger.

Key words: Inherited zircon, BSE imaging, LAM ICPMS U-Pb dating; isotopic profile.

5.2 Introduction

The creation and stabilization of continental crust is a multistage process involving magmatism, metamorphism and deformation. In many upper-crustal terranes, the sequence, roles, and associations among these processes are well constrained, but an understanding of their linkage with the underlying mid and lower crust is generally lacking. Lower crustal xenoliths provide a possible source of information, and some geochronological studies of xenolith suites have revealed evidence for complex polyphase metamorphic and magmatic lower crustal evolution (e.g. Rudnick and Cameron 1991; Davis 1997; Schmitz and Bowring, S.A., 2001; 2003). Recently, Davis et al. (2003) have reported magmatic and metamorphic ages from xenolith suites in the Slave Province that are coeval with those in the overlying crust, implying that linkages existed between the different crustal levels during the major crust-forming events. The relative scarcity of xenolith suites, and the comparable rarity of exhumed mid- to lower-crustal terranes (e.g. Ivrea-Verbano zone, European Alps; Kapuskasing Uplift, Superior Province, Canada), however, has significantly limited analysis of these potential correlations, prompting the need for new techniques that permit whole-crustal characterization.

Apart from direct analysis of xenolith suites and exhumed mid- and lower-crustal regions, indirect investigations of mid- and lower-crustal evolution may be conducted through geochemical and isotopic analyses of magmas formed in these reservoirs. A powerful complement to such studies involves the systematic examination of the refractory or 'inherited' zircon in these magmas. Inherited zircon analyses may represents

a virtually untapped reservoir of information about mid- and lower-crustal magma source regions that, when applied to dated magmatic rocks, also permits evaluation of the secular variations that occurred during crustal evolution. Such integrated studies are especially well suited to the Archean, when crust formation may have been more rapid than at later times in Earth history. In these regions the opportunity exists to isotopically 'profile' crustal evolution from its inception to final stabilization.

In this contribution, these techniques are applied to probe mid- and lower-crustal development of the Neoproterozoic Snare River terrane, southwestern Slave Province, where compositionally diverse, crustally-derived metaluminous and peraluminous granitoids that formed over ca. 90 M.y. were emplaced into the mid and upper crust during crust-formation and stabilization (Chapter 2; Bennett et al. 2005). Three principal themes are addressed: (1) characterization of mid- and lower-crustal evolution through inherited zircon analysis of nine plutons that punctuate the main stages of crustal evolution (isotopic profiling); (2) assessment of the role of Paleo- to Mesoproterozoic (pre-2.8 Ga) crust, which is widespread in the central Slave Province, in the genesis of younger magmas in the Snare River terrane; and (3) a description and evaluation of a novel method using inherited zircon age data to constrain interpretations of the Sm–Nd isotopic signatures of lower- and mid-crustally-derived magmas.

5.3 Zircon Inheritance

In silicate melts, zircon can occur as a magmatic-precipitate phase or as a premagmatic refractory phase; in the latter case originating from either the magma source

region (inherited zircon) or by entrainment during ascent (contaminant zircon; Miller et al. 2003). Since preservation of zircon in magmas is principally controlled by the solubility and dissolution kinetics of Zr, zircon in Zr-undersaturated melts consists almost entirely of magmatic precipitate grains (Watson and Harrison 1983; Harrison and Watson 1983; Hansmaan and Orberli 1991; Hanchar and Watson 2003). In contrast Zr-saturated melts contain appreciable quantities of premagmatic refractory zircon on which magmatic zircon commonly occurs as overgrowths. It is thus critical when undertaking U-Pb studies to distinguish between magmatic and premagmatic regions of individual zircon grains to avoid acquiring mixed U-Pb ages. Characterization of zoning by cathodoluminescence (CL) or back-scattered electron imaging (BSE) techniques is essential to delineate age domains. In multistage zircon crystals, subhedral to anhedral inherited cores are typically surrounded by compositionally and texturally distinct epitaxial rims, indicating growth in different environments (Paterson et al. 1992; Hanchar and Miller 1993; Belousova et al. 2002; Griffin et al. 2002; Corfu et al. 2003). Variable zoning patterns of inherited cores in a single sample imply different growth histories and a mixed inheritance (e.g. Harrison et al. 1987; Pidgeon and Compston 1992; Hanchar and Rudnick 1995; Corfu et al. 2003).

Numerous studies in the past twenty years have integrated U-Pb dating and BSE / CL imaging of inherited zircon populations to investigate the relationship between magma chemistry and inheritance trends (e.g. Harrison et al. 1987; Hansmann and Oberli 1991; Pidgeon and Compston 1992; Roddick and Bevier 1991; Chappell et al. 2000), and a powerful application of zircon inheritance has been to elucidate the lower crustal

composition and evolution recorded by the zircon populations in mafic xenolith suites (e.g. Rudnick and Cameron 1991; Hanchar and Rudnick 1995; Schmitz and Bowring 2000). A recent analysis of zircon from mafic xenoliths in the Slave Province has demonstrated the longevity of lower crustal evolution and its intimate relationship with the overlying mid and upper crust (Davis et al. 2003). We further examine this linked lower-, mid- and upper-crustal evolution in the Slave Province in this contribution using inherited zircon from Neoproterozoic metaluminous and peraluminous plutonic rocks of the Snare River terrane.

5.4 Geological Context

5.4.1 Regional Setting

The Slave Province, northwestern Canada (Fig. 5.1a), records a protracted history of crustal development from ca. 4.06 to 2.57 Ga. The main geological elements can be grouped into four broad lithotectonic units: (i) 4.06-2.8 Ga basement and its cover termed the Central Slave Basement Complex and Cover Sequence respectively (CSBC and CSCS respectively; Bleeker et al. 1999; Bowring and Williams 1999), (ii) two stages of greenstone-turbidite development from ca. 2.72-2.63 Ga, an older stage comprising 2.72-2.70 Ga tholeiitic and 2.66 Ga felsic volcanic rocks (Kam and Banting groups) and >2.66 Ga turbidites (Henderson 1970; Bleeker and Villeneuve 1995), and a younger stage comprising 2.68-2.66 Ga felsic and subordinate mafic volcanic rocks and <2.63 Ga turbidites (e.g. Pehrsson and Villeneuve 1999, Bennett et al. 2005); (iii) widespread plutonism, grouped into 2.63-2.60 Ga, (Defeat, Concession and Siege suites), and 2.60-

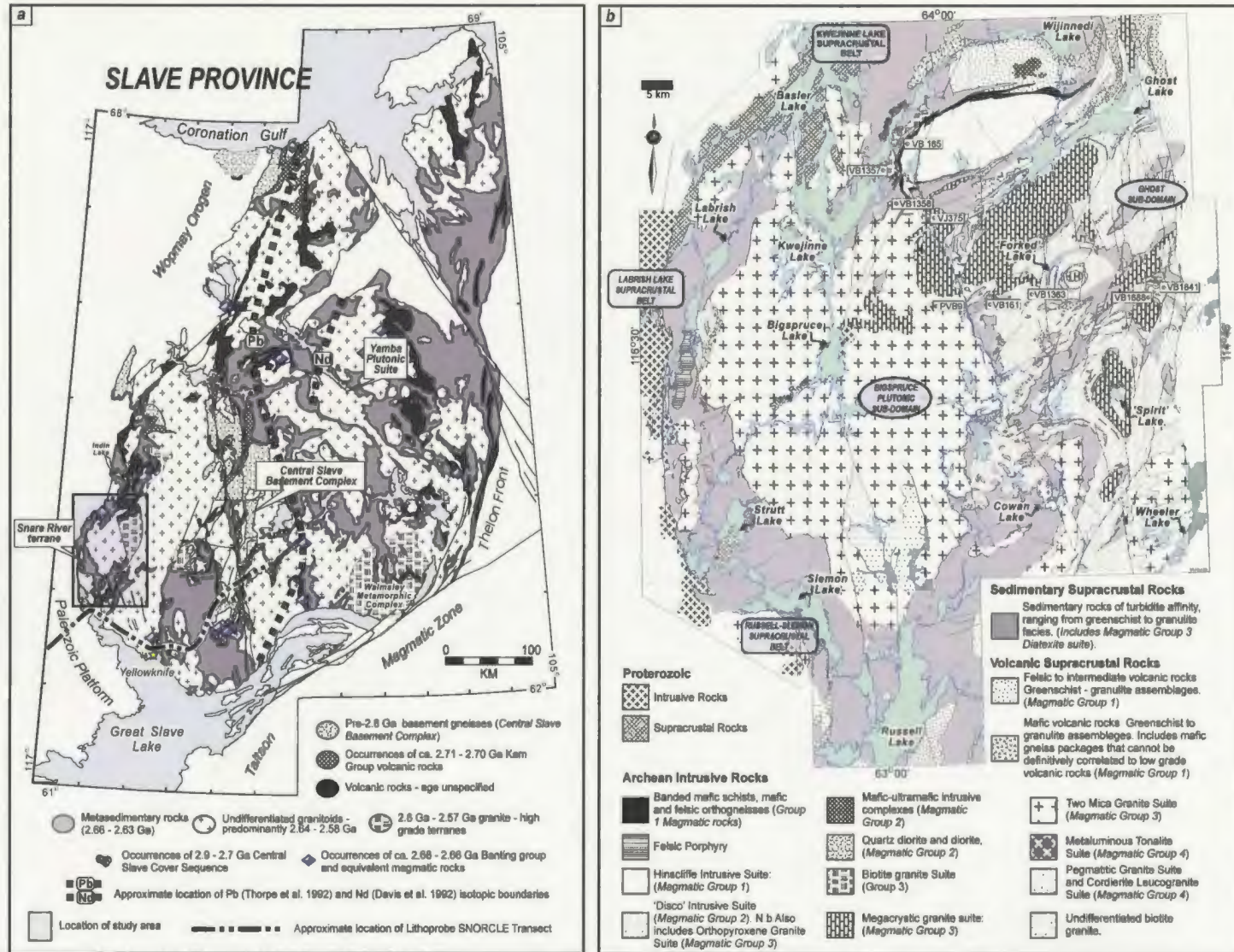


Figure 5.1: (a) Simplified geological map of the Slave Province (modified after Bleeker et al. 1999) showing location of the Snare River terrane and Fig.1b. (b) Geological map of the Snare River terrane, showing locations of samples analyzed in this study. Sources of information : Snare River area (Jackson 2003 and references therein); Wijinnedi Lake area (Henderson, 1998); Labrish Lake area (Brophy and Pell, 2002); Russell Lake area (Jackson 1999); Basler Lake area (McGlynn and Ross 1962, Lord 1942).

Henderson 1998; Bennett et al. 2005; Fig. 5.1b). Turbidites are the dominant supracrustal lithology and both pre- and post-2635 Ma packages have been identified.

The Snare River terrane exhibits evidence for three linked deformation/metamorphic events. D1/M1 (ca. 2640–2610 Ma) involved intercalation of turbidite and volcanic successions under greenschist- to amphibolite-facies conditions, D2/M2 (ca. 2610–2595 Ma) was the orogenic peak and in the mid-crustal Ghost subdomain took place under HT-LP granulite-facies conditions, and D3/M3 (2595–2580 Ma) involved extensional uplift and decompression of the Ghost subdomain. Pressures estimates, which range from 2.5-3.5 kbar in the supracrustal belts to 6.5-7 kbar in the high-grade gneisses (Appendix I; Chacko et al. 1995a, b), indicate burial from 9 to 25 km across the terrane. The concept of tectonic regimes was proposed by Bennett et al. (2005; Chapter 2) to describe episodes of deformation, metamorphism and magmatism that occur in a similar tectonic setting. The tectonic history of the Snare River terrane is subdivided into two broad tectonic regimes TR1 and TR2. Relationships among the various components of the study area integrated into the tectonic regime concept are shown in Fig. 5.2.

5.4.2 Magmatic rocks in the Snare River terrane

Magmatic rocks in the Snare River terrane range from metaluminous to peraluminous and are classified into four temporal groups. Group 1 (2674–2650 Ma, metaluminous) includes volcanic rocks and synvolcanic plutons ranging from basalt to rhyodacite and gabbro to tonalite, respectively; Group 2 (2637–2608 Ma, metaluminous) ranges in composition from ultramafic hornblendite to granodiorite; Group 3 (ca. 2600

2.58 Ga suites, (Stagg, Awry, Prosperous, Contwoyto and Yamba suites; Henderson 1985; Davis et al. 1994; van Breemen et al. 1992); and (iv) 2.60-2.57 Ga granite / high-grade metamorphic terranes characterized by polyphase deformation and metamorphism (Henderson 1994; Stubbley and Cairns 1998; Pehrsson et al. 2000; Jackson and Bennett 2003). Exposures of pre-2.8 Ga crust lie west of the Nd and Pb isotopic boundaries (Fig. 5.1a), which demarcate regions where extensive recycling of older crust was important during crustal evolution (Davis and Hegner 1992; Thorpe et al. 1992). Regional deformation and metamorphism was predominantly coeval with the 2.60-2.58 Ga plutonism.

The Snare River terrane, southwestern Slave Province (Fig. 5.1b), is a granite / high-grade metamorphic terrane characterized by high temperature/ low pressure (HT/LP) granulite- and amphibolite-facies gneissic and plutonic rocks (Ghost and Bigspruce subdomains), surrounded by upper-crustal greenschist- to amphibolite-facies volcano-sedimentary belts (Kwejinne Lake, Labrish Lake and Russell-Slemon belts; Henderson and Schaan, 1993; Pehrsson et al. 2000; Bennett et al. 2005). Supracrustal sequences consist of bimodal volcanic rocks, synvolcanic plutons and greywacke–mudstone turbidites, with high-grade tectonic lenses of these lithologies occurring in the Ghost subdomain. Two ages of felsic volcanism are recognized (ca. 2673 and 2658 Ma; Mortensen et al. 1992; Villeneuve and Henderson 1998), and synvolcanic intrusions include a composite assemblage of ca. 2674 Ma mafic to tonalitic orthogneiss mantling the ca. 2654 Ma trondhjemitic–granodioritic Hinscliffe complex (Villeneuve and

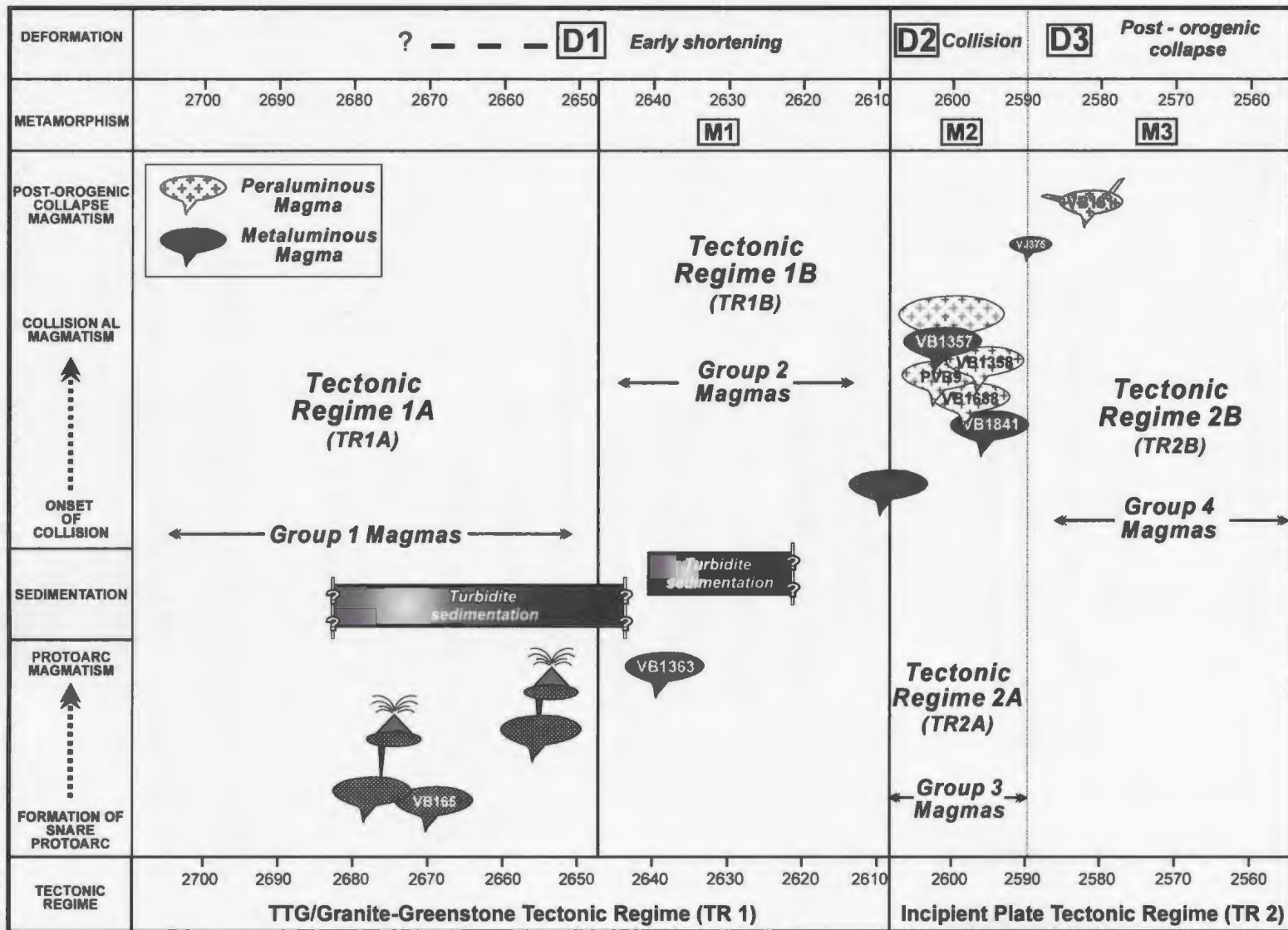


Figure 5.2: Summary diagram illustrating temporal relationships between magmatic group, tectonic regime and tectonometamorphic evolution of the Snare River Terrane.

Ma, metaluminous and peraluminous) is predominantly granitic; and Group 4 (2589-2585 Ma, metaluminous and peraluminous) comprises small-volume magmas ranging in composition from tonalite to pegmatitic granite. A summary of important geochemical and isotopic attributes of each magmatic group is given in Table 5.1.

5.5 Analytical Techniques

Nine representative samples (five metaluminous, four peraluminous) for which U-Pb crystallization ages and major, trace and Sm-Nd analyses had been acquired, were chosen for inherited zircon analysis. U-Pb data were collected from inherited grains in order to determine inheritance ages, the proportions of each inherited component, and variations in inheritance trends among samples. Between 50 and 90 grains were analyzed in each sample in order to generate statistically representative data on all significant populations and their proportions.

Zircon separates were extracted using standard crushing techniques, and heavy mineral concentrates were produced using a Wilfley™ table, heavy liquids and a Frantz™ isodynamic separator before hand-picking in ethanol under a binocular microscope. Grains were mounted in epoxy, polished and imaged using back-scattered electron (BSE) imaging techniques. Following grain characterization, samples were cleaned and loaded into the sample cell. Analysis of U-Pb isotopic ratios by LAM-ICP-MS is rapid, allowing acquisition of large datasets with which to assess the accuracy and frequency of each inherited age component. In this study, U/Pb and Pb/Pb isotopic ratios of the zircon standards and samples were measured using a VG PlasmaQuad 2S⁺ mass spectrometer

Table 5.1: Summary of geochemical characteristics of the magmatic groups of the Snare River terrane.

Magma Suite	Age (Ma)	Geochemical Characteristics	Melt Depletions	Melt Enrichments	Source	Characteristics/ Inferred Residual Phases	ϵ_{Nd}	Tectonic Affinity
GROUP 1								
Tholeiite (KLSB)	2674 Ma	Elevated and enriched, 20 - 30 x chondrite, unfractionated REE profiles; <i>Metaluminous</i> .	Sr	Ba	ultramafic - enriched	ol, minor opx	1.9	Plume
Tholeiite (RSSB)	2658 Ma	Fractionated, flat HREE profiles, comparable to Kam and Banting tholeiites; <i>Metaluminous</i> .	Nb	slight LREE, Th	ultramafic - metasomatized	ol, opx, cpx	2.2 to +2.8	Protarc-Onset
BBA (KLSB)	2674 Ma	Calc-alkaline affinity rocks interlayered with KLSB enriched tholeiite. Moderately fractionated; <i>Metaluminous</i> .	Nb, Sr, Zr	LREE, Th	ultramafic(?)	ol, opx, cpx, plag	1.4	Plume
TTG (KLSB)	2674 Ma	Moderately fractionated, calc-alkaline affinity felsic magmas, formed within plagioclase stability field; <i>Metaluminous</i> .	HREE, Nb, Sr	LREE, Th, Zr	mafic (hydrated)	grt, amph, rt	1.3 to +1.5	Plume
TTG (RSSB)	2658 Ma	Granodiorite - tonalite, equivalent to average TTG composition (as for ca. 2674 Ma); <i>Metaluminous</i> .	HREE, Nb, Sr,	LREE, Zr	mafic (hydrated)	grt, amph, rt	+ 2.4 to +3.0	Protoarc
Depleted Suite (RSSB)	2658 Ma	Strongly fractionated, calc-alkaline granodiorite, differentiate of coeval TTG; <i>Metaluminous</i> .	HREE, Nb	LREE, Sr, Zr	mafic (hydrated)	grt, amph, rt, ttn	2.5 to +3.1	Protoarc-crust
GROUP 2								
Disco Intrusive Suite	2635Ma	Strongly fractionated, calc-alkaline granodiorite - granite; <i>Metaluminous</i> .	HREE, Nb	LREE, Th, Zr, Eu	mafic (hydrated)	grt, amph, cpx, plag	1.0 to +1.9	Protoarc
Mafic Intrusive Complexes	Suite 1	Alkaline <i>fractionated</i> hornblende-quartz diorite, (sanukitoid); <i>Metaluminous</i> .	Nb, Sr, Zr	Th, LREE	ultramafic - metasomatized	ol, opx, cpx	1.1	Protoarc-Termination
	Suite 2	Alkaline <i>unfractionated</i> monzodiorite to monzonite, (sanukitoid); <i>Metaluminous</i> .	Zr,	Sr, Ba	ultramafic - metasomatized		1.3	Protoarc-Termination

Table 5.1: *Continued.*

Magma Suite	Age (Ma)	Geochemical Affinity	Melt Depletions	Melt Enrichments	Protolith Bulk	Characteristics/ Inferred Residual Phases	ϵ Nd	Tectonic Affinity
GROUP 3								
Upper-crustal Biotite Granite	2595 Ma	Moderately to strongly fractionated calc-alkaline granite; <i>Metaluminous</i>	HREE, Nb	LREE, Zr, Th, Sr	mafic (hydrated)	grt, amph, rt	2	Collision
Upper - Mid Crustal Biotite Granodiorite	2595 Ma	Strongly fractionated, calc-alkaline granodiorite; <i>Metaluminous</i> .	Nb, Sr, Eu, Zr	LREE, Th	mafic and metasedimentary	grt, amph, rt	0.4 to 0.6	Collision
Mid-crustal Orthopyroxene Granite	2597 Ma	Strongly fractionated, heterogeneous calc-alkaline granite, variably altered by chamokitization; <i>Metaluminous</i>	HREE, Nb, Sr	LREE, Eu, Zr	mafic / crustal assimilation	grt, amph, rt	- 0.5 to +1.1	Collision
Two Mica Granite / Diatexite	2597 Ma	Moderately fractionated, calc-alkaline granite and tonalite - granodiorite diatexite; <i>Peraluminous</i> .	Nb, Eu, Sr	LREE, Th	turbidite (greywacke - pelite)	plag, rt	0.9	Collision
Megacrystic Granite	2597 Ma	Moderately fractionated, calc-alkaline granite; <i>Peraluminous</i>	Nb, Sr, Eu, variable HREE	Th, LREE	grt rich pelite + MIC equivalent assimilation	plag, rt	0.6 to 1.0	Collision
GROUP 4								
Diorite Sanukitoid	2589 Ma	Moderately fractionated calc-alkaline diorite; <i>Metaluminous</i> .	Nb, Sr, HREE	LREE, Zr	ultramafic - metasomatized	grt, amph, rt	0.8	Post-orogenic collapse
Cordierite Leucogranite	2585 Ma	Strongly fractionated calc-alkaline granite, (decompression melt); <i>Peraluminous</i> .	HREE, NbTh	Sr, Eu, Zr	metasedimentary	grt, plag, rt	-0.4	Post-orogenic collapse
Pegmatitic Granite	2585 Ma	Variably fractionated, calc-alkaline granite; <i>Peraluminous</i> .	HREE, Nb, Zr, Sr	HREE, Nb	metasedimentary	plag, grt, rt	-0.8 to +0.8	Post-orogenic collapse

Notes: KLSB – Kwejinne Lake Supracrustal Belt; RSSB – Russell Slemon Supracrustal Belt; BBA – Basalt / Basaltic Andesite; TTG – Tonalite, Trondhjemite, Granodiorite MIC – Mafic Intrusive Complex; ol – olivine; opx- orthopyroxene; cpx – clinopyroxene; plag – plagioclase; grt – garnet; amph- amphibole; rt – rutile.

coupled to a Q-switched Nd:YAG 266 nm ultraviolet laser. Operating conditions were similar to those described by Košler et al. (2001, 2002) and Bennett et al. (2005; Chapter 2). Single-pass slow velocity rastering was adopted for this study.

5.6 Results and Methods of Data Treatment

5.6.1 Inherited zircon results

Inherited zircon age data are reported by magma composition (i.e., metaluminous and peraluminous) and by magmatic group. Complete data tables can be found in Appendix F (Tables F1 and F2). Inherited age populations in metaluminous and peraluminous samples are summarized in Tables 5.2 and 5.3. Back scattered electron images of representative grains in the five metaluminous samples are presented in Fig. 5.3a-e and the results are plotted on both concordia diagrams and cumulative probability histograms in Fig. 5.4a-e. Comparable data for the four peraluminous samples are given Figs. 5.3f-i and 5.5a-d. Brief descriptions of inherited zircon populations and individual ages are presented in Appendix G, and a full account of morphology and zonation trends of all zircon populations is given in Chapter 2. One metaluminous sample did not contain any inherited zircon, but in the remaining eight samples inherited grains were grouped into six inherited age components as outlined below. Examples of zircon cores that yielded the ages related to each inherited age component are illustrated in Figs. 5.4 and 5.5, relative proportions of each inherited age component are shown on pie diagrams in these figures, and the data are summarised in Tables 5.2 and 5.3. Additional analysis of age

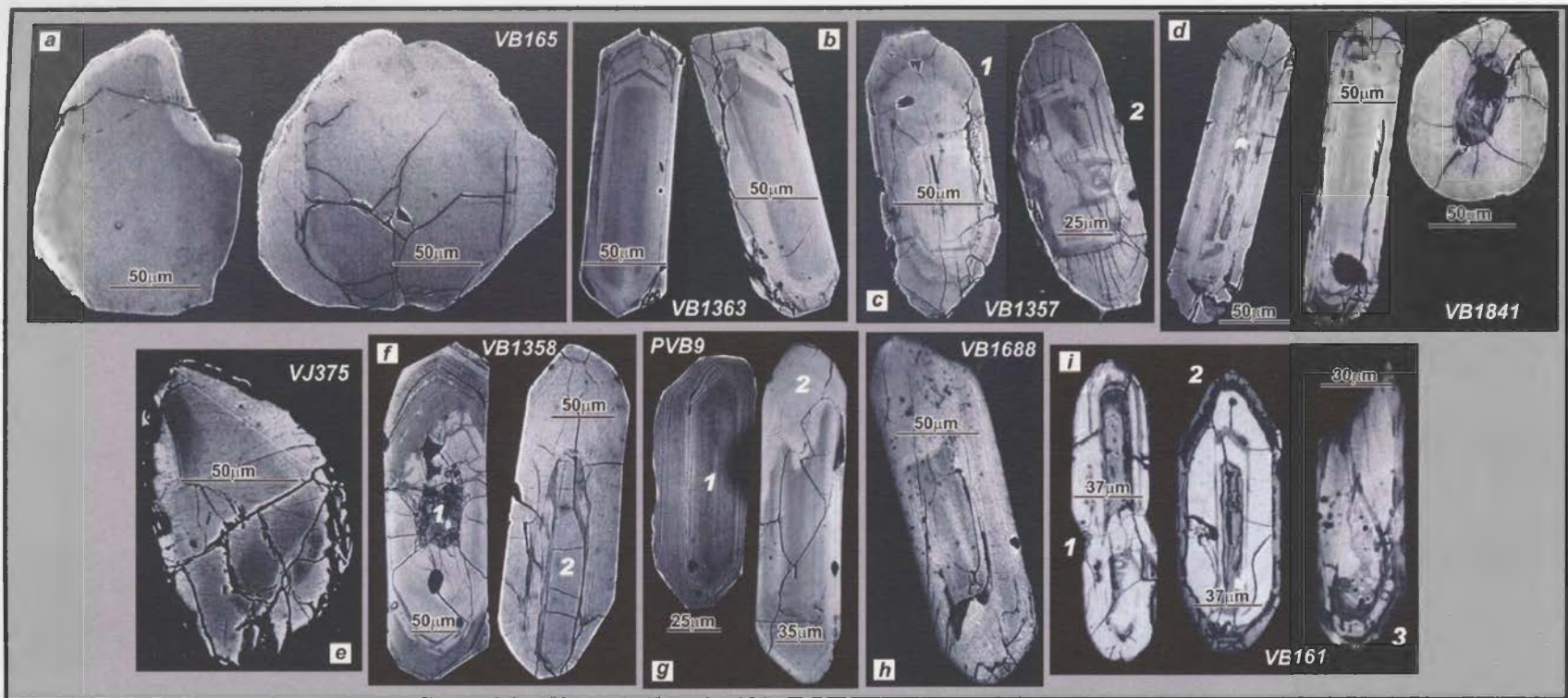


Figure 5.3: BSE images of representative inherited zircon grains in metaluminous intrusions. (a) *VB165 tonalite*. Rounded subhedral to anhedral grains exhibiting core and rim zoning patterns; grains consist of massive homogeneous cores (dark BSE) and partial to complete, thin rims (bright BSE); note crack truncation at epitaxial boundary in grain 2. (b) *VB1363 granodiorite*. Patchy recrystallized core with fine oscillatory zoned rim. (c) *VB1357*. Prism, oscillatory zoned inherited core with partial secondary crystallization; grain 1, broad diffusely zoned rim (dark BSE); grain 2, weak oscillatory-zoned mantle enclosing recrystallized core. (d) *VB1841*. Needle and prism morphologies, thick igneous and metamorphic rims mantling older inherited cores. (e) *VJ375*. Prism morphology, weak sector zoning, patchy recrystallization and partial rim (bright BSE, bottom right hand corner). (f) *VB1358*. Grain 1, needle, oscillatory zoning with minor disturbance in core, oscillatory zoned rim; grain 2, broad oscillatory zoning, homogeneous overgrowth. (g) *PVB9*. Prism and needle morphologies; grain 1, planar growth-zoned core, weak oscillatory-zoned outer rim, secondary transgressive recrystallization; grain 2, planar growth zoning, secondary convoluted zoning (top of image), fine oscillatory-zoned rim. (h) *VB1688*. Inherited core, diffuse relict planar zoning, oscillatory zoned rim, secondary transgressive recrystallization (top). (i) *VB161*. Needle; grain 1, relict fine oscillatory zoning, transgressive secondary recrystallization (lower portion of image, bright BSE patch); grain 2, thickened oscillatory zones enclosing thin inherited core; note sharp angle between core - rim crystal terminations; grain 3, prism, inherited core (bright BSE), mantled by rim, weak oscillatory-zoned patches, local recrystallization.

data for sample VJ375 is presented in Fig. 5.7.

Cumulative probability plots of $^{207}\text{Pb}/^{206}\text{Pb}$ age determinations are used in accordance with the methods of Compston and Kröner (1988) and Schiøtte and Compston (1990). This technique permits an assessment of whether dispersal of data is due to recent Pb loss from a single generation of zircon or to discrete inherited age populations. Populations were initially subdivided using clusters of $^{207}\text{Pb}/^{206}\text{Pb}$ ages that are within error of a single age at the 1σ confidence level. When non-random distribution occurs between the clusters of $^{207}\text{Pb}/^{206}\text{Pb}$ peaks, following Schiøtte and Compston (1990) the data are interpreted to represent unique age populations. Each resolved population was subsequently treated as an individual dataset and plotted on a concordia diagram to determine intercept and where possible concordia ages at the 2σ confidence level. Within-sample variation of $^{207}\text{Pb}/^{206}\text{Pb}$ ages was used to delineate inheritance trends, since the LAM ICP-MS measures Pb isotopic ratios with higher precision than U/Pb isotopic ratios in Precambrian rocks. Uncertainties on individual $^{207}\text{Pb}/^{206}\text{Pb}$ analyses were between ± 5 -14 Ma (1σ , average ± 9 Ma), whereas uncertainties on $^{238}\text{U}/^{206}\text{Pb}$ ratios ranged from ± 12 -40 Ma (1σ , average ± 22 Ma). $^{235}\text{U}/^{207}\text{Pb}$ ratios were measured with greater precision than $^{238}\text{U}/^{206}\text{Pb}$ ratios, with uncertainty on individual analyses ranging from ± 5 -20 Ma (1σ , average ± 10 Ma). However, despite the higher precision of the calculated $^{235}\text{U}/^{207}\text{Pb}$ ratios, the resultant ages were not used to identify inherited populations due to variable discordance. The discordance observed in the U/Pb analyses is attributed to at least three factors, including intragrain mobility of U and or Pb

Figure 5.4a-b: Resolved U-Pb zircon age populations for the 5 metaluminous samples. Each diagram includes; (i) cumulative probability and inherited population proportionality pie diagrams ($^{206}\text{Pb}/^{207}\text{Pb}$ age data), (ii) concordia diagrams of crystallization age; (iii – vi) youngest to oldest concordia diagrams for inherited components. Selected BSE images of analyzed grains illustrated on concordia. Crystallization ages quoted for each sample label after Bennett et al. (2005; Chapter 2). (a) *VB165*: ca. 2674 Ma tonalite (Group 1); (b) *VB1363*: ca. 2637 Ma biotite – hornblende granodiorite (Group 2).

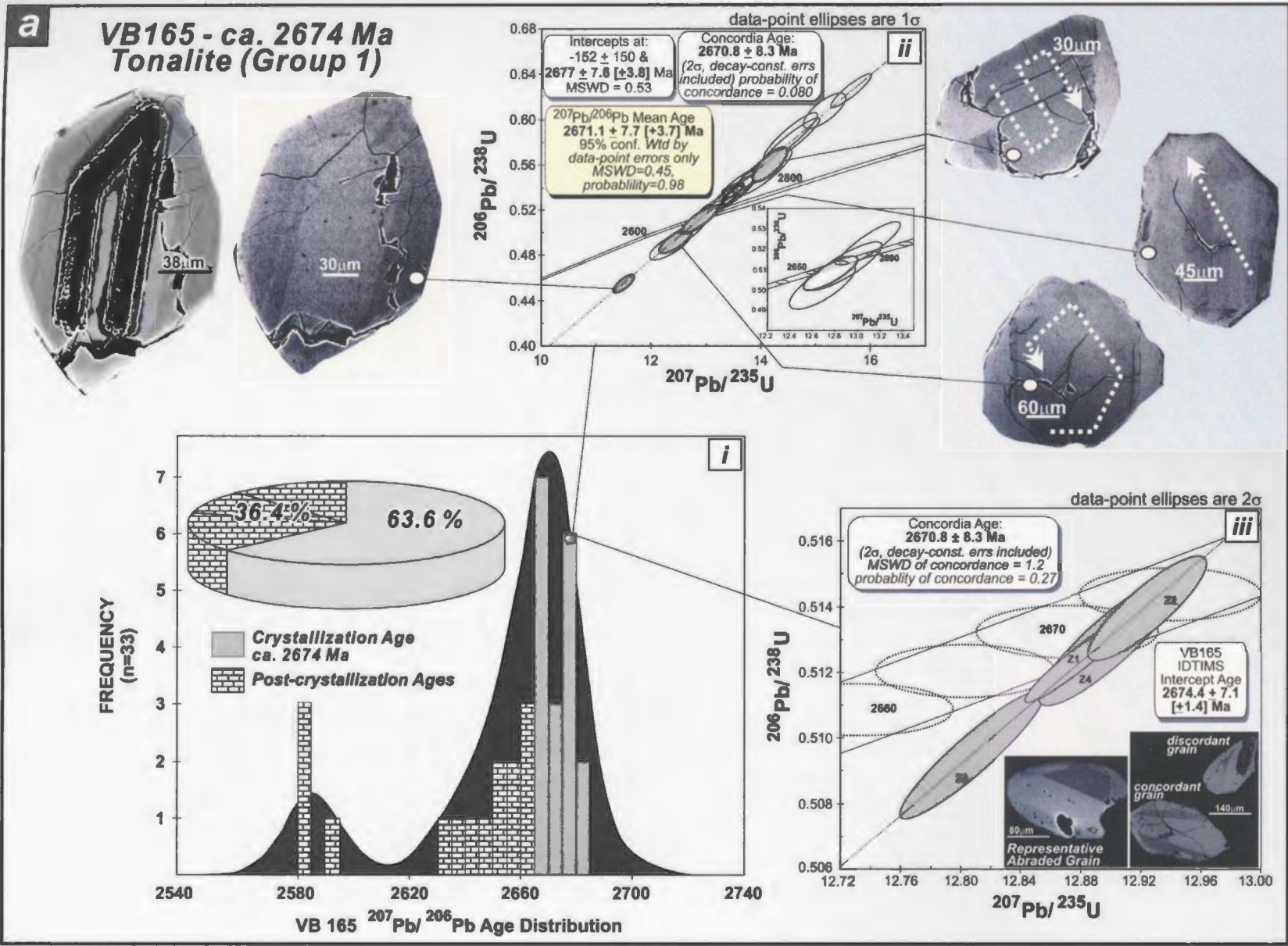


Figure 5.4a

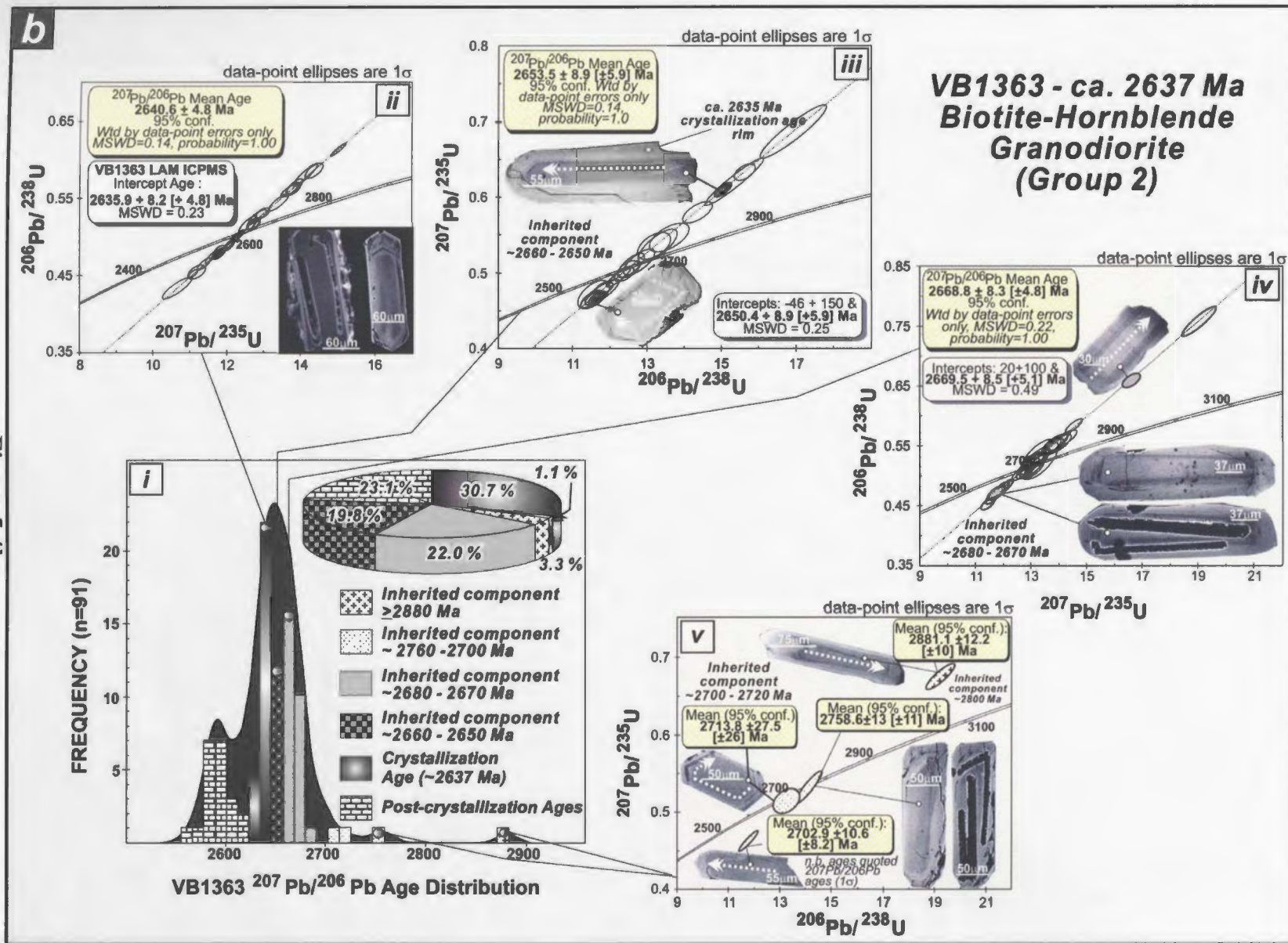


Figure 5.4b

Table 5.2: Summary of $^{206}\text{Pb}/^{207}\text{Pb}$ ages of inherited components in metaluminous samples. Note ages include decay constant errors. Uncertainties quoted represent 2σ confidence level.

	>2800 Ma (a) CSCG/ CSBC Component	>2700 Ma Kam Group Component	2690 - 2670 Ma Banting Group / Group 1- (b) KLSB Component	2660 - 2650 Ma Banting Group / Group 1- (c) RSSB Component	2640 - 2630 Ma Defeat Suite/ Group 2 - (d) DIS Component	2615 - 2605 Ma Concession Suite/ Group 2 - (e) MIC Component
Group 1 VB165 Tonalite (f)(2671±3 Ma)						
Group 2 VB1363 (g) Bt-Hbl granodiorite (2637±5 Ma)	2881 ± 24	2759 ± 26 2714 ± 56	2669 ± 8.3	2653 ± 9		
Group 3 VB1357 Bt Granite (2594±9)		2714 ± 12	2674 ± 8	2652 ± 9	2634 ± 9	
VB1841 Opx Granite (2598±7)		2713 ± 10	2673 ± 9	2652 ± 9	2633 ± 8	
Group 4 VJ375 Diorite (2589±4)						2612 ± 10

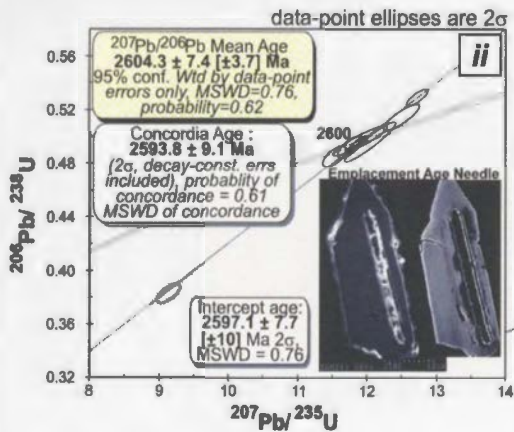
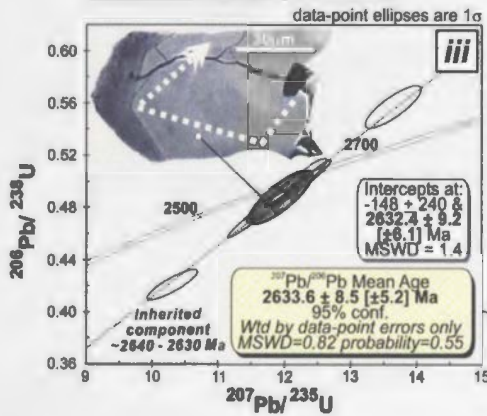
Notes: (a) CSBC / CSCG – Central Slave Basement Complex / Central Slave Cover Group (Bleeker et al. 1999); (b) KLSB – Kwejinne Lake supracrustal belt; (c) RSSB – Russell-Slemon supracrustal belt; (d) DIS – Disco Intrusive Suite; (e) MIC – Mafic Intrusive Complexes in the Snare River terrane; (f) Crystallization age quoted from Bennett et al. (2005; Chapter 2); (g) Mineral Abbreviations after Kretz (1983).

Figure 5.4c-d: Resolved U-Pb zircon age populations for the 5 metaluminous samples. Each diagram includes; (i) cumulative probability and inherited population proportionality pie diagrams ($^{206}\text{Pb}/^{207}\text{Pb}$ age data), (ii) concordia diagrams of crystallization age; (iii – vi) youngest to oldest concordia diagrams for inherited components. Selected BSE images of analyzed grains illustrated on concordia. Fig. 5.4c also indicates ϵNd_T data for respective inherited zircon populations ($\epsilon\text{Nd}_{T_{\text{inh}}}$) and measured $\epsilon\text{Nd}_{T_{\text{cryst}}}$ (Bennett et al. submitted; Chapter 4). See text for detail. Crystallization ages quoted for each sample label after Bennett et al. (2005; Chapter 2). (c) **VB1357:** ca. 2595 Ma biotite granite (Group 3); (d) **VB1841:** ca. 2597 Ma orthopyroxene granite (group 3).

C

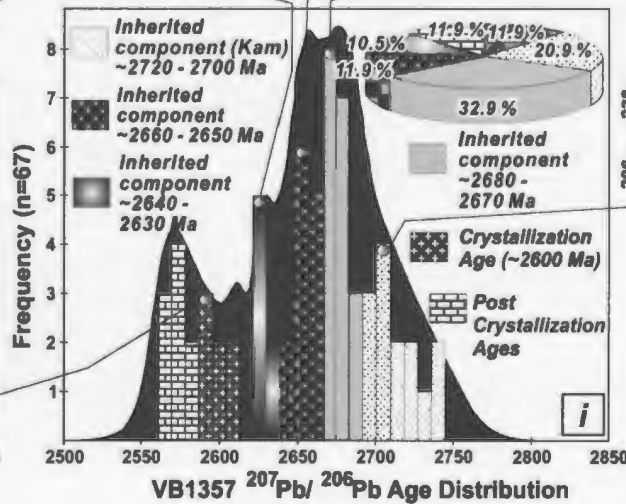
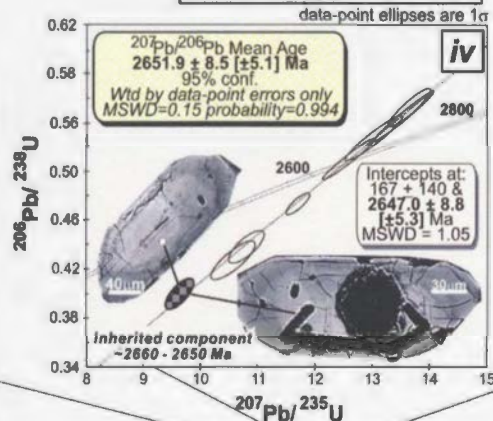
VB1357 - ca. 2595 Ma Biotite Granite (Group 3)

**Group 2 - Disco
Intrusive Suite Age
Component**
 $\epsilon Nd_{2597} = +1.1$

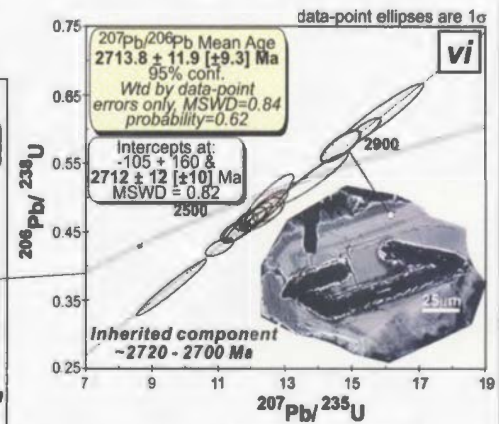
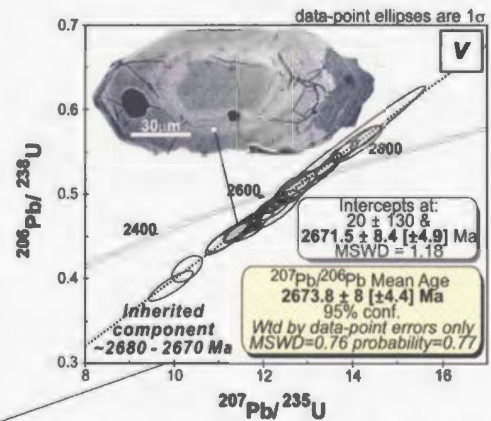


Crystallization Age $\epsilon Nd = +2.0$

**Hinscliffe Complex/
RSSB Volcanic
Age Component**
(ca. 2658 Ma)
 $\epsilon Nd_{2597} = +2.3$



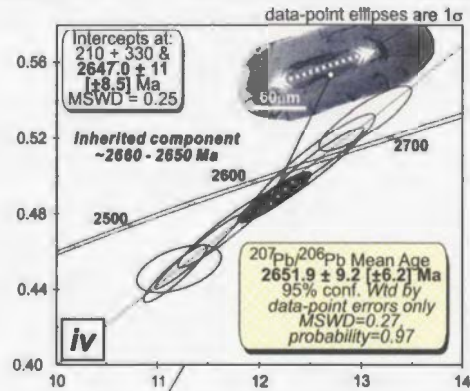
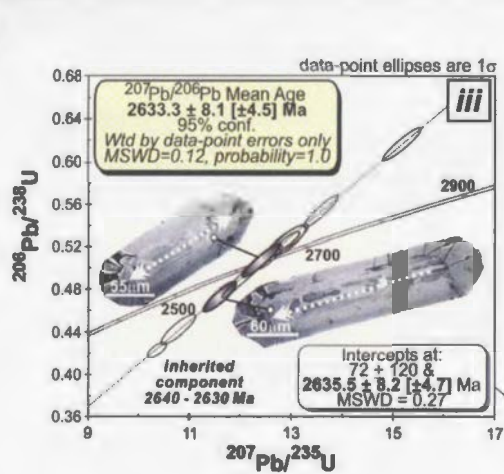
**KLSB Volcanic
Age (ca. 2674 Ma)
Component**
 $\epsilon Nd_{2597} = +1.1$



**Kam Age
Component
Ave ϵNd_{2597}
= +1.5**

Figure 5.4c

d



VB1841 - ca. 2597 Ma Orthopyroxene Granite (Group 3)

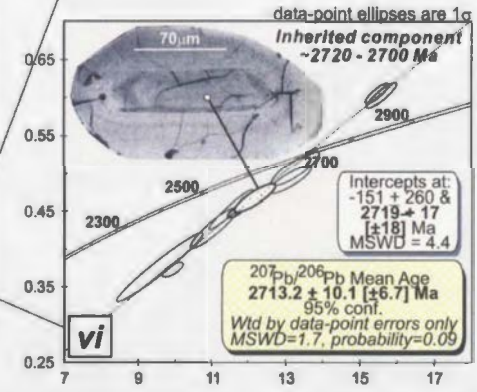
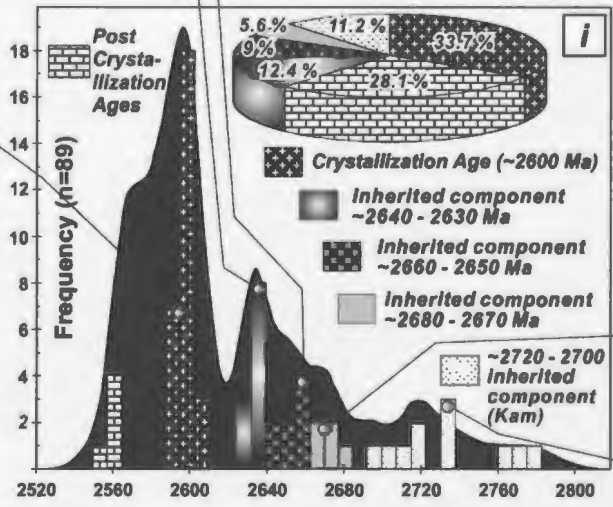
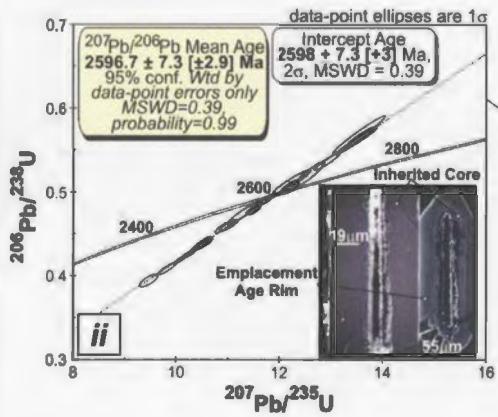
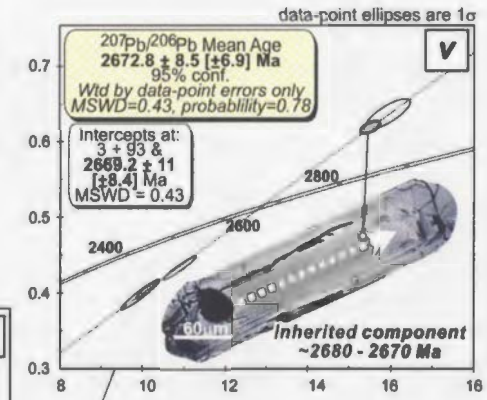
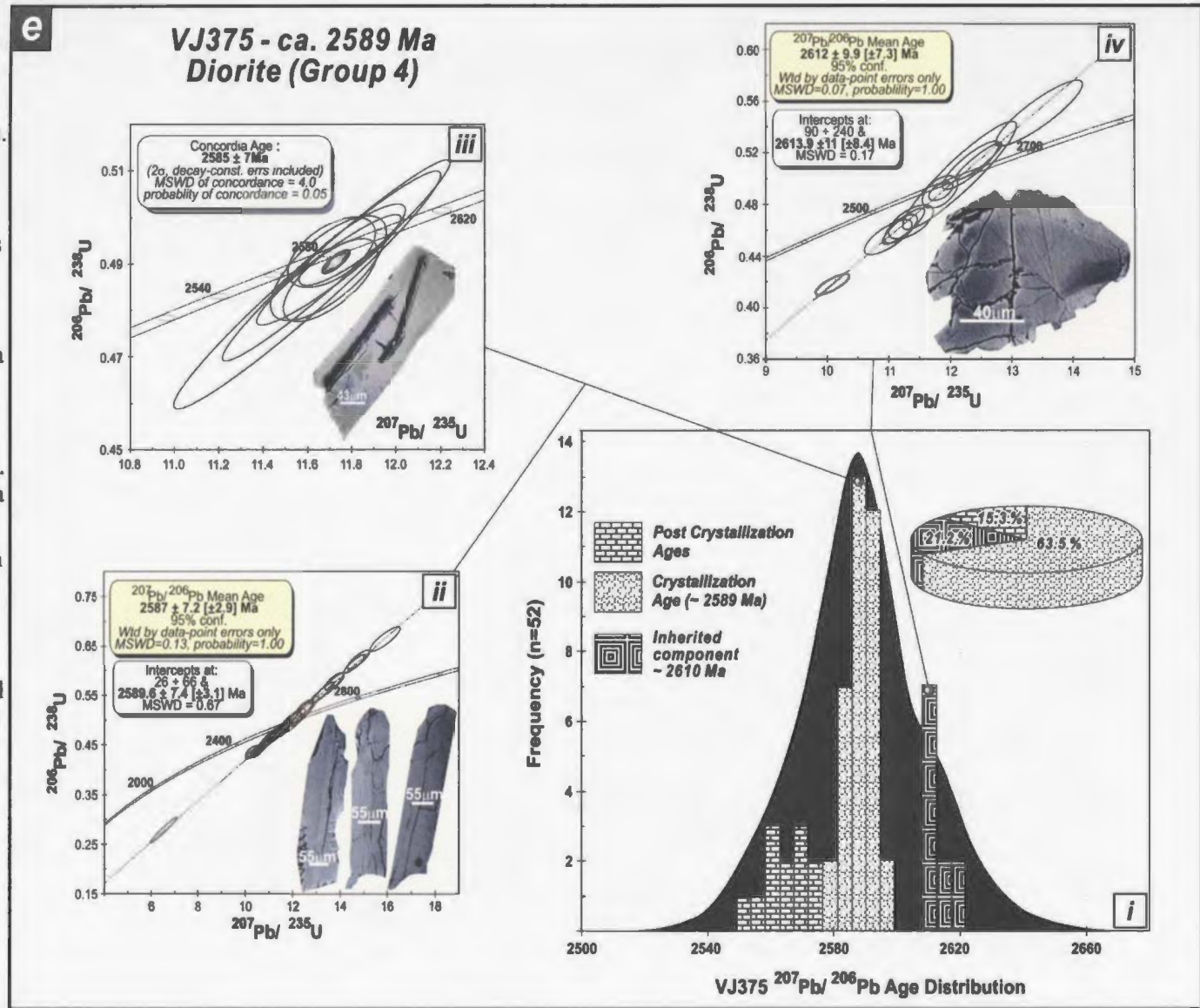


Figure S.4d

Figure 5.4: Resolved U-Pb zircon age populations for the 5 metaluminous samples for the 5 metaluminous samples. Each diagram includes; (i) cumulative probability and inherited population proportionality pie diagrams ($^{207}\text{Pb}/^{206}\text{Pb}$ age data), (ii) concordia diagrams of crystallization age; (iii - vi) youngest to oldest concordia diagrams for inherited components. Selected BSE images of analyzed grains illustrated on concordia. Fig. 5.4c also indicates $e\text{Nd}_T$ data for respective inherited zircon populations ($e\text{Nd}_{\text{Tinh}}$) and measured $e\text{Nd}_{\text{Tcryst}}$ (Bennett et al. submitted; Chapter 4). See text for detail. Crystallization ages quoted for each sample label after Bennett et al. (in press; Chapter 2). (e) VJ375: ca. 2589 Ma Diorite (Group 4).



in a closed system, open-system Pb loss, or mass-dependent fractionation of U and Pb during analysis.

The inherited age data reported here are grouped into six 'age components', which are described below with contemporary magmatic events from the Snare River terrane (*italics*) and Slave Province: (1) > 2800 Ma (CSCG / CSBC), (2) ca. 2760-2700 Ma (Kam Group), (3) ca. 2680-2670 Ma (Group 1 Kwejinne Lake belt magmas, Banting Group), (4) ca. 2660-2650 Ma (Group 1 Russell–Slemon volcanics, Hinscliffe plutonic complex, Banting Group), (5) ca. 2640-2630 Ma (Group 2 Disco Intrusive Suite, Defeat Suite), and (6) ca. 2615–2605 (Group 2 Mafic Intrusive Complexes, Concession Suite). Crystallization ages are summarized in Tables 5.2 and 5.3 and on Figs. 5.4 and 5.5.

U-Pb age uncertainties are reported at 1σ values in Tables F1 and F2 in Appendix F. Calculated U-Pb crystallization and inheritance ages presented on concordia diagrams (Figs. 5.4 and 5.5) are reported at 2σ confidence levels. Calculated ages for individual analyses are quoted at 1σ levels and data ellipses are plotted at 1σ . Two error estimates are provided for age determinations, including and ignoring U decay constant uncertainties, the latter in square brackets. Decay constant uncertainties are also plotted graphically on concordia diagrams. Reversely discordant data are considered to be real phenomena and not an artefact of the method (Chapter 2, Appendix B; Bennett et al. 2005) and are included in the datasets. Discussion of the significance of post-crystallization ages, which are plotted on Figs. 5.4 and 5.5, is not presented in this paper.

Figure 5.5a-b: Resolved U-Pb zircon age populations for the 4 peraluminous samples. Each diagram includes; (i) cumulative probability and inherited population proportionality pie diagrams ($^{206}\text{Pb}/^{207}\text{Pb}$ age data), (ii) concordia diagrams of crystallization age; (iii – vi) youngest to oldest concordia diagrams for inherited components. Selected BSE images of analyzed grains illustrated on concordia. Fig. 5.5b also indicates ϵNd_T data for respective inherited zircon populations ($\epsilon\text{Nd}_{T_{\text{inh}}}$) and measured $\epsilon\text{Nd}_{T_{\text{cryst}}}$ (Bennett et al. submitted; Chapter 4). See text for detail. Crystallization ages quoted for each sample label after Bennett et al. (2005; Chapter 2). *(a) VB1358:* ca. 2595 Ma two-mica granite (Group 2); *(b) PVB9:* ca. 2597 Ma megacrystic granite (Group 3).

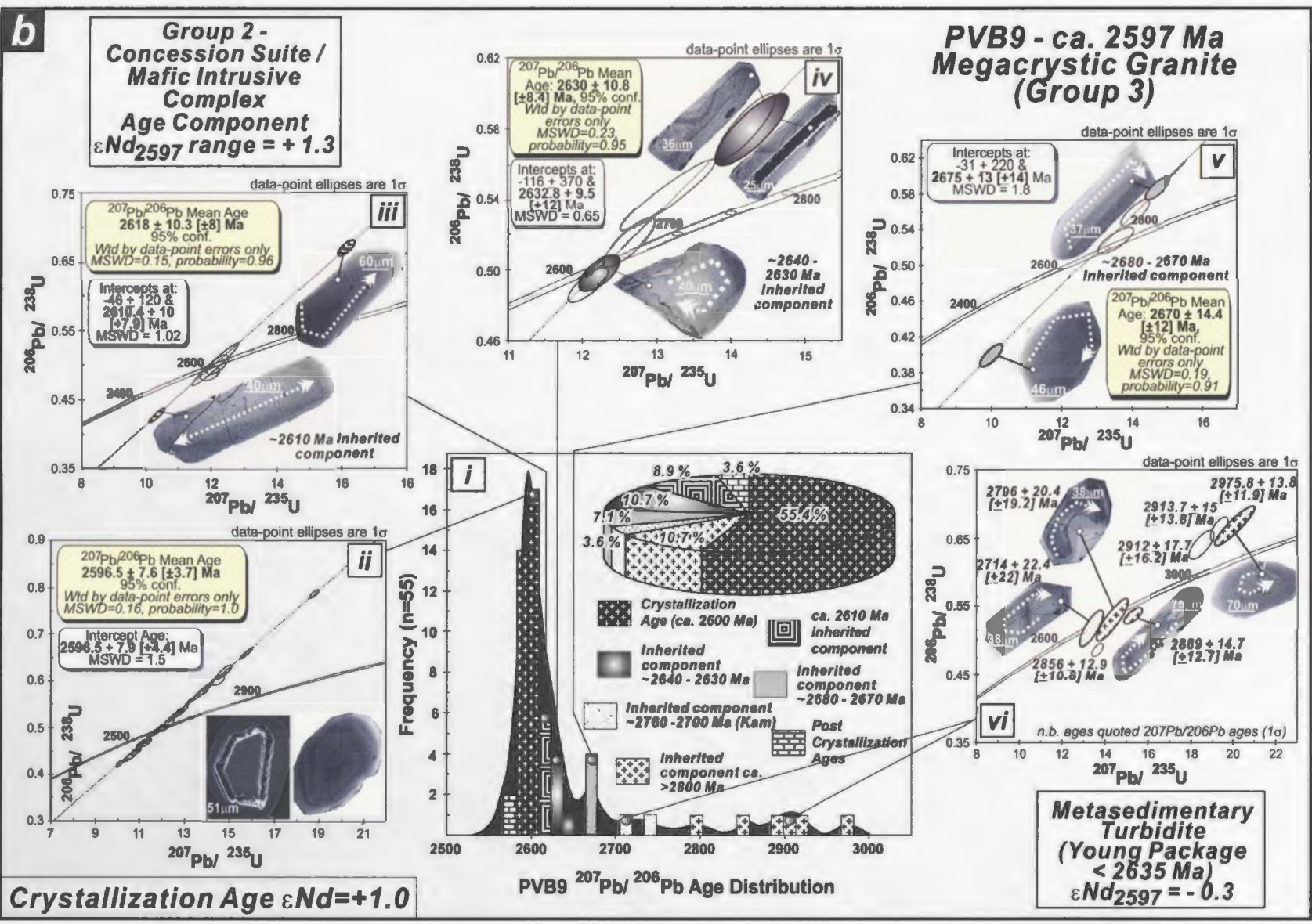


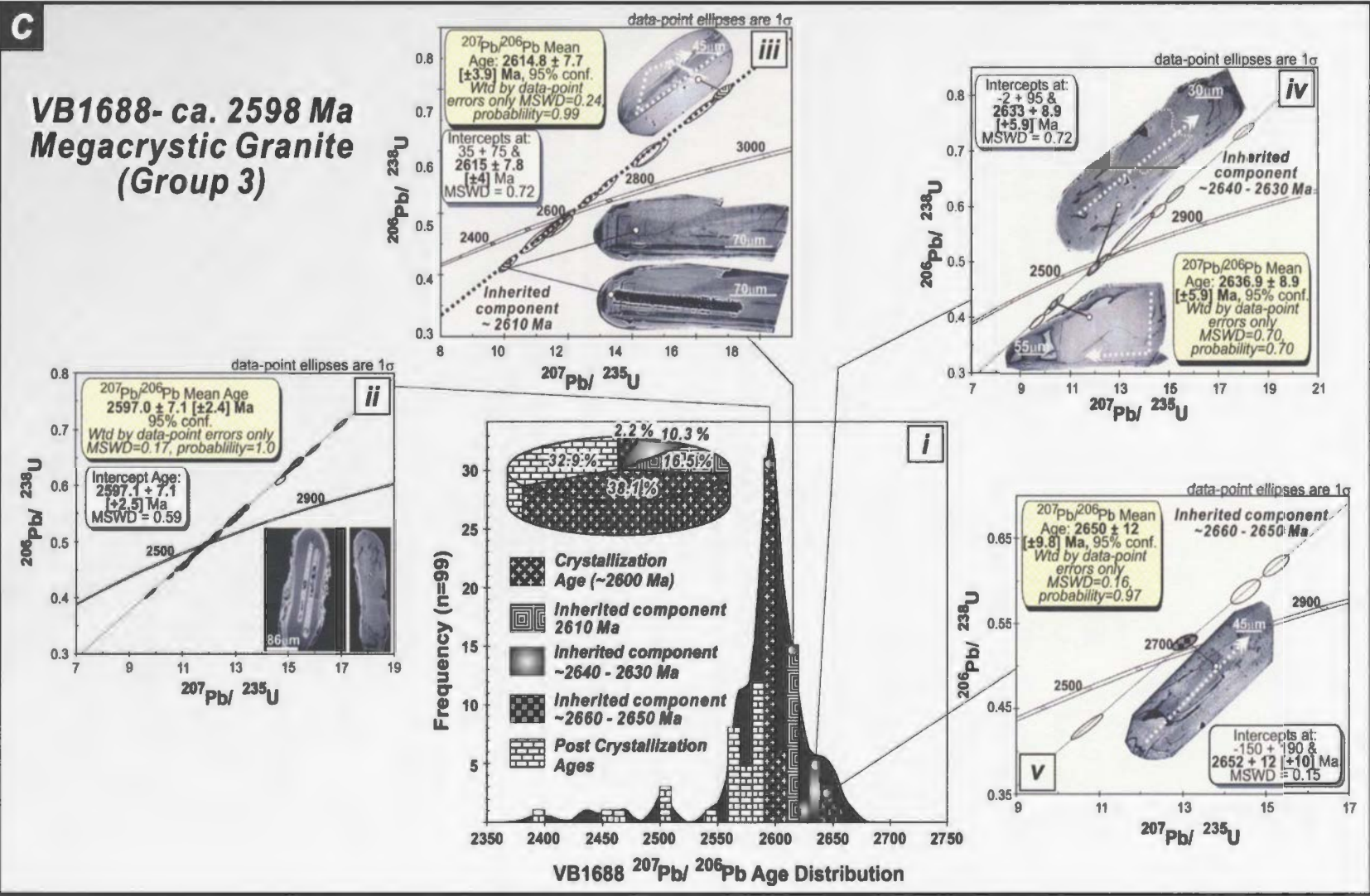
Table 5.3: Summary of $^{206}\text{Pb}/^{207}\text{Pb}$ ages of inherited components in peraluminous samples. Note ages include decay constant errors. Uncertainties quoted represent 2σ confidence level.

	>2800 Ma	>2700 Ma <2800 Ma	2690 - 2670 Ma	2660 - 2650 Ma	<2650 - 2630 Ma	2615 - 2605 Ma Concession Suite/ Group 2 – ^(b) MIC Magmatic Age Component	2600 Ma Group 3 Magmatic Age Component
	← ^(a) Age components observed in metaturbidite detrital zircon data →						
Group 3							
VB1358	3071 ± 24	2725 ± 11	2682 ± 15		2645 ± 10	^(d) 2618 ± 10	
Two-mica granite ^(c) (2595±8 Ma)	2809 ± 21						
PVB9	2976 ± 28	2796 ± 40	2670 ± 14		2630 ± 11		
Megacrystic granite (2597±8)	2914 ± 30 2912 ± 36 2889 ± 30 2856 ± 26	2714 ± 44					
VB1688				2650 ± 12	2637 ± 9	^(d) 2615 ± 8	
Megacrystic granite (2597±7)							
Group 4	2923 ± 30	2796 ± 30			2632 ± 10		2602 ± 12
VB161	2851 ± 30	2762 ± 36					
^(e) Crd leucogranite (2585±9)		2732 ± 13					

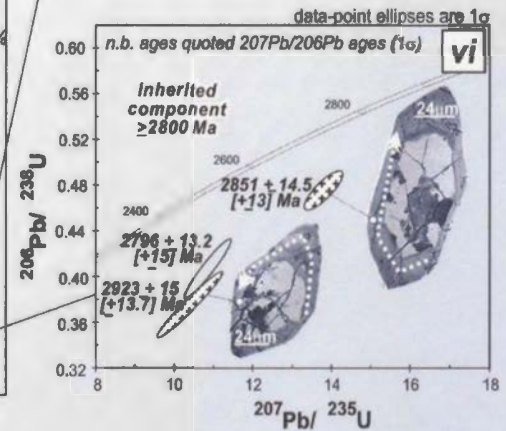
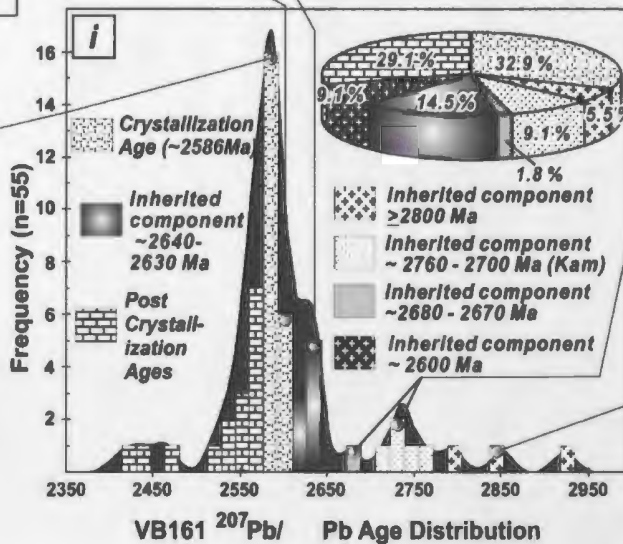
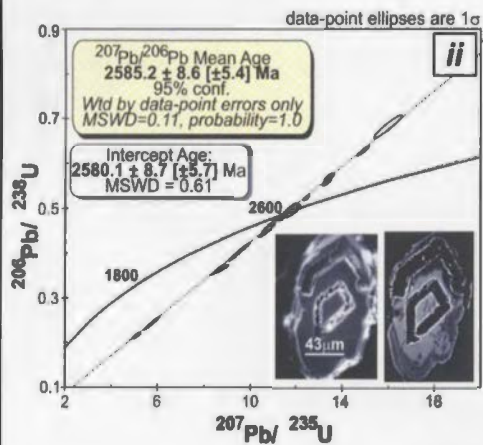
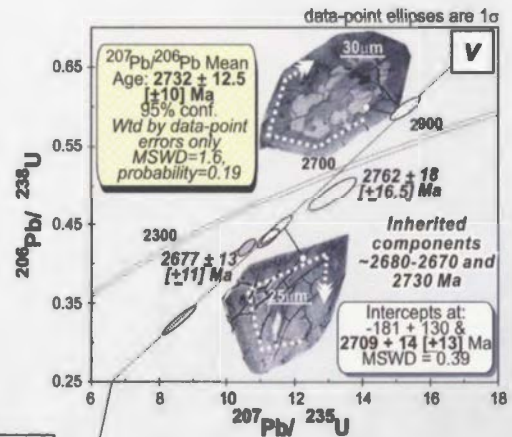
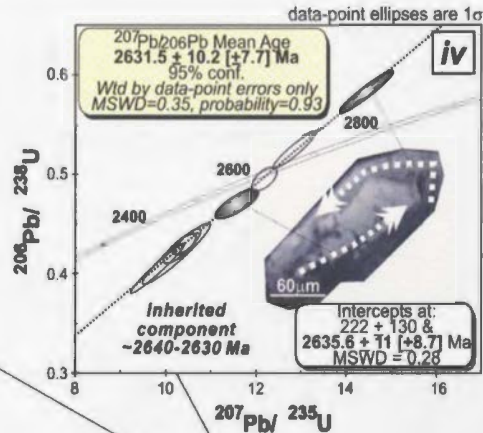
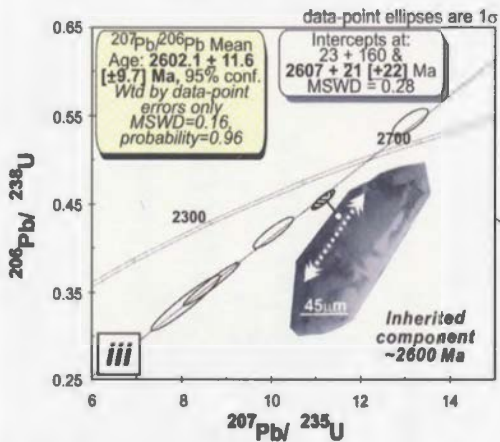
Notes: (a) Metaturbidite age components from Pehrsson and Villeneuve (1998) and Bennett et al. (2005; Chapter 2); (b) MIC – Mafic Intrusive Complexes in the Snare River terrane; (c) Crystallization ages from Bennett et al. (2005; Chapter 2); (d) calculated age, (including errors), falls within the range of Concession Suite crystallization ages; (e) mineral abbreviations after Kretz (1983).

Figure 5.5c-d: Resolved U-Pb zircon age populations for the 4 peraluminous samples. Each diagram includes; (i) cumulative probability and inherited population proportionality pie diagrams ($^{206}\text{Pb}/^{207}\text{Pb}$ age data), (ii) concordia diagrams of crystallization age; (iii – vi) youngest to oldest concordia diagrams for inherited components. Selected BSE images of analyzed grains illustrated on concordia. Crystallization ages quoted for each sample label after Bennett et al. (2005; Chapter 2). (c) *VB1688*: ca. 2598 Ma megacrystic granite (Group 3); (d) *VB161*: ca. 2565 Ma cordierite leucogranite (group 4).

C
VB1688- ca. 2598 Ma
Megacrystic Granite
(Group 3)



d VB161 - ca. 2585 Ma
Cordierite Granite
(Group 4)



5.6.2 ϵNd modelling data

The final dataset involves Sm-Nd data for two samples that are used as case studies to investigate the link between inherited zircon data and ϵNd isotopic mixing models. The samples, a mid-crustally-derived peraluminous megacrystic granite (PVB9) and a lower-crustally-derived metaluminous biotite granite (VB1357), both contain abundant inherited zircon and their geochemical and their isotopic signatures indicate negligible post-emplacement disturbance. Geochemical and temporal correlation of magmatic suites across the Slave Province (Chapter 4; Bennett et al. accepted) provides the rationale for the assignment of ϵNd_T values to each age component in the inherited zircon spectra. A Sm-Nd database (Appendix F, Table F3) was compiled to determine average ϵNd_T values and Nd concentrations for magmatic suites across the Slave Province, using the datasets of Davis and Hegner (1992), MacLachlan (1993), Davis et al. (1994), Yamashita et al. (1999a), Branstromm (2000), Cousens (2000), Cousens et al. (2002), Bennett et al. (submitted), and A. Alcazar and B. Cousens (unpublished data). These average values were assigned to each inherited component in the two samples. For example, the average ϵNd_T for ca. 2680-2670 Ma tholeiites in the Snare River terrane is +1.9, so this value is assigned to the ca. 2680-2670 Ma inherited zircon component in VB1357, a metaluminous magma interpreted to originate from tholeiitic protoliths. Note that this value represents the average ϵNd_T of this age component in the magma source, not that of the inherited zircon itself. A proportion is assigned to each inherited component based on the number of analyses of the component compared to the total number of analyses of inherited grains.

The inherited age components and proportions, crystallization ages, measured whole-rock ϵ_{Nd} values, assigned average ϵ_{Nd} values, and bulk protolith geochemistry for VB1357 and PVB9 are given in Table 5.4. Assigned ϵ_{Nd} values were calculated for $T=2597$ Ma, the approximate crystallization age of both samples. Petrogenesis of the peraluminous megacrystic granite suite involved a metaturbidite protolith and a proportion of its inherited zircon originated from this source. In order to characterise the turbidite component, detrital zircon data for a metaturbidite from the Kwejinne Lake supracrustal belt (Bennett et al. 2005) are included in Table 5.4 with the proportions and whole rock ϵ_{Nd} values of each major provenance population. Additional details are found in the discussion and Appendix H.

5.7 Interpretation

In evaluating the significance of the zircon inheritance age data, the implications in regard to the tectonic and petrogenetic evolution magmas in the Snare River terrane are examined and the importance of observed secular variations in the source regions of metaluminous magmas and the role of metasedimentary protoliths in the genesis of peraluminous magmas are highlighted. The discussion concludes with an evaluation of the dataset in the context of whole-rock ϵ_{Nd} data for two samples, which demonstrate that the zircon inheritance data can yield quantitative constraints for binary and multicomponent ϵ_{Nd} mixing models, and thus provide valuable insight into magma petrogenesis.

Table 5.4: Summary data to constrain binary and multicomponent mixing models for samples PVB9 and VB1357. Refer to Appendix F (Table F3) for original data sources.

	CSCG / CSBC Age Component (>2800 Ma)	Kam Group Component (>2700 Ma)	Banting Group / Group 1- KLSB Magmatic Age Component (~ 2670 Ma)	Banting Group / Group 1- RSSB Magmatic Age Component (~ 2658 Ma)	Defeat Suite/ Group 2 – DIS Magmatic Age Component (ca.2637 Ma)	Concession Suite/ Group 2 – MIC Magmatic Age Component (ca.2610 Ma)	Group 3 Magmatic Age Component (ca.2600 Ma)	^(a) Source rock Inferred from Magma Geochemistry (Table 5.1)
EXAMPLE 1: Upper-Crustal Metaluminous Biotite Granite (VB1357) – Multicomponent Mixing Data								
^(b) T _{inh} Prop ₍₆₁₎		27.5%	43.1%	15.7%	13.7%			Lower-crustal mafic source - <i>hydrated tholeiite?</i> [Amphibole –Rutile-Gamet residuals]
^(c) ²⁰⁶ Pb/ ²⁰⁷ Pb.		2714±12 [±9] Ma	2674±8 [±4.4] Ma	2652±8.5 [±5.1] Ma	2634±8.5 [±5.2] Ma		T _{crystallization} : 2594±9.1 Ma	
^(d) Nd (ppm)		8.2	17.4	12.2	19.6			
^(e) εNd ₂₅₉₇		(Ave +1.5)	(Ave +1.9)	(Ave +2.3)	(Ave +1.2)		+2.0	
EXAMPLE 2: Mid-Crustal Peraluminous Megacrystic Granite (PVB9) – Binary Mixing Data								
T _{inh} Prop ₍₂₃₎	27.3%	4.5%	18.2%	27.3%		22.7%		Mid-crustal mixed garnet-rich pelite (turbidite) and mafic (Concession Suite equivalent) protoliths. [Plagioclase - rutile residuals]
 77.3%.....							
²⁰⁶ Pb/ ²⁰⁷ Pb.	2975 - 2800Ma	2714±22 [±21]Ma	2670±14.4 [±12]Ma		2630±10.8 [±8.4]Ma	2610±10 [±7.9]Ma	T _{crystallization} 2597±7.3 [±2.9] Ma	
 ^(f) (Detrital Origin).....							
Nd (ppm)			15.7			43.5		
εNd ₂₅₉₇			- 0.3			+1.9	+1.0	
Turbidite data (Bennett et al. in press): ^(g) T _{sed} =2635Ma								
^(h) T _{det} Prop ₍₁₀₀₎	13.5%	39.6%	31.3%	10.4%	5.2%			
²⁰⁶ Pb/ ²⁰⁷ Pb.	~2870- 2780 Ma	2703 - -2744 Ma	2675±7.7 [±3.6] Ma	2653.1±8.9 [±5.9] Ma	2634±10 [±8.3] Ma			
⁽ⁱ⁾ εNd _{sed}							εNd ₂₅₉₇ = -0.3	

Notes: ^(a) Source rock: Geochemical source rock characteristics summarized from Bennett et al. (accepted; Chapter 4); ^(b) T_{inh} Prop₍₂₃₎: denotes the proportion, as a percentage, of individual inherited components, excluding crystallization and post-crystallization ages. Number of analyses used to calculate proportions in subscript; ^(c) ²⁰⁶Pb/²⁰⁷Pb: calculated inheritance, crystallization or detrital zircon age. Reported age errors are quoted both with and [without] U decay constant uncertainties; ^(d) Nd (ppm) assigned average Nd concentration in source component, determined from published data (see Appendix F; Table F3); ^(e) εNd₂₅₉₇: Epsilon Nd values assigned or measured for each age component, recalculated for the age of crystallization. Ave – represents an average εNd value where a range of data is available from published datasets. (See text for details); ^(f) (Detrital Origin): Whole rock geochemistry indicates a predominantly metasedimentary source, suggesting that inherited zircon ages represent detrital rather than igneous origin; ^(g) T_{sed} =2635Ma: Maximum sedimentation age of metaturbidite sample. Data presented in Bennett et al. (in press; Chapter 2); ^(h) T_{det} Prop₍₁₀₀₎: denotes the proportion, as a percentage, of individual detrital components, excluding metamorphic or reset zircon ages. Number of analyses used to calculate proportions in subscript; ⁽ⁱ⁾ εNd_{sed}: Epsilon Nd value of metaturbidite sample at time of sedimentation and recalculated to ~ 2597 Ma, which represents emplacement age of megacrystic granite.

5.7.1 Zircon inheritance in metaluminous magmas - Implications for Neoproterozoic lower crustal evolution

Metaluminous magmas punctuate the entire history of the Snare River terrane, from initial crust formation through orogenic thickening to final stabilization. Their geochemistry indicates a predominantly lower crustal origin and hence their inherited zircon populations provide the opportunity to profile lower crustal evolution through time. In the text that follows, we image three intervals of lower crustal evolution at ca. 2674, 2635 and 2600 Ma and briefly discuss the significance of inheritance in a 2589 Ma mantle-derived sanukitoid magma. Comparison of the profiles permits a first-order understanding of the secular evolution of the deep crust in the Snare River terrane.

5.7.1.1 Lower crustal profile at ca. 2674 Ma

Synvolcanic tonalite (VB165) and associated Group 1 TTG magmas were emplaced in the Snare River terrane at ca. 2674 Ma. As with similar magmas of this group, the analyzed tonalite is Zr-undersaturated (Chapter 6), so the absence of inherited zircon (Fig. 5.4a) cannot be taken to imply a lack of refractory zircon in the source region. Villeneuve and Henderson (1998) reported a single xenocrystic zircon with a $^{206}\text{Pb}/^{207}\text{Pb}$ age of 2791 ± 35 Ma from ca. 2673 Ma felsic volcanic rocks at Wijinnedi Lake (Fig. 1) that are correlated with Group 1 TTG magmas. This inherited age is suggestive of an older substrate predating 2674 Ma magmatism (Fig. 5.6), but the large error on the analysis hampers further interpretation. However, it is surmised on geochemical and isotopic grounds (Chapter 4) that the lower crust of the Snare River

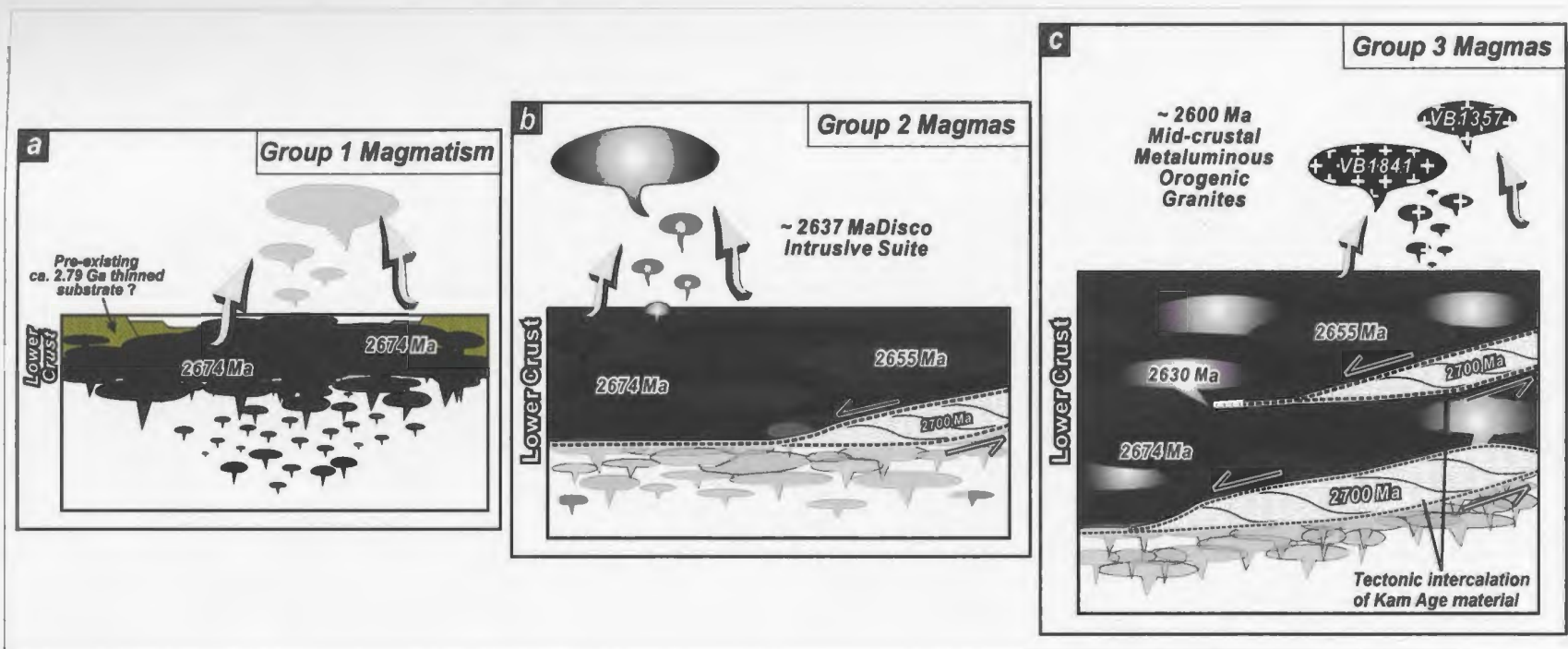


Figure 5.6: Summary diagram of lower crustal evolution of the Snare River terrane during crust formation, growth and orogenesis. Two mechanisms of lower-crustal growth are illustrated including both 'local' magmatic additions (5.6a-c) and subcretion of 'exotic' mafic tholeiitic components (5.6b & c).

terrane was characterized by a high degree of geochemical and isotopic homogeneity during the initial crust-forming episode associated with Group 1 magmas (TR1a; Fig 5.2) and was distinctive due to the negligible influence of pre-2.8 Ga crust.

5.7.1.2 Lower crustal profile at ca. 2637 Ma

A second window into lower-crustal evolution occurred ca. 40 M.y. after initial crust formation, with the age components of the lower crust at this time recorded in the inherited zircon populations of the Group 2 Disco Intrusive Suite (VB1363; Fig. 5.2). This suite, also of TTG affinity, is geochemically similar to Group 1 TTGs, reflecting a lower-crustal mafic source enriched in garnet and amphibole (Table 5.1). However, the Disco Intrusive Suite, which contains abundant inherited zircon, underwent a greater degree of intracrustal fractionation, as indicated by its positive Eu anomaly (Bennett et al. submitted; Chapter 4).

Four premagmatic components, with ages from ca. 2880 to 2650 Ma, are present in the inherited zircon population. The largest inherited components yield ages of ca. 2670 and 2653 Ma, which are comparable to crystallization ages determined for the upper-crustal Group 1 magmas (ca. 2674 Ma and 2658-2654 Ma, respectively). This is an important correlation as it demonstrates a temporal link between upper and lower crustal magmatism and implies that intermittent episodes of lower-crustal melting were an important mechanism for early crustal growth (Fig. 5.6). The origin of the older premagmatic zircon components is debatable. The single ca. 2881 Ma age may represent contaminant zircon derived from metaturbidites into which the suite was emplaced, as

metaturbidites across the Slave Province are known to contain detrital zircon of this age (e.g. Schärer and Allègre 1982; Pehrsson and Villeneuve 1999; Sircombe et al. 2001; Chapter 2). Due to the absence of 2760-2700 Ma granitoids in the Snare River terrane (at the present level of exposure), the three ca. 2760-2700 Ma premagmatic grains are inferred to represent either contaminant or inherited zircon. Detrital zircon from metaturbidites in both the Indin Lake and Kwejinne Lake supracrustal belts (Pehrsson and Villeneuve 1999; Bennett et al. 2005) include appreciable populations with an age of ca. 2760-2700 Ma and hence would be a suitable source of contaminant zircon for this age component. However, it must be noted that the oldest premagmatic age of 2758 ± 13 Ma overlaps with the inherited component identified in the ca. 2673 Ma Group 1 felsic volcanic rocks of TTG affinity (see above), and a distinct ca. 2760-2700 Ma inherited population occurs in ca. 2600 Ma metaluminous magmas (see below), indicating that the existence of a lower-crustal reservoir of this age should not be ruled out.

5.7.1.3 Lower-crustal profile at ca. 2600 Ma

The orogenic peak (TR2a) in the Snare River terrane occurred from ca. 2600-2595 Ma (Fig. 5.2) and was accompanied by emplacement of metaluminous granitic to granodioritic magmas in the upper and mid crust. Petrogenetic constraints for the analyzed upper-crustal biotite granite and mid-crustal orthopyroxene granite imply a mafic, garnet-rich lower crust, as was the case for the older Group 1 and 2 samples (Chapter 4), however, the inheritance profiles of the younger Group 3 magmas reveal

considerably greater heterogeneity in the source region. Four features of the inheritance trends in the ca. 2600 Ma metaluminous magmas are significant;

- (1) the similarity in resolved inheritance spectra between the ca. 2594 Ma upper- and ca. 2637 Ma and ca. 2598 mid-crustal granites (Table 5.2; Fig. 5.4c, d);
- (2) the occurrence in both upper- and mid-crustal suites of ca. 2680-2670 and 2660-2650 Ma inherited components (similar to VB1363 of the older Disco Intrusive suite), suggesting mafic rocks of these ages persisted as distinct components in the lower-crustal reservoir;
- (3) the presence of appreciable 2760-2700 Ma inherited grains, which in older magmas comprised a minor proportion of total inheritance;
- (4) the ca. 2674, 2653 and 2635 Ma inherited components are interpreted to reflect 'local' sources, as they correlate with the ages of plutons in the overlying mid- and upper-crust, whereas the 2760-2700 Ma population is termed 'exotic' as magmatic rocks of this age are not observed in the Snare River terrane.

The abundance of 'exotic' 2760-2700 Ma inherited ages in the ca. 2600 Ma metaluminous plutons, together with an absence of geochemical constraints supporting an origin by assimilation of metasediments, implies that 2760-2700 Ma mafic rocks had become an important reservoir in the lower crust by 2600 Ma. This age overlaps with Kam Group tholeiites (e.g. Chan and Crestaurum formations, $>2714 \pm 8$ Ma; Isachsen 1992), which are widespread in the central Slave Province. We therefore interpret the 2760-2700 Ma inherited component to imply that 'Kam' crust was tectonically intercalated into the lower crust of the Snare River terrane prior to the ca. 2600 Ma

orogenic peak. We envisage that intercalation involved underthrusting or subcretion (Fig. 5.6), akin to the shallow- or flat-subduction model of Smithies et al. (2003), in which underthrust mafic slabs are accreted to the lower crust and subsequently become a fertile source for TTG upper- and mid-crustal magmatism. In support of this model, seismic reflection data acquired across the SNORCLE transect west of Yellowknife ca. 100 km south of the Snare River terrane (Fig. 5.1) reveal several low angle west-dipping reflectors at depth that are interpreted to truncate Kam Group magmatic rocks exposed near Yellowknife (van der Velden and Cook 2002, their Fig. 3).

In summary, the similarity of inheritance profiles of the ca. 2600 Ma metaluminous magmas emplaced at different crustal levels, in combination with the secular changes observed in inheritance recorded in ca. 2674, 2635 and 2600 Ma metaluminous magmas, reveals that lower crustal growth occurred by both intermittent 'locally-derived' mafic magmatism, driven by thermal perturbations in the subjacent lithospheric mantle, and also by tectonic intercalation of 'exotic' mafic material that predated all exposed crustal components in the Snare River terrane.

5.7.1.4 Inheritance in 2589 Ma sanukitoid suite

The 10 M.y. interval following the ca. 2600 Ma orogenic peak in the Snare River terrane (TR2b; Fig. 5.2) involved major reorganization of the crustal architecture as a result of extensional uplift of the mid-crustal Ghost subdomain and emplacement of small-volume, mantle- and crustal-derived anatectic magmas (Chapters 2 and 4). A ca. 2589 Ma metaluminous diorite, VJ375, was selected for inheritance analysis in the hope

that it would profile the lower crust after post-orogenic collapse. However, geochemical data demonstrate the melt was an evolved sanukitoid, suggesting that petrogenesis involved mantle melting (Chapter 2), and hence zircon inheritance will not reflect the age composition of the lower crust at this time. Nonetheless, its inherited zircon is of interest. Excluding post-crystallization ages, two age components were observed among the 52 analyses of the sample (Fig 5.4e), but the precision of the LAM ICP-MS technique in this case does not clearly resolve the premagmatic population (Figs. 5.4e). At the 1σ confidence level, analyses of premagmatic grains yield ages that are greater than the ca. 2589 Ma crystallization age of the sample, but the error range overlaps with that of the magmatic grains, as is illustrated more clearly in Fig. 5.7a. To better define the premagmatic component, the magmatic ages were removed from the dataset and the remaining data were compared with the more precise crystallization age determined by ID-TIMS ($^{207}\text{Pb}/^{206}\text{Pb}$ crystallization age of 2589 ± 2.4 Ma 1σ ; Fig. 5.7b).

Figure 5.7b shows that the premagmatic component in sample VJ375 has an age of ca. 2610 Ma (2621 to 2603 Ma incorporating 2σ uncertainties), predating the crystallization age by about 20 M.y. Two contrasting scenarios involving either crustal contamination or a refractory origin from the mantle source could account for this older component. In the crustal contaminant model, lithologies with ages ranging from 2621 to 2603 Ma must have either predominated in the crustal column through which the sanukitoid magma ascended or been selectively incorporated during its ascent. However, field and geochronological evidence demonstrate the crust of the Snare River terrane was

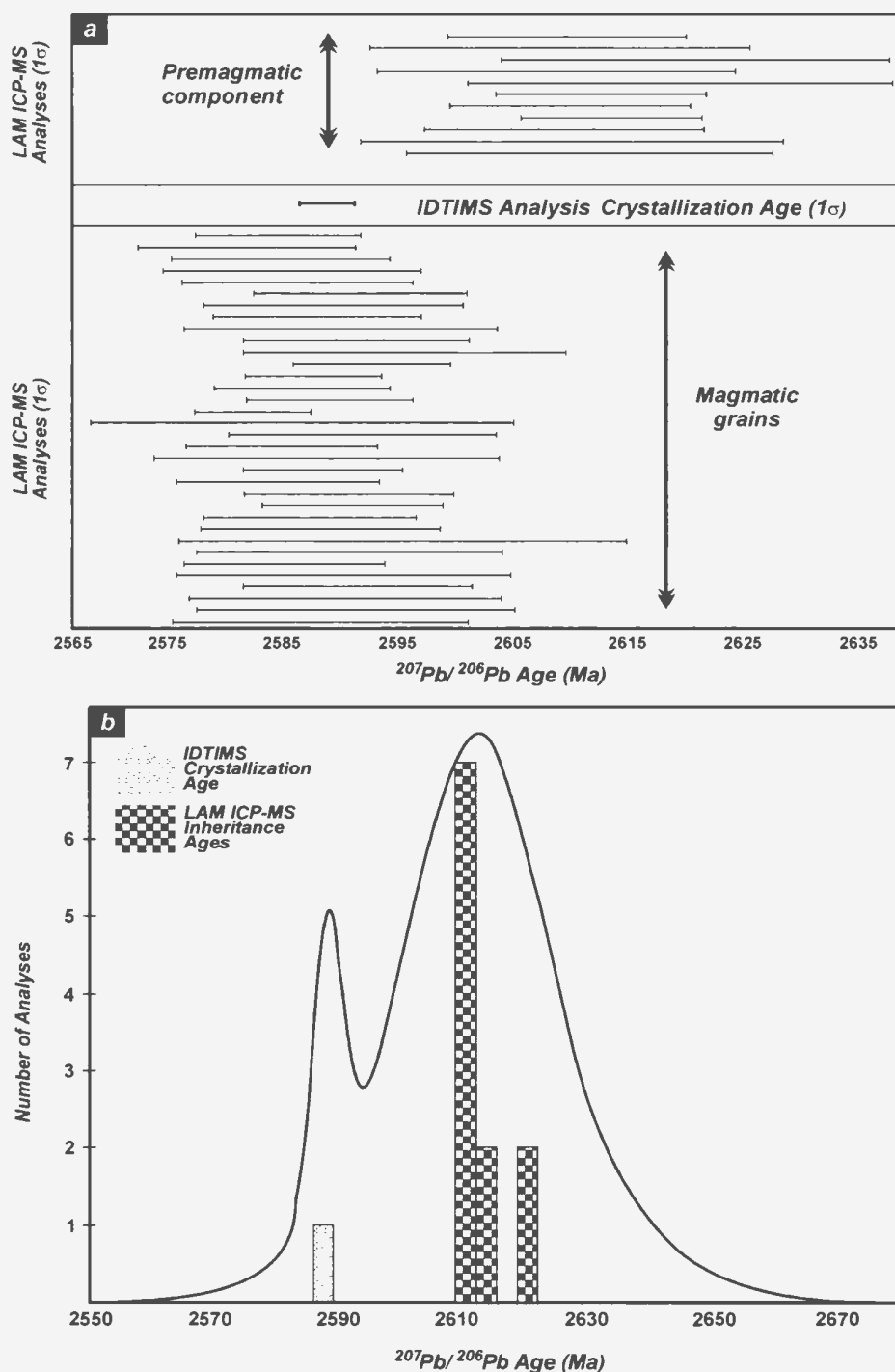


Figure 5.7: Comparison of premagmatic zircon component in VJ375 with magmatic zircon. (a) LAM ICP-MS error range for individual magmatic and premagmatic analyses compared to crystallization age determined by IDTIMS ($^{207}\text{Pb}/^{206}\text{Pb}$ age; 1σ). Figure demonstrates the overlap in maximum and minimum uncertainties in LAM ICP-MS analyses for two components at the 1σ confidence level. (b) Cumulative probability diagram resolving the older premagmatic age component in relation to the IDTIMS crystallization age.

composed of a diverse array of lithologies with detrital, inherited and crystallization ages ranging from ca. 3.0 to 2.59 Ga, so the occurrence of only a single ca. 2610 Ma population requires an alternative explanation.

It is argued here that the ca. 2610 Ma component is more readily understood if the zircon grains represent a restitic component of the mantle source. The calculated $^{207}\text{Pb}/^{206}\text{Pb}$ age of the premagmatic grains of 2612 ± 9.9 [± 7.3] Ma is remarkable in that it overlaps with the crystallization age of an earlier sanukitoid event at 2608.2 ± 3.4 [± 1.4] Ma (Chapters 2 and 4). Geochemical data indicate that both the ca. 2608 and 2589 Ma sanukitoid suites were derived from metasomatized mantle, and both are interpreted to result from delamination of the lower crust (Chapter 4). Given the similar petrogenetic and tectonic settings, it is tempting to conclude that the ca. 2610 Ma zircon population in the ca. 2589 Ma sanukitoid represents inherited zircon from the same mantle source that gave rise to the older sanukitoid suite. If correct, it would imply that the mantle source underwent negligible homogenization and/or melting during the ca. 20 M.y. interval separating the two events. In addition, zircon inheritance in the younger sanukitoid magma suggests that isolated mantle domains are capable of preserving a history of prior melting episodes. If this is so, then why is zircon, a mineral composed of strongly incompatible elements, retained in the mantle reservoir after melt extraction? Does metasomatism contribute to metastable Zr behaviour in these domains? Clearly, the problem of inherited zircon systematics in mantle-derived magmas requires further investigation.

5.7.2. Zircon inheritance in peraluminous magmas - Identifying metaturbidite contributions in inherited zircon spectra

The zircon inheritance spectra of peraluminous magmas in the Snare River terrane differ from their metaluminous counterparts in both the range and diversity of ages recorded. Furthermore, geochemical constraints demonstrate genesis of the peraluminous magmas from predominantly mid-crustal metasedimentary reservoirs (Chapter 4). Each of the four samples investigated contained abundant premagmatic zircon, which made determination of precise crystallization ages challenging. Ubiquitous inheritance is a characteristic attribute of peraluminous magmas (e.g. Chappell et al. 2000; Tikhomirova 2002; Miller et al. 2003) and indicates strongly Zr-saturated melts. Genesis of peraluminous melts in the Snare River terrane took place during and after the ca. 2600 Ma orogenic peak (TR2a).

5.7.2.1 Two-mica granite suite - deciphering the detrital connection

Geochemistry of the two-mica granite suite from the Snare River terrane and across the Slave Province indicates petrogenesis involved metaturbidite source rocks of predominantly pelitic composition (Davis et al. 1994; Yamashita et al. 1999a; Chapter 4). In the Snare River terrane, the geochemical similarity between metasedimentary diatexite, which represents anatexis of metaturbidites, and the two-mica granite suite implies similar metasedimentary protoliths. Consequently, inherited zircon in the suite is primarily considered to be detrital. Thus, successful interpretation of the inheritance profile of the two-mica granite is reliant on comparison with detrital zircon spectra for

metaturbidites from the region (Pehrsson and Villeneuve 1999; Bennett et al. 2005; Fig. 5.8a, b).

A distinctive feature of the inherited zircon spectrum in the two-mica granite sample is the prevalence of > 2800 Ma ages. Indeed, the oldest U-Pb zircon age (3071 ± 12 Ma) determined from the Snare River terrane is from an inherited grain in this sample, and a detrital grain with an age of 3048 ± 2 Ma was determined from the Indin Lake supracrustal belt to the north of the Snare River terrane (Fig. 5.1a) by Pehrsson and Villeneuve (1999). Figure 5.8b demonstrates that all inherited ages in the two-mica granite can be correlated with detrital provenance ages (Fig. 5.8a). A second important feature is the abundance of post-crystallization ages, and a comparable feature is also observed in the detrital spectra, in which post-sedimentation ages are common (Figs. 5.8a, b). Typically, the more protracted and complicated the history of an individual detrital zircon, the more susceptible it becomes to isotopic resetting and Pb loss when recycled (e.g. Balan et al. 2001; Zeck and Williams 2002; Riley 2003), a process that may account for the high proportion of both post-crystallization and post-sedimentary ages in the two-mica granite and metasedimentary turbidites, respectively.

The similarity between the inherited profile in the two-mica granite and the detrital zircon spectrum for the metaturbidite is consistent with the petrogenetic interpretation of a predominantly metasedimentary origin for the two-mica granite, and indicates that metaturbidite had been transported to the mid crust prior to the ca. 2600 Ma peak of peraluminous magmatism.

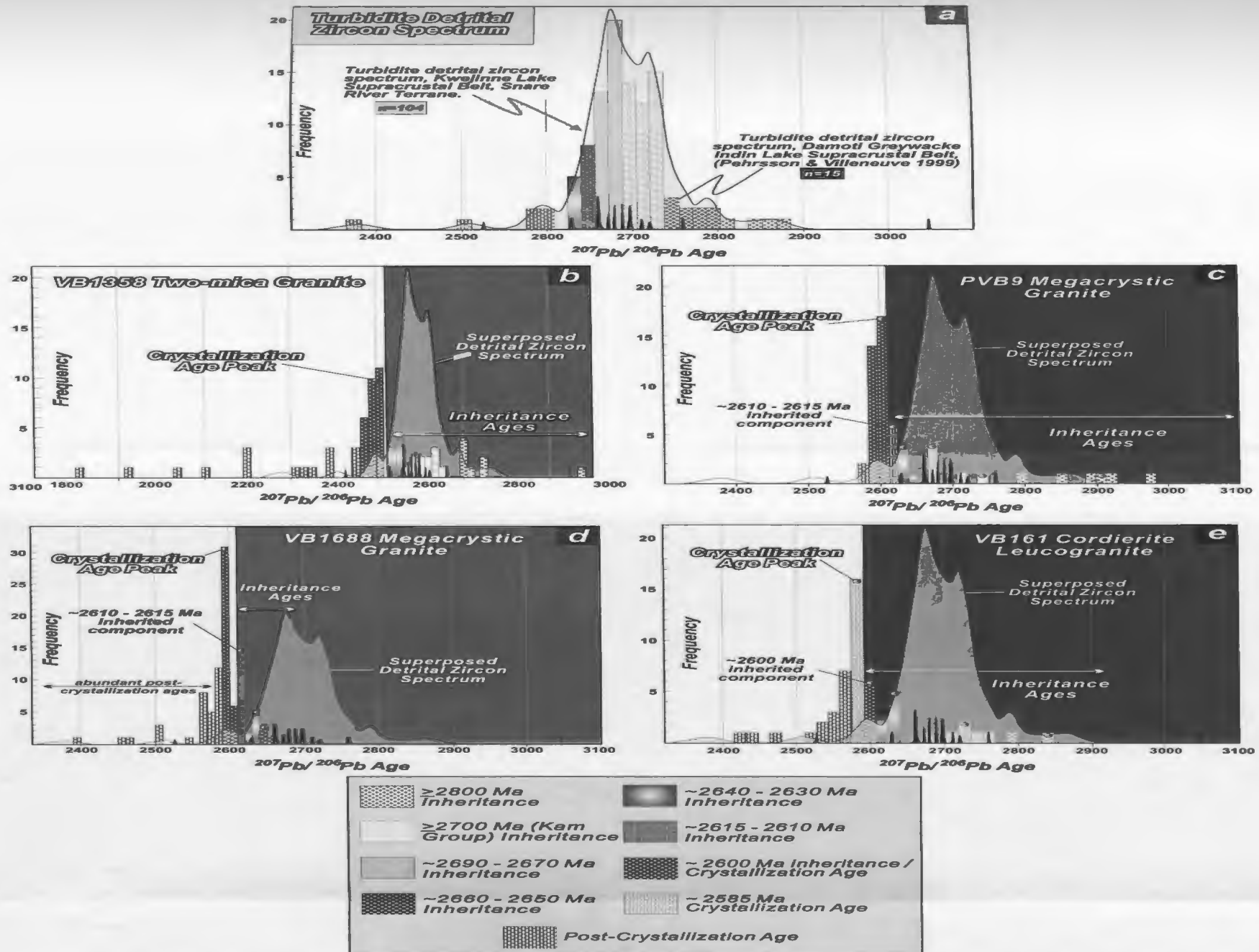


Figure 5.8: Comparison of cumulative probability diagrams and frequency histograms of turbidite detrital zircon spectra with peraluminous magma inherited zircon age spectra. (a) Turbidite detrital zircon spectra for samples analyzed in the Kwejinnie Lake and Indin Lake supracrustal belts (Bennett et al. in press; Pehrsson and Villeneuve 1999). (b) Comparative spectrum for two-mica granite suite, VB1358. (c) and (d) Comparative spectra for the upper and mid-crustal megacrystic granite suite, PVB9 and VB1688, respectively. (e) Comparative spectrum for the cordierite leucogranite suite, VB161.

5.7.2.2 Megacrystic granite suite - A record of mid-crustal heterogeneity

Two samples of megacrystic granite emplaced into amphibolite- and granulite-facies metamorphic zones of the mid crust have geochemical characteristics compatible with genesis by assimilation and/or mixing between metasedimentary and mafic melts (Chapter 4). However, zircon inheritance profiles reflect different attributes of their history. Sample PVB9, emplaced into amphibolite-facies crust, contains a few pre-2800 Ma ages and a high proportion of post-2800 Ma ages, including ca. 2700, 2680-2670 and 2630 Ma components that are interpreted to reflect detrital zircon populations of the metaturbidite component in the magma reservoir (Fig. 5.8b). In addition, a younger 'post-detrital' age of ca. 2610 Ma is present (Figs. 5.5b, 5.8b) that, despite poor precision, is within error of the emplacement age of the metaluminous Mafic Intrusive Complexes in the Snare River terrane. These data support and complement the interpretation presented in Chapter 4 based on geochemical data, that the megacrystic granite was derived from mixed metasedimentary and mafic sources. The megacrystic granite suite is geochemically and temporally correlated with the Yamba Suite of the eastern Slave Province (Fig. 5.1a), which was considered by Davis et al. (1994) to have been generated by mixing or assimilation of crustal melts with mafic magmas of the Concession Suite (with which the Mafic Intrusive Complexes are correlated).

VB1688, the mid-crustal megacrystic granite emplaced into granulite-facies mid crust, records a very different inheritance profile. No inherited grains older than ca. 2660 Ma were found, but the 2660-2650 and 2630 Ma populations are consistent with turbidite detrital ages and a 2610 Ma component, coeval with the Mafic Intrusive Complexes, is

abundant (Fig. 5.8c). The absence of a pre-2800 Ma component that is typically diagnostic of a detrital origin in these magmas is interpreted to be the result of selective recrystallization during syn- to post-emplacement HT/LP metamorphism, since zoning patterns demonstrate that recrystallization was pervasive in the inherited zircon population (Fig. 5.3h). It is inferred that recrystallization preferentially occurred in the oldest detrital zircon populations, which had the longest crustal histories and were therefore particularly susceptible to disturbance. The high proportion of post-crystallization ages in VB1688 compared to PVB9 reinforces this contention.

A significant feature of the inherited zircon profiles of PVB9 and VB1688 is the presence of components with an age equivalent to the Mafic Intrusive Complexes / Concession Suite (ca. 2610 Ma). This attribute supports the correlation of the two megacrystic granites and complements the geochemical interpretation that the suite formed from mixed metasedimentary and mafic sources.

5.7.2.3 Cordierite leucogranite - A record of turbidite evolution

Emplacement of the ca. 2585 Ma cordierite leucogranite suite, which occurs as small irregular bodies intruding granulite-facies diatexite, post-dated peak deformation and HT-LP metamorphism (TR2b; Fig 5.2). Field evidence is compatible with an origin by decompression melting and limited migration from the source region rather than in situ melting, and their strongly peraluminous character, HREE depletion and positive Eu, Sr and Zr anomalies demonstrate that they are evolved, fractionated magmas derived from garnet-rich protoliths (Table 5.1). Chapter 4 highlights their geochemical similarity

with the ca. 2600 Ma garnet–cordierite-bearing leucosomes in Ghost subdomain, which represent in situ melting of granulite-facies metapelitic rocks.

The inherited zircon profile determined for VB161 shows similarities to that of the ca. 2600 Ma peraluminous megacrystic granite, described above, compatible with derivation from a reservoir with corresponding age heterogeneity. The three oldest inherited components have comparable detrital zircon provenance ages (Fig. 5.8e), but since detrital ages younger than ca. 2630 Ma have not been recognized in turbidites in the Slave Province, the origin of the ca. 2600 Ma inherited component must correspond to the post-sedimentary history of the source. We suggest the ca. 2600 Ma zircon grains represent either resetting of detrital zircon grains and/or new metamorphic zircon growth in the source during HT/LP metamorphism at the orogenic peak. BSE imaging of zircon grains from this population reveals intricate zonation patterns (Fig. 5.3i, 5.5d), including complex recrystallization fronts, which may be a consequence of U and/or Pb diffusion during the high-temperature metamorphism.

In summary, the inherited zircon profile of the cordierite leucogranite suite reveals insight into the complex and protracted history of the precursor metaturbidite reservoir, from sedimentation and burial, through transport to the mid crust, high-grade metamorphism, anatexis, and melt extraction during decompression. Hence, understanding inheritance in derivative magmas requires a thorough understanding of the premagmatic history. The data are significant because they demonstrate that the metapelitic reservoir, although having undergone melt-extraction at the ca. 2600 Ma orogenic peak, not only remained Zr-saturated, but also retained inheritance comparable

to the original detrital zircon spectrum. Additionally, the inheritance data permit identification of major post-detriral (re)crystallization events in the source region of the cordierite leucogranite, which caused extensive metamorphic zircon growth and/or isotopic resetting.

5.7.3 Application of inherited zircon data to deconstruct ϵ_{Nd} mixing models

Binary ϵ_{Nd} mixing models work on the assumption that the measured Nd isotopic composition of a magma results from mixing of two end-member components of different isotopic composition (Faure 1986; DePaolo 1988). In practice, end-member compositions are generally assumed and combined in variable proportions until the desired Sm-Nd isotopic ratio is obtained (e.g. Yamashita et al. 1999). A major drawback of this approach is the non-unique nature of the results due to the lack of quantitative information about the composition, age proportions and heterogeneity of the source. This can result in inappropriate selection of end-members and the use of binary mixing when multicomponent mixing would be more applicable, potentially resulting in misleading interpretations. In this study, we use the inherited zircon spectra in PVB9 and VB1357 to estimate the number of source components and hence determine whether binary or multicomponent mixing is appropriate. We then assign an ϵ_{Nd} isotopic composition to each component which is incorporated into binary or multicomponent mixing equations. Details of the mixing calculations involved are given in Appendix H.

5.7.3.1 Binary mixing

As discussed above, petrogenesis of the ca. 2600 Ma megacrystic granite suite (sample PVB9) in the Snare River terrane is inferred to have involved mixing and/or assimilation in a two-component reservoir comprising a metasedimentary component and a mafic component of the ca. 2610 Ma Concession Suite/Mafic Intrusive Complexes (Davis et al. 1994; Chapter 4). 77.3% of the inherited zircon crystals in sample PVB9 are interpreted to have a detrital metasedimentary origin ($f_{\text{turbidite}} = 0.77$; Table 5.4; Fig. 5.9). The average ϵ_{Nd} value and Nd concentrations determined for metaturbidite in the Snare River terrane (- 0.3 and 15.7 ppm, respectively; Tables 5.4, Appendix F, Table F3) are used to represent this component. The ca. 2610 Ma component, which accounts for 22.7 % of inherited analyses in the sample ($f_{\text{Concession}} = 0.23$), is assigned the average ϵ_{Nd} and Nd concentration values of the Concession Suite/Mafic Intrusive Complexes (+1.9 and 43.5 ppm, respectively, Tables 5.4, Appendix F, Table F3). Substitution of these values (Table 5.4) into equation (H1, Appendix H) yields $\epsilon_{\text{Nd PVB9}} = + 0.65$, which is in agreement with the measured ϵ_{Nd} range of +0.6 to +1.0 (± 0.5) for the megacrystic granite suite (Yamashita et al. 1999; Chapter 4), suggesting that the method was successful and that inherited zircon datasets may be applied to quantify end-member parameters in binary mixing calculations. The binary mixing parameters in sample PVB9 are illustrated schematically in Fig 5.9a.

5.7.3.2 Multicomponent mixing

Multicomponent mixing is investigated using the ca. 2600 Ma metaluminous

Figure 5.9: Simplified diagram showing the principles behind two-component and multi-component mixing using inherited zircon data to determine the age and number of components. *(a)* The ca. 2600 Ma megacrystic granite sample (PVB9) is used to illustrate binary mixing in which the two end-members are defined from the inherited zircon spectrum in the sample. A turbidite and mafic Concession suite end-members are determined as principal source components for the sample. Mixing of components (average compositions determined from Table F3), in proportions equivalent to their modes of inheritance results in a 'back-calculated' ϵ_{Nd} value (+0.65), which is then compared to the measured ϵ_{Nd} value (+0.6 to +1.0). *(b)* The ca. 2600 Ma biotite granite suite is used to demonstrate the application of multicomponent mixing to understand measured ϵ_{Nd} value determined for the suite. Four inherited zircon components with age groups ca. 2720-2700 Ma, ca. 2674 Ma, ca. 2654 Ma and ca. 2635 Ma and which occur in variable proportions are assigned average compositions (Table F3) and mixed in proportions based on their modes in the inheritance spectrum. The back-calculated value of +1.8 agrees well with the measure ϵ_{Nd} value of + 2.0.

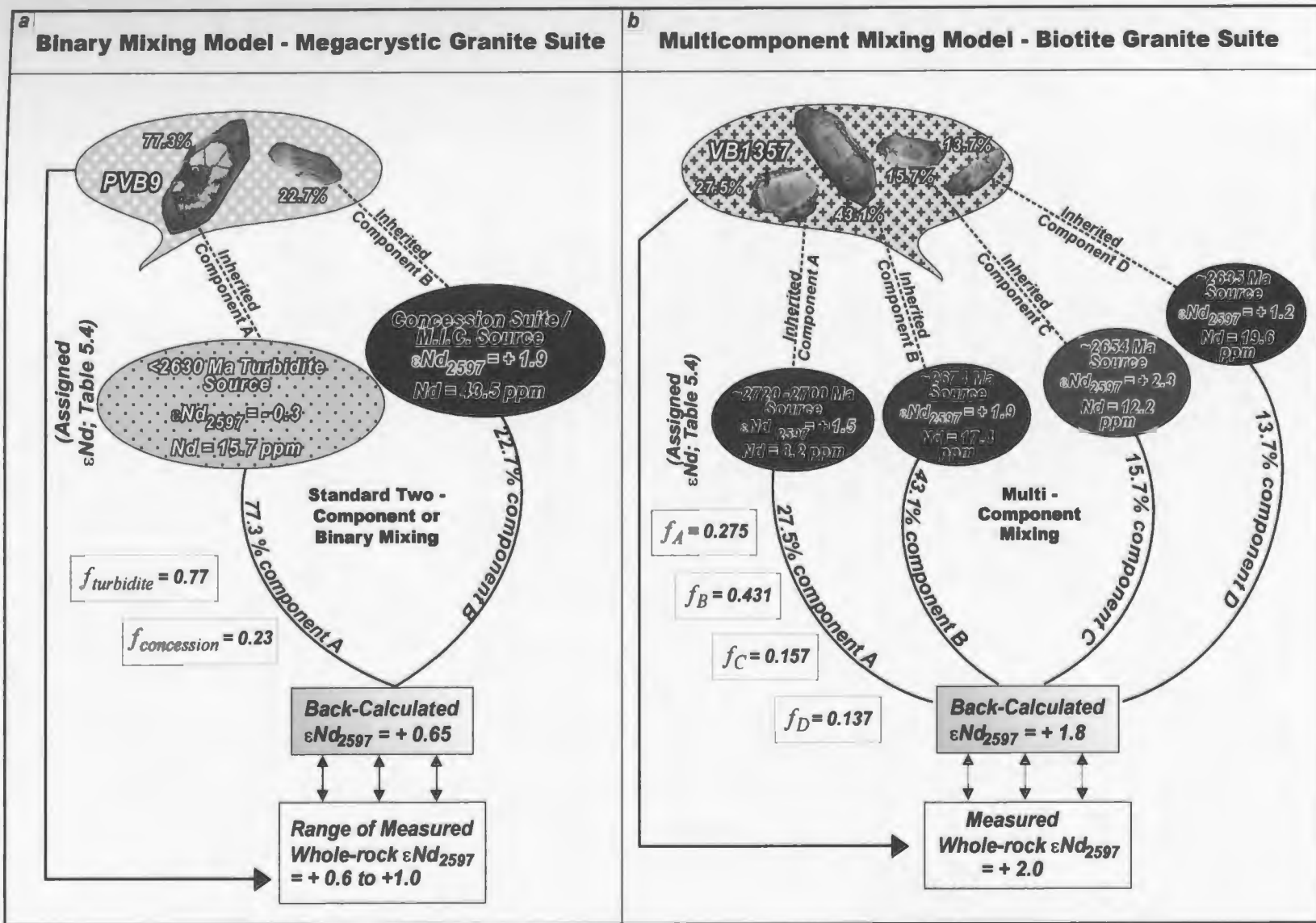


Figure 5.9: Caption see opposite

biotite granite (VB1357) of TTG affinity. Inherited zircon analyses delineate four components: 27.5 % yielded an age of ca. 2714 Ma (Kam Group equivalent) and are assigned ϵ_{Nd} and Nd concentration values of +1.5 and 8.2 ppm respectively determined from published analyses of the Crestaurum and Chan formations (Tables 5.4, Appendix F, Table F3); 43.1% of the analyses yielded an age of 2674 Ma, coeval to tholeiitic magmatism in the Snare River terrane, and have been assigned the ϵ_{Nd} and Nd concentration values characteristic of that unit of +1.9 and 17.4 ppm, respectively (Tables 5.4, Appendix F, Table F3); the ca. 2652 Ma component accounts for 15.7% of inheritance and has been assigned average ϵ_{Nd} values and Nd concentrations of +2.3 and 12.2 ppm respectively, which were measured for tholeiitic magmas of similar age in the Snare River terrane; and finally, for the ca. 2634 Ma inherited component, which represents 13.7% of inheritance, an ϵ_{Nd} value of + 1.2 and a Nd concentration of 19.6 ppm were assigned, these being values for the coeval Disco Intrusive Suite. Substituting these values into equation (H2, Appendix H) yields $\epsilon_{\text{Nd VB1357}} = + 1.8$, which is within error of the measured ϵ_{Nd} value of $+2.0 \pm 0.5$ determined for this sample (Chapter 4). This result is illustrated schematically in Fig. 5.9b.

5.7.3.3 Discussion

Binary mixing involving whole-rock Nd and Pb isotopic data was used by Yamashita et al. (1999) to characterize source regions of syn- to post-tectonic granitoids in the Snare River terrane, including the megacrystic granite sampled in this study

(correlated with their sample J-0397). In their mixing models, isotopic compositions for ca. 3.4 Ga basement were mixed in different proportions with typical mid-ocean ridge basalt and tholeiitic magmas of the upper Kam Group in an attempt to generate the observed isotopic ratios ($\epsilon_{Nd} = +0.6$). They concluded that the granitoids in the Snare River terrane were derived from 10-30 % old basement and 70-90 % juvenile crust. However, neither the inherited zircon data nor the modelling results presented here for the megacrystic granite support the occurrence of a significant pre-2.8 Ga crustal reservoir in the source region, except as a recycled component in metaturbidite. Detrital zircon data for a metaturbidite in the Snare River terrane indicate that ca. 13.5 % of ages have a pre-2.8 Ga provenance (Bennett et al. 2005; Chapter 2), which is consistent with the 10-30% range established by Yamashita et al. (1999). This suggests that the ancient basement component invoked by these authors potentially represents recycled material in a metaturbidite, presumably as Sm and Nd originally sequestered in clay minerals, rather than a major component of the crustal architecture of the Snare River terrane.

Furthermore, the inherited zircon data determined in this study suggest that the end-member components chosen by Yamashita et al. (1999) may not be representative of the magma reservoir. For instance, this study has shown that the megacrystic granite carries a ca. 2610 Ma population of inherited zircon that is correlated with the Concession Suite. However, the Concession Suite was not considered by Yamashita et al. (1999a) in their modelling, despite the fact that mixing of the suite with metaturbidite yields a back-calculated ϵ_{Nd} value of +0.65, which closely approximates their measured value (+0.6). These differences in interpretation highlight the importance of the inherited zircon data,

which provide not only a better understanding of the magma reservoirs, but also a method for assigning geologically realistic end-member compositions and proportions in mixing models.

With regard to multicomponent mixing in the biotite granite (VB1357), despite the increased number of variables, the agreement between back-calculated and measured ϵ_{Nd} values further highlights the advantage of using inherited zircon data to quantify mixing parameters. In this case, the isotopic composition assigned to the ca. 2634 Ma component may not be entirely representative of this age component because ϵ_{Nd} and Nd concentration values for a TTG rather than a tholeiite were used (there being no known tholeiitic magma of this age). However, the overlap of the result with the measured value suggests that the method has merit even in cases where data are missing and values have to be assumed. As with the binary mixing model for the megacrystic granite, the multicomponent mixing model for the biotite granite does not predict the presence of a significant pre-2.8 Ga basement component in the source region as invoked by Yamashita et al. (1999).

It must be stressed that despite the lack of measured values for certain age components, noted above, the reliability of the f parameter is the more questionable aspect of this technique. The obvious question arises: are the proportions of analyzed inherited zircon representative of the proportions of the components in the source region? They appear to be in the two test cases presented here, given that the calculated ϵ_{Nd} values are similar to the measured whole-rock values for these suites. However, the presence of Zr-undersaturated rocks (lacking inherited zircon) in the source region would

not be imaged by this method. Such magmas would contribute to the ϵ_{Nd} signature of the melt, but not its inherited zircon signature, causing the latter to be an incomplete record of the source. The significance of this caveat in lower- and mid-crustal melting remains to be established by additional testing and comparison with results from conventional binary and multicomponent mixing models.

5.8 Conclusions

In this contribution we have used the high spatial resolution and relatively high precision of the LAM ICP-MS technique to analyze inherited zircon grains in Neoproterozoic magmatic rocks from the Snare River terrane, southwestern Slave Province, to systematically characterize crust-formation through time (isotopic profiling). The results suggest that metaluminous and peraluminous magmas of the Snare River terrane were sourced from discrete lower- and mid-crustal reservoirs, respectively, and the inheritance profiles established for the five metaluminous and four peraluminous samples analysed have different implications with regard to crustal evolution. Secular variations characterized by inheritance in metaluminous magmas reflect protracted growth and development of a garnet-rich mafic lower crust by 'local' magmatic additions and by tectonic intercalation or subcretion of 'exotic' mafic material, interpreted to be tholeiitic magmas of Kam Group affinity. Mantle-derived, lower-crustal magmatic additions were coeval with mid- and upper-crustal magmatism, implying a linked mantle-crustal evolution. Furthermore, successive new additions to the lower crust subsequently became fertile sources from which younger metaluminous magmas were derived, indicating that

lower crustal development was a catalyst for mid- and upper-crustal formation and evolution. Significantly, in the context of the Slave Province, the inheritance profiles demonstrate an absence of a pre-2.8 Ga component during early lower-crustal evolution of the Snare River terrane, implying that evolution at this time took place in a setting that was distal from the old cratonic nucleus of the Slave Province, and that the two only became intercalated during subsequent collisional orogenesis. The inheritance profile of a mantle-derived sanukitoid, emplaced during post-orogenic collapse, raises the possibility of long-lived, chemically isolated domains in the lithospheric mantle that retained restitic zircon and preserved a record of melt-extraction events.

A striking similarity exists between inherited zircon age data in peraluminous magmas and measured detrital zircon ages in metaturbidites in the supracrustal belts, implying a genetic link between them. This observation serves to strengthen and complement geochemical interpretations which invoke metasedimentary material as the primary protolith for the peraluminous (S-type) magmas in general, and in the Snare River terrane in particular. With regard to the peraluminous megacrystic granite suite, inherited zircon data reveal the co-existence of two components in the source region, compatible with geochemical interpretations involving mixing of different source rocks. Understanding the premagmatic history of the metasedimentary reservoir of the peraluminous suites not only permits a valid interpretation of the inheritance profiles, but also provides an indirect method with which to document key stages of turbidite evolution, from sedimentation to melt extraction.

Finally, we have outlined a new technique that illustrates how the zircon inheritance data can be utilized to better constrain the number and compositions of end-members used in binary and multicomponent Sm-Nd isotope mixing models. In the Snare River terrane, petrogenetic implications derived from binary and multicomponent modelling for metaluminous and peraluminous magmas can be explained by mixing of source components that correspond to Kam Group (~2700 Ma) and younger lower- and mid-crustal reservoirs.

5 References

- Balan. E., Neuville, D.R., Trocellier, P., Fritsch, E., Muller, J-P., and Calas, G. 2001. Metamictization and chemical durability of detrital zircon. *American Mineralogist*, **86**: 1025 – 1033.
- Bennett, V., Rivers, T., Jackson, V.A., Relf, C., and Branstromm, M., accepted pending revisions. Formation, Growth and Evolution of Neoproterozoic crust: Constraints from the Snare River terrane, Slave Province, Canada. *Journal of Petrology*.
- Bennett, V., Tubrett, M., and Rivers, T., 2003. Laser Ablation ICP-MS, Reconnaissance or High Precision Dating Tool? A critical Evaluation using combined convention TIMS and LAM ICP-MS zircon datasets. In Geological Association of Canada – Mineralogical association of Canada – Society of Economic Geologists(GAC-MAC-SEG) Annual Meeting, Vancouver 2003, Program with Abstracts, 28: p.328
- Bennett, V., Jackson, V.A., Rivers, T., Relf, C., Horan, P and Tubrett, M, in press. Geology and U-Pb Geochronology of the Late Archean Snare River Terrane: Tracking Evolving Tectonic Regimes and Crustal Growth Mechanisms. *Canadian Journal of Earth Sciences*, **42**, LITHOPROBE Special Edition.
- Belousova, E.A., Griffin, W.L., O'Reilly, S.Y., and Fisher, N.I., 2002. Igneous zircon: trace element composition as an indicator of source rock type. *Contributions to Mineralogy and Petrology*, **143**: 602 – 622.
- Bleeker, W., and Villeneuve, M., 1995. Structural studies along the Slave portion of the SNORCLE Transect; in Slave-NORthern Cordillera Lithospheric Evolution (SNORCLE), Report of 1995 Transect Meeting, April 8-9, University of Calgary, edited by F. Cook and P. Erdmer, LITHOPROBE Report No. 44, p. 8-14.
- Bleeker W., Ketchum, J.W.F., Jackson, V.A., and Villeneuve, M.E., 1999. The Central Slave Basement, Part I: its structural topology and autochthonous cover. *Canadian Journal of Earth Sciences*, **36**: 1083-1109.
- Bowring, S.A., and Williams, I.S. 1999. Proterozoic (4.00 – 4.03 Ga) orthogneisses from northwestern Canada: *Contributions to Mineralogy and Petrology*, **134**: 3-16.
- Brannstrom, B.M., 2000. Chemical characteristics of Archean volcanic rocks from the Snare River Area (NTS 85O/13), S.W. Slave Province, N.W.T. Unpublished B.Sc. (Honours) Thesis. Simon Fraser University.
- Brophy, J.A., and Pell, J. 2002. Preliminary Geology of the Labrish Lake area, Southwestern Slave Province; Parts of 85N/09. NWT Open File 2002-06. DIAND, NWT Geology Division, Yellowknife. 1 map plus legend scale 1: 50 000.
- Chacko, T., Creaser, R.A., Farquhar, J. and Muehlenbachs, K. 1995a. The deep crust of the western Slave Province – Initial petrological and isotopic data from high grade rocks of the Ghost Domain. In Slave – Northern Cordillera Lithospheric Evolution Workshop

- (SNORCLE) Transect and Cordilleran Tectonics Workshop Meeting, 8 – 9 April, Calgary. Compiled by F. Cook and P. Erdmer. Lithoprobe Report 44, pp.4-7.
- Chacko, T., Farquhar, J., and Creaser, R.A. 1995b. A petrological study of granulites and associated rocks from the Ghost Lake area, southwestern Slave Province; In Geological Association of Canada – Mineralogical association of Canada (GACMAC) Annual Meeting, Victoria 1995, Program with Abstracts, 20: A-15.
- Chappell, B.W., White, A.J.R., Williams, I.S., Wyborn, D., and Wyborn, L.A.I., 2000. Lachlan fold belt granites revisited : high- and low-temperature granites and their implications. *Australian Journal of Earth Sciences* **47**, 123 – 138.
- Compston, W., and Kröner, A., 1988. Multiple zircon growth within early Archaean tonalitic gneiss from Ancient Gneiss Complex, Swaziland. *Earth and Planetary Science Letters*, **87**: 13 – 28.
- Corfu, F., Hanchar, J. M., Hoskin, P. W. O. & Kinny, P. 2003. Atlas of zircon textures. In: Hanchar, J. M. & Hoskin, P. W. O. (editors) *Zircon. Reviews in Mineralogy and Geochemistry*, **53**: 469–499.
- Cousens, B.L., 2000. Geochemistry of the Archean Kam Group, Yellowknife Greenstone Belt, Slave Province, Canada. *Journal of Geology*, **108**: 181 – 197.
- Cousens, B.L., Facey, K., Falck, H., 2002. Geochemistry of the late Archean Banting Group, Yellowknife greenstone belt, Slave Province, Canada: simultaneous melting of upper mantle and juvenile mafic crust. *Canadian Journal of Earth Sciences*, **39**: 1635 – 1656.
- Davis, W.J. and Hegner, E., 1992. Neodymium isotopic evidence for the tectonic assembly of Late Archean crust in the Slave Province, northwest Canada. *Contributions to Mineralogy and Petrology*, **111**: 493 –504.
- Davis, W.J., King, J.E., and Fryer, B.J. 1994. Geochemistry and evolution of Late Archean plutonism and its significance to the tectonic development of the Slave craton. *Precambrian Research*, **67**: 207 –241.
- Davis, W.J., 1997. U-Pb zircon and rutile ages from granulite xenoliths in the Slave Province: evidence for mafic magmatism in the lower crust coincident with Proterozoic dyke swarms. *Geology*, **25**: 343 – 346.
- Davis, W.J., Canil, J., MacKenzie, J.M., and Carbno, G.B., 2003. Petrology and U-Pb geochronology of lower crustal xenoliths and the development of a craton, Slave Province, Canada. *Lithos*, **71**: 541 – 573.
- DePaolo, D.J., 1988. *Neodymium Isotope Geochemistry: An Introduction*. Springer-Verlag, Heidelberg, 187pp.
- DePaolo, DJ and Wasserburg, G.J., 1979. Petrogenetic mixing models and Nd-Sr isotopic patterns: *Geochimica et Cosmochimica Acta*. **43**: 615-627.

- Faure, G., 1986. Principles of Isotope Geology (second edition): New York, John Wiley & Sons, 589 p
- Griffin, W.L., Wang, X., Jackson, S.E., Pearson, N.J., O'Reilly, S.Y., Xu, X., and Zhou, X., 2002. Zircon chemistry and magma mixing, SE China: In-situ analysis of Hf isotopes, Tonglu and Pingtan igneous complexes. *Lithos*, **61**: 237 – 269.
- Hanchar, J.M., and Miller, C.F., 1993. Zircon zonation patterns as revealed by cathodoluminescence and backscattered electron images: Implications for interpretation of complex crustal histories. *Chemical Geology*, **110**, 1 – 13.
- Hanchar, J. M., and Rudnick, R.L., 1995. Revealing hidden structures: The application of cathodoluminescence and back-scattered electron imaging to dating zircons from lower crustal xenoliths. *Lithos*, **36**: 289 – 303.
- Hansmaan, W., and Oberli, F., 1991. Zircon inheritance in an igneous rock suite from the southern Adamello batholith (Italian Alps). *Contributions to Mineralogy and Petrology*, **107**: 501 – 518.
- Harrison, T.M., and Watson., 1983. Kinetics of zircon dissolution and zirconium diffusion and granitic melts of variable water content. *Contributions to Mineralogy and Petrology*, **84**: 66 –72.
- Harrison, T.M., Aleinkoff, J.N., and Compston, W., 1987. Observations and controls on the occurrence of inherited zircon in Concord-type granitoids, New Hampshire. *Geochimica and Cosmochimica Acta*, **51**: 2549 – 2558.
- Henderson, J.B. 1970. Stratigraphy of the Yellowknife Supergroup, Yellowknife Bay – Prosperous Lake area, District of Mackenzie: Geological Survey of Canada, Paper 70-26.
- Henderson, J.B., 1985. Geology of the Yellowknife – Hearne Lake area, District of Mackenzie: A segment across an Archean Basin. Geological Survey of Canada, Memoir 414, 135 pp.
- Henderson, J.B., 1994. Geology of the Wijinnedi Lake area – a Paleoproterozoic (?) asymmetric uplift of Archean rocks on the southwestern Slave Province, District of Mackenzie, Northwest Territories; In: Current Research, 1994-C. Geological Survey of Canada, Paper 93-1C, pp. 71-79.
- Henderson, J.B. 2004. Geology of the Wijinnedi Lake area, District of Mackenzie, Northwest Territories. Geological Survey of Canada, Bulletin 576.
- Henderson, J.B. 2004. Geology, Wijinnedi Lake area, District of Mackenzie, Northwest Territories. Geological Survey of Canada, Map 2023A, scale 1:50 000.
- Henderson, J.B. and Schaan, S.E. 1993. Geology of the Wijinnedi Lake area: a transect into mid-crustal levels in the western Slave Province, District of Mackenzie, Northwest Territories. In: Current Research, Part C. Geological Survey of Canada, Paper 93-1C, pp. 83-91.

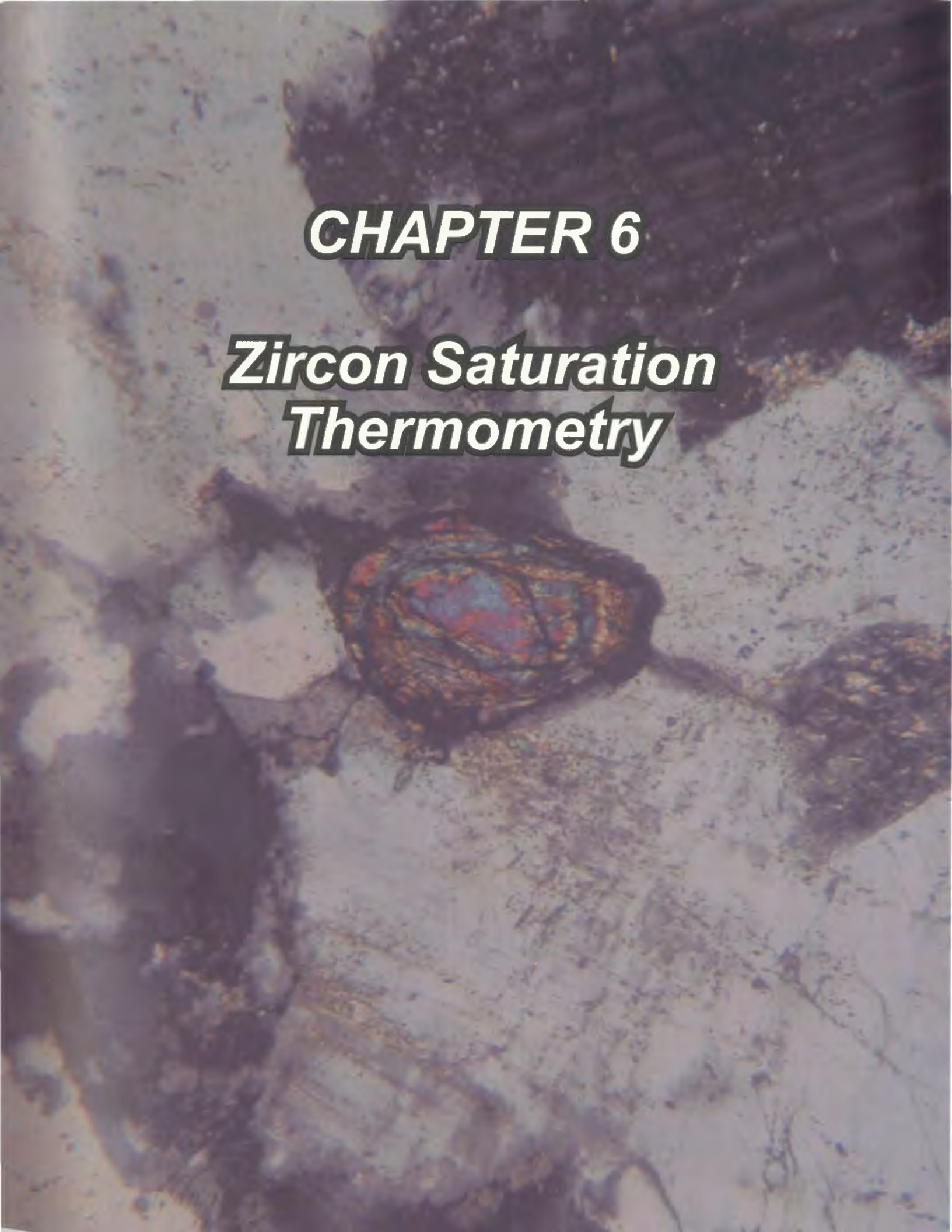
- Isachsen, C.E., 1992. U-Pb zircon geochronology of the Yellowknife Volcanic Belt and subjacent rocks, and mechanics of greenstone formation. Unpublished Ph.D. Thesis. Washington University, St Louis.
- Jackson, V.A., 1998. Preliminary Geology of the Kwejinne Lake area (parts of 85O/11, 12, 13): EGS Open File 1998-19. DIAND, NWT Geology Division, Yellowknife. 1 sheet with descriptive notes.
- Jackson, V.A., 2003. Preliminary compilation of the geology of the Snare River (1998-2002 results), Winjinnedi Lake, Labrish Lake and Russell Lake area; parts of 85N and 85O. C.S. Lord Northern Geoscience Centre, Yellowknife, NT. NWT Open Report 2003-002. Map, scale 1:100 000.
- Jackson, V.A., and Bennett, V., 2003. The Snare River Area: A unique greenschist to granulite grade Archean crustal section in the southwestern Slave Province, Northwest Territories, Canada In Geological Association of Canada – Mineralogical association of Canada – Society of Economic Geologists(GAC-MAC-SEG) Annual Meeting, Vancouver 2003, Program with Abstracts, 28: p.365
- Kretz, R. 1983. Symbols for rock-forming minerals. *American Mineralogist* **68**: 277 – 279.
- Košler, J., Tubrett, M., and Sylvester, P., 2001. Application of Laser Ablation ICP-MS to U-Th-Pb Dating of Monazite. *Geostandards Newsletter, The Journal of Geostandards and Geoanalysis*. **25**, no.2 , pp.12.
- Košler., J., Fonneland, H., Sylvester, P., Tubrett, M., and Pedersen, R., 2002. U-Pb Dating of detrital zircons for sediment provenance studies – a comparison of laser ablation ICP-MS and SIMS techniques. *Chemical Geology*, **182**: 605-618.
- Langmuir, C.H., Vocke, R.D., Hanson G.N., 1978. A general mixing equation with application to Icelandic Basalts. *Earth and Planetary Science Letters*, **37**: 380 – 192.
- Lord, C.S. 1942. Snare and Ingray Lake map areas, Northwest Territories. Geological Survey of Canada, Memoir 235.
- Ludwig, K.R. 1999. User's manual for Isoplot/Ex, v2.06. A geochronological toolkit for Microsoft excel. Berkeley Geochronological Centre Special Publication No. 1a, pp. 54.
- MacLachlan, K., 1993. Origin and evolution of the mafic dike complex in the Chan Formation, Yellowknife, NWT. M.Sc. thesis, Queens University, Kingston, Ontario,
- McGlynn, J.C., and Ross, J.V. 1962. Geology, Basler Lake, District of Mackenzie, Geological Survey of Canada, Map 18-1962, 1 inch to 1 mile map with marginal notes.
- Miller. C.F., McDowell S.M., and Mapes, R.W., 2003. Hot and cold granites? Implications of zircon saturation temperatures and preservation of inheritance. *Geology*, **31**: 529 – 532.

- Mortensen, J.K., Henderson, J.B., Jackson, V.A., and Padgham, W.A., 1992. U-Pb geochronology of the Yellowknife Supergroup felsic volcanic rocks in the Russell Lake and Clan Lake areas, southwestern Slave Province, Northwest Territories. In *Radiogenic Age and Isotopic studies, Report 5*. Geological Survey of Canada, Paper 91-2, pp. 1-7.
- Ootes, L., 2000. Petrogenesis of the Sleeping Bear Intrusion, Kwejinne Lake, southwestern Slave Province, Northwest Territories. Unpublished B.Sc. (Honours) Thesis. University of Saskatchewan.
- Ootes, L., 2003. Structural, Mineralogical, and Geochemical Analysis of the Crestaurum Gold Deposit Deposits, Yellowknife Volcanic Belt, NWT. Unpublished M.Sc. Thesis. University of New Brunswick.
- Paterson, B.A., Stephens, W.E., Rogers, G., Williams, I.S., Hinton, R.W., and Herd, D.A., 1992. The nature of zircon inheritance in two granite plutons. *Transaction of the Royal Society of Edinburgh: Earth Sciences*, **83**: 459 – 471.
- Pehrsson, S.J., and Villeneuve, M.E., 1999. Deposition and imbrication of a 2670-2629 Ma supracrustal sequence in the Indin Lake area, southwestern Slave Province, Canada. *Canadian Journal of Earth Sciences*, **36**: 1149-1168.
- Pehrsson, S.J., Chacko, T., Pilkington, M., Villeneuve, M.E., and Bethune, K., 2000. Anton terrane revisited: Late Archean exhumation of moderate-pressure granulite terrane in the western Slave Province. *Geology*, **28**: 1075-1078.
- Perks, M.A. 1997. The mid crust of the western Slave Province - Geological Mapping, geochemistry and U - Pb Geochronology of the Forked Lake Area, Southwestern Slave Province, NWT. M.Sc. thesis, University of Alberta, Edmonton, Alberta.
- Pidgeon, R.T., and Compston, W., 1992. A SHRIMP ion microprobe study of inherited and magmatic zircons from four Scottish Caledonian granites. *Transaction of the Royal Society of Edinburgh: Earth Sciences*. **83**: 473 – 483.
- Riley, B.C., and Garver, J.I., 2003. Low-temperatures thermal response of radiation damaged detrital zircon: Provenance and post depositional thermal history of Laramide synorogenic sediments, SE Arizona, Geological Society of America Abstracts with Programs, v. 35, n.5, p. 4.
- Roddick, J.C., and Bevier, M.L., 1992. U-Pb dating of granites with inherited zircon: Conventional and ion microprobe results from two Palaeozoic plutons, Canadian Appalachians. *Chemical Geology (Isotope Geoscience Section)*, **119**: 307 - 329
- Rudnick, R.L. and Cameron, K.L., 1991. Age diversity of the deep crust in northern Mexico. *Geology*, **19**: 1197-1200.
- Schärer, U., and Allègre, C.L., 1982. Investigation of the Archean crust by single-grain dating of detrital zircon: a graywacke of the Slave Province, Canada. *Canadian Journal of Earth Sciences*, **19**: 1910 – 1918.

- Schiøtte, L. and Compston, W., 1990. U-Pb age pattern for single zircons from early Archaean Akilia association south of Ameralik fjord, southern West Greenland. *Chemical Geology (Isotope Geoscience Section)*, **80**: 147-157.
- Schmitz, M.D., and Bowring, S.A., 2001. The significance of U-Pb zircon dates in lower crustal xenoliths from the southwestern margin of the Kaapvaal craton, southern Africa. *Chemical Geology*, **172**: 59 – 76.
- Schmitz, M.D., and Bowring, S.A., 2003. Ultrahigh-temperature metamorphism in the lower crust during Neoproterozoic Ventersdorp rifting and magmatism, Kaapvaal Craton, southern Africa: *Geological Society of America Bulletin*, **115**: 533-548.
- Sircombe K.N., Bleeker, W., and Stern R.A. 2001. Detrital zircon geochronology and grain-size analysis of a ~2800 Ma Mesoproterozoic proto-cratonic cover succession, Slave Province, Canada. *Earth and Planetary Science Letters*, **189**: 207-220.
- Smithies, R.H., Champion, D.C., and Cassidy, K.F., 2003. Formation of Earth's early Archean continental crust. *Precambrian Research*, **127**: 203 – 238
- Stubley, M.P. and Cairns, S.R. 1998. EGS Open File 1998-05. DIAND NWT Geology Division
- Tikhomirova, M., 2002. Zircon inheritance in diatexite granodiorites and its consequence on geochronology – a case in Lusatia and Erzgebirge (Saxo – Thuringia, eastern Germany). *Chemical Geology*, **191**: 209 – 224.
- Thorpe, R.I., Cumming, G.L., and Mortensen, J.K., 1992. A significant Pb Isotope boundary in the Slave Province and its probable relation to ancient basement in the western Slave Province. *In* Project Summaries, Canada - Northwest Territories Mineral Development Agreement 1987 - 91. Geological Survey of Canada, Open File Report no. 2484: 179-184
- van Breemen, O., Davis, W.J., and King, J.E., 1992. Temporal distribution of granitoid plutonic rocks in the Archean Slave Province, northwest Canadian Shield. *Canadian Journal of Earth Sciences*, **29**: 2186 – 2199.
- van der Velden, A.J., and Cook, F.A., 2002. Products of 2.65 – 2.58 Ga orogenesis in the Slave Province correlated with Slave – Northern Cordillera lithospheric evolution (SNORCLE) seismic reflection patterns. *Canadian Journal of Earth Sciences*, **38**: 1189 – 1200.
- Villeneuve, M.E., and Henderson, J.B., 1998. U-Pb geochronology of the Wijinnedi Lake area, Slave Province, District of Mackenzie, NWT. *In* Radiogenic Age and Isotopic studies: Report 11. Geological Survey of Canada, 1998-F, pp. 99-106.
- Watson, E.B., and Harrison, T.M., 1983. Zircon saturation revisited: temperature and composition effects in a variety of crustal magma types. *Earth Planetary Science Letters* **64**: 295-304.

Yamashita, K., Creaser, R.A., Stemler, J.U. and Zimaro, T.W., 1999. Geochemical and Nd-Pb isotopic systematics of Late Archean granitoids, southwestern Slave Province, Canada: Constraints for granitoid origin and crustal isotopic structure. *Canadian Journal of Earth Sciences*, **36**: 1131-1147.

Zeck, H.P., and Williams, I.S., 2002. Inherited and magmatic zircon from Neogene Hoyazo cordierite dacite, SE Spain – Anatectic source rock provenance and magmatic evolution. *Journal of Petrology*, **43**: 1089 – 1104.

The background of the slide is a photograph of a zircon crystal. The crystal is roughly oval-shaped and exhibits a complex internal structure with various colors, including shades of blue, red, and brown, which are characteristic of zircon crystals used in geochronology. The crystal is set against a light-colored, textured background, possibly a rock matrix or a thin section.

CHAPTER 6

Zircon Saturation Thermometry

**6 Thermal Effects of Neoproterozoic Magmatism on
Crustal Evolution and Orogenesis: Constraints
from Zircon Saturation Thermometry**

*V. Bennett¹, T.Rivers¹, C. Relf² and V. A. Jackson²

¹Department of Earth Sciences, Memorial University of Newfoundland, St. John's, NL.

A1B 3X5.

²NWT Geoscience Office, Yellowknife, NT, X1A 2R3

To submit to **Journal of Metamorphic Petrology**

NWT Geoscience Office Contribution number 0012.

6.1 Abstract

Zircon saturation thermometry is used to document the thermal character of Neoproterozoic magmatic rocks emplaced during 90 M.y. of growth and evolution of the Snare River terrane, southwestern Slave Province. The data constrain the contrasting thermal contributions of magmatism to the crustal heat budget during both steady state and perturbed geothermal settings. Refinement of zircon saturation temperatures was achieved by integrating information from whole-rock geochemistry, BSE imaging to discriminate inherited and magmatic zircon, and petrographic analysis of zircon textures, and the accuracy of the estimated temperatures was constrained by independent datasets. The results indicate the importance of removing the inherited Zr component where refractory zircon abundance is high. The corrected zircon saturation temperatures reveal secular changes during crustal evolution, which was characterized by: (i) a prolonged period of moderate-temperature (740-756 °C) TTG magmatism during crust formation and growth; (ii) a short period of orogenic magmatism involving several episodes of H₂O-rich, low-temperature (ca. 675 °C) and H₂O-poor, high-temperature (779-794 °C; 867 °C) plutonism; and (iii) a short period of low-temperature (657 °C) post-orogenic anatectic magmatism. Low-temperature orogenic plutons were emplaced into the upper crust, buffering and locally overprinting an older thermal regime, whereas high-temperature orogenic plutons emplaced into a 10 km thick section of the mid crust were the principal heat and fluid source for regional metamorphism. The onset of anhydrous conditions in the mid crust was related to emplacement of high-temperature orthopyroxene granite. Post-emplacement metamorphism of lower mid-crustal magmas

demarcates the maximum depth at which pluton-driven metamorphism was effective. Collectively, the data illustrate the diachroneity and variable roles of magmatic heat in crustal metamorphism.

6.2 Introduction

Intracrustal magmatism was a fundamental process in the growth and cratonization of Neoproterozoic crust (e.g., Champion and Sheraton 1997; Oberthür et al. 2002; Chamberlain et al. 2003; Bédard et al. 2003). To a first approximation, crustal evolution can be subdivided into three stages, an initial stage of steady-state or intermittent crustal growth, an intermediate orogenic stage of pervasive crustal reworking, and a terminal stage involving cratonization, typically followed by a return to steady-state conditions. Analysis of the secular geochemical trends in crustal magmas formed during each of these stages can aid in defining the nature and rate of crustal maturation (e.g., Wiedenbeck and Watkins 1993; Moyen et al. 2003; Chapter 4), but a complementary understanding of the thermal effects of these magmas in a time–space context is generally lacking. Published thermometric datasets of initial melting and/or magma crystallization temperatures are limited (e.g., Bédard 2003), but such studies have the potential to provide important constraints on the heat budget, which during the Neoproterozoic is generally agreed to have been at least 2–3 times greater than the present (Pollack 1997). Given the abundance of crustal magmatism, the prevalence of high temperature / low pressure (HT/LP) metamorphism in the Neoproterozoic, and the continuing debate concerning causes of perturbed geothermal gradients (e.g., Fyfe 1973; Percival 1994;

Kramers et al. 2001), the lack of such datasets on magmatic temperatures is surprising. Application of zircon saturation thermometry (Watson and Harrison 1983; Hancher and Watson 2003) potentially provides a method to characterize the thermal behaviour of crustal melts, although it has seldom been applied to Archean magmas (e.g. Barrie 1995).

In this contribution, we use zircon saturation thermometry to characterize the thermal evolution of the Snare River terrane, southwestern Slave Province (Fig. 6.1), a well-exposed Neoproterozoic HT/LP metamorphic belt recording peak orogenic conditions well in excess of a steady-state geotherm. Magmatism punctuated the entire evolution of the belt and was particularly voluminous during the orogenic stage, which involved emplacement of magmas into the mid and upper crust. The coeval magmatism and HT/LP metamorphism in the belt provides an excellent opportunity to investigate the consequences of magmatism on the thermal budget of metamorphism. In order to determine crystallization temperatures for magmatic rocks emplaced in the Snare River terrane during its ca. 90 M.y. history, we have integrated inherited zircon studies (Bennett et al. Chapter 5) with zircon saturation data to characterize the thermal contribution of Neoproterozoic magmatism. An outline of the methodology used, which specifically accounts for the several sources of error associated with the thermometer, is given before the implications of the dataset are assessed. Two fundamental issues are addressed: (i) relationships among secular variation in magma geochemistry, crustal evolution and temperature; and (ii) an assessment of the role of magmatic heat in HT metamorphism (i.e., principal heat source versus heat buffer).

6.3 Geological setting

The Snare River terrane is located in the southwestern Slave Province, a small Archean craton of approximately 190 000 km² recording over 1.5 B.y. of punctuated crustal history. Four first-order lithotectonic components are recognized in the Slave Province: Paleo- to Mesoarchean basement complexes, Neoproterozoic volcano-sedimentary belts, Neoproterozoic plutonic rocks, and LP/HT granite-granulite domains (Bowring and Williams 1999; Bleeker et al. 1999; Mortensen et al. 1988; Isachsen et al. 1991; Davis et al. 1994; Pehrsson et al. 2000). Of these, the Neoproterozoic plutonic rocks are the most voluminous at the present level of erosion, comprising approximately 60% of the surface area of the craton and exhibiting a broad secular variation from older metaluminous to younger peraluminous compositions (Davis et al. 1994; Yamashita et al. 1999, 2000). Occurrences of HT/LP metamorphic belts are associated with Neoproterozoic magmas, suggesting a genetic link. The thermal peak of HT/LP metamorphism in supracrustal belts across the province occurred at ca. 2.6 Ga and peak temperatures varied from 400 °C to 750 °C (Thompson 1978; Relf 1992).

The Snare River terrane (Fig. 6.1), the largest HT/LP belt, is characterized by a core of granulite- and amphibolite-facies rocks and voluminous magmatic suites (Ghost and Bigspruce sub-domains; Henderson and Schaan 1993; Pehrsson et al. 2000; Bennett et al. 2005) surrounded by greenschist- to amphibolite-facies supracrustal belts (Kwejinne Lake, Labrish Lake and Russell-Slemon supracrustal belts). The supracrustal belts consist of ca. 2674-2635 Ma bimodal volcanic rocks, syn-volcanic plutons and greywacke-mudstone metaturbidites that are intruded by ca. 2608-2595 Ma

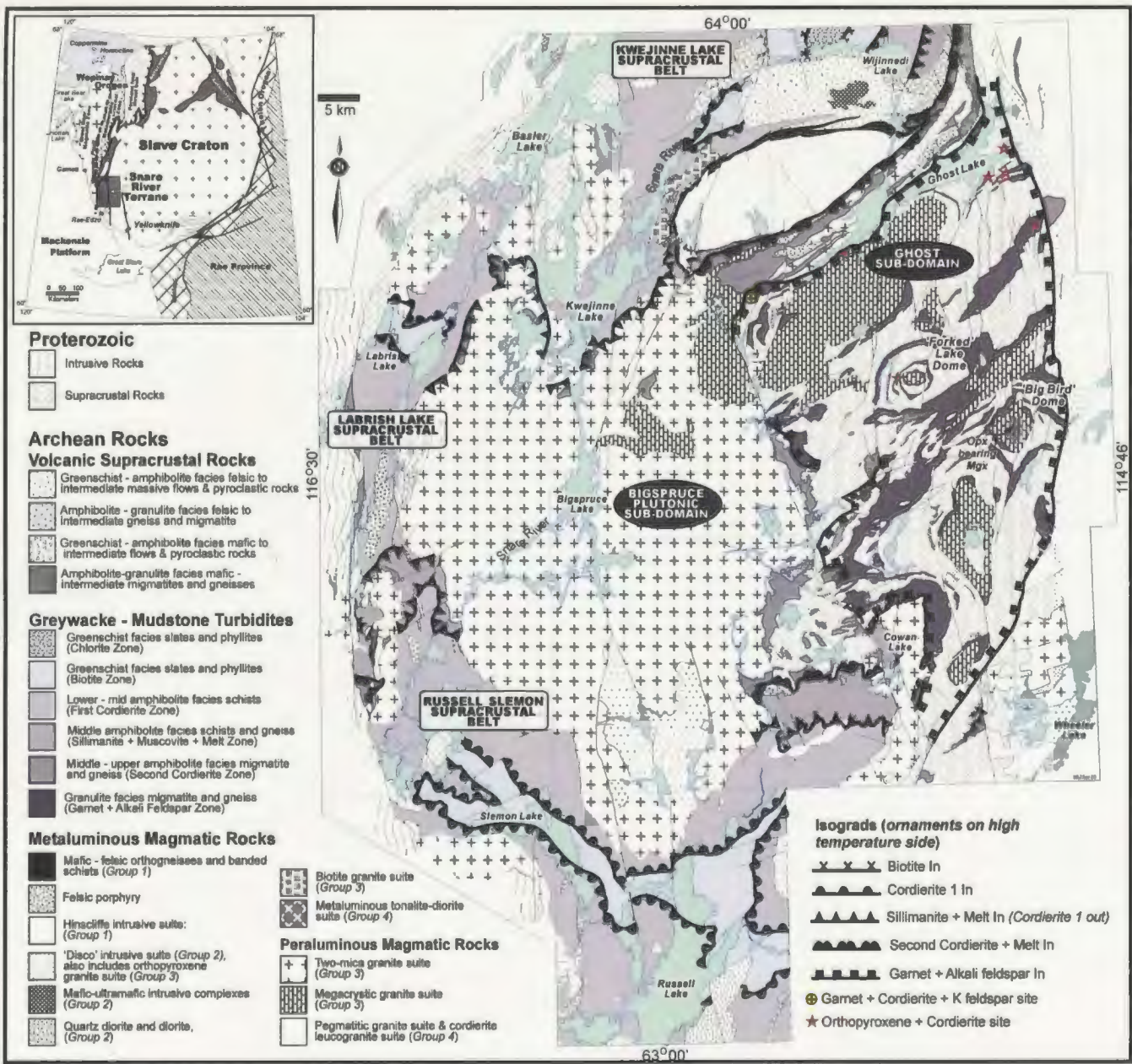


Figure 6.1: Geological map of the Snare River terrane with regional metamorphic isograd sequence marked. Sources of information: Snare River area (Jackson 2003 and references therein); Wijinnedi Lake area (Henderson 1998); Labrish Lake area (Brophy and Pell 2002); Russell Lake area (Jackson 1999); Basler Lake area (McGlynn and Ross 1962; Lord 1942). Inset box shows location of the Snare River terrane in the Slave Province, modified after Hoffman and Hall (1993). Mgx, megacrystic granite

metaluminous and peraluminous magmas (Mortensen et al. 1992; Villeneuve and Henderson 1998; Bennett et al. 2005). The high-grade core is predominantly composed of ca. 2630-2590 Ga plutonic rocks with tectonic lenses of the ca. 2674-2635 Ma volcano-sedimentary lithologies (Jackson and Bennett 2003; Bennett et al. 2005; Chapter 2).

The deformation history in the Snare River terrane comprised three events (D1 to D3; Chapter 3), similar to the Slave Province as a whole. D1, which peaked between ca. 2640-2610 Ma, resulted in penetrative folding and fabric development and the intercalation of volcanic and sedimentary lithologies (Pehrsson and Villeneuve 1999). D2 involved crustal thickening and was coeval with HT granulite-facies metamorphism between ca. 2610-2600 Ma. Evidence for D3 includes open folds and pre-2585 Ma conjugate shear sets.

Magmatic rocks in the Snare River terrane are subdivided into four groups on the basis of age and composition (Bennett et al. accepted). Groups 1 and 2 are metaluminous, whereas both metaluminous and peraluminous compositions occur in groups 3 and 4. Group 1 magmas occur predominantly in the supracrustal belts and include volcanic rocks and syn-volcanic plutons, ranging from basalt to rhyodacite and gabbro to tonalite respectively, that crystallized episodically between ca. 2674-2650 Ma. Group 2 magmas are plutonic, intruded syn- to post-D1/M1 from ca. 2635-2608 Ma and range in composition from ultramafic hornblendite to hornblende-biotite granodiorite. Magmas of Group 3 are granitic in composition, intruded syn- to late D2 at ca. 2597 Ma and were associated with upper-amphibolite- to granulite-facies metamorphism. Group 3 metaluminous magmas consist of abundant orthopyroxene granite, which occurs

exclusively within the Ghost subdomain, and less abundant biotite±hornblende granite emplaced into Ghost subdomain and the surrounding supracrustal belts. Group 3 peraluminous magmas include numerous bodies of megacrystic granite in Ghost and Bigspruce subdomains and the voluminous two-mica granite suite in Bigspruce subdomain and adjacent supracrustal belts. Group 4 magmas are small volume melts, ranging from metaluminous tonalite to peraluminous cordierite leucogranite and pegmatitic granite, which intruded during or post- D3 from ca. 2590-2585 Ma. Important field relationships and petrographic features are illustrated in Fig. 6.2.

Three phases of Neoproterozoic metamorphism (M1 to M3) are recognized in the Snare River terrane. M1 coincided with D1 and involved low temperature – low pressure (LT-LP) metamorphism (Pehrsson 1998). A titanite cooling age of 2610 ± 4 Ma from the Hinscliffe plutonic complex (Fig. 6.1) is suggested to represent a maximum age of M1 in the Kwejinne Lake supracrustal belt (Villeneuve and Henderson 1998). M2 involved high temperature – low to medium pressure (HT-L/MP) metamorphism and was coeval with D2 and Group 3 magmatism. The M2 thermal peak is constrained by 2592 ± 5 Ma metamorphic zircon in mafic granulite at Forked Lake (Perks 1997) and ca. 2596-2590 Ma metamorphic monazite in tonalitic gneiss north of Ghost Lake (Henderson 2004). A prograde HT/LP M2 metamorphic sequence comprising six zones and five isograds in metapelitic rocks has been defined (Figs. 6.1 and 6.3; Table 6.1; Appendix I). From lowest to highest grade the isograds are: (i) Biotite-In, (ii) Cordierite 1-In, (iii) Sillimanite+Melt-In (Cordierite 1-Out), (iv) Cordierite+Melt-In, and (v)

Figure 6.2: Field and petrographic relationships of magmatic suites in the Snare River terrane. Hammer and lens cap are approximately 45 cm long and 5 cm in diameter. Scale and fields of view (FOV) for polished slabs and photomicrographs are indicated. (a) Melt-rich and melt-absent zones adjacent to intrusions of upper-crustal granitic dyke within *Sil + Melt* zone. Note that bedding is preserved above dyke. (b) Variable effect of emplacement of biotite granite on adjacent cordierite zone turbidites. Local H₂O-present incipient melting overprints cordierite grade metamorphism, Kwejinne Lake supracrustal belt. (c) Contact between two-mica granite and *Sil + Melt* grade turbidites. No appreciable prograde metamorphic effect is apparent. *Sil + Melt* zone assemblages are continuous several kilometers from pluton contact. (d) Polished slabs of megacrystic granite at upper amphibolite- and granulite-facies conditions, respectively. Geochemistry and U-Pb age data indicate petrogenetic link between two samples. (e) Polished slabs of metaturbidite adjacent to and as enclaves within megacrystic granite. Note *Grt + Melt* assemblage in enclave compared to *Crd (2) + Melt* assemblage in adjacent country rocks. (f) Photomicrograph illustrating *Grt + Melt* formation as a result of *Crd + Bt* breakdown within metaturbidite enclave in megacrystic granite. (g) Spatial association of diatexite and intrusions of megacrystic granite (h) Metamorphic monazite overgrowing older magmatic zircon in megacrystic granite located within the margin of megacrystic granite intrusion coring 'Big Bird' structural dome, Ghost subdomain.

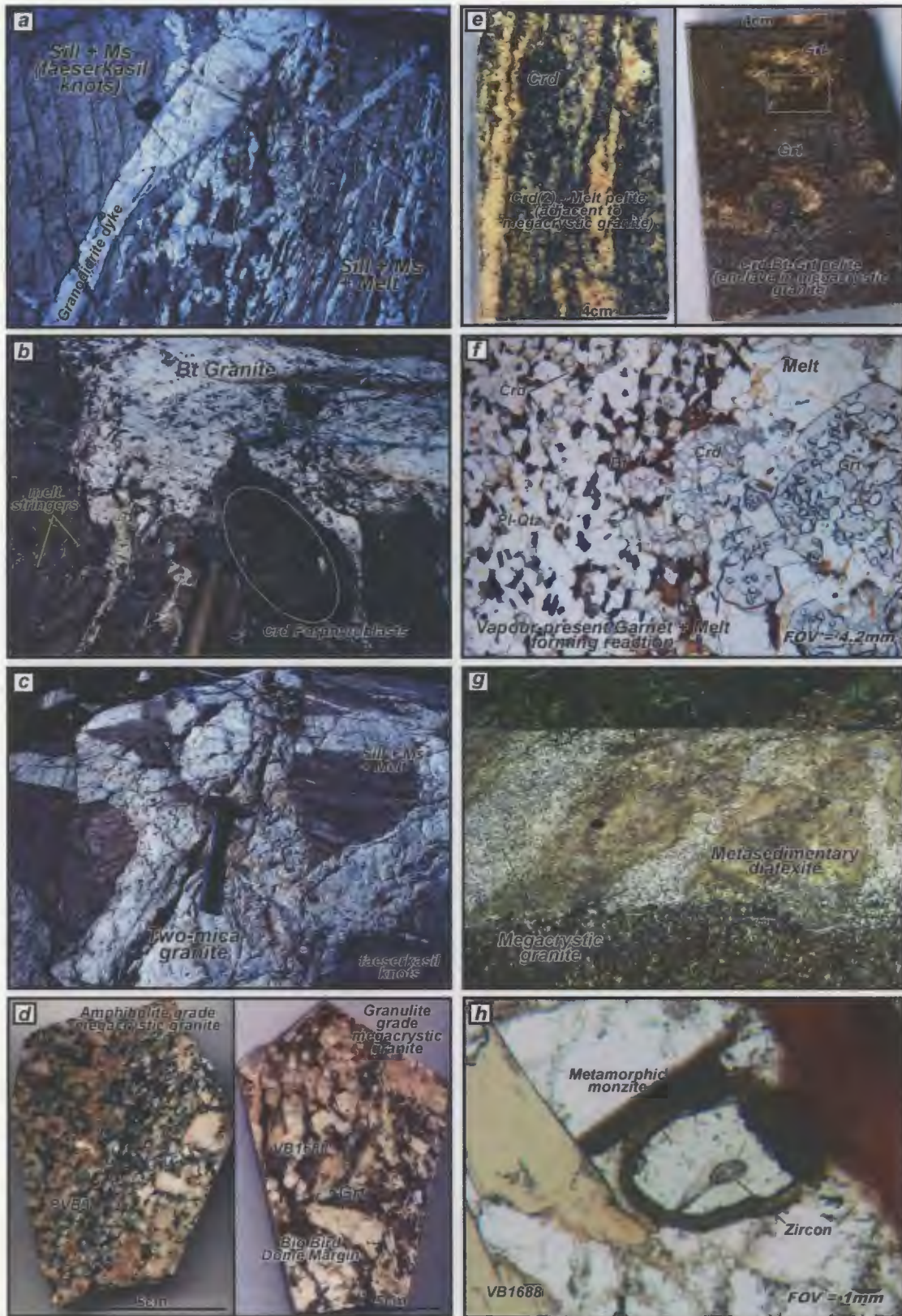


Figure 6.2: Caption see opposite

Figure 6.2: Field and petrographic relationships of magmatic suites in the Snare River terrane. Hammer and lens cap are approximately 45 cm long and 5 cm in diameter. Scale and fields of view (FOV) for polished slabs and photomicrographs are indicated. *(i)* Contact relations between Disco Intrusive Suite and crosscutting orthopyroxene granite. Photomicrograph of *Bt* and *Hbl* dehydration within Disco Intrusive Suite, indicating anhydrous metamorphic conditions related to intrusion of orthopyroxene granite. *(j)* Photomicrograph illustrating biotite dehydration and metamorphic orthopyroxene formation in orthopyroxene granite suite adjacent to core of 'Forked Lake' structural dome, Ghost subdomain. *(k)* Polished slabs of orthopyroxene granite at lowest and highest levels of the Ghost subdomain. Field photograph illustrating alteration occurring at deepest level where sample on left was collected (c.f. Newton 1990). *(l)* Mafic enclave within orthopyroxene granite with dehydration metamorphic rind. *(m)* Photomicrographs of *Hbl-Bt* core and *Opx-Pl* rim of mafic enclaves illustrated in *(l)*. *(n)* Photomicrographs of orthopyroxene granite immediately adjacent to *Grt + Kfs* isograd. Biotite dehydration is responsible for formation of garnet at these localities. *(o)* Photomicrographs and polished slabs of megacrystic granite occurring in 'Big Bird' structural dome core. Figure illustrates the progressive breakdown of *Grt* and *Bt* and correlative formation of *Opx* as dome core is traversed.

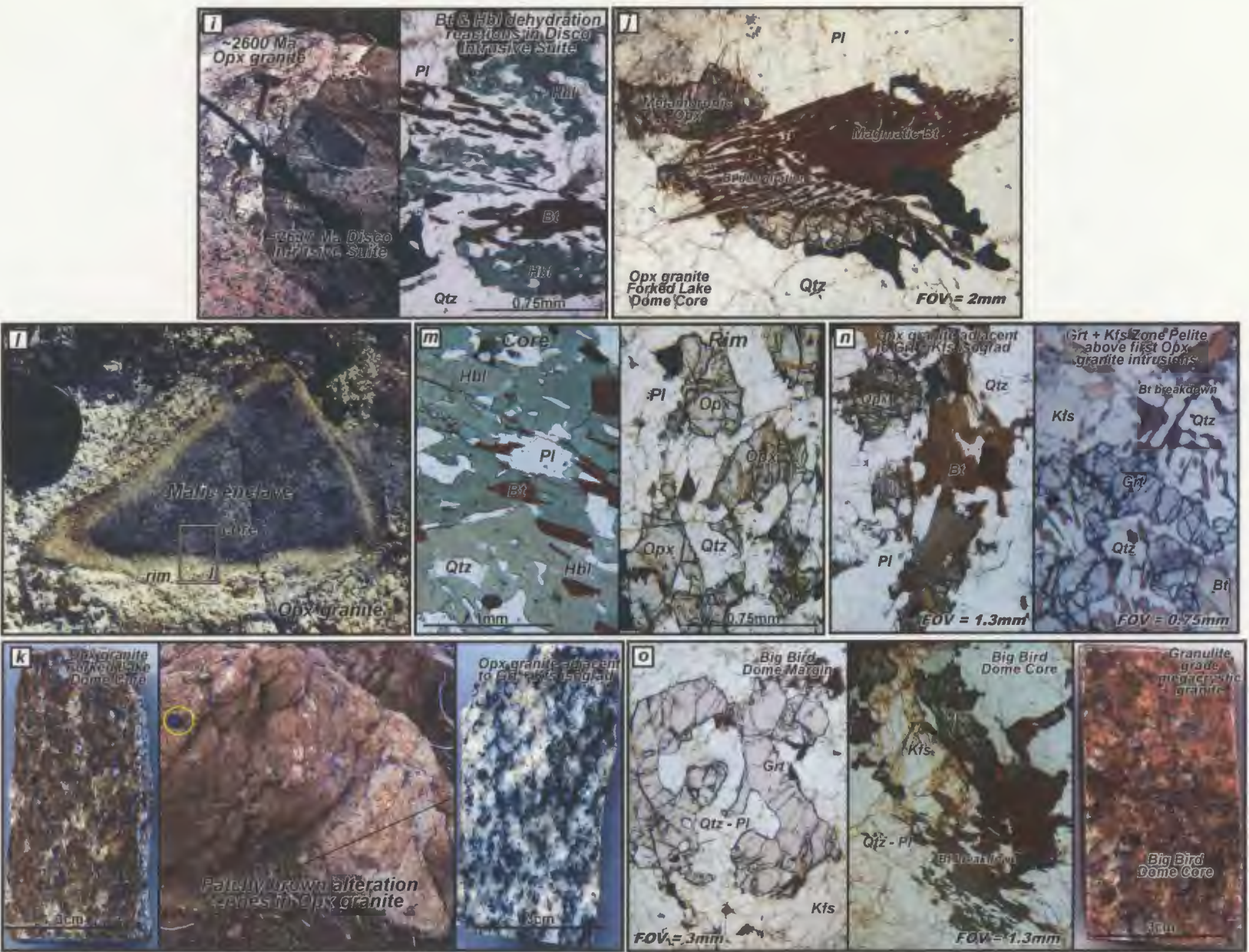


Figure 6.2: Caption see opposite

Table 6.1: Summary of peak metamorphic conditions (M2) at different crustal levels during the ca. 2600 Ma orogenic peak and associated plutons and magmatic groups emplaced into respective metamorphic zones.

ISOGRAD/ ZONE	METAMORPHIC MINERAL ASSEMBLAGE	REACTIONS	^(a) P-T RANGE	PEAK ESTIMATE	CRUSTAL LEVEL	SYNCHRONOUS MAGMATIC GROUP
GREENSCHIST FACIES						
Chl Zone	Chl - Ms					
Bt Zone (Fig 6.3a)	Chl - Ms - Bt	(1) Chl + Kfs = Ms + Bt + Qtz + H ₂ O	300 - 400 °C ≤ 2 kbar	400°C 2 kbar	Upper Crust (4 - 7 km)	<i>not observed</i>
LOWER AMPHIBOLITE FACIES						
Crd (1) Zone (Figs. 6.3b,c)	Crd - Bt - Ms ± And	(2) Mg-Chl + And = Mg-Crd + H ₂ O (3) Mg-Chl + Ms = Mg-Crd + Phl + H ₂ O (4) Chl + Ms = Crd + Bt + And + H ₂ O (5) Phl + Ms = Crd + Kfs + H ₂ O	500 - 570 °C 2 - 3.2 kbar	570°C 3.2 kbar	Upper Crust (7 - 11 km)	Gp 3 Bt granite suite Gp 3 Two-mica granite
MIDDLE AMPHIBOLITE FACIES						
Sil + Melt Zone (Figs. 6.3d, e)	Sil - Bt - Ms - Melt ± Crd	(6) Ms + Crd = Sil + Bt + Qtz + H ₂ O (Faserkeisel Crd replacement) (7) H ₂ O Pelite saturated solidus (8) Ms + Qtz = Sil + Kfs + L	550 - 650 °C 3.2 - 4 kbar	650 - 670°C 3.5 - 4 kbar	Upper Crust (11 - 14 km)	Gp 3 Bt granite Gp 3 Two-mica granite
UPPER AMPHIBOLITE FACIES						
Crd (2) + Melt Zone (Figs. 6.3f,g,h)	Crd (2) - Bt - Sil ± Kfs	(9) Bt + Sil + Qtz = Crd + Kfs + H ₂ O (10) Bt + Kfs + Sil + H ₂ O = Crd + L (11) Bt + Sil + Qtz + H ₂ O = Crd + L (12) Bt + Crd + Kfs + H ₂ O = Sil + L	650 - 770°C 4 - 4.7 kbar	730°C 4 kbar	Upper - Mid Crust (14 - 16.5 km)	Gp 3 Two-mica granite Gp 3 Megacrystic granite
GRANULITE FACIES - Upper Ghost subdomain						
Grt + Kfs Zone (Figs. 6.i - l)	Grt - Kfs - Crd - Melt	(13) Bt + Sil + Pl + Qtz = Grt + Kfs + L (14) Bt + Sil = Grt + Crd + Kfs + L	740 - 830°C 4.7 - 5.9 kbar	^(b) 740°C 4.7 kbar	Mid Crust (16.5 - 21)	Gp 3 Megacrystic granite Gp 3 Opx granite suite
GRANULITE FACIES - Lower Ghost subdomain						
Crd + Opx Associated with Reactions (13) & (14)	Crd - Opx - Kfs- Grt	(15) Grt + Bt + Qtz = Opx + Kfs + Crd + L	^(c) 845 - 920 °C 5.9 - 7.4 kbar	not established	Mid Crust (21 - 26 km)	Gp 3 Megacrystic granite Gp 3 Opx granite suite

Notes: (a) P/T determinations presented in Appendix I. (b) P-T estimate of Grt + Kfs isograd. (c) Thermobarometric determinations of Chacko et al. (1995, 1996) for the northern Ghost Subdomain. P-T estimates calculated using Grt-Pl-Opx-Qtz barometer and aluminum-in-Opx thermometer (Fitzsimmons and Harley 1994; Pattison and Begin 1994).

Figure 6.3: Representative images of metamorphic indicators for each metamorphic zone in the Snare River terrane. Hammer and pen are approximately 45 cm and 10 cm long respectively, lens cap is approximately 5 cm in diameter. (a) Primary flame structures in Biotite zone. (b) *And* + *Crd* porphyroblasts in *Crd* (1) zone. (c) Zoned cordierite porphyroblasts in *Crd* (1) zone. (d) Faeserkasil replacement of *Crd* by *Sil* at onset of *Sil* + *Melt* zone. (e) *Sil* replacement of *Crd* in addition to onset of melting within *Sil* + *Melt* zone. (f) Formation of second cordierite (iolite) and melt in *Crd* (2) + *Melt* zone. (g) Diatexite with large irregular grains of *Crd* + *Kfs* and rafts of metasedimentary material within *Crd* (2) + *Melt* zone. (h) Close up of cordierite crystal in diatexite. (i) Subrounded alkali feldspar grain in granulite grade metasedimentary diatexite in *Grt* + *Kfs* zone. (j) Very large cordierite associated with thin alkali feldspar bearing-melt within granulite grade diatexite, *Grt* + *Kfs* zone. (k) *Grt* + *Kfs* + *Crd* assemblage in granulite grade diatexite, *Grt* + *Kfs* zone. (l) Layered pelite with *Grt* + *Crd* bearing leucosome, *Grt* + *Kfs* zone.



Figure 6.3: Caption see opposite

Garnet+Kfeldspar-In. Andalusite is widespread, but no regional andalusite isograd is recognized. Garnet-cordierite-orthopyroxene-Kfeldspar assemblages occur locally (Fig. 6.1). Metamorphic temperatures and pressures range from ca. 300 °C / < 2 kbar in the chlorite zone to ≥ 920 °C / 7.4 kbar in the garnet-K feldspar zone (Farquhar and Chacko 1996; Henderson 2004). Peak M2 *P-T* conditions, principal reactions, crustal depths, and related coeval magmatic suites are summarized in Table 6.1 and Appendix I. The terminal M3 event involved overprinting of M2 assemblages and decomposition of M2 garnet and cordierite to form spinel-cordierite-sillimanite-biotite \pm ilmenite symplectite, indicating widespread decompression. U-Pb data from igneous and metamorphic rocks demonstrate that M3 was a protracted event between ca. 2590-2563 Ma (Perks 1997; Villeneuve and Henderson 1998; Bennett et al. 2005, unpublished data).

6.4 Zircon saturation thermometry

Zircon saturation thermometry is an underutilized tool that, with careful application, may in some cases permits accurate and robust estimates of crustally-derived magma temperatures using the solubility model of Watson and Harrison (1983). The thermometer is dependent on the saturation behaviour of Zr in the melt, which is positively correlated with the alkalinity of the bulk rock as measured on a molar basis (Dietrich 1968; Watson 1979; Watson and Harrison 1983; Hanchar and Watson 2003). H₂O abundance also affects zircon solubility, but for melts with more than ~2 wt.% H₂O, Zr saturation is typically independent of H₂O content. Zirconium solubility experiments indicate the thermometer is not reliable for peralkaline and anhydrous melts. Since Zr

saturation is dependent on the alkalinity (M value; Hanchar and Watson 2003; Appendix J), melt geochemistry must be assessed in terms of the degree of fractionation. Melt segregation has been suggested to remove refractory zircon (Miller et al. 2003), so Zr in subsequent magmas would occur only in solution, thus calculated temperatures would be different for each melt fraction. However, for Zr-saturated, crustally-derived magmas with abundant inherited zircon, fractionation is commonly inferred to be limited (Miller et al. 2003) and the inherited zircon is taken to imply that Zr saturation occurred early and crystallization was close to the source. In contrast, an absence of inherited zircon suggests Zr undersaturation and late zircon crystallization (i.e., close to the level of emplacement). Any refractory zircon in such melts would quickly dissolve and subsequently reprecipitate as magmatic zircon.

For successful application of the zircon saturation thermometer, four criteria must be satisfied: (1) precise determination of the whole-rock, major- and trace-element melt composition and a corresponding assessment of the fractionation state of the magma; (2) an alkalinity value (M) within the experimentally determined calibration range of Watson and Harrison (1983); (3) H₂O contents \geq 2 Wt.%; and (4) an estimation of the proportion of inherited Zr in the melt.

6.5 Results

In this study we have utilized the zircon saturation thermometer to constrain zircon crystallization temperatures (T_{Zir}) for a suite of 42 samples, comprising 29 metaluminous magmas (groups 1 to 4) and 13 peraluminous magmas (groups 3 and 4),

using data from the studies of Perks (1997), Yamashita (1999), Ootes (2000), Bennett et al. (accepted) and unpublished results of A. Alcazar and B. Cousens. For the nine samples presented in Chapter 5 for which zircon inheritance data were available, the effect of Zr inheritance on the accuracy of the resultant temperature is estimated. For these samples, back-scattered electron (BSE) images of representative zircon crystals (25 to 47 grains per sample) were used to calculate average proportions of magmatic and refractory (inherited) zircon in each sample (Fig. 6.8). Aspect ratios of zircon grains varied from 1:1 to 1:6 (Fig. 6.4). Calculations using image analysis software (ImageJ v. 1.32J) were done on an area basis, as the cores were commonly irregular in shape due to magmatic resorption and shapes in the third dimension were unknown. Application of an area rather than a volume correction for the presence of inherited zircon introduces a source of error to the method, but the significance of the resultant uncertainty is not readily estimated. Once the average area proportion of inherited Zr present in each melt was estimated, it was subtracted from the total whole-rock Zr concentration.

The significance of the calculated T_{Zir} values with respect to the relative timing of crystallization was considered by examination of both the magma chemistry and the in situ petrographic context of the zircon. In the absence of such evidence, T_{Zir} values are generally interpreted to represent maximum (i.e., melting) temperatures, which can potentially overestimate emplacement conditions, particularly for Zr-saturated magmas. Petrographic associations and textural relations of zircon relative to magma fractionation state are outlined in Table 6.2 and illustrated in Fig. 6.5. A summary of magmatic suite, rock type, crystallization age, molar alkalinity value (M), Zr concentration, and

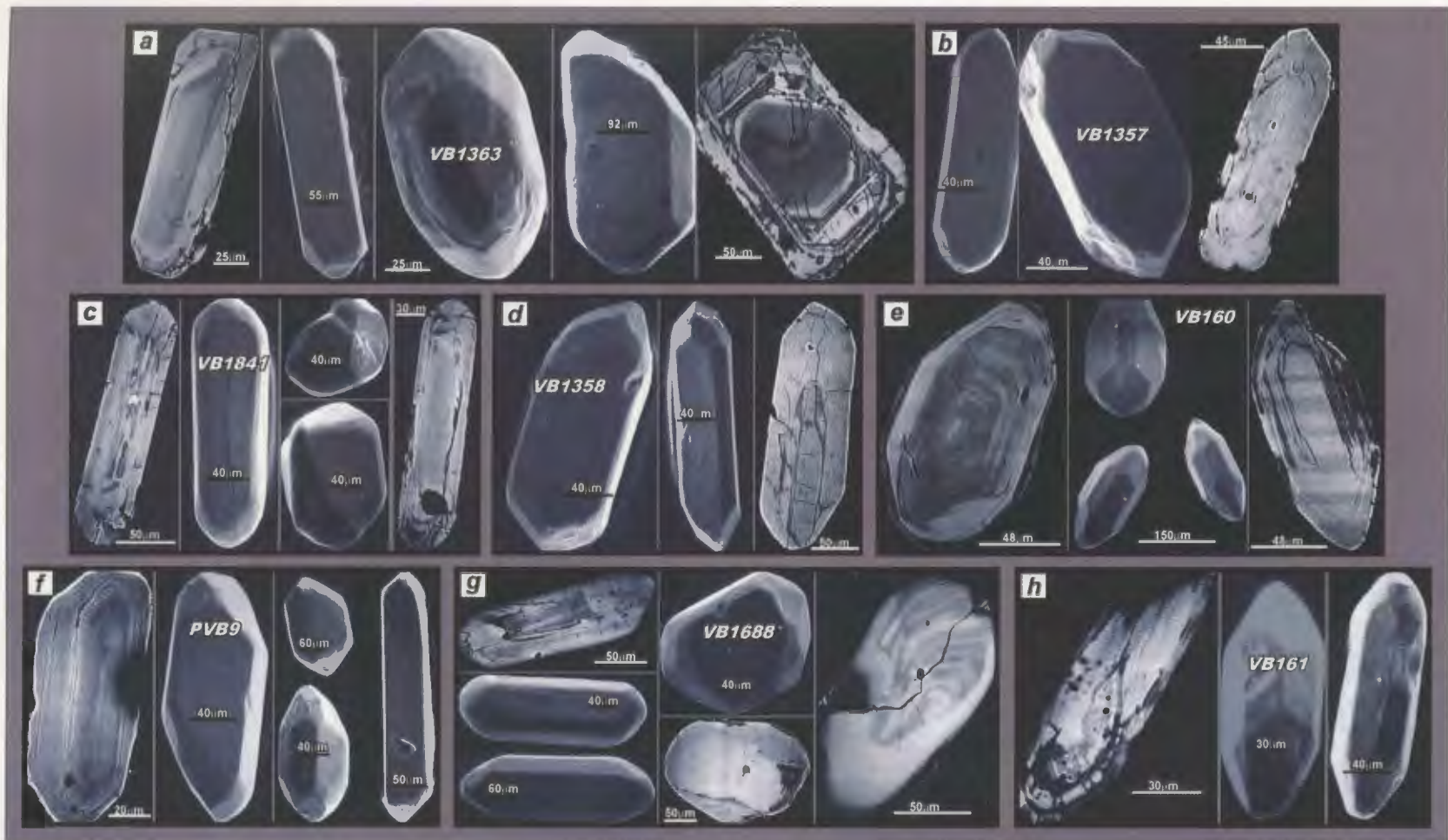


Figure 6.4: Zircon morphologies and representative inherited zircon zonation trends for 8 magmatic suite, illustrating diverse and complex trends involving inherited zircon. (a) *VB1363*, ca. 2637 Ma Disco Intrusive Suite. (b) *VB1357*, upper-crustal ca. 2600 Ma Biotite granite suite. (c) *VB1841*, mid-crustal, ca. 2600 Ma Orthopyroxene granite suite. (d) *VB1358*, ca. 2600 Ma upper-crustal Two-mica granite. (e) *VB160*, granulite grade metasedimentary diatexite. (f) *PVB9*, ca. 2600 Ma high-level intrusion of Megacrystic granite suite. (g) *VB1688*, ca. 2600 Ma mid-crustal Megacrystic granite suite. (h) *VB161*, ca. 2585 Ma Cordierite leucogranite suite.

Table 6.2: Summary of whole-rock trace-element composition, mineralogy, and zircon petrographic observations to determine relative timing of magmatic zircon crystallization.

SAMPLE (Magmatic Group)	MAGMA TRACE ELEMENT CHARACTERISTICS		FRACTIONATION (Relative) Degree	BOWENS SERIES MINERALOGY (in decreasing abundance)	INHERITANCE % (Calculated from BSE database)	ZIRCON / MAJOR MINERAL OBSERVATIONS (decreasing importance)		RELATIVE TIMING OF ZIRCON CRYSTALLIZATION (interpretation)
	Enrichment	Depletion				Association	Location	
METALUMINOUS GRANITES								
VB165 TTG GROUP 1	Zr, LREE	Sr, Nb, HREE melt	^(a) FC Not significant – approximates initial composition	Pl – Qtz – Hb - Kfs – Bt	None observed	1. Zrn – Qtz, Pl, Kfs 2. Zrn in Pl, Kfs Qtz 3. Zrn in Bt, Hb	Grain Boundary Intragrain Grain Margin	Late-stage zircon crystallization (<i>Emplacement</i>)
VB1692 Granodiorite GROUP 1	Sr, Zr, Eu LREE	Nb, HREE	Feldspar FC - TTG Differentiate	Pl – Qtz – Bt – Hb - Kfs	Not calculated (observed in thin section ; Fig. 6.5)	1. Zrn – Qtz, Pl, Bt 2. Zrn in Pl, Qtz 3. Zrn in Bt	Grain Boundary Intragrain Grain Margin	Late-stage zircon crystallization (<i>Emplacement</i>)
VB1363 Granodiorite GROUP 2	Zr, Eu LREE	Sr, Nb HREE	Minor feldspar FC; Approximates initial melt composition	Qtz – Pl – Bt - Kfs – Hbl	60.3 %	1. Zrn – Qtz, Pl, Bt 2. Zrn in Qtz, Pl 3. Zrn in Bt 4. Zrn in Qtz (<i>cojoined grains</i>)	Grain Boundary Intragrain Grain Margin Intragrain	Late-stage zircon crystallization (<i>Emplacement</i>)
VB1357 Bt Granite GROUP 3	Zr, Sr LREE	Nb, HREE	Feldspar FC Fractionate melt	Qtz – Pl – Kfs- Bt	73.5%	1. Zrn in Bt – Qtz 2. Zrn – Bt 3. Zrn in Qtz, Pl, Kfs	Grain Boundary Grain Margin Grain Margin	Late-stage zircon crystallization (<i>Emplacement</i>)
VB1841 Opx Granite GROUP 3	Eu, Zr LREE	Sr, Zr, Eu HREE	Feldspar FC - Fractionate melt	Qtz – Kfs – Pl - Opx – Bt(magmatic)	23 %	1. Zrn – Qtz, Pl, Kfs 2. Zrn in Qtz	Grain Boundary Intragrain	Late-stage zircon crystallization (<i>Emplacement</i>)
^(b) FL24, 74 Opx Granite GROUP 3	Zr, ±Eu LREE	Weak Sr HREE	Minor feldspar FC Intermediate stage Fractionate melt	Qtz – Pl – Kfs Opx – Bt	Not Calculated (observed in thin section ; Fig. 6.5)	1. Zrn – Qtz, Pl, Kfs, Opx, Bt 2. Zrn in Qtz 3. Zrn in Opx	Grain Boundary Intragrain Grain Margin	Late-stage zircon crystallization (<i>Emplacement</i>)
PERALUMINOUS GRANITES								
VB 1358 Two – Mica Granite GROUP 3	LREE	Sr, Eu, Zr Nb	Moderate feldspar removal	Qtz – Kfs – Pl - Bt – Ms	65.3%	1. Zrn – Qtz, Bt, Pl, Kfs, Ms 2. Zrn in Qtz, Pl, Kfs 3. Zrn in Bt	Grain Boundary Intragrain/Margin Grain Margin	Late-stage zircon crystallization (<i>Emplacement</i>)

Table 6.2: continued

SAMPLE (Magmatic Group)	MAGMA TRACE ELEMENT CHARACTERISTICS		FRACTIONATION (Relative) Degree	BOWENS SERIES MINERALOGY (in decreasing abundance)	INHERITANCE % (Calculated from BSE database)	ZIRCON / MAJOR MINERAL OBSERVATIONS (decreasing importance)		RELATIVE TIMING OF ZIRCON CRYSTALLIZATION (interpretation)
	Enrichment	Depletion				Association	Location	
VB 160 Diatexite GROUP 3	LREE	Sr, Eu, Zr Nb	Moderate feldspar removal	Qtz - Pl - Crd Bt - Kfs	56%	1. Zm - Qtz, Bt, Crd, Pl 2. Zm in Qtz - <i>cojoined grains</i> 3. Zm in Bt, Pl, Crd	Grain Boundary Grain Margin Grain Margin	Late-stage zircon crystallization (<i>Emplacement</i>)
PVB9 Megacrystic Granite GROUP 3	Zr, LREE	Sr, Nb	FC Not significant approximates initial melt composition	Qtz - Kfs - Pl - Bt - Ms	50.8%	1. Zm - Qtz, Bt, Pl, Kfs 2. Zm - Qtz, Bt 3. Zm - Qtz, Pl, Kfs, Bt 4. Zm in Qtz, Pl, Kfs, Bt	Grain Boundary Grain Margin Grain Margin Intragrain	Late-stage zircon crystallization (<i>Emplacement</i>)
VB1688 Megacrystic Granite GROUP 3	Zr, LREE	Sr, Nb	FC Not significant approximates initial melt composition	Qtz - Kfs - Pl - Bt - Grt	32%	1. Zm - Qtz, Pl, Kfs, Bt 2. Zm in Bt 3. Zm in Monazite 4. Zm -Bt breakdown	Grain Boundary Grain Margin Intragrain Grain Margin	Late-stage zircon crystallization (<i>Emplacement</i>)
VB 161 Cordierite Leucogranite GROUP 3	Ba, Eu, Sr, Zr	Nb HREE	Significant feldspar FC	Qtz - Pl - Kfs - - Bt - Crd	56%	1. Zm - Qtz, Pl, Kfs 2. Zm in Qtz, Pl, Kfs 3. Zm in Qtz, Pl, Kfs 4. Zm in Crd	Grain Boundary Grain Margin Intragrain Grain Margin	Late-stage zircon crystallization (<i>Emplacement</i>)

Notes: (a) FC - Fractionation; (b) Equivalent samples collected at approximate sites of Perks (1997).

Figure 6.5: Petrographic relationships between zircon and host minerals. Field of view (FOV) indicated. (a) *VB1692*, ca. 2654 Ma Hinscliffe complex. Late-stage zircon growth occurring at boundary between *Pl* and *Qtz*. Inherited cores occur within *Pl* grain. (b) *VB1363*, grain-boundary zircon growth. Inherited cores are evident, magmatic zircon growth associated with *Qtz-Pl* grains. (c) *VB1841*, large inherited zircon grain at margin of orthopyroxene. Thin magmatic rim in contact with quartz, indicating late stage crystallization of zircon. (d) *VB1841*, inherited zircon with magmatic rim on grain-boundary. (e) *VB1357*, zircon needles at *Bt-Qtz* grain boundary. (f) *VB1357*, zircon needle in alkali feldspar grain. (g) *VB1358*, zircon needles in *Bt* and *Qtz*. (h) *VB1358*, zircon needle with small inherited core in quartz grain adjacent to biotite grain margin.

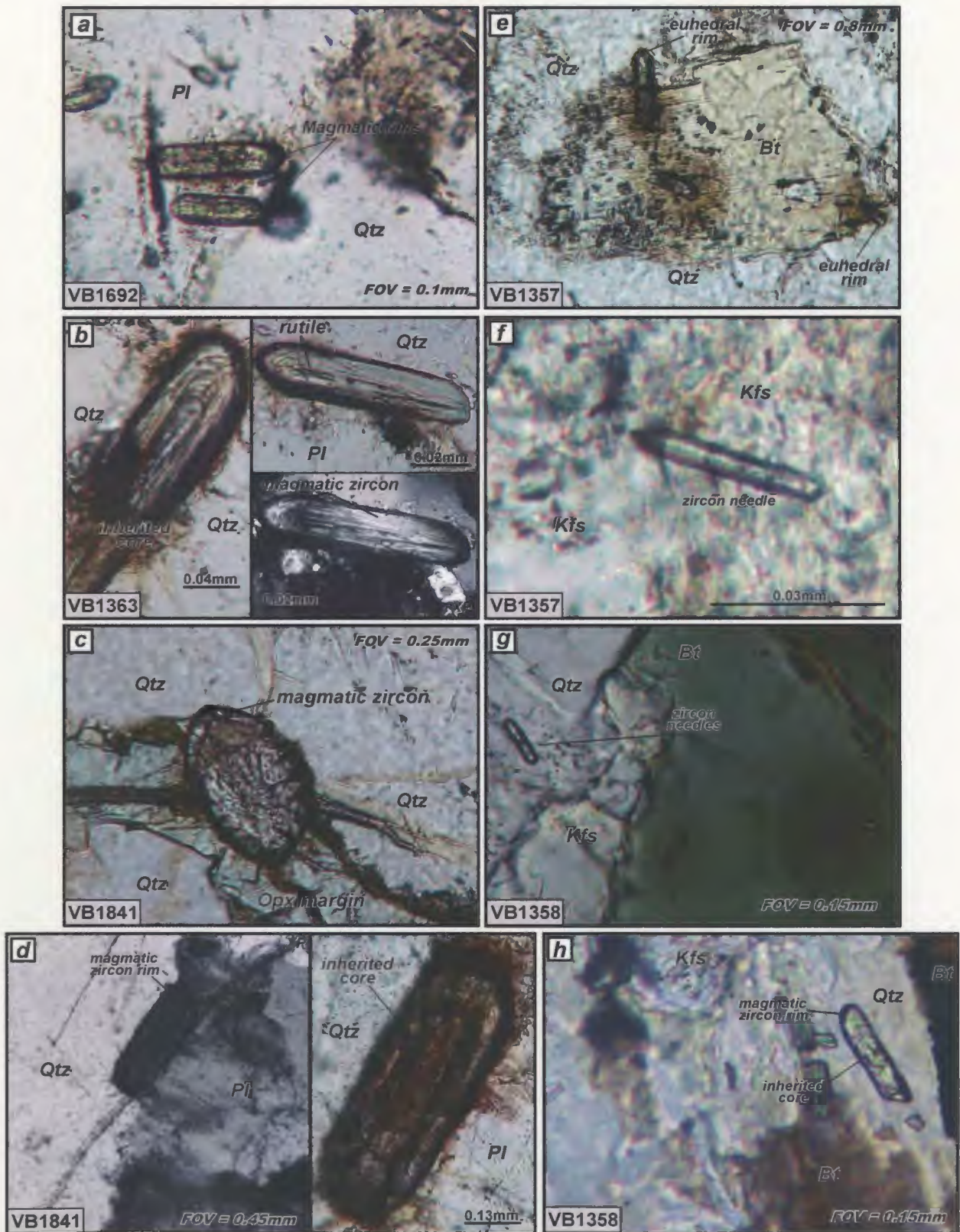


Figure 6.5: Caption see opposite

Figure 6.5: Petrographic relationships between zircon and host minerals. Field of view indicated. *(i)* Large zircon with inherited core and magmatic rim at Bt-Qtz-Crd grain boundary, VB160. *(j)* Cojoined quartz grains in quartz grain margin, VB160. *(k)* Zircon needle associated with interstitial growth of quartz, PVB9. *(l)* Zircon grain with inherited core and small rim at Bt-Qtz grain boundary. *(m)* Large zircon grain at Qtz-Pl_Kfs grain boundary with distinct inherited core, VB1688. *(n)* Blocky zircon exhibit three distinct phases of zircon growth and associated with biotite breakdown texture, VB1688. *(o)* Irregular zircon prism with magmatic tip occurring and cordierite grain margin (altered), VB161. *(p)* Zircon grain at Qtz – kfs grain boundary, VB161.

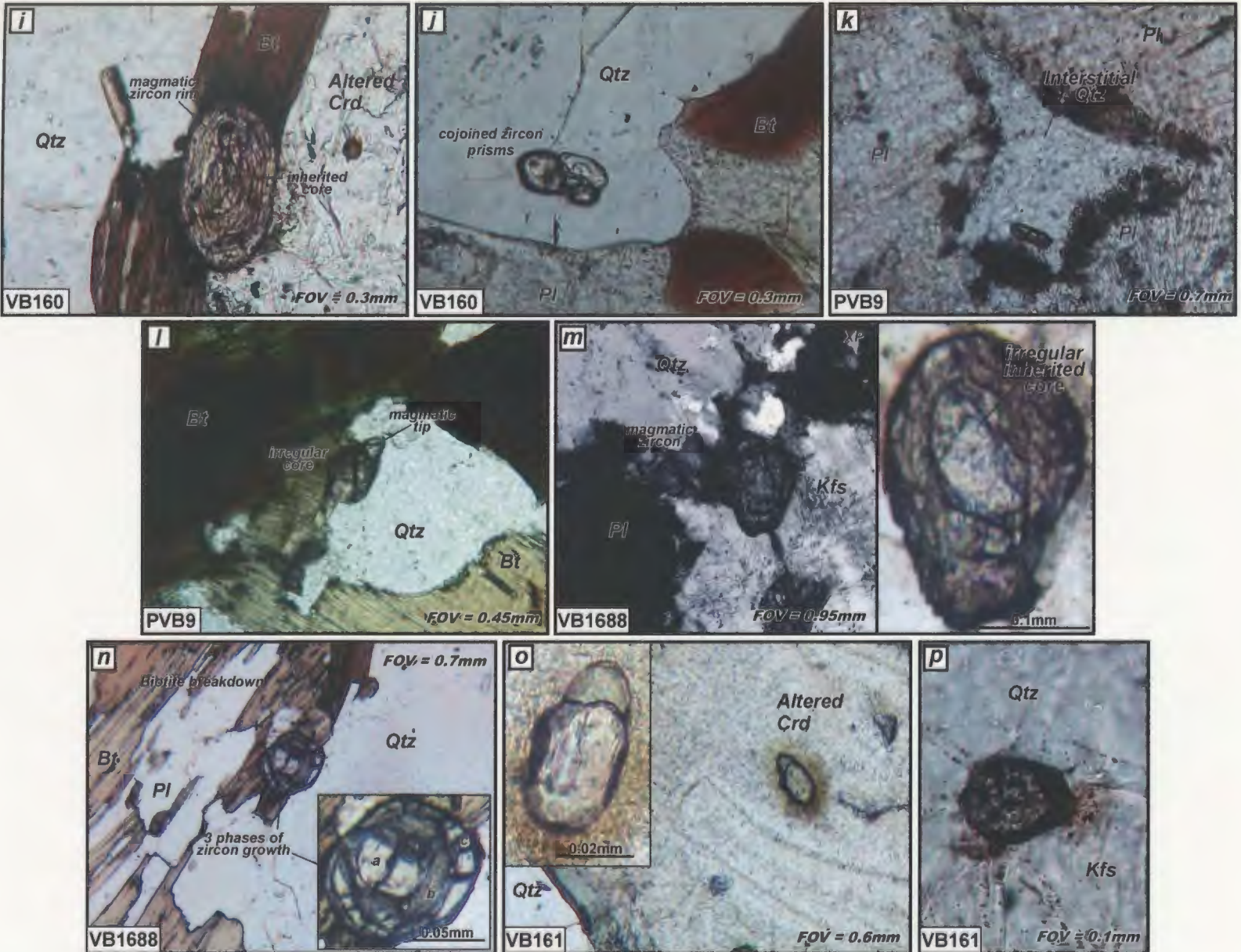


Figure 6.5: Caption see opposite

calculated individual maximum and average maximum temperatures is reported in Tables 6.3 and 6.4 for metaluminous and peraluminous suites, respectively. Further detail of the data summarized in Tables 6.3 and 6.4 is provided in Appendix J. Additional information on magma chemistry is available in Bennett et al. (accepted; Chapter 4). M values determined for magmas are plotted against Zr concentration and compared to the experimental zircon solubility results of Watson and Harrison (1983) in Fig. 6.6. In order to apply the thermometer, samples must plot within the range $M = 0.85$ to ≤ 2.0 .

Maximum temperature (T_{Zir}) variations within and between each magmatic group are illustrated graphically in Figs. 6.7a – c. Transparent grey boxes represent maximum average temperatures for the magmatic group. Magmas excluded from Fig. 6.7 because their alkalinity values lie outside the calibration range include a ca. 2674 Ma tonalite-diorite (VB165), the ca. 2610 Ma Mafic Intrusive Complexes (MIC), and a ca. 2589 Ma diorite of sanukitoid affinity (VJ375). Error estimates on all zircon saturation temperature determinations are considered to be ± 30 °C (B. Watson pers. comm). Corrected T_{Zir} values were determined for 9 samples using the method outlined above to remove inherited Zr from the total Zr budget (Fig. 6.8). A comparison of T_{Zir} uncorrected (maximum), T_{Zir} average (maximum), and T_{Zir} (corrected) values is illustrated in Fig. 6.9 and Table 6.4 summarizes the best estimate of crystallization temperature for each magmatic group. Petrographic observations indicate that zircon occurs as a late-stage precipitate in all samples studied so estimated T_{Zir} are considered to reflect magma emplacement temperatures (Table 6.2; Fig. 6.5). Additionally, complementary geochemical data demonstrate that the melts have not undergone significant segregation.

Table 6.3: Metaluminous samples - summary of age data, M values, Zr concentrations and zircon saturation temperatures. Temperature uncertainties are $\pm 30^\circ\text{C}$. Temperatures presented graphically in Figure 6.7.

Sample		Age (Ma)	^(a) M	Zr total (ppm)	^(b) T _{Zr} (max°C)	Data Source
Group 1 Magmas						
<i>Banting Equivalent TTG Suite</i>						
VB165B	Tonalite - Diorite	~2674	2.18	126	^(d) n.b. 713	^(c) Bennett et al. (submitted)
FV1806	Felsic volcanic	~2674	1.62	220	797	Bennett et al. (submitted)
Ru-1	Felsic Magma		1.47	176	788	^(e) Cousens & Alcazar
Ru-2	Felsic Magma		1.58	165	775	Cousens & Alcazar
Average					786	
<i>Banting Equivalent Depleted TTG Suite</i>						
Sn-1	Felsic tuff	~2658	1.46	99	741	Cousens & Alcazar
Sn-2	Felsic dyke		1.47	84	728	Cousens & Alcazar
VB1692	Granodiorite	~ 2654	1.35	154	787	Bennett et al. (submitted)
Average					752	
Group 2 Magmas						
<i>Disco Intrusive Suite (crustal differentiates of TTG)</i>						
VB1363	Granodiorite	~2635	1.34	268	837	Bennett et al. (submitted)
VB1356			1.49	226	810	Bennett et al. (submitted)
PVB29	Granite		1.52	170	782	Bennett et al. (submitted)
FL28			1.49	151	774	Perks (1997)
FL2A			1.35	156	787	Perks (1997)
FL98			1.54	147	768	Perks (1997)
FL20A			1.62	93	726	Perks (1997)
FL84A			1.80	168	761	Perks (1997)
J0398			1.47	219	808	Yamashita et al. (1999)
Average					784	
<i>Mafic Intrusive Complex (Sanukitoid Magmas)</i>						
VB1359A	Monzogabbro	~2608	2.20	21	^(d) n.b. 593	Bennett et al. (submitted)
J-0391	quartz diorite	~2605	1.91	18	^(d) n.b. 598	Yamashita et al. (1999)
lo1027	Monzogabbro		2.06	189	^(d) n.b. 752	Ootes (2000)
Group 3 Magmas						
<i>Uppercrustal Biotite Granite Suite</i>						
VB1357	Granite	~2600	1.38	147	780	Bennett et al. (submitted)
lo1025			1.32	122	769	Ootes (2000)
lo1014'b			1.35	141	779	Ootes (2000)
Average					776	

Table 6.3: continued

Sample	Age (Ma)	^(a) M	Zr total (ppm)	^(b) T _{Zr} (max°C)	Data Source
Group 3 Magmas - continued					
<i>Biotite Granodiorite Suite</i>					
J-0400 Granite	~2593	1.43	274	833	Yamashita et al. (1999)
ML20A	~2590	1.43	172	790	Yamashita et al. (1999)
Average				811	
<i>Orthopyroxene Granite Suite</i>					
VB1841 Granite	~2600	1.32	75	728	Bennett et al. (submitted)
FL24		1.55	149	769	Perks (1997)
FL74		1.70	107	731	Perks (1997)
HBA-0505-93		1.37	484	894	Yamashita et al. (1999)
Average				781	
Group 4 Magmas					
<i>Sanukitoid Suite</i>					
VJ375 Diorite	~2589	2.19	346	^(d) n.b. 794	Bennett et al. (submitted)

Notes : (a) Molar Alkalinity ratio = [(Na + K + 2Ca)/Al.Si]; (b) Temperature estimate calculated from zircon saturation thermometer of Watson and Harrison (1983); (c) Geochemical data used to calculate M value and T_{Zr} from Bennett et al. (submitted; Chapter 4); (d) ^{n.b.}: T_{Zr} estimate unreliable, M value outside calibration range of Watson and Harrison (1983), refer to Fig 6.7; (e) unpublished data.

Table 6.4: Peraluminous samples - summary of age data, M values, Zr concentrations and calculated zircon saturation temperatures. Temperature uncertainties are $\pm 30\text{C}^\circ$.

Sample		Age (Ma)	^(a) M	Zr total (ppm)	^(b) T _{Zr} (max°C)	Data Source
Group 3 Magmas						
<i>Two Mica Granite Suite</i>						
VB 1358	Two mica granite	~2598	1.21	94	754	^(c) Bennett et al. (submitted)
VB1590	^(d) Diatexite (amphibolite)	~2600	1.33	143	781	^(e) Bennett
VB160	Diatexite (granulite)	~2600	0.70	161	841	Bennett
Average					792	
<i>Megacrystic Granite Suite</i>						
PVB 9		~2597	1.32	334	860	Bennett et al. (submitted)
VB1688		~2598	1.26	71	728	Bennett et al. (submitted)
VB 1848			1.36	392	873	Bennett et al. (submitted)
J-0397			1.25	224	828	Yamashita et al. (1999)
FL96			1.52	257	819	Perks (1997)
Average					822	
Mid-crustal Average ^(f)					840	
Group 4 Magmas						
<i>Cordierite Leucogranite Suite</i>						
VB 161		~2585	1.10	52	716	Bennett et al. (submitted)
<i>Pegmatitic Granite Suite</i>						
VB 1864	Pegmatite Dyke	~2585	1.15	18	639	Bennett et al. (submitted)
VB 1229A	Pegmatite Dyke	~2585	1.09	34	684	Bennett et al. (submitted)
VB1886	Pegmatite Dyke		1.32	42	686	Bennett
VB1697	Pegmatite Dyke		1.05	8	590	Bennett
Average					650	

Notes: (a) Molar Alkalinity ratio = [(Na + K + 2Ca)/Al.Si]; (b) Temperature estimate calculated from zircon saturation thermometer of Watson and Harrison (1983); (c) Geochemical data used to calculate M value and T_{Zr} from Bennett et al. (submitted; Chapter 4); (d) Diatexite – metasedimentary diatexite with geochemical affinity to two mica granite; (e) unpublished data from Snare River terrane used to calculate temperature. (f) undisturbed samples used to calculate average value.

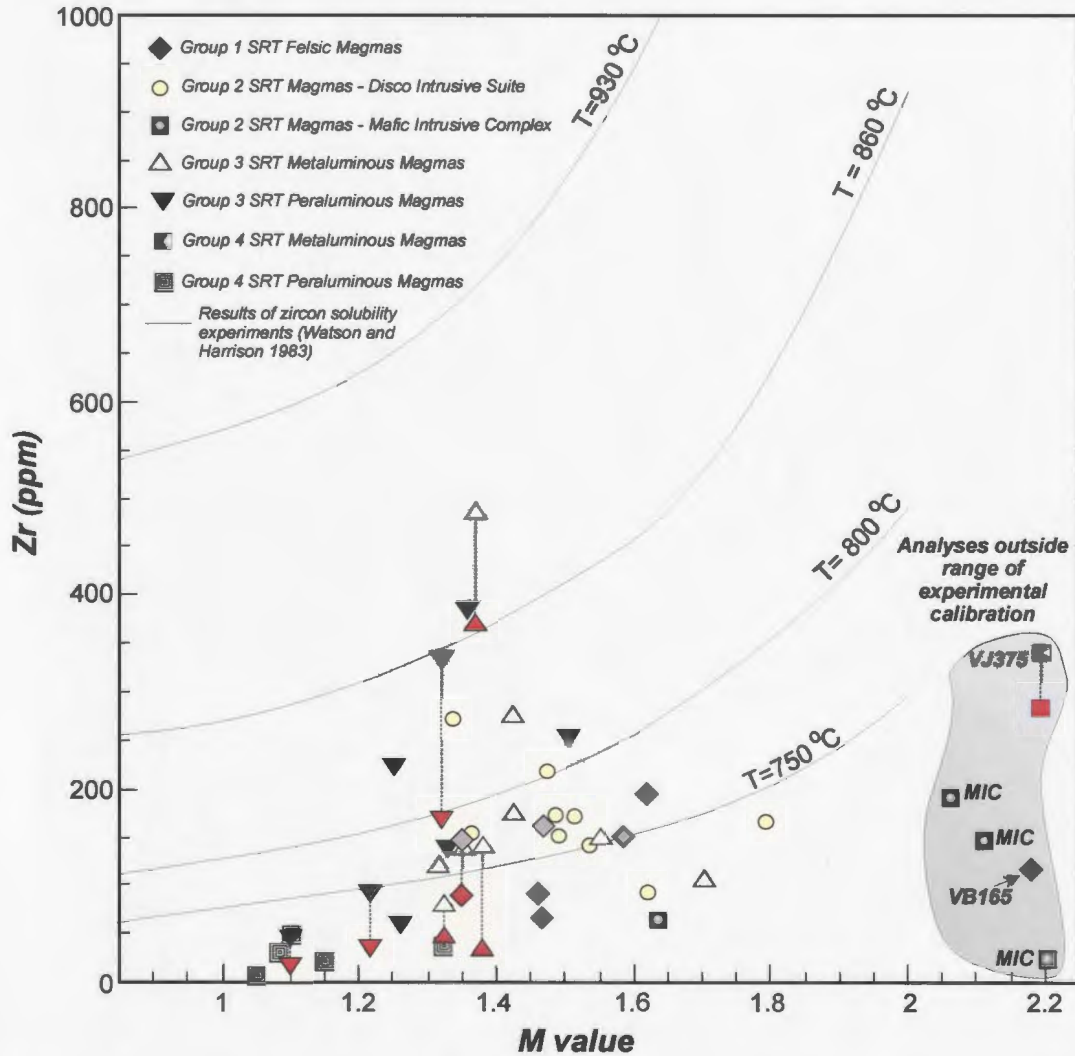


Figure 6.6: Zr vs M value plot with experimental zircon solubility curves plotted on for reference (after Watson and Harrison 1983). Diagram illustrates the range of M values for samples examined in this study and defines samples for which the zircon saturation thermometer of Watson and Harrison (1983) cannot be applied (grey shaded area). Also shown in red are corrected Zr abundances (ppm) for 8 samples where the proportions of magmatic and inherited zircon could be estimated from BSE image datasets.

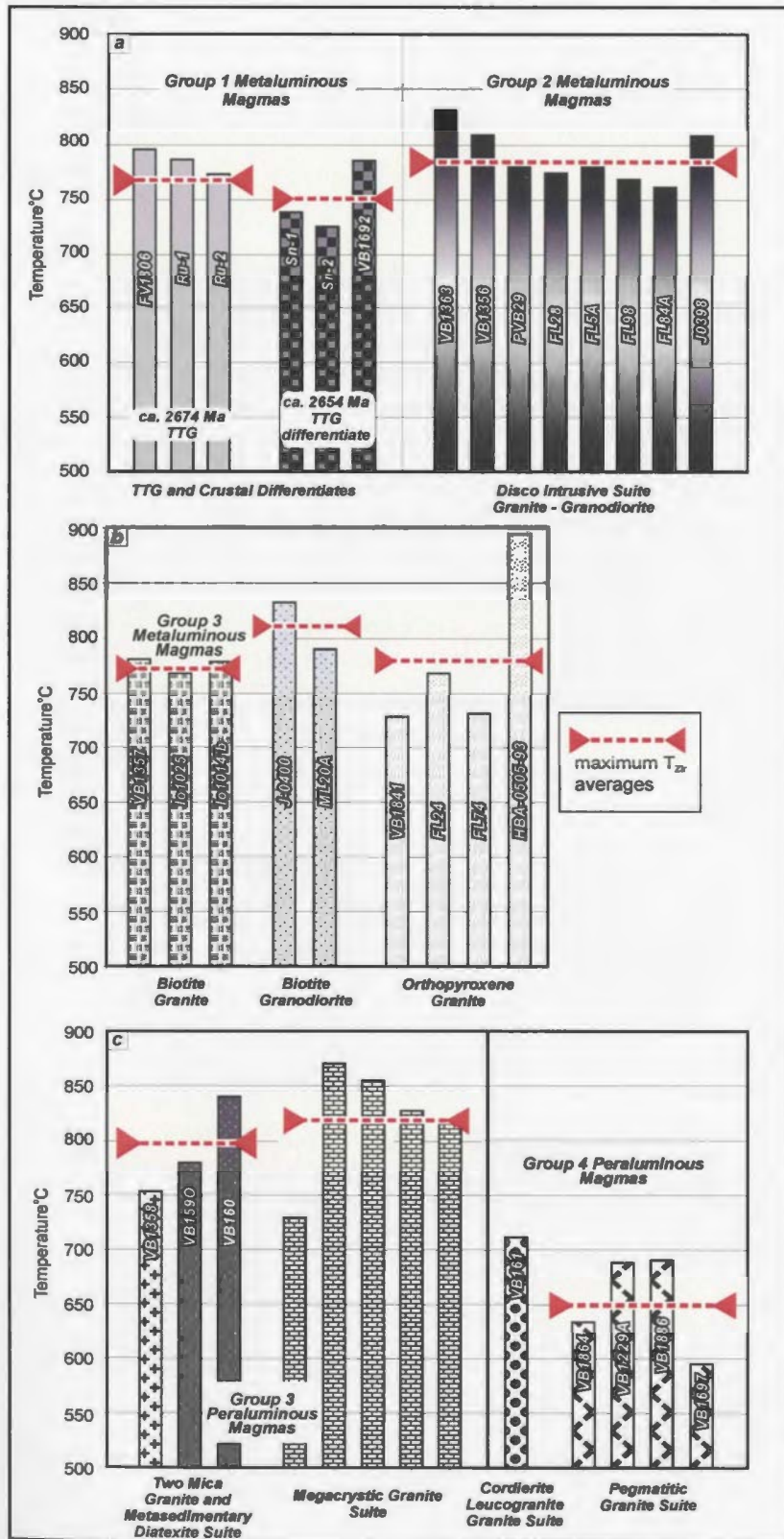


Figure 6.7: Temperature histograms illustrating zircon saturation estimates of zircon saturation temperatures for metaluminous and peraluminous samples. Data presented in Tables 3 and 4. Transparent grey shaded box superimposed on individual samples represents average temperature estimate for each group. Note the M values of samples VB165 and VJ375 lie outside the calibration range defined by Watson and Harrison (1983) and hence the temperature estimates are considered invalid. Errors for each estimate are $\pm 30^{\circ}\text{C}$ (B. Watson pers. comm) (a) Groups 1 and 2 metaluminous magmas. (b) Groups 3 and 4 metaluminous magmas. (c) Groups 3 and 4 peraluminous magmas.

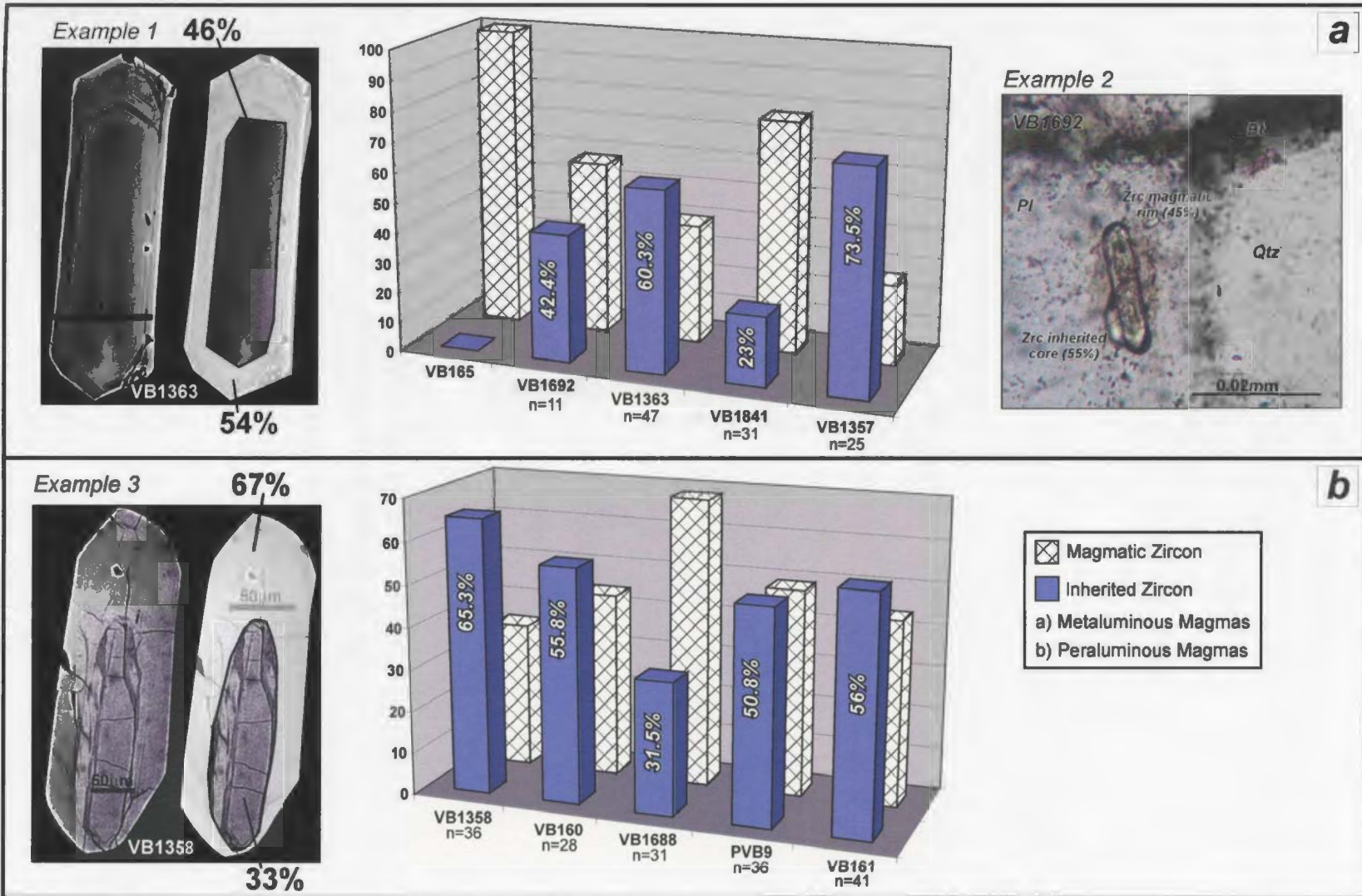


Figure 6.8: Diagram illustrating the proportion of inherited zircon to magmatic zircon within a) metaluminous and b) peraluminous samples selected for inherited zircon analysis. Note: n = the number of BSE images used to determine the average area of magmatic zircon compared to inherited zircon within each sample. Area of magmatic and inherited zircon was calculated using the digital BSE imaging software. Examples (VB1363 and VB1358) are given. Transmitted light images were used to estimate proportion of inheritance for VB1692 (example given).

Application of the method to all samples except the orthopyroxene granite suite was straightforward and yielded consistent results. The latter suite is discussed in more detail below.

6.5.1 Orthopyroxene granite suite

Calculated uncorrected individual maximum T_{Zir} values for the orthopyroxene granite suite vary widely from 728 to 894 °C (Table 6.5) with lowest and highest temperature estimates corresponding to the geochemically most (VB1841) and least (HBA-0505-93) fractionated melts of the suite (Bennett et al. accepted; Chapter 4). Analyses of 31 inherited grains in VB1841 indicate ~ 23% inherited zircon, which after removal from the total Zr budget corresponds to a corrected T_{Zir} value of 708 °C (Table 6.5; Fig. 6.9). In contrast, HBA-0505-93 yields uncorrected and corrected temperatures of 894 and 867 °C, respectively (assuming 23% inherited zircon as in VB1841). Assuming the inheritance correction is approximately accurate, two processes may account for the wide range of estimated temperature for the orthopyroxene granite suite. Firstly, the samples exhibit important trace-element anomalies, with VB1841, exhibiting strong enrichments in Sr, Eu and Zr, indicative of feldspar accumulation and early removal of Zr from the source region, whereas HBA-0505-93 displays strong Sr depletion and weak Eu enrichment (Table 6.2; Chapter 4). Consequently the disparity could be explained by melt fractionation processes, with the least fractionated sample having the highest temperature. Alternatively, it could be argued from the presence of dehydration reaction rims on mafic enclaves (Figs. 6.2l and m) and from the interpretation that orthopyroxene granites

Table 6.5: Comparison of maximum uncorrected, corrected and average zircon saturation temperatures for metaluminous and peraluminous samples with associated inherited zircon U-Pb age data presented in this study. Temperature uncertainties are $\pm 30\text{C}^\circ$.

Sample	^(a) M	Zr Total (ppm)	^(b) Inher %	Zr cryst (ppm)	T(max) °C	^(c) T _{corr} °C	^(d) Diff. °C	^(e) T _{Max} Average
Metaluminous Samples								
VB165B Tonalite	2.18	126	0 - <5	126	713	<i>n/a</i>	<i>n/a</i>	786
VB1692 Granodiorite	1.35	154	42.4	88.7	787	740	46	752
VB1363 Granodiorite	1.34	268	60.3	106	837	756	81	784
VB1357 Biotite granite	1.38	147	73.5	39	780	677	103	776
VB1841 Orthopyroxene granite	1.32	75	23	57	728	708	20	782
^(f) HBA-0505-93 Orthopyroxene granite	1.37	484	23	373	894	867	27	781
VJ375 Tonalite	2.19	346	18	283	794	<i>n/a</i>	<i>n/a</i>	<i>n/a</i>
Peraluminous Samples								
VB 1358 Two-mica Granite	1.21	94	65.3	33	754	675	79	792
VB 160 Diatexite	0.70	161	56	70.8	841	767	74	792
PVB 9 Megacrystic Granite	1.32	334	50.8	164	860	794	66	822
VB1688 Megacrystic Granite	1.26	71	31.5	48	728	699	29	822
^(g) Average(<i>undisturbed</i>) Megacrystic Granite	1.38	291	50.8	144	840	779	61	840
VB 161 Cordierite Granite	1.10	52	56	23	716	657	59	<i>n/a</i>

(a) Molar Alkalinity ratio = $[(\text{Na} + \text{K} + 2\text{Ca})/\text{Al.Si}]$; (b) Proportion of inherited zircon as determined from BSE images analyzed in study; (c) Corrected temperature estimate after removal of inherited Zr from total Zr budget; (d) Difference between temperature calculated with total Zr abundances to that determined from magmatic Zr concentrations only. (e) average maximum temperature for magmatic suite. (f) Least post-magmatically disturbed sample, corrected for Zr inheritance assuming inherited Zr concentration is similar to VB1841. (g) Average data for geochemically undisturbed mid-crustal megacrystic granite, corrected for Zr inheritance assuming a proportion similar to PVB9.

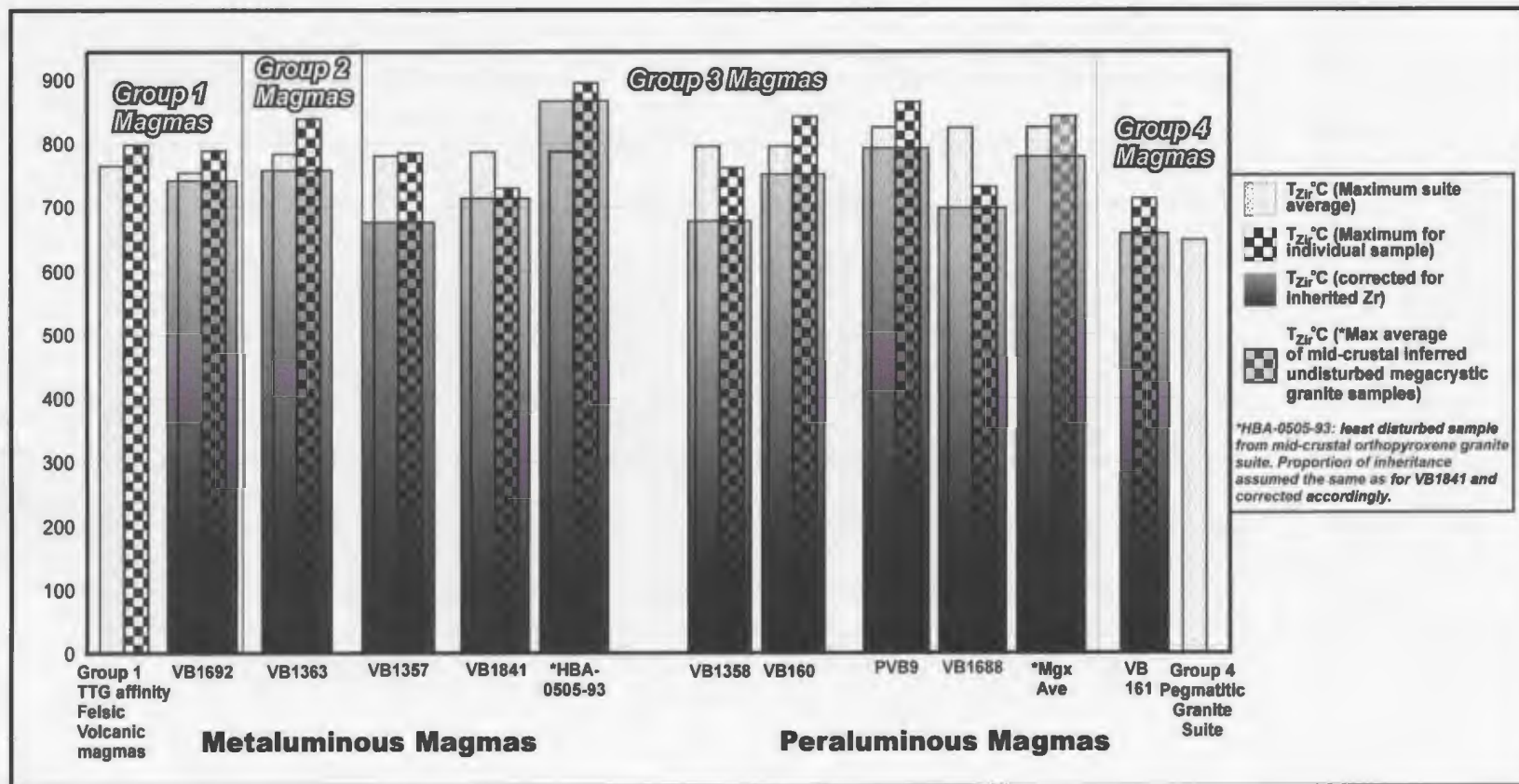


Figure 6.9: Temperature histogram illustrating difference between corrected and uncorrected zircon saturation temperatures for individual samples where inherited zircon data are available. Also plotted are maximum average T_{Zir} estimates for each suite. Uncorrected T_{Zir} average and maximum uncorrected individual T_{Zir} data for Group 1 volcanic magmas are shown. T_{Zir} datum for HBA-0505-93 is considered most representative for orthopyroxene granite suite. The average mid-crustal T_{Zir} estimate of megacrystic granite suite plotted in addition to samples PVB9 and VB1688.

commonly host CO₂-rich fluids at some stage of their petrogenesis (e.g., Newton 1992; Frost et al. 2000; Fig. 6k) that anhydrous conditions prevailed in this suite and therefore the criterion requiring a hydrous magma (>2 wt.% H₂O) cannot be unequivocally demonstrated. In addition, the M values determined for this suite may not be primary magmatic values as there is widespread evidence for post-magmatic metamorphism involving biotite dehydration melting by the reaction $Bt + Pl + Qtz = Opx + Kfs + L$ (Fig. 6.2j). In this case, the measured alkalinity ratio in the protolith will likely differ from the original magmatic M value due to the production and subsequent removal of an alkali-rich melt phase. Additionally, magmatic temperature estimates for orthopyroxene granites from other high-grade regions range from 845 to ≥ 1045 °C (e.g., Kilpatrick and Ellis 1992; Bédard 2003), so the corrected T_{Zir} estimates are considered to be minimum values at best. In their geochemical analysis of this suite, Bennett et al. (accepted; Chapter 4) suggested that sample HBA-0505-93 had undergone the least post-magmatic disturbance and therefore we use the individual maximum temperature calculated for this sample (T_{Zir} = 894 °C; Table 6.3, Fig 6.7b) as the best (uncorrected) estimate for the suite. Petrographic observations of several samples of the suite suggest early crystallization of orthopyroxene, as indicated by its grain shape and lack of zircon inclusions, followed by late-stage precipitation of remaining magmatic phases, including zircon (Fig. 6.5d). Hence, the T_{Zir} estimate is interpreted as the emplacement temperature for the suite.

6.6 Interpretation

In the discussion that follows we consider the implications of the magma crystallization temperatures (T_{Zir}) in the context of the contribution of Neoproterozoic magmatism to the metamorphic thermal budget in the Snare River terrane. The area is an excellent natural laboratory in which to assess the results as coeval upper- and mid-crustal magmatism are associated with a well exposed regional metamorphic gradient extending from greenschist to granulite facies, for which the prevailing P - T conditions are known (Table 6.1; Appendix I). The T_{Zir} dataset is evaluated in regard to the themes of secular variation in zircon saturation temperature and its relationship to magma petrogenesis and crustal evolution, and the role of orogenic magmatism during HT/LP metamorphism.

6.6.1 Secular variations in magma crystallization temperature

The ca. 90 M.y. period of crustal evolution of the Snare River terrane was punctuated by intermittent magmatism. Bennett et al. (accepted; Chapter 4) described a three-stage model of secular variation in magma geochemistry involving an initial long-lived stage (ca. 65 M.y.) of metaluminous crust-forming TTG magmatism, followed by a short period (ca. 15 M.y.) of bimodal metaluminous and peraluminous magmatism during orogenesis, and terminating with another short period (ca. 5 M.y.) of small-volume post-orogenic peraluminous magmatism. The T_{Zir} dataset exhibits three distinct stages (Fig. 6.10) that correspond to those based on geochemistry. The implications of this secular

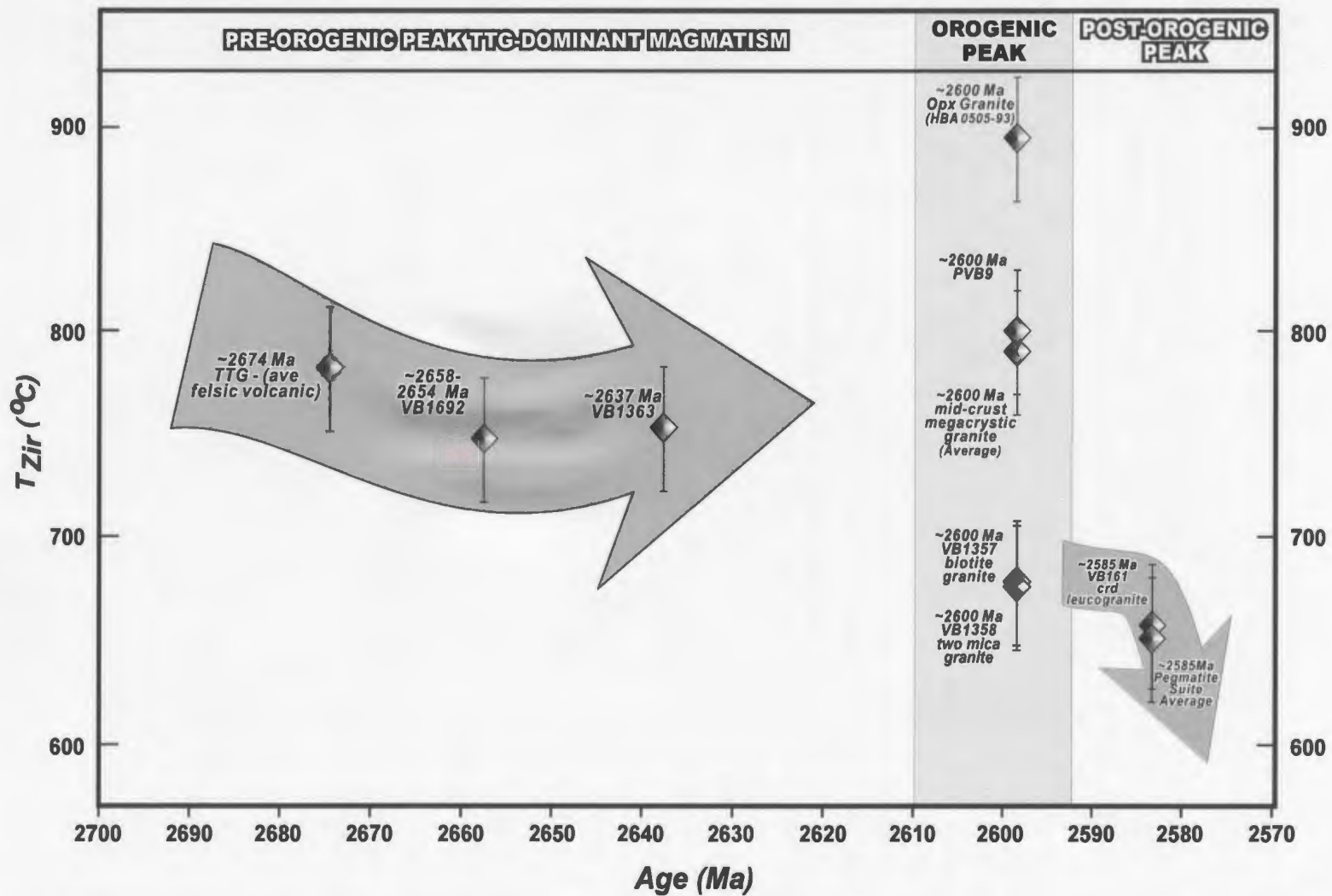


Figure 6.10: Temperature versus time diagram illustrating the evolution in zircon saturation temperatures throughout the evolution of the Snare River terrane. An initial TTG-dominant phase prevailed prior to the orogenic peak and was characterized by uniform melting temperatures (within error), suggesting that constancy of lower-crustal melting conditions. However, by the orogenic peak, diverse magma compositions formed in consequence to a variety of melting reactions and were emplaced throughout the thickened crustal column. Post-orogenic collapse occurred soon after the peak and resulted in mid-crustal uplift and low-temperature, low volume anatexic melts.

change in regard to petrogenesis and tectonism are addressed in more detail in the text that follows.

6.6.1.1 Crust-forming TTG magmatism (ca. 2674 – 2608 Ma)

Combined geochemical and inherited zircon datasets demonstrate that mid and upper crustal growth occurred principally through emplacement of TTG magmas (Bennett et al. accepted, Chapter 5). Successive TTG crustal melts exhibit similar geochemistry and ϵNd values over approximately 40 M.y. and zircon inheritance profiles of these magmas record intermittent growth of a mafic lower crustal reservoir during this interval. Collectively these data imply a stable tectonic setting and petrogenetic conditions for the formation of groups 1 and 2 magmas, a feature also reflected in their crystallization temperatures (Fig. 6.10). The corrected T_{Zir} values range from ca. 740-756 °C with individual maximum temperatures within error of these corrected values (Tables 6.3, 6.5; Figs. 6.7, 6.9). The accuracy of the thermal dataset is supported by experimental studies, in which TTG melting temperatures are constrained to 650-850 °C (Martin 1994; Rapp et al. 1991; Springer and Zeck 1997), and also by studies utilizing the Blundy and Holland (1990) plagioclase – hornblende thermometer on natural Archean TTG samples (e.g., 680-789 °C; Stone 2000; Bédard 2003).

The uncorrected and corrected temperature estimates for VB1363 demonstrate the overestimation of T_{Zir} when large quantities of inherited Zr are not accounted for (Table 6.5; Fig.6.9). Maximum uncorrected T_{Zir} estimates for this sample, although within the experimentally determined range for TTG genesis, are distinctly higher than those for

both older and coeval magmas (Fig. 6.7a). However, after removal of the inherited Zr component, the resultant T_{Zir} value is indistinguishable from the remainder of the TTG dataset.

6.6.1.2 Orogenic Magmatism (ca. 2608 – 2597 Ma)

The ca. 10 M.y. orogenic peak in the Snare River terrane (ca. 2608-2597 Ma) was accompanied by major changes in crustal architecture and composition as the older metaluminous, lower and mid crust was intercalated with the metasedimentary and volcano-plutonic upper crust during pervasive deformation. Perhaps the most significant change was the introduction of hydrous metasedimentary material into the mid crust, which permitted the onset of peraluminous magmatism. The diversity of orogenic magmatic processes is reflected in the coexistence of high- and low-temperature metaluminous and peraluminous melts.

Lower-crustal thermal heterogeneity

The metaluminous *biotite granite suite* is an upper crustal, TTG-affinity magma that was sourced from a mafic lower-crustal reservoir (Bennett et al. accepted, in prep). The corrected T_{Zir} estimate (677 °C; Table 6.5) is slightly lower than T_{Zir} estimates for Group 1 TTGs, but the discrepancy can be understood when melt fractionation is considered. Prominent LREE, Sr and Zr, and minor Eu enrichments (Table 6.2) indicate that its petrogenesis involved significant feldspar and zircon fractionation, hence the suite is interpreted as an evolved fractionate melt. Zr enrichment is consistent with the high

proportion of zircon inheritance in the suite (73.5 %; Fig. 6.9). Collectively, these constraints imply that melt segregation was important, and hence magma compositions do not reflect original source compositions and calculated T_{Zir} estimates do not reflect source melting temperatures. Additionally, significant heat loss during ascent may have occurred, particularly since ascent distances are surmised to have been 25-30 km and pluton sizes, based on exposed areal dimensions, are comparatively small. Although heat-loss amounts and original melting temperatures are unconstrained, broad geochemical and Nd isotopic similarities to older TTGs suggests that ambient lower-crustal melting temperatures in the range of 700-800 °C may be realistic for the biotite granite suite.

Petrogenesis of the mid-crustal orthopyroxene granite suite involved both lower-crustal melting and crustal assimilation. The T_{Zir} estimates are greater than those of the coeval upper-crustal biotite granite suite. Maximum temperatures indicate emplacement conditions in excess of 850 °C, implying hotter ambient temperatures in the lower-crustal source. The occurrence of coeval high- and low-temperature metaluminous magmas indicates thermal heterogeneity in the lower-crust during orogenesis. Furthermore, genesis of abundant orthopyroxene granite requires perturbation of the thermal regime that prevailed during TTG magmatism.

Coeval mid-crustal muscovite and biotite dehydration melting

Geochemical and inherited zircon data indicate petrogenesis of the voluminous two-mica granite suite from predominantly metasedimentary protoliths. Dehydration melting of biotite-bearing metapelitic rocks, which typically takes place from 700-850 °C

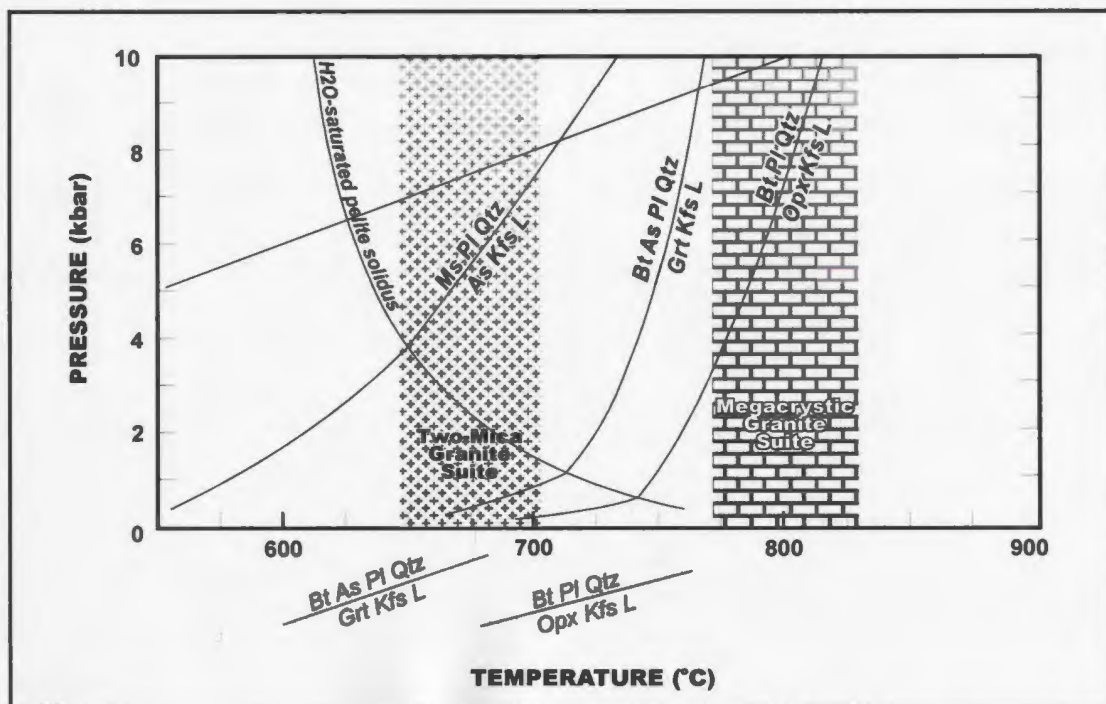


Figure 6.11: Pressure-Temperature diagram showing major dehydration melting reactions for pelitic rocks and the calculated T estimates for two-mica and megacrystic granite suites. The diagram implies petrogenesis of the two-mica and megacrystic granite suites principally involved dehydration melting of muscovite and biotite, respectively. Modified after Le Breton and Thompson (1988), Clemens and Wall (1981) and Clemens (1984). T estimates are interpreted as source melting temperatures. Refer to text for details.

(Clemens and Vielzeuf 1987; Vielzeuf and Montel 1994; Fig. 6.11), was inferred by Bennett et al. (accepted) to be the principal melt-forming reaction. If this was the case, melting temperatures must have been greater than the T_{Zir} estimate of 675 °C. Two mechanisms that could have lowered T_{Zir} are a reduced initial melting temperature due to melt fractionation and heat loss during magma ascent. However, neither seems to be viable in this case. With respect to fractionation, the magma geochemistry is similar to the most likely sources, amphibolite-facies metaturbidite and metasedimentary diatexite (Bennett et al. accepted), suggesting melt segregation was not significant. Furthermore, Miller et al. (2003) indicated that for inheritance-rich plutons (the two-mica granite contains 65.3 % inherited zircon; Fig. 6.8b), T_{Zir} values represent a maximum estimate of protolith melting temperatures. The other possible mechanism, heat loss during ascent, is inferred to have been minimal due to both the vast size of the unit (which occupies most of Bigspruce subdomain; Fig 1), and the fact that it is underlain by higher temperature upper-amphibolite- to granulite-facies rocks (700 to \geq 900 °C; Table 6.1). Therefore the T_{Zir} estimate for the two-mica granite suite is considered to represent both the initial source melting temperature and the temperature of crystallization. At such low temperatures (<700 °C), biotite dehydration melting is unlikely to be extensive and dehydration melting of muscovite is more plausible (Fig. 6.11). However, generation of large melt volumes by muscovite dehydration melting is problematic as, for typical pelite compositions, this reaction yields only a limited quantity of melt that is commonly not liberated from the source region, but rather results in extensive migmatite domains (Clemens and Vielzeuf 1987; Brown 2001). Thus, for muscovite dehydration to be the

primary melt-forming reaction, specific tectonic conditions must have prevailed that maintained muscovite stability at depth. Ingress of external H₂O-rich fluids into the mid crust provides a plausible method to achieve these conditions and also to generate appreciable quantities of water-saturated melt (e.g., Clemens and Vielzeuf 1987; Miller et al. 2003). The deformation history of the Snare River terrane indicates that transport of metaturbidite from the hydrous near-surface environment to the mid crust occurred during D2 prior to formation and emplacement of the two-mica granite suite (Chapter 3). In this setting, fertile muscovite-bearing metasedimentary material could have been transported into the mid crust, with thrust faults providing pathways for the introduction of H₂O-rich fluids, thereby depressing the solidus temperature of the source rocks and resulting in generation of the two-mica granite magma. In this model, melting would continue as long as muscovite, plagioclase and quartz remained and H₂O-rich fluids were delivered to the mid crust, with the voluminous size and homogeneity of the two-mica granite suite suggesting that the process resulted in almost complete melting of the metaturbidite protolith.

Field and U-Pb data for the megacrystic granite suite indicate it was emplaced as sheets concurrently into the mid crust and lowermost levels of the upper crust. Geochemical, Sm-Nd isotopic and inherited zircon data indicate that the suite was derived from metasedimentary and mafic protoliths (Bennett et al. accepted, in prep). Trace element data lack evidence of feldspar fractionation (i.e., no Ba, Sr and Eu anomalies) and Zr enrichments reflect the partitioning of Zr into the melt from a Zr-saturated source, consistent with the high proportions of inheritance observed (Fig. 6.8b).

The deepest intrusions (ca. 26 km; 779 °C) yield corrected T_{Zir} estimates that are within error of those for the highest level intrusions (ca. 14 km; 794 °C), demonstrating adiabatic magma ascent through ca. 12 km of crust and implying that the zircon saturation temperatures constrain both protolith melting and emplacement temperature.

Furthermore, the temperature is consistent with melt generation by biotite dehydration of the metasedimentary source component (700-850°C; Clemens and Vielzeuf 1987; Fig. 6.11) and/or by biotite and amphibole dehydration melting of a mafic source (850-925 °C; Skjerlie and Johnston 1996). Subsequent mixing and/or assimilation between the two components would result in the temperatures recorded for the suite.

The occurrence of both low- and high-temperature peraluminous magmatic suites derived from mid-crustal protoliths has significant implications with regard to crustal fertility. Specifically, the T_{Zir} data demonstrate that the orogenic mid crust of the Snare River terrane was characterized by high a_{H_2O} regions that were the sites of low-temperature melting, and low a_{H_2O} domains where high temperature melting prevailed.

6.6.1.3 Post-Orogenic Magmatism (ca. 2585 Ma)

The voluminous plutonism that accompanied orogenesis was followed by a brief, terminal magmatic episode at ca. 2589-2585 Ma during which small intrusions of cordierite leucogranite and pegmatitic granite were emplaced. Intrusions of the cordierite leucogranite suite occur in the Ghost subdomain, where they truncate peak metamorphic assemblages. Geochemical and inherited zircon data indicate genesis from metapelitic protoliths and Ba, Sr, Eu and Zr enrichments indicate significant feldspar and zircon

accumulation. The suite is interpreted as a product of crustal anatexis (Bennett et al. accepted, in prep.) and the T_{Zir} estimate (657°C) constrains emplacement temperature. During the orogenic stage, low temperature magmas were emplaced only at upper-crustal levels, so intrusion of the low-temperature cordierite leucogranite suite into the orogenic mid crust suggests either cooling and/or exhumation of the Ghost subdomain to upper-crustal levels. Uplift is supported by the widespread occurrence of cordierite-spinel±sillimanite±biotite symplectite formed at the expense of garnet in adjacent metasedimentary rocks.

Emplacement of post-tectonic pegmatitic granite was unrelated to crustal level as defined by the metamorphic field gradient. Geochemical data indicate derivation by anatexis of metasedimentary protoliths (Bennett et al. accepted) and T_{Zir} estimates (ca. 590-686 °C) indicate an analogous low temperature history to the cordierite leucogranite. Collectively, these data reveal that major changes in terms of magmatic style, volume, and thermal conditions had occurred by 15 M. y. after the orogenic peak.

6.6.2 Orogenic magmatism, HT/LP metamorphism and thermal structure

The prevalence of HT/LP metamorphic belts in Neoproterozoic crust has been attributed to the higher geothermal gradients characteristic of that era (Fyfe 1973; Condie 1984). However, while the geothermal regime may have been a contributing factor, it is now well established from detailed metamorphic studies (e.g., Harley 1989; Percival 1994) that the HT/LP conditions were transient and significantly perturbed above steady-state geotherms. Typically the underlying mechanism controlling elevated geothermal

gradients is advective heat transfer related to magmatism within or external to the crust. For this to be so, metamorphism must accompany magmatism as it proceeds through the crustal column (Wells 1980; Lux et al. 1986).

In this section we address these thermal considerations and evaluate connections between coeval magmatism and metamorphism by integrating zircon saturation temperatures for upper- and mid-crustal orogenic magmas with field and metamorphic constraints from metapelitic rocks. Exposure of crustal depths exceeding 22 km in the Snare River terrane provides a rare opportunity to investigate depth-dependent changes between magmatism and metamorphism and permits consideration of first-order crustal-scale variations in orogenic heat distribution.

6.6.2.1 Upper-crustal magmatism – buffering a pre-existing thermal regime?

The two-mica granite and biotite granite suites intruded the upper crust of the Snare River terrane at the ca. 2600 Ma orogenic peak (Fig. 6.1) and both suites are characterized by similar emplacement levels and crystallization temperatures (ca. 7-14 km; ca. 675 °C). The highest level intrusions are post-deformational and straddle the *Crd* (1) and *Sil + Melt* metamorphic zones (Figs. 6.1, 6.3) for which estimated conditions range between $P = 2-3$ kbar, $T = 550-570$ °C and $P = 3-4$ kbar, $T = 650-670$ °C respectively (Table 6.1; Appendix I). The relationship between the geometry of the isograds and the margins of exposed plutons can be examined in Fig. 6.1. At some locations, contact metamorphic effects occur and isograds are subparallel to pluton boundaries (e.g., eastern Labrish Lake); however elsewhere, the distribution of lower-

and mid-amphibolite-facies isograds are unrelated to plutonism. This is evident in the Kwejinne Lake supracrustal belt, where no contact metamorphic aureoles are recognized, granites transect metamorphic zones that are unrelated to pluton margins, and metaturbidite enclaves in two-mica granite show no evidence for metamorphic reaction with the surrounding granite (Figs. 6.1 and 6.2b, c). These observations imply metamorphism predated pluton emplacement at this crustal level.

Collectively, the zircon saturation data and metamorphic evidence indicate that the principal thermal role of these magmas was to buffer pre-existing metamorphic heat in the upper crust. Additionally, syn- and post-deformational growth of cordierite porphyroblasts in the *Crd (1)* metamorphic zone (Chapter 3) is compatible with prolonged mineral growth that may have been in part a result of locally advected magmatic heat adjacent to late D2 plutons. Despite the limited thermal role of upper crustal plutonism, crystallization of the two granite suites appears to have liberated significant quantities of H₂O that served to reduce the pelite solidus in surrounding rocks and induce appreciable local melting in proximity to pluton and dyke boundaries (Fig. 6.2a).

6.6.2.2 Mid-crustal pluton-driven metamorphism

The mid-crustal megacrystic and orthopyroxene granite suites appear to have played a fundamental role in the HT/LP metamorphism of the Snare River terrane based on information from the transition zone underlying the Kwejinne Lake supracrustal belt. In this area, the *Crd (2) + Melt* and *Grt + Kfs* isograds are parallel and in close proximity

to the structurally highest sheets of megacrystic and orthopyroxene granite, respectively (Figs. 6.1 and 6.3), implying that they formed as a result of post-emplacement heat and/or fluid transport associated with these magmas. Integration of zircon saturation data with the field and metamorphic constraints also supports pluton-driven mid-crustal metamorphism at the orogenic peak.

Intrusions of megacrystic granite underlie the *Crd (2) + Melt* zone in the Kwejinne Lake supracrustal belt and the *Crd (2) + Melt – In* isograd is parallel to the upper contacts of megacrystic granite sheets (Figs. 6.1, 6.2d). Metamorphic assemblages, reactions and textural evidence all support fluid-present metamorphic conditions (Appendix I), consistent with voluminous metatexite and diatexite in this zone (Fig. 6.2g). Peak metamorphic conditions in the *Crd (2) + Melt* zone ($P = 4$ kbar, $T = 730$ °C) suggest an approximately isobaric temperature increase from the adjacent *Sil + Melt* zone (Fig. 6.12; Appendix I). These metamorphic observations are consistent with emplacement of megacrystic granite beneath the *Crd (2) + Melt* zone, followed by release of magmatic heat into the overlying rocks. Zircon saturation temperatures for the megacrystic granite suite ($T_{\text{Zir}} = 779\text{-}794$ °C) are compatible with peak metamorphic conditions in the adjacent turbidite sequence ($T_{\text{peak}} = \text{ca. } 730$ °C; Appendix I). Garnet-bearing metaturbidite enclaves in megacrystic granite sheets reflect the higher magmatic temperatures within the plutons. Textural evidence (Fig. 6.2e, f) demonstrates that garnet and melt in the enclaves formed at the expense of biotite and cordierite by the H_2O -present reaction $\text{Crd} + \text{Bt} + \text{Qtz} + \text{H}_2\text{O} = \text{Grt} + \text{Melt}$, which occurs at temperatures slightly less than 800 °C (Vielzeuf and Holloway 1988; Appendix I), compatible with the

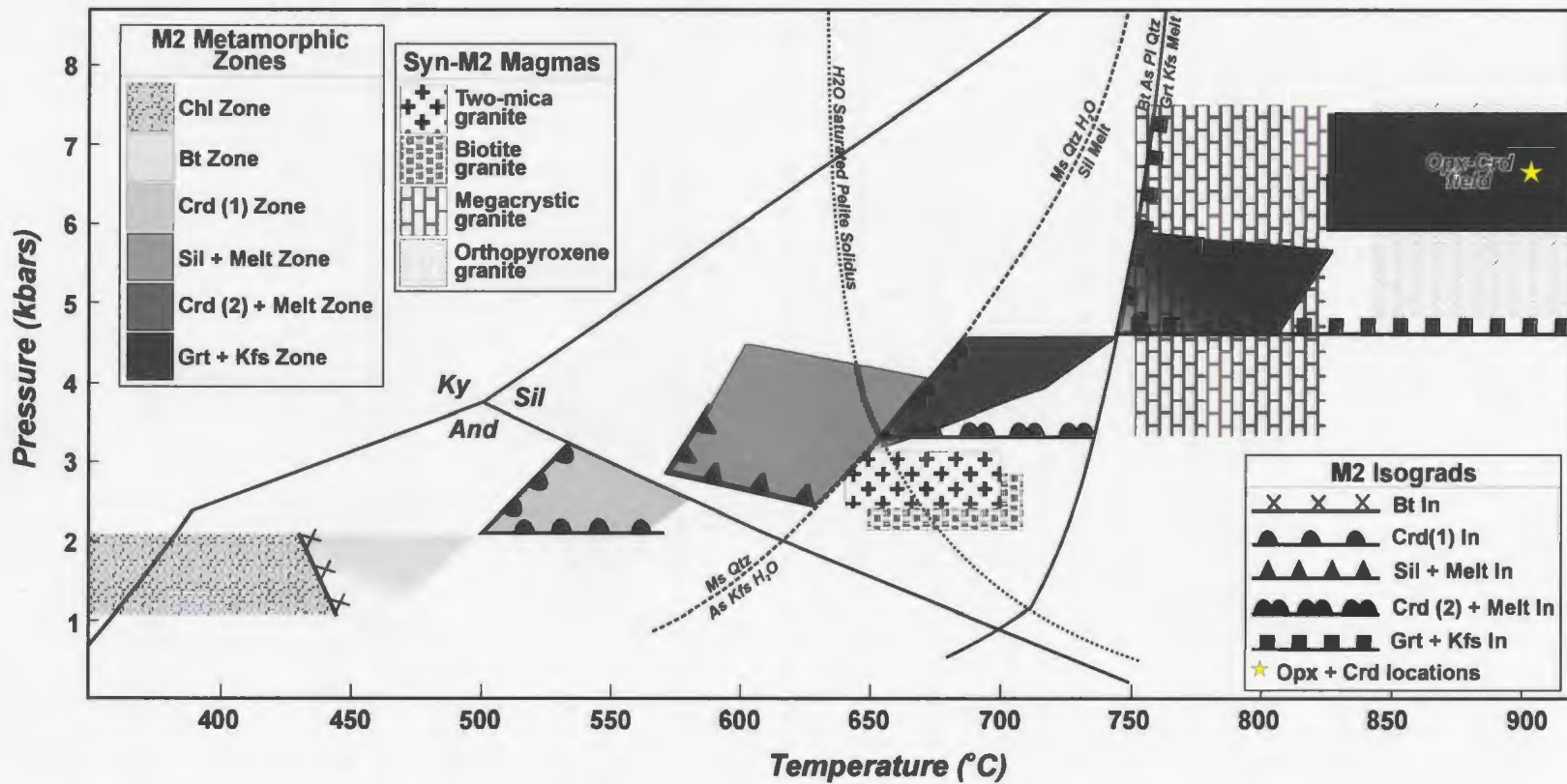


Figure 6.12: Comparison of P-T constraints for each metamorphic zone in the Snare River terrane and upper- and mid-crustal orogenic magmatic suites. Pressure constraints for orogenic magmas reflect emplacement levels with respect to ambient metamorphic grade. Temperature estimates are interpreted as emplacement temperatures. Conditions of greenschist-facies metamorphism are poorly constrained. Diagram illustrates the association between the *Crd (2) + Melt* and *Grt + Kfs* isograds with temperatures and emplacement levels of the megacrystic and orthopyroxene granite suites, respectively. Isograd reactions are given in Appendix I.

zircon saturation temperatures for the megacrystic granite suite. The integrated datasets imply this suite was a significant source of heat and H₂O during formation of the overlying *Crd (2) + Melt* zone, in which extensive fluid-present melting occurred.

The orthopyroxene granite suite played an analogous role at higher metamorphic grade and emplacement of this suite can be linked to the onset of granulite-facies conditions in adjacent metasedimentary turbidites. The *Grt + Kfs* isograd occurs immediately above and parallel to exposed contacts of the orthopyroxene granite suite (Fig. 6.1), but in contrast to the fluid-present metamorphic conditions of the *Crd (2) + Melt* zone, predominantly anhydrous conditions prevailed in this zone. Assemblages and reactions textures observed in samples close to the *Grt + Kfs* isograd indicate initial garnet formation occurred by biotite dehydration melting, i.e., $Bt + Sil + Pl + Qtz = Grt + Kfs + Melt$ (Fig. 6.2n; Appendix I). Consequently, this isograd marks the transition between hydrous upper-crustal and anhydrous mid-crustal conditions. Maximum zircon saturation temperatures ($T_{Zir} = 850-900$ °C) are consistent with metamorphic observations (Fig. 6.12), and the close proximity of the *Grt + Kfs* isograd to the contacts of the intrusion suggests a steep thermal gradient. The assemblage *Grt-Crd-Kfs* appears 1-2 km from the *Grt + Kfs* isograd (Appendix I) and is interpreted to result from the modified biotite dehydration melting reaction: $Bt + Sil = Grt + Crd + Kfs + Melt$.

The onset of anhydrous assemblages also appears to relate to conditions prevailing in orthopyroxene granite suite. Metamorphic reactions involving biotite and

hornblende dehydration occur in mafic enclaves (Fig. 6.2j, m) and in the ca. 2637 Ma Disco intrusive suite, which is extensively intruded by the orthopyroxene granite (Fig. 6.2i), implying that these magmas were an important vehicle for heat transfer and reduction of the ambient $a_{\text{H}_2\text{O}}$. Similar reactions were observed in charnockite in the Ashuanipi Complex, Superior Province, where they were attributed to low $a_{\text{H}_2\text{O}}$ in the host magma (Percival 1994).

The case for pluton-driven, granulite-facies metamorphism at deeper crustal levels in the Ghost subdomain, where peak metamorphic temperatures are close to or exceed maximum uncorrected zircon saturation temperatures ($T = 845\text{-}920$ °C; Farquhar and Chacko 1996), is less convincing. Field and petrographic evidence in Forked Lake and Big Bird structural domes (Fig. 6.1) indicate that both the megacrystic and orthopyroxene granite suites experienced post-emplacment metamorphism. In the Big Bird structural dome, which is cored by a sheet of garnet-bearing megacrystic granite, an early phase of post-emplacment metamorphism in the outer margins of the sheet is indicated by an absence of primary magmatic textures and abundant metamorphic monazite, commonly overgrowing igneous zircon (Fig. 6.2h). However, in the central part of the sheet, garnet and biotite breakdown coincide with orthopyroxene formation (Fig. 6.2o), indicating a second phase of post-emplacment metamorphism affected the intrusion. At crustal levels above the orthopyroxene granite, megacrystic granite shows no evidence for prograde metamorphism, so the early phase of post-emplacment mid-crustal metamorphism may be attributed to heating induced by emplacement of the orthopyroxene granite suite. Metamorphism of the orthopyroxene granite suite primarily involved biotite dehydration

and orthopyroxene formation and is most evident around the Forked Lake dome (Figs. 6.1 and 6.2j, k). Post-emplacement metamorphism of this suite is significant as it implies ambient thermal conditions exceeded emplacement temperatures and it therefore delimits the lower depth at which pluton-driven metamorphism took place.

In summary, the megacrystic and orthopyroxene granite suites were important heat and/or fluid sources responsible for pluton-driven metamorphism in the mid-crust of the Snare River terrane. The *Crd* (2) + *Melt* isograd delimits the upper structural level at which this pluton-driven metamorphism took place, whereas the maximum lower limit occurs at the depth where these suites experienced post-emplacement metamorphism.

6.6.2.3 Orogenic thermal structure

Exposure of ~22 km of Neoproterozoic crust in the Snare River terrane permits assessment of depth-dependent variations in heat distribution associated with metamorphism and magmatism. To this end, we have constructed a crustal-scale thermal profile of the Snare orogen for peak orogenic conditions (Fig. 6.13). Four principal observations can be made from the profile. (1) A first-order thermal stratification of heat existed at the orogenic peak, with increasing temperature positively correlated with palaeodepth. (2) Contrasting fluid regimes occurred within the crust. At greenschist- and amphibolite-facies conditions (≤ 17 km), the crust was characterized by high $a_{\text{H}_2\text{O}}$, which exerted a profound control on the style of metamorphism and melting. The onset of granulite-facies conditions in Ghost subdomain at 17-26 km marked the transition to predominantly anhydrous crust. (3) Different modes of metamorphism occurred at

Figure 6.13: Schematic diagram illustrating the variation in ca. 2600 Ma orogenic magma temperature and ambient metamorphic grade with depth. Low-temperature upper-crustal granites intruded following establishment of greenschist- to amphibolite-facies metamorphic conditions (> 2600 Ma). These magmas primarily buffered upper-crustal heat and prolonged amphibolite facies conditions. Local ingress of H₂O resulted in depression of the pelite solidus and melting. The megacrystic granite suite intruded mid and upper mid-crustal levels. Heat and H₂O fluid released upon crystallization drove upper-amphibolite facies metamorphism (ca. 2600 Ma) and melting within the *Crd* (2) + *Melt* zone. At highest emplacement levels within in this zone, the suite was not affected by prograde metamorphic conditions, whereas in the Ghost subdomain it records evidence for post-emplacement metamorphism (post – 2600 Ma) related to the intrusion of the orthopyroxene granite suite and a subsequent event unrelated to orogenic magmatism. The high-temperature orthopyroxene granite suite is restricted to mid-crustal levels and correlates to the location of the *Grt* + *Kfs* isograd and the onset of anhydrous metamorphic conditions. The lowest emplacement levels exposed were affected by post-emplacement metamorphism. The thermal profile illustrates crustal-scale diachroneity of the orogenic HT-LP metamorphism. The oldest phase of metamorphism (ca. 2608 – 2600 Ma) occurred in the uppercrust and was overprinted by ca. 2600 Ma pluton-driven metamorphism that occurred in a 10km thick zone in the mid-crust. This, in turn was overprinted at the lowest exposed levels by a younger phase of the HT-LP metamorphic event. T_{Zir} data presented in the text and metamorphic P-T data provided in the appendix were integrated with field data to construct the profile. Temperature fluctuations represented graphically on diagram in the mid-crustal *Grt* + *Kfs* metamorphic zone reflect the variation in thermometric determinations across the Ghost subdomain (Chacko et al. 1995).

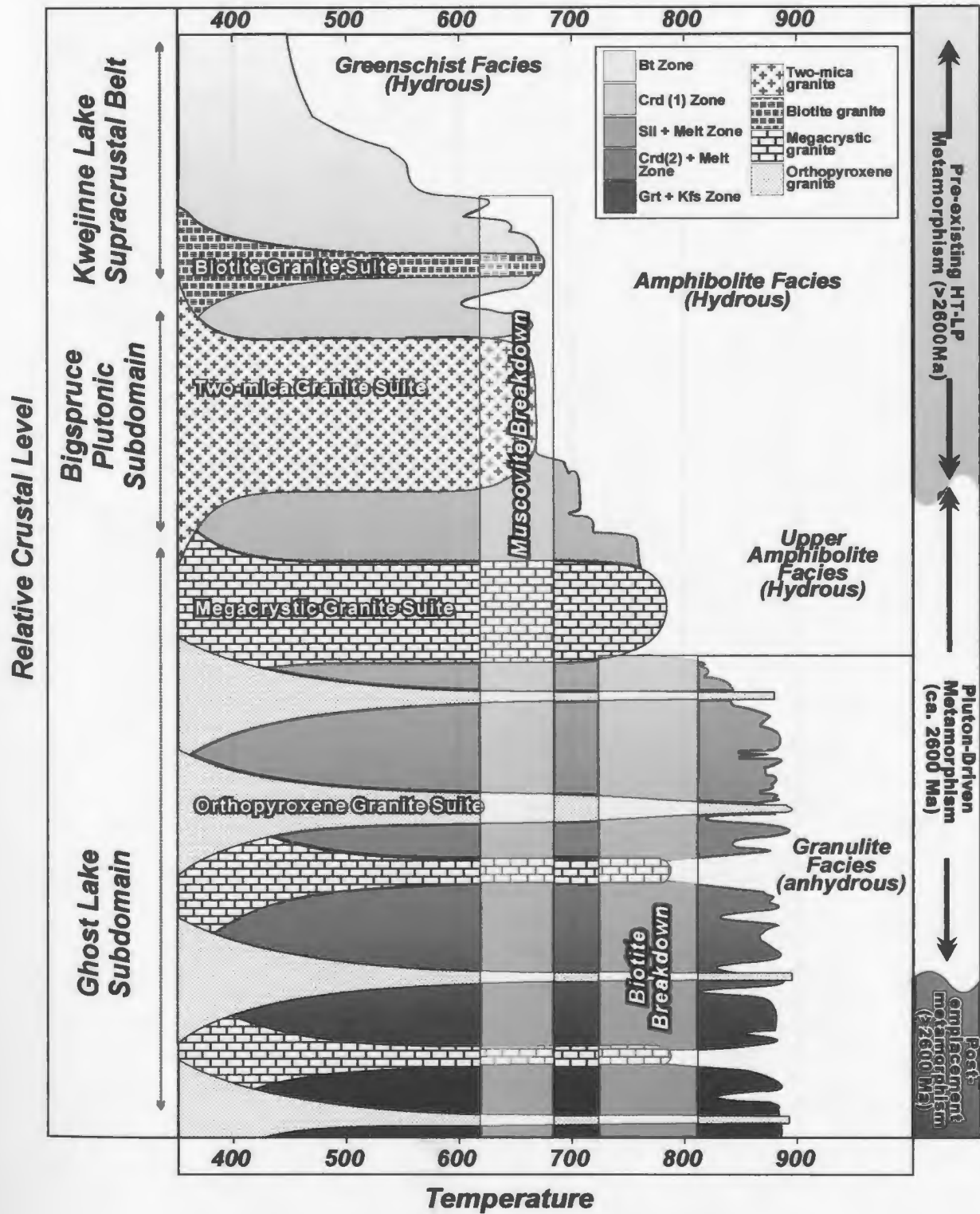


Figure 6.13: Caption see opposite

different crustal levels. Upper-crustal HT/LP metamorphism was buffered, but not driven by emplacement of low-temperature orogenic magmas. Local solidus depression due to release of H₂O from crystallizing magmas induced melting, but did not create prograde conditions. In contrast, at depths of ca. 17-26 km, heat from high temperature mid-crustal orogenic magmas was the driving force for upper-amphibolite and granulite-facies metamorphism. Below ca. 26 km, pluton-driven metamorphism was ineffective due to overprinting by a higher temperature thermal regime. Delineation of the role of pluton-driven metamorphism in the Snare River terrane affirms the role of magmatism as a major agent of heat transfer and HT/LP metamorphism in crust characterized by grossly perturbed geotherms, as previously suggested by others (e.g., Vernon 1990; Ashwal et al. 1992; Bethune et al. 1999; Brown 2001). (4) Metamorphism was diachronous on a crustal scale. However, as opposed to a series of discrete unrelated metamorphic episodes, the different phases of metamorphism are interpreted to reflect successive thermal waves of a metamorphic front. The earliest phase of metamorphism (i.e., the first thermal wave) is reflected in the HT/LP greenschist- and amphibolite-facies metamorphism in the upper crust. Overprinting by ca. 2600 Ma orogenic magmas demarcates the onset of a mid-crustal pluton-driven metamorphism. Finally, post-emplacement metamorphism of mid-crustal magmas is considered to represent a third thermal wave.

Collectively, these findings illustrate the dynamic nature of orogenesis in the Snare River terrane. The cause of the initial perturbation of the steady-state geotherm that prevailed during TTG magmatism remains unconstrained, but for peak *P-T* conditions in the andalusite and sillimanite fields, mantle heat flux and crustal radiogenic heat

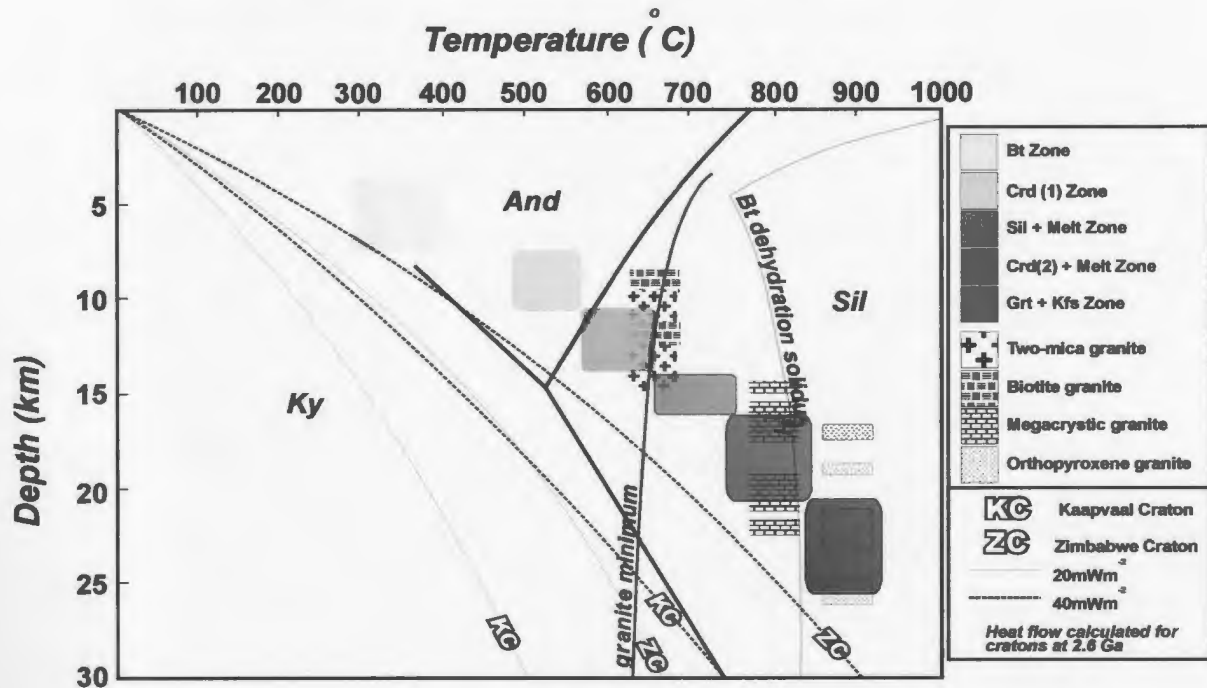


Figure 6.14: Temperature versus depth diagram illustrating the steady-state geotherms determined by Kramers et al. (2001) for the Zimbabwe and Kaapvaal cratons at ca. 2.6 Ga and compared with metamorphic and magmatic data from the Snare River terrane. Steady-state geotherms were calculated using the average concentrations of heat-producing elements occurring in these cratons. Concentrations of heat producing elements (K, Th & U; see Chapter 4) observed in the pre-orogenic rocks (i.e. > 2608 Ma) of the Snare River terrane overlap in abundance measured average concentrations determined for the Zimbabwe craton. Geotherms determined for this craton are considered a reasonable estimate of steady-state geotherms characteristic in the study area prior to orogenesis. Peak orogenic conditions in the Snare River terrane exceed these geotherms, despite high-levels of radiogenic heat production, suggesting that anomalous, elevated mantle heat-flow may have contributed to perturbation of the steady-state geotherm in the study area.

production must have been high (De Yoreo et al. 1989, 1991). Figure 6.14 shows a comparison of the magmatic and metamorphic datasets presented here with steady-state geotherms calculated for Neoproterozoic orogenic crust in the Kaapvaal and Zimbabwe cratons, taking into account the abundance of heat-producing elements and elevated rate of radiogenic heat production during the Archean, for model mantle heat fluxes of 20 and 40 mW m⁻² (Kramers et al. 2001). It shows that metamorphic conditions and magmatic temperatures at different crustal depths in the Snare River terrane significantly exceed those for the hottest steady-state geotherm modelled, indicating either increased radiogenic heat production or a mantle heat flux in excess of 40 mW m⁻², or both, is necessary to account for the perturbed geothermal conditions. Bennett et al. (accepted) noted that orogenesis was preceded by the emplacement of mantle-derived sanukitoids that were interpreted to have formed in response to slab delamination. Such a model, which predicts removal of lower crust and an upwelling of mantle heat, may provide an appropriate setting for the observed extreme perturbation of the steady-state geotherm, which would have subsequently controlled the style of orogenic evolution.

6.7 Conclusions

We have demonstrated that careful application of zircon saturation thermometry to Neoproterozoic magmas in the Snare River terrane, southwestern Slave Province, can yield geologically meaningful magma crystallization temperatures. Correction for the proportion of zircon inheritance, coupled with complementary petrogenetic and petrographic studies, was essential to ensure realistic results. Comparison of zircon

saturation temperatures with regional metamorphic data, in which conditions vary from greenschist- to granulite-facies over a crustal depth range of approximately 22 km, yields an independent measure of crustal temperature at the level of magma emplacement. We have utilized this association to assess the significance of zircon saturation temperatures with respect to Archean petrogenetic, metamorphic and tectonic evolution.

Integration of datasets for the Snare River terrane has revealed that secular thermal variations accompanied successive phases of tectonism during its ca. 90 M.y. evolution. Specifically, the data demonstrate each tectonic episode was characterized by a distinct magmatic style, chemistry, magma melting and emplacement temperatures. During several pulses of TTG magmatism over the ca. 66 M.y. period of crust formation, moderate temperature magmatism prevailed, and the consistent geochemistry and zircon saturation temperatures support the notion of a stable magma reservoir and melting conditions over this period. Orogenesis was characterized by significant magma diversification and heterogeneous melting conditions in the lower and mid crust involving both H₂O-rich low-temperature and H₂O-poor high-temperature magmatism. Post-orogenic crustal stabilization was characterized by low-temperature, small-volume crustal anatexis.

Comparison of zircon saturation data for orogenic magmas with the ambient metamorphic conditions has yielded new information regarding the HT/LP metamorphism that affected the region. Low-temperature magmas emplaced in the upper crust buffered the pre-existing metamorphic regime, whereas high-temperature magmas emplaced into the mid-crust were the source of heat and/or fluids that resulted in a ca. 10

km thick zone of HT mid-crustal metamorphism. Emplacement of individual magmatic suites was intimately associated with the onset of fluid-present upper-amphibolite-facies and fluid-absent granulite-facies metamorphic zones. Post-emplacement metamorphism of high-temperature granites at the lowest exposed structural levels delimits the maximum depth of pluton-driven metamorphism. Integration of field, magmatic and metamorphic datasets has enabled characterization of the heat distribution in the orogenic crust and identification of a crustal-scale metamorphic diachroneity characterized by younger HT/LP metamorphism at increasing palaeodepth. Geothermal perturbations due to elevated radiogenic heat production and mantle heat flux are necessary to explain the voluminous crustal melting and HT metamorphism.

The results of this application of zircon saturation thermometry lead us to believe it has an essential place in studies involving magma petrogenesis, characterization of the thermal behaviour of magmatic rocks, and the source(s) of metamorphic heat. However, we stress that careful geochemical, petrographic and zircon inheritance studies are crucial for its successful application.

6 References

- Baragar, W.R.A., and McGlynn, J.C., 1976. Geochemistry of the Yellowknife volcanic rocks, Canadian Journal of Earth Sciences, 3: 9 – 30.
- Barrie, C.T., 1995, Zircon thermometry of high-temperature rhyolites near volcanic-associated massive sulfide deposits, Abitibi subprovince, Canada: *Geology*, 23: 169–172.
- Bédard, J.H., 2003. Evidence for pluton-driven, high-grade metamorphism in the Archean Minto Block, northern Superior Province, Canada. *The Journal of Geology*, 111: 183–205
- Bédard, J.H., Brouillette, P., Madore, L., and Berclaz, A., 2003. Archean cratonization and deformation in the northern Superior Province: an evaluation of plate tectonic versus vertical tectonic models. *Precambrian Research*, 127: 61 – 87.
- Bennett, V.R.C., and Dunning, G.R., 1998. Geological Transect across the southern Indin Lake supracrustal belt to the central Ghost Lake granulite domain. *In: 26th Yellowknife Geoscience Forum*. Indian and Northern Affairs Canada, NWT Chamber of Mines and Resources, Wildlife and Economic Development, Program and Abstracts of Talks and Posters, pp. 14-16.
- Bennett, V., Dunning, G.R., and Indares, A., 2000. Preliminary data from the Kwejinne Lake supracrustal belt-Ghost Lake granulite domain transect: impact of a steep thermal gradient on upper crustal rocks. *In 28th Yellowknife Geoscience Forum ; Indian and Northern Affairs Canada, NWT Chamber of Mines and Resources, Wildlife and Economic Development, Program and Abstracts of Talks and Posters*, pp. 10-11.
- Bennett, V., Rivers, T., Relf., 2002. Where East meets West: Formation, growth and collapse of the Snare River Terrain, southwestern Slave Province. *In 30th Yellowknife Geoscience Forum ; Indian and Northern Affairs Canada, NWT Chamber of Mines and Resources, Wildlife and Economic Development, Program and Abstracts of Talks and Posters*, pp. 1-2.
- Bleeker, W., and Beaumont-Smith., 1995 C. Thematic structural studies in the Slave Province: preliminary results and implications for the Yellowknife domain, Northwest Territories. *In Current Research, part C. Geological Survey of Canada, Paper 1995-C*, pp.87-96.
- Bethune, K.M, Villeneuve, M.E., and Bleeker, W. 1999. Laser $^{40}\text{Ar}/^{39}\text{Ar}$ thermochronology of Archean rocks in the Yellowknife Domain, Slave Province. Canada. *Canadian Journal of Earth Sciences*, 36: 1189 - 1206.
- Bleeker W., Ketchum, J.W.F., and Davis, W.J., 1999b. The Central Slave Basement, Part II: Age and tectonic significance of high strain zones along the basement-cover contact. *Canadian Journal of Earth Sciences*, 36: 1111-1130.
- Bleeker W., Stern R., and Sircombe, K., 2000. Why the Slave Province got a little bigger. *In Current Research, 2000-C. Geological Survey of Canada*, 9 pp.1999a,b, 2000;

- Bowring, S.A., Williams, I.S., and Compston, W., 1989. 3.96 Ga gneisses from the Slave Province Canada, Northwest Territories, Canada. *Geology*, **17**: 971-975
- Brown, M., 2001. Orogeny, migmatites and leucogranites: A review. *Proceedings of the Indian Academy of Science, Earth and Planetary Science*, **110**: 313 – 336.
- Cairns, S., Relf, C., MacLachlan, K., and Davis, W., in press. Late Archean decoupling of upper and mid crustal tectonothermal domains in the southeast Slave Province; evidence from the Walmsley Lake area. *Canadian Journal of Earth Sciences*, LITHOPROBE Special Edition.
- Chamberlain, K.R., Frost, C.D., and Frost, B.R., 2003. Early Archean to Mesoproterozoic evolution in the Wyoming Province: Archean origins to modern lithospheric architecture. *Canadian Journal of Earth Sciences*, **40**: 1357 - 1374
- Champion, D.C., and Sheraton, J.W., 1997. Geochemistry and Nd isotope systematics of Archean granites of the Eastern Goldfields, Yilgarn Craton, Australia: implications for crustal growth processes. *Precambrian Research*, **83**: 109 – 132.
- Clemens, J.D. and Wall, V.J., 1981. Crystallization and origin of some peraluminous (S-type) granitic magmas. *Canadian Mineralogist*, **19**: 111–132.
- Clemens, J.D., and Vielzeuf, D., 1987. Constraints on melting and magma production in the crust. *Earth and Planetary Science Letters*, **86**: 287 – 306.
- Conrad, W.K., Nicholls, I.A., and Wall, V.J., 1988. Water-saturated and –undersaturated melting of metaluminous and peraluminous crustal composition at 10kb: evidence for the origin of silicic magmas in the Taupo volcanic zone, New Zealand and other occurrence. *Journal of Petrology*, **29**: 765 – 803.
- Davies, G.F., 1992. On emergence of plate tectonics. *Geology*, **20**: 963 – 966.
- Davis, W.J., and Bleeker, W. 1999. Timing of plutonism, deformation and metamorphism in the Yellowknife Domain, Slave Province, Canada. *Canadian Journal of Earth Sciences*, **36**: 1169-1187.
- De Yoreo, J.J., Lux, D.R., and Guidotti, C.V., 1989. The role of crustal anatexis and magma migration in the thermal evolution of regions of thickened continental crust. In: Daly, J.S., Cliff, R.A., and Yardley B.W.D. (eds) 1989. *Evolution of Metamorphic Belts*, Geological Society Special Publication No. 43, pp187 – 202.
- Dietrich, R.V., 1968. Behaviour of zirconium in certain artificial magmas under diverse P-T conditions. *Lithos* **1**: 20 – 29.
- Drummond, M.S., and Defant. M.J., 1990. A model for trondjemite-tonalite-dacite genesis and crustal growth via slab melting: Archean to modern comparisons, *Journal of Geophysical Research*, **95**: 21 503 – 21 522.

- Emon, K.E., Jackson, V.A., and Dunning, G.R., 1999. Geology and U-Pb geochronology of the Eukok Uplift: a pre-2.8 Ga basement terrane in the northwestern Slave Structural Province, Northwest Territories, Canada. *Canadian Journal of Earth Sciences*, **36**: 1061-1082.
- Frith, R.A., Loveridge, W.D., and Van Breeman, O., 1986. U-Pb ages from basement granitoids of the western Slave Structural Province, northwestern Canadian Shield, *In Current Research, Part A. Geological Survey of Canada, Paper 86-1A*, pp. 113 - 119.
- Frith, R.A., and Loveridge, W.D., 1982. Ages of Yellowknife Supergroup volcanic rocks, granitoid intrusive rocks and regional metamorphism in the northeastern Slave Province, *In Current Research, Part A. Geological Survey of Canada, Paper 82-1A*, pp. 225 – 237.
- Fyfe, W.S., 1973. The granulite facies, partial melting and the Archean crust. *Philosophical Transactions of the Royal Society of London*, **A273**: 457 – 461.
- Hanchar, J.M., and Watson, E.B., 2003. Zircon Saturation Thermometry, In: J.M. Hanchar and P.W.O. Hoskin (editors), *Zircon, Reviews in Mineralogy and Geochemistry*, vol. **53**, chapter 4, pp. 89-112. Mineralogical Society of America, Washington D.C.
- Henderson, J.B. 1998. Preliminary geology, Wijinnedi Lake area, District of Mackenzie, Northwest Territories; Geological Survey of Canada, Open File 3609, scale 1: 50 000.
- Henderson, J.B. and Chacko, T. 1995. A reconnaissance of the high grade metamorphic terrane south of Ghost Lake, southwestern Slave Province, Northwest Territories. *In Current Research, 1995-C. Geological Survey of Canada*, pp. 77-85.
- Henderson, J.B., Loveridge, W.D., and Sullivan, R.W., 1982. U-Pb study from granitic basement beneath the Yellowknife Supergroup, Point Lake, District of Mackenzie, *In Rb-Sr and U-Pb Isotopic Age Studies, Report 5. Geological Survey of Canada, Paper 82-1C*, pp. 173 – 178.
- Henderson, J.B., van Breemen, O., and Loveridge, W.D., 1987. Some U-Pb zircon ages from Archean basement, supracrustal and intrusive rocks, Yellowknife – Hearne Lake area, District of Mackenzie. *In Radiogenic Age and Isotopic Studies: Report 1. Geological Survey of Canada, Paper 87-2*, pp. 111-121.
- Hoffman, P.F., 1986. Crustal accretion in a 2.7 – 2.5 Ga “granite-greenstone” terrane, Slave Province, N.W.T.: a prograding arc – trench system? In: M.J. de Witt and L.D. Ashwall (editors), *Tectonic Evolution of Greenstone belts. Lunar Planetary Institute Report 86 – 10*: 120.
- Isachsen, C.E., Bowring, S.A., and Padgham, W.A., 1991. Geochronology of the Yellowknife Volcanic Belt, N.W.T., Canada : new constraints on the timing and duration of greenstone belt magmatism. *Journal of Geology*, **99**: 55 - 67.
- Isachsen, C.E., and Bowring, S.A., 1997. The Bell Lake group and Anton Complex: a basement –

cover sequence beneath the Archean Yellowknife greenstone belt revealed and implicated in greenstone belt formation. *Canadian Journal of Earth Sciences*, **34**: 169-189.

Jackson, V.A., 1998. The Snare River Project : Objectives and initial results; *In* 26th Yellowknife Geoscience Forum. Indian and Northern Affairs Canada, NWT Chamber of Mines and Resources, Wildlife and Economic Development, Program and Abstracts of Talks and Posters, pp.61-63.

Jackson, V.A., 1999. Preliminary 1:100 000 scale compilation of the geology of the Snare River area (1998 and 1999 results); EGS Open File 1999-18. DIAND, NWT Geology Division, Yellowknife.

Jackson, V.A., 2000a. Descriptive Notes for the Snare River 1:50 000 scale maps to accompany EGS Open File 1998-18 and EGS Open File 2000-10. DIAND, NWT Geology Division, Yellowknife. Text, 23 pages.

Jackson, V.A., 2000b. Preliminary Geology of the part of the Snare River area; Parts of 85N/16 and 85O/5-7; 10-13: EGS Open File 2000-10. DIAND, NWT Geology Division, Yellowknife. Data on 3 maps and assay tables, scale 1:50 000 and CD in Autocad R14 and .pdf formats.

Jackson, V.A., 2000c. The Snare River Project: results from mapping; *In* 28th Yellowknife Geoscience Forum. Indian and Northern Affairs Canada, NWT Chamber of Mines and Resources, Wildlife and Economic Development, Program and Abstracts of Talks and Posters, pp.33-34.

Jackson, V.A., 2001. The 2001 Snare River Project: Mapping results with focus on the high grade rocks. *In* 29th Yellowknife Geoscience Forum. Indian and Northern Affairs Canada, NWT Chamber of Mines and Resources, Wildlife and Economic Development, Program and Abstracts of Talks and Posters, pp.28-29.

Jackson, V.A., 2002a. Preliminary Geology of the part of the Snare River area, Southwestern Slave Province; Parts of 85O and 85N. NWT Open File 2002-02. DIAND, NWT Geology Division, Yellowknife. 4 maps plus legend, scale 1:50 000. Assay tables to accompany maps.

Jackson, V.A., 2002b. The Snare River project (parts of 85N and 85O): Results from 2002 mapping, the final field season. *In* 30th Yellowknife Geoscience Forum. Indian and Northern Affairs Canada, NWT Chamber of Mines and Resources, Wildlife and Economic Development, Program and Abstracts of Talks and Posters, pp. 27-28.

James, D.T., and Mortensen, J.K., 1992. An Archean metamorphic core complex in the southern Slave Province: basement-cover structural relations between the Sleepy Dragon Complex and the Yellowknife Supergroup, *Canadian Journal of Earth Sciences*, **29**: 2133 – 2145.

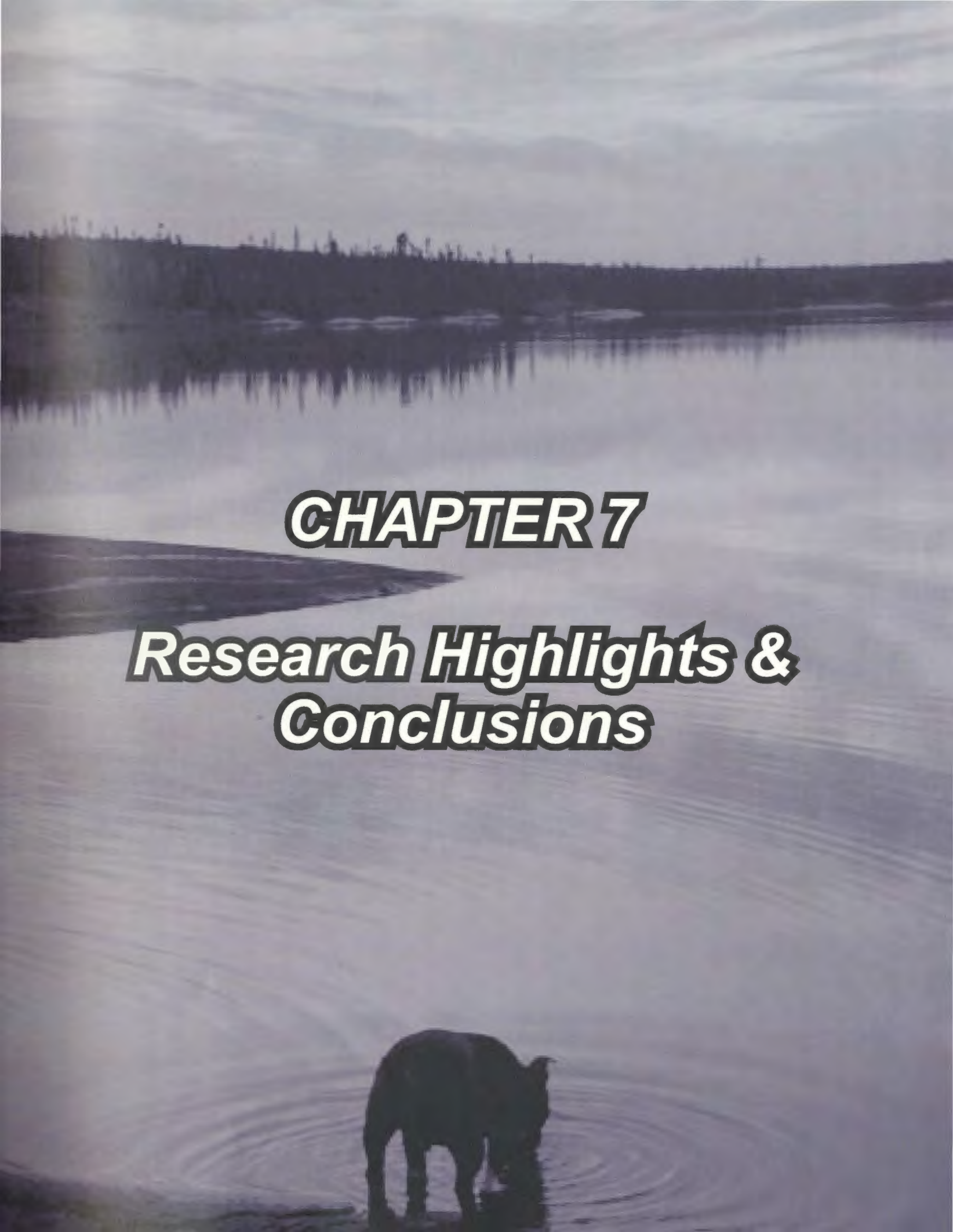
Jenner, G.A.; Fryer, B.J. & McLennan, S.M., 1981. Geochemistry of the Archaean Yellowknife Supergroup. *Geochimica. et Cosmochemica. Acta.*, **45**: 1111-1129

- Ketchum, J., and Bleeker, W. 1998. U-Pb geochronology of the Sleepy Dragon complex in the Morose – Patterson Lake areas, southwestern Slave Province, with tectonic implications. *In Slave – Northern Cordillera Lithospheric Evolution Workshop (SNORCLE) Transect and Cordilleran Tectonics Workshop Meeting, 6 – 8 March, Simon Fraser University. Compiled by F. Cook and P. Erdmer. Lithoprobe Report 64, pp. 25-30.*
- Ketchum, J., and Bleeker, W. 1999. The Central Slave Cover Group and Central Slave Basement Complex: a progress report on U-Pb geochronological studies. *In Slave – Northern Cordillera Lithospheric Evolution Workshop (SNORCLE) Transect and Cordilleran Tectonics Workshop Meeting, 5 – 7 March, Calgary. Compiled by F. Cook and P. Erdmer. Lithoprobe Report 69, pp. 21-29.*
- Ketchum, J., and Bleeker, W. 2000. New field and U-Pb data from the Central Slave Cover Group near Yellowknife and the Central Slave Basement Complex at Point Lake. *In Slave – Northern Cordillera Lithospheric Evolution Workshop (SNORCLE) Transect and Cordilleran Tectonics Workshop Meeting, 25 – 27 February, Calgary. Compiled by F. Cook and P. Erdmer. Lithoprobe Report 72, pp. 27-31.*
- Kramers, J.D., Kreissig, K., and Jones, M.Q.W., 2001. Crustal heat production and style of metamorphism between two Archean high grade provinces in the Limpopo Belt, southern Africa. *Precambrian Research, 112: 149 – 163.*
- Krogh, T.E., and Gibbons, W., 1978. U-Pb isotopic ages of basement and supracrustal rocks in the Point Lake area of the Slave Structural Province, Canada. *In Geological Association of Canada – Mineralogical association of Canada (GAC-MAC) Annual Meeting, Program with Abstracts, 3: p.478*
- Lambert, M.L., and van Breemen, O., 1991. U-Pb zircon ages from the Sleepy Dragon Complex and a new occurrence of basement rocks within the Meander Lake Plutonic Suite, Slave Province, N.W.T., *In Radiogenic age and isotopic studies: Report 4. Geological Survey of Canada, Paper 90-2, pp 79 - 84.*
- Le Breton, N., and Thompson, A.B., 1988. Fluid absent (dehydration) melting of biotite in metapelites in the early stages of crustal anatexis. *Contributions to Mineralogy and Petrology, 99: 226 – 237.*
- Lux, D.R., De Yoreo, J.J., Guidotti, C.V., and Decker, E.R., 1986. The role of plutonism in the formation of low pressure metamorphic belts. *Nature, 323: 794 – 797.*
- Martin, H., 1987. Petrogenesis of Archean trondhjemites, tonalites and granodiorites from eastern Finland: Major and trace element geochemistry. *Journal of Petrology, 228: 921- 953.*
- Martin, H., 1994. The Archean gneisses and genesis of the continental crust. In *Condie, K.C., (Ed), Archean Crustal Evolution: Amsterdam, Elsevier, 205-259.*
- Mortensen, J.K., Thorpe, R.I., Padgham, W.A., King, J.E. and Davis, W.J., 1988. U-Pb zircon ages for felsic volcanism in the Slave Province, N.W.T., *In Radiogenic age and isotopic studies: Report 2. Geological Survey of Canada, Paper 88-2, pp 85-95.*

- Moyen, J.-F. , Martin, H., Jayananda, M. et Auvray, B., 2003. Late-Archaean granites: a typology based on the Dharwar Craton (India). *Precamb. Res.*, 127:103-123.
- Oberthür, T., Davis, D.W., Blenkinsop, T.G., and Höhndorf, A., 2002. Precise U-Pb mineral ages, Rb-Sr and Sm-Nd systematics for the Great Dyke, Zimbabwe – constraints on late Archean events in the Zimbabwe craton and Limpopo belt. *Precambrian Research*, 113: 293 – 305.
- Ootes, L., 2000. Petrogenesis of the Sleeping Bear Intrusion, Kwejinne Lake, southwestern Slave Province, Northwest Territories. Unpublished B.Sc. (Honours) Thesis. University of Saskatchewan.
- Padgham, W.A., and Fyson, W.K. 1992. The Slave Province: A distinct Archean craton. *Canadian Journal of Earth Sciences*, 29: 2072 – 2086.
- Patiffo Douce, A.E., and Harris, N., 1998. Experimental constraints on Himalayan Anatexis. *Journal of Petrology*, 39, 689-710.
- Pattison, D.R.M. & Bégin, N.J., 1994. Zoning patterns in orthopyroxene and garnet in granulites: implications for geothermometry. *Journal of Metamorphic Geology*, 12: 387-410.
- Pehrsson, S.J. 1998. Deposition, deformation and preservation of the Indin Lake supracrustal belt, Slave Province, Northwest Territories. Unpublished Ph.D. thesis, Queens University, Kingston, Ontario.
- Pehrsson, S.J., and Chacko, T. 1997. Contrasting styles of deformation and metamorphism between mid and upper crustal rocks of the western Slave Province, Northwest Territories. *In Current Research, 1997-C*. Geological Survey of Canada, pp. 15-25.
- Percival, J.A., 1994. Archean High-grade Metamorphism. In: Condie, KC (Ed.), *Archean Crustal Evolution*. Elsevier, Oxford, pp. 357 - 410
- Perks, M.A., 1997. The mid crust of the western Slave Province - Geological Mapping, geochemistry and U - Pb Geochronology of the Forked Lake Area, Southwestern Slave Province, NWT. M.Sc. thesis, University of Alberta, Edmonton, Alberta.
- Pollack, H.N., 1997, Thermal characteristics of the Archean Earth, in *Tectonic Evolution of Greenstone Belts*. In: M. de Wit and L. Ashwal, (Editors), Oxford University Press, pp.223-232.
- Powers, R.E., and Bohlen, S.R., 1985. The role of synmetamorphic igneous rocks in the metamorphism and partial melting of metasediments, N.W. Adirondacks. *Contributions to Mineralogy and Petrology*, 90: 401–409.
- Rapp, R.P., Watson, E.B., and Miller, C.F., 1991. Partial melting of amphibolite/eclogite and the origin of Archean trondhjemites and tonalites. *Precambrian Research*, 51: 1 – 25.

- Relf, R., Chouinard, A., Sandeman, H., and Villeneuve, M., 1994. Contact relations between Anialik River volcanic belt and the Kangguyak gneiss belt, northwestern Slave Province, Northwest Territories, *In* Current Research, 1994-C. Geological Survey of Canada, pp 49 – 59.
- Relf, R., Sandeman, H., and Villeneuve, M., 1999. Tectonic and thermal history of the Anialik River area, northwestern Slave Province, Canada. *Canadian Journal of Earth Sciences*, **36**: 1207 – 1226.
- Sircombe, K.N., Bleeker, W., Stern, R.A., 2001. Detrital zircon geochronology and grain-size analysis of a ~ 2800 Ma Mesoarchean proto-cratonic cover succession, Slave Province, Canada. *Earth and Planetary Science Letters*, **189**: 207-220.
- Skjerlie, K.P., and Johnston, A. D., 1996. Vapor-absent melting from 10 to 20 kbar of crustal rocks that contain multiple hydrous phases: Implications for anatexis in the deep to very deep continental crust and active continental margins. *Journal of Petrology*, **37**: 661-691.
- Springer, W., and Zeck, H.A., 1997. Partial fusion of basic granulites at 5 to 15kbar: implications for the origin of TTG magmas. *Contributions to Mineralogy and Petrology*, **127**: 30 – 45.
- Stern, R.A., and Bleeker, W., 1999. Age of the worlds oldest rocks refined using Canada's SHRIMP: The Acasta Gneiss Complex, Northwest Territories, Canada. *Geoscience Canada*. **25**, 27 – 31.
- Stone, D., 2000. Temperature and pressure variations in suites of Archean felsic plutonic rocks , Berens River area, northwest Superior Province, Ontario, Canada. *The Canadian Mineralogist*, **38**: 455 – 470.
- Stubley, M.P., Jaegli, S., Bilben, S. and Tyler, T. 1995. Geology of the Nardin Lake area, south-central Slave Province, parts of NTS 85P/5 and 12, 85O/8 and 9. EGS Open File 1995-04. 1:50 000 map with marginal notes. Yellowknife: DIAND NWT Geology Division.
- van Breemen. O., Henderson, J.B., Sullivan, R.W., and Thompson, P.H., 1987. U-Pb zircon and monazite ages from the eastern Slave Province, Hearley Lake area, N.W.T., *In* Radiogenic age and isotopic studies: Report 1. Geological Survey of Canada, Paper 87-2, pp 101 – 110.
- Vernon, R.H., Clarke, G.L. and Collins, W.J. 1990: Local mid-crustal granulite facies metamorphism and melting: an example in the Mount Stafford area, central Australia. In Ashworth, J.R. and Brown, M. (editors): *High-temperature Metamorphism and Crustal Anatexis*, Unwin Hyman, London, 272-319.
- Vielzeuf, D., and Montel, J.M., 1994, Partial melting of metagreywackes: Part 1. Fluid-absent experiments and phase relationships: *Contributions to Mineralogy and Petrology*, **117**: 375–393.

- Vielzeuf, D., and Clemens, J.D., 1992. The fluid-absent melting of phlogopite quartz: Experiments and models. *American Mineralogist*, **77**:1206–1222.
- Villeneuve M.E., Jackson, V.A., and Thompson, P.H., 1993. Geochronological evidence for the existence of pre-Yellowknife Supergroup supracrustal sequences in the Slave Province. Geological Association of Canada – Mineralogical Association of Canada, Program with Abstracts, **18**: A107.
- Villeneuve, M.E., Henderson, J.R., Hrabi, R.B., Jackson, V.A., and Relf, C., 1997. 2.70 – 2.58 Ga plutonism and volcanism in the Slave Province, District of Mackenzie, Northwest Territories. *In* Radiogenic Age and Isotopic studies: Report 8. Geological Survey of Canada, 1997-F, pp. 37-60.
- Watson, E.B., 1979. Zircon saturation in felsic liquids: experimental results and applications to trace element geochemistry. *Contributions to Mineralogy and Petrology*, **70**: 407 – 419.
- Wiedenbeck, M. and Watkins, K.P., 1993. A time scale for granitoid emplacement in the Archean Murchison Province, Western Australia, by single zircon geochronology. *Precambrian Research*, **61**: 1-26.
- Yamashita, K., Creaser, R.A., and Villeneuve, M.E., 1999b. Integrated Nd isotopic and U-Pb detrital zircon systematics of clastic sedimentary rocks from the Slave Province, Canada: evidence for extensive crustal reworking in the early- to mid-Archean. *Earth and Planetary Science Letters*, **174**: 283 – 299.
- Yamashita, K., Creaser, R.A., Jensen, J.E., and Heaman, L.M. 2000. Origin and evolution of the mid- to late-Archean crust in the Hanikahimajuk Lake area, Slave Province, Canada; evidence from U-Pb geochronological, geochemical and Nd-Pb isotopic data. *Precambrian Research*, **99**: 197-224.



CHAPTER 7

Research Highlights & Conclusions

7 HIGHLIGHTS AND CONCLUSIONS

7.1 Preliminary Statement

The research presented in the preceding chapters has investigated the nature, diversity, and interconnections among the principal processes responsible for crustal growth and evolution as recorded in the low-grade upper-crustal and high-grade mid-crustal rocks in the Neoproterozoic Snare River terrane, southwestern Slave Province. A four-dimensional approach to the understanding of crustal evolution is evident from the temporal, geochemical, architectural and thermal datasets presented in Chapters 2-6. As independent datasets and as integrated multidisciplinary studies, they demonstrate that crustal development in the Snare River terrane was characterized by a broad secular evolution involving two distinct tectonic regimes, a tonalite–trondhjemite–granodiorite (TTG)–greenstone regime (TR1) that is inferred to have developed in an oceanic setting, and an incipient collisional plate-tectonic regime (TR2). The primary control on the tectonic evolution from TR1 to TR2 was the occurrence and distribution of Mesoproterozoic crust (the Central Slave Basement Complex) that served as a nucleus onto which Neoproterozoic crustal material was accreted and reworked. The tectonic history of the Snare River terrane supports the contention that lateral accretion of juvenile marginal Neoproterozoic terranes onto a Mesoproterozoic protocraton was an important mechanism of crustal growth during the latter stages of Archean cratonic evolution in the Slave Province.

7.2 Highlights of Research Methods

Three approaches were crucial for the execution of this study of the Snare River terrane:

1. The variable scale of the field mapping, undertaken at both regional (1:50 000) and transect (1:30 000) scales, provided insight into regional problems while at the same time allowing time for detailed outcrop-scale mapping, observations and sampling. In this respect, the collaborative mapping effort between the author and members of the Northwest Territories Geoscience Office was invaluable;
2. The application LAM ICP-MS analyses to solve petrologic and tectonic problems;
3. The integration of multidisciplinary datasets to examine the connections among the various components and processes characterizing crustal evolution.

7.2.1 Field Mapping

The contribution of detailed field mapping to the study becomes apparent from a cursory comparison of the recent compilation map of the Snare River area with the most notable previous compilation (Lord 1942; Fig. 7.1). Examination of Fig. 7.1a shows that the first-order interpretation of the map-scale crustal elements defined by Lord (1942) is that of an upper-crustal granite–greenstone terrane, in which greenschist- to amphibolite-facies supracrustal belts are intruded by younger granitic plutons. In contrast, the recent compilation map (Fig. 7.1b) reveals the presence and juxtaposition of contrasting low-

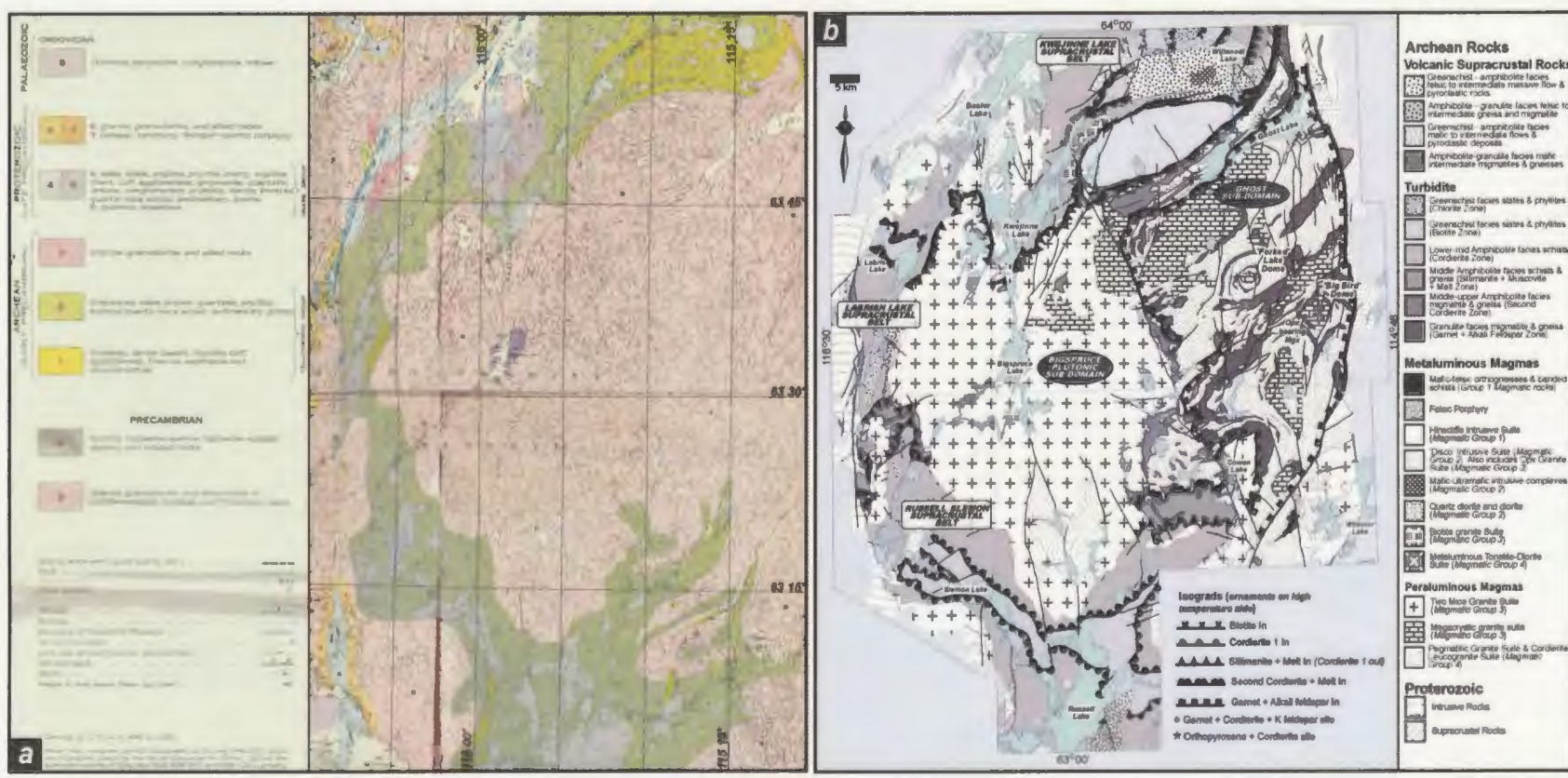


Figure 7.1: Geological maps of the Snare River terrane. (a) Compilation of Lord (1942). (b) Recent compilation. Sources of information in (b) : Snare River area (Jackson 2003 and references therein); Wijinnedi Lake area (Henderson, 1998); Labrish Lake area (Brophy and Pell, 2002); Russell Lake area (Jackson 1999).

grade upper crust and high-grade mid crust, a fundamentally different tectonic association reflecting a correspondingly different style of crustal evolution. Recognition of upper- and mid-crustal domains separated by an intervening transitional zone has provided new three-dimensional insight into the crustal evolution of this part of the Slave Province, and indeed to the Slave Province as a whole, which previously had been viewed through the prism of Neoproterozoic upper-crustal granite-greenstone belts and Mesoproterozoic basement. Integration of regional mapping across the study area over the past decade has enabled delineation of the 'Snare River terrane', a region of distinct crust and orogenic development in the southwestern Slave Province that forms the framework upon which the research presented in this thesis was based.

Furthermore, detailed field observations in the Snare River terrane were essential for the establishment of a robust relative chronology of magma emplacement on which much of the analytical work in this study was based. Without the firm observational and mapping base, the validity of the erroneous ID TIMS emplacement ages (due to zircon inheritance and/or recrystallization) might not have been recognized and could have led to incorrect interpretations concerning the sequence of magma genesis and crustal evolution. In summary, the mapping and field-based observations provide a fundamental underpinning to this study that should not be overlooked.

7.2.2 LAM ICP-MS

Application of the rapidly evolving technique of LAM ICP-MS analysis permitted significant progress in several aspects of the study and was critical in obtaining several of

the major datasets. In particular, the enhanced spatial resolution, rapid analysis and ongoing improvements in precision and accuracy of the method for U-Pb dating encouraged investment of time and effort in the development of new and refined analytical protocols that resulted in a significantly improved data and thereby enhanced understanding of the processes responsible for crust formation and reworking. New sampling strategies developed by the author resulted in improved spatial resolution and precision of the technique and hence have broadened the scope of its application, particularly in the field of zircon geochronology. Resolution of polyphase histories recorded in different zircon populations within individual samples, presented in Chapters 2 and 5, was achieved through integrated BSE imaging and LAM ICP-MS analysis, an approach that is becoming widely adopted. In the view of the author, the potential of LAM ICP-MS as an important research tool to solve petrologic and tectonic problems such as those presented in the preceding chapters is now well established, but the scope for innovation using well characterized samples and new analytical approaches remains large.

7.2.3 Integration of Multidisciplinary Datasets

Acquisition and subsequent integration of multidisciplinary datasets was a primary aim of this thesis and was instrumental in identifying fundamental relationships among the various mechanisms associated with crustal development in the Snare River terrane. Geophysical datasets were important for comparison with structural and compositional whole-rock data acquired from mid-crustal Ghost subdomain (Chapter 2).

Integration of relative and absolute temporal constraints on the sequence of deformation and magmatism demonstrate the importance of secular change in crustal evolution (Chapters 3 and 4). Integration of BSE imaging and U-Pb studies by LAM ICP-MS greatly aided understanding and interpretation of ID TIMS U-Pb age data for complex magmatic rocks, and documentation of epitaxial relationships in zircon by BSE imaging was crucial to understand the significance of the zircon inheritance data determined for magmas emplaced into the upper and mid crust. Additionally, zircon inheritance studies contributed to a greatly improved understanding of both magma petrogenesis and source region compositions (Chapter 5). Integration of geochemical and zircon datasets with field and metamorphic data was essential for assessment of the applicability of the zircon saturation thermometer and the accuracy of the results (Chapter 6). In summary, integration of multidisciplinary field and analytical datasets has been central to this study and has enabled insight into the rates, styles and mechanisms of crustal evolution in the Snare River terrane.

7.3 Detailed Contributions

The five preceding chapters present data that constrain the temporal, architectural, geochemical and thermal evolution of the Snare River terrane and provide a broad framework in which to interpret its crustal evolution. Specifically, the profiles determined for each magmatic component have elucidated both the role of Mesoarchean crust during crustal growth and development and also delineated the sequence of crustal construction at different crustal levels (i.e., provided a three-dimensional understanding of crustal

evolution). Three features, in particular, are highlighted by this study, the internal consistency of conclusions with respect to the changing style of tectonism derived from each dataset, the secular variations exhibited within individual datasets (i.e. first-order variations in crustal evolution), and the diachroneity of certain processes during a single phase of crustal evolution.

7.3.1 Zircon Geochronology: Magmatic, Detrital and Inherited Studies

U-Pb studies of magmatic and refractory zircon in plutonic rocks and detrital zircon in metasedimentary rocks, presented in chapters 2 and 5, provide an absolute temporal framework in which to interpret field and other analytical datasets. When integrated with field data, the U-Pb results permit a four-dimensional understanding of crustal evolution in the Snare River terrane. Zircon was the primary chronometer employed due to its ability to record a spectrum of events associated with crustal evolution.

Important contributions from the magmatic and detrital U-Pb zircon study of Chapter 2 can be summarized as follows.

1. Recognition of two contrasting tectonic regimes of crust formation, with secular evolution from a granite–greenstone regime (TR1; 2674–2608 Ma) to an accretionary, incipient plate-tectonic regime (TR2; 2608–2585 Ma);
2. Punctuated metaluminous magmatism at ca. 2674, 2658–2654, 2637, 2608, 2597 and 2589 Ma that reflects the importance of lower-crustal and mantle melting events during crustal construction in the study area;

3. Peraluminous plutonism at ca. 2597 and 2589 Ma, reflecting the tectonic burial of metaturbidite and the rise of the melting zone to mid-crustal depths;
4. Recognition of a first-order age stratification of the crust in the Snare River terrane, with older lithologies formed during TR1 predominating in the greenschist-facies upper crust and younger lithologies associated with TR2 centred in the granulite-facies mid crust;
5. Diachronous turbidite sedimentation including a pre-2637 Ma package that is most common in the mid crust and a post-2633 Ma package occurring in the upper crust;
6. Mesoarchean crust (>2.8 Ga) has not been identified in the Snare River terrane, but its influence in crustal evolution has been monitored through detrital zircon populations in metaturbidites and inherited zircon in igneous lithologies, respectively (see below);

With regard to the inherited zircon U-Pb study presented in Chapter 5, the most significant contributions include the following.

1. The secular growth of the lower crust through melting in 'local' lower- and mid-crustal source regions at ca. 2680–2670, 2660–2650, 2640–2630 and 2600 Ma, and tectonic intercalation of 'exotic' mafic crust (with an age >2700 Ma);
2. Correlation of lower crustal inheritance ages with upper-crustal magmas in the study area and across the Slave Province (e.g., Kam and Banting Groups; Defeat and Concession suites), which indicates that lower crustal evolution was a catalyst for development of the overlying mid and upper crust;

3. An absence of Mesoarchean crust in lower-crustal magma reservoirs for the duration of crustal evolution in the Snare River terrane;
4. Recognition of genetic links between voluminous peraluminous magmatism and metasedimentary protoliths as revealed by overlapping detrital and inheritance ages;
5. A new application of inherited zircon datasets, acquired through LAM ICP-MS techniques, to better interpret binary and multicomponent Sm-Nd isotope mixing models.

7.3.2 Three-dimensional Architecture

Integrated studies of the evolution of deformation and metamorphism permit analysis of the gross pre-orogenic, orogenic and post-orogenic architectural development of the Snare River terrane. Specifically, Chapter 3 outlines the deformation mechanisms responsible for the formation of the partial (mid to upper) crustal section. Structural and metamorphic transitions, which occur where the partial section is preserved, involve a gradational change in structural architecture with palaeodepth. They are characterized by steep structures in the greenschist- to lower-amphibolite-facies upper-crust, moderately dipping structures in the transitional mid- and upper-amphibolite-facies migmatite zone, and moderately- to gently-dipping structures in the granulite-facies mid crust. A model involving progressive contractional deformation and nappe tectonics following collision of the Snare River terrane with the leading edge of a Mesoarchean protocraton (the Central Slave Basement Complex) provides a resolution to the 'structural versus seismic

paradox' of steep structures in the upper crust overlying shallow structures in the mid to lower crust.

Analysis of the deformation history of the Snare River terrane has led to the following conclusions:

1. Superposition of three major phases of Neoproterozoic deformation and one phase of post-Neoproterozoic (Paleoproterozoic) deformation has resulted in the juxtaposition of steeply-dipping low-grade supracrustal belts with the gently-dipping high-grade mid crust. Two types of locally superposed contacts are observed between the low- and high-grade domains, Neoproterozoic ductile shear zones and Paleoproterozoic brittle faults;
2. The transitional migmatite zones exhibit continuity with the overlying upper crust and underlying mid crust and have proven to be key areas to correlate structures and deformation histories throughout the crust;
3. Three principal deformation mechanisms operated during crustal evolution of the Snare River terrane, lateral crustal shortening by fold–thrust tectonics (D1), nappe tectonics involving progressive imbrication of the upper plate (Snare River terrane) and overriding of the lower plate (leading edge of the Central Slave Basement Complex) during D2, and extensional collapse and mid-crustal uplift (D3);
4. Recognition of diachroneity and variable overprinting of D2, with older structures well preserved in the upper crust, younger structures predominating in the mid crust, and the intervening transition zones recording the effects of both older and younger phases of deformation;

5. Contrasting styles of fold superposition in the upper and mid crust, with coaxial refolding (type III hook-type interference structures) characteristic of the steep upper crust, but non-coaxial refolding (types I and II dome-and-basin and asymmetric mushrooms styles) prevailing in the mid crust. The transitional migmatite zones record evidence of both early coaxial and late non-coaxial fold superposition;
6. Dome-and-basin interference structures in the mid crust formed primarily as a result of progressive D2 deformation, but their geometry was amplified during later deformation;
7. Interpretation of the 'seismic versus structural paradox' as the combined effects of progressive nappe tectonics during protoarc–continent collision, upper-crustal decoupling, and amplification of structural contrasts during extensional exhumation.

7.3.3 Magma Geochemistry

Geochemical analysis of the mantle- and crustally-derived melts that intruded the upper and mid crust of the Snare River terrane was essential to assess the role of magmatism during crustal evolution. Magmatism was a fundamental process controlling all stages of crustal development in the Snare River terrane. The geochemical and Sm-Nd isotopic studies presented in Chapter 4 constrain the compositional variations of magmatic contributions to the crust through time and permit further resolution of the two tectonic regimes (i.e., granite–greenstone and incipient plate tectonic) into four stages of crustal growth and evolution (TR1a, b and TR2a, b). Specific highlights include the following:

1. Recognition that mantle-melting episodes (at ca. 2674, 2660, 2608 and 2589 Ma) subdivide crustal evolution into four stages of crust-formation, crustal growth, orogenesis and orogenic collapse. The close relationship between mantle melting and crustal evolution implies a coupled crust–mantle system was important during the development of the Snare River terrane;
2. Crustal magmatism demonstrates the transition from lower-crustal melting during early crust formation to predominantly mid-crustal melting during and after the orogenic peak, the changing locus of magmatism reflecting the maturation and thickening of the crustal column;
3. HREE-depleted metaluminous magmatism prevailed throughout the four stages of crustal evolution, implying progressive growth of a garnet-rich mafic lower crust;
4. Peraluminous magmas, which were derived predominantly from metasedimentary sources, occur after the onset of orogenesis (i.e., in TR2), indicating that metasedimentary material had not entered the mid crust until this time;
5. The crust of the Snare River terrane is compositionally stratified, with the older, low-grade upper crust characterized by metaluminous magmas, whereas the younger, high-grade mid crust is composed of both metaluminous and voluminous peraluminous magmas;
6. The four stages of crustal evolution that have been identified are correlated with four distinct tectonic settings: (a) initial crust-formation in an oceanic plateau environment (tholeiites and coeval TTG magmatism); (b) crustal growth in a protoarc setting as a result of shallow subduction or subcretion (TTG magmatism); (c) rapid orogenic

reworking in a continent–protoarc collisional environment (voluminous bimodal metaluminous and peraluminous magmatism); and (d) post-orogenic collapse speculated to be the result of lower crustal instability and subsequent delamination (mantle-derived sanukitoids and decompressional anatectic crustal melts);

7. Sm-Nd isotopic data preclude significant involvement of Mesoarchean crust during petrogenesis of magmas in the Snare River terrane.

7.3.4 Thermal Evolution of Crust

The thermal evolution of Archean crust is perhaps one of the most poorly constrained aspects of crustal analysis. Calculation of zircon saturation temperatures for magmatic rocks in the Snare River terrane demonstrates the potential of this thermometer to contribute to resolution of petrogenetic, metamorphic and tectonic problems.

Significant contributions of the zircon saturation studies presented in Chapter 6 include the following:

1. Secular variation in pluton emplacement temperatures broadly correlates with the four stages of crustal evolution recognized for the study area. Initial crustal growth was characterized by intermittent, moderate-temperature (740–756 °C) TTG magmatism. Orogenic magmas consisted of H₂O-rich low-temperature (677 and 675 °C) and H₂O-poor high-temperature melts (794–779 °C; 867°C); and post-orogenic magmas were low-temperature anatectic melts (657 °C);
2. Comparison of emplacement temperatures of orogenic magmas with metamorphic constraints at both upper- and mid-crustal levels demonstrates an intimate link

between magmatism and HT-LP metamorphism in the Snare River terrane. At the highest crustal levels, low-temperature magmas overprinted and buffered the pre-existing metamorphic thermal regime. In contrast, pluton-driven, upper-amphibolite- and granulite-facies metamorphism prevailed across a 10 km thick zone in the mid crust. At the lowest observed crustal levels, pluton-driven metamorphism is superseded by regional post-emplacement metamorphism;

3. High-grade metamorphic isograds are spatially associated with the emplacement of moderate- and high-temperature magmas. Intrusions of megacrystic granite are closely associated with upper-amphibolite-facies, hydrous metamorphic conditions in overlying metapelitic rocks. Similarly, the onset of anhydrous granulite-facies conditions is spatially correlated with intrusions of high-temperature orthopyroxene granite;
4. Integration of the zircon saturation temperature with field and metamorphic constraints demonstrates crustal-scale diachroneity in the timing of metamorphism, with the oldest phase of metamorphism occurring in the upper crust and progressively younger phases (or fronts) occurring at successively deeper crustal levels.

7.4 Four-Dimensional Crustal Evolution in the Snare River Terrane.

7.4.1 Tectonic Evolution

Integration of the multidisciplinary datasets presented in Chapters 2–6 permits reconstruction of the tectonic evolution of the Snare River terrane. Four distinct tectonic

settings are recognized over the ca. 90-100 M.y history of the region: plume, protoarc, collisional (orogenic), and post-orogenic collapse settings (Fig. 7.2). Furthermore, the succession from plume tectonics to post-orogenic collapse represents the transition from a long-lived (ca. 66 M.y.) episode of TTG–greenstone tectonism (TR1) to a comparatively short-lived (ca. 23 M.y.) interval of incipient plate tectonics (TR2).

Stage 1: Plume tectonics to onset of protoarc (2674 - 2654 Ma)

Vigorous plume activity, which began at ca. 2674 Ma and was characterized by subaqueous eruption of bimodal tholeiitic and calc-alkaline TTG magmas in an oceanic plateau setting distal to the Central Slave Basement Complex, marked the onset of new crust formation in the Snare River terrane (TR1a; Fig. 7.2a). Tholeiitic magmatism was characterized by high degrees of partial melting of a chemically primitive mantle in an oceanic plateau environment. After rapid magmatic thickening of the crust, partial melting at its base led to TTG magmatism. A thin older (>2750 Ma) substrate may have been present, but if so it had minimal influence on magma genesis as the juvenile character of the 2674 Ma TTG magmas precludes a significant role for older crust and/or mantle during their petrogenesis. Moderate temperature magmatism (~750 °C) characterized this period of lower-crustal melting. Magmatism in the Snare oceanic plateau was approximately coeval with turbidite sedimentation in distal depocentres offshore from the Central Slave Basement Complex, which was located to the east (present coordinates). Creation of the Snare plateau was controlled principally by mantle and lower-crustal magmatism in response to a mantle plume. The onset of protoarc

tectonics occurred after ca. 2660 Ma and coincided with the termination of plume tectonics in the region. Protoarc development is surmised to have been a consequence of lateral crustal motions, driven by extensional thinning in Central Slave Basement Complex to the east in response to the impingement of coeval mantle plume(s). Interaction of plumes with this Mesoarchean block is suggested to have instigated lateral motions and resulted in dismemberment and oblique dispersal of the Snare oceanic plateau prior to ca. 2654 Ma. Encroachment of the Central Slave Basement Complex from the east towards the Snare plateau delimited the beginning of protoarc tectonics (TR1b), and related tholeiitic and TTG magmatism are inferred to represent products of shallow, west-dipping subduction or subcretion beneath the dissected oceanic plateau (Fig. 7.2b).

Stage 2: Protoarc evolution – subcretion to subduction (2654 - 2608 Ma)

The evolution from subcretion to subduction reflects maturation of the Snare protoarc during this ca. 45 M.y interval. Mantle and moderate-temperature lower-crustal magmatism continued as the primary modes of crust building. Increased crustal thicknesses led to greater intracrustal magma differentiation and abundant local and distal turbidite sedimentation. The youngest sedimentation observed (i.e., post-2635 Ma packages) is suggested to have occurred west of the protoarc, whilst ongoing diachronous sedimentation characterized ocean basins in the east (Fig. 7.2b). Initial subcretion was succeeded by subduction as the eastern crust moved closer to the Snare protoarc. Contractual deformation (D1) and early subgreenschist- and greenschist-facies

metamorphism accompanied crustal shortening, which culminated in intercalation of turbidite packages with the older, dismembered, volcano-plutonic crust. Growth of the lower crust continued in response to magmatic events (i.e., at ca. 2660 and 2637 Ma), and minor tectonic intercalation of >2700 Ma material into the magmatic lower crust is inferred to be the result of subcretion tectonics. Ensuing collision of unsubductable buoyant crust with the Snare protoarc significantly altered ambient stress regimes such that the subducting slab delaminated into the underlying lithospheric mantle. Renewed metasomatized mantle magmatism occurred in response to delamination at ca. 2608 Ma and emplacement of these sanukitoid magmas coincided with cessation of protoarc

Figure 7.2a: Schematic model of crust-formation in the Snare River terrane at ca. 2674 Ma by plume tectonics (Tectonic Regime 1a). Crustal products are tholeiite and TTG. Distal turbidite sedimentation adjacent to the Central Slave Basement Complex, the leading edge of which comprises voluminous >2700 Ma Kam-equivalent mafic material. Note that a plume is also inferred beneath the Central Slave Basement Complex.

Figure 7.2b: Schematic model of crustal growth in the Snare River terrane through protoarc tectonics involving a transition from subcretion to subduction (Tectonic Regime 1b). Crustal products are tholeiite, TTG, turbidite. Corresponding magmatism to the east (Defeat Suite), derived from mixed mantle and crustal sources is shown.

Figure 7.2c: Cessation of protoarc tectonics and the onset of Tectonic Regime 1b as a result of delamination of subducted slab when the leading edge of Central Slave Basement Complex reaches the Snare protoarc. Crustal products are sanukitoid magmas.

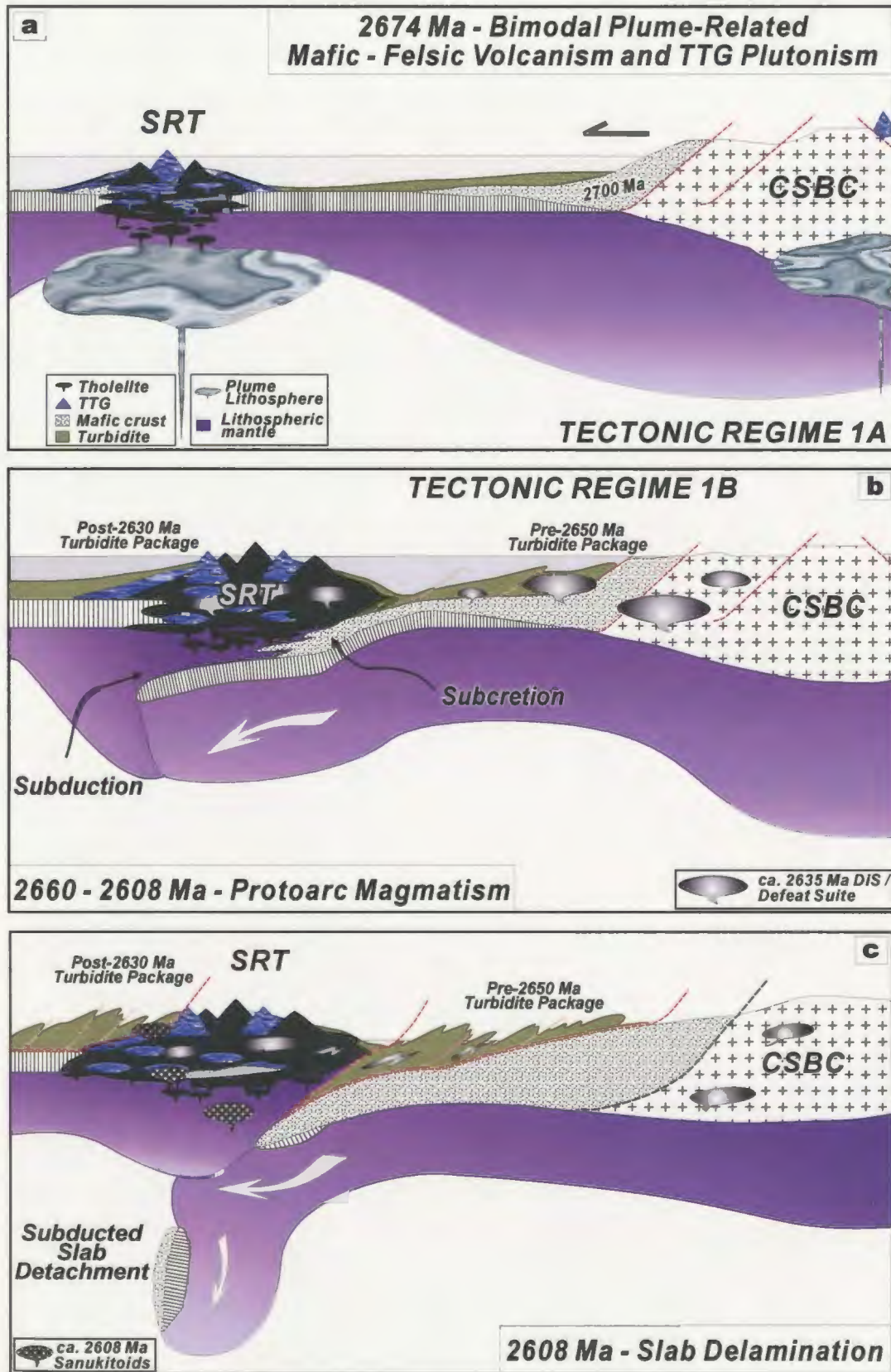


Figure 7.2a -c: Caption see opposite

tectonics and the onset of collisional orogenesis (Fig. 7.2c). Removal of the underlying slab and associated upwelling of hot mantle resulted in gross perturbation of the prevailing TTG thermal regime, creating the HT–LP conditions that characterized the collisional episode.

Stage 3: Protoarc–continent collisional orogenesis (2608 - 2597 Ma)

Initiation of protoarc–continent collision heralded a penetrative, short-lived period of HT-LP orogenesis (Snare Orogen; TR2a) and resulted in crustal reworking and voluminous growth and thickening of the mid crust. The leading edge of the crust to the east was composed predominantly of metaturbidite, ca. 2640-2420 Ma TTG magmas (Defeat Suite), and >2700 Ma mafic crust (Kam Group equivalent), with subordinate ca. 2680-2660 Ma volcano-plutonic fragments (Banting Group equivalent). As collision progressed, this crust was tectonically intercalated at both mid- and lower-crustal depths resulting in a wedge-shaped or indented orogenic geometry (Fig. 7d), with denser mafic material (>2700 Ma) incorporated into the lower crust and TTGs and fluid-rich metaturbidite intercalated into the mid crust of the Snare Orogen. Upper-crustal shortening resulted in refolding of D1 structures through progressive nappe tectonics (D2), such that the upper plate, primarily comprised of interleaved ca. 2674–2654 Ma volcano-plutonic crust and post-2635 Ma turbidite packages, overrode the lower plate composed of continental crust derived from the east. Deformation in the lower regions of the superstructure outlasted that in the upper crust as revealed by the occurrence of successively younger structures at progressively deeper levels. Underthrusting of the

lower plate and overthrusting of the upper plate through crustal-scale nappe tectonics resulted in formation of low- to moderately-dipping structures in the mid and lower crust.

The perturbed thermal regime coupled with the introduction of fertile mafic and metasedimentary protoliths into mid and lower crust resulted in diachronous HT-LP metamorphism and voluminous high- and low-temperature plutonism. Coeval magmatism and tectonic underthrusting were the principal agents of mid-crustal thickening in the Snare Orogen. Similarly, local magmatism and tectonic intercalation of exotic older crust (>2700 Ma) were instrumental in lower-crustal orogenic development. Continued extraction of HREE-depleted TTG magmas during TR1a-b and also during collision (TR2a) contributed to growth of a dense garnet-rich lower crust into which the older exotic material was incorporated.

Mesoarchean basement per se (i.e. >2.8 Ga crust) did not directly interact with the crust of the Snare River terrane at any crustal level, but remained distal to it (Fig. 7.2d). The dynamic nature and rapidity of orogenesis resulted in creation of a thickened crustal column in the accreted Snare River terrane, characterized by gross thermal and density instabilities. Orogenic collapse (TR2b) succeeded collision and was an important crustal stabilization process.

Stage 4: Post-orogenic collapse (2597 to \leq 2585 Ma)

Collapse of the Snare orogen took place in the 15 M.y. interval following the collisional peak (Fig. 7.2e). Removal of the dense lower crustal root by delamination resulted in magmatism derived from the rejuvenated metasomatized mantle (2589 Ma

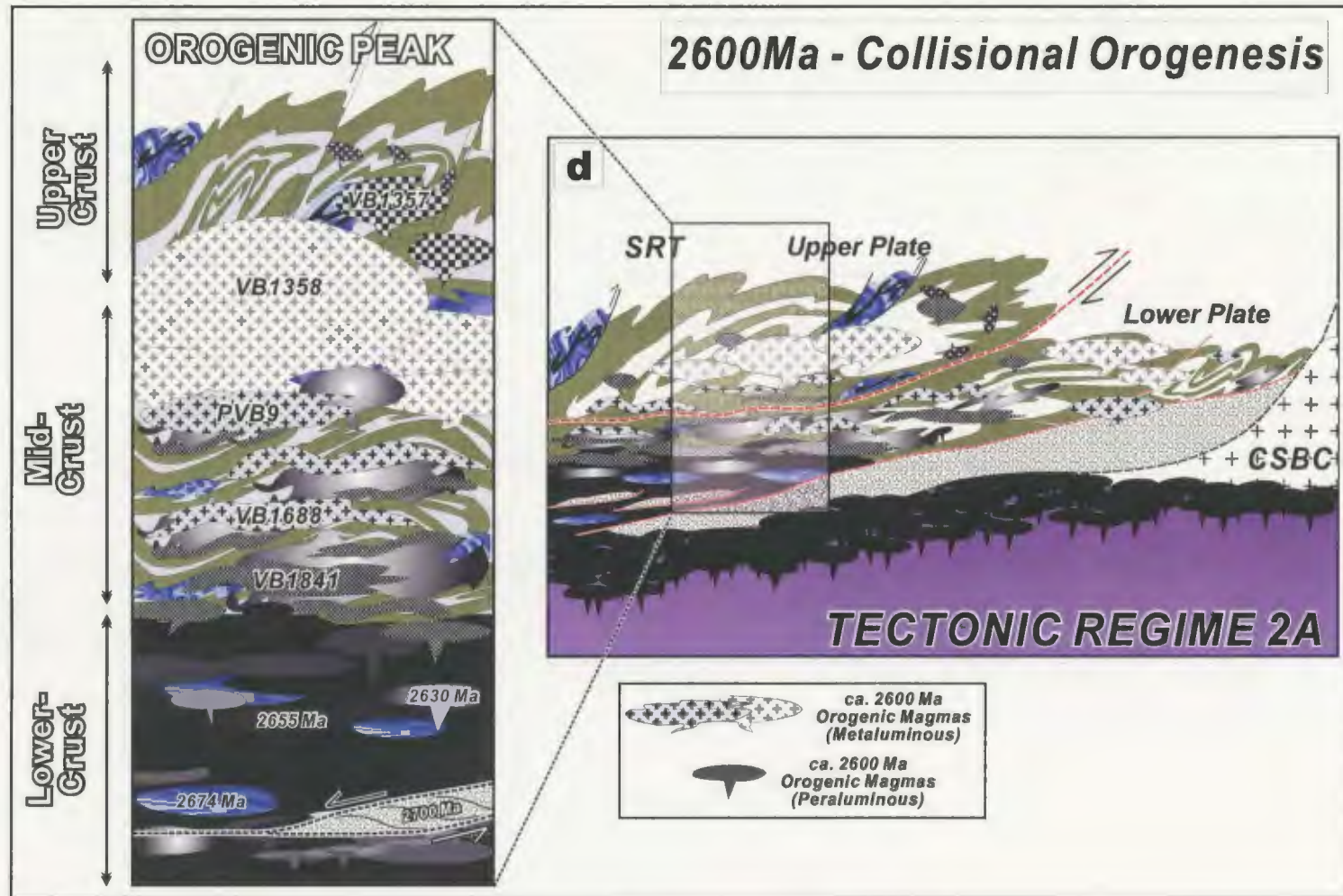


Figure 7.2d: Collisional orogenesis (Tectonic Regime 2a). Voluminous mid-crustal magmatism accompanies diachronous metamorphism and deformation. Intercalation of fertile metasedimentary and mafic material into the mid- and lower crust, respectively. Crustal products are metaluminous and peraluminous magmas.

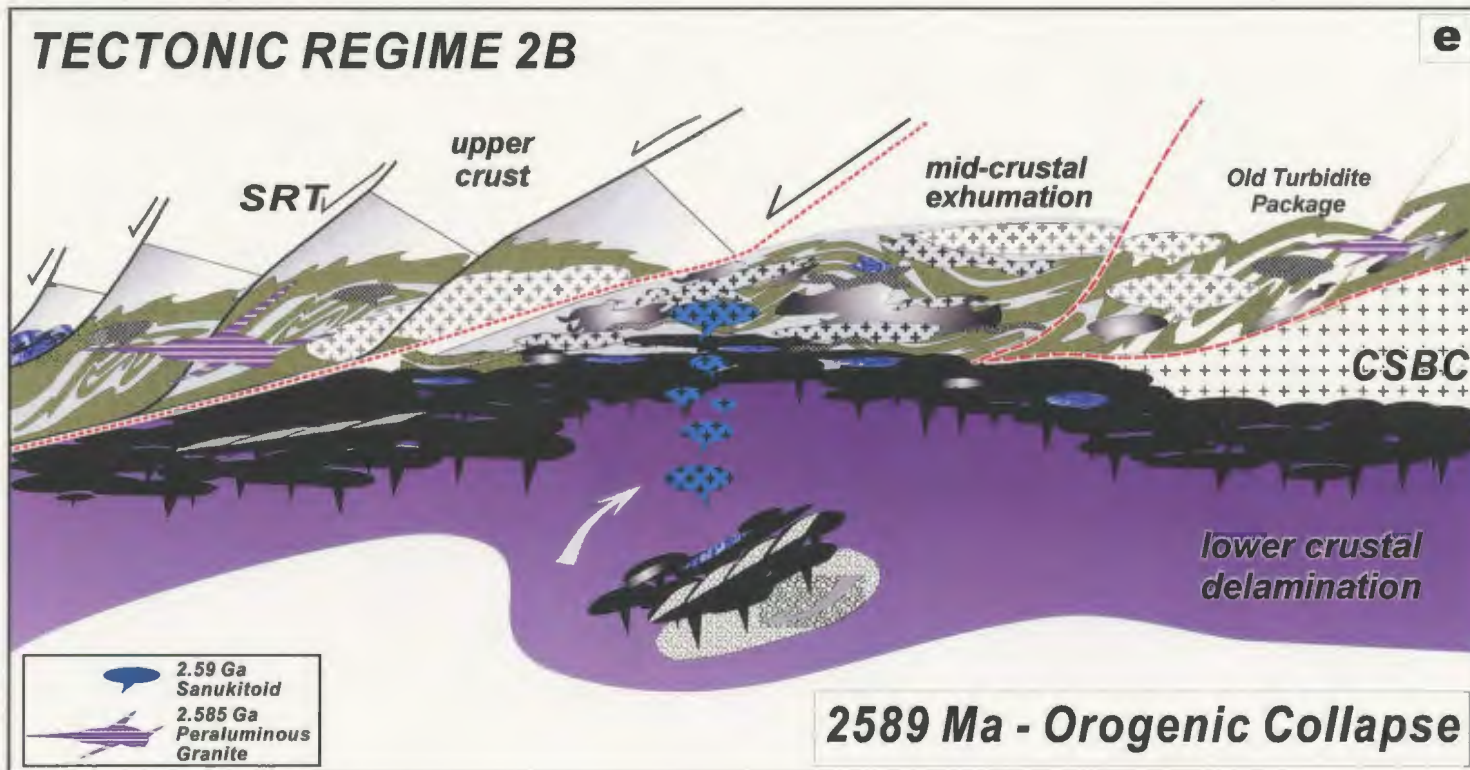


Figure 7.2e: Post-orogenic collapse (Tectonic Regime 2b). Overthickened orogenic crust is unstable and delamination of dense lower-crustal root initiates crustal extension and mid-crustal uplift. Crustal products are mantle sanukitoids and anatectic decompressional crustal melts.

sanukitoid suite), crustal extension and mid-crustal exhumation (D3). Decompression metamorphism (M3) overprinted peak M2 assemblages in upper-amphibolite- and granulite-facies rocks of the mid-crust. Asymmetric uplift of the mid-crust, achieved principally by operation of pervasive ductile conjugate extensional faulting, resulted in telescoping of the prograde M2 isograd sequence, but continuity of metamorphic zones was maintained. Low-temperature decompressional anatexis (cordierite leucogranite and pegmatitic granite suites), which in part post-dated extensional faulting, was the terminal process through which crustal stability was ultimately achieved.

7.4.2. Implications of crustal stratigraphy

A consistent theme addressed throughout this study is that of a ‘crustal stratigraphy’. Recognition of metamorphic continuity and the occurrence of a ca. >22 km depth profile from low-grade upper-crustal volcano-sedimentary belts to the high-grade mid-crustal Ghost subdomain has permitted documentation of various attributes of the crustal stratigraphy that characterizes the region. The datasets presented in chapters 2–6 have examined the age, compositional, deformational, thermal and metamorphic variations as a function of depth and thus constrain the four-dimensional evolution of Neoproterozoic crust.

Multidisciplinary datasets from the Kapuskasing Uplift in the Superior Province have revealed that crustal processes affected different crustal levels at different times. Specifically, the diachronous nature of magmatic, deformational and metamorphic processes has been shown to be central to crustal development. Data presented in

chapters 2–6 mirror several of the first-order observations from the Kapuskasing Uplift (Fig. 7.3), specifically in regard to the following:

1. The depth-dependence of crustal–growth ages (i.e., older upper crust versus younger mid crust);
2. The gross compositional zonation of the crust, characterized by a volcano-sedimentary (predominantly mafic) upper-crust, a plutonic (granitoid) mid-crust and a mafic lower crust;
3. The importance of magmatism during all phases of crustal evolution and the evolution of magma compositions with time corresponding to progressive crustal thickening and maturity;
4. The crustal-scale metamorphic zonation from a greenschist-facies upper crust to a granulite-facies mid crust;
5. The diachronous nature of deformation and metamorphism throughout the crustal column;
6. The similarity in structural architecture between the two areas, with steep upper-crustal structures and low- to moderately-dipping mid-crustal dome-and-basin geometries, consistent with seismic reflection datasets.

The thermal and inherited zircon datasets presented in chapters 5 and 6 provide unique insight into the crustal stratigraphy and demonstrate the intimate feedback relationships occurring between crustal levels in response to crustal evolution. Inherited zircon data support the existing understanding of the development and evolution of the lower crust as a consequence of mafic magmatic additions and subsequent melt

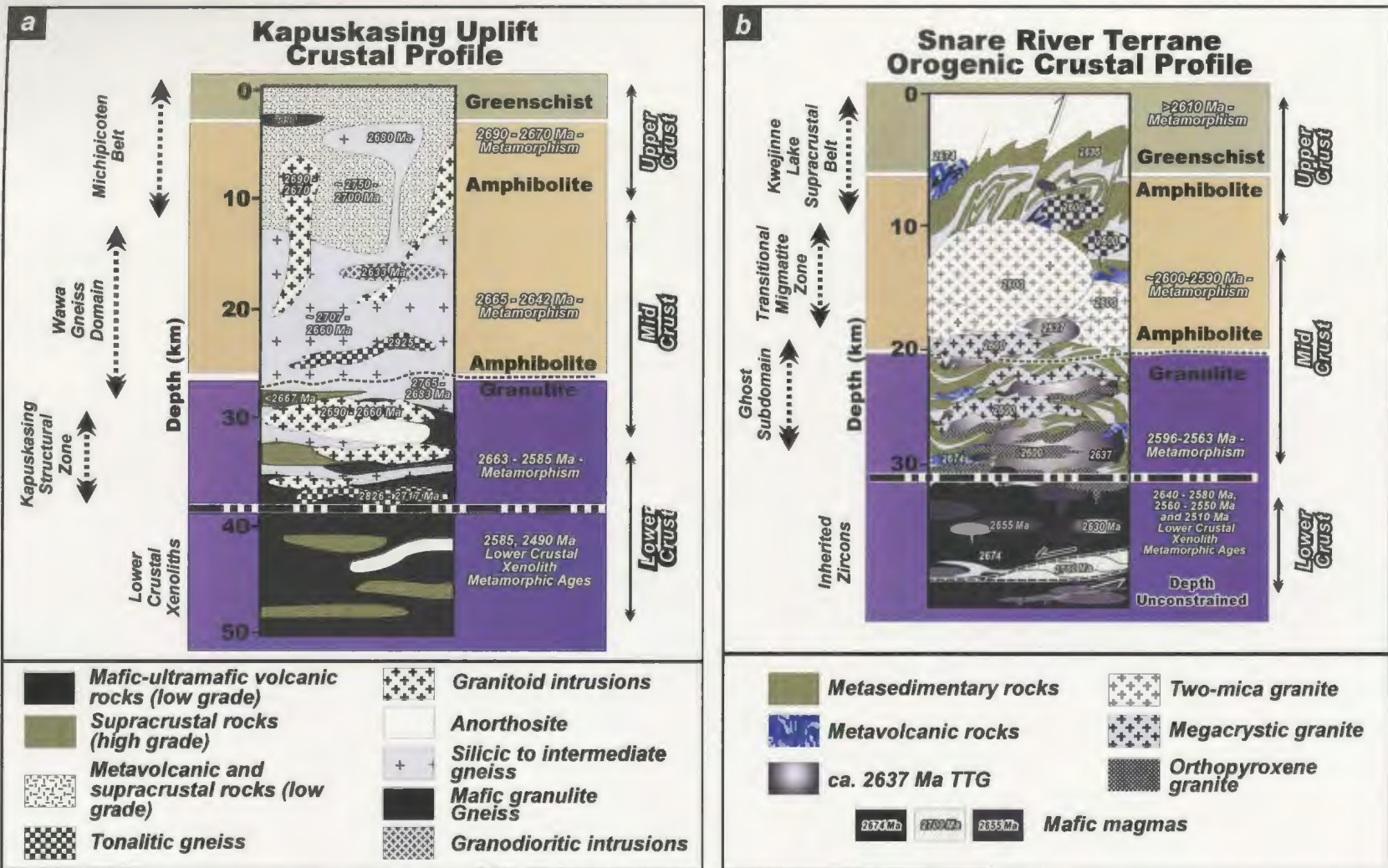


Figure 7.3: Schematic crustal stratigraphy of (a) the Kapuskasing structure, Superior Province (modified after Percival et al. 1992; U-Pb ages from Krogh and Moser 1994, Percival and West (1994), Moser 1994 and Moser et al. 1996), and (b) the Snare River terrane (this study; lower crustal xenolith metamorphic ages from Davis et al. 2003). Diagram illustrates second-order metamorphic layering of the crust, superimposed on broad transition from first-order dominantly silicic upper crust to largely plutonic mid crust through to mafic and ultramafic lower-crust. Note also the steep low grade upper crust and subhorizontal high grade mid crust. Protolith formation ages are noted on respective lithological units and predominant metamorphic ages are given adjacent to each crustal-scale stratigraphic column.

extraction. Additionally, the inherited zircon age data demonstrate the importance of tectonic intercalation during development of both the mid and lower crust.

The thermal dataset confirms the importance pluton-driven HT-LP metamorphism in the mid crust, but indicates that the primary source of heat was in the underlying lithospheric mantle. Furthermore, it provides an understanding of the distribution of heat throughout the orogenic crustal column and provides an explanation for the metamorphic diachroneity.

The Snare River terrane contrasts with the Kapuskasing Uplift in the causative mechanism responsible for mid-crustal uplift. Whereas in the Kapuskasing Uplift it was a result of a later (Paleoproterozoic) episode of compressional exhumation (i.e., polycyclic origin), in the Snare River terrane it was primarily the consequence of extensional tectonics that occurred in a single cycle of Neoproterozoic crustal evolution (locally overprinted during the Paleoproterozoic).

Collectively, the crustal profiles of the Kapuskasing Uplift and the Snare River terrane (Fig. 7.3) demonstrate the importance of and interplay among local magmatism, sedimentation, deformation, metamorphism and large-scale tectonic intercalation of exotic cratonic elements during crustal evolution. The four-dimensional datasets presented in this study indicate that the first-order mechanism of Neoproterozoic crustal growth was lateral accretion, which preceded second-order vertical crustal growth during accretion of outboard terranes.

7.5 Future Work

The Snare River terrane is an excellent natural laboratory in which to conduct crustal analysis and, as with the Kapuskasing Uplift, warrants detailed study and the acquisition of additional multidisciplinary datasets that build upon those presented in this thesis. The following studies would significantly improve the current understanding of crustal evolution in the Snare River terrane:

1. Absolute age constraints on the sequence of polyphase deformation at both the upper- and mid-crustal levels in order to constrain the degree of diachroneity;
2. Resolution of the timing of metamorphism in the upper and mid crust;
3. Detailed metamorphic petrology to better constrain the time-space variations in peak P-T conditions and provide estimates of the amount of uplift across the Ghost subdomain;
4. Improved resolution of the crustal architecture of the region, including better definition of the geometry of mid-crustal uplift;
5. Geophysical surveys to determine the thickness and structure of the crust under the Ghost subdomain;
6. Detrital zircon analysis to document the distribution of old and young turbidite packages to determine whether sedimentation was diachronous across the Slave Province or occurred in discrete events;
7. An outstanding issue with regard to the lower-crustal delamination and orogenic collapse model is the absence of voluminous magmatism. Was the asthenospheric

mantle sufficiently depleted in volatiles that further melting could not take place?

Combined mantle xenolith and crustal metamorphic studies to constrain the thermal regime that accompanied post-orogenic collapse would help resolve this issue.

7 References

- Brophy, J.A., and Pell, J. 2002. Preliminary Geology of the Labrish Lake area, Southwestern Slave Province; Parts of 85N/09. NWT Open File 2002-06. DIAND, NWT Geology Division, Yellowknife. 1 map plus legend scale 1: 50 000.
- Henderson, J.B., 1998. Preliminary geology, Wijinnedi Lake area, District of Mackenzie, NWT, GSC, Open file 3609, scale 1:50 000.
- Jackson, V.A. 1999. Preliminary 1:100 000 scale compilation of the geology of the Snare River area (1998 and 1999 results); EGS Open File 1999-18. DIAND, NWT Geology Division, Yellowknife.
- Jackson, V.A., 2003. Preliminary compilation of the geology of the Snare River (1998-2002 results), Winjinnedi Lake, Labrish Lake and Russell Lake area; parts of 85N and 85O. C.S. Lord Northern Geoscience Centre, Yellowknife, NT. NWT Open Report 2003-002. Map, scale 1:100 000.
- Lord, C.S. 1942. Snare and Ingray Lake map areas, Northwest Territories. Geological Survey of Canada, Memoir 235.
- Percival, J.A., Fountain, D.M., and Salisbury, M.H., 1992. Exposed crustal cross sections as windows on the lower crust. In D.M. Fountain and R.J. Arculus and R.W. Kay (eds). Continental lower crust. Elsevier, Amsterdam, pp. 317 – 362.

Appendix B

Supplementary Data – Reverse Discordance in U-Pb LAM

ICP-MS Datasets

B1 - Introduction

As noted in the text, reversely and normally discordant analyses in individual samples are a noticeable feature of the LAM ICP-MS dataset. In this appendix we provide supplementary data to investigate the causes of reverse discordance including a discussion of whether the results represent a real phenomenon due to within-grain redistribution of Pb and/or U in the analysed zircons and/or whether the data are an artefact of the analytical method, i.e., due to instrument-induced elemental fractionation. We begin with a discussion of the instrumental causes of reverse discordance in LAM ICP-MS data sets, then present data for internal standards used during data collection, and conclude with a discussion the correlation between zircon zonation and discordant data.

B2 – Elemental fractionation and LAM ICP-MS

The simplest explanation for the reversely discordant analyses presented in Chapters 2 and 5 is instrument and/or laser-induced elemental fractionation. Fractionation in LAM ICP-MS can occur at the ablation site, during aerosol transport of material to the ICP-MS, and within the plasma itself when atomization of particles is incomplete or random (Günther et al. 2003; Košler et al. 2005). In recent years, the effect of particle size distribution and its control on elemental fractionation has been examined (e.g. Guillong and Günther 2002; Košler and Sylvester 2003; Košler et al. 2005), and it has been shown that generation of large particle fractions during ablation can lead to significant matrix effects and non-stoichiometric sampling of material (Guillong and

Günther 2002; Košler et al 2005). This has been interpreted to indicate that when the concentration of large aerosol compounds delivered to the ICP increases, ionization efficiency decreases and preferential vaporization of compounds with higher volatility leads to elemental fractionation in the ICP (Günther et al. 2003). A major control on particle size is laser wavelength and smaller particles are generally produced with shorter wavelengths (Bruguier et al. 2001; Günther et al. 2003). Specifically, particle sizes produced by 266 nm wavelength Nd: YAG lasers are significantly greater than those produced by 193 nm excimer laser systems. Other factors that have been shown to exert control on particle size are ablation rate and penetration depth; in this case it has been argued that shallow penetration depths are characterized by greater laser energy per unit area sampled, consequently enhancing the potential for more efficient breaking of chemical bonds and ionization (Günther et al. 2003). However Košler et al. (2005) demonstrated that, in addition to fractionation caused by large particle size, small particle size can also lead to anomalously high Pb/U ratios.

Given the amount of reverse discordance in the U-Pb datasets presented in this thesis, it is difficult to rule out the effect of non-representative sampling of particles based on their size. Use of the slow line-profiling technique during this study (Fig. B1), although resulting in a low fractionation index (Li et al. 2001), does not rule out the possibility of time-dependent fractionation, and Guillong and Günther (2002) considered that the low fractionation index more likely reflected stability of the ablation process rather than the absence of fractionation. The significant reduction in ablation speed that

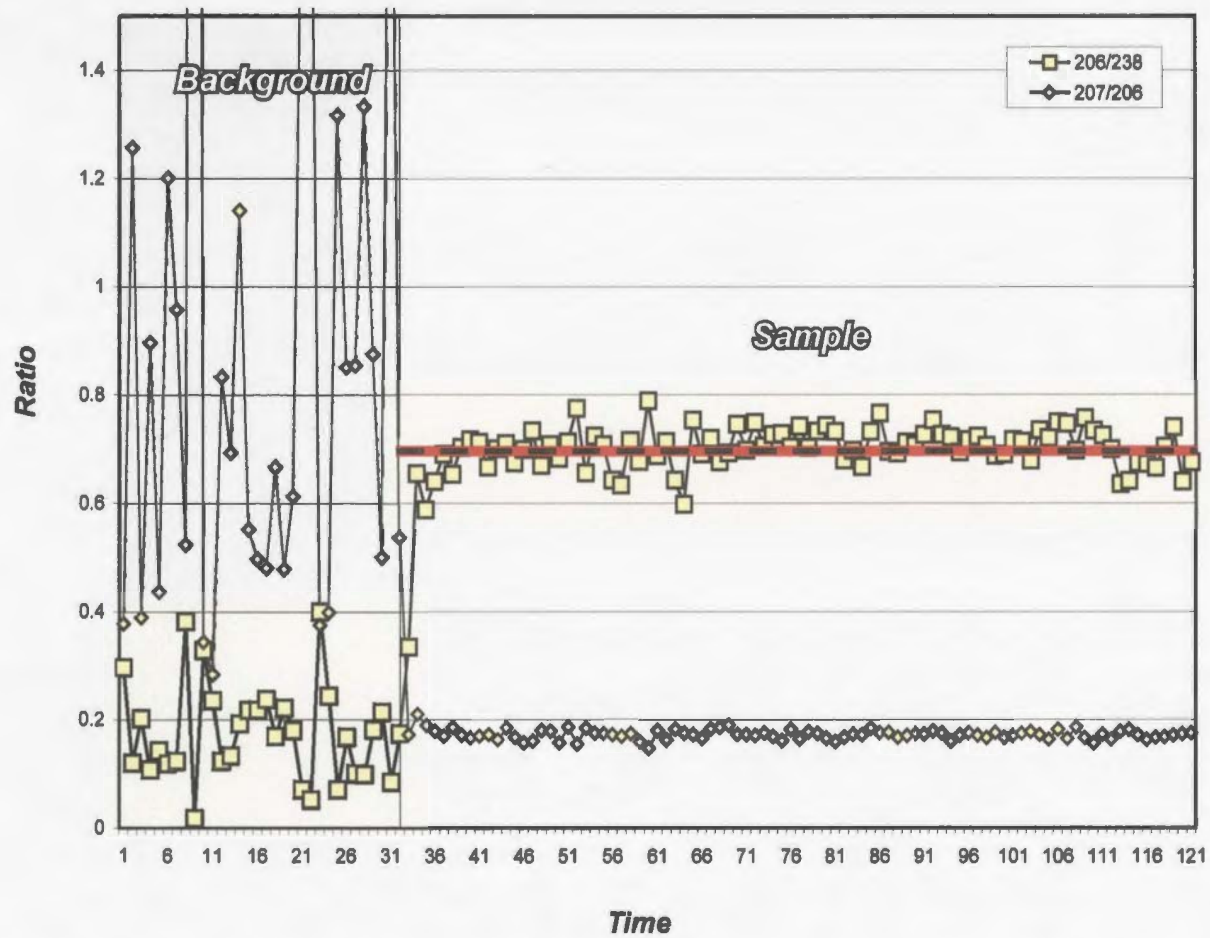


Figure B1: Time-resolved $^{206}\text{Pb}/^{238}\text{U}$ and $^{207}\text{Pb}/^{206}\text{Pb}$ ratios during the course of a single analysis. Diagram illustrates limited time-dependent elemental fractionation or more specifically a constancy of ablation in the zircon grain analysed

was employed in this study during data collection (i.e. the slow raster technique) is speculated to have resulted in generation of smaller particle sizes and, as illustrated by Košler et al. (2005), anomalously high Pb/U ratios and hence, reversely discordant data. However, as we show below, despite these instrumental concerns, the accuracy of the U-Pb data presented in the research was carefully monitored by external calibration using the chosen reference materials (02123 and VB165)

B3 - Analyses of standards

LAM ICP-MS analyses (Tables B1, B2) of the standard 02123 and the internal standard VB165 were routinely interspersed with analyses of the unknowns (typically analyses of two unknowns were followed by analysis of a standard). The U and Pb concentrations and ratios of 02123 and VB165 were determined independently by ID TIMS before their use as standards in the LAM ICP-MS study. ID TIMS analyses of 02123 yielded a concordant age of 295 ± 1 Ma (excluding decay constant uncertainties; reported in Ketchum et al. 2001, analyst G. Dunning). ID TIMS analysis of VB165, reported in Table 2.1 and Fig. 2.7a in Chapter 2, gave an age of 2674 ± 1.4 Ma (excluding decay constant uncertainties). Discordance of the 4 single grain abraded analyses of VB165 ranged from 0.1-0.9% (Table 2.1). Despite the slight differences in discordance of individual single grain fractions, VB165 was used as an internal standard because of its similarity in age to the other unknowns in this study and its consistent $^{207}\text{Pb}/^{206}\text{Pb}$ ratio.

Table B1: LAM ICP-MS U-Pb age data for Standard 02123. Age calculations follow the method of Ludwig (1999). 1 and 2 σ error are stated for calculated ratios. 1 σ errors are stated for calculated ages. Weighted mean $^{207}\text{Pb}/^{206}\text{Pb}$ ages reported in brackets without U decay constant uncertainties.

	Concordia Columns				Rho	$^{207}\text{Pb}/^{206}\text{Pb}$		2 σ %		2 σ %		2 σ %		AGES Ma		$^{206}\text{Pb}/^{238}\text{U}$		$^{207}\text{Pb}/^{206}\text{Pb}$		%disc
	$^{207}\text{Pb}/^{235}\text{U}$	1 σ	$^{206}\text{Pb}/^{238}\text{U}$	1 σ		$^{207}\text{Pb}/^{206}\text{Pb}$	1 σ	$^{207}\text{Pb}/^{235}\text{U}$	$^{206}\text{Pb}/^{238}\text{U}$	$^{207}\text{Pb}/^{206}\text{Pb}$	$^{207}\text{Pb}/^{235}\text{U}$	1 σ	$^{206}\text{Pb}/^{238}\text{U}$	1 σ	$^{207}\text{Pb}/^{206}\text{Pb}$	1 σ				
1	0.334	0.003	0.046	0.000	0.606	0.052	0.000	1.651	1.469	1.394	292.3	2.1	290.2	2.1	289.6	15.9	-0.2			
2	0.333	0.006	0.046	0.001	0.393	0.052	0.001	3.311	2.376	3.228	292.1	4.2	289.0	3.4	306.8	36.8	5.8			
3	0.340	0.007	0.048	0.001	0.197	0.052	0.001	3.933	2.265	4.135	297.2	5.1	300.2	3.3	268.6	47.4	-11.8			
4	0.334	0.003	0.046	0.000	0.730	0.052	0.000	1.633	1.567	1.177	292.4	2.1	291.6	2.2	276.6	13.5	-5.4			
5	0.338	0.007	0.047	0.001	0.350	0.052	0.001	4.132	2.997	5.199	295.9	5.3	293.1	4.3	301.5	59.3	2.8			
6	0.341	0.004	0.046	0.000	0.283	0.053	0.001	2.228	1.400	2.271	298.1	2.9	291.9	2.0	327.8	25.8	10.9			
7	0.341	0.003	0.047	0.000	0.561	0.052	0.000	1.772	1.595	1.585	297.7	2.3	298.3	2.3	269.1	18.2	-10.9			
8	0.340	0.003	0.048	0.000	0.386	0.052	0.000	1.936	1.402	1.902	297.4	2.5	299.2	2.0	273.0	21.8	-9.6			
9	0.335	0.003	0.046	0.000	0.561	0.052	0.000	1.772	1.595	1.585	293.1	2.3	290.6	2.3	269.1	18.2	-8.0			
10	0.334	0.003	0.046	0.000	0.386	0.052	0.000	1.936	1.402	1.902	292.8	2.5	291.4	2.0	273.0	21.8	-6.7			
11	0.342	0.007	0.047	0.001	0.475	0.052	0.001	3.917	2.712	3.552	298.3	5.1	298.0	3.9	276.8	40.7	-7.7			
12	0.341	0.007	0.047	0.001	0.177	0.052	0.001	3.907	2.436	4.222	297.6	5.0	298.8	3.6	272.9	48.4	-9.5			
13	0.345	0.005	0.048	0.001	0.836	0.054	0.000	2.783	2.483	1.534	300.9	3.6	300.1	3.6	358.5	17.3	16.3			
14	0.340	0.005	0.047	0.000	0.448	0.053	0.001	2.810	1.217	2.512	297.1	3.6	295.8	1.8	347.9	28.4	15.0			
15	0.337	0.003	0.047	0.000	0.479	0.053	0.000	1.869	1.225	1.673	295.2	2.4	294.9	1.8	337.7	19.0	12.7			
16	0.331	0.004	0.047	0.000	0.392	0.052	0.001	2.383	1.518	2.268	290.1	3.0	295.3	2.2	280.5	26.0	-5.3			
17	0.334	0.003	0.047	0.000	0.465	0.053	0.000	1.876	1.655	1.837	292.8	2.4	295.3	2.4	307.4	20.9	4.0			
18	0.338	0.003	0.047	0.000	0.415	0.053	0.001	2.021	1.189	1.871	295.8	2.6	293.7	1.7	348.2	21.2	15.7			
19	0.338	0.005	0.047	0.001	0.604	0.054	0.001	2.759	2.323	2.294	295.7	3.5	295.2	3.4	352.5	25.9	16.3			
20	0.339	0.005	0.047	0.000	0.406	0.052	0.001	2.973	1.647	2.753	296.2	3.8	294.7	2.4	295.4	31.4	0.2			
21	0.335	0.004	0.046	0.000	0.611	0.052	0.001	2.600	1.889	2.079	293.2	3.3	291.5	2.7	303.9	23.7	4.1			
22	0.337	0.005	0.047	0.001	0.514	0.052	0.001	2.759	2.546	2.621	294.8	3.5	296.4	3.7	272.0	30.0	-9.0			
23	0.338	0.003	0.047	0.000	0.798	0.052	0.000	1.832	1.805	1.155	295.7	2.4	295.4	2.6	282.2	13.2	-4.7			
24	0.334	0.004	0.047	0.000	0.506	0.052	0.001	2.549	1.826	2.264	292.5	3.2	294.5	2.6	270.3	26.0	-9.0			
25	0.332	0.004	0.047	0.000	0.443	0.051	0.001	2.445	1.503	2.233	291.5	3.1	296.3	2.2	243.5	25.7	-21.7			
26	0.342	0.005	0.047	0.000	0.699	0.052	0.001	2.746	2.064	1.969	298.4	3.6	296.6	3.0	302.9	22.4	2.0			
27	0.338	0.003	0.047	0.000	0.526	0.052	0.000	2.002	1.656	1.806	295.9	2.6	293.5	2.4	300.7	20.6	2.4			
28	0.339	0.004	0.047	0.000	0.579	0.052	0.001	2.553	1.807	2.107	296.7	3.3	294.9	2.6	292.9	24.1	-0.7			
29	0.341	0.003	0.046	0.000	0.402	0.053	0.000	1.710	1.511	1.770	298.1	2.2	292.6	2.2	325.7	20.1	10.2			
30	0.339	0.003	0.047	0.000	0.699	0.052	0.000	2.025	1.583	1.458	296.6	2.6	297.4	2.3	293.0	16.6	-1.5			
31	0.336	0.007	0.047	0.001	0.615	0.052	0.001	3.939	3.224	3.209	293.9	5.0	296.7	4.7	275.8	36.8	-7.6			
32	0.339	0.005	0.047	0.001	0.715	0.053	0.001	2.817	2.183	1.978	296.3	3.6	294.6	3.1	331.7	22.4	11.2			
33	0.337	0.005	0.047	0.000	0.384	0.052	0.001	2.734	1.574	2.579	294.9	3.5	296.6	2.3	285.5	29.5	-3.9			
34	0.338	0.004	0.046	0.000	0.528	0.053	0.001	2.489	1.693	2.147	295.6	3.2	291.5	2.4	327.9	24.4	-11.1			
35	0.343	0.011	0.046	0.001	0.730	0.057	0.002	6.334	4.906	8.048	299.8	8.2	289.9	7.0	484.6	88.8	40.2			
36	0.339	0.006	0.047	0.001	0.732	0.054	0.001	3.542	2.631	2.413	296.7	4.6	294.1	3.8	379.2	27.1	22.4			
37	0.337	0.003	0.047	0.000	0.498	0.054	0.001	1.954	1.828	1.899	294.9	2.5	298.4	2.7	352.4	21.5	15.3			
38	0.339	0.005	0.047	0.001	0.715	0.052	0.001	2.991	2.427	2.111	296.7	3.8	296.9	3.5	285.2	24.1	-4.1			
39	0.336	0.007	0.047	0.001	0.267	0.055	0.001	3.985	2.487	4.095	293.8	5.1	294.1	3.6	427.2	45.7	31.2			
40	0.336	0.010	0.047	0.001	0.139	0.055	0.002	6.195	2.363	6.315	293.8	7.9	293.8	3.4	423.3	70.5	30.6			
41	0.339	0.015	0.047	0.001	0.388	0.055	0.002	8.679	3.395	8.000	296.6	11.2	297.8	4.9	424.0	89.3	29.7			
42	0.342	0.014	0.047	0.001	0.144	0.052	0.002	8.162	4.288	8.656	298.5	10.6	298.4	6.3	283.9	99.0	-5.1			
43	0.339	0.007	0.046	0.001	0.432	0.053	0.001	3.931	2.791	3.709	296.4	5.1	292.1	4.0	307.6	42.2	5.0			
44	0.336	0.016	0.047	0.001	0.365	0.052	0.002	9.371	5.398	8.947	294.1	12.0	297.3	7.8	302.1	102.0	1.6			
45	0.336	0.008	0.047	0.001	0.404	0.053	0.001	4.690	2.340	4.314	294.0	6.0	294.5	3.4	312.6	49.1	5.8			
46	0.331	0.005	0.048	0.001	0.442	0.051	0.001	3.217	2.257	3.004	290.7	4.1	299.5	3.3	258.3	34.5	-16.0			
47	0.342	0.005	0.047	0.000	0.494	0.055	0.001	3.082	1.542	2.679	299.0	4.0	294.1	2.2	392.1	30.1	25.0			
48	0.342	0.006	0.047	0.001	0.440	0.052	0.001	3.442	2.529	3.252	298.3	4.4	296.9	3.7	291.8	37.1	-1.8			
49	0.339	0.009	0.047	0.001	0.354	0.052	0.001	5.148	2.610	4.878	296.4	6.6	296.1	3.8	273.7	55.9	-8.2			
50	0.340	0.007	0.046	0.001	0.550	0.053	0.001	4.191	2.791	3.533	297.3	5.4	292.4	4.0	347.9	39.9	16.0			
51	0.337	0.006	0.047	0.000	0.352	0.052	0.001	3.401	2.101	3.309	294.8	4.4	295.8	3.0	298.3	37.7	0.8			
52	0.338	0.004	0.047	0.000	0.336	0.053	0.001	2.494	1.584	2.464	295.9	3.2	294.9	2.3	307.6	28.1	4.1			
53	0.343	0.006	0.047	0.001	0.340	0.053	0.001	3.571	2.273	4.513	299.3	4.6	293.4	3.3	338.2	51.1	13.2			
54	0.337	0.004	0.047	0.001	0.568	0.053	0.001	2.550	2.223	2.238	295.0	3.3	297.0	3.2	314.8	25.5	5.7			
55	0.343	0.006	0.046	0.000	0.236	0.054	0.001	3.218	1.743	3.278	299.6	4.2	290.2	2.5	374.3	36.9	22.5			
56	0.342	0.006	0.046	0.000	0.188	0.053	0.001	3.480	1.930	3.648	298.6	4.5	292.2	2.8	340.2	41.3	14.1			
57	0.337	0.004	0.047	0.000	0.263	0.052	0.001	2.375	1.973	2.659	294.9	3.0	294.0	2.8	305.6	30.3	3.8			
58	0.332	0.006	0.047	0.001	0.392	0.051	0.001	3.526	2.767	3.526	290.8	4.5	296.8	4.0	241.6	40.6	-22.8			
59	0.332	0.006	0.046	0.001	0.259	0.052	0.001	3.784	2.665	4.024	291.0	4.8	291.9	3.8	281.9	46.0	-3.5			
60	0.337	0.005	0.047	0.000	0.176	0.052	0.001	3.218	1.514	3.307	295.1	4.1	296.9	2.2	293.1	37.8	-1.3			
61	0.340	0.007	0.046	0.001	0.094	0.054	0.001	4.191	2.180	4.538	297.2	5.4	289.5	3.1	380.2	51.0	23.8			
62	0.333	0.008	0.047	0.001	0.340	0.052	0.001	4.647	2.279	5.406	291.5	5.9	296.4	3.3	298.5	61.7	0.7			
63	0.336	0.005	0.047	0.000	0.300	0.051	0.001	3.037	1.672	3.483	294.1	3.9	296.9	2.4	225.9	40.3	-31.5			
64	0.334	0.005	0.046	0.000	0.098	0.051	0.001	2.799	1.796	3.174	292.5	3.6	291.9	2.6	255.8	36.5	-14.1			
65	0.345	0.005	0.047	0.000	0.098	0.052	0.001	2.771	1.702	3.107	301.3	3.6	296.0	2.5	292.0	35.5	-1.4			

(continued on next page)

Table B1: continued

66	0.327	0.007	0.046	0.000	0.300	0.050	0.001	4.049	2.013	4.607	287.2	5.1	292.5	2.9	189.7	53.6	-54.2
67	0.340	0.004	0.046	0.000	0.308	0.052	0.001	2.405	1.400	2.381	297.0	3.1	289.4	2.0	282.5	27.2	-2.4
68	0.341	0.006	0.046	0.001	0.590	0.053	0.001	3.782	2.354	3.055	297.6	4.9	291.9	3.4	349.9	34.5	16.6
69	0.332	0.006	0.046	0.000	0.485	0.052	0.001	3.747	1.975	3.282	291.1	4.7	292.4	2.8	291.2	37.5	-0.4
70	0.334	0.006	0.047	0.001	0.624	0.052	0.001	3.502	3.200	2.918	292.3	4.4	294.7	4.6	304.5	33.2	3.2
71	0.338	0.011	0.047	0.001	0.389	0.053	0.002	6.275	3.515	5.879	295.6	8.0	297.3	5.1	309.4	66.9	3.9
72	0.344	0.008	0.046	0.001	0.502	0.054	0.001	4.427	2.511	3.840	299.9	5.7	292.6	3.6	368.1	43.3	-20.5
73	0.338	0.007	0.047	0.001	0.431	0.053	0.001	4.403	2.441	4.010	295.4	5.6	294.1	3.5	324.1	45.5	9.3
74	0.346	0.010	0.048	0.001	0.123	0.053	0.002	5.597	3.102	6.055	301.6	7.3	301.8	4.6	321.3	68.8	6.1
75	0.345	0.007	0.047	0.001	0.561	0.053	0.001	3.927	2.343	3.253	300.7	5.1	296.9	3.4	337.8	36.8	12.1
76	0.337	0.005	0.047	0.000	0.512	0.051	0.001	2.795	1.951	2.457	294.7	3.6	297.9	2.8	254.9	28.2	-16.9
77	0.336	0.007	0.047	0.001	0.582	0.054	0.001	3.894	2.177	3.166	294.3	5.0	293.3	3.1	360.4	35.7	18.6
78	0.335	0.004	0.047	0.000	0.399	0.053	0.001	2.493	1.510	2.344	293.5	3.2	296.1	2.2	344.9	26.5	14.1
79	0.341	0.006	0.046	0.000	0.362	0.055	0.001	3.519	2.063	3.375	298.0	4.5	292.1	2.9	411.2	37.7	28.9
80	0.335	0.004	0.047	0.000	0.531	0.054	0.001	2.685	2.053	2.360	293.1	3.4	294.9	3.0	387.9	26.5	24.0
81	0.332	0.004	0.046	0.000	0.484	0.052	0.001	2.161	1.663	1.989	291.3	2.7	290.6	2.4	294.3	22.7	1.3
82	0.339	0.004	0.047	0.000	0.593	0.053	0.000	2.243	1.585	1.824	296.4	2.9	293.8	2.3	309.2	20.8	5.0
83	0.334	0.004	0.047	0.000	0.522	0.052	0.000	2.099	1.370	1.811	292.6	2.7	297.2	2.0	268.3	20.8	-10.7
84	0.334	0.004	0.047	0.000	0.382	0.051	0.001	2.545	1.611	2.437	292.9	3.2	298.0	2.3	261.0	28.0	-14.2
85	0.343	0.006	0.047	0.001	0.721	0.052	0.001	3.669	3.011	2.566	299.5	4.8	296.3	4.4	289.3	29.3	-2.4
86	0.342	0.004	0.046	0.000	0.368	0.056	0.001	2.448	1.295	2.310	298.6	3.2	287.5	1.8	453.6	25.6	36.6
87	0.332	0.005	0.047	0.000	0.422	0.054	0.001	3.221	2.104	3.013	291.4	4.1	293.8	3.0	355.7	34.0	17.4
88	0.341	0.006	0.046	0.000	0.680	0.053	0.001	3.559	2.136	2.626	297.8	4.6	290.8	3.0	321.9	29.8	9.7
89	0.335	0.006	0.047	0.000	0.418	0.052	0.001	3.538	2.017	3.258	293.7	4.5	295.2	2.9	273.1	37.3	-8.1
90	0.341	0.004	0.048	0.000	0.489	0.052	0.001	2.082	1.708	1.942	297.6	2.7	299.3	2.5	269.9	22.3	-10.9
91	0.344	0.007	0.048	0.001	0.677	0.052	0.001	4.015	3.322	3.018	300.1	5.2	301.0	4.9	300.7	34.4	-0.1
92	0.337	0.005	0.047	0.001	0.801	0.053	0.000	3.070	2.470	1.840	295.0	3.9	296.3	3.6	345.8	20.8	14.3
93	0.336	0.006	0.047	0.000	0.112	0.051	0.001	3.389	1.950	3.716	294.4	4.3	295.1	2.8	219.9	43.0	-34.2
94	0.336	0.005	0.046	0.000	0.379	0.051	0.001	2.794	1.854	2.704	294.4	3.6	291.5	2.6	237.4	31.2	-22.8
95	0.334	0.005	0.047	0.000	0.150	0.052	0.001	2.959	1.697	3.183	292.6	3.8	296.6	2.5	265.8	36.5	-11.6
96	0.339	0.003	0.048	0.000	0.413	0.051	0.000	1.948	1.365	1.860	296.1	2.5	300.5	2.0	256.0	21.4	-17.4
97	0.332	0.005	0.047	0.000	0.182	0.052	0.001	3.293	1.746	3.435	291.4	4.2	294.5	2.5	271.2	39.4	-8.6
98	0.340	0.005	0.047	0.000	0.550	0.052	0.001	2.919	2.094	2.487	297.3	3.8	294.6	3.0	287.7	28.4	-2.4
99	0.335	0.006	0.047	0.000	0.315	0.051	0.001	3.507	1.617	3.367	293.7	4.5	296.5	2.3	255.8	38.7	-15.9
100	0.341	0.004	0.047	0.000	0.561	0.052	0.000	2.082	1.576	1.771	297.6	2.7	294.6	2.3	306.3	20.2	3.8
101	0.335	0.003	0.047	0.000	0.487	0.052	0.001	2.055	1.714	1.932	293.4	2.6	294.1	2.5	287.4	22.1	-2.3
102	0.336	0.005	0.047	0.001	0.574	0.052	0.001	2.848	2.274	2.419	294.2	3.6	295.3	3.3	289.0	27.6	-2.2
103	0.342	0.003	0.047	0.000	0.543	0.052	0.000	2.026	1.377	1.724	298.9	2.6	295.9	2.0	305.4	19.6	3.1
104	0.339	0.005	0.046	0.000	0.546	0.053	0.001	2.844	1.818	2.396	296.5	3.7	291.1	2.6	326.4	27.2	10.8
105	0.333	0.004	0.047	0.000	0.010	0.052	0.001	2.264	1.935	2.963	291.9	2.9	293.3	2.8	278.7	33.9	-5.2

(concluded)

Table B2: LAM ICP-MS U-Pb age data for Neoproterozoic Standard VB165. Age calculations follow the method of Ludwig (1999). 1 and 2 σ error are stated for calculated ratios. 1 σ errors are stated for calculated ages.

	Concordia Columns		Rho	$\frac{^{207}\text{Pb}}{^{206}\text{Pb}}$		2 σ %		2 σ %		2 σ %		AGES Ma		$\frac{^{206}\text{Pb}}{^{238}\text{U}}$		$\frac{^{207}\text{Pb}}{^{206}\text{Pb}}$		%disc
	$\frac{^{207}\text{Pb}}{^{235}\text{U}}$	1 σ		$\frac{^{206}\text{Pb}}{^{238}\text{U}}$	1 σ	$\frac{^{207}\text{Pb}}{^{235}\text{U}}$	1 σ	$\frac{^{207}\text{Pb}}{^{235}\text{U}}$	$\frac{^{206}\text{Pb}}{^{238}\text{U}}$	$\frac{^{207}\text{Pb}}{^{206}\text{Pb}}$	$\frac{^{207}\text{Pb}}{^{235}\text{U}}$	1 σ	$\frac{^{206}\text{Pb}}{^{238}\text{U}}$	1 σ	$\frac{^{207}\text{Pb}}{^{206}\text{Pb}}$	1 σ		
1	12.221	0.090	0.488	0.003	0.690	0.182	0.001	1.476	1.403	1.135	2621.5	6.9	2560.4	14.8	2671.5	9.4	4.2	
2	13.222	0.105	0.524	0.003	0.659	0.183	0.001	1.581	1.282	1.212	2695.6	7.5	2714.7	14.2	2677.1	10.0	-1.4	
3	13.579	0.122	0.538	0.005	0.620	0.183	0.002	1.799	1.957	1.643	2720.8	8.5	2776.7	22.1	2679.9	13.6	-3.6	
4	12.769	0.174	0.507	0.006	0.731	0.182	0.002	2.732	2.499	1.932	2662.8	12.9	2642.8	27.1	2671.2	16.0	1.1	
5	11.709	0.127	0.468	0.005	0.611	0.182	0.002	2.174	2.188	1.924	2581.4	10.2	2473.6	22.5	2667.0	15.9	7.3	
6	13.839	0.194	0.550	0.008	0.974	0.183	0.001	2.800	2.975	0.686	2738.8	13.3	2825.7	34.0	2676.2	5.7	-5.6	
7	11.591	0.146	0.461	0.006	0.821	0.182	0.001	2.511	2.522	1.505	2571.9	11.7	2445.2	25.7	2670.8	12.5	8.4	
8	12.291	0.097	0.489	0.004	0.540	0.182	0.001	1.577	1.649	1.548	2626.9	7.4	2564.5	17.4	2674.1	12.8	4.1	
9	13.569	0.222	0.543	0.010	0.824	0.181	0.002	3.266	3.624	2.074	2720.1	15.4	2797.6	41.1	2662.1	17.2	-5.1	
10	12.224	0.150	0.484	0.007	0.708	0.182	0.002	2.458	2.886	2.080	2621.8	11.5	2545.6	30.3	2672.6	17.2	4.7	
11	12.696	0.074	0.505	0.003	0.708	0.182	0.001	1.171	1.207	0.909	2657.4	5.5	2633.9	13.0	2670.4	7.5	1.4	
12	12.868	0.118	0.510	0.004	0.784	0.182	0.001	1.836	1.636	1.156	2670.0	8.6	2657.8	17.8	2673.1	9.6	0.6	
13	12.904	0.106	0.514	0.004	0.569	0.182	0.001	1.636	1.590	1.498	2672.7	7.7	2672.0	17.4	2671.5	12.4	0.0	
14	13.004	0.119	0.517	0.004	0.593	0.182	0.001	1.828	1.683	1.588	2680.0	8.6	2688.5	18.5	2672.1	13.1	-0.6	
15	12.772	0.167	0.508	0.007	0.918	0.182	0.001	2.621	2.608	1.060	2663.0	12.3	2646.7	28.3	2671.6	8.8	0.9	
16	13.363	0.128	0.529	0.005	0.762	0.183	0.001	1.914	1.817	1.290	2705.7	9.0	2736.3	20.3	2679.4	10.7	-2.1	
17	16.073	0.201	0.645	0.008	0.917	0.182	0.001	2.495	2.456	1.012	2881.1	11.9	3208.2	31.0	2671.6	8.4	-20.1	
18	13.100	0.154	0.523	0.006	0.875	0.183	0.001	2.344	2.418	1.191	2686.9	11.1	2710.8	26.8	2679.8	9.9	-1.2	
19	12.471	0.106	0.496	0.004	0.755	0.182	0.001	1.702	1.671	1.181	2640.5	8.0	2597.8	17.9	2671.9	9.8	2.8	
20	14.779	0.143	0.587	0.005	0.683	0.183	0.001	1.935	1.569	1.434	2801.1	9.2	2978.3	18.7	2678.3	11.9	-11.2	
21	12.963	0.120	0.512	0.005	0.760	0.183	0.001	1.852	1.907	1.302	2677.0	8.7	2664.7	20.8	2683.3	10.8	0.7	
22	12.869	0.129	0.514	0.005	0.834	0.182	0.001	2.006	1.855	1.121	2670.1	9.5	2675.6	20.3	2673.1	9.3	-0.1	
23	12.884	0.140	0.514	0.004	0.662	0.181	0.001	2.167	1.634	1.637	2671.2	10.2	2674.8	17.9	2666.4	13.6	-0.3	
24	14.534	0.121	0.576	0.004	0.672	0.183	0.001	1.663	1.509	1.292	2785.2	7.9	2934.0	17.8	2675.8	10.7	-9.6	
25	12.383	0.106	0.490	0.003	0.657	0.183	0.001	1.713	1.418	1.324	2633.9	8.0	2569.6	15.0	2676.3	11.0	4.0	
26	14.542	0.177	0.580	0.007	0.924	0.182	0.001	2.441	2.298	0.937	2785.8	11.6	2948.0	27.2	2671.9	7.8	-10.3	
27	12.015	0.065	0.478	0.002	0.727	0.182	0.001	1.083	1.034	0.784	2605.6	5.1	2517.5	10.8	2670.6	6.5	5.7	
28	12.714	0.109	0.507	0.003	0.571	0.182	0.001	1.717	1.377	1.464	2658.7	8.1	2642.3	14.9	2669.2	12.1	1.0	
29	12.316	0.093	0.487	0.003	0.701	0.183	0.001	1.516	1.357	1.121	2628.8	7.1	2558.2	14.3	2676.8	9.3	4.4	
30	12.810	0.108	0.509	0.004	0.741	0.182	0.001	1.687	1.684	1.212	2665.8	7.9	2653.5	18.3	2672.5	10.0	0.7	
31	12.436	0.094	0.491	0.003	0.605	0.183	0.001	1.511	1.363	1.284	2637.9	7.1	2573.4	14.5	2682.5	10.6	4.1	
32	15.741	0.177	0.623	0.007	0.922	0.182	0.001	2.253	2.170	0.879	2861.2	10.8	3122.3	26.8	2673.8	7.3	-16.8	
33	12.260	0.137	0.485	0.005	0.705	0.183	0.002	2.240	2.245	1.724	2624.5	10.5	2547.7	23.6	2682.4	14.3	5.0	
34	13.481	0.103	0.533	0.004	0.520	0.183	0.001	1.525	1.532	1.498	2714.0	7.2	2753.6	17.2	2682.0	12.4	-2.7	
35	12.104	0.149	0.483	0.005	0.528	0.182	0.002	2.455	2.191	2.269	2612.5	11.5	2538.6	23.0	2670.1	18.8	4.9	
36	11.691	0.080	0.466	0.003	0.578	0.182	0.001	1.368	1.226	1.198	2580.0	6.4	2466.5	12.6	2672.0	9.9	7.7	
37	12.931	0.113	0.515	0.004	0.934	0.182	0.001	1.743	1.705	0.626	2674.6	8.2	2677.3	18.7	2672.1	5.2	-0.2	
38	11.960	0.081	0.475	0.003	0.803	0.182	0.001	1.361	1.304	0.838	2601.3	6.4	2505.4	13.5	2672.9	6.9	6.3	
39	12.579	0.091	0.498	0.004	0.842	0.182	0.001	1.441	1.616	0.874	2648.7	6.8	605.6	17.3	2671.1	7.2	2.5	
40	12.868	0.152	0.514	0.006	0.966	0.181	0.001	2.364	2.324	0.616	2670.1	11.1	2674.6	25.4	2660.1	5.1	-0.5	
41	12.677	0.080	0.501	0.003	0.773	0.183	0.001	1.269	1.195	0.833	2656.0	6.0	2618.5	12.9	2675.9	6.9	2.1	
42	12.949	0.096	0.513	0.004	0.845	0.182	0.001	1.484	1.544	0.846	2676.0	7.0	2671.4	16.9	2670.2	7.0	0.0	
43	11.649	0.095	0.466	0.004	0.640	0.183	0.001	1.639	1.512	1.341	2576.6	7.7	2468.1	15.5	2676.0	11.1	7.8	
44	11.884	0.093	0.473	0.003	0.797	0.183	0.001	1.563	1.442	0.964	2595.3	7.3	2495.0	14.9	2681.2	8.0	6.9	
45	13.268	0.207	0.527	0.008	0.937	0.182	0.001	3.117	2.930	1.088	2698.9	14.7	2730.7	32.6	2674.5	9.0	-2.1	
46	12.583	0.106	0.501	0.004	0.899	0.182	0.001	1.689	1.669	0.757	2648.9	7.9	2617.1	18.0	2675.0	6.3	2.2	
47	12.522	0.091	0.500	0.004	0.873	0.182	0.001	1.454	1.535	0.757	2644.4	6.8	2611.9	16.5	2668.6	6.3	2.1	
48	14.219	0.176	0.565	0.007	0.901	0.182	0.001	2.472	2.473	1.102	2764.4	11.7	2887.4	28.8	2667.4	9.1	-8.2	
49	11.850	0.127	0.472	0.005	0.630	0.182	0.002	2.151	2.020	1.799	2592.6	10.1	2492.5	20.9	2669.7	14.9	6.6	
50	13.067	0.141	0.521	0.006	0.921	0.183	0.001	2.153	2.236	0.876	2684.5	10.2	2701.7	24.7	2676.2	7.2	-1.0	
51	11.109	0.110	0.444	0.004	0.814	0.182	0.001	1.988	2.005	1.216	2532.3	9.3	2368.8	19.9	2673.7	10.1	11.4	
52	11.284	0.105	0.446	0.003	0.463	0.184	0.002	1.862	1.467	1.757	2546.9	8.7	2377.5	14.6	2687.7	14.5	11.5	
53	11.267	0.147	0.446	0.005	0.897	0.183	0.001	2.612	2.354	1.154	2545.5	12.2	2378.3	23.4	2681.1	9.5	11.3	
54	10.852	0.117	0.432	0.005	0.781	0.182	0.001	2.165	2.323	1.492	2510.6	10.1	2315.3	22.6	2671.7	12.3	13.3	
55	12.931	0.118	0.514	0.005	0.808	0.182	0.001	1.828	1.936	1.171	2674.7	8.6	2674.4	21.2	2674.3	9.7	0.0	
56	12.890	0.105	0.513	0.004	0.847	0.182	0.001	1.630	1.611	0.898	2671.6	7.7	2668.7	17.6	2672.9	7.4	0.2	
57	13.591	0.249	0.541	0.010	0.975	0.182	0.001	3.662	3.847	0.862	2721.6	17.3	2785.6	43.5	2675.7	7.1	-4.1	
58	11.659	0.111	0.462	0.004	0.575	0.183	0.001	1.905	1.562	1.626	2577.4	8.9	2447.5	15.9	2678.1	13.5	8.6	
59	13.876	0.153	0.554	0.006	0.955	0.182	0.001	2.210	2.235	0.671	2741.3	10.5	2842.4	25.7	2668.4	5.6	-6.5	
60	11.415	0.071	0.452	0.003	0.577	0.182	0.001	1.240	1.164	1.108	2557.7	5.8	2404.6	11.7	2674.4	9.2	10.1	
61	12.252	0.097	0.486	0.003	0.824	0.182	0.001	1.579	1.246	0.896	2623.9	7.4	2551.5	13.1	2669.9	7.4	4.4	
62	12.540	0.126	0.501	0.004	0.855	0.182	0.001	2.002	1.795	1.043	2645.7	9.4	2618.1	19.3	2668.8	8.6	1.9	
63	12.943	0.121	0.515	0.005	0.936	0.182	0.001	1.872	1.899	0.676	2675.5	8.8	2679.2	20.8	2674.9	5.6	-0.2	
64	11.945	0.139	0.476	0.006	0.962	0.181	0.001	2.320	2.336	0.639	2600.1	10.9	2511.7	24.3	2661.6	5.3	5.6	

(Continued on next page)

Table B2: Continued

65	11.786	0.076	0.467	0.003	0.765	0.182	0.001	1.294	1.264	0.878	2587.6	6.1	2468.8	13.0	2670.4	7.3	7.6
66	11.085	0.073	0.439	0.003	0.773	0.183	0.001	1.314	1.293	0.878	2530.3	6.1	2344.2	12.7	2675.9	7.3	12.4
67	12.894	0.114	0.513	0.004	0.832	0.183	0.001	1.770	1.755	1.021	2671.9	8.3	2668.9	19.2	2679.3	8.4	0.4
68	12.474	0.089	0.494	0.004	0.834	0.181	0.001	1.425	1.464	0.834	2640.8	6.7	2588.5	15.6	2664.9	6.9	2.9
69	13.074	0.092	0.519	0.003	0.803	0.182	0.001	1.406	1.253	0.846	2685.0	6.6	2696.0	13.8	2673.3	7.0	-0.9
70	12.834	0.098	0.511	0.004	0.863	0.182	0.001	1.522	1.616	0.828	2667.6	7.2	2659.8	17.6	2673.4	6.8	0.5
71	12.961	0.284	0.514	0.011	0.898	0.182	0.002	4.389	4.114	1.935	2676.8	20.7	2674.0	45.0	2672.2	16.0	-0.1
72	13.482	0.151	0.537	0.006	0.859	0.183	0.001	2.236	2.194	1.178	2714.0	10.6	2769.4	24.7	2677.4	9.7	-3.4
73	13.926	0.152	0.552	0.006	0.825	0.183	0.001	2.189	2.004	1.253	2744.7	10.4	2832.4	23.0	2676.8	10.4	-5.8
74	11.602	0.135	0.459	0.004	0.753	0.183	0.001	2.330	1.868	1.537	2572.9	10.9	2433.7	18.9	2676.5	12.7	9.1
75	13.858	0.258	0.553	0.009	0.882	0.183	0.002	3.718	3.212	1.751	2740.0	17.6	2835.6	36.8	2677.1	14.5	-5.9
76	11.682	0.117	0.467	0.004	0.890	0.182	0.001	1.995	1.872	0.913	2579.3	9.3	2471.6	19.2	2668.3	7.6	7.4
77	12.928	0.206	0.514	0.008	0.961	0.183	0.001	3.193	3.127	0.885	2674.4	15.0	2674.5	34.2	2679.6	7.3	0.2
78	11.846	0.108	0.477	0.005	0.866	0.182	0.001	1.818	2.066	1.032	2592.3	8.5	2513.1	21.5	2675.4	8.5	6.1
79	12.515	0.202	0.501	0.008	0.874	0.184	0.001	3.233	3.104	1.595	2643.8	15.2	2619.7	33.4	2688.0	13.2	2.5
80	12.146	0.176	0.486	0.007	0.884	0.182	0.001	2.893	2.848	1.381	2615.7	13.6	2555.4	30.0	2671.1	11.4	4.3
81	11.837	0.338	0.469	0.014	0.979	0.183	0.001	5.718	5.829	1.194	2591.6	26.8	2480.0	60.0	2677.4	9.9	7.4
82	13.262	0.275	0.528	0.011	0.983	0.182	0.001	4.146	4.085	0.758	2698.5	19.6	2734.7	45.5	2673.5	6.3	-2.3
83	14.746	0.200	0.589	0.008	0.867	0.182	0.001	2.717	2.846	1.443	2799.0	12.9	2983.4	34.0	2670.0	11.9	-11.7
84	14.888	0.155	0.592	0.006	0.900	0.182	0.001	2.079	2.004	0.916	2808.1	9.9	2999.1	24.0	2673.9	7.6	-12.2
85	12.552	0.161	0.498	0.006	0.937	0.182	0.001	2.569	2.550	0.907	2646.7	12.1	2604.9	27.3	2673.1	7.5	2.6
86	13.379	0.252	0.535	0.009	0.922	0.182	0.001	3.767	3.223	1.478	2706.8	17.8	2764.3	36.2	2673.9	12.2	-3.4
87	11.765	0.082	0.470	0.003	0.723	0.182	0.001	1.389	1.186	0.976	2585.9	6.5	2485.6	12.2	2673.8	8.1	7.0
88	12.464	0.117	0.497	0.005	0.769	0.183	0.001	1.877	1.960	1.305	2640.0	8.8	2599.1	21.0	2678.4	10.8	3.0
89	10.657	0.101	0.421	0.004	0.716	0.184	0.001	1.895	2.073	1.505	2493.7	8.8	2266.8	19.8	2686.1	12.4	15.6
90	11.544	0.187	0.457	0.007	0.888	0.182	0.001	3.243	3.237	1.532	2568.2	15.2	2426.5	32.7	2672.8	12.7	9.2
91	10.138	0.098	0.406	0.003	0.617	0.182	0.001	1.935	1.572	1.569	2447.4	8.9	2196.9	14.6	2672.3	13.0	17.8
92	10.855	0.104	0.435	0.004	0.692	0.182	0.001	1.917	1.852	1.480	2510.8	8.9	2327.3	18.1	2673.0	12.2	12.9
93	10.819	0.170	0.434	0.007	0.581	0.183	0.003	3.146	3.333	2.972	2507.7	14.6	2323.3	32.5	2682.8	24.6	13.4
94	11.999	0.100	0.480	0.004	0.677	0.182	0.001	1.670	1.504	1.284	2604.4	7.8	2528.0	15.7	2673.6	10.6	5.4
95	12.566	0.118	0.501	0.004	0.862	0.183	0.001	1.872	1.776	0.964	2647.7	8.8	2616.5	19.1	2679.5	8.0	2.4
96	12.352	0.107	0.494	0.004	0.717	0.183	0.001	1.735	1.593	1.258	2631.6	8.1	2587.4	17.0	2680.7	10.4	3.5
97	10.532	0.085	0.418	0.003	0.711	0.183	0.001	1.622	1.670	1.252	2482.7	7.5	2253.2	15.9	2676.2	10.4	15.8
98	12.585	0.105	0.501	0.004	0.820	0.182	0.001	1.676	1.503	0.968	2649.1	7.9	2617.0	16.2	2673.9	8.0	2.1
99	12.856	0.096	0.512	0.004	0.729	0.182	0.001	1.497	1.691	1.188	2669.1	7.0	2663.7	18.4	2675.0	9.8	0.4
100	12.941	0.081	0.514	0.003	0.619	0.182	0.001	1.255	1.092	1.035	2675.4	5.9	2672.6	11.9	2673.5	8.6	0.0
101	12.931	0.086	0.514	0.003	0.842	0.183	0.001	1.334	1.202	0.723	2674.7	6.3	2674.8	13.2	2676.4	6.0	0.1
102	11.746	0.131	0.466	0.005	0.939	0.182	0.001	2.236	2.352	0.808	2584.4	10.5	2467.5	24.1	2673.5	6.7	7.7
103	14.050	0.160	0.560	0.005	0.577	0.183	0.002	2.282	1.941	1.965	2753.1	10.8	2866.8	22.5	2676.6	16.3	-7.1
104	12.864	0.091	0.512	0.004	0.822	0.183	0.001	1.412	1.382	0.835	2669.7	6.7	2664.6	15.1	2675.7	6.9	0.4
105	13.138	0.084	0.519	0.004	0.910	0.182	0.001	1.273	1.374	0.569	2689.6	6.0	2694.2	15.1	2669.4	4.7	-0.9
106	12.382	0.086	0.490	0.003	0.819	0.183	0.001	1.396	1.390	0.839	2633.8	6.6	2569.8	14.7	2678.1	6.9	4.0
107	12.066	0.095	0.480	0.004	0.839	0.182	0.001	1.580	1.576	0.896	2609.5	7.4	2525.5	16.5	2669.9	7.4	5.4
108	14.161	0.234	0.564	0.009	0.980	0.183	0.001	3.305	3.283	0.651	2760.6	15.7	2882.4	38.1	2680.8	5.4	-7.5
109	12.969	0.105	0.514	0.004	0.917	0.183	0.001	1.619	1.593	0.655	2677.4	7.6	2675.2	17.4	2676.9	5.4	0.1
110	13.978	0.126	0.559	0.005	0.887	0.182	0.001	1.798	1.703	0.836	2748.2	8.5	2863.3	19.7	2669.5	6.9	-7.3
111	12.931	0.135	0.514	0.006	0.630	0.182	0.002	2.090	2.204	1.850	2674.7	9.8	2674.5	24.1	2673.4	15.3	0.0
112	12.928	0.142	0.514	0.005	0.849	0.183	0.001	2.204	1.971	1.170	2674.4	10.4	2675.3	21.6	2684.6	9.7	0.3
113	17.113	0.224	0.680	0.009	0.929	0.183	0.001	2.618	2.644	0.995	2941.2	12.6	3342.9	34.5	2683.4	8.2	-24.6
114	13.637	0.223	0.547	0.009	0.974	0.182	0.001	3.276	3.122	0.752	2724.9	15.5	2812.7	35.6	2671.8	6.2	-5.3
115	12.954	0.124	0.513	0.004	0.832	0.183	0.001	1.915	1.636	1.063	2676.3	9.0	2671.3	17.9	2682.1	8.8	0.4
116	11.609	0.127	0.461	0.005	0.838	0.182	0.001	2.182	2.111	1.222	2573.4	10.2	2444.7	21.5	2675.0	10.1	8.6
117	11.573	0.230	0.462	0.009	0.910	0.181	0.002	3.968	3.853	1.663	2570.5	18.5	2449.7	39.3	2664.9	13.8	8.1
118	13.485	0.134	0.537	0.005	0.963	0.183	0.000	1.990	2.040	0.548	2714.3	9.4	2771.1	23.0	2676.0	4.5	-3.6
119	13.793	0.219	0.546	0.008	0.951	0.182	0.001	3.172	2.994	0.981	2735.6	15.0	2809.4	34.1	2674.6	8.1	-5.0
120	13.786	0.217	0.550	0.008	0.971	0.182	0.001	3.143	2.896	0.767	2735.1	14.9	2825.3	33.1	2671.6	6.4	-5.8
121	12.569	0.130	0.496	0.005	0.894	0.183	0.001	2.070	1.834	0.928	2647.9	9.7	2598.2	19.6	2679.7	7.7	3.0
122	12.209	0.136	0.485	0.005	0.905	0.183	0.001	2.230	2.090	0.949	2620.6	10.5	2547.3	22.0	2681.1	7.8	5.0
123	10.780	0.124	0.432	0.005	0.927	0.182	0.001	2.293	2.285	0.874	2504.3	10.7	2316.7	22.2	2672.8	7.2	13.3
124	13.712	0.378	0.548	0.016	0.974	0.182	0.001	5.511	5.787	1.306	2730.0	26.1	2817.3	66.0	2670.0	10.8	-5.5
125	15.593	0.210	0.621	0.008	0.956	0.183	0.001	2.696	2.734	0.806	2852.2	12.9	3112.4	33.7	2681.8	6.7	-16.6
126	13.687	0.103	0.543	0.005	0.841	0.183	0.001	1.511	1.687	0.918	2728.3	7.1	2796.0	19.1	2678.2	7.6	-4.4
127	11.154	0.109	0.444	0.004	0.883	0.182	0.001	1.946	1.944	0.941	2536.1	9.1	2367.3	19.3	2675.2	7.8	11.5

(Table concluded)

Figures B2a and b show concordia plots for the LAM ICP-MS analyses of the two standards. The difference in their behaviour is immediately apparent. Analyses of 02123 are approximately concordant and the concordia age determined from 105 LAM ICP-MS analyses is 294.71 ± 0.55 Ma, within error of the age determined by ID TIMS (295 ± 1 Ma). On the other hand, the 113 analyses for internal standard VB165 are normally to reversely discordant, defining a chord that intersects concordia at 2674 ± 1.6 Ma, with the 25 most concordant analyses yielding a concordia age of 2675 ± 2.4 Ma (Fig. B1b), both of which are identical (within error) to the ID TIMS age of 2674 ± 0.8 Ma and the $^{207}\text{Pb}/^{206}\text{Pb}$ age of 2673.9 ± 1.4 Ma (2σ). These data suggest that the LAM ICP-MS results are statistically both precise and accurate and that the difference in behavior between the two standards is not a function of the instrument, but rather of the grains analyzed.

BSE images of 6 grains of the internal standard VB165 are shown in Fig. B2c. Two types of zoning are evident: (i) primary igneous growth zoning parallel to grain boundaries; and (ii) secondary wispy, diffuse and irregular zoning unrelated to grain boundaries, considered to have developed during a later metamorphic event as a result of diffusion (referred to as within-grain secondary recrystallization or metamorphic zoning in the literature). During the course of the LAM ICP-MS sessions, it became apparent that grains with primary igneous zoning typically yielded concordant or normally discordant data, whereas some analyses of grains with evidence of secondary recrystallization yielded reversely discordant results. This implies the existence of a

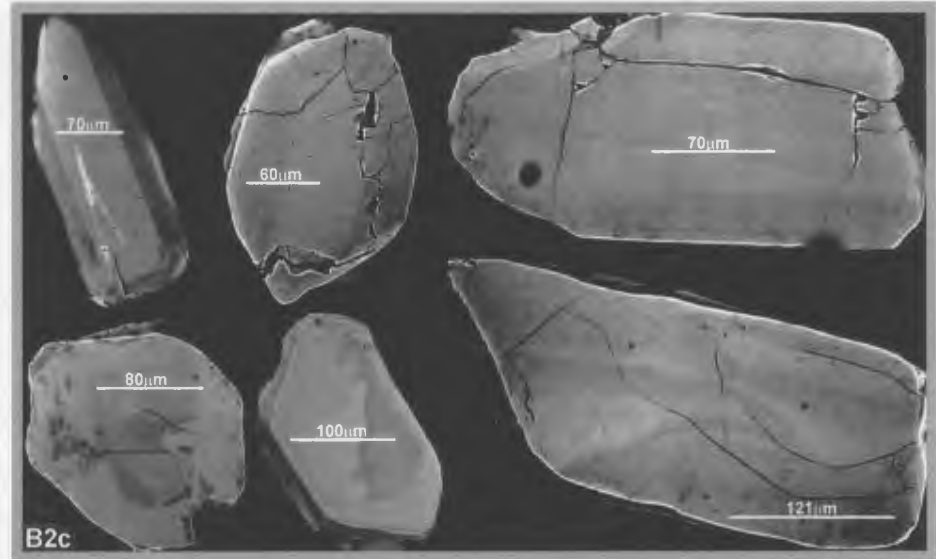
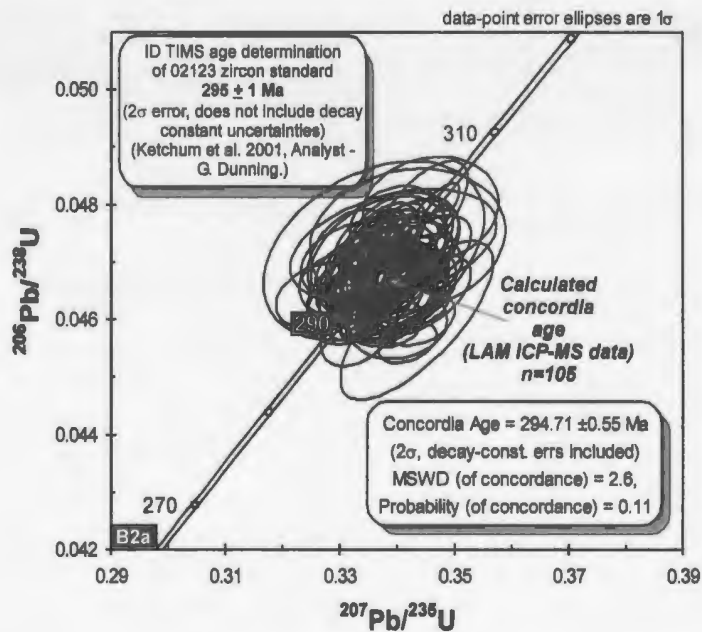
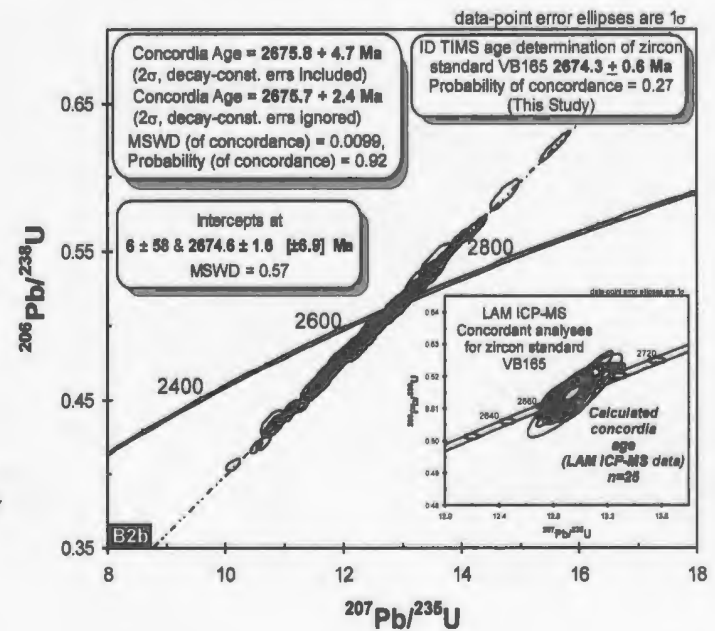


Fig. B2a & b: U-Pb analyses of zircon standards 02123 and VB165 used in LAM ICP-MS. Data collected over a period of 4 months, 105 analyses of zircon standard 02123 are presented in concordia plot B1a, (30 analyses not included in age calculations). 113 analyses are presented in concordia plot B1b, 25 concordant analyses, 88 normal to reversely (-16 to 17.8 %) discordant analyses, (12 analyses not included in age calculations). Discarded data considered to be due to instrument drift, surface contamination and / or surface irregularities and ablation irregularities. Size of individual error ellipse dependent on the noise of signal, which is considered to be dependent on i) length of analysis time, ii) quality of surface polish, iii) proximity to previous ablation pit fallout zones and iv) ablation technique employed, (e.g. single pass versus multipass rastering).

B2c: Representative BSE images of internal zircon standard VB165. Top row illustrates grains with primary zoning that yield concordant to normally discordant U-Pb age data. Bottom row images illustrates grains with secondary (metamorphic) due to diffusional processes that yield reversely discordant U-Pb age data.



spatial relationship between zoning and the type of discordance, which is investigated in more detail below.

B4 - Analyses of a single zoned grain

Figure B3a is a BSE image of a zircon which displays a partial dull rim on the left side of the grain and a diffusely zoned core comprising a dull region at the top right grading into a brighter region at the bottom left of the grain. The diffuse zoning in the core is interpreted to be a result of secondary recrystallization. The location and ablation direction of a single S-shaped pit in the core of the grain are shown and the pit is divided into three time–space segments. The time resolved $^{207}\text{Pb}/^{235}\text{U}$, $^{206}\text{Pb}/^{238}\text{U}$ and $^{207}\text{Pb}/^{206}\text{Pb}$ signals collected for this analysis are shown in Figs. B3c and d and the three time intervals are also marked on these figures. The $^{207}\text{Pb}/^{235}\text{U}$ and $^{206}\text{Pb}/^{238}\text{U}$ ratios determined for each interval, together with the total $^{207}\text{Pb}/^{235}\text{U}$ and $^{206}\text{Pb}/^{238}\text{U}$ ratios determined for the analysis, are presented on a concordia diagram in Fig. B3b. Age data for the standard 02123 and the internal standard VB165 collected immediately before and after analysis of the unknowns are shown in Figs. B3e-f. This dataset is important in that it relates the internal zonation revealed in BSE imaging to variations in U/Pb isotopic ratios collected over the course of a single analysis. Several features are apparent:

1. Reversely discordant analyses of the dull zone of the BSE image compared to normally discordant analyses of the brighter zone.
2. Normally discordant total signal, which includes analyses of both the dull and bright zones of the crystal. This may be comparable to a whole grain analysis such as would result from ID TIMS method.

3. Distinct variations in the $^{207}\text{Pb}/^{235}\text{U}$ and $^{206}\text{Pb}/^{238}\text{U}$ signals (Figs. B2c-d) as the gradational boundary between the dull and brighter zones is crossed, compared to a constant $^{207}\text{Pb}/^{206}\text{Pb}$ ratio.
4. Agreement between the calculated ages of the internal standards and their independently determined ID TIMS ages of 295 ± 1 Ma and 2674 ± 0.8 Ma respectively (see Figs. B2, B3e and f).

These data demonstrate a correlation between discrete chemical domains within the zircon grain and discordance, and two factors are speculated to have exerted control on this; (i) variation in particle size production between different chemical zones as a consequence of variable ablation behaviour, and/ or (ii) differential within-grain diffusion of U and/or Pb whereby either gain of Pb or loss of U within the dull zone and/or the converse in the brighter zone has occurred. Importantly, a review of ablation pit location, internal zoning and resultant U-Pb behaviour with respect to concordia suggests that ablation of zones characterized by dull BSE (i.e., lower mean atomic number, and therefore lower concentrations of U, Th and Pb) more often result in reversely discordant data.

The viability of intragrain diffusion of U and Pb as a function of temperature and time has been evaluated in several experimental and modelling studies. The study of Lee et al. (1997) concluded that at 1100°C diffusion of Pb in zircon was up to four orders of magnitude faster than that of U and Th. These relative rates are compatible with the mineral chemistry of zircon, in which U and Th commonly substitute for Zr in the zircon lattice and would therefore occupy stable sites and be relatively immobile, whereas there

Figure B3: (a) BSE image of zircon grain exhibiting diffuse zonation. Location of LAM ICP-MS raster straddling dull and bright BSE zones. Raster pit subdivided into three time/space segment (1-3). (b) Concordia diagram of three segments of LAM analysis illustrated in Figure A2.2a and total resolved signal (grey fill). (c) Time resolved $^{207}\text{Pb}/^{235}\text{U}$ ratio for analysis illustrated in (a) and presented on concordia plot in (b). Intervals correspond to segments on (a). (d) Time resolved $^{206}\text{Pb}/^{238}\text{U}$ and $^{206}\text{Pb}/^{207}\text{Pb}$ ratios for analysis illustrated in B2a and presented on concordia plot in (b). Intervals correspond to segments on (a). Note variation of $^{206}\text{Pb}/^{235}\text{U}$ ratio compared to relatively flat signal of $^{206}\text{Pb}/^{207}\text{Pb}$. (e) Concordia diagram and calculated ages of internal zircon standard 02123. Data collected before and after analysis presented in figure (a-d). (f) Concordia diagram and calculated ages of internal zircon standard VB165. Data collected before and after analysis presented in figure (a-d).

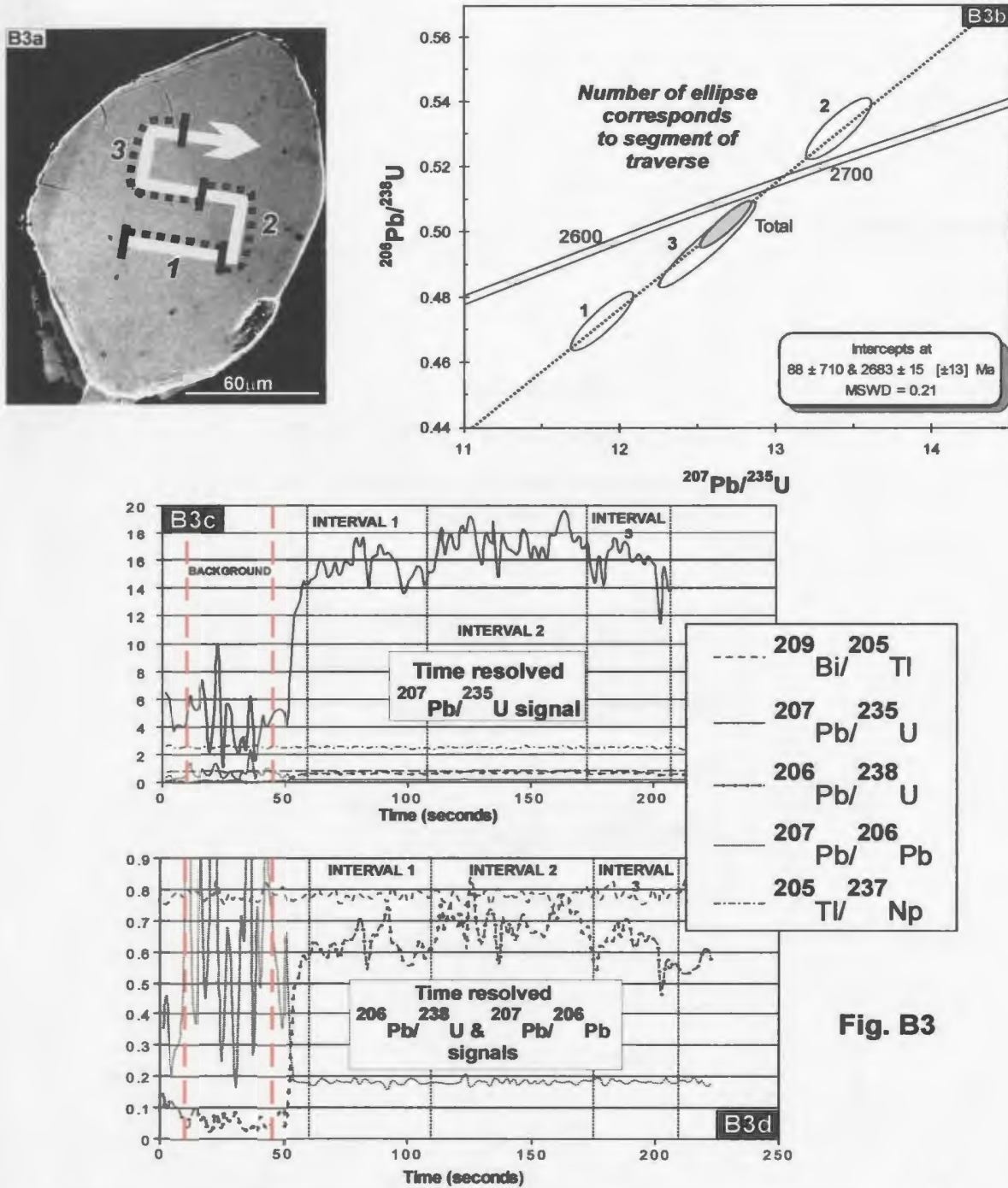
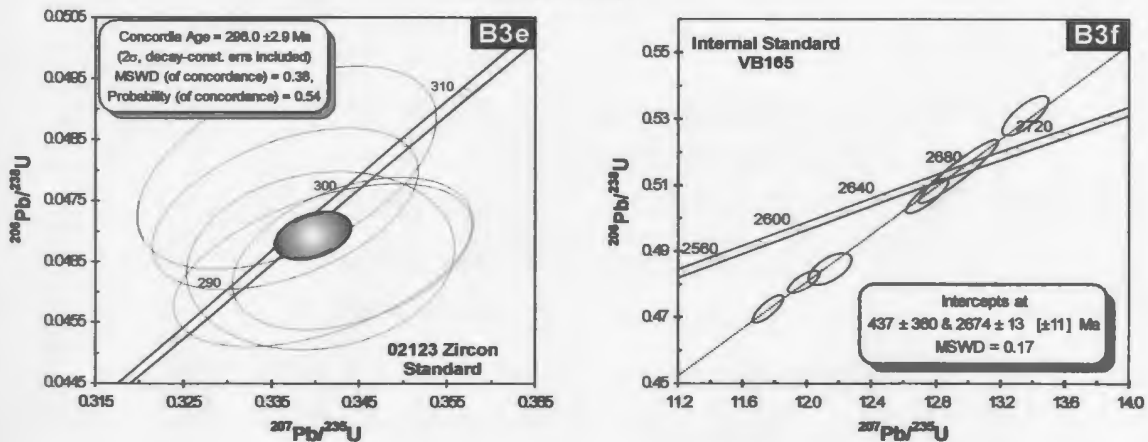


Fig. B3



is no known site that can accommodate Pb (Cherniak and Watson 2003). Nonetheless, Cherniak and Watson (2000) suggested that U mobilization may also be a contributing factor to reverse discordance because of the effects of radiation damage, fracturing due to differential lattice expansion, fluid leaching, and pressure release crystallization on the zircon lattice.

In conclusion, the occurrence of reverse discordance in the datasets presented is not well understood and warrants further investigation to assess whether it is due to natural diffusion processes, laser and or instrument induced fractionation or a combination of the two.

Appendix B - References

- Bruguiere, O., Telouk, P., Cochérie, A., Fouillac, A.M., and Albarède, F. 2001. Evaluation of Pb-Pb and U-Pb laser ablation ICP-MS zircon dating using matrix-matched calibration samples with a frequency quadrupled (266 nm) nd-yag laser. *Geostandards Newsletter*, **25**: 361-373.
- Cherniak, D.J., and Watson, E.B. 2000. Pb Diffusion in zircon. *Chemical Geology*, **172**, p. 5-24.
- Cherniak, D.J., and Watson, E.B. 2003. *Diffusion in Zircon*, In: *Zircon*, ch. 5, pp. 113-143 *Reviews in Mineralogy and Geochemistry*, vol. 53, J.M. Hanchar and P.W.O. Hoskin, Eds.), Mineralogical Society of America, Washington D.C.
- Guillong, M., and Günther, D. 2002. Effect of particle size distribution on ICP-induced elemental fractionation in laser ablation – inductively coupled plasma-mass spectrometry. *Journal of Analytical Atomic Spectrometry*, **17**: 831 – 837.
- Günther, D., Hattendorf, B., Latkoczy, Ch. 2003. LA-ICP-MS – it's particle size that really matters. *Analytical Chemistry (A-pages)*, **75**: 341A-347A
- Ketchum, J.W., Jackson, S.E., Culshaw, N., and Barr, S.M. 2001. Depositional and tectonic setting of the Paleoproterozoic Lower Aillik Group, Makkovik Province, Canada: evolution of a passive margin-foredeep sequence based on

petrochemistry and U-Pb (TIMS and LAM-ICP-MS) geochronology. *Precambrian Research*, **105**: 331-356.

Košler, J., Wiedenbeck, M., Wirth, R., Hovorka, J., Sylvester, P., and Mikova, J., 2005. Chemical and phase composition of particles produced by laser ablation of silicate glass and zircon – implications for elemental fractionation during ICP-MS analysis. *Journal of Analytical Atomic Spectrometry*, **20**: 402 – 409.

Košler, J., and Sylvester, P. 2003. Present trends and the future of zircon in geochronology: laser ablation ICPMS. In: Hanchar, JM and Hoskin, PWO (eds), *Zircon. Reviews in Mineralogy & Geochemistry*, **53**: 243-275.

Lee, J.K.W., Williams, I.S., and Ellis, D.J. 1997. Pb, U and Th diffusion in natural zircon. *Nature*, **390**: 159-161.

Li, X., Liang, X., Sun., M and Malpas, J.G., 2001. Precise $^{206}\text{Pb}/^{238}\text{U}$ age determination on zircons by laser ablation microprobe – inductively coupled plasma – mass spectrometry using continuous laser ablation. *Chemical Geology*, **175**: 209 – 219.

Appendix C

IDTIMS

SIZE – WEIGHT TABLE

INTRODUCTION

As outlined in Chapter 2, the ID-TIMS work for this research involved imaging of abraded grains prior to dissolution and single grain analysis. The long axes of abraded grains ranged from approximately 70 to > 150 μm , and abrasion resulted in reduction of their original size by up to 50%, rendering handling difficult. In addition, the single grain nature of the analyses increased the handling difficulties at all stages of the dissolution procedure, including pre-cleaning, weighing and loading into teflon bombs.

Subsequent to BSE imaging, grains were carefully removed from the epoxy grain mount under distilled water using a sharp needle-shaped instrument. Use of distilled water on the grains reduces the risk of grain loss after extraction, H_2O being better than alcohol in this regard because of its higher viscosity. The extracted grains were then removed from the H_2O using tweezers. In order to minimize loss, each grain was examined under a binocular microscope and compared to a size–weight table (Fig. C1) that was constructed in-house by the author. Determining the grain weight using the table eliminated the use of the electronic balance, which had previously been demonstrated to be a significant potential source of grain loss. The imaged and abraded grains were particularly difficult to see and even more difficult to handle, especially when the flat polished surface was face down on the aluminum boats used to house the grains during weighing.

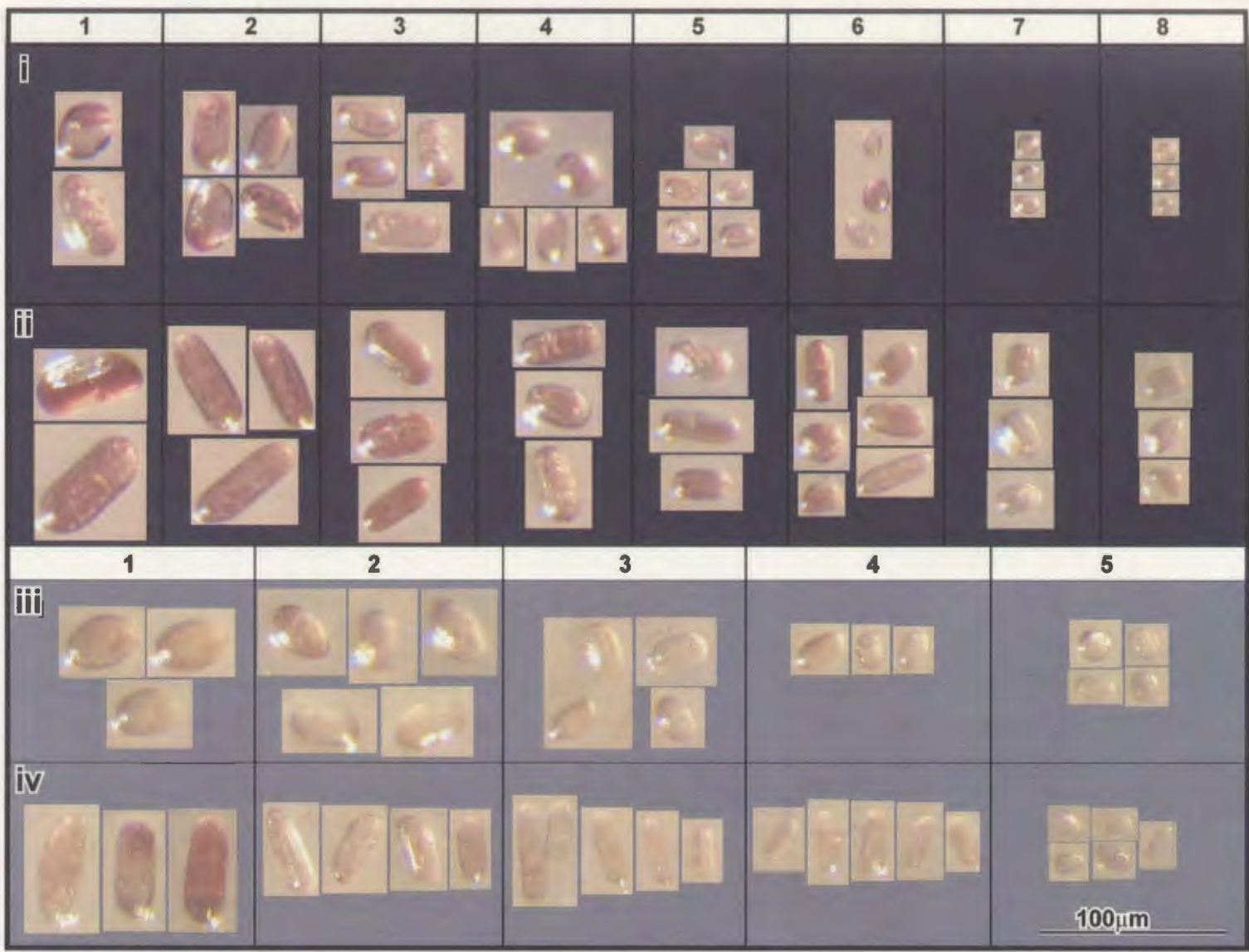


Figure C1: Four reference zircon groups used for estimation of grain weights. (i) medium to large pink prisms; (ii) large pink - brown needles; (iii) medium - small yellow - tan needles; (iv) medium to small yellow needles

CONSTRUCTION OF SIZE–WEIGHT CHART

The size–weight table was created using zircon from the 13 samples presented in this thesis. Four zircon groups were selected (i-iv) on the basis of zircon morphology and colour. Groups i and ii, pink prisms and needles, respectively, were divided into 8 size categories. Each category was comprised of 1–5 grains of different size, which were each independently weighed. The average weight for the group was then calculated and used as the best weight estimate for individual grains of that size range in that particular grouping. For group i, pink prisms (Fig. Ci), average grain weights ranged from 0.0093 to 0.0003 mg. For Group ii, pink to dark brown needles (Fig. Cii), average grain weights ranged from 0.0161 to 0.0010mg. Groups iii and iv, yellow- light brown to tan prisms and needles, respectively, were divided into 5 weight catagories. Two to 5 grains were used in each weight class to calculate an average weight. Average grain weights for group iii (Fig. Civ) ranged from 0.0055 to 0.0009 mg and for group iv, 0.0070 to 0.0008 mg). Table C1 summarizes the weight dataset and averages used for each of the four categories. A comparison of grain weights determined using the balance and the reference tables demonstrated that the table yielded results that were within error of those determined with the electronic balance (Table C2). All weight estimates after the initial testing stage were determined using the reference table.

Table C1: Size / Weight table – dataset. Zircon sizes for each group shown in Fig. C1, weights in mg.

GROUP	1.	2.	3.	4.	5.	6.	7.	8.
	0.0093	0.0054	0.0044	0.0027	0.0017	0.0012	0.008	0.0005
GROUP i		0.0055	0.0044	0.0029	0.0019	0.0012	0.008	0.0003
Pink Prisms		0.0061	0.0045	0.0033	0.0021	0.0015	0.009	0.0003
(PVB9; VB1358)		0.0063	0.0048	0.0031	0.0021			
		0.0071			0.0025			
AVERAGE	0.0093	0.006	0.0045	0.0030	0.0021	0.0013	0.0008	0.0003
GROUP ii	0.0141	0.0091	0.0071	0.005	0.0034	0.0024	0.0017	0.0010
Dark Brown –	0.0181	0.0093	0.0071	0.0063	0.0035	0.0025	0.0021	0.0011
Pink Needles		0.0096	0.0073		0.0036	0.0028		
(VB1229A)		0.0103	0.0076		0.0040	0.0029		
		0.0111	0.0081		0.0045	0.0031		
AVERAGE	0.0161	0.0099	0.0074	0.0057	0.0038	0.0027	0.00019	0.00010

GROUP	1.	2.	3.	4.	5.
GROUP iii	0.006	0.0034	0.0025	0.0013	0.0008
Yellow	0.0056	0.0037	0.0026	0.0013	0.0010
Prisms	0.0050	0.0041	0.0028	0.0017	
(VB161)		0.0045	0.0029	0.0019	
			0.0030		
AVERAGE	0.0055	0.0039	0.0028	0.0016	0.0009
GROUP iv	0.0073	0.0041	0.0024	0.0013	0.0006
Light brown	0.0070	0.0047	0.0027	0.0017	0.0008
- tan needles	0.0060	0.0055	0.0035	0.0019	0.0010
(VB166; VJ375)					
AVERAGE	0.0070	0.0048	0.0029	0.0017	0.0008

Table C2: Comparison of grain weights determined using balance versus reference chart.

Sample	^a. Weight - Balance (mg)	Weight – Chart (mg)	Difference (mg)
<i>PVB 9</i>			
grain 1	0.00145	0.00150	+ 0.0005
grain 2	0.0029	0.0031	+ 0.0002
<i>VB166</i>			
grain 1	0.0018	0.0014	- 0.0002
grain 2	0.0008	0.0013	+ 0.0005

a. Error on balance \pm 0.0005mg

D. Appendix

Geochemical Analytical Techniques

1. Major and Trace Element analysis

Light major elements (Na, Mg, Al, Si, P, K, Ca, Sc, Ti, V, Cr, Mn, Fe, Ba, and Ce) were analysed by XRF using fused borate glass beads composed of 1.5 g of sample, 6 g of lithium metaborate and 1.5 g of lithium tetraborate. Intermediate weight major elements (K through Fe) and trace elements (Sc, V, Cr, Ni, Cu, Zn, Ga, As, Rb, Sr, Y, Zr, Nb, Ba, Ce, Pb, Th, U) were determined on pressed powder pellets made with 5 g of rock powder and 0.7 g of phenolic resin. Analyses were performed using a Fisons/Applied Research Laboratories model 8420+ sequential wavelength-dispersive X-ray spectrometer for both qualitative and quantitative determination of elements. Quality control was carried out by analyzing four reference materials with the samples during each data collection run and comparing the results to published datasets. Detection limits for pressed pellets range from 0.7 ppm (Nb) to 41 ppm (Ce) with estimated precision 0.2 – 3.1% (Cox et al. 1998). Fused beads have detection limits of 0.006 % (K_2O and TiO_2) and 0.079 % (Al_2O_3) and a precision range of 0.2 – 3.2 % (Cox et al. 1998). Loss on ignition was determined from weight difference of sample before and after heating to 1050 °C. Following a sodium peroxide sinter, REE concentrations were determined using a Perkin-Elmer SCIEX ELAN model 250 solution ICP-mass spectrometer. Full details of

the procedure are outlined in Jenner et al. (1990) and Longerich et al. (1990). XRF analyses are compared to AGV-1, DNC-1, JG-2 and BCR-2 (Govindaraju 1989; Table D1). ICP-MS analyses are compared to chondrite, Govindaraju, MRG-1 (gabbro) and NIST SRM 688 (Table D2). Detection limits range from 0.001 ppm (Lu) to 0.015 ppm (Yb). Quality control of the ICP-MS data was carried out by comparison with XRF determinations, e.g., Ba, Nb, Y, Th, and Ce (Fig. D1). Precision, determined from multiple analyses of several international standards and duplicate analyses of unknowns, ranges from 3 – 10 %, depending on the concentration of the individual element.

2. Sm – Nd Isotopic Analyses

Sm-Nd isotopic analyses were performed at the Radiogenic Isotope Facility, Department of Earth & Atmospheric Sciences, University of Alberta by isotope dilution mass spectrometry. Whole rock powders were spiked with a mixed $^{149}\text{Sm} - ^{150}\text{Nd}$ tracer prior to dissolution. Sm and Nd were separated by standard cation and HDEHP chromatography following the method outlined in Creaser et al. (1997). Isotopic compositions of purified fractions of Sm and Nd were analyzed using a Micromass Sector 54 thermal ionization mass spectrometer. With the exception of two samples with low Nd concentrations that were analyzed in static mode, Nd isotopic analyses were performed using a dynamic multicollector routine, where all ratios were normalized to $^{146}\text{Nd}/^{144}\text{Nd} = 0.7219$ (Wasserburg et al. 1981). Sm isotopic analyses were measured in static multicollector mode and raw ratios were normalized to $^{152}\text{Sm}/^{154}\text{Sm} = 1.17537$ (Wasserburg et al. 1981). Procedural blanks for Nd and Sm are <0.1 pg. Analyses of

standard jNdi -1 (Shin Etsu) carried out during the course of data collection yielded mean values of $^{143}\text{Nd}/^{144}\text{Nd} = 0.512210 \pm 0.0000136$ (2σ , $n = 17$). For the low Nd samples, the value of $^{143}\text{Nd}/^{144}\text{Nd}$ for jNdi -1 was $^{143}\text{Nd}/^{144}\text{Nd} = 0.512107 \pm 0.000018$ (1σ , $n = 4$). Both mean values are in agreement with values determined by Tanaka et al. (2000). Data were subsequently normalized to $^{143}\text{Nd}/^{144}\text{Nd} = 0.512107$, which is equivalent to a value for the La Jolla Nd standard of 0.511850. Four samples were analyzed using the Nu Plasma multicollector. Measurements of the 'α' standard during analysis of these samples gave a mean $^{143}\text{Nd}/^{144}\text{Nd} = 0.512225$. The data were subsequently normalized to $^{143}\text{Nd}/^{144}\text{Nd} = 0.512265$, which is equivalent to a value for the La Jolla Nd standard of 0.511850.

Epsilon values at time T were calculated using the relation:

$$\epsilon_{\text{Nd}}^T = \left[\left(\frac{^{143}\text{Nd}/^{144}\text{Nd}_{\text{sample}}^T}{^{143}\text{Nd}/^{144}\text{Nd}_{\text{CHUR}}^T} \right) - 1 \right] \times 10000$$

where CHUR is the Chondritic Uniform Reservoir and T is time of formation of the rock.

The 2σ uncertainty in the ϵ_{Nd} values is estimated to be ± 0.5 epsilon units, based on replicate analyses.

Table D1: XRF reference material geochemical data.

	AGV-1					DNC-1					JG-2				BCR-2					
SiO2	58.79	59.61	59.7	59.24	59.42	47.04	43.72	43.98	43.95	43.77	79.65	74.78	74.86	74.88	74.87	54.06	55.42	55.64	55	55.5
TiO2	1.05	1.01	1	1.01	1.03	0.48	0.45	0.46	0.46	0.46	0.04	0.05	0.05	0.05	0.05	2.24	2.3	2.29	2.3	2.3
Al2O3	17.14	16.77	16.71	16.65	16.65	18.3	18.8	18.81	18.93	18.77	12.41	13.5	13.45	13.57	13.51	13.64	14.49	14.47	14	14.4
Fe2O3	6.76	6.73	6.73	6.74	6.73	9.93	9.98	10	10.03	9.98	0.92	1.06	1.06	1.05	1.06	13.41	13.01	13.06	13	13
Mno	0.09	0.1	0.1	0.1	0.09	0.15	0.15	0.14	0.15	0.15	0.02	0.02	0.02	0.02	0.02	0.18	0.19	0.19	0.2	0.19
MgO	1.53	1.48	1.47	1.45	1.48	10.05	10.04	10.09	10.07	10.03	0.04	0.12	0.11	0.12	0.12	3.48	2.99	2.99	3	2.98
CaO	4.94	4.89	4.87	4.89	4.87	11.27	11.08	11.1	11.17	11.06	0.8	0.77	0.78	0.78	0.76	6.95	6.96	6.98	7	6.94
Na2O	4.26	3.85	3.82	3.84	3.85	1.87	2.06	2.03	2.04	2.02	3.55	3.62	3.61	3.62	3.63	3.27	3.3	3.29	3.3	3.29
K2O	2.91	2.8	2.8	2.78	2.79	0.23	0.27	0.26	0.26	0.26	4.72	4.55	4.51	4.54	4.58	1.69	1.8	1.81	1.8	1.84
P2O5	0.49	0.47	0.46	0.45	0.46	0.09	0.1	0.09	0.1	0.1	0	0.03	0.03	0.03	0.03	0.36	0.3	0.3	0.3	0.3
Ni	16	6	4	7	3	247	241	239	240	243	2	4	na	4	0	13	1	na	2	0
Cu	60	55	57	59	56	96	86	85	86	85	0	0	na	0	1	19	21	21	19	18
Zn	88	69	65	73	68	66	52	50	52	47	13	19	20	25	17	130	98	93	97	99
Ga	20	21	21	21	20	15	16	13	14	15	19	20	18	19	18	22	25	23	21	24
As	1	na	na	5	na	0	11	2	na	2	1	6	2	na	na	0	13	na	6	na
Rb	67.3	70.3	70.7	69.6	70	4.5	3.6	3.3	3.5	3.3	297	287.1	287.5	283.3	288.1	47.2	48.8	48.4	48	48.9
Sr	662	687.5	689.2	684.4	688	145	145.5	143.6	145	143.5	16	15.7	15.4	15.8	15.3	330	349.3	349	348	350
Y	20	17.6	17.3	18.2	17.3	18	16.3	16	16.2	16.5	89	71.3	70.4	72.6	71	38	33.1	33.7	34	33.6
Zr	227	245.7	246.7	259.8	246.7	41	34.2	34.4	38.7	35	97	89.5	88	89.9	86.6	190	199.4	198.4	204	200
Nb	15	16.6	17.3	17.3	16.7	3	1.5	1.8	2.1	1.3	15	15.8	15.9	17.3	15.4	14	14.4	14.2	14	14.2
Ba	1226	1260	1265	1235	1248	114	123	97	96	104	67	69	66	56	44	681	699	722	695	715
Ce	67	73	78	65	60	11	na	na	na	na	46	21	30	59	49	54	34	40	30	4
Pb	36	36	37	18	34	6	13	3	na	7	33	27	27	0	26	14	16	16	na	9
Th	7	6	6	7	7	0	1	0	0	1	30	26	27	22	28	6	7	6	6	7
U	2	3	0	3	2	0	0	0	0	0	13	12	12	9	14	2	4	2	1	4
S	26	725	748	758	721	392	1139	1195	1240	1182	9	546	552	622	579	410	505	531	673	511
Cl	119	655	699	683	643	37	974	944	868	894	0	675	679	828	701	59	287	320	412	283
Sc	12	16	15	18	13	31	37	39	31	35	2	5	3	1	3	33	30	30	33	33
V	121	108	108	116	113	148	139	147	150	144	3	0	2	1	3	407	410	432	416	413
Cr	10	na	na	0	na	285	292	294	299	299	8	na	0	0	1	16	12	8	11	9

Table D2: ICP-MS Reference material geochemical data

	MRG-1	MRG-1(MUN Ave)			dup		trip			BR-688	dup					
Ba	61.00	49.40	49.67	51.14	51.01	51.44	46.20	66.58	65.43	163.33	174.70	174.91	163.37	159.15	207.36	208.57
Ta	0.80	0.74	0.80	0.83	0.83	0.79	0.80	0.47	0.82	0.18	0.22	0.29	0.25	0.28	0.21	0.27
Nb	20.00	22.30	27.79	26.35	27.92	27.87	24.65	39.80	29.58	4.87	5.45	5.75	4.21	4.15	7.65	5.76
Hf	3.76	3.89	4.10	4.16	4.17	4.12	3.88	3.76	4.29	1.54	1.75	1.71	1.65	1.62	1.44	1.63
Zr	108.00	107.00	116.15	118.59	120.73	121.61	110.39	172.23	130.88	59.15	65.24	65.44	63.85	62.63	86.91	65.72
Y	14.00	11.50	11.41	11.44	11.58	11.64	10.94	11.64	11.40	17.81	18.94	18.83	18.00	17.82	17.29	16.89
Th	0.93	0.82	0.73	0.75	0.75	0.78	0.72	0.68	0.78	0.33	0.35	0.34	0.31	0.32	0.27	0.33
La	9.80	8.83	8.68	8.52	8.66	8.61	8.13	8.89	8.92	4.98	5.34	5.03	4.91	4.94	4.85	4.92
Ce	26.00	25.80	25.09	24.64	25.18	25.03	23.19	25.28	25.12	11.55	12.30	11.90	11.60	11.54	11.13	11.15
Pr	3.40	3.71	3.72	3.62	3.68	3.66	3.38	3.79	3.76	1.65	1.79	1.74	1.65	1.67	1.63	1.63
Nd	19.20	14.60	17.61	17.51	17.82	17.71	16.58	17.88	18.49	8.03	8.64	8.37	7.97	8.08	7.87	8.02
Sm	4.50	4.34	4.36	4.37	4.41	4.50	4.17	4.44	4.74	2.30	2.47	2.49	2.37	2.39	2.21	2.40
Eu	1.39	1.38	1.42	1.40	1.43	1.42	1.32	1.42	1.53	0.94	1.01	0.99	0.96	0.96	0.92	1.00
Gd	4.00	3.97	4.12	4.10	4.13	4.20	3.89	3.65	4.45	2.88	3.12	3.05	3.02	2.93	2.51	3.04
Tb	0.51	0.52	0.54	0.55	0.56	0.56	0.52	0.49	0.58	0.48	0.51	0.50	0.49	0.50	0.42	0.50
Dy	2.90	3.00	2.94	2.90	2.98	2.95	2.79	2.62	3.05	3.21	3.52	3.38	3.25	3.30	2.83	3.32
Ho	0.49	0.49	0.51	0.51	0.51	0.51	0.47	0.45	0.52	0.70	0.76	0.75	0.74	0.72	0.60	0.72
Er	1.12	1.16	1.22	1.18	1.22	1.23	1.15	1.04	1.24	2.10	2.32	2.17	2.13	2.10	1.74	2.04
Tm	0.11	0.14	0.15	0.15	0.15	0.15	0.14	0.13	0.15	0.30	0.33	0.32	0.31	0.31	0.26	0.30
Yb	0.60	0.79	0.81	0.82	0.85	0.82	0.76	0.73	0.85	2.00	2.18	2.16	2.07	2.00	1.73	2.00
Lu	0.12	0.11	0.11	0.11	0.11	0.11	0.10	0.10	0.12	0.30	0.34	0.32	0.30	0.31	0.28	0.32

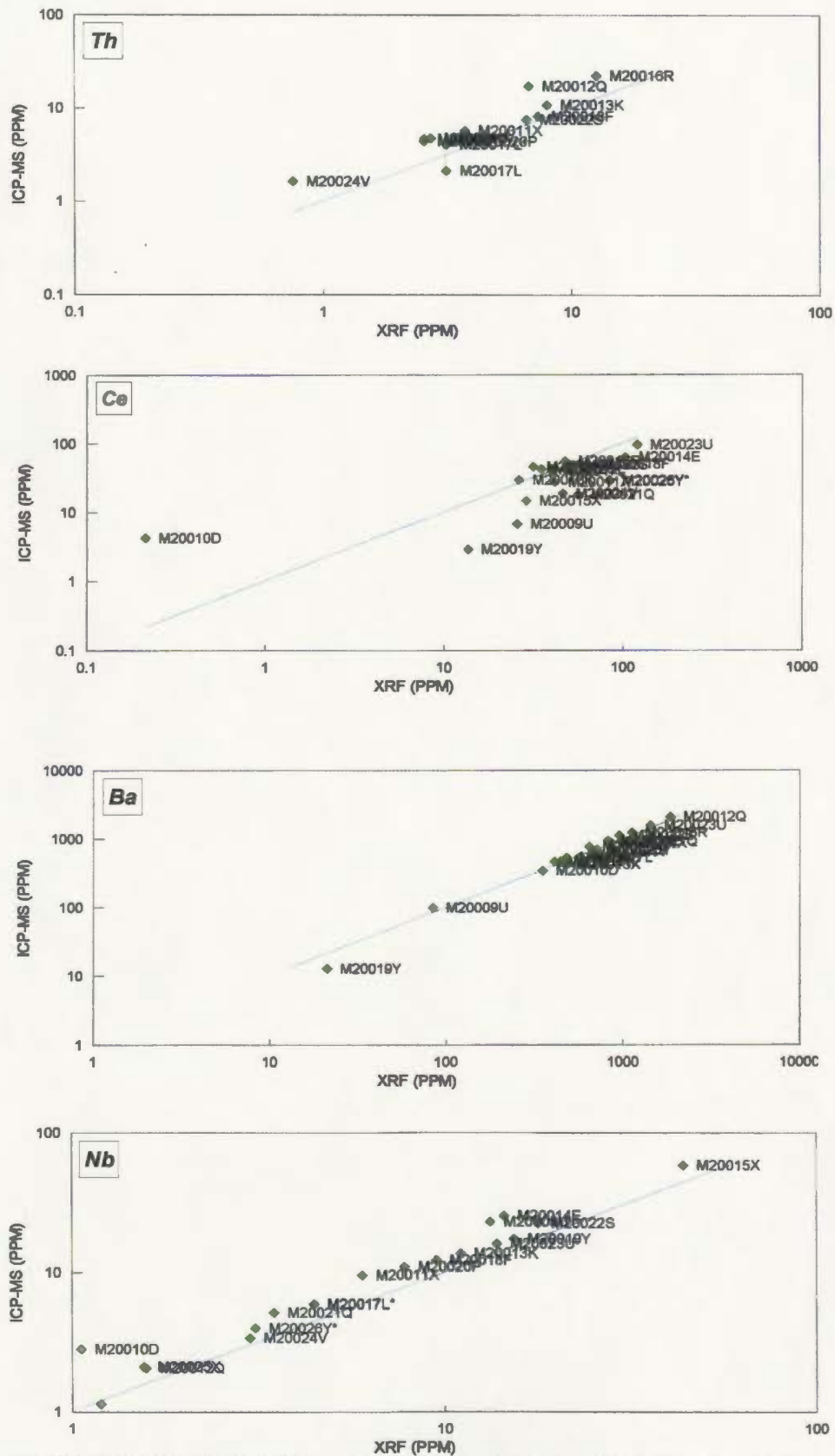


Figure D1: XRF vs ICP-MS trace element concentration comparison

APPENDIX G
Inherited Zircon Population and
Age Descriptions

Introduction

Supplementary details are provided that briefly describe inherited zircon populations, internal zonation trends, and inherited age calculations for each component defined from the LAM ICP-MS dataset. Samples are described by age and composition with the oldest metaluminous samples of Group 1 presented first and the youngest peraluminous magmas of Group 4 presented last. Errors on ages are quoted at the 2σ level. Two uncertainties on each age are given, including and excluding uncertainties on the U decay constants (the latter in square brackets).

Metaluminous Samples

Group 1: 2674 Ma – VB165 Calc-alkaline TTG Suite

Thirty grains from zircon populations not previously used to determine the crystallization age of the sample were selected for analysis. Grains with visible pink to dark brown, irregular, anhedral to subhedral cores were targeted. BSE imaging (Figs. 5.3a, 5.4a) and revealed planar, concentric and sector growth zoning, as well as featureless, bright embayed rims, truncating the planar, oscillatory- or sector-zoned cores. Examples of ablation pits in zircon cores are illustrated in Fig. 5.4a. Thirty-three analyses were obtained from the 30 grains selected (Tables F1, F2; Fig. 5.4a). No inherited populations were observed in VB165, in which approximately 64% (n=21) of the analyses yielded $^{207}\text{Pb}/^{206}\text{Pb}$ ages within error of the crystallization age of the sample. The weighted $^{207}\text{Pb}/^{206}\text{Pb}$ age is 2671 ± 7.6 [± 3.8] Ma (*Banting equivalent population*).

No further testing for inheritance was undertaken, as all zircon populations in this sample had previously undergone extensive independent analysis to assess the potential of this sample as an internal standard for data collection associated with this study. During this period, 113 grains were analyzed (see Appendix B; Bennett et al. in press) and no inheritance was observed.

Group 2: 2635 Ma – VB1363 Disco Intrusive Suite

VB1363 yielded light brown to pink prism and needle populations.

Crystallization-age zircon occurs as rims mantling inherited cores in both morphologies. BSE imaging of the needle population (Figs. 5.3b, 5.4b) revealed dull diffuse, patchy or weak oscillatory zoned cores, mantled by concentric, oscillatory-zoned brighter rims. The prism population exhibits cracked dull cores with relict planar, sector and oscillatory zoning, mantled by oscillatory-zoned rims (Fig. 5.4b). Ninety-one core and rim analyses were obtained from 71 grains and approximately 46% of analyses yielded inheritance ages (Tables 5.2, F1; Fig. 5.4b). Six $^{207}\text{Pb}/^{206}\text{Pb}$ ages were defined (4 single grain and 2 resolved group ages) that are interpreted as 4 inherited components. From oldest to youngest, the ages are; 2881 ± 12.2 [± 10] Ma (single grain age; *CSBC/CSCG* equivalent), 2713.8 ± 27.5 [± 26] Ma, 2758.6 ± 13 [± 11] Ma and 2712.9 ± 10.6 [± 8.2] Ma, single grains, *Kam Group* equivalents), 2668.8 ± 8.3 [± 4.8] Ma (resolved group age; *Banting Group* and *Kwejinne Lake Group* equivalent), and 2653.3 ± 8.9 [± 5.9] (resolved group age; *Banting Group* and *Hinscliffe Complex* equivalent).

Group 3: 2597 Ma – VB1357 Upper-crustal Biotite Granite Suite

VB1357 yielded three zircon populations, dark brown to pink prisms, light pink to brown elongate prisms and light pink to translucent needles. BSE imaging of the prism populations revealed cores with oscillatory, sector and planar growth zoning truncated and overgrown by dull recrystallized rims with wispy or patchy zoning (Figs. 5.3c, 5.4c). The needle population exhibits oscillatory- and growth-zoned cores mantled by featureless recrystallized rims. Sixty-seven analyses were obtained from 50 grains. All populations were analyzed and inheritance was observed in 76% of the data (n=51; Table 5.2) with 4 populations recognized. Resolved group $^{207}\text{Pb}/^{206}\text{Pb}$ ages cluster into 2713.8 ± 11.9 [± 9.1] Ma (*Kam Group* equivalent), 2673.8 ± 8 [± 4.4] Ma (*Banting Group* and *Kwejinne Lake Group* equivalent), 2651.9 ± 8.5 [± 5.1] Ma (*Banting Group* and *Hinscliffe complex* equivalent), and 2633.6 ± 8.5 [± 5.2] Ma (*Defeat Suite* and *Disco Intrusive Suite* equivalent).

Group 3: 2597 Ma – VB1841 Mid-crustal Orthopyroxene Granite Suite

VB1841 yielded four populations, equidimensional prisms, well faceted stubby prisms, elongate needles and aggregate grains. BSE imaging of prism morphologies (Figs. 5.3d, 5.4d) shows diffuse concentrically and sector zoned cores modified by secondary patchy recrystallization. Needles exhibit cores with relict oscillatory and planar growth zoning overprinted by irregular recrystallized domains. All populations were analyzed, with 89 core and rim analyses determined from 80 grains (Table 5.2, F1). Approximately 38% of analyses (n=34) produced inherited ages with 4 populations

recognized. Resolved group $^{207}\text{Pb}/^{206}\text{Pb}$ ages cluster at 2713.2 ± 10.1 [± 6.7] Ma, (Kam Group equivalent), 2672.8 ± 8.5 [± 6.9] Ma (*Banting Group* and *Kwejinne Lake Group* equivalent), 2651.9 ± 9.2 [± 6.2] (*Banting Group* and *Hinscliffe Complex* equivalent), and 2633.3 ± 8.1 [± 4.5] Ma (*Defeat Suite* and *Disco Intrusive Suite* equivalent).

Group 4: 2589 Ma – VJ375 Calc-alkaline Tonalite Suite

VJ375 yielded needle and prism populations, both of which were analyzed. Overgrowths were not observed in either population. BSE imaging of the prism and needle morphologies (Figs. 5.3e, 5.4e) revealed faint planar, oscillatory and weak sector zoning overprinted by recrystallized patchy domains. Fifty-two analyses were obtained from obtained from 48 grains, with approximately 21% of the data (n=11) interpreted to define a single inherited population (Tables 5.2, F1). The weighted mean $^{207}\text{Pb}/^{206}\text{Pb}$ age is 2612 ± 9.9 [± 7.3] Ma (*Concession Suite* and *Mafic Intrusive Complex* equivalent). Thirty-four analyses yielded $^{207}\text{Pb}/^{206}\text{Pb}$ ages within error of the crystallization age with a weighted mean of 2587 ± 7.2 [± 2.9] Ma.

Peraluminous Samples

Group 3: 2597 Ma – VB1358 Two-Mica Granite Suite

VB1358 yielded needle and prism populations, which were selected for analysis. BSE imaging (Figs. 5.3f, 5.5a) revealed cores characterized by diffuse oscillatory and planar growth zoning mantled by oscillatory zoned or dull featureless rims. Seventy core and rim analyses were obtained from 55 grains and Approximately 38% of the data

(n=25) yielded inheritance ages (Tables 5.3, F2). Five $^{207}\text{Pb}/^{206}\text{Pb}$ ages were defined (1 single grain and 4 resolved group ages) that are considered to represent 4 inherited components. From oldest to youngest, the resolved ages are; A single grain $^{207}\text{Pb}/^{206}\text{Pb}$ ages of 3071 ± 12 [± 9.3] Ma (CSBC equivalent; oldest inherited zircon age determined for this study), 2809 ± 21 [± 20] Ma (resolved group age, CSBC/CSCG equivalent), 2725.1 ± 11 [± 8.8] Ma (group age, Kam Group equivalent), 2682 ± 15.1 [± 13] Ma (resolved group age, Banting Group and Kwejinne Lake Group equivalent), of 2645.4 ± 10.2 [± 7.8] Ma (resolved group age, Defeat Suite and Disco Intrusive Suite equivalent).

Group 3: 2597 Ma – PVB9 Megacrystic Granite Suite

PVB9 yielded needles, elongate leaf-shaped, euhedral, subhedral to anhedral prisms. BSE imaging of needle and prism populations (Figs. 5.3g, 5.5b) revealed diffuse planar zoning overprinted by unzoned recrystallized patches and rims. Grains from all populations were analyzed with 55 analyses completed on 48 grains (Tables 5.3, F2). Approximately 41% of analyses (n=23) yielded inheritance ages. Ten $^{207}\text{Pb}/^{206}\text{Pb}$ ages were determined (7 single grain and 3 resolved group ages), which are interpreted to represent 5 inherited components. From oldest to youngest, the $^{207}\text{Pb}/^{206}\text{Pb}$ ages are; 2975.8 ± 13.8 [± 11.9] Ma, 2913.7 ± 15 [± 13.8] Ma, 2912 ± 17.7 [± 16.2] Ma, 2889 ± 14.7 [± 12.7] Ma, 2856 ± 12.9 [± 10.8] Ma, 2796 ± 20.4 [± 19.2] (single grain ages; CSBC, CSCG and turbidite detrital spectrum equivalent; Pehrsson and Villeneuve 1999; Chapter 2); 2714 ± 22.4 [± 22] Ma (single grain ages; Kam Group equivalent), 2670 ± 14.4 [± 12] Ma (resolved group age; Banting Group and Kwejinne Lake Group equivalent), $2630 \pm$

10.8 [± 8.4] Ma (resolved group age; *Defeat Suite* and *Disco Intrusive Suite* equivalent), and 2618 \pm 10.3 [± 7.9] Ma (resolved group age; *Concession Suite* and *Mafic Intrusive Complex* equivalent).

Group 3: 2597 Ma – VB1688 Megacrystic Granite Suite

VB1688 yielded elongate needles, euhedral and stubby prisms, all of which were analyzed. BSE imaging (Figs. 5.3h, 5.5c) of the needle and elongate prism populations revealed faint growth zoning truncated by patchy, recrystallized domains. The stubby prism population appears homogeneous and unzoned. Ninety-nine core and rim analyses were obtained from 48 grains (Tables 5.33, F2). Approximately 29% of the analyses (n=27) were inherited ages with 3 populations recognized. Resolved group $^{207}\text{Pb}/^{206}\text{Pb}$ ages cluster at 2650 \pm 12 [± 9.8] Ma (*Banting Group* and *Hinscliffe Complex* equivalent), 2636.9 \pm 8.9 [± 5.9] Ma (*Defeat Suite* and *Disco Intrusive Suite* equivalent), and 2614.8 \pm 7.7 [± 3.9] Ma (*Concession suite* and *Mafic Intrusive Complex* equivalent).

Group 4: 2585 Ma – VB161 Cordierite Granite Suite

VB161 yielded needle and prism populations both characterized by translucent to pale yellow overgrowths. BSE imaging (Figs. 5.3i, 5.5d) revealed concentric oscillatory and planar zoning extensively modified by secondary zone thickening. Dull, featureless cores and rims retain relics of primary growth structures that are partially overprinted by recrystallized domains. Both populations were analyzed and 55 analyses were obtained from 38 grains (Tables 5.3, F2). Approximately 40% of analyses (n=22) resulted in

inherited ages. Eight $^{207}\text{Pb}/^{206}\text{Pb}$ ages were defined (5 single grain and 3 resolved group ages) that are considered to represent 5 inherited components. From oldest to youngest, the $^{207}\text{Pb}/^{206}\text{Pb}$ ages are; 2923 ± 15 [± 13.7] Ma, 2851 ± 14.5 [± 13] Ma and 2796 ± 15 [± 19.2] Ma, 2762 ± 18 [± 16.5] (single grain ages; *CSBC/ CSCG* and *turbidite* equivalent), 2732 ± 12.5 [± 10] Ma (resolved group age; *Kam Group* equivalent), 2677 ± 10.2 [± 7.7] Ma (single grain age; *Banting Group* and *Kwejinne Lake Group* equivalent), 2631.5 ± 10.2 [± 7.7] Ma (resolved group age; *Defeat Suite* and *Disco Intrusive Suite* equivalent) and 2602 ± 11.6 [± 9.7] Ma (*resolved group age*; equivalent of ca. *2600 Ma Group 3 magmas*).

APPENDIX H
 ϵ Nd Modelling Methodology

Methodology for ϵ Nd Modelling using inherited zircon age populations

1. The inherited zircon age data are used to delineate *source region ages* and the number of *discrete components* for each sample. For each sample, the estimated percentile of each inherited end-member component is determined from the proportion of analyses of each end-member compared to the total number of inherited analysis (*f value*).
2. Geochemical data are used to infer the *bulk geochemistry of the reservoir* represented by each component of the inherited zircon spectrum (e.g., ca. 2658 Ma TTG magmas were derived from garnet-hornblende-bearing hydrated tholeiitic sources in the lower crust). Understanding of protolith geochemistry is essential to assigning geologically meaningful isotopic compositions to each defined end-member inherited component.
3. ϵ Nd values and Nd concentrations are assigned to each end-member based on the geochemical–temporal magmatic association, in this case for Neoproterozoic magmas of the Slave Province (Chapter 4). For example in the case of the Disco Intrusive Suite (VB1363), a ca. 2637 Ma lower crustally-derived TTG magma, three major inherited components with ages of ca. 2700, 2670, 2650 Ma were identified. The ca. 2700 Ma inherited component is temporally equivalent to the Kam Group tholeiites of the central Slave Province (Cousens 2000), so the occurrence of inherited grains of this age in a younger TTG

magma is compatible with Kam-type tholeiitic material in the lower crustal source region. Hence, ϵ Nd and Nd concentration data are assigned using average values for the Kam Group. A similar process is carried out for all age components and the data are presented in the appendix (Table F3) and summarized in Table 5.4.

4. The ϵ Nd data are mixed in proportions determined by their f values in binary or multicomponent mixing models to test whether the defined parameters fit, within error, the measured Sm-Nd isotopic ratio of the magma.

The algebraic expression describing binary mixing using the epsilon notation is well established (e.g., Langmuir et al. 1978; DePaolo and Wasserburg 1979) and can be written as:

$$\epsilon^{\text{Nd}}_{\text{Mix}} = \frac{\epsilon^{\text{Nd}}_{\text{A}} \cdot \text{Nd}_{\text{A}}(f) + \epsilon^{\text{Nd}}_{\text{B}} \cdot \text{Nd}_{\text{B}}(1-f)}{\text{Nd}_{\text{A}}(f) + \text{Nd}_{\text{B}}(1-f)} \quad (\text{H1})$$

where Nd_{A} and Nd_{B} are the concentrations of Nd in components A and B, $\epsilon^{\text{Nd}}_{\text{A}}$ and $\epsilon^{\text{Nd}}_{\text{B}}$ are their assigned ϵ Nd values, and f represents the weight fraction of component A in the mixture.

The equation describing a multicomponent mix is an extension of the binary mixing equation, but it is only solvable if all parameters are known quantities. The equation can be written as:

$$\epsilon^{\text{Nd}}_{\text{Mix}} = \frac{\epsilon^{\text{Nd}}_{\text{A}} \cdot X_{\text{A}}(f_{\text{A}}) + \epsilon^{\text{Nd}}_{\text{B}} \cdot X_{\text{B}}(f_{\text{B}}) + \epsilon^{\text{Nd}}_{\text{C}} \cdot X_{\text{C}}(f_{\text{C}}) + \epsilon^{\text{Nd}}_{\text{D}} \cdot X_{\text{D}}(f_{\text{D}})}{X_{\text{A}}(f_{\text{A}}) + X_{\text{B}}(f_{\text{B}}) + X_{\text{C}}(f_{\text{C}}) + X_{\text{D}}(f_{\text{D}})} \quad (\text{H2})$$

where Nd_A , Nd_B , Nd_C and Nd_D are the concentrations of Nd in each of four components A, B, C and D, ϵ^{Nd}_A , ϵ^{Nd}_B , ϵ^{Nd}_C and ϵ^{Nd}_D are the assigned ϵ Nd values of each component, and f_A , f_B , f_C , and f_D represent the proportions or weight fractions of each component in the mixture.

Application of the binary mixing equation (H1) to sample PVB9 yields the expression:

$$\epsilon^{Nd}_{PVB9} = \frac{(-0.3) \times 15.7 + (1.9 \times 43.5) \times (1 - 0.77)}{(15.7 \times 0.77) + 43.5 \times (1 - 0.77)}$$

for which the resultant $\epsilon^{Nd}_{PVB9} = + 0.65$.

Application of the multicomponent mixing equation (H2) to sample VB1357 yields the expression:

$$\epsilon^{Nd}_{VB1357} = \frac{(1.5 \times 7.4 \times 0.275) + (1.9 \times 16.7 \times 0.431) + (2.3 \times 12.2 \times 0.157) + (1.1 \times 17.4 \times 0.137)}{(7.4 \times 0.275) + (16.7 \times 0.431) + (12.2 \times 0.157) + (17.4 \times 0.137)}$$

for which the resultant ϵ Nd value is $\epsilon^{Nd}_{VB1357} = + 1.8$.

Appendix I

Supplementary Pressure-Temperature data for Major Metamorphic Zones in the Snare River Terrane

Introduction

The only published studies of the high-temperature low- to medium-pressure metamorphic history of the Snare River terrane are the thermobarometric calculations of Chacko et al. (1995) and Farquhar and Chacko (1996) conducted on a suite of granulite-facies metapelites from south of Ghost Lake (Fig. 6.1) and the descriptive reports associated with 1:50 000 regional mapping (Henderson 2004; Jackson 2003 and references therein). Currently, no synthesis is available that constrains the P - T conditions in each of the metamorphic zones defined in the Snare River terrane. As we have used a large amount of unpublished P - T data from the metapelitic rocks to assign the crustal level of magma emplacement and to characterize the ambient thermal conditions, a brief account of the important metamorphic assemblages and reaction isograds that constrain the P - T conditions in each metamorphic zone is provided here. Petrographic evidence of important reactions is given in Fig. I1 and petrogenetic grids that delimit the prograde P - T fields of each zone are illustrated in Fig. I2. Observations were based on a detailed transect southeast from the Kwejinne Lake supracrustal belt to the western boundary fault in the centre of Ghost subdomain. Mineral abbreviations follow Kretz (1983).

Chlorite and biotite zones

In contrast to the large regions underlain by amphibolite- and granulite-facies rocks, greenschist-facies chlorite- and biotite-bearing slate and phyllite are limited to comparatively a small area of northern Snare River terrane near Kwejinne and Wijinnedi

Lakes (Fig. 6.1). A chlorite zone and biotite isograd were identified by Henderson (2004) east of Wijinnedi Lake, but they have not been recognized in the transect area, where the lowest grade rocks are in the biotite zone. Chlorite zone metaturbidites consist of the sub-assembly *Pl-Qtz-Chl* with secondary white mica. Minor phases include tourmaline, epidote and carbonate (Henderson 2004). The more extensive biotite zone is distinguished in the field by its coarser grain size and the ubiquitous presence of biotite (Henderson 2004) and consists of diagnostic mineral assemblage *Chl-Ms-Bt-Qtz-Pl±Kfs* with minor titanite, tourmaline and magnetite. In some samples, large titanite porphyroblasts accompany the biotite. Biotite initially occurs as medium to large porphyroblasts overprinting an earlier fabric and enclosed in a fine-grained mica-quartz matrix (Fig. I1a). Inclusions within biotite include *Qtz, Ms, Chl,* and *Kfs*. Termination of the biotite zone is marked by the appearance of small zoned cordierite porphyroblasts, and as the cordierite isograd is approached biotite increases in abundance and occurs as both finer grained matrix material and medium sized porphyroblasts.

The KFMASH reaction of Spear and Cheney (1989) involving consumption of chlorite and alkali feldspar adequately accounts for the mineral assemblages and textures observed at the biotite isograd and across the biotite zone (Fig. I2a):



Solid solution in chlorite and K feldspar would render the reaction at least divariant and the *P-T* conditions at which it takes place are not well constrained experimentally; however it has been suggested to occur between temperatures of 300 – 400 °C at pressures below 2 kbar within bathozone 1 (Carmichael 1978; Spear 1993).

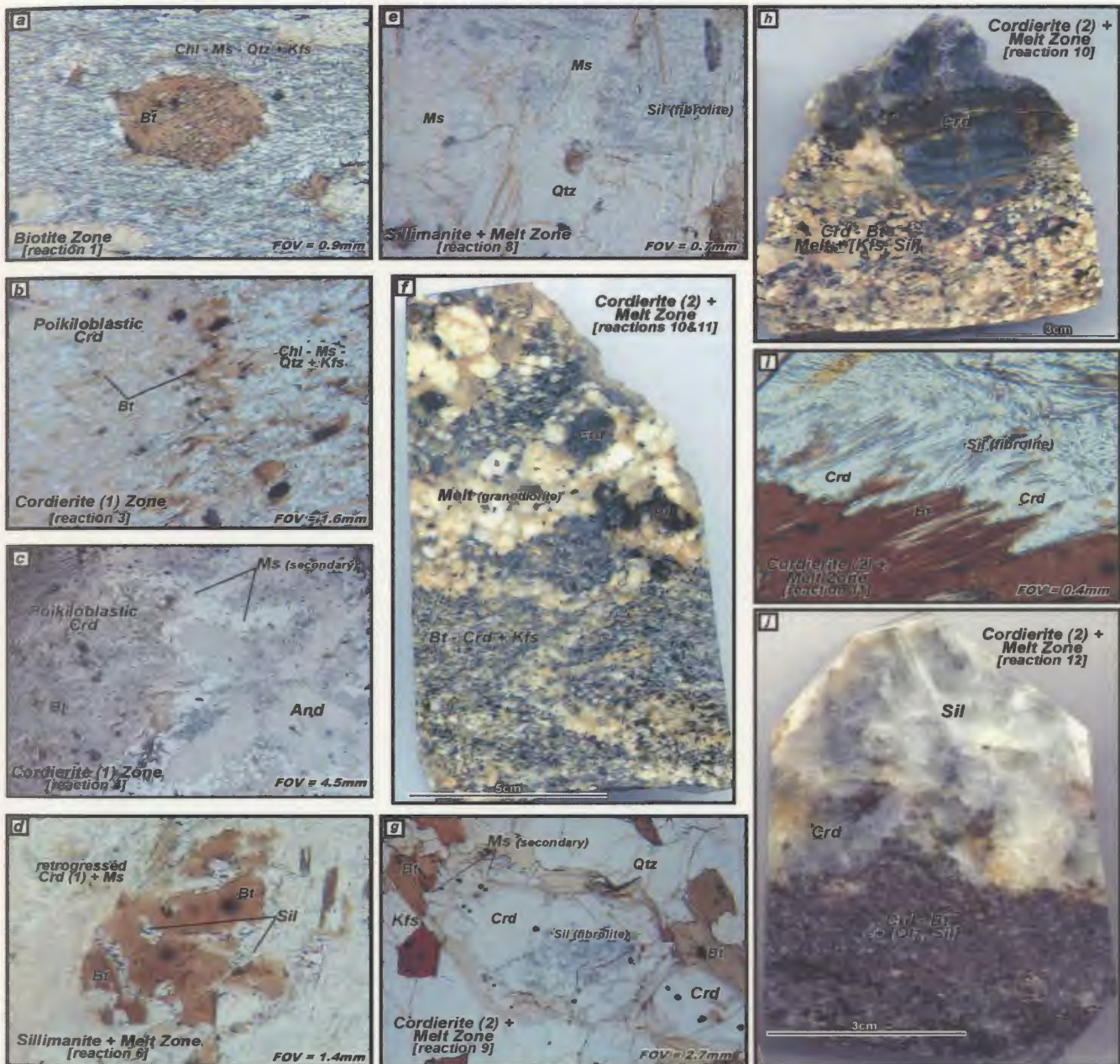


Figure I1: Photomicrographs and polished slabs indicating important metamorphic assemblages and reactions occurring in each metamorphic zone of the Snare River terrane. Field of view and scale indicated. All observations are from samples collected across a NNW to SSE transect from the Kwejinne Lake supracrustal belt to the eastern margin of the Ghost subdomain. (a) Biotite porphyroblast overprinting early fabric in $Qtz\text{-}Pl\text{-}Ms\text{-}Chl\text{-}Kfs$ matrix, *Biotite zone*. (b) Formation of large cordierite porphyroblast and biotite at the expense of muscovite and chlorite, *Cordierite zone*. (c) Large cordierite and andalusite porphyroblasts, *Cordierite zone*. (d) Formation of $Bt + Sil$ in centre of large cordierite porphyroblast, *Sillimanite + melt zone*. (e) Reaction of $Ms + Qtz$ to form sillimanite (fibrolite), *Sillimanite + melt zone*. (f) Polished slab illustrating formation of second cordierite in associated with melt, *Second Cordierite + Melt zone*. (g) Cordierite formation at expense of $Bt + Sil$. Retrograde formation of muscovite is also evident, *Second Cordierite + Melt zone*. (h) Polished slab of large cordierite within upper-amphibolite facies diatexite, *Second Cordierite + Melt zone*. (i) $Bt + Sil$ breakdown to form cordierite, *Second Cordierite + Melt zone*. (j) Rare strongly aluminous leucosome, $Sil + Crd + Kfs$, with in $Crd\text{-}Bt$ bearing pelites, *Second Cordierite + Melt zone*.

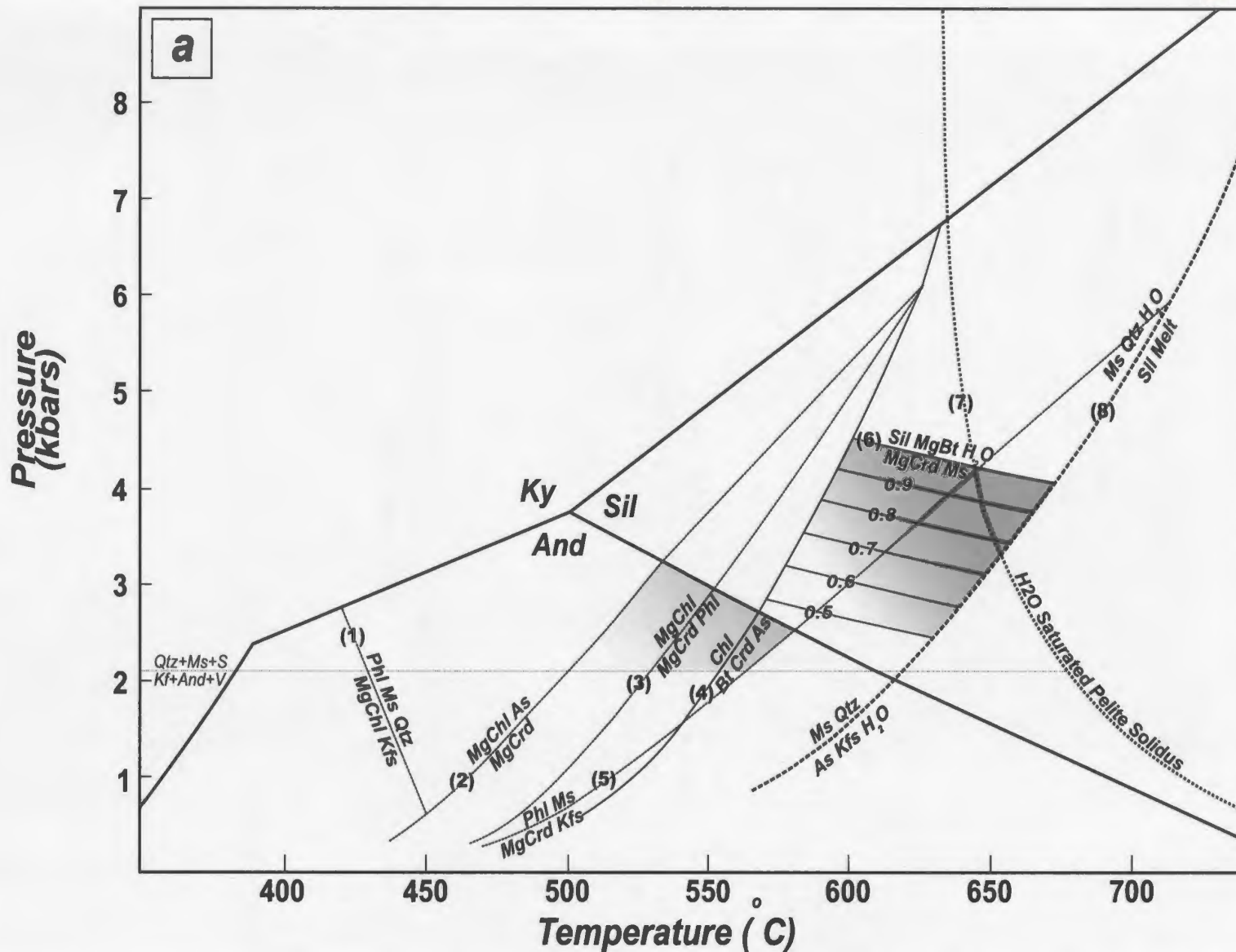


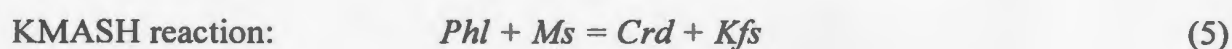
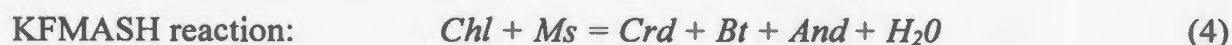
Figure 12: Petrogenetic grids defining maximum P-T conditions for each metamorphic zone across the Snare River terrane. All grids use the aluminosilicate curves of Holdaway (1971). (a) Constraints for chlorite, biotite, cordierite (1) and sillimanite + melt zones. Reactions from H₂O-present KMASH and KFMASH grids of Spear & Cheney (1989) and Pattison et al. (2002). Isopleths for reaction 6 plotted for Mg-rich compositions reaction (Pattison et al. 2002). Muscovite dehydration curve and pelite saturated solidus after Kerrick (1972) and Spear (1993), respectively. Bathograd zone 1 after Carmichael (1978). Reaction curves numbered 1 - 8 (see text for details). aH₂O = 1.

First cordierite zone

The first cordierite zone represents the onset of amphibolite-facies conditions in the study area. It is defined by the appearance of poikiloblastic cordierite in the mica-rich schistose tops of graded metaturbidites. Close to the isograd the poikiloblasts are small and sparse, but they increase in size and abundance across the zone until their breakdown at the termination of the zone. The cordierite poikiloblasts are zoned at both meso- and microscopic scales, which is inferred to be due to variable Mg and Fe concentrations, although since unaltered cordierite has not been observed this has not been proven. Where retrogression is incomplete, relict sector zoning can be observed. Andalusite-bearing assemblages are restricted to aluminous horizons and adjacent to quartz veins. Garnet-bearing assemblages are uncommon, occurring in discontinuous horizons. The diagnostic peak assemblage for the zone is: *Crd*-*Ms*-*Bt*-*Qtz*±*And*±*Grt*±*Chl*, with minor phases including tourmaline, magnetite, epidote and titanite. Inclusion phases within cordierite poikiloblasts include *Ms*, *Bt*, *Qtz* and *Chl*, with primary chlorite inclusions being restricted to adjacent to the isograd. The upper limit of the first cordierite zone is marked by the formation of sillimanite at the expense of cordierite.

Four K(F)MASH reactions (2-5; Spear and Cheney 1989) that bracket the range of *P-T* conditions for the cordierite zone are listed below in order of increasing temperature and illustrated on Fig. I2a. Where Mg end-member reactions are presented, the Fe contents in natural samples will cause the reactions to take place at slightly lower temperatures and hence estimates are maxima. However the lack of garnet, staurolite and a regional andalusite isograd are suggestive of Mg-rich compositions in these

metaturbidites and so these reactions should provide reasonable P - T constraints for the first cordierite zone. A vapor phase is considered to have been present in all assemblages (i.e. $a_{\text{H}_2\text{O}} \approx 1$).



Evidence for reactions (3) and (4) was commonly observed (Figs. I1b, I1c).

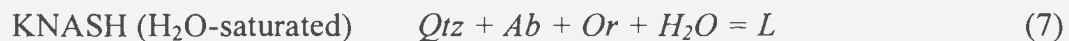
Reaction (2) represents the lower temperature limiting reaction for the first cordierite zone and is restricted to aluminous horizons. The absence of biotite breakdown textures associated with cordierite growth implies reaction (5) did not occur, which constrains the maximum temperature conditions in the first cordierite zone. When plotted on a petrogenetic grid with the Al silicate stability fields and muscovite breakdown reaction (Holdaway 1971; Kerrick 1972), reactions (3) and (4) suggest that temperatures across the cordierite zone ranged from 500-570 °C (Fig. I2a), and a maximum pressure of ca. 3.2 kbar is established from the intersection of reaction (2) with the *And-Sil* reaction boundary. This P - T range is consistent with determinations for the cordierite isograd elsewhere in the Slave Province (e.g., 550 °C and 3 kbar; Ramsay 1974; Pehrsson 1998).

Sillimanite - melt zone

The sillimanite zone, which succeeds the first cordierite zone, varies from ca. 0.5-2 km in width in the transect area. The onset of the zone is marked by replacement of 0.5-30 mm cordierite porphyroblasts by sillimanite in the form of faeserkasil knots. This is

abruptly followed (typically within 100 m) by thin, discontinuous melt stringers parallel to the main mica fabric. Termination of the sillimanite–melt zone is marked by the appearance of a second generation of cordierite and the breakdown of muscovite. Outcrop-scale granitoid intrusions are pervasive throughout the zone. The peak mineral assemblage of the sillimanite zone is *Sil-Ms-Bt-Qtz-L±Crd*, with minor tourmaline, magnetite, epidote, monazite, zircon and titanite. Biotite is more abundant than primary muscovite, which occurs as fine-grained flakes between quartz and feldspar grains. The former cordierite 1 porphyroblasts are composed of heterogeneous assemblages of muscovite, biotite, sillimanite, and retrograde fine white mica. Melt stringers are granodioritic in composition consisting of *Qtz-Pl-Kfs±Bt*. The persistence of muscovite throughout the zone, despite the presence of melt, suggests H₂O-saturated melting.

Field and petrographic evidence indicate 3 main reactions (6) – (8) occurred in the sillimanite–melt zone (Figs. I1d, e and I2a). In order of increasing temperature they are:



Reactions are presented on the grid at their ideal end-member locations, so the reactions in natural samples would occur at slightly lower temperatures. The *P-T* range for cordierite breakdown is constrained using the recent KFMASH grid of Pattison et al. (2002). For cordierite compositions with $X_{MgO} \geq 0.5$, the formation of sillimanite occurs between 550–650 °C and 2.5–4.5 kbar (Fig. I2a). Based on the proximity of the faeserkasil knots to the first cordierite zone, the lower *P-T* range for this part of the sillimanite zone

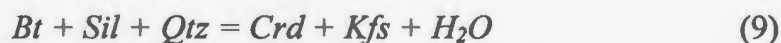
is inferred to be similar, i.e., ca. 550 °C / 3 kbar. The rarity of alkali feldspar implies that the operation of reaction (8) was minimal. Peak metamorphic conditions for the sillimanite zone are established from localities where the coexistence of reactions (6) to (8) occurs. Intersection of the H₂O-saturated pelite solidus with the muscovite + cordierite breakdown curve indicates peak of 650-670 °C and 3.5-4 kbar (Kerrick 1972; Spear 1993; Pattison et al. 2002).

Second cordierite zone

The appearance of a second cordierite zone characterized by the subassemblage *Crd-L* upgrade and structurally below the sillimanite zone defines the onset of uppermost amphibolite-facies conditions in the Snare River terrane. The second cordierite zone is a broad transition with abundant mesoscopic granitic intrusions that is superseded upgrade by the appearance of garnet in shallow-dipping domal structures. Second generation cordierite is distinguished from the zoned poikiloblasts of the first cordierite zone by its dark blue to purple colour (iolite) and the comparative lack of inclusions. Large-scale melting is ubiquitous in the second cordierite zone and a complete transition can be observed from migmatite through metatexite to diatexite. Large cordierite and alkali feldspar grains from 5-10 cm in diameter are common in the diatexite. Biotite and cordierite increase in abundance across the zone, but a corresponding increase in alkali feldspar content does not occur. The peak assemblage for this zone is *Crd-Bt-Qtz-Pl-L±Kfs±Sil*, with minor phases including abundant zircon and monazite and subordinate tourmaline, magnetite and ilmenite. Peraluminous leucosomes, consisting of ≥ 90 %

sillimanite, are a distinctive feature of the zone (Fig. I1j). Retrograde muscovite intimately associated with biotite is a ubiquitous alteration product of cordierite (Fig. I1g).

The diversity of mineral assemblages and melt phases across the second cordierite zone implies a complex array of reactions took place that is best understood by examination of fluid-present KFMASH subsolidus and melting reactions (Vielzeuf and Holloway 1988; Wei et al. 2004). The predominant reactions in order of increasing temperature are:



These KFMASH reactions define a broad field in P - T space in which peak assemblages of the second cordierite zone are stable (Fig. I2b). Minimum P - T conditions are constrained by peak conditions established in the structurally overlying sillimanite zone (650 °C; 3.5-4 kbar). Maximum pressures are constrained by the lowest pressure limits determined for the structurally underlying Ghost subdomain (5.9 kbar; Chacko et al. 1996) and maximum temperatures are limited by the onset of garnet-producing reactions that define the garnet-Kfeldspar isograd (ca. 740-750 °C) described below. Hence the maximum conditions across the second cordierite zone range from 650-770 °C and 4-5.9 kbar. The lack of abundant alkali feldspar across the zone suggests that (9) was not a significant cordierite-forming reaction. Reactions (9), (11) and (12) were observed at one

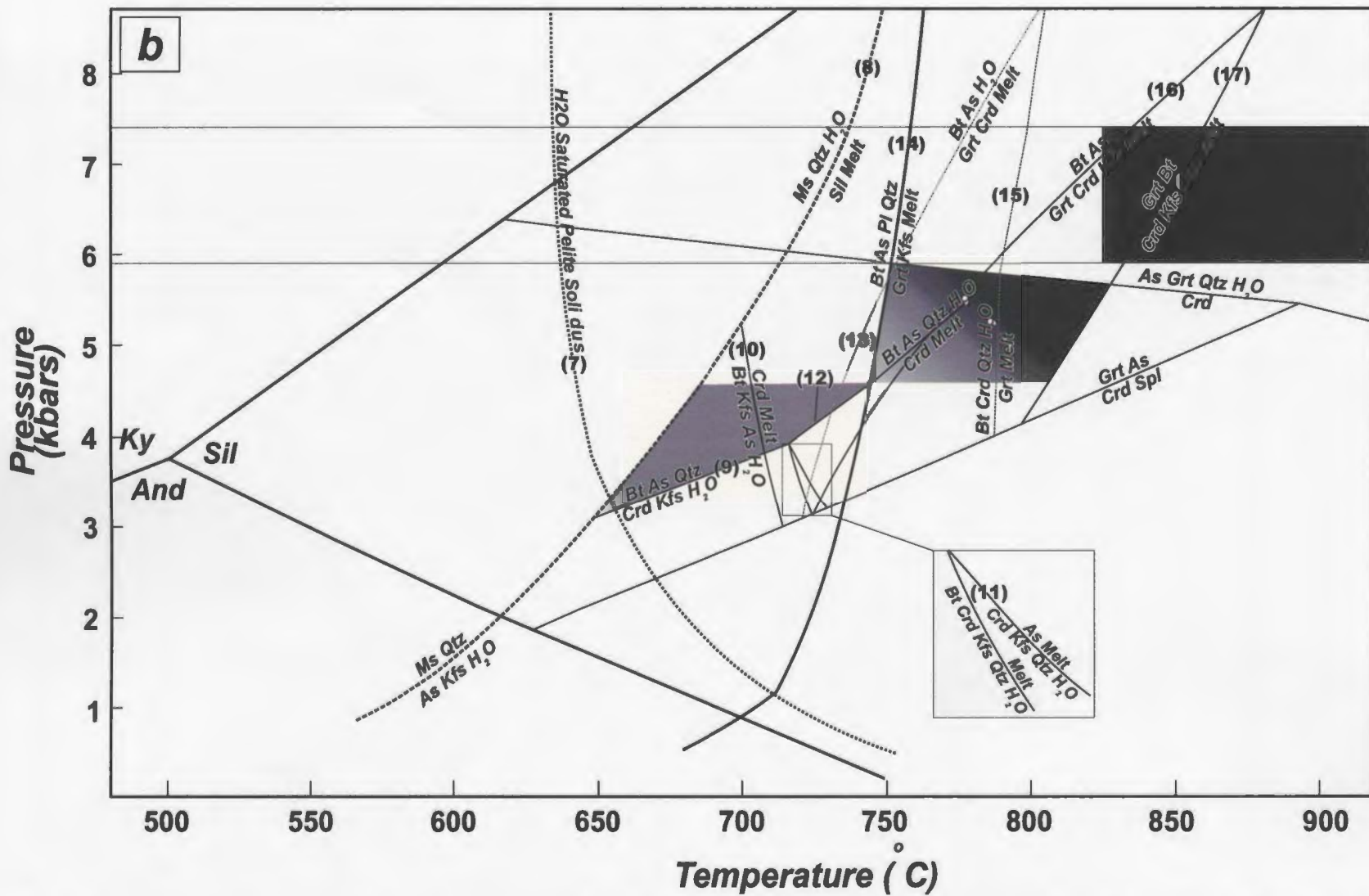


Figure 12 continued: Petrogenetic grids defining maximum P-T conditions for each metamorphic zone across the Snare River terrane. All grids use the aluminosilicate curves of Holdaway (1971). **(b)** Constraints for *second cordierite + melt* and *garnet + K feldspar* zones. *Crd (2) + melt* zone reactions from H₂O-present KFMASH grids of Vielzeuf & Holloway (1988) and Wei et al. 2004. H₂O is considered important in this metamorphic zone. H₂O-absent, KFMASH reactions of Wei et al. (2004) constrain *Grt + Kfs + Crd* and *Opx + Crd + Kfs* assemblages across Ghost subdomain. Thermobarometric estimates of Farquhar and Chacko (1996) determined across the northern Ghost subdomain are plotted. Reaction curves numbered 9 - 17 (see text for details).

site in the middle of the zone (vb1696). The intersection of these three reaction lines in P - T space constrains conditions to ca. 730 °C and 4 kbar, suggesting a nearly isobaric increase in temperature and high $a_{\text{H}_2\text{O}}$ characterized the second cordierite zone.

Garnet–K feldspar zone and orthopyroxene localities

The appearance of the subassemblage garnet-alkali feldspar in metapelitic rocks on a regional scale in the Snare River terrane marks the onset of granulite-facies conditions. In the transect area, the transition is abrupt and the isograd is parallel to the boundaries of major plutons (Fig. 6.1). The onset of the garnet-K feldspar zone also delimits the uppermost structural levels the Ghost sub-domain, below which orthopyroxene-bearing assemblages occur (e.g., Chacko et al. 1996). No regional orthopyroxene isograd has been mapped. P - T estimates for garnet- and orthopyroxene-bearing assemblages are described separately. As in the second cordierite zone, melting is widespread. However a notable contrast between the two zones is the greater abundance of alkali feldspar in melts of granitic composition. The stable peak mineral assemblage at the garnet isograd is $Grt-Bt-Pl-Qtz-Kfs-L\pm Sil$. Cordierite intergrown with spinel is associated with the breakdown of garnet and is inferred to have formed during a subsequent decompression event (Fig. I1o). Minor phases included abundant monazite and zircon, and unidentified opaque phases. Leucosome mineralogy consists of $Grt-Qtz-Pl-Kfs\pm Bt$ (Fig. I1n). Inclusion phases, which are concentrated in the garnet cores, include Qtz, Bt, Sil and Pl (Fig. I1m). Approximately 1 km upgrate from the isograd, garnet, cordierite and melt coexist (Fig. I1p) in the assemblage $Grt-Crd-Kfs-Bt-Sil-Qtz-Pl-L$. A prominent textural feature that distinguishes this zone from the second cordierite

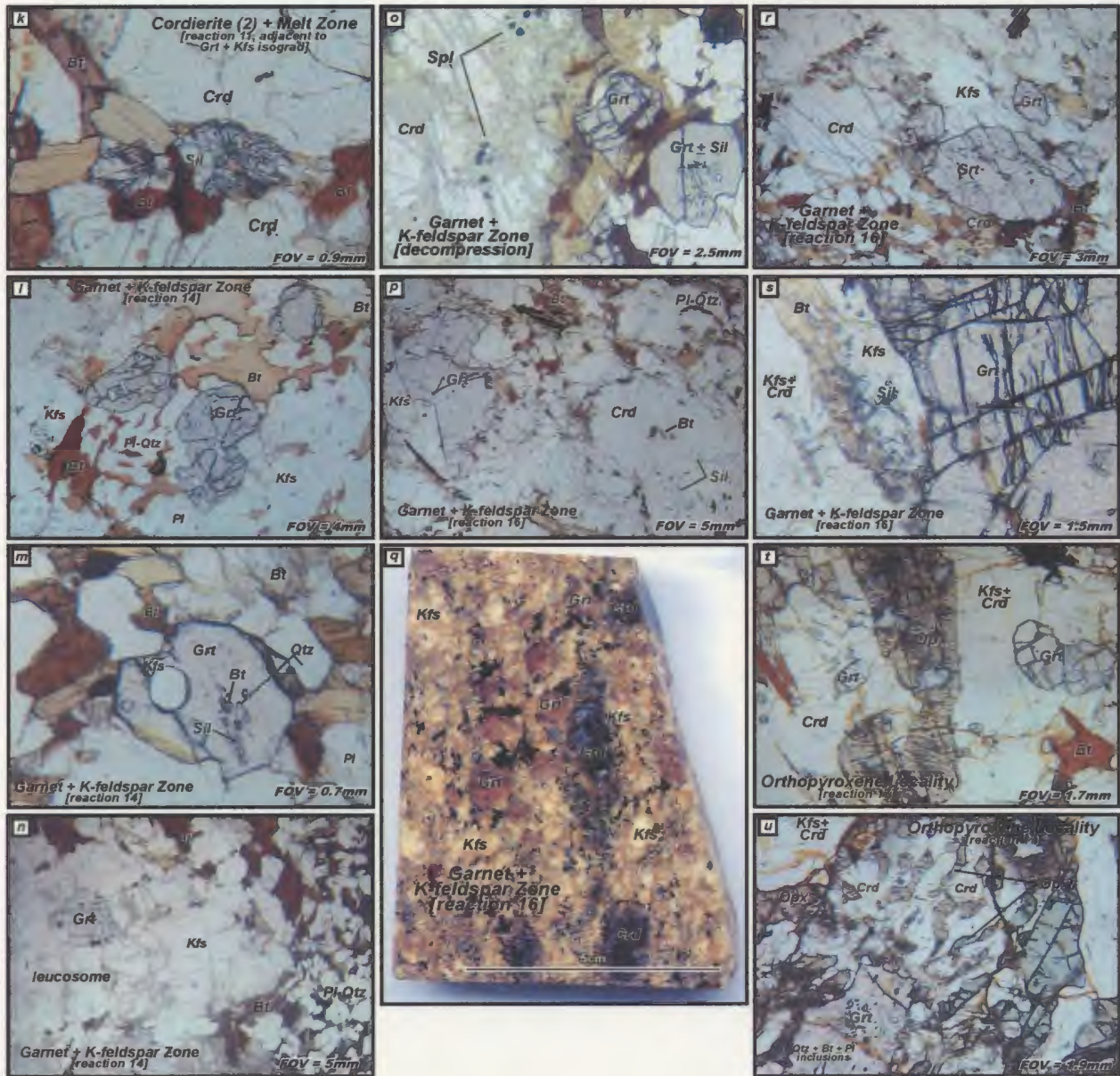
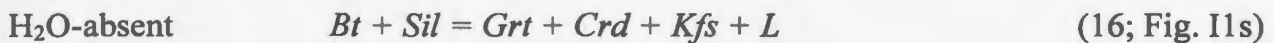
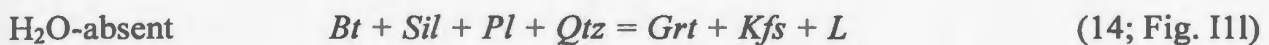


Figure 11 continued: (k) Reaction of $Bt + Sil$ to form cordierite adjacent to $Grt + Kfs$ isograd. (l) $Grt + Kfs$ formation due to biotite breakdown at $Grt + Kfs$ isograd. (m) $Sil + Bt + Qtz$ inclusions in garnet, Garnet + K-feldspar zone. (n) Leucosome-forming reaction associated with garnet growth adjacent to $Grt + Kfs$ isograd. (o) $Crd + Spl$ formed from garnet breakdown during decompression, Garnet + K-feldspar zone. (p) $Grt + Crd + Kfs$ assemblage occurring approximately 1km from $Grt + Kfs$ isograd. $Bt + Sil$ inclusion occur within large cordierite grain. (q) Polished slab of $Grt + Crd + Kfs$ bearing diatexite, Ghost subdomain. (r) Stable coexistence of $Grt + Crd + Kfs$, the most pervasive reaction across the Ghost subdomain. (s) $Bt + Sil$ consumption to form $Grt + Kfs + Crd$, Ghost subdomain. (t) and (u) Garnet breakdown to form $Opx + Crd + Kfs$.

zone is the breakdown of biotite associated with the formation of garnet and alkali feldspar (Fig. I1l).

Five possible KFMASH reactions (Vielzeuf and Holloway 1988; Wei et al. 2004) could account for the appearance of garnet in vapour-present and vapour-absent conditions. In order of increasing temperature, they are:



The appearance of alkali feldspar and absence of prograde cordierite in garnet-bearing assemblages on and adjacent to the garnet–K feldspar isograd suggests the reactions involving H₂O were not involved in garnet formation. This is consistent with textural observations indicative of biotite breakdown by dehydration melting and implies reaction (14) was the predominant isograd reaction. Minimum *P-T* is constrained by peak conditions estimated for the overlying second cordierite zone (730 °C / 4 kbar). The *P-T* conditions prevailing at the isograd can be determined by the intersection of reaction (11), which took place on the low temperature side of the isograd, with reaction (14) on the high-temperature side (Fig. I1k), yielding a temperature and pressure of ca. 740 °C and 4.7 kbar. The occurrence of *Grt-Crd-Kfs-L* assemblages implies the operation the higher temperature, vapour-absent reaction (16; Fig. I1p,r). Maximum pressures are constrained by the lowest pressure estimate for the underlying Ghost subdomain (5.9

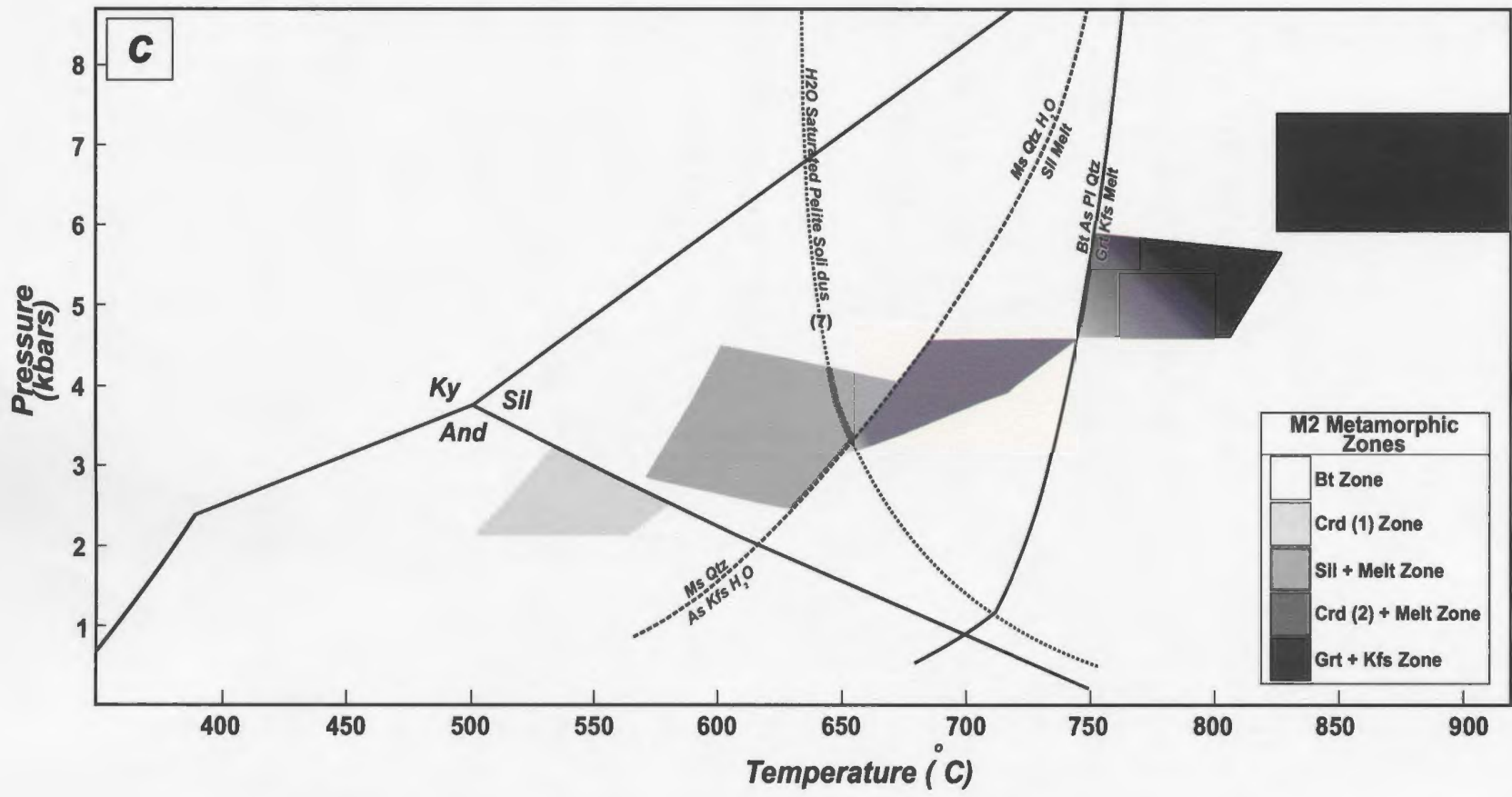


Figure I2 continued: (c) Diagram illustrating metamorphic field gradient across the Snare River terrane in P-T space.

kbar; Chacko et al. 1996) and maximum temperatures are delimited by the garnet-consuming reaction



which marks the first appearance of orthopyroxene and takes place at ca. 800-830 °C. These constraints bracket the *P-T* range for the garnet-Kfeldspar zone overlying the Ghost subdomain to 4.7-5.9 kbar and 740-830 °C (Fig. I2b).

Orthopyroxene-bearing pelites from northern Ghost subdomain (Fig. 6.1) were used by Chacko et al. (1995) and Farquhar and Chacko (1996) to determine peak *P-T* conditions. They described *Grt-Opx* and *Grt-Opx-Crd* assemblages from several sites and applied the aluminum-in-*Opx* thermometer and *Grt-Pl-Opx-Qtz* barometer (Fitzsimmons and Harley 1994; Pattison and Begin 1994), which yielded temperatures and pressures of 845-920 °C and 5.9-7.4 kbar respectively. Other localities in the centre of Ghost subdomain were observed in this study to consist of the peak assemblage *Grt-Crd-Opx-Pl-Qtz-Kfs* (Figs. I1q, t, u). Textural features involving the breakdown of garnet to form cordierite and orthopyroxene suggest the operation of reaction (17), indicating temperatures in excess of 800 °C prevailed at these localities (Fig. I2b).

Appendix I - References

- Carmichael, D.G. 1978. Metamorphic bathozones and bathograds: A measure of the depth post-metamorphic uplift and erosion and the regional scale. *American Journal of Science*, **278**: 769 – 797.
- Chacko, T., Creaser, R.A., Farquhar, J. and Muehlenbachs, K., 1995. The deep crust of the western Slave Province – Initial petrological and isotopic data from high grade rocks of the Ghost Domain. *In*: Slave – Northern Cordillera Lithospheric Evolution Workshop

- (SNORCLE) Transect and Cordilleran Tectonics Workshop Meeting, 8 – 9 April, Calgary. *Compiled by* F. Cook and P. Erdmer. Lithoprobe Report 44, pp.4-7.
- Farquhar, J., and Chacko, T. 1996. Thermobarometry of high-temperature granites and granulites of the western Slave Province, District of Mackenzie, NWT, Canada. In 1996 spring Meeting, EOS, American Geophysical Union, V. 77, no. 17, supplement, p 283 – 284.
- Fitzsimmons, I.C.W., and Harley, S.L. 1994. The influence of retrograde cation exchange on granulite P-T estimates and a convergence technique for the recovery of peak metamorphic conditions. *Journal of Petrology*, **35**: 543 – 576.
- Henderson, J.B. 2004. Geology of the Wijinnedi Lake area, District of Mackenzie, Northwest Territories. Geological Survey of Canada, Bulletin 576, 115p.
- Holdaway, M.J. 1971. Stability of andalusite and the aluminum silicate phase diagram. *American Journal of Science*, **271**: 97 – 131.
- Jackson, V.A., 2003. Preliminary compilation of the geology of the Snare River (1998-2002 results), Winjinnedi Lake, Labrish Lake and Russell Lake area; parts of 85N and 85O. C.S. Lord Northern Geoscience Centre, Yellowknife, NT. NWT Open Report 2003-002. Map, scale 1:100 000.
- Kerrick, D.M. 1972. Experimental determination of muscovite + quartz stability with $\text{PH}_2\text{O} < \text{Ptotal}$. *American Journal of Science*, **272**: 946 – 948.
- Kretz, R. 1983. Symbols for rock-forming minerals. *American Mineralogist* **68**: 277 – 279.
- Pattison, D.R.M., and Bégin, N.J. 1994. Zoning patterns in orthopyroxene and garnet in granulites: implications for geothermometry. *Journal of Metamorphic Geology*, **12**: 387 - 410.
- Pattison, D.R.M., Spear, F.S., Debuhr, C.L., Cheney, J.T., and Guidotti, C.V. 2002. Thermodynamic modelling of the reaction muscovite + cordierite $\rightarrow \text{Al}_2\text{SiO}_5$ + biotite + quartz + H_2O : constraints from natural assemblages and implications for the metapelitic petrogenetic grid. *Journal of Metamorphic Geology*, **20**: 99 – 118.
- Pehrsson, S.J., 1998. Deposition, deformation and preservation of the Indin Lake supracrustal belt, Slave Province, Northwest Territories. Unpublished Ph.D. thesis, Queens University, Kingston, Ontario.
- Ramsay, C.R. 1974. The cordierite isograd in Archean metasediments near Yellowknife, N.W.T., Canada – variations on an experimentally established reaction. *Contributions to Mineralogy and Petrology*, **47**: 27 – 40.
- Spear, F.S. 1993. *Metamorphic Phase Equilibria and Pressure – Temperature – Time paths*. Mineralogical Society of America, Washington D.C. 799p.

- Spear, F.S., and Cheney, J.T. 1989. A petrogenetic grid for pelitic schists in the system $\text{SiO}_2 - \text{Al}_2\text{O}_3 - \text{FeO} - \text{MgO} - \text{K}_2\text{O} - \text{H}_2\text{O}$. *Contributions to Mineralogy and Petrology*, **101**: 149 – 164.
- Vielzeuf, D., and Holloway, J.R. 1988. Experimental determination of the fluid-absent melting relations in the pelitic system. Consequences for crustal differentiation. *Contributions to Mineralogy and Petrology*, **98**: 257 – 276.
- Wei, C.J., Powell, R., and Clarke, G.L. 2004. Calculated phase equilibria for low- and medium-pressure metapelites in the KFMASH and KMnFMASH systems. *Journal of Metamorphic Geology*, **22**: 495 – 508.

APPENDIX J

Zircon Saturation Thermometry: Methodology and Sample Descriptions

Introduction

Zircon saturation temperatures (T_{Zir}) were calculated by rearranging the solubility model of Watson and Harrison (1983) into the formula:

$$T_{Zir} = 12900 / (2.95 + 0.85M + (\ln C_{Zr}^{melt} / C_{Zr}^{zircon})),$$

where C_{Zr}^{melt} = concentration of Zr in the melt determined from whole rock analysis, C_{Zr}^{zircon} = stoichiometric concentration of Zr in zircon (assumed to be constant in nature; ~ 497 646 ppm), T = temperature (K) and M = cation ratio (Na + K + 2Ca) / (Al*Si) (molar form). M values were calculated using the molar proportions of the major elements measured by XRF whole-rock analysis and Zr concentrations were measured by whole-rock solution ICP-MS analysis. Details regarding the analytical techniques used are outlined in Bennett et al. (submitted). The analytical uncertainties in measuring these parameters are a significant source of error affecting the zircon saturation thermometer. In some instances as much as a 50% error in Zr abundance can occur, which propagates to a temperature uncertainty of ± 35 °C (Hanchar and Watson 2003). In addition, error in calculation of the M value over the range of 1.3 to 1.9 translates to an uncertainty of ± 25 °C. However, Miller et al. (2003) noted that despite these potentially significant analytically-induced uncertainties in the Zr and M values, the resultant uncertainty in

calculated temperature is relatively small. For T_{Zir} values calculated in this study, an error of ± 30 °C has been assigned (B. Watson pers. comm.).

Sample Descriptions

Metaluminous Magmas

Group 1 magmatic rocks, consisting of tonalite-trondhjemite-granodiorite (TTG) and volcanic equivalents, are subdivided into older (ca. 2674 Ma) and younger suites (ca. 2654 Ma; Table 6.2). M values range from 1.35 to 1.62 and Zr concentrations from 84 to 220 ppm (Fig. 6.6; Table 6.3). Resultant T_{Zir} estimates vary from 728-797 °C, with averages of 786 °C for the older suite and 752 °C for the younger, more differentiated suite (Table 6.3; Fig 6.7a). The M value of VB165 (2.18) occurs outside the calibration range of the thermometer and hence the T_{Zir} (uncorrected) value of 713 °C is invalid. Inherited zircon is absent in this sample implying a Zr-undersaturated melt (Fig. 6.5).

Minor inheritance was identified in the older, ca. 2674 Ma volcanic suite (Villeneuve and Henderson 1998), so the temperature estimate ($T_{Zir} = 797$ °C) is considered to approximate the time of zircon crystallization, albeit a maximum value, for the Group 1 magmas.

Petrographic observations for a younger suite sample (VB1692) reveal inherited cores with magmatic overgrowths on zircon located at grain boundaries, indicative of early zircon saturation, but late zircon crystallization (Fig. 6.5a). Zircon separates were unavailable for this sample, but several large zircons ($n = 11$) with well defined epitaxial relationships in thin section were used to estimate the areal proportion of inherited cores. The resultant corrected T_{Zir} value for the sample is 740 °C, 46 °C less than the maximum

uncorrected value (Table 6.5; Fig. 6.9), a result that is similar to T_{Zir} estimates for volcanic samples in the older suite (Table 6.3). Collectively, the data indicate that the TTG suite was characterized by Zr-undersaturated to weakly saturated magmas and calculated T_{Zir} values are interpreted as eruption and emplacement temperatures of the volcanic and plutonic rocks, respectively. Low inherited Zr concentrations (i.e. < 20 %), such as observed in this suite, do not appreciably alter T_{Zir} estimates (Miller et al. 2003), so the average uncorrected value (786 °C) for Group 1 is considered to represent a reasonable estimate of the temperature of zircon crystallization (Fig. 6.9; Table 6.5). The corrected T_{Zir} value for VB1692 (740 °C), in addition to providing evidence for grain boundary growth of magmatic zircon, is considered a reliable temperature estimate for the emplacement temperature of the younger differentiated suite.

Group 2 magmas comprise the ca. 2637 Ma granitic to granodioritic Disco Intrusive Suite and the quartz dioritic to monzogabbroic Mafic Intrusive Complexes. M values for the Disco Intrusive Suite (1.34-1.80; Table 6.2, Fig. 6.6) fall within the calibration range. Zr abundances range from 93 to 268 ppm and individual maximum T_{Zir} estimates range from 726-837 °C, with an average maximum T_{Zir} value of 784 °C (Fig. 6.7a). M values (1.91-2.20) for the Mafic Intrusive Complex magmas lie outside the calibration range and hence temperature estimates calculated are not experimentally constrained and are considered invalid. Analysis of 47 zircon BSE images from sample VB1363 (Disco Intrusive Suite) indicates that ~ 60 % of Zr is premagmatic (Fig. 6.8). Removing this amount from the Zr budget translates to a corrected T_{Zir} value of 756 °C, an 81 °C temperature difference between maximum and corrected values (Table 6.5; Fig.

6.9). In combination with textural evidence (Fig. 6.5), the corrected T_{Zir} value of 756 °C is considered to represent the magma emplacement temperature, an interpretation that is tentatively extended to the Disco Intrusive Suite as a whole.

Group 3 metaluminous magmas, emplaced at the ~2600 Ma orogenic peak, consist of 3 suites, an upper-crustal biotite granite suite, a mid- to upper-crustal biotite granodiorite suite, and a mid-crustal orthopyroxene granite suite. M values for all three suites (1.32 to 1.70; Fig. 6.6) are within the calibration range and Zr abundances range from 75 to 484 ppm. Calculated individual maximum T_{Zir} values for the *biotite granite suite* range from 769-780 °C (average 776 °C). Analysis of 25 inherited zircons from sample VB1357 indicates ~ 74 % of Zr is inherited (Fig. 6.7), and removal of this proportion from the Zr budget corresponds to a corrected T_{Zir} value of 677 °C (a reduction of 103 °C), which is considered the best estimate of emplacement temperature (Table 6.5; Fig. 6.9). Calculated individual maximum T_{Zir} values for the *biotite granodiorite suite* range from 790-833 °C (average 811 °C). No inherited zircon analysis was undertaken for this suite and hence these values are considered maxima.

Calculated uncorrected individual maximum T_{Zir} values for two samples of the *orthopyroxene granite suite* vary widely from 728 to 894 °C (Table 6.5). Analyses of 31 inherited grains in VB1841 indicate ~ 23% inherited zircon, which after removal from the total Zr budget corresponds to a corrected T_{Zir} value of 708 °C (Table 6.5; Fig. 6.9). In contrast, HBA-0505-93 yields uncorrected and corrected temperatures of 894 and 867 °C, respectively (assuming the same proportion of inherited zircon – 23%, as in VB1841). Assuming the inheritance correction is approximately correct, two processes may account for the wide range of estimated temperature for the orthopyroxene granite suite. Firstly,

the samples exhibit important trace-element anomalies, with the most fractionated member, VB1841, exhibiting strong enrichments in Sr, Eu and Zr, indicative of feldspar accumulation and early removal of Zr from the source region, whereas the least fractionated member, HBA-0505-93, displays strong Sr depletion and weak Eu enrichment (Table 6.2). Consequently the disparity could be explained by melt fractionation processes, with the least fractionated sample having the highest temperature. Alternatively, it could be argued from the presence of dehydration reaction rims on mafic enclaves (Fig. 6.2) and from the interpretation that orthopyroxene granites commonly host CO₂-rich fluids at some stage of their petrogenesis (e.g., Newton 1992; Frost et al. 2000) that anhydrous conditions prevailed in this suite and therefore the criterion requiring a hydrous magma (>2 wt.% H₂O) cannot be unequivocally demonstrated. In addition, the M values determined for this suite may not be primary magmatic values as there is widespread evidence for post-magmatic metamorphism involving biotite dehydration melting by the reaction $Bt + Pl + Qtz = Opx + Kfs + L$ (Fig. 6.2) and subsequent rehydration of orthopyroxene to biotite. In this case, the measured alkalinity ratio in the protolith will likely differ from the original magmatic M value. Additionally, temperature estimates for orthopyroxene granites from other high-grade regions range from 845 to ≥ 1045 °C (e.g., Kilpatrick and Ellis 1992; Bédard 2003), so the corrected T_{Zir} estimates are considered to be minimum values at best. In their geochemical analysis of this suite, Bennett et al. (submitted) suggested that sample HBA-0505-93 had undergone the least post-magmatic disturbance and therefore we use the individual maximum temperature calculated for this sample ($T_{Zir} = 894$ °C; Table 6.3, Fig 6.7b) as the best (uncorrected) estimate for the suite. Petrographic observations of several samples

of the suite suggest early crystallization of orthopyroxene, as indicated by its grain shape and lack of zircon inclusions, followed by late-stage precipitation of remaining magmatic phases, including zircon (Fig. 6.5). Hence, the T_{Zir} estimate is interpreted as the emplacement temperature for the suite.

Group 4 metaluminous magmas include *sanukitoid-affinity tonalite – diorite* that post-dated the orogenic peak by ca. 10 Ma (Table 6.1). A single sample was analyzed but yielded an M value outside the calibration range ($M = 2.19$; Fig. 6.5), so reliable crystallization temperatures could not be established.

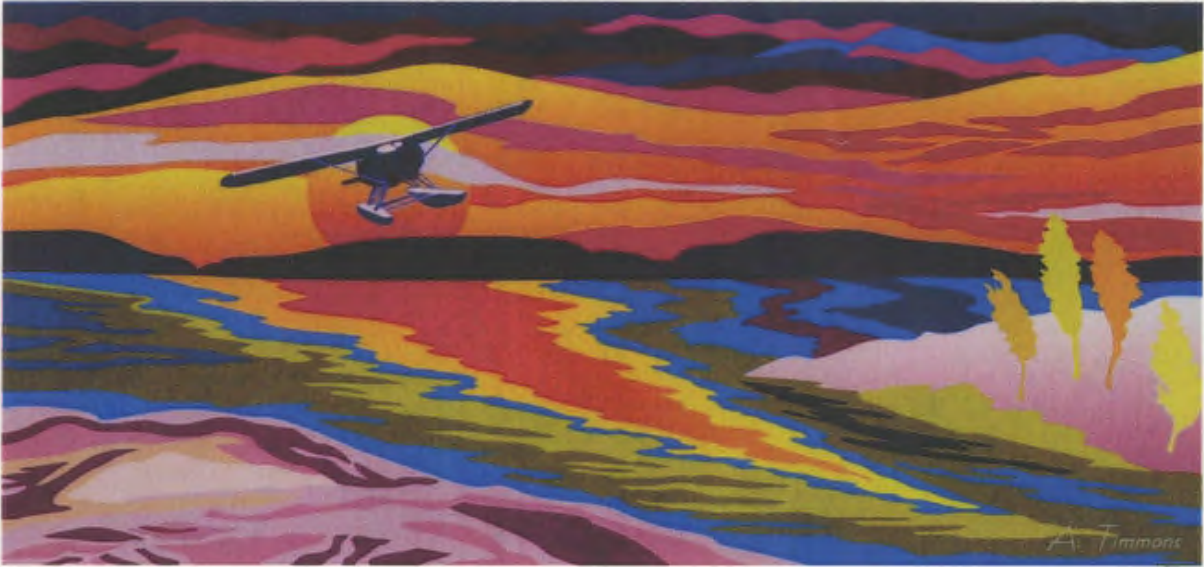
Peraluminous Magmas

Group 3 peraluminous magmas were emplaced during the ~2600 Ma orogenic peak and consist of an upper-crustal two-mica granite / diatexite suite and a mid- to upper-crustal megacrystic granite suite. M values fall within the calibration range of the zircon saturation thermometer (0.70 to 1.52; Fig. 6.6, Table 6.4) and Zr abundances range from 71 to 392 ppm. For the *two-mica granite / diatexite*, calculated individual maximum T_{Zir} values range from 754-841 °C (average 792 °C). BSE imaging of 36 and 23 zircon grains from samples VB1358 and VB160, respectively, indicates ca. 65% and 56% Zr inheritance (Fig. 6.8). After removal, the corrected T_{Zir} values were 675 °C and 767 °C, decreases of 79 and 74 °C respectively (Table 6.5; Fig. 6.9). Abundant inheritance in both samples indicates strongly Zr-saturated magmas, geochemistry indicates limited melt segregation, and textural observations confirm zircon as a late-stage precipitate (Table 6.2, Fig. 6.5). The corrected T_{Zir} values are considered good estimates of emplacement temperatures.

Calculated individual maximum T_{Zir} values for the *megacrystic granite suite* range from 728-873 °C (average 822 °C; Table 6.4; Fig. 6.7). Zircon image analysis of 36 grains in PVB9 indicates ~ 51 % inherited Zr, which after removal corresponds to a corrected T_{Zir} value of 794 °C, a ca. 66 °C temperature decrease (Fig. 6.8, Table 6.5). The corrected T_{Zir} value is considered a maximum estimate of the emplacement temperature at this crustal level (Fig. 6.9). Image analysis of 31 zircon grains in VB1688 indicates ca. 32 % inherited Zr, which equates to a corrected T_{Zir} value of 699 °C, a 29 °C difference (Fig. 6.8, Table 6.5). However, the sample exhibits evidence for significant post-magmatic metamorphism, with formation of orthopyroxene and pervasive biotite breakdown (Fig. 6.5). VB1688 has an anomalously low Zr abundance with respect to the other samples in the suite, which have correspondingly higher zircon saturation temperatures (Table 6.3). As discussed above, biotite dehydration melting will yield a melt fraction that upon removal from the protolith will alter the original magmatic alkali content (M value), so the calculated temperature must be considered a minimum. Additionally, the proportion of zircon inheritance at the time of magma emplacement may have been greater than 32 %, as zircon has undergone extensive recrystallization in this sample (Fig. 6.4), rendering discrimination between inherited and precipitate (magmatic) zircon difficult or impossible. If the three remaining mid-crustal samples in the suite (VB1848, J-0387 and FL96), are averaged and corrected for ~ 51% inheritance, a T_{Zir} estimate of 779 °C is determined (Table 6.5; Fig. 6.9). Petrographic evidence from samples VB1848 and FL96 support greater abundances of inherited zircon and importantly, all samples exhibit predominant grain-boundary growth of zircon indicating late-stage crystallization (Fig. 6.5). The corrected *average mid-crustal* T_{Zir} , which

overlaps within error with upper-crustal sample PVB9 (794 °C), is consistent with magma geochemistry for the suite, which indicates that minimal fractionation or melt segregation occurred between the various samples analyzed (Bennett et al. submitted). Hence, the corrected average T_{Zir} estimate (779 °C) is considered a good approximation of zircon crystallization temperatures of the megacrystic granite suite during its emplacement into mid-crust.

Group 4 peraluminous magmas were emplaced at ~2585 Ma and coincide with the M3 decompressional event. Two suites intruded during this interval, a cordierite leucogranite suite and a pegmatitic granite suite. M values for both suites are within the calibration range for the thermometer (1.05 to 1.32; Table 6.4) and Zr abundances range from 8 to 52 ppm. The individual maximum T_{Zir} value for the *cordierite leucogranite suite* is 716 °C (Table 6.4). Analysis of inherited zircon from sample VB161 indicates ~56 % of Zr is inherited, which corresponds to a corrected T_{Zir} value of 657 °C, a 59 °C decrease, which together with evidence for grain-boundary zircon growth is considered to represent the crystallization temperature for this suite (Figs. 6.5, 6.8; Table 6.5). Calculated individual maximum T_{Zir} values for the *pegmatitic granite suite* range from 590 to 686 °C (average 650 °C). Zr concentrations are low in this suite and the calculated T_{Zir} value does not change significantly after removal of the inherited Zr component. The average T_{Zir} value for the suite (650 °C) is considered a good estimate of the emplacement temperature for the suite (Table 6.3).



THE END

2583 88

